AD-A247 043

# PROCEEDINGS OF

# Technology Showcase

7-9 AUGUST 1990

Sponsored By

THE RESEARCH, DEVELOPMENT, AND
ENGINEERING CENTER

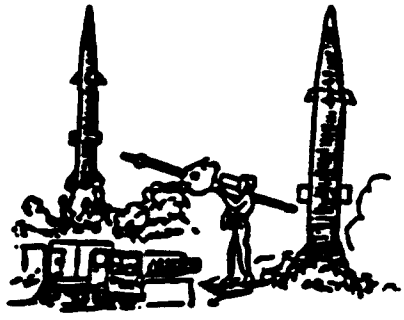

U.S. ARMY MISSILE COMMAND
Redstone Arsenal, Alabama 35898-5000

CLEARED FOR PUBLIC RELEASE; DISTRIBUTION IS UNLIMITED

91-17276

SMI FORM 1021, 1 AUG 85 PREVIOUS EDITION IS OBSOLETE

## DESTRUCTION NOTICE

FOR CLASSIFIED DOCUMENTS, FOLLOW THE PROCEDURES IN DoD 5200.22-M, INDUSTRIAL SECURITY MANUAL, SECTION II-19 OR DoD 5200.1-R, INFORMATION SECURITY PROGRAM REGULATION, CHAPTER IX. FOR UNCLASSIFIED, LIMITED DOCUMENTS, DESTROY BY ANY METHOD THAT WILL PREVENT DISCLOSURE OF CONTENTS OR RECONSTRUCTION OF THE DOCUMENT.

## DISCLAIMER

THE FINDINGS IN THIS REPORT ARE NOT TO BE CONSTRUED AS AN OFFICIAL DEPARTMENT OF THE ARMY POSITION UNLESS SO DESIGNATED BY OTHER AUTHORIZED DOCUMENTS.

## TRADE NAMES

USE OF TRADE NAMES OR MANUFACTURERS IN THIS REPORT DOES NOT CONSTITUTE AN OFFICIAL ENDORSEMENT OR APPROVAL OF THE USE OF SUCH COMMERCIAL HARDWARE OR SOFTWARE.

U.S. ARMY MISSILE COMMAND
RESEARCH, DEVELOPMENT, AND ENGINEERINC CENTER

# TECHNOLOGY SHOWCASE

7-9 August 1990

Tom Bevil Center
Huntsville, Alabama

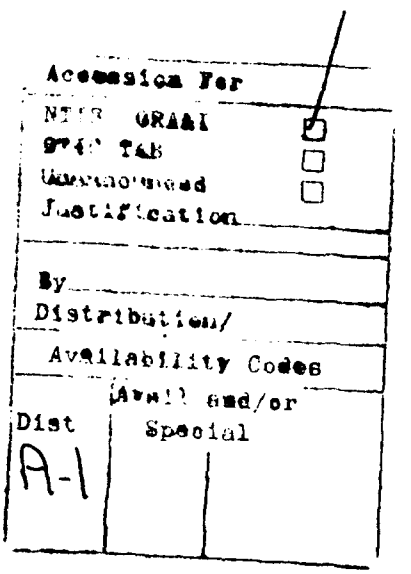

TABLE OF CONTENTS


Page

**SESSION I. RESEARCH**

Integrated Photonics for Signal Processing and Optical Computing..... 1

UV-IR and Focal Plane Array Material Evaluation Using Faraday Rotation..... 17

Hydrogen Fluoride Overtone Laser Technology..... 31

Mantest-Microcircuit Chip Thermal Screening System..... 43

Automated Hermetic Sealing of Microcircuit Packages Using Nd:YAG Laser Welding..... 51

**SESSION II: SENSORS**

Combined Arms Multipurpose Missile..... 63

Synthetic Discriminant Functions for Use in Pattern Recognition..... 79

Monopulse Angular Error Reduction for Complex Targets Using High Range Resolution..... 91

Infrared Seeker Developments for Indirect Fire Applications... 113

Laser Line of Sight Guidance..... 129

Measuring Radar Cross Section Using a CW Track-While-Scan Radar..... 141

**SESSION III: GUIDANCE AND CONTROL**

The Development and Application of Automatic Target Cueing Technology for Man-in-the-Loop Fire Control System..... 157

Lock-On-After-Launch (LOAL) Testbed Facility..... 169

Winding and Environmental Testing of Polarization-Maintaining Fibers..... 191

Control Systems Development..... 199

Page

Microprocessor Technology Utilization Program..... 219

Real Time Executive for Missile Systems (RTEMS)..... 245

**SESSION IV: STRUCTURES**

Aerothermal and Materials Testing Using Hypervelocity Sleds..... 269

Evolution of High Performance Small Rocket Motors..... 323

Clustered High Performance Rocket Motor Flight Demonstration.. 341

Development of Full Scale Hypersonic Kinetic Energy Missile/Penetrator Sled Testing Techniques..... 359

Metallurgical Failure Analyses of Maraging Steel Missile Motorcases..... 375

**SESSION V: SYSTEM SIMULATION AND AEROBALLISTICS**

Mission Augmented Airborne Platform Application of Artificial Intelligence to Air Defense Systems..... 393

Target and Scenario Signal Generation for Microwave and Millimeter Wave HWIL Missile Guidance Simulation..... 409

Dynamic Infrared Scene Projection Technology..... 437

SIMSTAR - Anatomy of a Modern Hybrid Computer..... 445

Simulation as a Tool in Assessing Millimeter-Wave Smart Weapon Systems..... 455

CFD in Tactical Missile Aero-Propulsion Technology..... 481

**SESSION VI. PROPULSION**

Safe Disposal of Rocket Motors..... 495

Insensitive Munitions Solid Propellant Development..... 505

Page

Composite Motor Case Technology..... 517

Rocket Motor Testing at the Propulsion Directorate..... 529

An Overview of the Army Rocket Motor Service Life Program..... 543

Bipropellant Gels..... 559

- SESSION I -

RESEARCH

# Integrated Photonics for Signal Processing and Optical Computing

Paul Ashley, Mark Bloemer, and Charles Bowden

Research Directorate, AMSMI-RD-RE-OP
Research, Development, and Engineering Center
U.S. Army Missile Command
Redstone Arsenal, AL 35898-5248

ABSTRACT: We present theoretical predictions and experimental results and comparisons for spheroidal microparticles of gold, silver, and platinum in linear host materiels, such as Schott glass. Specifically, experimental results are analyzed with respect to our theoretical model for a four-wave-mixing configuration and the frequency dependence of the conjugate signal is examined. We show, among other characteristics, that frequency and optical depth dependence of the conjugate intensity can be used to determine average shape parameters for the particle.

Conditions for intrinsic optical bistability and subpicosecond optical switching times are predicted for surface plasmon response of the particles embedded in the host and using effective medium theory to calculate the composite effective dielectric function, which is determined to be nonlinear.

We show that materials of this type can be useful for ultrafast optical switches and limiters for intense laser radiation, as well as being relatively cost effective. Limiting action can apply to device protection as well as biological, and composites can be easily fabricated using sol gels.

# 1. INTRODUCTION

Light scattering in inhomogeneous media has been an active research area with a broad range of problems[1]. Recent work on nonlinear effects has established conditions of resonant enhancement of these nonlinearities and sought to use them to increase the magnitude of physical effects, such as optical phase conjugation,[2,3] or to introduce new phenomena, such as intrinsic optical bistability.[4,5] Of course, this research has its roots in the studies of surface-enhanced Raman scattering[6], where, for example, the Raman cross section observed from molecular monolayers upon a silver substrate was enhanced by several orders of magnitude.

The enhancement of the Raman scattering cross section is due to the large increase of the local field, both inside and outside the metal particles near its surface, at the surface-plasmon resonance. Silver has a sharp resonance feature, but the resonance in gold and other metals can also lead to strong Raman scattering.

We predict that intrinsic optical bistability should be observed in silver particle composites. This optically bistable phenomenon is a local condition in the material and occurs without optical feedback, as from a cavity. The bistable behavior is due to the local field effect associated with the particles embedded in the dielectric host material. For spherical particles, the switching intensities are expected to be ~ 200 MW/cm$^2$; this magnitude is determined by the magnitude of the imaginary part of the metal's dielectric constant[5,7]. The design of experiments with ellipsoidal particles and a nonlinear host medium for the particles can lead to a significant reduction of the switching intensities. This is possible because the resonance frequency can now be chosen so as to minimize the imaginary part of the dielectric constant.

Degenerate four-wave mixing (DFWM) measurements in metal colloids reveal that a small silver or gold sphere has $\chi^{(3)} = 10^{-8} - 10^{-9}$ esu in the vicinity of the surface plasmon resonant with response times of the order of picoseconds.[2,3] It has been proposed that the $\chi^{(3)}$ for small metal particles results from an intrinsic $\chi_m^{(3)}$ of the plasmon excitation. The conjugate signal is proportional to the local field factor to the eighth power. The local field factor's dependence on shape has been illustrated many times in surface-enhanced Raman scattering experiments. In addition, it is possible to shift the resonant energy of the surface plasmon by varying the shape of the particle.[8] We found that it was important to make a more detailed examination of these enhancement effects. We present results from studies of the linear absorption as well as of the conjugate signal in DFWM experiments. Analysis of these experiments gives detailed information about the particle shapes.

Using results from the effective-medium theory[7], we evaluate the effects of absorption, both linear and nonlinear, and the particle shape on the DFWM conjugate signal.

## 2. RESULTS FROM THE EFFECTIVE-MEDIUM THEORY

In a composite dielectric material that has metal particles dispersed in it, the medium behaves on the average as a homogeneous medium with an effective dielectric tensor $\bar{\epsilon}$. To calculate the elements of this tensor, statistical theories have been developed that examine the effects of multiple scattering of the applied electromagnetic fields on linear media.[7,9-12] More recently, these theories have been extended to cover nonlinear systems.[7] We follow the results of Ref. 7, from which the effective dielectric tensor can be determined through the self-consistency condition

$$0 = \left\langle \left\{ 1 + \left[ \epsilon(x) - \bar{\epsilon} \right] \cdot \Gamma \right\}^{-1} \left[ \epsilon(\vec{x}) - \bar{\epsilon} \right] \right\rangle , \qquad (1)$$

where $1$ is the unit tensor, $\epsilon(\vec{x})$ is the inhomogeneous dielectric tensor of the medium, and $\Gamma$ is the depolarization tensor. The average in Eq. (1) contains uniform weighting of the particle positions, as is consistent with their random positions, and also an average over the weighted orientations of the particles.

The dielectric constant in the inhomogeneous medium is that of either the host dielectric matrix, $\epsilon_h(\vec{E}_L)$, or the metallic particles, $\epsilon_m(\vec{E}_L)$. Both may be nonlinear functions of the electric field, but the field is not identical for each environment. Outside the conducting particles, the field is the applied field plus the induced dipole field. Inside the particles, the local field drives the optical nonlinearities of that medium. For each material we assume a Kerr medium, which for degenerate field is written as

$$\epsilon_h = \epsilon_{hL} + \chi_h^{(3)} : \vec{E}_h(\omega)\, \vec{E}_h(\omega) \qquad (2a)$$

for the host medium and

$$\epsilon_m = \epsilon_{mL} + \chi_m^{(3)} : \vec{E}_m(\omega)\, \vec{E}_m(\omega) \qquad (2b)$$

for the embedded material. In general, the coefficients $\chi_\alpha^{(3)}$ are fourth-rank tensors.

The linear dielectric tensors are denoted by a subscript L . We will make the further assumption below that these tensors have degenerate principal values, i.e., they are isotropic media. This does not imply that the effective-medium dielectric functions are isotropic; for ellipsoidal particles the angular distribution of the scattered light depends on the particles' shape and orientation. When the particle orientations are correlated, this is manifest by polarization dependence in the scattered light. For gold particles of dimensions < 30 nm the linear optical properties are dominated by absorption, with < 10% of the total cross section being due to scattering. Spheroidal gold particles support two dipole modes with a moment aligned along the minor axis of the particle. Therefore the frequency dependence of the absorption cross section for polarized light is sensitive to the spheroids' orientation. The effective-medium theory can incorporate this polarization difference by an anisotropic dielectric tensor for the effective medium.

The field inside the ellipsoidal-shaped particles is uniform but not necessarily in the same direction nor of the same magnitude as the applied field $\vec{E}_c$ . For the ellipsoids of metal particles embedded in an effective medium, we have the local field

$$\vec{E}_m(\omega) = \gamma^m(\omega) \cdot \vec{E}_c(\omega) \tag{3a}$$

and for ellipsoids of the host material we have its local field

$$\vec{E}_h(\omega) = \gamma^h(\omega) \cdot \vec{E}_c(\omega) . \tag{3b}$$

The local fields may be quite different from the applied field. Their value is determined by the tensors $\gamma^\alpha$ , where $\alpha = m$ or $\alpha = h$; these are related to the depolarization tensor and the dielectric tensors:

$$\gamma^m(\omega) = \left\{ 1 + \Gamma(\omega) \left[ \epsilon_m(\omega) - \bar{\epsilon}(\omega) \right] \right\}^{-1} \tag{4a}$$

and

$$\gamma^h(\omega) = \left\{ 1 + \Gamma(\omega) \left[ \epsilon_h(\omega) - \bar{\epsilon}(\omega) \right] \right\}^{-1} \tag{4b}$$

Since they provide the magnitude of the enhancement effects of the local field, we will denote these coefficients as *enhancement factors*. These factors determine the

resonance position in the denominator, which is controlled by the principal values of the depolarization tensor.

For random orientation of the spheroids, the enhancement factors in Eqs. (4), which refer to a coordinate system fixed to the spheroid, now have different contributions because the applied field is changing its direction relative to this coordinate system. The lack of a single local field for particles with different orientations means that the self-consistency condition, Eq. (1), incorporates a complicated angular dependence in the nonlinear coefficients. A simple expression for the effective-medium dielectric function is no longer possible; instead the effective medium is expanded as a power series in the applied field.

A useful expression for the nonlinear coefficient $\bar{\chi}^{(3)}$ is obtained when the host medium is linear, $\chi_h^{(3)} = 0$, and for small concentrations the result is

$$\bar{\chi}^{(3)} \simeq f \frac{\chi_m^{(3)}}{\epsilon_{hl}} \left\{ \frac{\frac{8}{15}\left|\gamma_x^m\right|^2 + \frac{2}{15}\left|\gamma_z^m\right|^2}{\left[\left(1-A_x\right)\bar{\epsilon}_L + A_x\epsilon_{mL}\right]^2} + \frac{\left(\frac{2}{15}\left|\gamma_x^m\right|^2 + \frac{3}{15}\left|\gamma_z^m\right|^2\right)}{\left[\left(1-A_z\right)\bar{\epsilon}_L + A_z\epsilon_{mL}\right]^2} \right\} . \quad (5)$$

Here, $A_x$ and $A_z$ are depolarization factors, i.e., $A_x = \bar{\epsilon}_x \Gamma_{xx}$, $A_z = \bar{\epsilon}_z \Gamma_{zz}$.

This expression has denominators with two surface-plasmon resonances. The strongest resonances occur when the enhancement factors in the numerator have their resonance at the same frequency as the denominator, as they are in the first and last terms of Eq. (5). However, because of the mixing of these resonant terms, enhancements of the susceptibility occur between the frequencies. At the surface-plasmon resonances the effective nonlinearity can be enhanced by several orders of magnitude over the value $\chi_m^{(3)}$. The actual enhancement factor depends on the metal. In silver the resonance is sharp in the visible, and 8 to 10 orders of magnitude enhancement are possible. This is reduced by the volume fraction, f, which multiplies these factors.

The conjugate reflectivity is defined as

$$R = \frac{\left|E_c(0)\right|^2}{\left|E_s(0)\right|^2} = 4\left|\beta\right|^2 \frac{e^{-2\alpha L}\left|\sinh\left(\frac{\alpha L}{2}\right)\right|^2}{\alpha^2}\left|E_F(0)\right|^2\left|E_B(L)\right|^2, \qquad (6)$$

where $\beta = 3\omega^2 \bar{\chi}^{(3)}/(2c^2\kappa)$ and $\alpha = \omega^2 \operatorname{Im}(\bar{\epsilon})/(c^2\kappa)$ are the nonlinear coupling and absorption coefficients, respectively. Here $E_F$ and $E_B$ are the forward and backward pump field amplitudes, respectively, and $E_c(0)$ and $E_s(0)$ are the conjugate and probe fields of the input.

A more accurate expression valid for large nonlinear coupling can be found in Ref. 13, but these expressions are not needed for the discussion that follows. Equation (6) contains $|\bar{\chi}^{(3)}|^2$, which contains the enhancement factors to the eighth power. The absorption coefficient, $\alpha$, contains the first power of the enhancement factor; therefore the overall reflectivity has a sixth power of the enhancement for the multiplicative coefficient of the hyperbolic sine.

## 3. THEORETICAL RESULTS

The description of heterogeneous nonlinear-optical materials given in the previous sections is useful for a wide range of materials; these include semiconductor colloids and glasses and, under certain restrictions on the size, heterogeneous polymer solutions. In nonconducting media, the transparency is usually large enough that high-volume fractions can be considered.

The pump fields are taken as equal and small, such that $\chi_m^{(3)}\left|E_B(0)\right|^2 = 0.01$. In Fig. 1 the conjugate reflectivity for spheroidal particles is shown from Eq. (6). The length of the medium is taken as $L = 2$ nm; the maximum conjugate reflectivity occurs at a value $\alpha L \simeq 1.5$. At small concentrations only a single maximum is observed, but the high concentrations show the appearance of a second peak, which eventually dominates the reflectivity. Over a range of concentrations the reflectivity changes from a single peak to a broad double-peaked structure. A second peak at the second surface plasmon resonance eventually dominates the reflectivity.

The second peak occurs because $\bar{\chi}^{(3)}$ is enhanced at this frequency owing to the second surface-plasmon resonance, and the absorption has not yet become the limiting factor in the maximum of the conjugate reflectivity. The peak in $R_c$ can switch from one resonance to another; this provides a sensitive test of the average particle shape.

## 4. EXPERIMENTAL RESULTS

We examined the linear- and nonlinear-optical properties of glass containing gold particles. The glasses are RG6 filters obtained from Schott. The volume fraction of gold in the RG6 is fixed; therefore we varied the sample thickness to investigate the effects of absorption on the DFWM signal. Three samples of 1-, 2-, and 3-mm thicknesses provided $\alpha L$ = 1.6, 3.1, 4.7, respectively, at $\lambda$ = 0.545 μm. Recall that the maximum conjugate reflectivity occurs at $\alpha L \simeq 1.5$. Nearly all the loss in the RG6 glass is due to the gold particles, and little is due to the glass matrix.

DFWM was performed at different frequencies using an excimer-pumped dye laser at a 10-Hz repetition rate. The pulse duration was 12 nsec for all frequencies. We do not have electron micrographs of the gold particles in the RG6 glass, but it is not unreasonable to assume that the particles' shape may deviate from a perfect sphere. The particles would also be expected to have a range of shapes in the actual glass.

Figure 2 shows the conjugate signal versus wavelength at a constant pump intensity of 8 MW/cm$^2$. For the thinnest sample, L = 1 mm, one broad peak is observed. The thickness L = 2 mm shows an overall reduction of the reflectivity and two peaks in the spectrum, which is characteristic of the two surface-plasmon resonance frequencies supported by a nonspherical particle. For L = 3 mm, the dominant peak in the reflectivity has shifted to the longer wavelength, and the overall reflectivity has been reduced by a factor of ~ 3 compared with the 1-mm sample. A dip in the conjugate signal versus wavelength is predicted for spherical particles but only at values of $\alpha L$ larger than those of the RG6 samples examined here.

## 5. OPTICAL BISTABILITY

Optical bistability without an optical cavity [called instrinsic optical bistability (IOB)] has been observed in a number of materials[14] and theoretical descriptions have been given for this phenomenon[15]. Recently, this IOB phenomenon has been predicted for a single-semiconductor microparticle[16]. We extend these predictions by considering the effects of a composite consisting of a collection of conducting microparticles randomly distributed throughout a transparent host material. The particles are considered to possess a sharp size distribution.

To be specific, we consider a material made up of small spherical metallic particles of radius $a$, with volume fraction $f$, and they are embedded in a dielectric host medium with coefficient $\epsilon_d$. The metal grains are small enough that surface effects are important and are driven by a strong applied field so that

they will have a nonlinear response which turns out to be of the Kerr type for gold and silver particles.

A material composed of microscopic particles that are randomly and independently distributed throughout the medium has a dielectric constant that varies from point to point in the medium $\epsilon(r)$. The medium is described by an effective dielectric function $\epsilon^*$, which accounts for the multiple-scattering effects of the heterogeneous medium in an averaged manner. The expression relating $\epsilon^*$ to the microscopic properties of the medium is determined by the self-consistency condition. In our case, this general expression involves the volume fraction $f$ and the dielectric constants. However, the concentrations of metal spheres we will explore are low enough that the effective dielectric function for the medium can be approximated by linear terms in the concentration (Maxwell-Garnett approximation)

$$\epsilon^* \approx \epsilon_c + f\left[3\epsilon_d / \left(2\epsilon_d + \epsilon_m\right)\right]\left(\epsilon_m - \epsilon_d\right) \tag{7}$$

The steady-state Maxwell equation for the applied, propagating electric field is $[E(r,t) = E_c(r)\, e^{-i\omega t}]$

$$\nabla^2 E_c + \left(\omega^2/c^2\right)\epsilon^* E_c = 0. \tag{8}$$

To develop the theory further, first we introduce the slowly varying envelope approximation and use one-way propagation of the electromagnetic field. To be specific we assume the electromagnetic field is propagating along the positive $z$ axis:

$$E_c = E_\epsilon\, e^{ikz} \tag{9}$$

The wave number $k$ is chosen to eliminate the real, linear contribution to the dielectric function $\epsilon^*$ in Eq. (7),

$$k^2 = \left(\omega^2/c^2\right) \mathrm{Re}\left\{\epsilon_\ell^*\right\} \tag{10}$$

where $\epsilon_\ell^* = \epsilon^*\ (E_L = 0)$. The transverse effects are neglected: their contribution can be important for small Fresnel numbers as we have found for the nonlinear oscillator model, but the results for the on-axis intensity were not affected in that study down to Fresnel numbers of unity. As the two problems are quite analogous,

we expect the same results for this model. The backward-propagating wave is negligible in the present case because we restrict our numerical results to small concentrations of metal spheres, $f << 1$. In this limit the nonlinear changes of the real part of dielectric function are small. The Maxwell field equation (8), in a slowly varying envelope approximation (SVEA), is reduced to

$$\frac{dE_\epsilon}{dz} - i\kappa E_\epsilon = 0 . \qquad (11)$$

The coefficient appearing in Eq. (11) is

$$\kappa = \left[\epsilon'' - Re\left(\epsilon_\ell''\right)\right] \omega/2c \sqrt{Re\left(\epsilon_\ell''\right)} \qquad (12)$$

These equations provide the basis for studying propagation effects in composite media.

In the following we take the spherical particles to be composed of silver and use the dielectric constant which was developed for small particles to include the quantum-mechanical confinement of the electrons. The linear dielectric constant in Eq. (5) is given by

$$\epsilon_0 = \epsilon_\infty + \left[\omega_p^2/\left(\Omega^2 - \omega^2 - i\omega\Gamma\right)\right] . \qquad (13)$$

The coefficient $\epsilon_\infty = 4.66$. The resonance frequency $\Omega^2$ and the damping coefficient, $\Gamma$, are functions of the particle size:

$$\Omega = \sqrt{\xi}\ v_F/a \quad , \quad \Gamma = \Gamma_b + \left(v_F/a\right) , \qquad (14)$$

where the Fermi velocity $v_F = 1.29 \times 10^8$ cm/s and $\Gamma_b = 2.5 \times 10^{13}\ s^{-1}$ in silver.The plasma frequency is related to the density of the electrons in our case, $\omega_p^2 = 4\pi ne^2\backslash m_c \approx 4.0 \times 10^{31}\ s^{-2}$. The electric fields are scaled to the parameter $\chi_3$, which we assume to be real and positive.

The bistable behavior arises from the nonlinear relation between the local field inside the metal particle $E_L$ and the propagating field $E_0$. The condition on tuning of the laser frequency to observe bistability is that

$$\mathrm{Re}\left(2\epsilon_d + \epsilon_{mi}\right) < 0$$

and

$$\left|\mathrm{Re}\left(2\epsilon_d + \epsilon_{mi}\right)\right| > 3\left|\mathrm{Im}\left(2\epsilon_d + \epsilon_{mi}\right)\right| \qquad (15)$$

The first inequality is based on the assumption that $\chi_3 > 0$. The second inequality is violated near the resonance frequency $\Omega$ and we do not find optical bistability for this regime. Furthermore, the bistable characteristics for a laser tuned near this frequency would be very sensitive to tiny fluctuations in size and shape of the particles. The curve of the local field intensity versus the propagating field intensity is shown in Fig. 3 for particles of size $a = 5$ nm at a wavelength of 500 nm. At this wavelength the penetration depth of the electric field is about eight times larger than the particle radius $2\pi a\sqrt{\mathrm{Re}\,(\epsilon_{mi})}/\lambda \approx 0.13$ and our use of the quasistatic approximation is justified.

Equation (11) is integrated using a forward-difference scheme. At each new point at which the propagating-electric field is found, we require that the local-field intensity $|E_L|^2$ be determined from Eq. (2) together with Eq. (3); the result is a cubic equation. In the regions of propagating-field intensity where three real roots are found, the solution chosen depends on the intensity of the input electromagnetic field and its previous history. If the input intensity is ramped up sufficiently slowly from zero, then the steady-state solution on the lower branch of the local-field intensity is chosen and it remains on this branch until the turning point marked A is reached in Fig. 3. Along the lower branch, the medium is highly dispersive and $|\mathrm{Re}\,(2\epsilon_d + \epsilon_m)| >> \mathrm{Im}\,(2\epsilon_d + \epsilon_m)$. The absorption of the propagating-electric field in the medium is small for solutions along this branch. Six solutions that exemplify this behavior are shown in Fig. 4. They are labeled 1-6 and curve 6 is close to the turning point A in Fig. 3.

For input fields ramped to higher values of the intensity than turning point A in Fig. 3, the local-field intensity in the metal becomes large. Now the medium is driven into resonance by the local field and the medium is highly absorbing. The local field in the particles remains on the high branch until it reaches the turning point marked B in Fig. 3. The local field jumps discontinuously, but the propagating field remains continuous in the medium.

It should be noted that this switch in local fields occurs inside the medium, say at length $L$ and that at $L$, the effective-medium dielectric function undergoes a discontinuity. This boundary separating the high and low local field branches would

scatter radiation in the backward direction, as does a similar boundary analyzed earlier for a different system[17], as well as for the nonlinear oscillator model[18]. However, for the concentrations in this paper, $f = 10^{-3}$, the discontinuity in $\epsilon^*$ is quite small.

The occurrence of the dielectric boundary is exhibited in Fig. 4 by curves 7-10. The knee in the curve separates a high-absorption regime from a low-absorption regime. As the input field is increased, the knee in the propagating intensity curve moves to the right; and as it is decreased, the knee moves to the left until it continuously moves back to the input and the local field is then on the lower branch throughout the entire medium.

We can study different effects of the internal boundary by observing the transmission characteristics for the silver composite cut to two different lengths. We show two examples in Figs. 5 and 6. In Fig. 5, the medium is short enough that the boundary does not appear in the medium. The transmitted intensity decreases when the input intensity reaches point A, but the output intensity is greater than that at point B (Fig. 3). Increasing the output intensity does not significantly change the absorption in the medium, so the transmission is again linear with the input field. As the input field is decreased, a change in slope occurs in the transmitted intensity and the output intensity remains nearly constant. The absorption in the medium is no longer constant; the knee in the intensity curve discussed in Fig. 4 is inside the medium. A further lowering of the input intensity will result in the motion of the boundary out of the medium at the input face and eventually the transmitted intensity will smoothly join the low-intensity solutions.

In Fig. 6, the medium has a length that is longer than can sustain the large local field, corresponding to the upper-branch solution, across the sample. The boundary now appears inside the medium. The contrast between high- and low-output intensities is greater and the nearly constant output intensity is sustained over a much larger range of input intensities.

## 6. CONCLUSIONS AND OBSERVATIONS

We find that the metal composite glasses can exhibit optical bistability when driven by a strong laser. The bistability is intrinsic since it does not require the use of an external cavity or other forms of optical feedback, and its features are analogous to the nonlinear oscillator model[18]. Our results are not restricted to photochromic glasses or metal colloids, but they could also be applicable to inhomogeneous polymer solutions that have a larger $\chi_3$ with metal particles dispersed in them to increase the effective nonlinearity.

We find that further tuning of the laser frequency toward the blue can give a significant decrease of the input intensities and the results presented here are not

significantly altered for 20% variations of the particle sizes. In our studies the backward propagating wave is entirely negligible, and in higher particle concentrations the absorption may be too large to allow a significant reflected intensity from occurring at a boundary inside the medium.

The response time of these materials is determined by the relaxation time of the electrons excited by the applied field. According to Hache, Ricard, and Flytzanis[3], $\chi_3$ can be enhanced in small particles by quantum size effects on the free electrons. This is due to a breakup of the continuum into a quasicontinuum. Therefore, the response time is of order $\Gamma^{-1}$; this is less than 1 ps for silver. For silver, they also calculate $\chi_3$ (Ag) = 2.4 X $10^{-9}$ esu. With this value we estimate the intensity levels for the bistable switching to be around 100 MW/cm$^2$ at a wavelength of 450 nm.

## REFERENCES


1. J. C. Gardland and D. B. Turner, eds., *Electrical Transport and Optical Properties of Inhomogeneous Materials*, AIP Conf. Proc. 40 (1978); D. Richard, "Nonlinear optics at surfaces and in composite materials," in *Nonlinear Optics: Materials and Devices*, C. Flytzanis and J. L. Oudar, eds. (Springer-Verlag, Berlin, 1986), p. 154.

2. D. Ricard, Ph. Roussignol, and Chr. Flytzanis, Opt. Lett. 10, 511 (1985).

3. F. Hache, D. Ricard, and C. Flytzanis, J. Opt. Soc. Am. B3, 1647 (1986).

4. K. M. Leung, Phys. Rev. A33, 2461 (1986); C. M. Bowden, R. Inguva, J. W. Haus, and N. Kalyaniwalla, Opt. News 13(9), 116 (1987).

5. J. W. Haus, N. Kalyaniwalla, R. Inguva, and C. M. Bowden, J. appl. Phys., 65, 1420 (1989).

6. R. K. Chang and T. E. Furtak, *Surface Enhanced Raman Scattering* (Plenum, New York, 1982).

7. J. W. Haus, R. Inguva, and C. M. Bowden, "Effective medium theory of nonlinear ellipsoidal composites," submitted to Phys. Rev. A41, 1670 (1990).

8. M. J. Bloemer, M. C. Buncick, R. J. Warmack, and T. L. Ferrell, J. Opt. Soc. Am. B5, 2552 (1988).

9. L. K. H. Van Beek, "Dielectric behavior of heterogeneous systems," in *Progress in Dielectrics*, J. B. Birks, ed. (CRC, Cleveland, OH, 1967), Vol. 7, p. 69.

10. D. Stroud, Phys. Rev. B12, 3368 (1975).

11. G. S. Agarwal and R. Inguva, Phys. Rev. B30, 6108 (1984).

12. D. Stroud and P. M. Hui, Phys. Rev. B37, 8719 (1988).

13. A. Yariv and P. Yeh, *Optical Waves in Crystals*, (Wiley, New York, 1984), p. 563.

14. J. Hajto and I. Janossy, Philos. Mag. B47, 346 (1983); M. Dagenais and W. F. Sharfin, Appl. Phys. Lett. 45, 210 (1984); D. A. B. Miller, A. C. Gossard, and W. Wiegman, Opt. Lett. 9, 162 (1984).

15. C. M. Bowden and C. C. Sung, Phys. Rev. A19, 2393 (1979); F. A. Hopf and C. M. Bowden, Phys. Rev. A32, 268 (1985); J. W. Haus, C. C. Sung, C. M. Bowden, and J. M. Cook, J. Opt. Soc. Am. B2, 1920 (1985). Y. Ben-Aryeh, C. M. Bowden, and J. C. Englund, Phys. Rev. A34, 3917 (1986).

16. D. S. Chemla and D. A. B. Miller, Opt. Lett. 11, 522 (1986).

17. Y. Ben-Aryeh, C. M. Bowden, and J. C. Englund, Opt. Comm. 61, 147 (1987).

18. J. W. Haus, S. Wang, M. Scalora, and C. M. Bowden, Phys. Rev. A38,4043 (1988).

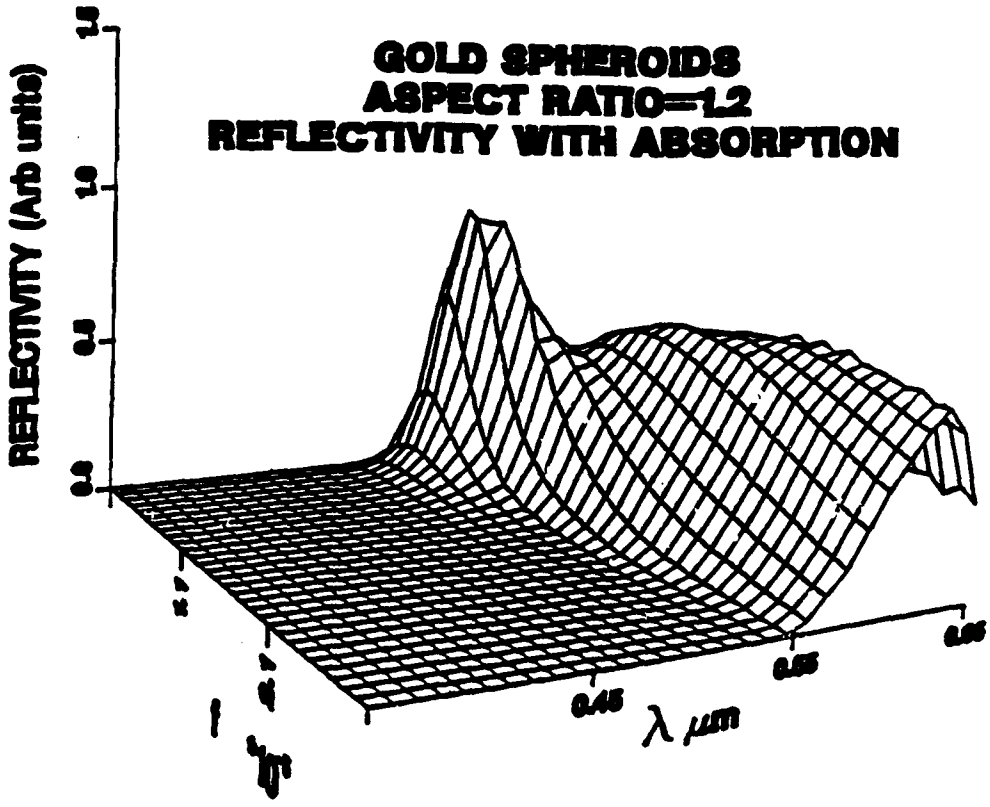


Figure 1. Conjugate reflectivity for spheroids plotted as the concentration and wavelength is varied: use Eq. (28)..8

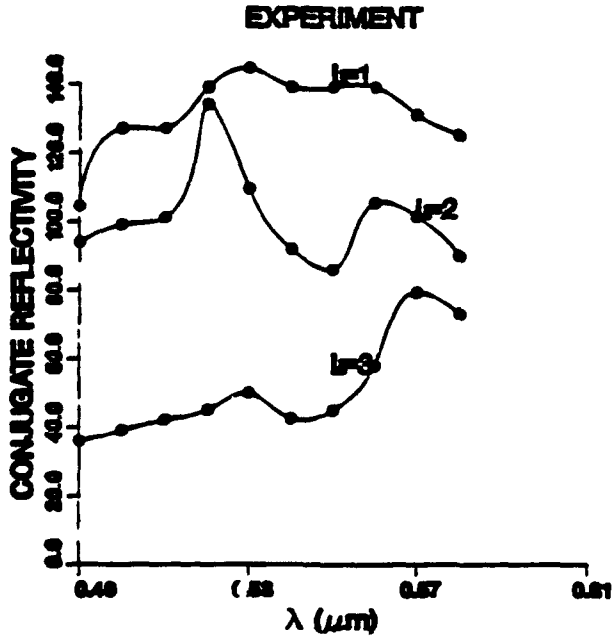


Figure 2. Conjugate reflectivity data for the RG6 glasses. The curves are a spline fit to the data and are not from the theory.

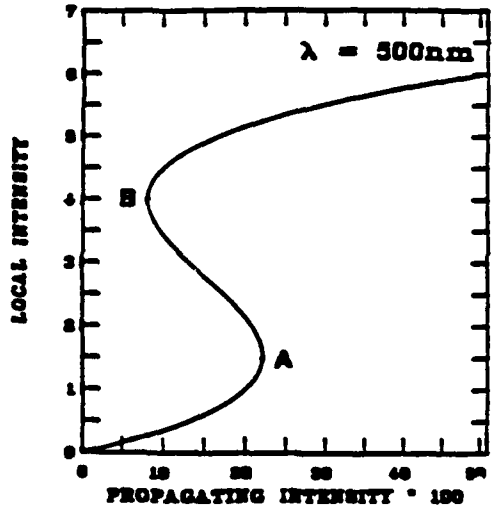


Figure 3. Local-field intensity vs propagating intensity from Eq. (8). The particle radius is 5 nm.

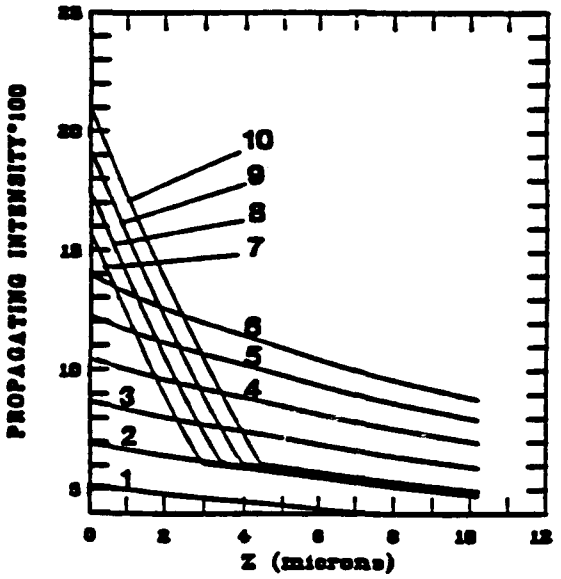


Figure 4. Intensity of light in the medium. The input intensities are regularly spaced.

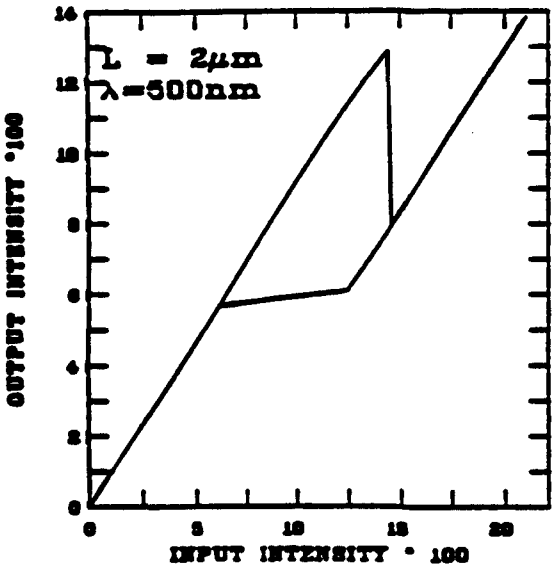


Figure 5. Input vs output intensities for a 2-μm-thick sample. The particle radius is 5 nm.

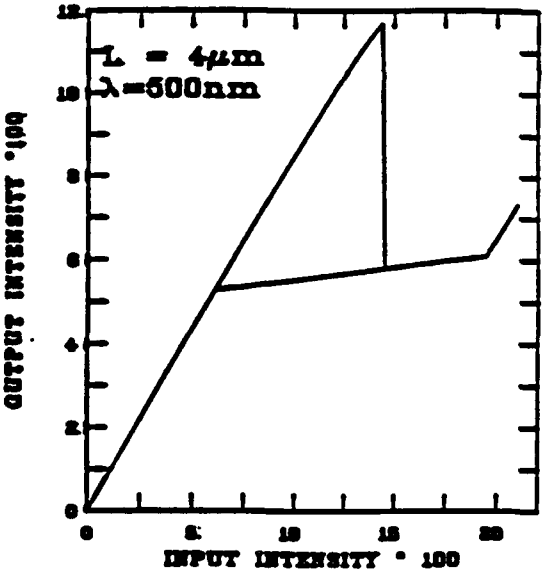


Figure 6. Same as in Figure 5 with a 4-μm-thick sample.

# UV-IR Detector and Focal Plane Array Material Evaluation Using Faraday Rotation

Dr. Charles R. Christensen, Dr. George A. Tanton, Mr. John A. Grisham ,
and Dr. John Stensby †
Research Directorate, Research, Development, and Engineering Center, U.S. Army Missile Command, Redstone Arsenal, AL
35898-5248

## Introduction

Our objective is to develop innovative noncontact methods that can be applied in ultraviolet (UV) and long wavelength infrared (LWIR) detector manufacturing to increase yield, reduce production costs, and to improve traceability throughout the manufacturing process.

Conventional methods used to characterize semiconductor material do not quickly or efficiently identify areas of a wafer that will produce useful detectors or focal plane arrays. This results in lower production yields and higher unit cost. In the technique described here [1,2] the material of interest is positioned in an amplitude modulated magnetic field and scanned with a linearly polarized laser beam. As the laser beam passes through the material it undergoes Faraday Rotation (FR) proportional to the free carrier concentration in that particular part of the wafer. Since detector device characteristics, such as effective resistance and capacitance, are functions of the free carrier concentration parts of a wafer that will not yield good detectors can be identified in the early stages of manufacturing using this technique. The yield would be significantly increased and the unit cost decreased by identifying and culling wafers or parts of wafers that do not meet specifications at the beginning of the fabrication process. It is expected that this FR technique can be utilized as a universal evaluation tool that will make manufacturing traceability possible by correlating device performance for any part of a wafter with fundamental parameters. This technique is applicable to all major detector materials of Army interest, e.g. mercury cadmium telluride (HgCdTe), cadmium sulfide (CdS), indium antimonide (InSb), platinum silicide (PtSi), and gallium arsenide (GaAs).

Major advantages of this technique are: a) no contacts need be alloyed with the wafer, hence no wafer material contamination. b) surface preparation is not required, c) it is a rapid CAM technique and does not require a skilled operator, and d) automated wafer mapping is

† Permanent Address: Electrical and Computer Engineering
University of Alabama in Huntsville
Huntsville, AL

possible. An objective of the effort reported here was to demonstrate the applicability of FR for the measurement of electronic homogeneity of wafers in the UV to IR Spectral region. The first steps in accomplishing this goal appear to be successful. The method, apparatus, and measurement results to date are reported here. Although these results are limited at present to only a few samples measured at ambient temperature, extensive measurements on the bulk material demonstrate the method for MCT and CdS. Future improvements now in the design phase include the addition of a cryogenic capability and a longer wavelength source to map wafers at 77 K.

## EXPERIMENTAL SETUP

The bench setup is shown schematically in Fig. 1.

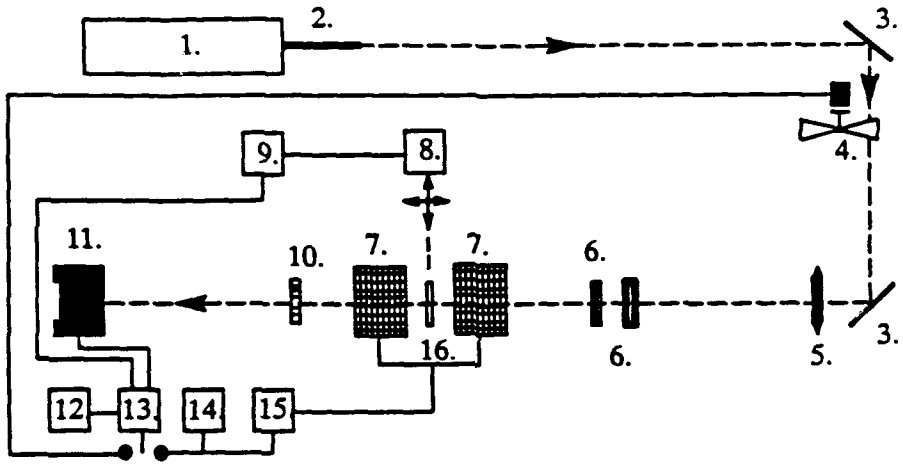


| | |
|---|---|
| 1. LASER, 2 WATTS CW @ 10.6 MICRONS | 2 ATTENTUATOR |
| 3. MIRROR | 4. CHOPPER |
| 5. FOCUSING LENS | 6. POLARIZER, ZnSe WIRE GRID |
| 7. SPLIT ELECTRO-MAGNET, 2.4 kG | 8. X/Y TRANSLATION STAGES |
| 9. IBM PC | 10. ANALYZER, ZnSe |
| 11. DETECTOR, HgCdTe @ 77 K | 12. RECORDER, STRIP CHART |
| 13. LOCK-IN, AMPLIFIER | 14. SINE WAVE GENERATOR |
| 15. MAGNET DRIVER POWER AMPLIFIER | 16. SAMPLE |

Fig. 1. Faraday Rotation, Mapper.

The wafer was probed with a $CO_2$ laser beam at a wavelength of 10.6 micrometers. The sample was positioned in a magnetic field by X/Y translation stages with a positioning precision of 0.005 mm. The free carrier concentration in a particular part of the wafer was determined by the Faraday rotation as the laser beam passed through the material. The reference plane of polarization was established by two wire grid ZnSe polarizers shown in Fig. 2 and an analyzer, rotated at a bias angle $\Theta$ was placed after the wafer.

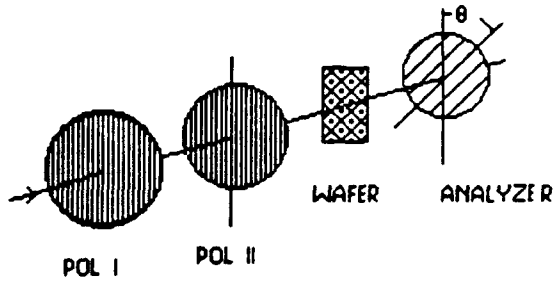


Fig. 2 Faraday Rotation Optical Train

A 25 mm focal length ZnSe lens in front of polarizer I focused the beam to 0.3 mm diameter at the wafer, resulting in a flux density of 10 - 50 W/cm$^2$. The split magnet shown in Fig. 3 produced a 10 Hz amplitude modulated magnetic field of $\pm$ 2. 4 KG. The magnetic field was directed parallel to the propagation axis of the probe beam.

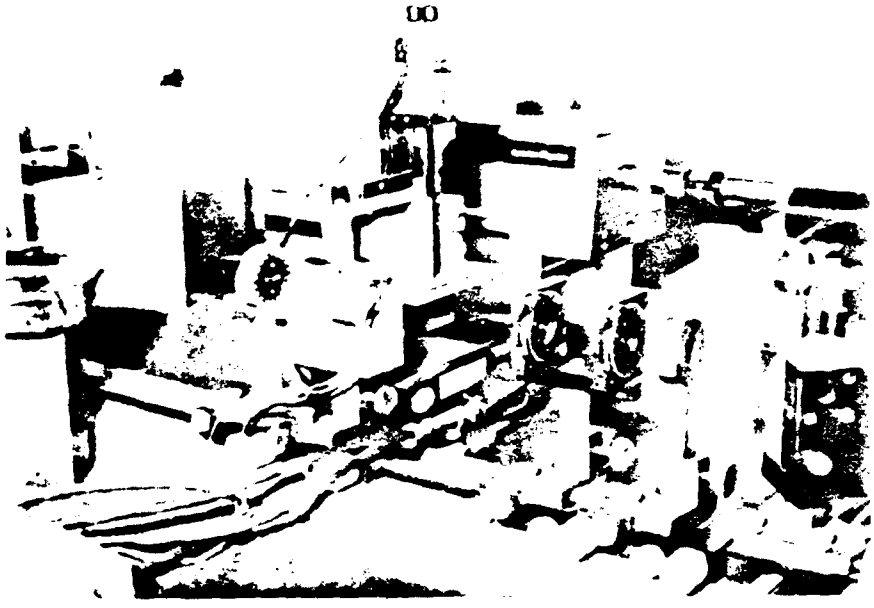

Fig. 3. Split Magnet for FR Measurements

The change in intensity of the probe beam caused by rotation of the plane of polarization (Faraday rotation) and propagation through the zinc selenide Brewster window analyzer was measured by a mercury cadmium telluride detector cooled to 77 K. All system components were located away form any stray magnetic fields that might have affected their performance. A high sensitivity lock-in amplifier, tuned to the modulating frequency of the magnetic field, amplified the detector output and fed it into an IBM PC. The computer was programmed to execute the sequences to control the scanning hardware and collect and reduce the data. Details of the software and theory of operation can be found in another report[3].

## BACKGROUND THEORY

According to classical theory at wavelengths long compared to the bandgap wavelength. FR due to free carriers is given by.[4]

$$\delta = \lambda^2 Be^3 NL / 2\pi c^4 nm^{*2} \qquad (1)$$

a result that is well established for binary semiconductors. In Eq. (1) $\delta$ is the Faraday rotation angle in radians, e = 4. 8 x $10^{-10}$esu, the free carrier effective mass $m^*$ was assumed to be 0.015m for MCT and 0.2m for CdS at 300 K, m = 9.1x $10^{-28}$gm. n = index of refraction of the material, N [$cm^{-3}$ ] is the free carrier concentration. B = 2400 Gauss, L and $\lambda$ are the thickness of the sample and wavelength in units of cm, respectively, and $\pi$ has its usual meaning. The band gap energy, $E_g$, of CdS is 2.4 eV. It was calculated for MCT from an expression given by Hansen et al.[5]

$$E_g = - 0.302 + 1.93x - 0.81x^2 + 0.832x^3 + 0.535\ T\ (1-2x)/1000 \qquad (2)$$

where x = percent concentration of Cd. The band gap at T = 300 K for long wavelength IR MCT with x = 0.200-0. 220 yields a cut-off wavelength = $E_g$ [eV] / 1. 239 < 8 micrometers. Therefore the output from a $CO_2$ laser operating at 10.6 micrometers could be used for the probe beam for FR measurements of both MCT and CdS at ambient temperature.

## MCT RESULTS

Sample MCT4 was reported to be n-type bulk grown by the travelling heater method and it was investigated in the most detail. The remaining three were supplied as LPE samples. Faraday rotation was proportional to the magnetic field strength B as expected from Eq. 1, Fig. 4 shows the FR signal level plotted against B at an arbitrary position on MCT4. B was determined from the ac voltage across a 1 Ohm precision resistor in series with the magnet coils and from a direct measurement with a Gauss meter.

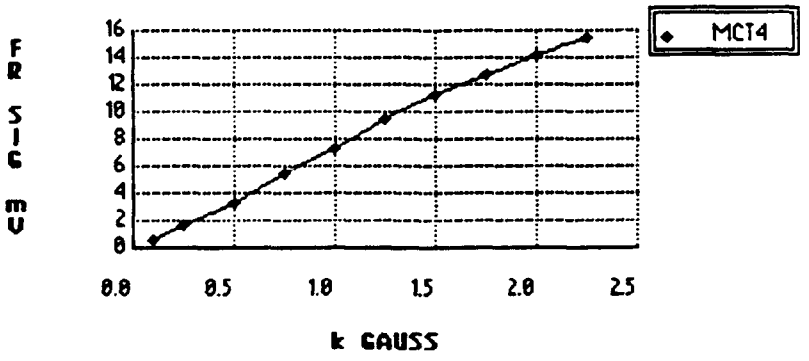


Fig. 4. Faraday Rotation Signal vs Magnetic Field Strength

Fig. 5 shows a comparison of normalized FR as a function of wafer position measured on different days and demonstrates that system repeatability was quite good. Laser fluctuations, although a potential source of scatter in the data, do not appear to be a problem.

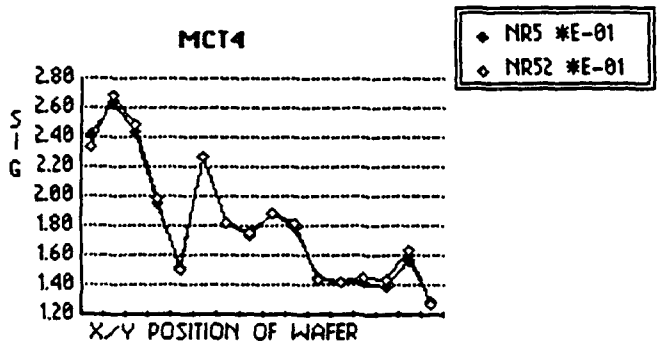


Fig. 5 Faraday Rotation in MCT4 @ 300K. Repeatability Test.

The magnitude of the Faraday rotation angle was measured directly by plotting the detector output as a function of $\Theta$, the angle through which the analyzer was rotated from parallel orientation to polarizer $\Pi$ ($\Theta = 90^{o}$ would be the fully crossed position), Fig. 2. A constant polarization reference plane was maintained for the radiation incident on a sample by rotating the analyzer and keeping the polarizers fixed. Fig. 6shows the optical train when no sample was in the beam. The beam was chopped at 10 Hz to provide a reference signal for the lock-in amplifier. Fig. 7 shows the resulting detector output as a function of analyzer angle.

The chopper was turned off when a sample was in the modulated field and the amplitude modulated signal generated by Faraday rotation in the sample provided the ac signal necessary for the lock-in amplifier. With sample MCT4 in the modulated field, the detector output had a maximum near $87^{o}$, Fig. 8. The difference between the maximum in Fig. 7 corresponds to a FR of approximately 3 degrees.

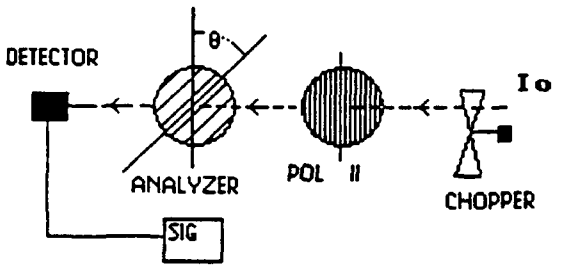


Fig. 6. System Initialization Setup Without Sample

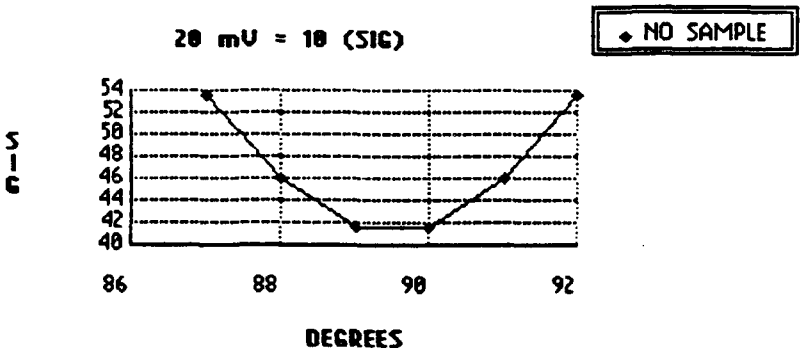


Fig. 7. Detector Output vs Analyzer Angle - No Sample

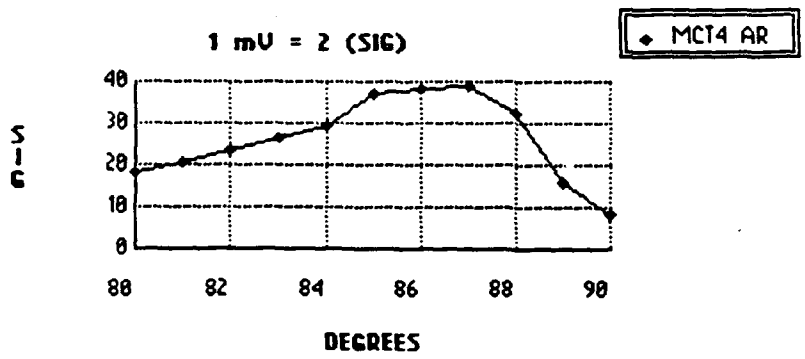


Fig. 8. Faraday Rotation Signal vs Analyzer Angle for MCT4 at 300 K

A more anaytical determination of the FR is obtained from the following analysis. From Beer's law and Malus' law the intensity I at the detector is given as

$$I = I_o \exp(-aL) \cos^2(\Theta + \delta) \qquad (3)$$

where $I_o$ = intensity of the laser beam at polarizer II, a = absorption coefficient; L, $\delta$ and $\Theta$ are the water thickness, FR angle, and fixed angle between analyzer and polarizer, respectively.

The percent change in I found from Eq. 3 leads to:

$$dI/I = 2\delta \, (d\delta) \, \tan(\Theta + \delta) \qquad (4)$$

A representative value for the magnitude of the FR in MCT4 was calculated from Eq. 1 using the rotation angle determined as follows: A plot of the normalized Faraday rotation vs tan ($\Theta$), at an arbitrary position on the sample very closely approximately a straight line for $\Theta$ less than about 80°, as expected from the small $\delta$ limit of Eq. 4. The departure from a straight line seen in Fig. 9 for $\Theta > 80°$ is due to the contribution of $\delta$.

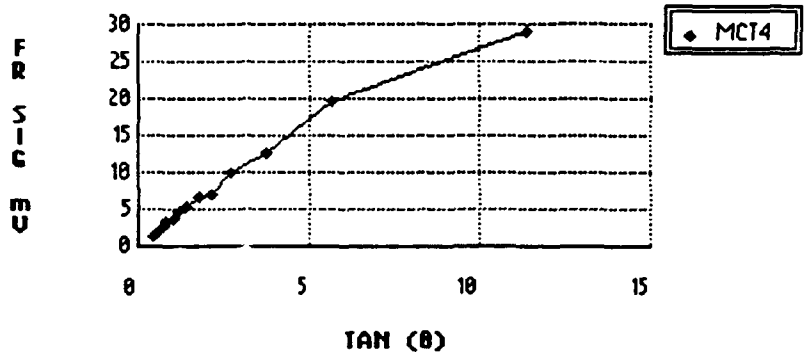


Fig. 9. Faraday Rotation Signal vs Tangent of Analyzer Angle.

The small $\delta$ becomes a significant contributing factor as $\Theta$ approaches 90 degrees because then the system sensitivity to FR theoretically approaches infinity, Eq. 4. In our measurements the gain in sensitivity from setting $\Theta = 80^{o}$ instead of $45^{o}$ was determined experimentally to be equal to 4.5 for both CdS and MCT, compared to the theoretical value calculated from Eq. 4, i.e. tan (80)/tan (45) = 5.7. The difference between the experimentally determined curve and the extrapolated tan ($\Theta$) function yields a value of -3 degrees for $\delta$ as Fig. 10 shows in good agreement with the value estimated directly from the relatively course scale marked in two degree increments on the analyzer holder.

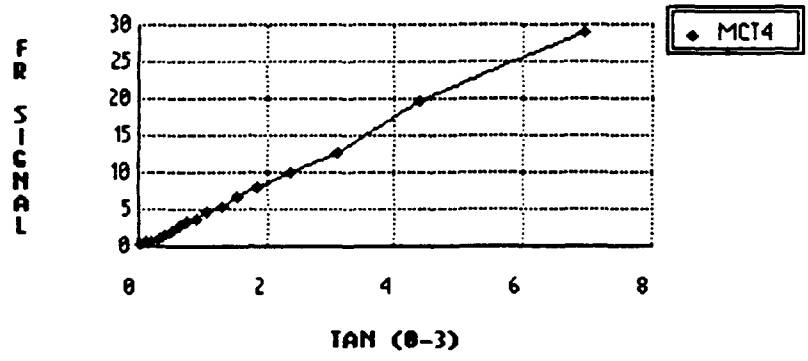


Fig. 10 FR signal vs. Tan ($\Theta$ - 3)

Solving Eq. 1 for N, here determined at only one arbitrary spot on the wafer, yields N = 6.7 ($10^{15}$ ) $cm^{-3}$ using $^{6}$ n = 3.55. This value is somewhat lower than the calculated intrinsic free carrier concentration , n(i) = 2 *$10^{16}$ for x = 0.22 and T = 300 K, but is consistant with

Hall and FR measurements on CdS at 300 K described later. No attempt was made to measure $\delta$ at a position in the wafer corresponding to the calculated mean value of N, only to show that $\delta$ obtained as described above is a reasonable value.

The relative free carrier densities were measured in the bulk grown sample MCT4 at room temperature using the automated equipment developed in this laboratory.

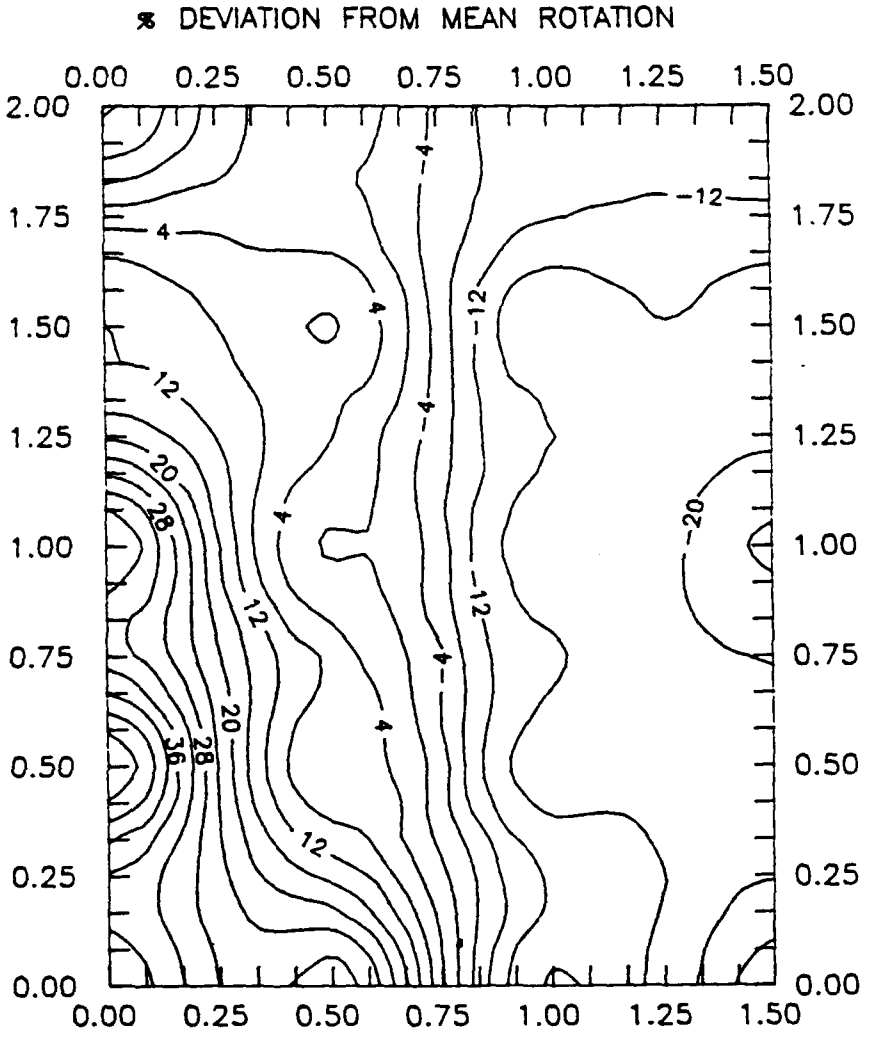


Fig. 11. High Resoluation Map of MCT4 (63 Data Points)

Fig. 11 is a high resolution map of MCT4 generated from 63 data points. The acquisition time in both cases was approximately 20 sec/point. The analyzer angle $\Theta$ was 80°. The free carrier concentration was found to vary 50% or more in sample MCT4. Although it may be desirable to perform measurements on cooled samples Nemiorovsky and Finkman[7] have pointed out that measurement of the intrinsic carrier concentration at room temperature can be

used to determine the composition and band gap of n-type wafers if the wafer is known to be intrinsic at room temperature.

COMPARISONS WITH LPE RESULTS:

The relative amplitudes of the FR signal in n and p type LPE samples at 300 K are compared in Table I with n-type bulk grown material. Table I also shows the free carrier concentrations at 77 K determined by Hall measurements. Although a direct comparison of FR with Hall results must be made at the same wafer temperature because of possible extrinsic effects.

---

TABLE I. RELATIVE FARADAY ROTATION (FR) PER CM IN MCT @ 300 K

| MCT# | TYPE | THICKNESS | N @ 77 K *10E14/cm$^3$ | FR (mV/cm)$^+$ | x |
|---|---|---|---|---|---|
| 1 | p-LPE | 18 microns | 100 | 55.5 | 0. 200-0. 220 |
| 2 | n-LPE | 18 microns | 2 | 30 | 0. 200-0. 220 |
| 3 | p-LPE | 23 microns | 80 | 40 | 0. 295 |
| 4 | n-BULK | 864 microns$^+$ | 2 | 31.8 | 0. 200-0.220 |

Except where marked with $^+$, samples and data in Table I were provided by Michael Grenn, CNVEO, U.S. Army, CECOM

---

The significant features in this Table are:

1. The Faraday rotation per unit length (FR/cm) increased with increased N as expected.

2. For a given N the magnitude of FR/cm was very close to the same value for n-type LPE and n-type bulk MCT. The FR results were virtrally the same for both LPE and bulk grown material even though sample thicknesses differed by a factor of 48. This indicates that the method of growth made no significant difference in the Faraday rotation. Possible extrinsic effects and other factors limit the extent to which one can compare Hall measurements made at 77 K to these FR results made at 300 K. However they appear to be in reasonable agreement.

## CdS RESULTS

Faraday Rotation measurements combined with theory and Hall measurements at 300 K give a consistent description of the free carrier concentration over a very wide range of detector and focal plane array material parameters, and demonstrated the applicability of the FR

technique to materials used in the spectral range from UV to IR. In previous work[2] with CdS, Faraday rotation and Hall measurements were made on the same wafers to determine the relation between free carrier concentration and Faraday rotation for this material. Fig. 12 shows a map of free carrier concentration determined by Faraday rotation measurements on a CdS wafer designated as GD4N3A. This map was generated from 25 measurements[2] over the wafer surface made with a 2mm diameter beam.

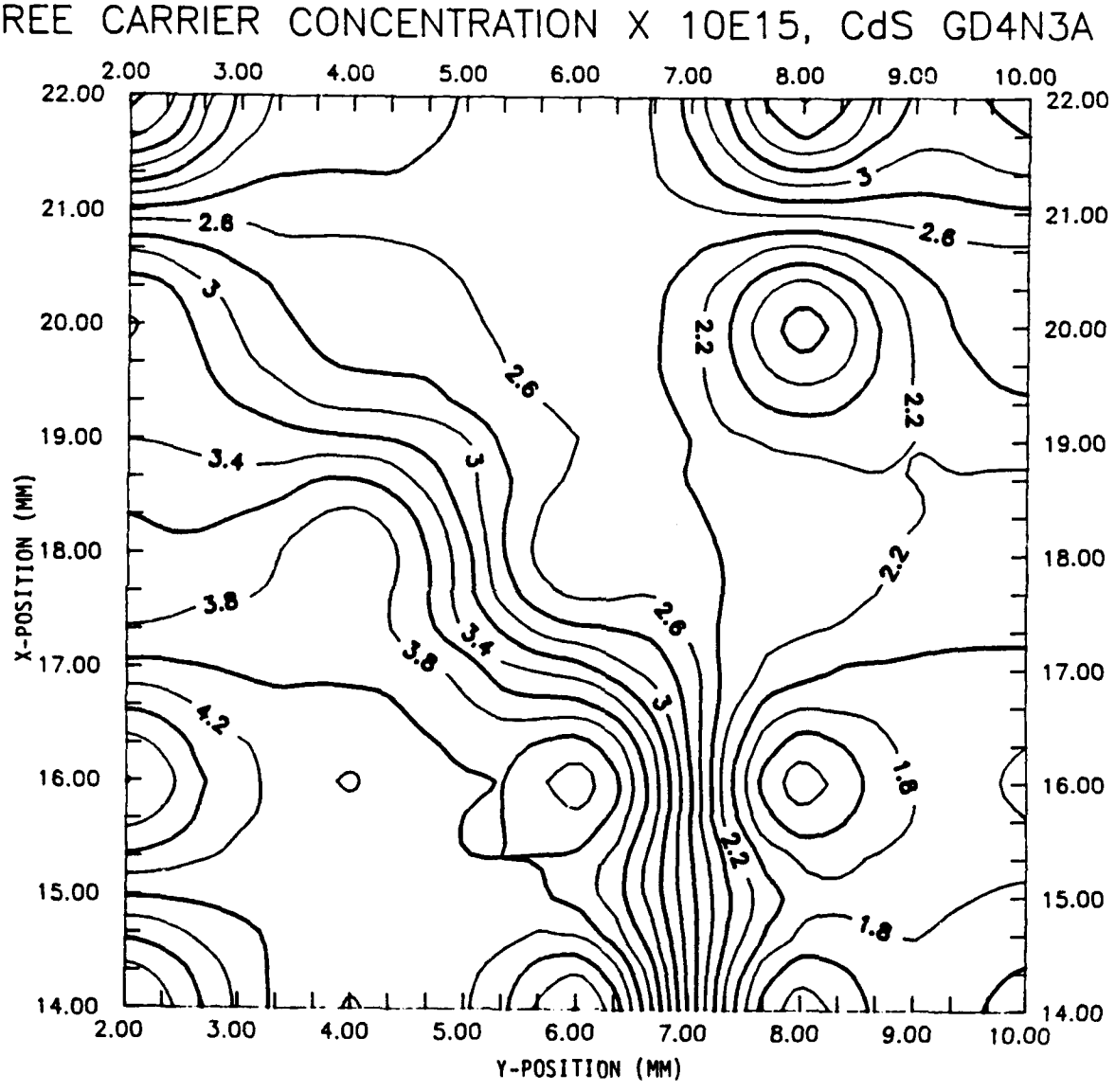


Fig 12. Map of a CdS wafer (25 data points)

Although a similar data base of Hall and Faraday rotation measurements has not yet been generated for MCT, Eq. 1 can be used to calculate N for MCT4 from Hall and FR measurements on CdS and known values for M* and n.

Eq. 1 yields the following relationship

$$N_{(MCT)} = \delta_{(MCT)} * [N_{(CdS)} / \delta_{(CdS)}] * 0.009 \qquad (5)$$

since $0.009 = (m^{*2}n)_{(MCT)} / (m^{*2}n)_{(CdS)}$

Room Temperature Hall measurements on two CdS wafers, designated as #7 and #12B, gave free carrier concentrations $N_{(CdS)} = 11.4 * 10^{15}$ cm$^{-3}$ and $2.7 * 10^{15}$ cm$^{-3}$, respectively. Using Eq. 5 with the maximum and minimum values of FR measured for CdS#7 yields a calculated range of $N_{(MCT)}$ between $2*10^{15}$ cm$^{-3}$ and $6.5*10^{15}$ cm$^{-3}$. The maximum and minimum values of FR in CdS#12B yield a calculated range of $0.9*10^{15}$ cm$^{-3}$ to $6.7*10^{15}$ cm$^{-3}$ for $N_{(MCT)}$. These values are consistent with the value of $6.7*10^{15}$ cm$^{-3}$ calculated for MCT4 using $\delta_{(MCT)} = 3^{o}$ measured at a single point as previously described.

## CONCLUSIONS

Major conclusions from this effort are summarized as follows:

a. The first high resolution mapping using the FR technique to determine free carrier concentraction uniformity of MCT as a function of position on a wafer was demonstrated.

b. Qualitative results of FR are consistent with those reported for LPE and bulk grown n-type material.

c. Quantitative consistency between results of Hall measurements, FR, and theory was demonstrated over a wide range of material parameters covering the spectral range from UV to IR.

d. In the limited circumstances of this first MCT FR mapping demonstration, the FR method appears to be a viable technique applicable to semiconductors that operate anywhere between the UV and LWIR. FR measurements at cryogenic temperatures on additional samples are needed to demonstrate the full capability of this technique.

## ACKNOWLEDGEMENTS

The cooperation extended by the Center for Night Vision and Electro-Optics (CNVEO), CECOM, by providing the MCT samples and Hall data used in Table I, taken by Michael Grenn (CNVEO), is acknowledged. The work reported here was made possible through the support of the Systems Engineering and Production Directorate and Research Directorate, MICOM. Technical assistance of Rachel Wright is gratefully acknowledged.

## REFERENCES

1. M. Balkanski and E. Amzallag, phys. stat. sol. 30, 407 (1968).

2. G. A. Tanton, J. A. Grisham, C. R. Christensen, and S. Razi, "Proc. Electronics and E-0 Materials for Smart Munitions Workshop", p. 105-114, 13-14 May 1987, Redstone Arsenal, AL, GACIAC PR-87-01.

3. John Stensby, C. R. Christensen, G. A. Tanton, andJ. A. Grisham, "A Computer Controlled System for Measurement of Faraday Rotation in Semiconductors," U. S. Army Missile Command Technical Report TR-RD-RE-90-5, 1990.

4. M. J. Stephan and A. B. Lidard, J. Phys. Chem. Solids, 9, 43 (1958).

5. G. L. Hansen, J. L. Schmit, T. N. Casselman, J. Appl. Phys. (USA) vol. 53 #10 (1982) p. 7099-101.

6. John Brice and Peter Capper, Properties of Mercury Cadmium Telluride, INSPEC, The Institution of Electrical Engineers, The Gresham Press, 1987.

7. Y. Nemirovsky and E. Finkman, J. Appl. Phys. (USA) vol. 50 #12 Dec 79, p. 8107-11.

# HYDROGEN FLUORIDE OVERTONE CHEMICAL LASER TECHNOLOGY

William A. Duncan, Barbara J. Rogers
Miles E. Holloman, and Stanley P. Patterson
U. S. Army Missile Command
Redstone Arsenal, AL 35898

## Abstract

The Hydrogen Fluoride Overtone Chemical Laser Technology Program has exploited the technology base developed over the last two decades for hydrogen fluoride lasers and successfully demonstrated a short wavelength chemical laser. This technology development centers on overtone lasing of the hydrogen fluoride molecule to produce laser radiation at 1.33 micrometers rather than the conventional fundamental lasing at 2.8 micrometers. The overtone wavelength can lead to significant improvements in brightness potential as well as atmospheric propagation properties. The concept has matured from initial demonstrations at the ten watt scale to the currently demonstrated multi-kilowatt level. In the course of these test programs it was necessary to develop new highly reflective coatings that permitted short wavelength lasing while completely suppressing lasing on the fundamental. This paper briefly reviews the performance of both discharge driven and combustion driven chemical laser devices, and the optical configurations employed in the scalability steps. Appropriate diagnostics are discussed, including power, efficiency, spectra, and small signal gain.

## I. Introduction

High power hydrogen fluoride (HF) chemical lasers have been the subject of research in the United States of America for approximately two decades. The basic principle of operation for continuous wave chemical lasers has been presented in several places.[1,2,3] During this period the technology advanced from the laboratory scale to major demonstration systems including Baseline Demonstration Laser (BDL), Navy-ARPA Chemical Laser (NACL), Mid-IR Advanced Chemical Laser (MIRACL) and ALPHA. Cylindrical as well as linear concepts have been investigated. Reference 4 presents a review of the High Power Laser programs. Emphasis during this period was placed on improvements in efficiency, scalability of concepts, and improvements in beam quality. For space-based applications size and weight considerations are critical. Planned growth to include addressing responsive strategic threats requires substantial increase in power as well as efficiency. An alternate approach to increasing the power requirements on the laser is to shorten the wavelength, thereby increasing brightness. Several efforts are ongoing to address this issue; however, success in the area is limited.[5] Among the potential candidates for a shorter wavelength laser is the overtone chemical laser that builds directly on the hydrogen fluoride technology base. The overtone chemical laser uses the same chemical reaction and produces the same excited populations as does the conventional hydrogen fluoride laser. It differs in that the optics employed suppress lasing at 2.8 micrometers and allow lasing at 1.33 micrometers (see Fig. 1).

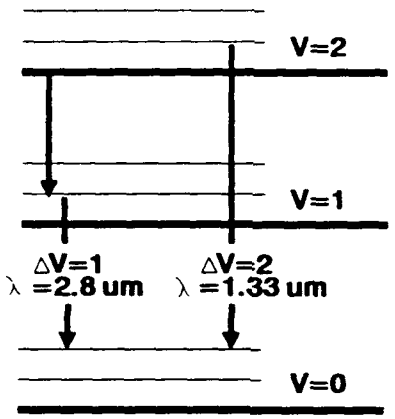


Fig. 1. Overtone Concept

## II. Subsonic Experiments

Prior to this development under the Overtone Chemical Laser Program, overtone lasing had been observed at very low levels using techniques not scalable to the power levels necessary for the envisioned applications.[6] Overtone lasing has been observed at low levels in other laboratories but no attempts were made to improve the modest performance.[10,11] In 1984, a Helios CL-I chemical laser (Fig. 2) demonstrated approximately 10 watts of laser energy at approximately 1.33 micrometers. Significantly, this level represented approximately 20% of the corresponding lasing power on the fundamental transition. Only the optics were changed to allow the overtone lasing. Transmissive optics designed for Nd-YAG applications were used in the demonstration test. The device illustrated in Fig. 2 measures 15 centimeters in gain length. Improvements were made in the optics, eventually allowing the demonstration of 21% of the fundamental power at the shorter wavelength.[9] Limited scalability of the concept was achieved by increasing the gain length to 30, 45, and finally 75 centimeters by combining individual 15 centimeter modules (Fig. 3). The performance of these devices is summarized in Fig. 4. The data illustrated in Fig. 4 suggests an upper performance limit of approximately 30% of the fundamental. Suppression of the fundamental lasing in the longer gain length devices tended to be a problem. Techniques of multiple mirror resonator designs prevented the fundamental wavelength from achieving lasing threshold by multiple reflections. Figure 5 illustrates the four mirror design used in the 75 centimeter device experiments. Representative spectra for these lasing tests are illustrated in Fig. 6.

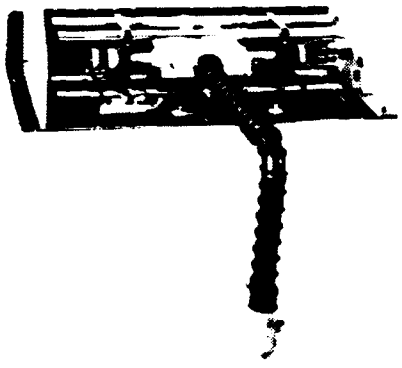

Fig. 2. CL-I Laser

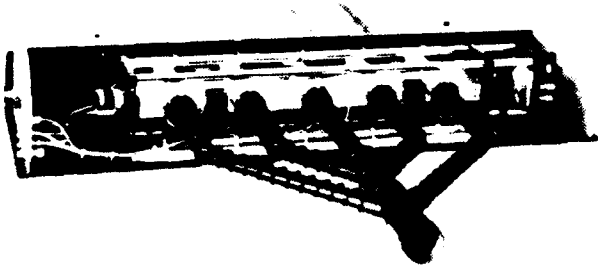

Fig. 3. CL-IV Laser

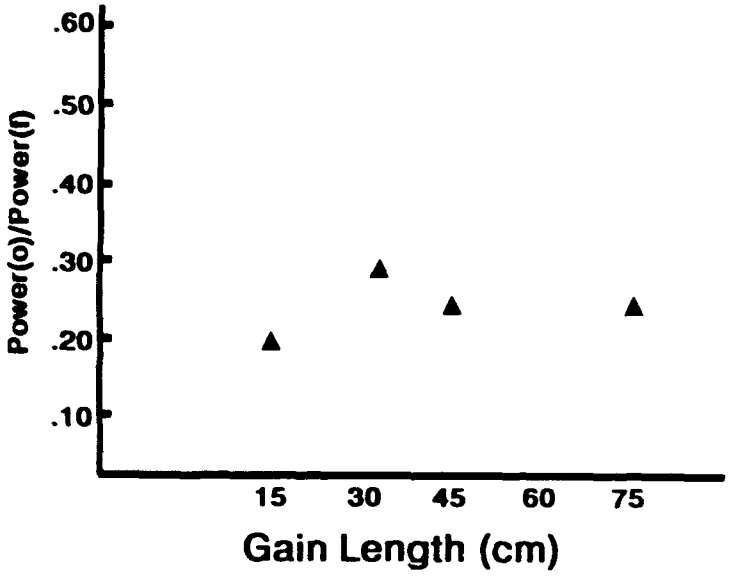


Fig. 4. Subsonic Device Performance Summary

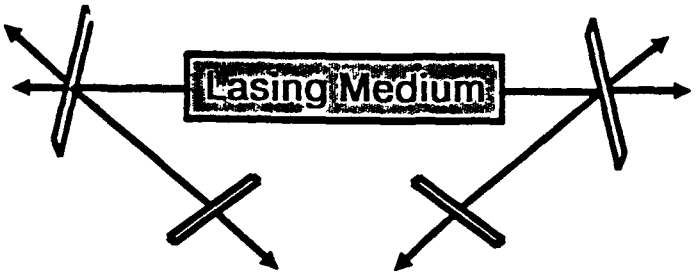


Fig. 5. Four Mirror Configuration

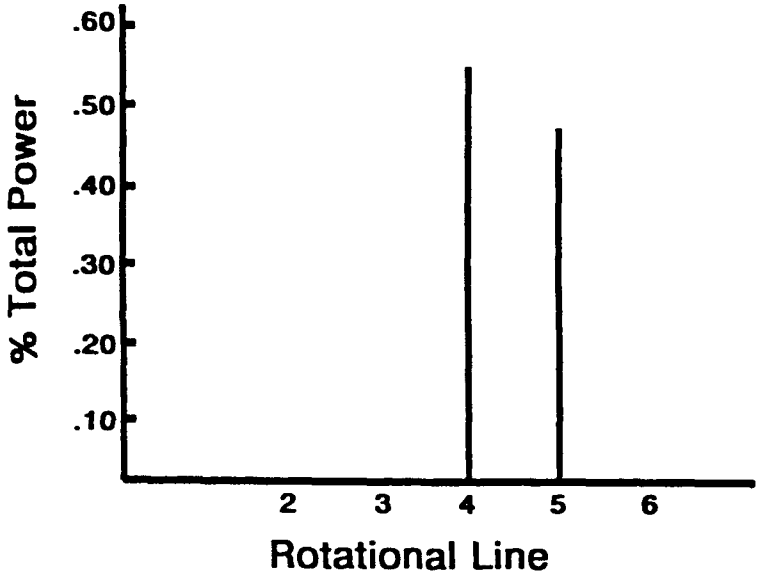


Fig. 6. CL-I Spectrum

The multiple optical surfaces required to suppress the fundamental introduced an additional source of loss in the cavity design, which to the low gain overtone laser was significant. Subsonic performance was improved by the introduction of a new nozzle design of greater flow height, optics/optical coatings specifically designed to suppress the fundamental and support overtone lasing, and hemispherical calorimeters designed to measure any radiation scattered from the highly reflective mirror surfaces. This improved design called the ZEB laser has demonstrated 55% of the fundamental performance at overtone power levels of approximately 200 watts or approximately an order of magnitude power scalability with a doubling of the efficiency.

## III. Supersonic Experiments

The subsonic designs do not lend themselves to being scalable to truly high power levels analogous to BDL, NACL, MIRACL, etc. The Overtone Chemical Laser Development Program transitioned into scalable supersonic chemical laser hardware in 1986. Tests performed at TRW demonstrated overtone performance at 24-35% of the fundamental using two chemical laser hardware configurations, the Hypersonic Wedge Nozzle (HYWN) and the Hypersonic Low Temperature (HYLTE) Nozzle conceptually illustrated in Figs. 7 and 8. A referenced paper describes these laser concepts in more detail.[7] The reactants used were nominally deuterium, flourine, hydrogen, and helium as a diluent. Mode lengths were found to be somewhat shorter than for the fundamental and the lasing spectra were as expected from the Helios experiments (Fig. 9). The resonator configuration consisted of transmissive Nd-YAG mirrors as in the initial Helios subsonic tests.

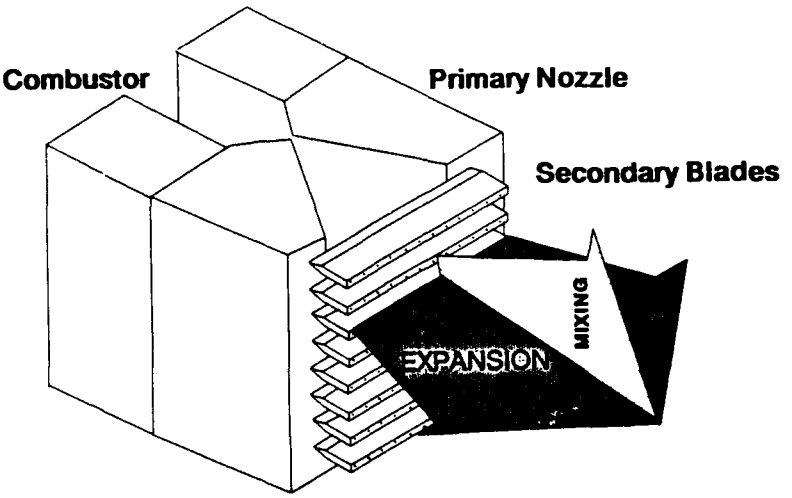


Fig. 7. HYWN Nozzle

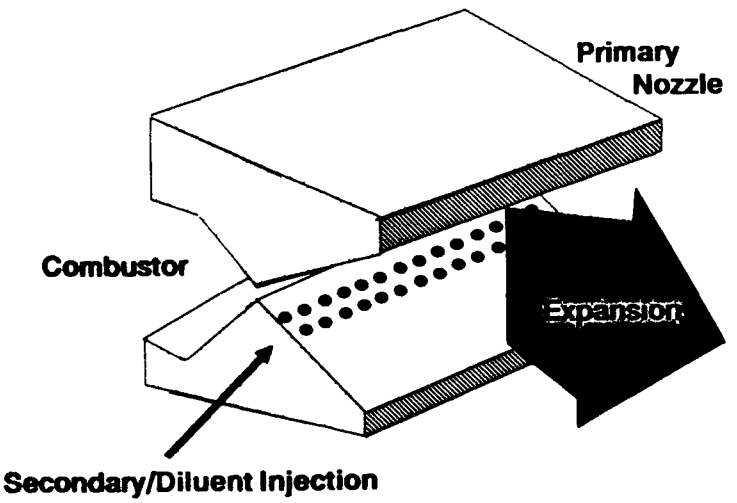


Fig. 8. HYLTE Nozzle

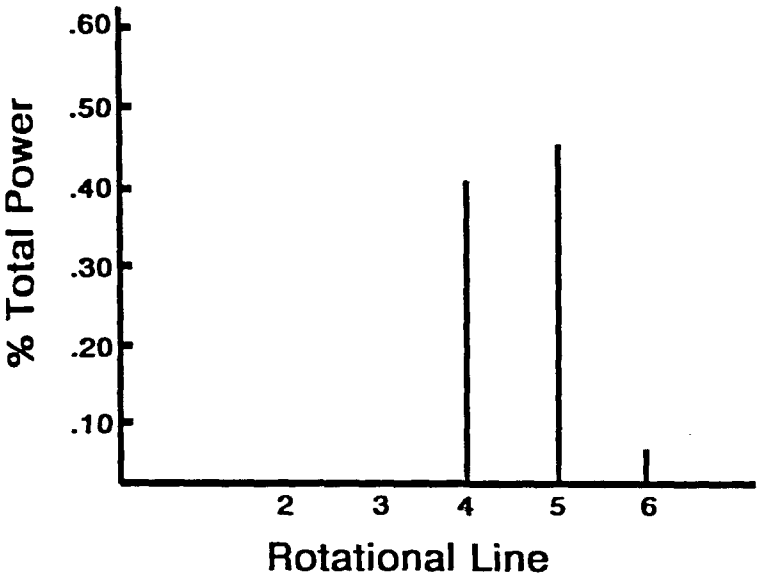


Fig. 9. HYLTE Spectrum

The success of these first supersonic experiments was somewhat misleading as to the true understanding of the overtone chemical laser concept. This fact was dramatically illustrated in the failure to demonstrate the scalability to higher power levels using larger nozzle hardware, ALPHA Verification Module (VM). To scale to higher power levels the more conventional closed cavity reflective optics were used. The gain length of the VM was such that the reflectivity suppression of the first generation optical coatings was inadequate to prevent fundamental lasing. The initial tests failed due to inadequate optical discrimination at the low fundamental rotational transitions. Improvements were made in coating design that achieved complete suppression of the fundamental transitions and allowed the demonstration of overtone performance at 25% of the fundamental at a total power level of approximately 4 kilowatts. However, these results were limited by repeated optical coating failure at flux levels greater than 30 $kw/cm^2$. The following section will discuss the optical coating development in more detail. These VM tests did provide a much better understanding of the difficulties in the design of optical coatings highly reflective at one wavelength, totally absorbing in another, and having a characteristic damage threshold sufficiently high to support high power lasing.

Differences in mode lengths between the overtone and fundamental lasing indicated that the optimum overtone nozzle design would not necessarily be identical to that for the fundamental laser. All supersonic lasing tests to this point had been run using existing hardware residual from previous chemical laser technology development programs that addressed fundamental lasing. The ZEBRA nozzle, Fig. 10, was designed, fabricated and tested to better understand the geometric influences of the HYWN nozzle on overtone lasing. This hardware, along with redesigned optics and resonator configuration demonstrated overtone lasing at 56% of the fundamental at a total power level in excess of 4 kilowatts. The overtone lasing spectrum is again simple as compared to the transition rich fundamental. Figure 11 provides a chronological summary of the overtone performance data.

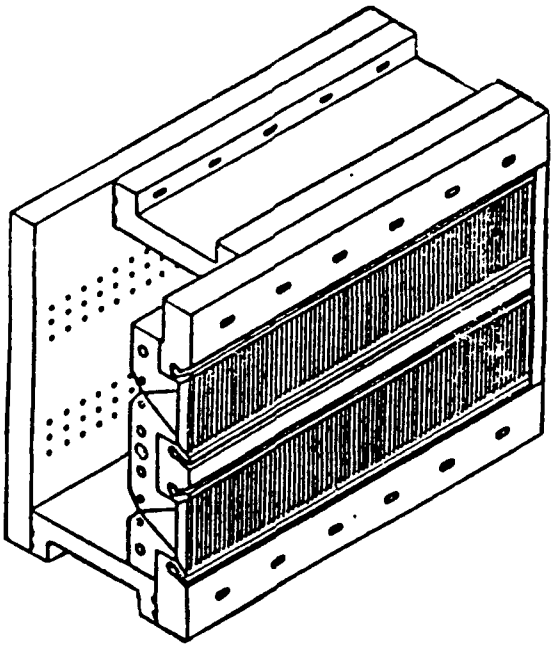

Fig. 10. ZEBRA Nozzle

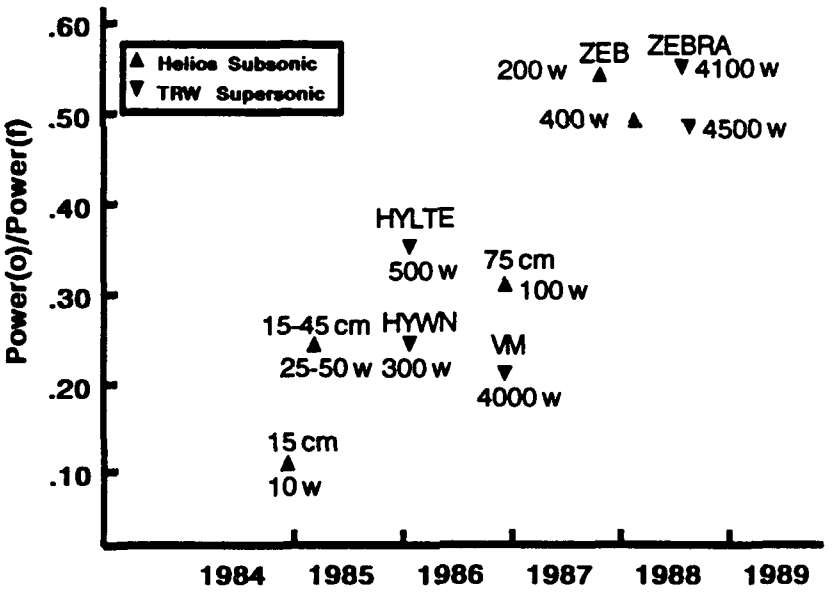


Fig. 11. Overtone Lasing Performance Summary

Previous calculations and experiments indicated a large difference between the magnitude of the small signal gains (SSG) of the HF overtone transitions as compared to the HF fundamental, thereby creating a difficult gain competition to overcome. Experimental SSG data is vital to guide optical coating and resonator design requirements to achieve discrimination and efficient overtone operation. The ZEBRA device was used to make experimental SSG measurements. Figure 12 shows typical SSG traces in scanning from the centerline of a primary nozzle throat to the centerline of an intervening base region between nozzles. Figure 13 is a summary of the vibrational and rotational transitions included in the measurements.

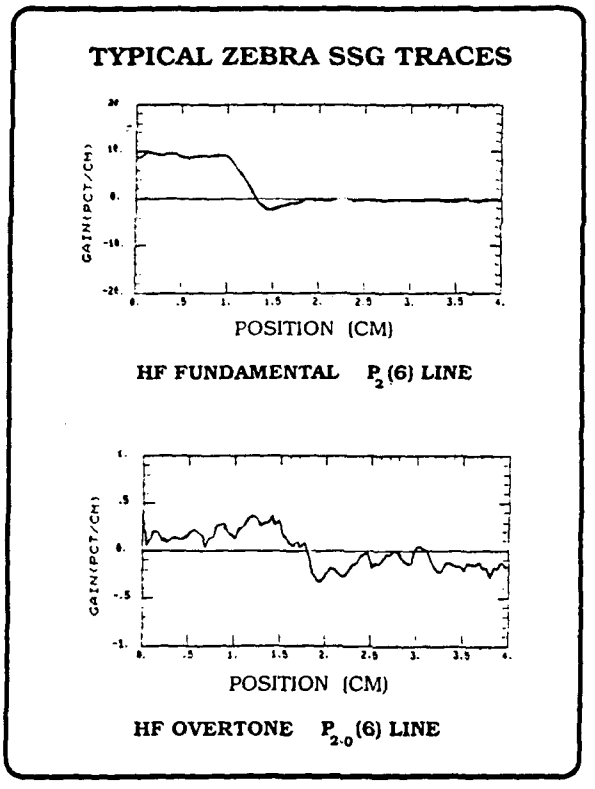


Fig. 12. Typical ZEBRA SSG Traces

## ZEBRA SMALL SIGNAL GAIN SUMMARY

- HF Fundamental v=2-1 Transitions
  Measured ssg of $P_2(3)$, $P_2(4)$, $P_2(5)$, $P_2(6)$, $P_2(8)$ Lines

  v=1-0 Transitions
  Measured ssg of $P_1(3)$, $P_1(4)$, $P_1(5)$, $P_1(6)$, $P_1(8)$ Lines

- HF Overtone v=2-0 Transitions
  Measured ssg of $P_{2\text{-}0}(3)$, $P_{2\text{-}0}(4)$, $P_{2\text{-}0}(5)$, $P_{2\text{-}0}(6)$ Lines

- SSG Summary
  $HF_f$ Range 3 - 12 %/cm

  $HF_o$ Range 0.1 - 0.4 %/cm

Fig. 13. ZEBRA Small Signal Gain Summary

## IV. Optics/Optical Coating Development

The development of unique optical coatings has proven to be critical to the current success of the overtone chemical laser development and will likely continue to be a critical component. Initially the role of the optical coating was not totally appreciated or understood. Several iterations in the development of successful coatings have been necessary to support overtone lasing at the current levels. It was understood that coatings must be developed that were highly reflective to the overtone transition and nearly totally absorbing to the fundamental. These coatings had to be such that the absorbed energy was transmitted efficiently to the cooled mirror substrate and also withstand relatively high power fluxes. What was not initially appreciated was the wavelength band over which the fundamental lasing had to be suppressed. An error was made in the specification of the coating characteristics for the early Verification Module tests. Fundamental lasing typically occurred at wavelengths from 2.7 to 2.9 micrometers in this hardware. The coatings developed adequately suppressed lasing in this band. However, this suppression caused the lasing process to occur at shorter wavelengths, approximately 2.6 micrometers on lasing transitions not normally observed. The optical coating developed and used in these early tests had sufficient reflectively in this region to allow inefficient fundamental lasing to occur. Subsequent developments in the optical coatings for the overtone chemical laser progressed to the point of approximately 0.3% reflectivity over the entire fundamental lasing band and highly reflective in the overtone lasing band. Figure 14 summarizes the development in optical coatings and illustrates performance of current designs. Typical designs are multi-layer stacks of approximately 25 layers. Typical stack materials are ZnS, $ThF_4$, and SiO.

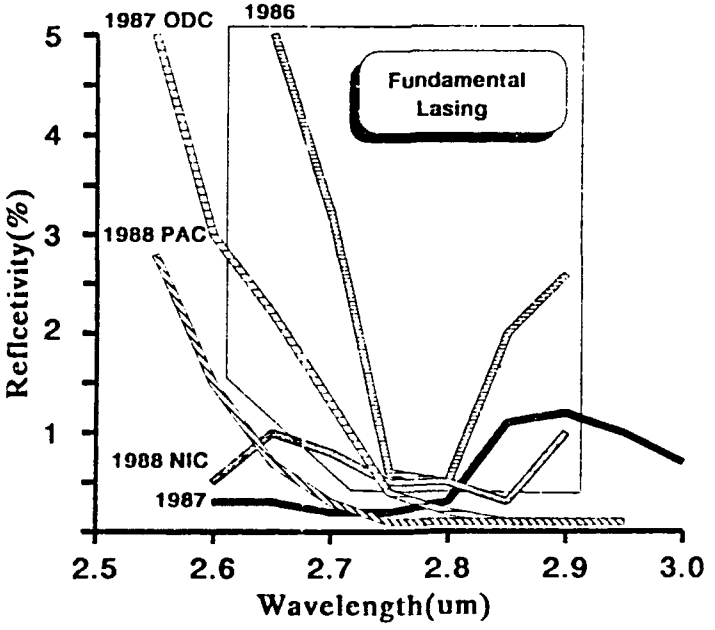


Fig. 14. Overtone Lasing Optics Summary

The coating designations on Fig. 14 are identified as follows:

1986, 1987 - Multilayer Dielectric Coatings (MLDC) from Optical Coating Laboratory (OCLI) for tests on the Alpha Verification Module.

1987 ODC - Optical Diagnostic Coating from Deposition Sciences, Inc. (DSI).

1988 PAC - Partially Absorbing Coating from DSI for metal substrate, heat exchanger mirrors.

1988 NIC - Normal Incidence Coating from DSI.

Details of the DSI coatings are available upon request from the authors at MICOM.

## VI. Acknowledgements

The authors would like to acknowledge the contributions of the following individuals and organizations for their invaluable contributions to the rapid advance of this exciting technology:

HF Overtone Laser Experiments:

William Q. Jeffers
Helios, Inc.
Longmont, CO

Jeffrey L. Sollee
TRW Space & Technology Group
Redondo Beach, CA

Analytical Modeling & Data Evaluation

Wilford Smith, Robert Acebal
Science Applications International Group
Marietta, GA

Optical Coating Design and Analysis

Gary F. Morr, Phillip Goede, William Hansen
W. J. Schafer Associates, Inc.
Woodland Hills, CA

Optical Coating Production

Dennis Kitchens
Deposition Sciences, Inc.
Santa Rosa, CA

## References


1. K. L. Kompa, Chemical Lasers, 37 (Springer-Verlag, New York, 1973).

2. R. W. F. Gross and J. F. Bott, Handbook of Chemical Lasers (John Wiley & Sons, Inc., New York, 1976).

3. W. R. Warren, Jr., Astronautics & Aeronautics, 13, 4, 36, (1975).

4. J. Miller, Proceedings of the International Conference on Lasers 87, Soc. for Optical & Quantum Electronics, p. 190, Dec. 7-11, 1987.

5. C. R. Jones, Proceedings of the International Conference on Lasers, 87, Soc. for Optical & Quantum Electronics, p. 1139, Dec. 7-11, 1987.

6. S. N. Suchard and G. C. Pimental, Applied Phys. Lett. 18, 530 (1971).

7. J. M. Walters, Proceedings of the International Conference on Lasers 88, Soc. for Optical & Quantum Electronics, Dec. 4-9, 1988.

8. W. Q. Jeffers, "Scalable Overtone HF Chemical Laser," U.S. Patent Application 700,123, Filed Feb. 11, 1985.

9. W. Q. Jeffers, AIAA Journal, January 1989, p. 64.

10. J. F. Hon and J. R. Novak, "Chemically Pumped Hydrogen Fluoride Overtone Laser," IEEE J. Quantum Electronics, QE-11, 698-699, (Aug. 1985).

11. A. S. Bashkin, U. I. Ogoshin, Yu S. Leonov, A. N. Oraevskii, and O.E. Porodinkov, "An Investigation of a Chemical Laser Emitting Due to an Overtone of the HF Molecule," Sov. J. Quantum Electronics, 7, p. 626, (May 1977).

12. G. W. Holleman and H. Injeyan, "Multi-Wavelength 2-5 Micrometer Laser," AFWAL-TR-80-1047, p. 14-22 (June 1980). Also: "CW DF Overtone Laser Demonstration," Topical Meeting on Infrared Lasers, Univ. of So. California (Dec. 3-5, 1980).

13. W. Q. Jeffers, "Short Wavelength Chemical Laser Technology Development."

# MANTEST - MICROCIRCUIT CHIP THERMAL SCREENING SYSTEM

Daron C. Holderfield
U.S. Army Missile Command
AMSMI-RD-SE-MT

## I. INTRODUCTION

Hybrid Microelectronic Assembly (HMA) manufacturers are faced with many producibility concerns as the complexity of military hardware continues to increase. These problems are componded by Government requirements for low volumes of complex HMA types. Custom HMAs are used extensively in missile systems as method of intergrating, or packaging, custom electronic functions such as missile guidance and control subsystems.

Semiconductor chips are mounted into the HMA along with other discreet electronic devices, during a labor intensive, costly manufacturing process. The HMA package is then tested, at hot and cold temperature extremes, and hermetically sealed as an assembly.

This paper provides the results of a research and development effort conducted by the Army Missile Command's Research, Development and Engineering Center, which addresses HMA producibility concerns. This effort focused on developing techniques for electrically probing the individual semiconductor chips under concurrent thermal stress prior to assembly into HMAs.

The MANTEST - Microcircuit Chip Thermal Screening System, shown in figure 1, was designed and developed by the Manufacturing Technology Division. The system is semi-automatic, and provides a non-destructive method for probing individual chips at ambient and hot/cold temperature extremes. When coupled with a an electrical test system, MANTEST provides a unique capability for environmentally stress screening individual semiconductor chips.

Of major importance is the system's ability to perform full dynamic screening with a single probe of each chip.

This low-cost system provides a viable approach to improving HMA producibility while lowering production costs. MANTEST can be used to screen selected, critical chip types to validate electrical performance prior to HMA manufacturing.

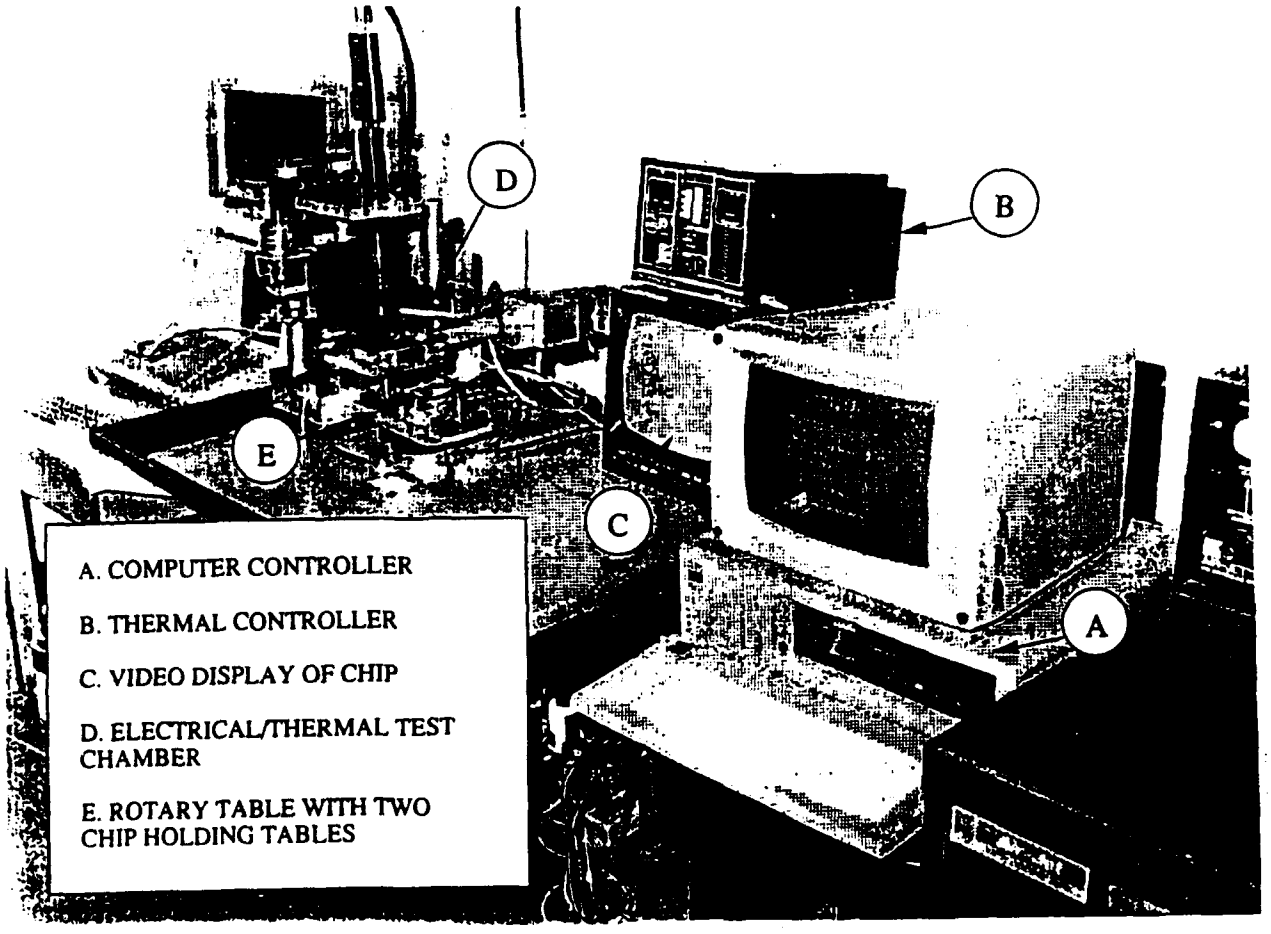


Figure 1. MANTEST - Microcircuit Chip Thermal Screening System

## II. ELECTRICAL/THERMAL PRESCREENING

Military specifications require HMAs to be operated at ambient temperature, and at -55 and +125 degrees Celsius prior to acceptance. The conventional method for determining individual chip acceptability is wafer probing, where chips are static tested (DC capacitance test) at room temperature. This is followed by statistical sampling where only one to five percent of the wafer lot is electrically tested at the temperature extremes. During statistical sampling chips are mounted in custom test fixtures and are retained for future testing and validation purposes. The fixturing allows dynamic electrical testing at hot and cold temperature extremes. Using test results predictions are made concerning the remainder of the lot. Therefore, individual chip reliability is not verified until testing is performed on the HMA. Chip failures discovered at the HMA level result in costly troubleshooting, HMA rework, and repair, and lower the reliability of the HMA.

The Manufacturing Technology Division identified the need for an Electrical/Thermal Prescreening (E/TP) process to pre-test

chips prior to HMA manufacturing. This led to the development of an E/TP process, and the design and development of a prototype system.

The E/TP process consists of electrically probing a single chip at varying temperatures inside a temperature chamber. Hot and cold air is blown around the chip during test cycles. An electrical probe card, similar to a wafer probe card, is lowered to the chips surface. The probe card connects to a user provided electrical test system, and multiple dynamic tests may then be conducted at any temperature over the range from -55°C to +125°C. A thermocouple is positioned inside the thermal chamber to provide real-time temperature feedback.

Chip handling, which is a major concern to HMA manufacturers is accomplished by an operator loading and unloading chips with a vacuum pencil. A rubber tip on the pencil prevents damage; all other E/TP processes have the chip in a fixed location held in place by a vacuum applied to the backside of the chip. The vacuum handling should minimize chip damage concerns.

The MANTEST E/TP process, including electrical probing, is non-destructive and gives the HMA manufacturer a capability to screen chips at varying electrical parameters. MANTEST offers a viable process to increase yields of HMAs by screening select chip types suspected of hot/cold failures. MANTEST can also be used as a part of the chip design verification process to assess operability of new semiconductor designs over a broad range of temperatures.

## III. THE MANTEST PROTOTYPE

Considerable engineering time was spent on the design of the prototype microcircuit chip thermal screening system. The thermal chamber is the center of all activities, yet chip input and output, alignment of electrical probes to the chip, and computerized process control were of equal concern and technical complexity.

Manufacturing Technology Division personnel developed the MANTEST machine concept and prototype design with engineering support provided by contractors. The MANTEST design had to address the following needs:

a) handle multiple types and sizes of chips;
b) input and output to standard chip carriers;
c) non-destructive electrical probing;
d) thermal stress cycle over the range from -55 to +125°C;

e) interface to user-provided electrical test systems;
f) computer controlled processes with minimum operator training and intervention; and
g) man-machine interfacing.

The following paragraphs describe the various modules of the MANTEST prototype.

A. Chip Table

The chip table, shown in figure 2, is the holding mechanism for the individual semiconductor chips. The operator must load and unload chips into the cut-out on the table using a vacuum pencil. Gross alignment of the chip to the electrical probes is accomplished by placing the chip firmly into the cut-out. A hole is provided in the table through which a vacuum is applied to hold the chip in place during the E/TP process.

The design of the table also provides good thermal transfer characteristics. Air flows under the copper table cap to provide thermal transfer to the backside of the chip. The housing is constructed from machinable Macor ceramic.

A theta rotation mechanism is provided to allow the operator to adjust the chip's position with respect to the electrical probes as the entire table is rotated. However, the cut-out and loading process described above is used to align the chip so that electrical probing is possible with little or no manual theta adjustment.

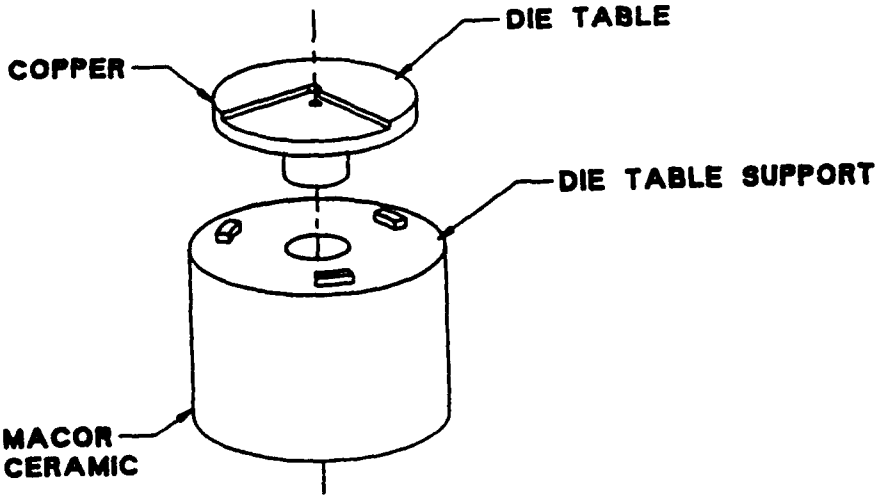


Figure 2. Chip Table

B. Rotary Transfer Arm

The rotary transfer arm provides two chip tables which can be loaded and unloaded while the second is in the E/TP test position (inside the thermal chamber). This eliminates idle test time by allowing the operator to load/unload chips during concurrent E/TP on the second chip table.

The transfer arm rotates exactly 180 degrees between the two positions and is restrained by magnetic stops. The operator manually rotates the table and a magnet locks the transfer arm into the test position while the electrical probes are down and in contact with the chips surface. Once testing is complete, the probes are raised to a safe location and the arm is unlocked.

C. Thermal Chamber

A thermal test chamber, shown in figure 3, was designed and developed to interface with a closed-loop thermal forcing unit. The chamber allows a positive air flow onto the chip under test and provides the integration point for the chip and electrical probes.

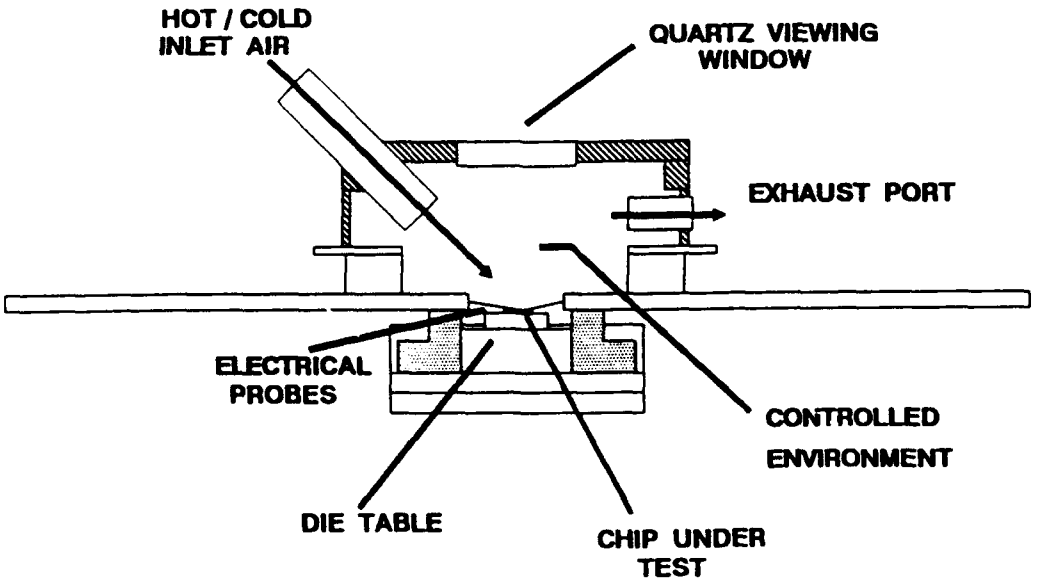


Figure 3. MANTEST Thermal Chamber

The chamber has a total volume of approximately 1.5 cubic inches and was optimized for distributed air flow. Thermal forcing is accomplished by a commercial unit which uses compressed air or nitrogen to achieve a desired temperature at a controlled level of air flow. The unit is computer controlled and uses a thermocouple, mounted inside the thermal chamber, to maintain the desired temperature. With the present MANTEST prototype system configuration, a temperature cycle of ambient, -55 and +125$^{o}$C can be accomplished in less than one minute.

Two exhaust ports are used for exit air flow from the thermal chamber. A quartz viewing window, located in the top of the chamber, is provided for the final chip alignment process. A closed circuit video camera, with an appropriate lens set, is used to view the chip and electrical probes. Display is accomplished via a 12 inch video monitor.

An electrical mother board assembly is mounted inside the thermal chamber. An electrical probe card, which is chip specific, is then mounted to the mother board assembly. This capability allows rapid change-over from one card/chip type to another. An output electrical interface is provided by the mother board assembly for connecting to user provided electrical test systems.

The thermal chamber, with electrical probe card is lowered to the chip table (Z axis alignment) during the E/TP process. The chamber is mounted on a vernier mechanism which is motor diven, and is raised and lowered to pretaught positions under computer control. A seal is provided on the chip table such that once the probes are lowered to the chips surface, the thermal chamber is closed to assure control of air flow.

X and Y axis alignment is also accomplished through the thermal chamber assembly. Micrometer driven sliding mechanisms allow the electrical probes, mounted to the chamber, to be acurately positioned by the operator. This is accomplished while viewing the chip and electrical probes on the video monitor.

D. Video System

The MANTEST video system consists of a video camera, appropriate lens, and a 12 inch display monitor that provides a magnified view of the chip under test. The camera looks straight down through the temperature chamber window at the probes and chip.

The video camera is equipped with a zoom 6000 6.5 power lens. Illumination of the test area is achieved with a high-intensity fiber optic annular light source. Alignment of electrical probes to the chip under test is simplified by the video display and the manual, micrometer driven, X and Y axis mechanism described earlier.

E. Computer Controller

MANTEST E/TP processes are controlled by an IBM PC-XT compatible computer system. The standard XT has an IEEE-488 bus which links the MANTEST control software to the Z axis motor, rotary table locking mechanism, thermal forcing unit, and the user provided electrical test system.

Process parameters are stored integral to the computer control software. This includes, Z axis location of the chip (electrical probes contact the chip surface), and hot and cold temperature settings.

The software is user friendly, and provides detailed prompts and menus displayed on the computer screen, to lead the operator through the MANTEST E/TP process. All MANTEST options are listed and the operator can select the appropriate function. The software is structured to prevent operator keyboard entry errors, and escape sequences allow orderly system shutdown in the event of a software error.

The software was written in compiled C code, and uses windowing techniques to provide the user with machine information and process parameters.

IV. MANTEST E/TP PROCESS STEPS

The following process steps are typical of a dynamic chip test. This assumes that the operator has setup temperature parameters using the MANTEST software schema, and has taught the Z axis location of the chip.

a) operator loads a single chip onto the chip table;
b) operator rotates the transfer arm 180 degrees;
c) Z axis automatically lowers to a safe position with the probes just above the chips surface, transfer arm is locked into place;
d) operator manually adjusts X, Y and theta alignment
e) operator accepts alignment by keyboard response to the computer;
f) Z axis automatically lowers to the chip surface;

g) computer initiates thermal cycle providing the desired temperatures;
h) electrical tests are performed while operator loads the second chip table;
i) operator accepts test results by keyboard response and the Z axis is raised to a safe position and the transfer arm is unlocked; and
j) the process is repeated beginning at step b.

While the process is semi-automatic and subject to operator error, it has been proven to be highly reliable and repeatable. The key process steps are operator handling of the chips, and alignment of the electrical probes to the chip. Therefore, operator performance is critical.

## SUMMARY AND CONCLUSIONS

The MANTEST system is currently available to the industrial base for implementation, and a demonstration model is set up at at Redstone Arsenal for user evaluations. Technical support is available to the industrial base to assist in the technology transfer of the MANTEST system and the thermal forcing concept.

Test results, to date, have demonstrated the validity of thermal prescreening as a means to reduce HMA manufacturing cost. This technology can be applied to the manufacture of HMAs to improve yield at burn-in and reduce labor intensive rework.

# AUTOMATED HERMETIC SEALING OF MICROCIRCUIT PACKAGES USING Nd:YAG LASER WELDING

Daron C. Holderfield
U.S. Army Missile Command
AMSMI-RD-SE-MT

## I. INTRODUCTION

An Automatic Hybrid Package Sealing System (AHPSS) was developed by the U.S. Army Missile Command under the DoD Manufacturing Technology (MANTECH) Program.

The MANTECH Program provides a mechanism to improve the producibility of military hardware through research and development (R&D) appropriations. Focusing on manufacturing processes, equipment, materials, and other associated manufacturing elements, the MANTECH Program objective is to reduce military production costs through the development and implementation of generic manufacturing technologies.

The AHPSS, shown in figure 1, is a fully-automated system for hermetically sealing microcircuit packages. A laser subsystem is used to weld lids on packages; robotic subsystems transport packages through the laser welding processes, and computer control provides complete system integration.

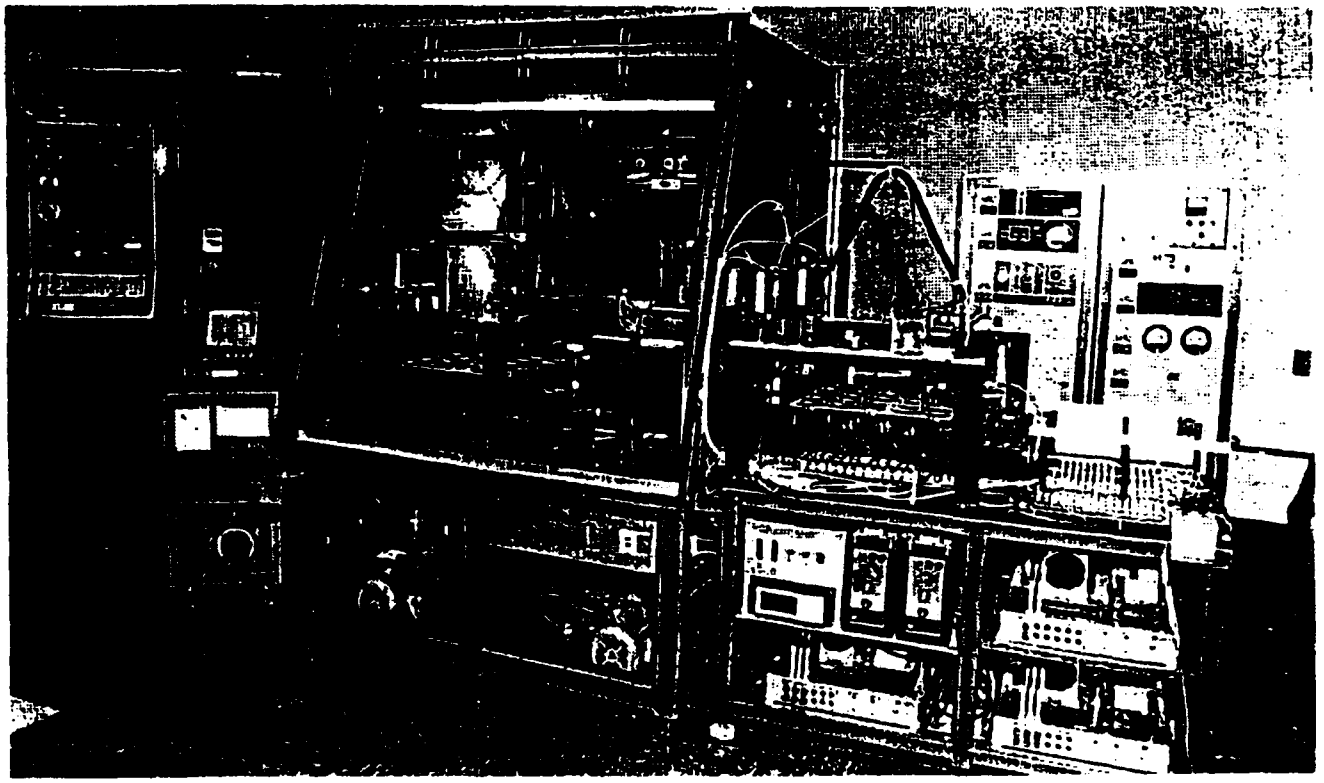

Figure 1. AHPSS with front cover removed

This paper will present a technical description of the AHPSS and discuss the parameters associated with quality Nd:YAG laser welding. The system is currently located in building 8972, Redstone Arsenal, AL. On site demonstrations and additional technical data are available to individuals and enterprises eligible under DODD 5230.5, through the RD&E Center's MANTECH Technology Transfer program.

## II. THE NEED FOR HERMETIC SEALING

Hermetic sealing is required for hybrid microelectronic assemblies used in military weapon systems which must withstand extreme thermal stress, moisture, and long-term storage. Hybrid microcircuit packages, shown in figure 2, are used in missile systems due their relatively small size and weight, custom performance offerings, and overall electronic integration characteristics.

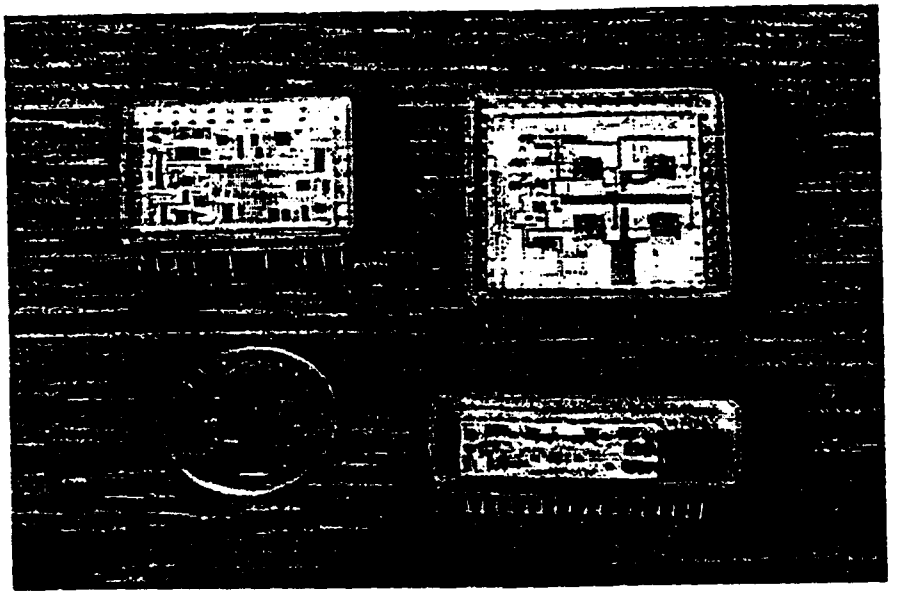

Figure 2. Typical Hybrid Microcircuit Packages without Lids

While conventional microcircuit package hermetic sealing methods have been adequate for most military applications, the processes are labor intensive, operator sensitive, and cannot accommodate some custom military package types due to non-conventional shapes and package/lid material combinations.

The Manufacturing Technology Division, System Engineering and Production Directorate which is part of the Research, Development and Engineering Center, identified the need for improved and automated hermetic sealing processes in 1984. Detailed engineering concepts and baseline designs were developed which included robotic package handling to reduce manual, labor intensive, handling processes; laser welding to provide welding process flexibility; and computer control to reduce process parameter errors (operator mistakes) which are inherent in conventional sealing equipment.

MANTECH Task 1095, entitled "Automatic Sealing of Hybrid Microelectronic Packages" was initiated in 1985 with the following technical objectives:

1) Develop a fully automated manufacturing system for hermetically sealing hybrid microcircuit packages
2) Develop laser welding based sealing techniques
3) Develop robotic material handling and computer control
4) Transfer new hermetic sealing techniques to the industrial base

The key thrust of the MANTECH Task was laser welding due to the need for greater flexibility to process non-conventional package shapes and material combinations. This was a major concern in 1984 and continues to be a producibilty/manufacturing concern today.

## IV. THE AUTOMATIC HYBRID PACKAGE SEALING SYSTEM

The AHPSS integrates Nd:YAG laser welding with moving optics, robotic package handling, and computer control to provide a unique capability for hermetic sealing of microcircuit packages. Automated processes include:

1) moisture bake-out in a vacuum bake oven,
2) package and lid alignment at the weld site,
3) laser welding in a controlled inert atmosphere,
4) robotic package loading and unloading, and
5) fine leak detection.

The following paragraphs describe each system module and peripheral tooling which are used in the automated hermetic sealing process.

### A. AHPSS TRAY

An 18 inch by 18 inch tray was designed as a carrying fixture for AHPSS batch processing. The tray design accommodates twenty-five microcircuit packages, which are located on a carrying fixture called a pallet. Trays are moved through the AHPSS on a rail mechanism with motor driven push-pull arms. Tooling pins on the tray provide a known location and a hold-down mechanism for each of the twenty-five pallets. The tray is made of aluminum and is fabricated in a manner to minimize overall weight.

### B. AHPSS PALLET

The pallet was designed as a carrying fixture for individual microcircuit packages during AHPSS processing. Four corner stops are provided to restrain the package and lid in the desired orientation. The pallet design also provides a constant distance, 125 mm, from the lens. Both of these features are essential to AHPSS operations, and require a custom pallet design for each

configuration of package processed on the AHPSS. Currently, pallets are machined from aluminum stock and require approximately one hour to fabricate. Two holes are provided in the pallet for handling by the overhead gantry robot's grippers.

C. MOBILE VACUUM BAKE OVEN

The vacuum bake oven was designed as a mobile unit, independent of the AHPSS, to allow multiple units to support off-line vacuum bake-out. Any vacuum bake oven unit may be connected to and integrated with the AHPSS as required. The oven consists of a vacuum vessel, exterior frame with metal housing mounted on wheels for mobility, a vacuum pumping system, automatic temperature control, manual operated door for loading trays of packages, and an automatic door coupled to the environmental chamber for unloading trays. A vertical conveyor inside the oven allows stacking of 8 trays with each containing a maximum of twenty-five microcircuit packages/lids. The conveyor presents each tray to the automatic door for insertion into the AHPSS environmental chamber.

D. GANTRY ROBOTS

The pallets are handled through AHPSS processes by three overhead mounted gantry robots with integral grippers. These are called the load gantry, the shuttle gantry, and the unload gantry. Each gantry consists of a combination of single-axis, permanent magnet, synchronous linear reluctance stepper motors. The linear motors use a moving element called a forcer, which travels along a ferromagnetic track called a platen. The load gantry and unload gantry each have X and Y axis motion and use dual forcers and platens. The shuttle gantry only travels in the X axis and uses a single forcer and platen. The gantry robots run in an open-loop mode using micro-stepping techniques for high resolution and repeatability at 0.040 inch resolution and 0.002 inch repeatability.

E. GANTRY ROBOT GRIPPER ASSEMBLIES

A gripper end effector assembly, shown in figure 3, is attached to each of the three gantry robots. The gripper picks up and deposits a single pallet at various process points of the AHPSS. The grippers are air-solenoid driven, with spring return pivotal mechanisms (male tooling pins) which mate with bushed tooling holes on AHPSS pallets. When activated, the mechanism grips the pallet, raises vertically to a preset clearance, and then is positioned to the next desired location by the gantry robot. The gripper's tooling pins are retractable, meaning if an error in positioning occurs, the tooling pin prevents Z axis crashing and resultant damage. The load gantry gripper has a detection switch to identify if a lid accompanies the desired package, and serves as a lid hold-down mechanism while the pallet, package, and lid are transferred from the input tray to the rotary table where welding is accomplished.

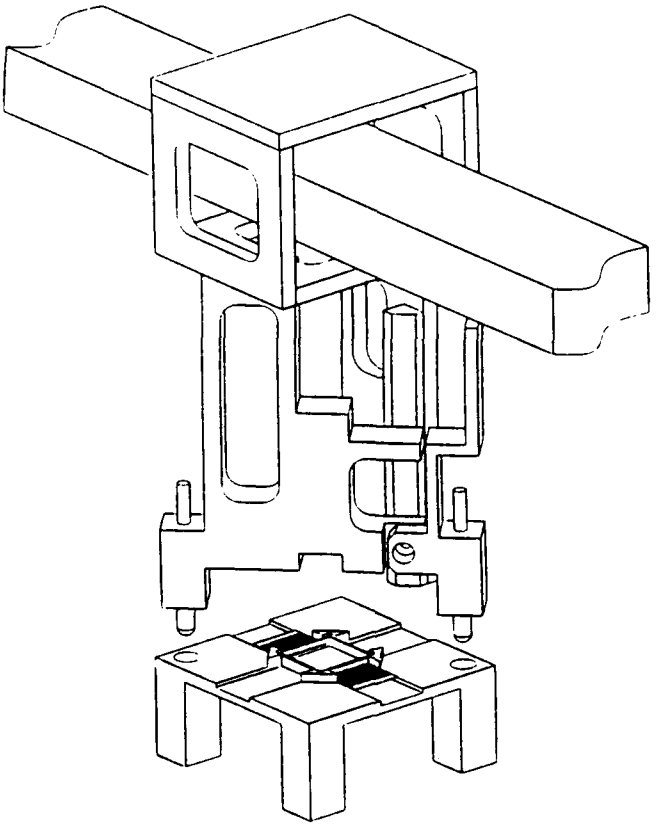

Figure 3. Gantry Gripper with Pallet and Package

## F. ROTARY TABLE AND PACKAGE/LID ALIGNMENT MODULE

A pallet with a package and lid, is transferred by the input gantry robot to a rotary table at the initiation of a welding sequence. The rotary table, with four pallet locations, steps in 90 degree increments for pallet/package loading, welding, and unloading. The fourth location is not used unless the AHPSS is in the "fully-automatic" mode.

An electro-mechanical centering mechanism, shown in figure 4, is used for package-to-lid alignment which also aligns the combinations both with respect to the position of laser beam. The centering mechanism consists of four spring-loaded fingers mounted on linear rack and pinion slides. The fingers are driven in pairs to push the package in the X and Y axis utilizing a slip-clutch concept. The continuous slip-clutches allow one pair of alignment fingers to continue moving after the other has made contact with the package. A second set of fingers, which work the same way, are used for lid alignment.

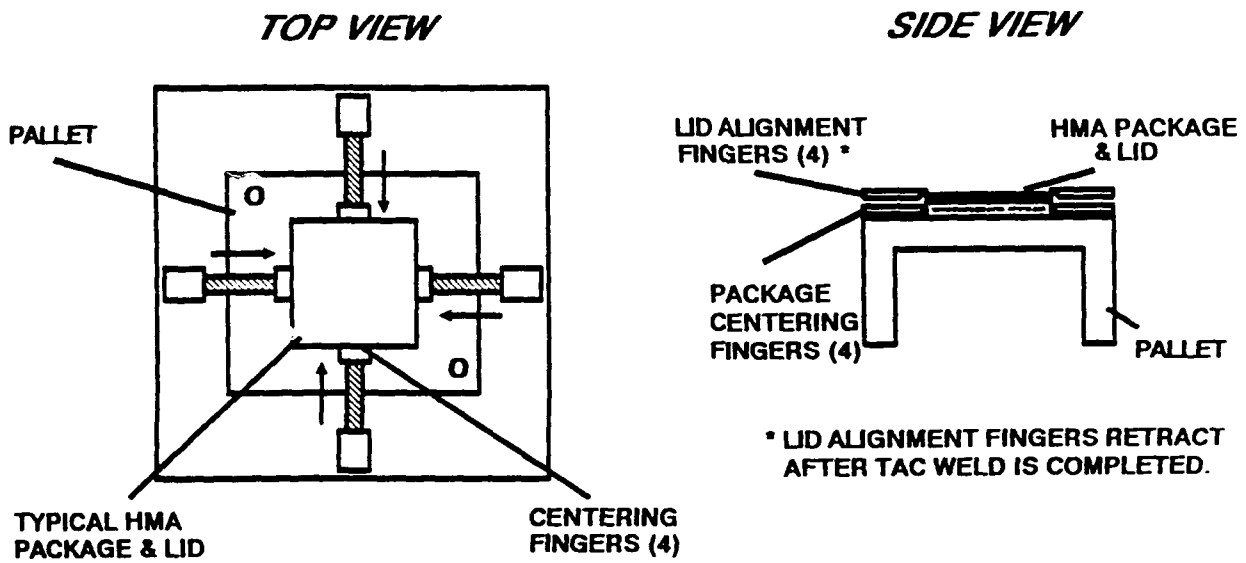


Figure 4. Package and Lid Alignment Module

G. Nd:YAG LASER SUBSYSTEM

Laser welding is accomplished with a pulsed Nd:YAG laser which can produce up to 400 watts average power. Laser components include a laser optical assembly, power supply, programmable controller with multiple input/output ports, operator interface (console), and gas control system. A low-power helium-neon (HeNe) laser is integrated with the YAG for optics alignment and programming of weld paths/programs. The laser optics assembly is rigid-mounted to the AHPSS frame, and is self-contained in a lockable laser casket.

The Nd:YAG (neodymium-doped yttrium-aluminium-garnet) laser rod measures 0.375 inches in diameter and 6.25 inches in length. The rod is mounted at the center focal point of a double ellipse cavity. A krypton flashlamp is at each of the two minor foci of the ellipse. The lamps and rod are mounted in a block called the laser head, which is cooled with three parallel water flows. Lasing is created by interaction between the laser head and mirrors when energy is pumped in through the flashlamps. The laser head and mirrors form an oscillator cavity approximately 16 inches in total length (the cavity contains one fold to reduce size). A curved mirror with 100% reflectivity and a partially reflective flat output mirror produce intracavity feedback, inducing laser action. This produces a laser beam with 15 mrads divergence.

Laser pulse characteristics are controlled by parameter settings in the programmable controller. Through front panel (operator console) settings or pre-taught software, laser pulses can be varied from 0 to 5 joules per millisecond, from 0 to 20 milliseconds in length, at up to 200 pulses per second. The maximum average power is 400 watts, with 50 joules maximum energy per pulse. The beam is invisible infrared, with a wavelength of

1.06 um. Upon exiting the oscillator cavity, the laser beam passes through a collimator which doubles the beam diameter and reduces divergence to about 8 mrads.

After exiting the laser casket, the beam is directed through a measurement cabinet which contains a pyrometer that can be moved into the beam-path when measurements to evaluate laser power are required. This is used to monitor the power performance of the laser system.

H. MOVING OPTICS MODULE

Beam positioning within the AHPSS work area is accomplished by a moving optics module. X and Y axis servo motors provide positioning of two orthogonal mirrors to precisely direct the beam to the AHPSS work area. The module is mounted to the AHPSS overhead frame and uses slide mechanisms with lead screws for high accuracy beam positioning. The optics module is controlled by the laser controller. This provides full electro-mechanical integration for process control. Final beam shaping in the Z axis is accomplished by a 125 mm focal length lens which places a beam of approximately 0.035 inches diameter on the target. The focus can be manually controlled by a motorized micrometer.

A key feature of the moving optics module is the integration of a video camera, mounted behind the final mirror, which is used to view the laser beam path in the work area. Display is accomplished via a 9 inch video monitor with approximately 30 power magnification. This capability provides the method for an operator to develop new weld beam paths using the HeNe beam. The display is also used to monitor YAG beam positioning during actual welding sequences.

I. ENVIRONMENTAL CHAMBER

The AHPSS environmental chamber encloses the system's frame along with robotic package handling and moving optics modules. Ante-chambers are provided for interfacing the vacuum bake oven with the environmental chamber, shuttling welded packages on a pallet to the leak detection module, and output of empty trays. Therefore the chamber is quite large as compared to conventional sealing dry-boxes due to the automation elements.

A front cover panel viewing port is provided with eye safe shielding to permit observation of YAG laser operations. This allows the AHPSS to operate as a Class I laser system.

The AHPSS purification system is self-contained and provides a 40 cfm recirculation blower, moisture and oxygen removal to less than one part per million, pressure control system, and automatic regeneration. A parallel regeneration loop is provided with an additional 100 cfm filtration. This exhausts all by-products produced during laser welding. The environment is maintained at 90% argon with 10% helium as a tracer (leak detection) gas.

## J. LEAK DETECTION MODULE

This module was developed as an AHPSS in-process hermetic evaluation and not to meet MIL-STD-883 specifications. This provides immediate feedback as to the quality of laser welding processes to the host computer. A standard commercial leak detection system was integrated with the AHPSS for remote programming and control. This helium mass spectrometer leak detection system detects leaking tracer gas from packages sealed in the AHPSS chamber. Packages are loaded into a leak detection chamber by the unload gantry robot.

## K. AHPSS HOST COMPUTER AND SOFTWARE

The system is controlled by an IBM PC-AT compatible computer host system with RS-232 serial interfacing to individual system modules and subsystems. While the laser controller provides control of the laser, rotary table, and moving optics module, all other AHPSS functions are controlled by the host computer. The laser controller is fully integrated with the host computer which monitors each task.

The AHPSS host computer is menu-driven with operator interface via a mouse-device and keyboard. The software is extremely efficient and modular. From the main menu the operator can select the desired option. Most options from the main menu call other menus. If run-one-part is selected at the main menu, a run-one-part menu is displayed.

Any function of the AHPSS can be operated independent of other subsystem functions under host computer control using the "single-step" mode. This was very useful during the development and debugging of each subsystem module. The "run-one-part" mode automatically sequences one package through all AHPSS processes. In the "fully-automatic" mode, the system will continuously run packages, without operator intervention, and allows the AHPSS to perform some tasks in parallel to increase system throughput.

The host computer is hardware and software interfaced to numerous limit switches and sensors to monitor AHPSS operations and process errors. The host computer controller also interfaces with the leak detection module to allow desired leak detection parameters to be stored integral to the AHPSS.

# V. Nd:YAG LASER WELDING PROCESSES

The following paragraphs describe the AHPSS hermetic sealing and leak detection processes, and the methodology for programming the system to operate under computer control.

Parts flow through the AHPSS, shown in figure 5, in a batch mode. Process steps, after a tray of parts has been transferred from the mobile vacuum bake oven, are as follows:

1) Package and lid are transported to the rotary table;
2) Rotary table moves 90 degrees to present the package to the weld station;
3) Alignment module centers package and lid with respect to the laser beam;
4) Laser fires to perform tack welds;
5) Laser fires to perform hermetic seal;
6) Sealed package is transported to leak detection chamber;
7) Leak detection is performed; and
8) Package is transported to output tray.

The AHPSS is structured such that the operator must set up the hardware, software, and operating parameters, and monitor the Nd:YAG laser welding activities for safety purposes. All processes are fully-automatic and under computer control.

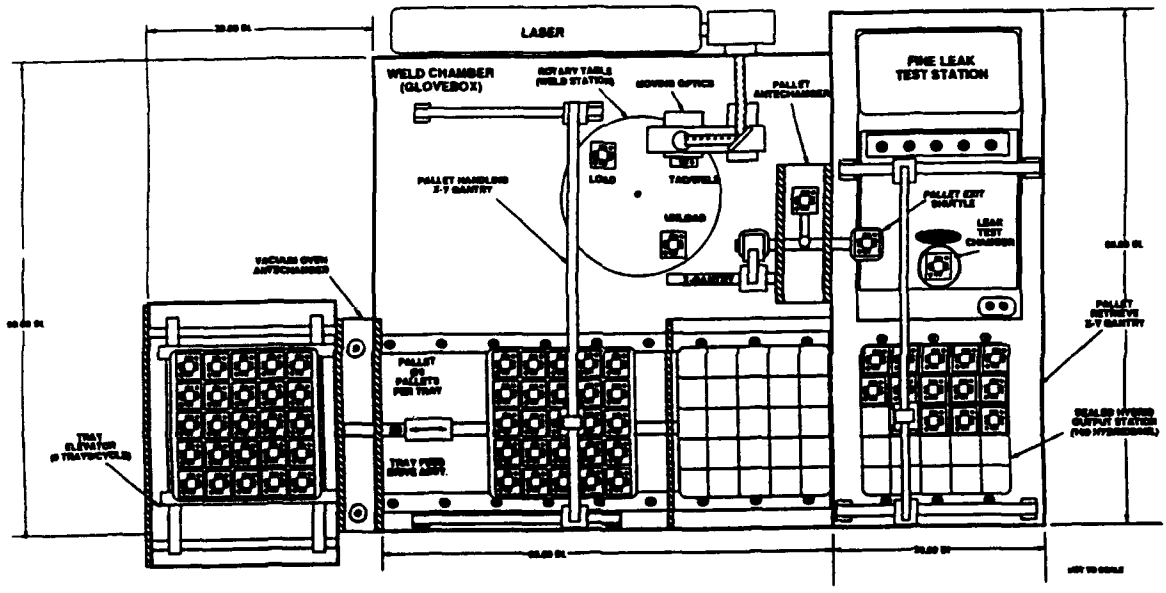


Figure 5. AHPSS Plan View

## VI. LASER WELDING PARAMETERS

Prior to running the AHPSS, the operator must develop a welding program on the laser controller (required for each different package type). The program defines the X and Y positioning of the laser beam on the hybrid package for tack and continuous welds, and laser firing parameters such as energy, pulse length, pulse width, speed of the moving optics, and the number of warm-up shots required.

X and Y locations are taught by the AHPSS operator using the laser controller console, the video camera/monitor which displays a magnified view of the work area, and the low-power HeNe laser.

The HeNe beam, which is visible to the operator, and package are viewed simultaneously on the 9 inch video monitor. The operator will usually select a package corner as a starting point and simply select a beam path (X and Y coordinates) through visual alignment of the HeNe beam to the package. Coordinates are displayed on the laser controller console, and are incorporated into the laser welding program. X and Y coordinates are established for tack weld locations and for continuous welding start and stop locations.

Laser parameters are defined as part of the laser welding program. This includes energy, pulse width and length, and the number of shots (pulses).

A typical set of parameters for a nickel plated Kovar package is as follows:

- WARMUP SHOTS
  - Energy = 0.6 joules
  - Pulse Rate = 30 shots per second
  - Length = 10 milliseconds
  - Number of Shots = 30

- TACK WELD
  - Energy = 0.8 joules
  - Pulse Rate = 30 shots per second
  - Length = 10 milliseconds

- CONTINUOUS WELD
  - Energy = 0.8 joules
  - Pulse Rate = 30 shots per second
  - Length = 10 milliseconds
  - Speed = 15 inches per minute

Warm-up shots are used to excite and energize the laser flash lamps. This capability allows the laser to be "warmed" to 100% average power prior to actual welding, and insures that actual welding parameters are at the desired level.

Parameters for tack and continuous welding must be evaluated and optimized for each packages type. The parameters vary as packages are made up of multiple types of materials such as nickel plated Kovar, gold plated Kovar, and other combinations.

After completing a laser welding program, the operator must save the program to floppy disk. The program can then be executed stand-alone, or in an automated manner with the AHPSS. Programs can also be retrieved from floppy disk as required.

## VII. FUTURE AHPSS GOALS AND OBJECTIVES

Manufacturing Technology Division personnel are currently concentrating on developing and optimizing laser welding process

parameters to support a wide range of package types and materials combinations.

Additional AHPSS and hermetic sealing efforts are planned under the MANTECH Program. This work will focus on developing laser welding parameters and specific processes which are applicable to military microcircuit requirements. Our intent is to transition this technology from the laboratory to the production environment, thus enhancing the industrial base for microelectronics. Resultant data will be offered free to U.S. companies through our Technology Transfer Program.

The AHPSS prototype is installed at the Manufacturing Technology Division's manufacturing research lab at Redstone Arsenal, Alabama. Additional information and on-site demonstrations are available upon request.

## - SESSION II -

SENSORS

# COMBINED ARMS MULTIPURPOSE MISSILE

Jimmy R. Duke
Advanced Sensors Directorate
Research, Development, and Engineering Center

## ABSTRACT

Combined Arms Multipurpose Missile (CAMM) is a Missile Command research and development program being conducted inhouse with industry support to demonstrate an innovative missile guidance concept offering major performance improvements for anti-air weapon system applications.

A multiguidance concept is being developed to extend the use of terminal homing seekers against long range, low signature targets in clutter by combining the features of terminal homing and command guidance into a single, lightweight missile for multipurpose roles. Three modes of operation would be available to cover a wide variety of target and conditions; a lock-on-before-launch fire-and-forget mode always used when the target signature-to-clutter ratio permits, a line-of-sight command guidance mode used when this ratio is low and target lock-on is not possible or in severe countermeasure environments, and finally, a lock-on-after-launch mode that uses command guidance early to guide the missile and point the seeker towards the target to enable the earliest possible target lock-on-after-launch for moderate signature/clutter conditions. The flight demonstration of this third mode is the primary objective of this program. The other two modes separately are well within current technology capability.

Begun in 1988 with the selection of the HELLFIRE missile as a test bed, the program is nearing the completion of hardware development. Static, captive, and missile environment testing is in progress. Flight tests are planned in 1991-92. Design details will be given.

## INTRODUCTION

Combined Arms Multipurpose Missile (CAMM) is a MICOM 6.2 funded technology demonstration program that combines fire-and-forget terminal homing seeker guidance with command guidance on the same missile to achieve a major performance improvement in missile guidance capability. In this case sophisticated target acquisition and guidance hardware is carried on board the missile to achieve higher terminal accuracy at longer range than can be obtained with command or terminal homing guidance alone.

The CAMM program is aimed at demonstrating the availability and maturity of technology to implement this dual guidance concept to allow missiles to operate more effectively at longer ranges.

## OBJECTIVE

Previously, the Army Missile Command has developed lock-on-before-launch (LOBL) seeker technology for its fire-and-forget capability, but with the missile operating range limited to the lock-on range capability of the seeker. Now, with technology advances, the missile range can be extended by flying part of the way with command guidance until the seeker and its processor can lock onto the target and complete the engagement in the terminal homing mode. Demonstration of this lock-on-after-launch (LOAL) capability required to implement a dual guidance concept is the key objective of the CAMM program.

## APPLICATIONS

The CAMM concept, as depicted in Figure 1, has application to a wide variety of lightweight launch platforms and targets, hence the term "multi-purpose." Included in the launch platforms are the future light helicopter (LHX) for the aviation role and a Pedestal Mounted Stinger type of light vehicle platform for the air defense role. The target set includes both air and ground targets. The most difficult target from a seeker lock-on standpoint is the long range helicopter hovering in clutter. The armored target is the most difficult from a warhead viewpoint. Both of these tend to increase missile diameter. The maneuvering fixed wing target drives the missile kinematics which leads to a larger length-of-diameter ratio or longer missile.

The CAMM program is focusing on the first problem of engaging long range, low signature targets in clutter. To this end the innovative dual guidance concept based on the most advanced seeker and image processor technology is being developed. Its objective is to demonstrate a means to rapidly engage any line-of-sight target detected by the platform fire control sensor suite, even when the target signature to clutter ratio is too low to permit LOBL. Flight demonstrations of this technology and concept are planned using the HELLFIRE missile as a test bed. The issues of warhead sizing, airframe kinematics and platform sensor suite development will be left for a future weapon system development program such as The Army Counter Air Weapon System (TACAWS).

## DUAL GUIDANCE

Dual guidance extends the operating range and application of the host missile by adding the capabilities of the two guidance modes. The mid-course command guidance will be accomplished by CO2 laser beamrider due to availability of hardware. Millimeter wave command guidance is another candidate approach for this function. Terminal homing guidance will be implemented initially using TV seekers as surrogates for the more tactically suitable Imaging Infrared (IIR) seekers. Actual flights with IIR seekers are planned for later after proving out the test bed missile with the lower cost TV seeker.

As illustrated in Figure 2, three distinct operating modes are available with the dual guidance concept. The classical lock-on-before-launch, true fire-and-forget mode is available and would always be used when the target signature, clutter and countermeasures environment allow. The lock-on range and use of this mode can be severely restricted by these conditions.

The command guidance mode all the way to intercept is available for adverse conditions when signature, clutter or countermeasures does not allow target lock-on by the seeker. In this mode the missile is tethered to the platform for guidance and its long range accuracy is limited.

By combining the two guidance modes on a single missile, as shown at the bottom of the figure, a third mode which extends the missile operating range and performance is possible. A target "filter" is obtained from the platform's computer library of target optical images and is loaded into the missile seeker before launch. This tells the missile seeker what target to look for within its narrow field-of-view. It is based on all of the information known about the target from the platform's sophisticated sensor suite or from external inputs. The seeker is pointed toward the target while the missile is flown by command guidance toward the target. When the Automatic Target Recognition (ATR) processor is able to establish a correlation between the stored target filter and the seeeker provided video, which includes target and clutter, handover occurs to the seeker target tracker and the engagement is completed in the terminal homing mode. The target filter may also be used for terminal aimpoint selection to provide information to the tracker to obtain the most effective aimpoint for each target.

It is this third mode of operation that is the technology challenge of the CAMMS program and for which hardware is being developed for proof-of-principal flight demonstrations. The first two modes are considered to be well within current capability.

An additional capability is being investigated in which the seeker video also would be transmitted back to the platform to permit operator input and trajectory adjustment. Implementation of this could be by means of a modulated laser retro-reflector in the aft of the missile.

The command guidance approach chosen for CAMMS is a CO2 laser beamrider raster scan implementation, shown in Figure 3. The center of the scan is placed on the line-of-sight (LOS) to the target by virtue of its being boresighted to the TV or FLIR target tracking sensor. The time of arrival of the laser beam on the missile receiver is unique for each position within the raster. The missile is thus able to determine it position and maintain itself on the LOS to the target.

A simplified version of the ATR processor is shown in Figure 4. The target filter consists of a 256 X 256 X 8 bit array of numbers representing the target image in the frequency domain for every 10 degrees of target aspect. Several target filters are required for target growth to cover band of range-to-go. A corresponding array is developed in real time during

flight from the seeker image using a two-dimensional FFT processor. The 256 X 256 array and a 2.2 degree field-of-view produce an instantaneous field-of-view of 150 microradians. This results in 10 pixels within a 3.0 meter dimension of a target at a range-to-go of 2.0 kilometers. This is the CAMM ATR baseline.

A two-dimensional correlation surface, such as is shown in Figure 5, is produced by multiplying these two arrays element by element and taking the IFFT of the result row-by-row and then column-by-column. An analysis of this surface by a general purpose processor identifies the target coordinates corresponding to the best correlation. The target tracker is locked onto the target at these coordinates and hand-over is completed. The target is then tracked to intercept in the terminal homing mode.

## CAMMS HARDWARE

The CAMMS test bed missile, shown in Figure 6, is divided into two parts; the CAMMS unique forward section with its seeker, processing electronics and telemetry package and the back section which is HELLFIRE except for the rearward looking CAMMS command guidance CO2 laser receiver and associated hardware.

The completion of the design and fabrication of the first prototype missile is expected this year. This missile will be used to validate the design and all electrical and mechanical interfaces. Subsequently, up to six flight missiles will be assembled with TV seekers for flight tests in FY91.

Examples of CAMMS hardware in-hand are in Figures 7 through 10. The TV seekers were obtained from Boeing and are a variant of the FOG-M seeker. A gimbal mounted Sony XC-37/47 CCD camera/optics provides a 2.0 degree field-of-view with an RS170 format output. A low drift rate in the rate mode of less than 60 degrees per hour in the pitch plane (0.33 degrees, 1 sigma, during a 20 second flight) is obtained through the use of an improved Northrop 2-axis rate gyro. This helps insure that the target will remain in the seeker's field-of-view during the command guidance phase.

The tripod mounted CO2 laser beamrider beam projector was obtained through Ford Aerospace and is related to their AAWS-M effort. This projector can provide command guidance to the maximum range of the HELLFIRE test bed missile if needed. The wing-mounted command guidance receiver includes a cryogenically cooled HgCdTe detector, filter, optics, and preamp. It provides a 4.0 mm diameter aperture with a 30 degree field-of-view.

The biggest technical challenge of the program has been the packaging of the ATR and guidance electronics into the HELLFIRE test bed missile even though it is 7.0 inches in diameter and the warhead has been removed. Shown is one of eight PC boards that go into the front of the missile behind the seeker to do the CAMMS function. Four of them are associated with the ATR processor. Each of these boards is multilayer with one having eight layers.

Further downsizing of the electronics can be expected in the future with advancements in processing density and speed as would be required for a 4 to 5-inch diameter tactical implementation.

## SUMMARY

As a summary, the schedule of Figure 11 shows that hardware design and development has been essentially completed. Component testing and algorithm development are on schedule this year and should lead to TV seeker flights in FY91 at the Eglin AFB, FL HELLFIRE test range. If affordable IIR seekers can be obtained, they could be integrated into the test bed missile and flown in FY92 to be ready for TACAWS, an Advanced Technology Transition Demonstration (ATTD) planned to start in FY93.

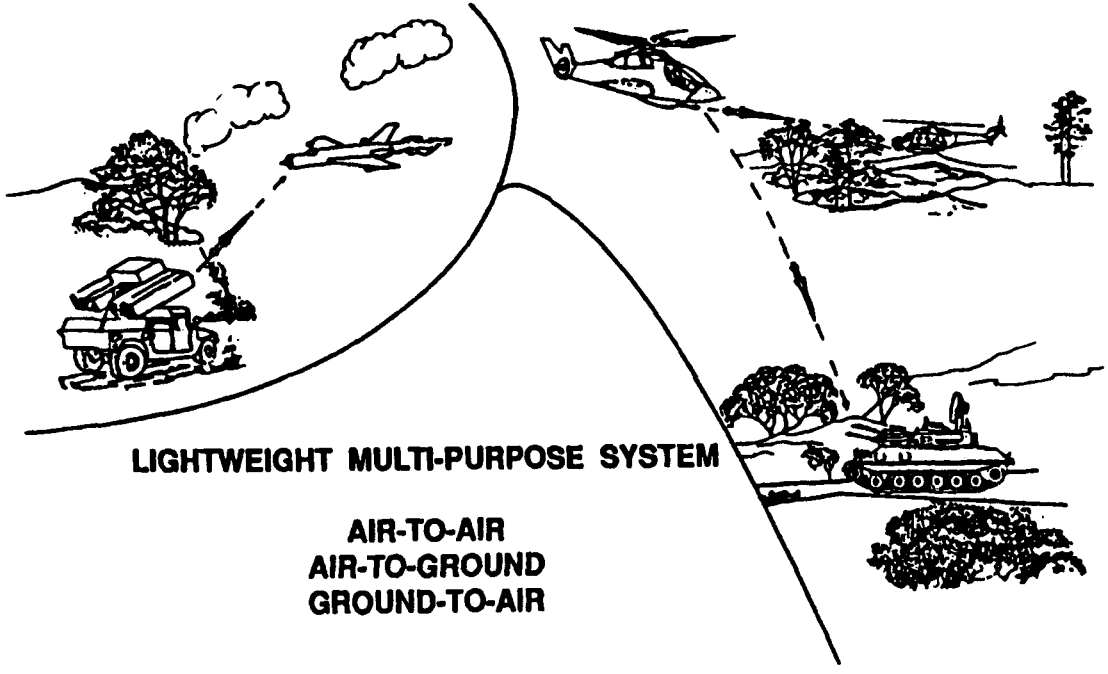


Figure 1. CAMMS Applications

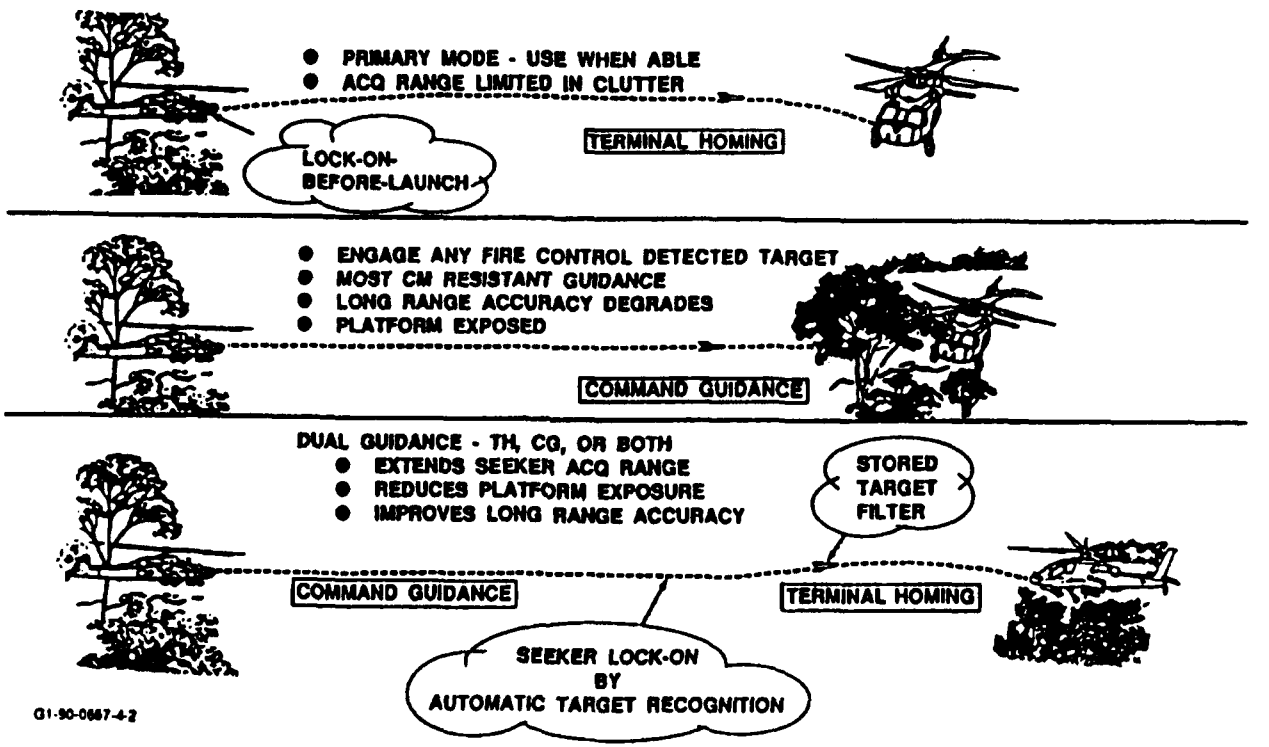


Figure 2. Dual Guidance Concept.

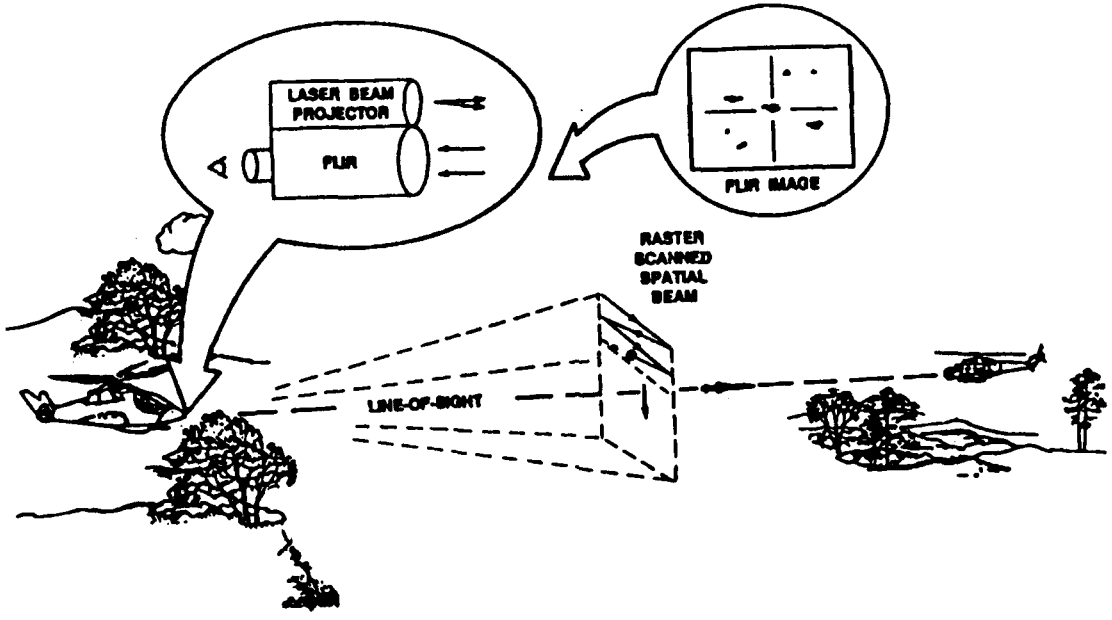


Figure 3. Laser Beamrider Guidance Concept.

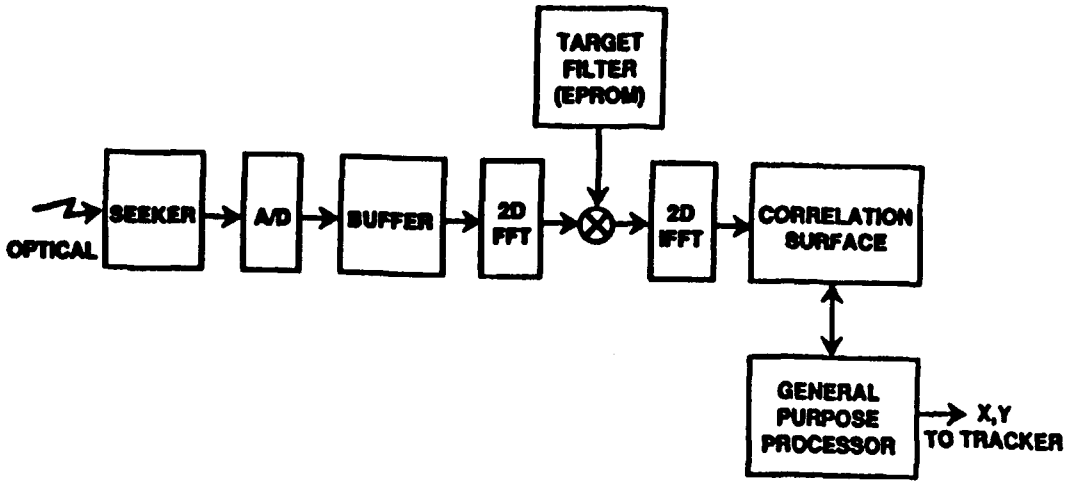


Figure 4. ATR Processor.

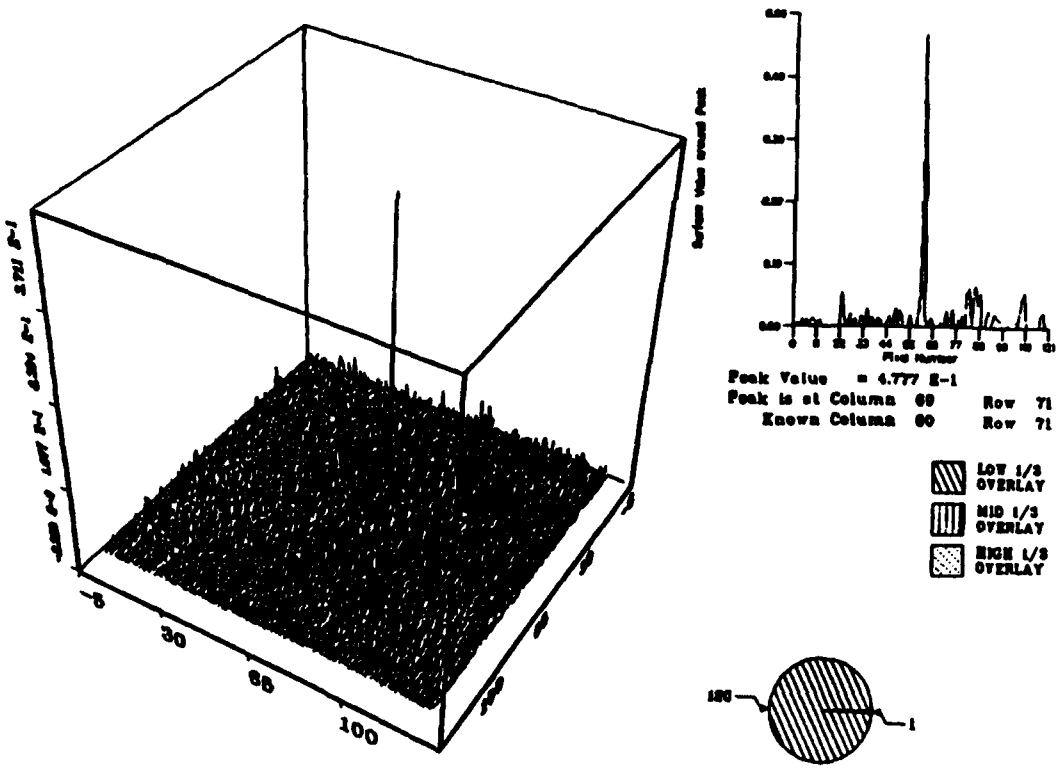


Figure 5. Typical Correlation Surface.

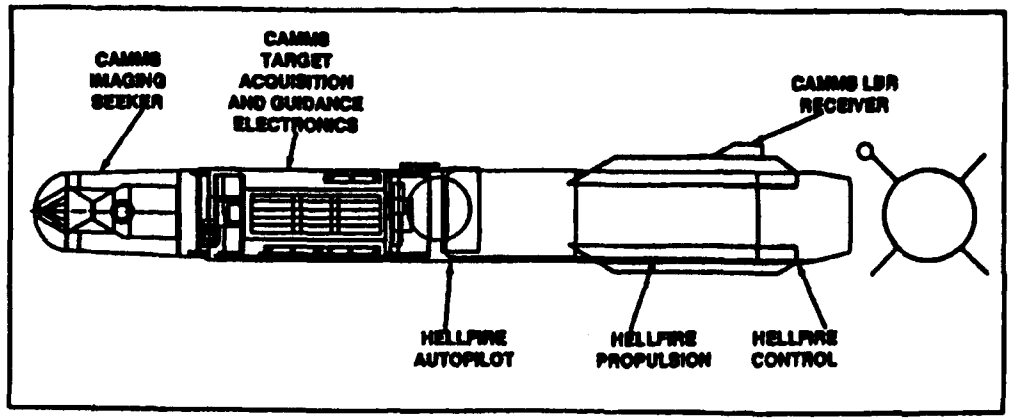


Figure 6. CAMMS Test Bed Missile.

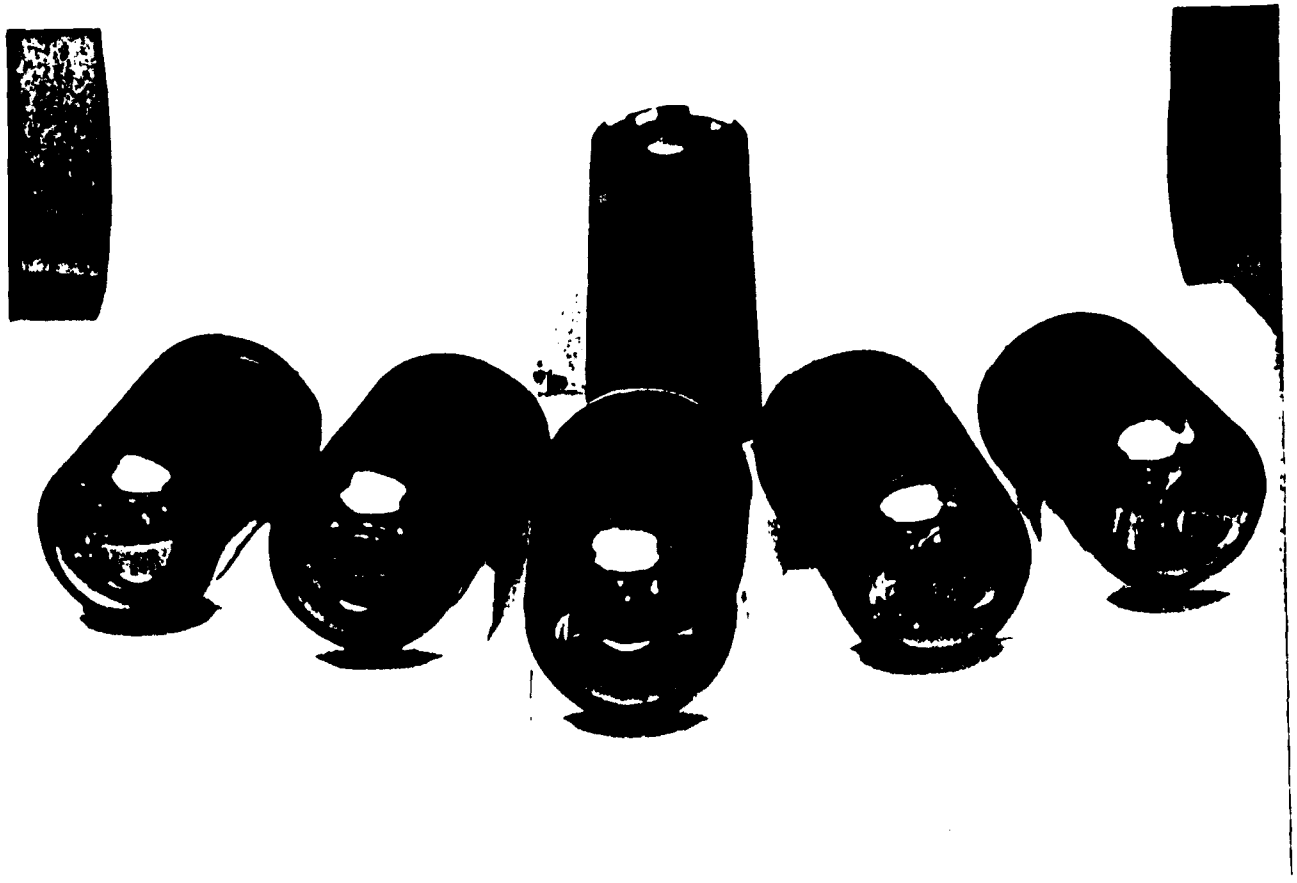

Figure 7. CAMMS TV Seekers.

Figure 8. C02 Laser Beamrider Beam Projector.

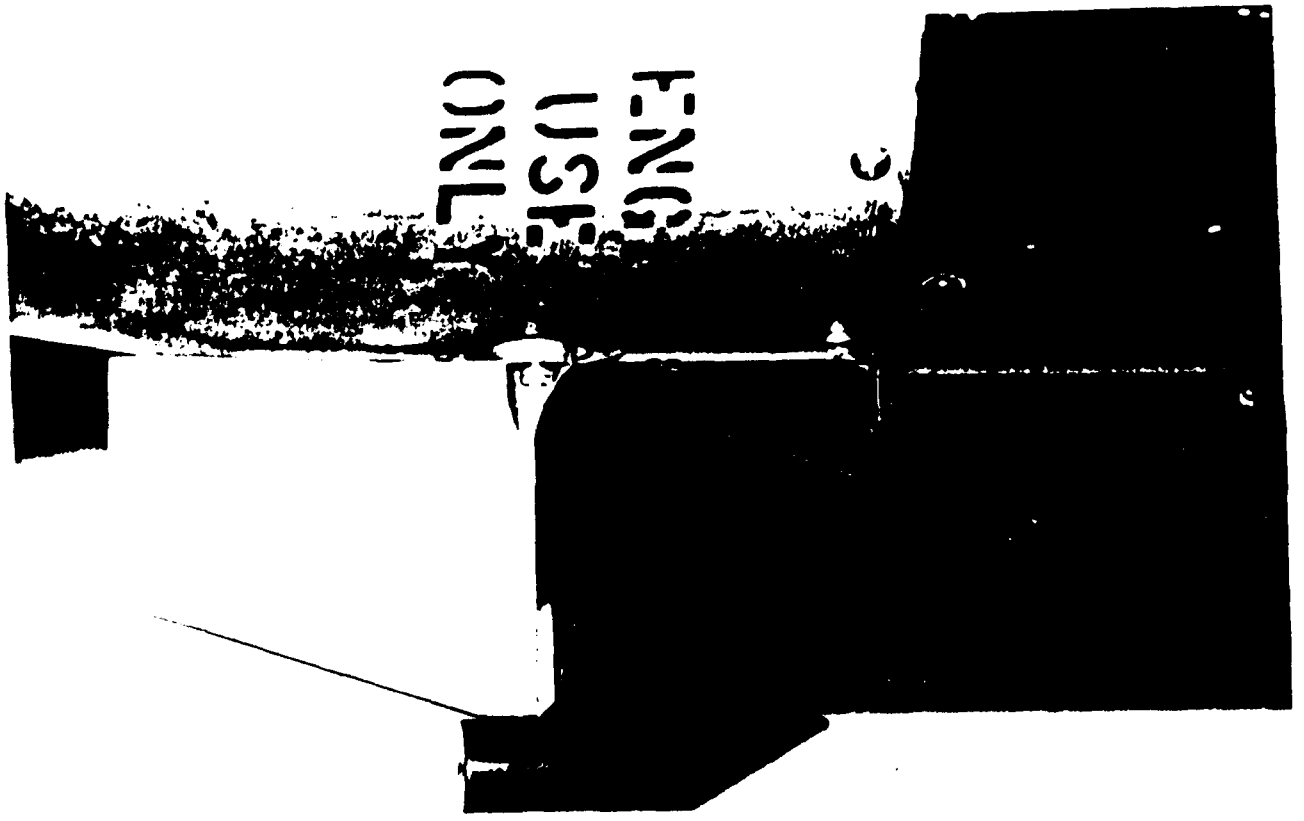

Figure 9. Laser Beamrider Receiver.

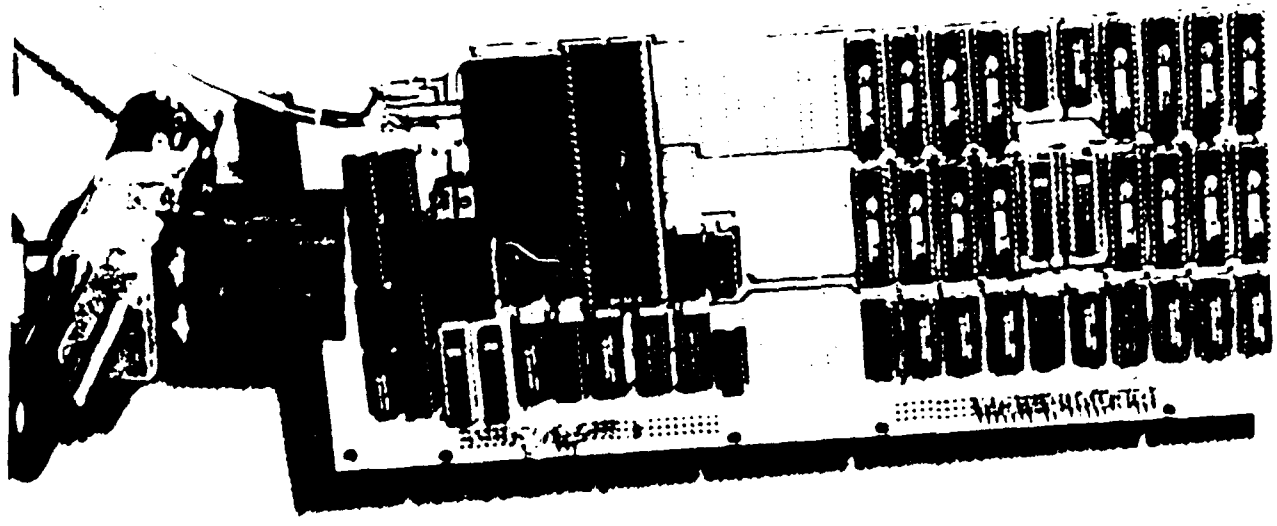

Figure 10. One of Eight PC Boards in CAMMS Processor.

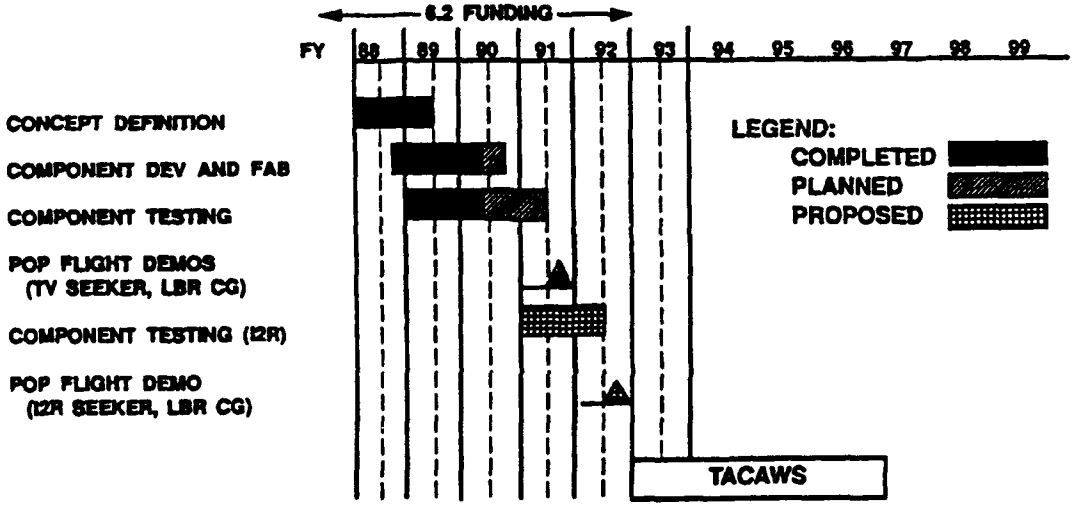


Figure 11. CAMMS Schedule.

# *Synthetic Discriminant Functions for use in Pattern Recognition*

S. Richard F. Sims
and
Jonathan A. Mills

U.S. Army Missile Command
Research Development and Engineering Center
AMSMI-RD-AS-SS
Redstone Arsenal, Alabama 35898-5253

**ABSTRACT**

Synthetic Discriminant Functions have had several different names over the last ten years of their development from the earliest type called linear combinatorial filters to one of the latest versions called the minimum average correlation energy filter. The ten years of development produced many different variations and efforts toward significant advancement over two dimensional matched filters. Most of this filter development was oriented toward optical implementations, however, the test results presented here are selected from many filters tested digitally and are considered exemplary of the major types for use in both optical and digital implementations.

## 2. SDF Development Stages

We categorize three major stages in SDF development each of which is considered an improvement over the previous one. The original or first SDF method is a linearly combined reference set[1] using the technique outlined in Figure 1[2].

The limitation of this original approach is that the correlation surface is not guaranteed to be anything specific or defined except at the registered position. In other words there is no control over the output correlation surface except at one point. This result is of course in general much different than a matched filter would produce and was not very useful until phase encoding schemes were introduced.[3] The phase only encoding, shown in Figure 2, and the binary phase encoding produce dramatically improved results.

Standard SDF using N training images d elements long where $d \gg N$.

$$\bar{h} = \sum_{i=1}^{N} a_i \bar{x}_i = \text{SDF filter}$$

$$\bar{h}^T \bar{x}_j = v_j$$

$$\sum_{i=1}^{N} a_i \bar{x}_i^T \bar{x}_j = v_j = \sum_{i=1}^{N} a_i R_{ij}, \quad j=1,2,3, - - - N$$

$$\bar{R}\,\bar{a} = \bar{v}$$

$$\bar{a} = \bar{R}^{-1}\bar{v}$$

The values of $v_j = 1$. The $x_i$ are the training images.

Figure 1

## PHASE ENCODING

- Complex frequency domain pixel = x + iy
- Rectangular to polar phase encoding

PHASE:

$$\Theta = \tan^{-1}\frac{y}{x}$$

AMPLITUDE:

Amplitude is set to a constant = 1

- Polar to rectangular conversion

Figure 2

The second category of SDF techniques is called the Correlation SDF[4] and has an intuitive aspect which is easily visualized.[5]. The information used in building the SDF are the references themselves and noting the fact that the system of equations in Figure 1 is under determined the insertion of constants at desired places using a duplication of offset references creates control points on the correlation surface. This technique is used to create a distinctive correlation surface at and around the registered position. In addition this second method retains the limitation of the original SDF method in that it does not control the correlation anywhere except at the defined control points and the surface can take on uncontrolled values at all other positions. This uncontrollability is not necessarily a problem if a subsequent correlation stage uses an ideal result cross correlation to extract the unique surface shape sculpted by the control points selected. This approach does however add that additional computation. For other than single pass cross correlation for near term digital implementation this methodology, as shown in the Results Tables under the E2Z5TFAB100, S5E2TFAB1, and E2Z5TFAB1 performs better than the phase encoded methods and shows more potential detectability.

The third category looks at a more comprehensive way of developing the SDF filters in that they strive to minimize the variance[6] and then in another more easily computed method to minimize the average correlation energy (MACE)[7]. These methods vary significantly from the earlier techniques in that these approaches try to control the overall correlation surface by implicitly minimizing a global feature. An outline of the development of the MACE filter is shown in Figure 3 and Figure 4.

$$g_i(n) = x_i(n) \odot h(n)$$

$$E_i = \sum_{n=1}^{d} |g_i(n)|^2 = (1/d) \sum_{k=1}^{d} |G_i(k)|^2$$

$$= (1/d) \sum_{k=1}^{d} |H(k)|^2 |X_i(k)|^2$$

In vector form can also be written as

$$E_i = H^* D_i H$$

where $D_i(k,k) = |X_i(k)|^2$

and the correlation peak amplitude constraint is

$$g_i(0) = X_i^* H = u_i$$

Figure 3

$$E_{AV} = (1/N)\sum_{i=1}^{N} E_i = (1/N)\sum_{i=1}^{N} H^* D_i H$$

letting $D = \sum_{i=1}^{N} \alpha_i D_i$ if all $\alpha_i = 1$

then

$$E_{AV} = (1/N) H^* D H$$

By minimizing $E_{AV}$ subject to $X^* H = u$ using the method of Lagrange multipliers the solution for the MACE filter is

$$H = D^{-1} X (X^* D^{-1} X)^{-1} u$$

Figure 4

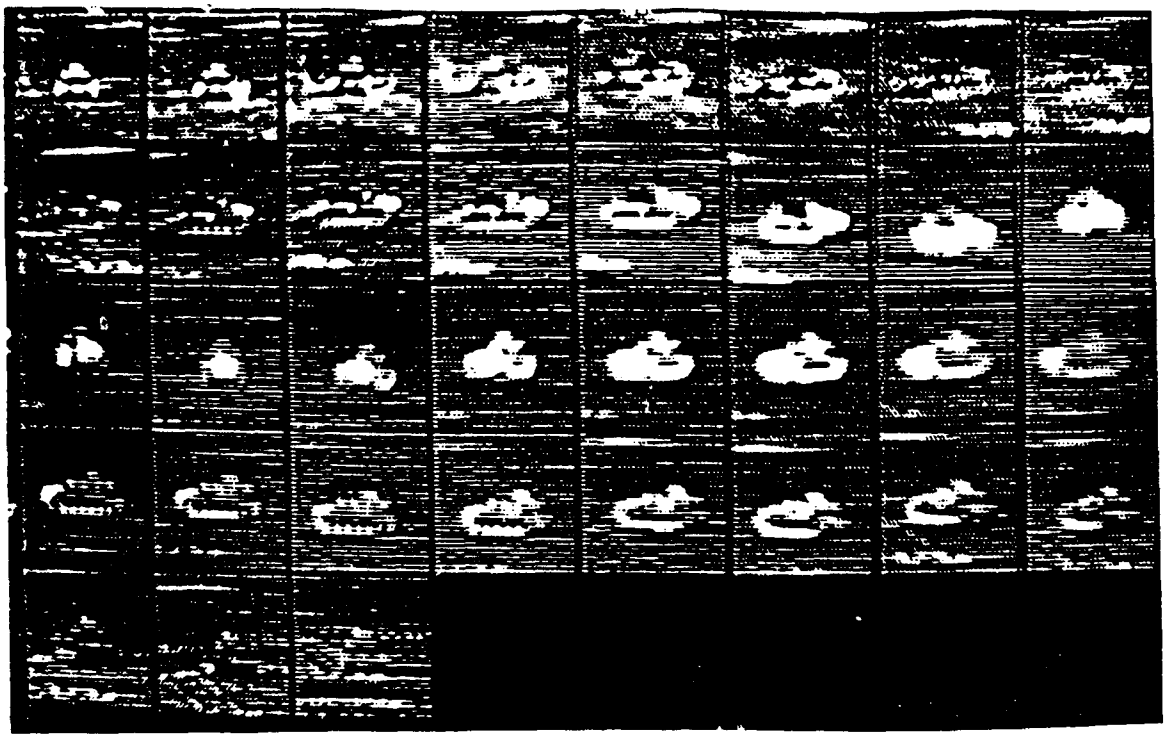

**Figure 5** - Large Object Reference Set

### 3. Filter Testing

Filters were developed using two data sets shown in Figure 5 and Figure 6. Performance results of the major filter types are presented in Results Tables 1 and 2. Results Table 1 (RT1) was generated using the cross correlation of the specified filter with the input images that consisted of the reference object with its actual background as shown in Figure 5 and Figure 6. Results Table 2 (RT2) was generated using the cross correlation of the specified filter with each reference used to build the filter, hence RT2 shows the best possible performance achievable. The testing of the frequency domain SDF development methods which are the phase only, binary phase only and the minimum average correlation energy filters, involved several steps in the process common to all frequency domain methods as depicted in Figure 7. To define the zero offset position the images used to build the filter or the input image must be quadrant swapped to give a point of reference in the correlation surface. This swapping essentially places the center of the images in the upper left corner as shown in Figure 8.

As shown in RT1 the performance using the phase only encoding (PHASE ENCODED) produced generally poor results, but the insertion of a D.C. notch significantly enhanced the performance (see PHASE NOTCH). The optimum size of the frequency notch is clearly object dependent.

The PHASE NOTCH technique results shown are a results of using the optimum notch size. The binary phase only encoded (BINARY PHASE in RT2) SDF has the inherent feature of on axis bleed through of the test reference[8] and consequently makes the probability for use with a digital implementation quite low, however, this does not of course impede its use optically. We did not chose to test the BINARY PHASE SDF with the background data set because of its relatively poor performance against its own reference set.

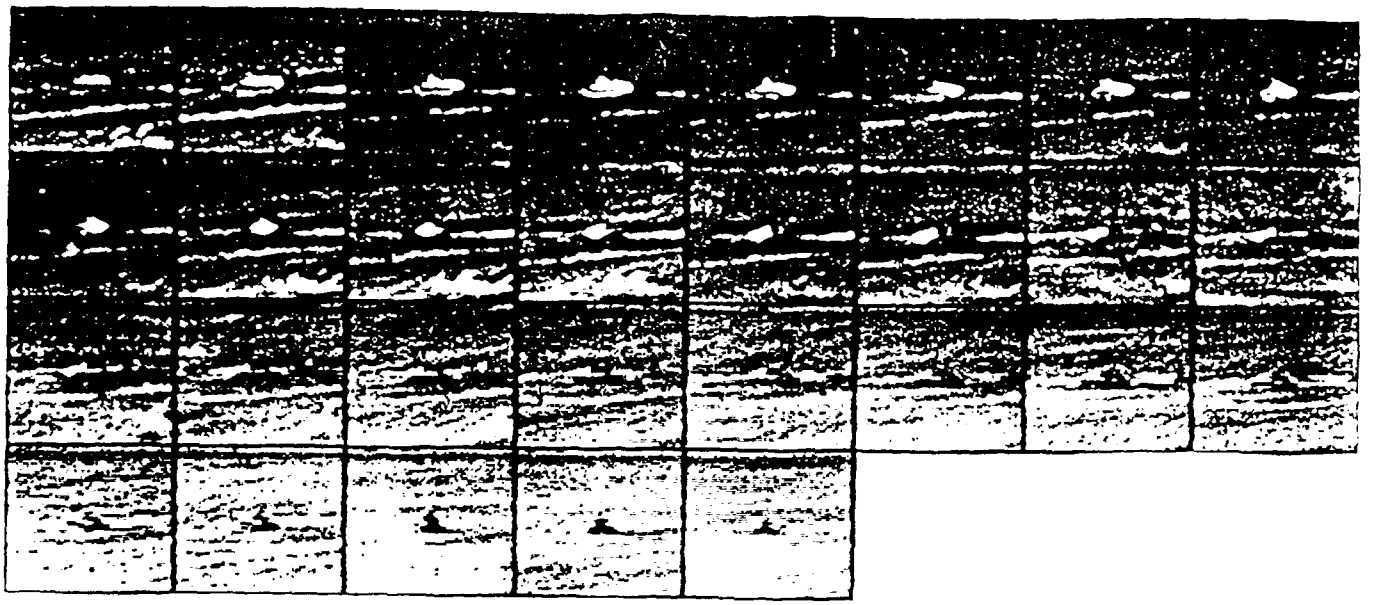

Figure 6 - Small Object Reference Set

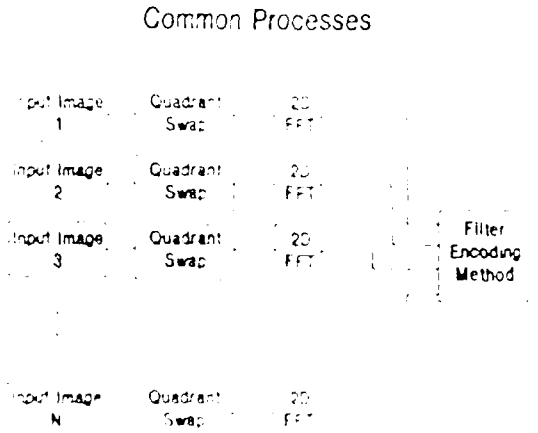


Figure 7

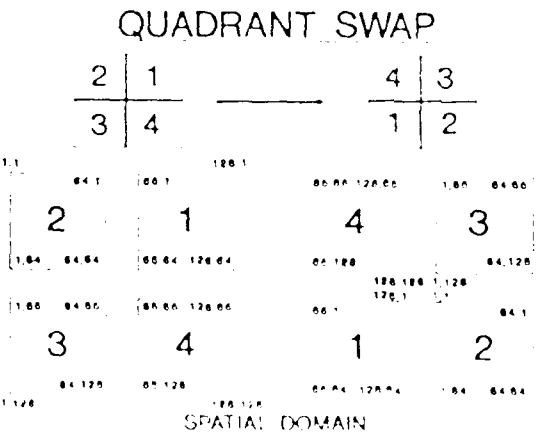


Figure 8

In addition to the full reference set (every 10 degree object aspect) testing, several filters of each type were implemented with half of the reference set (every other object aspect) incorporated. This half filter was a test to evaluate the distortion tolerance or sensitivity of each filter method. The result tables depict this performance under the Half References section.

The background grayscale value used in all filter development was the target mean value and it should be noted that performance was not as tractable using other values such as the image mean or any other experimental value.

## 4. Summary of Results

The statistics of the overall results are shown in Results Tables 1 and 2. The best and worst case MACE correlation surfaces are also shown with detailed statistics in Appendix A. The SDF file naming convention for use in interpreting the results table is described in Appendix A. It is clear the MACE SDF produces the best single pass correlation results.

The MACE SDF performs well when the background value used in the filter is the target mean. The resultant output can generally contains low frequency components which translate to slowly rolling hills in the correlation surface, however, these were removed using a nonlinear D.C. notch filter post process on the correlation surface itself. This low frequency component was also removed using frequency notching in the frequency plane which generated less than optimum but useable results.

Several additional filter types which have been published such as the minimum variance SDF were undergoing testing, however, comprehensive results were not available for this paper but will be included at a later date.

## Results Table 1 (RT1)

| BACKGROUND SET | Number of Exact Hits | Peak Within 2 Pixels | Peak Within 5 Pixels | Peak Within 10 Pixels | Peak Within 20 Pixels | Peak Within 30 Pixels | >30 |
|---|---|---|---|---|---|---|---|
| All References | | | | | | | |
| MACENOISE | 32 | **32** | 0 | 0 | 1 | 0 | 2 |
| MACE | 31 | **31** | 1 | 0 | 1 | 0 | 2 |
| E2Z5TFAB100 | 17 | **27** | 1 | 4 | 3 | 0 | 0 |
| S5E2TFAB1 | 16 | **27** | 2 | 2 | 2 | 2 | 0 |
| E2Z5TFAB1 | 17 | **26** | 1 | 4 | 4 | 0 | 0 |
| PHASE NOTCH | 19 | **23** | 2 | 3 | 4 | 2 | 1 |
| S9E2TFAB1 | 10 | **22** | 2 | 6 | 4 | 1 | 0 |
| PHASE ENCODED | 11 | **19** | 1 | 3 | 6 | 3 | 3 |
| S5TFAB1 | 4 | **13** | 1 | 6 | 12 | 3 | 0 |
| S9TFAB1 | 8 | **12** | 6 | 4 | 11 | 2 | 0 |
| Half References | | | | | | | |
| S5E2HTFAB1 | 16 | **24** | 4 | 5 | 2 | 0 | 0 |
| S9E2HTFAB1 | 13 | **24** | 2 | 4 | 5 | 0 | 0 |
| MACENOISEH | 17 | **21** | 0 | 2 | 5 | 5 | 2 |
| MACE HALF | 17 | **20** | 0 | 7 | 5 | 0 | 3 |
| S5HTFAB1 | 10 | **19** | 1 | 5 | 6 | 4 | 0 |
| S9HTFAB1 | 9 | **17** | 5 | 3 | 8 | 2 | 0 |
| Small References | | | | | | | |
| MACE SMALL | 19 | **23** | 0 | 2 | 0 | 0 | 4 |
| MACE SMALL HALF | 13 | **23** | 1 | 1 | 0 | 1 | 3 |
| S5E2TFAB1 SMALL | 0 | **14** | 5 | 7 | 2 | 1 | 0 |
| E2Z5TFAB100 SMALL | 1 | **13** | 2 | 7 | 4 | 1 | 2 |

## Results Table 2 (RT2)

| REFERENCE SET | Number of Exact Hits | 2 | Peak Within 5 Pixels | 10 | 20 | 30 | >30 |
|---|---|---|---|---|---|---|---|
| All References | | | | | | | |
| MACENOISE | 35 | **35** | 0 | 0 | 0 | 0 | 0 |
| MACE | 35 | **35** | 0 | 0 | 0 | 0 | 0 |
| E2Z5TFAB100 | 32 | **35** | 0 | 0 | 0 | 0 | 0 |
| E2Z5TFAB1 | 32 | **35** | 0 | 0 | 0 | 0 | 0 |
| S5E2TFAB1 | 30 | **35** | 0 | 0 | 0 | 0 | 0 |
| PHASE NOTCH | 33 | **33** | 0 | 1 | 0 | 1 | 0 |
| S5TFAB1 | 19 | **30** | 1 | 0 | 3 | 1 | 0 |
| S9E2TFAB1 | 24 | **28** | 7 | 0 | 0 | 0 | 0 |
| S9TFAB1 | 18 | **28** | 3 | 1 | 3 | 0 | 0 |
| PHASE ENCODED | 25 | **26** | 0 | 1 | 5 | 3 | 0 |
| BINARY PHASE | 21 | **23** | 0 | 3 | 6 | 3 | 0 |
| Half References | | | | | | | |
| S9E2HTFAB1 | 21 | **29** | 3 | 3 | 0 | 0 | 0 |
| S5E2HTFAB1 | 21 | **27** | 1 | 5 | 2 | 0 | 0 |
| MACE HALF | 18 | **25** | 3 | 6 | 1 | 0 | 0 |
| S5HTFAB1 | 14 | **21** | 4 | 4 | 6 | 0 | 0 |
| S9HTFAB1 | 11 | **17** | 5 | 3 | 10 | 0 | 0 |
| MACENOISEH | 18 | **26** | 3 | 5 | 1 | 0 | 0 |
| Small References | | | | | | | |
| MACE SMALL | 29 | **29** | 0 | 0 | 0 | 0 | 0 |
| S5E2TFAB1 SMALL | 12 | **26** | 1 | 2 | 0 | 0 | 0 |
| E2Z5TFAB100 SMALL | 10 | **24** | 2 | 3 | 0 | 0 | 0 |
| MACE SMALL HALF | 16 | **23** | 6 | 0 | 0 | 0 | 0 |

## Appendix A

The SDF naming convention for the file names has evolved where all filter names have the general form 'ppppTFsss'. The 'pppp' represents a series of prefixes, indicating whether enhancement, shifting, or other features were used in constructing the filter. The 'sss' represents a series of suffixes, which is more standardized, indicating whether or not the flat image was used, etc. The 'TF' stands for 'TestFilter', which is the name of the program which computes correlation surfaces.

Prefix characters for SDF file names:

- E - Enhancement, Type 1
- E2 - Enhancement, Type 2 (Sobel)
- Sn - Shifting, n pixels in cross pattern
- H - Filter built from only half the reference set
- B - A typical background patch was used in the reference set
- X - The reference background mean was set to the mean of a typical background patch
- Zn - Shifting, n pixels in cross and diagonal pattern

Suffix:

- AB1 -- The flat image was used to suppress DC shifts
- ABn -- The flat image was used to suppress DC shifts with the value n
- NB1 -- The flat image was not used.

The 'B1' part of the suffix refers to features which were not varied in this study. For example the filter S9TFAB1 uses the flat image for DC suppression, and was built using shifting, the shifting distance being 9 pixels. The filter S9E2TFAB1 is identical, except that enhancement filter 2 was used in addition to the shifting. In this naming scheme, filter TFNB1 is the classical SDF filter, without any additional property.
For the MACE SDF and phase encoded SDF the naming convention is as follows:

HALF - The filter is built from only half the reference set (same as H)

SMALL - The filter is built from objects one half the size of the large reference set

NOISE - The filter is built using 5 samples of background plus the reference set

```
-----------------------------------------------------------
FILTER SET        =     M.A.C.E. REFERENCE SET
IMAGE NUMBER      =     1  ( THE IDEAL CORRELATION SURFACE )
-----------------------------------------------------------

PEAK COL, PEAK ROW        =          64          65
MAXPEAK COL, MAXPEAK ROW  =          64          65
SIGNAL AT MIN POINT                          =  2.6019336E-12
SIGNAL WITHIN 3 PIXELS (USED FOR RATIOS)  =   1.000005

MEAN = 0.1123E-02 VARIANCE = 0.6882E-04 SIGMA = 0.8296E-02

.........................KNOWN..........MAXIMUM.........
SIGNAL AT PEAK        =   1.000          1.000
RMS NOISE             =  0.2945E-02     0.2945E-02
CONTRAST              =  0.9941         0.9941
SIGNAL/MEAN           =   890.2          890.2
SIGNAL/RMS NOISE      =   339.2          339.2
SIGNAL/MAX SIDE LOBE  =   15.39          15.39
.........................................................

MISS DISTANCE         =     0.00

ON TARGET             = YES    EXACT HIT                = YES

WITHIN TWO  PIXELS    = YES    WITHIN TWENTY PIXELS     = NO
WITHIN FIVE PIXELS    = NO     WITHIN THIRTY PIXELS     = NO
WITHIN TEN  PIXELS    = NO     OVER   THIRTY PIXELS     = NO

% X,Y TO ONTARGET CENTER =   100.00 %   100.00 %

PEAK WIDTH TO 1/2(PEAK VAL-MEAN)+MEAN     =          1.00
PEAK WIDTH IN X DIRECTION                 =          1
PEAK WIDTH IN Y DIRECTION                 =          1

MAXPEAK WIDTH TO 1/2(PEAK VAL-MEAN)+MEAN  =          1.00
MAXPEAK WIDTH IN X DIRECTION              =          1
MAXPEAK WIDTH IN Y DIRECTION              =          1
```

# M.A.C.E. REFERENCE 1

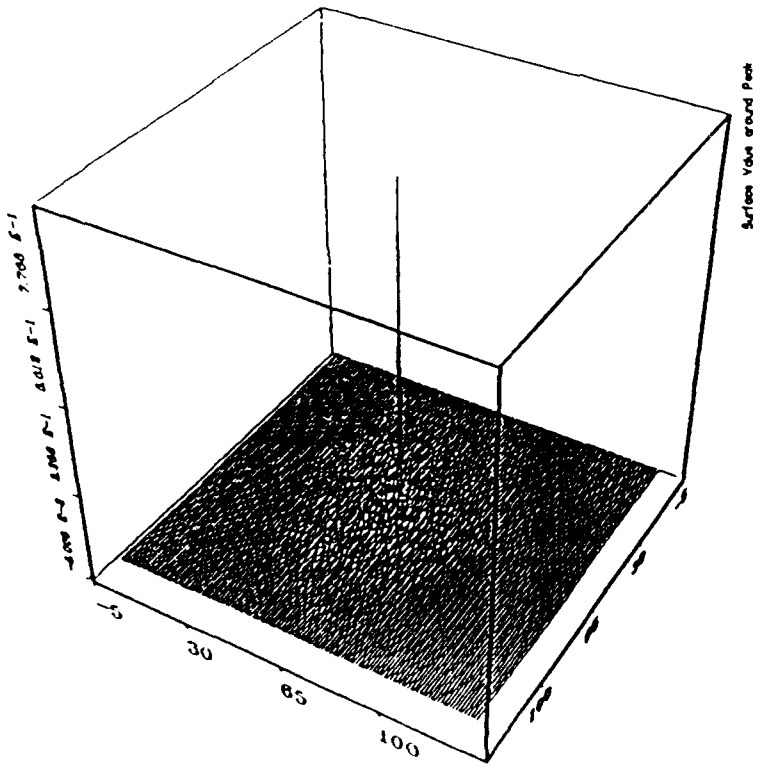


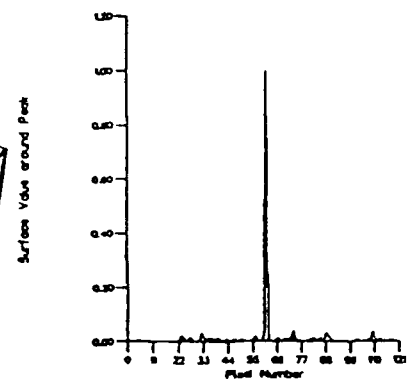


Peak Value = 1.000
Peak is at Column 64 Row 65
Known Column 64 Row 65

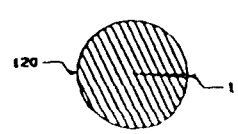

```
-----------------------------------------------------------
FILTER SET        =     M.A.C.E. BACKGROUND SET
IMAGE NUMBER      =     5  ( THE BEST CORRELATION SURFACE )
-----------------------------------------------------------

PEAK COL, PEAK ROW        =          59          65
MAXPEAK COL, MAXPEAK ROW  =          59          65
SIGNAL AT MIN POINT                          =  1.8452162E-11
SIGNAL WITHIN 3 PIXELS (USED FOR RATIOS)     =  0.8744556

MEAN = 0.6434E-02 VARIANCE = 0.1439E-03 SIGMA = 0.1200E-01

.........................KNOWN..........MAXIMUM.........
SIGNAL AT PEAK        =   0.8745          0.8745
RMS NOISE             =   0.9866E-02      0.9866E-02
CONTRAST              =   0.9777          0.9777
SIGNAL/MEAN           =    135.9           135.9
SIGNAL/RMS NOISE      =    87.98           87.98
SIGNAL/MAX SIDE LOBE  =    4.022           4.022
.........................................................

MISS DISTANCE         =     0.00

ON TARGET             = YES    EXACT HIT                = YES

WITHIN TWO  PIXELS    = YES    WITHIN TWENTY PIXELS     = NO
WITHIN FIVE PIXELS    = NO     WITHIN THIRTY PIXELS     = NO
WITHIN TEN  PIXELS    = NO     OVER   THIRTY PIXELS     = NO

% X,Y TO ONTARGET CENTER =   100.00 %   100.00 %

PEAK WIDTH TO 1/2(PEAK VAL-MEAN)+MEAN     =          1.00
PEAK WIDTH IN X DIRECTION                 =          1
PEAK WIDTH IN Y DIRECTION                 =          1

MAXPEAK WIDTH TO 1/2(PEAK VAL-MEAN)+MEAN  =          1.00
MAXPEAK WIDTH IN X DIRECTION              =          1
MAXPEAK WIDTH IN Y DIRECTION              =          1
```

# M.A.C.E. BACKGRND 5

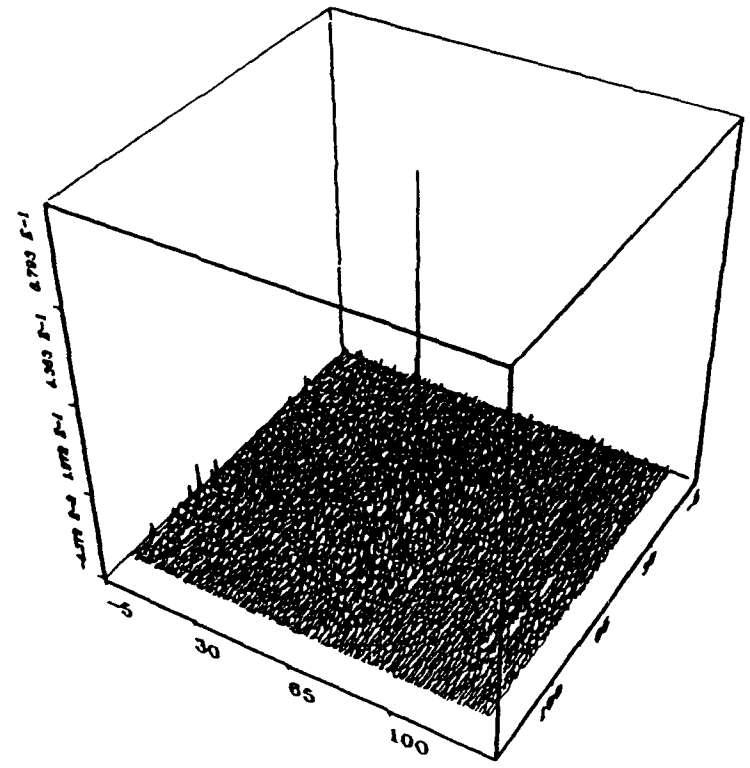


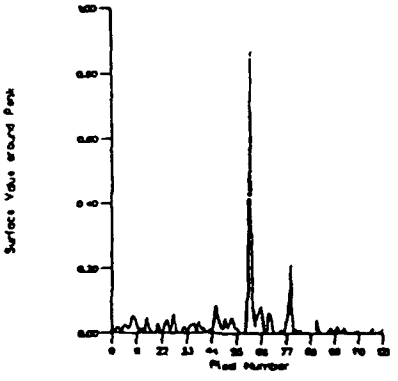


Peak Value = 8.744 E-1
Peak is at Column 59 Row 65
Known Column 59 Row 65

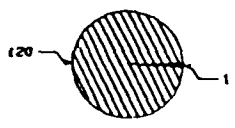

FILTER SET = M.A.C.E. BACKGROUND SET
IMAGE NUMBER = 20 ( THE WORST CORRELATION SURFACE )

PEAK COL, PEAK ROW = 61 64
MAXPEAK COL, MAXPEAK ROW = 29 94
SIGNAL AT MIN POINT = 1.1746849E-13
SIGNAL WITHIN 3 PIXELS (USED FOR RATIOS) = 5.9494589E-02

MEAN = 0.4063E-02 VARIANCE = 0.3514E-04 SIGMA = 0.5928E-02

| | KNOWN | MAXIMUM |
|---|---|---|
| SIGNAL AT PEAK | 0.5949E-01 | 0.7058E-01 |
| RMS NOISE | 0.5947E-02 | 0.5949E-02 |
| CONTRAST | 0.8183 | 0.8445 |
| SIGNAL/MEAN | 14.64 | 17.37 |
| SIGNAL/RMS NOISE | 9.322 | 11.18 |
| SIGNAL/MAX SIDE LOBE | 0.8429 | 1.013 |

MISS DISTANCE = 43.86

ON TARGET = NO EXACT HIT = NO

WITHIN TWO PIXELS = NO WITHIN TWENTY PIXELS = NO
WITHIN FIVE PIXELS = NO WITHIN THIRTY PIXELS = NO
WITHIN TEN PIXELS = NO OVER THIRTY PIXELS = YES

PERCENT X,Y TO ONTARGET CENTER = N/A

PEAK WIDTH TO 1/2(PEAK VAL-MEAN)+MEAN = 3.24
PEAK WIDTH IN X DIRECTION = 1
PEAK WIDTH IN Y DIRECTION = 1

MAXPEAK WIDTH TO 1/2(PEAK VAL-MEAN)+MEAN = 1.00
MAXPEAK WIDTH IN X DIRECTION = 1
MAXPEAK WIDTH IN Y DIRECTION = 1

# M.A.C.E. BACKGRND 20

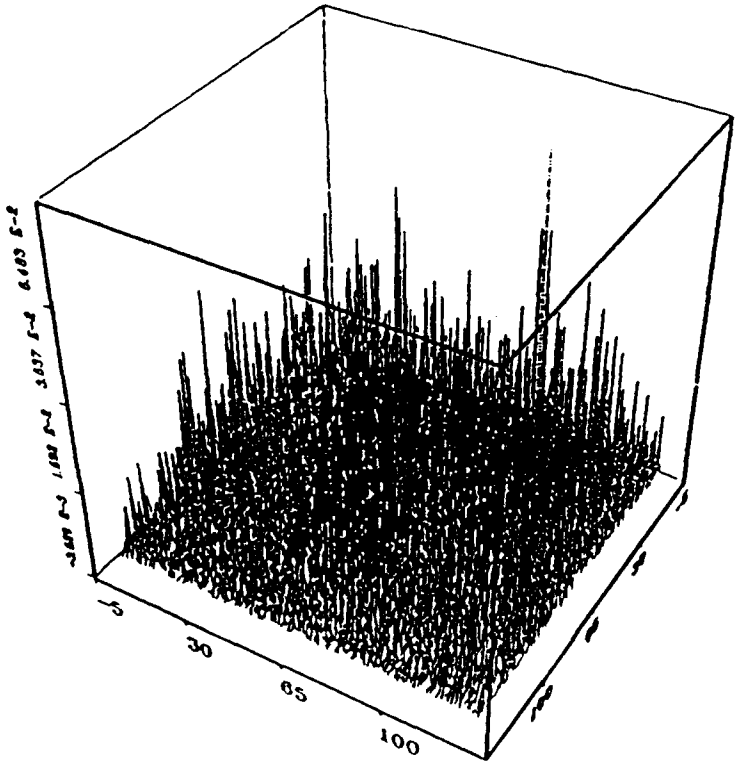


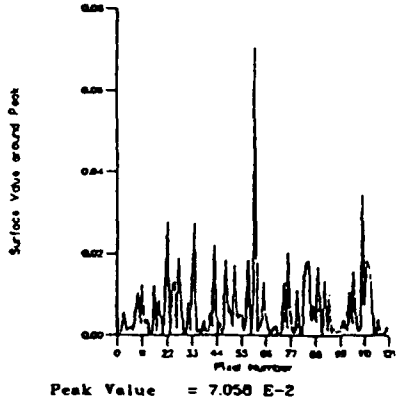


Peak Value = 7.058 E-2
Peak is at Column 29 Row 94
Known Column 61 Row 64
Miss Distance = 4.386 E1

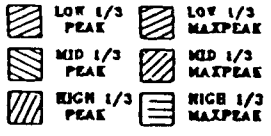


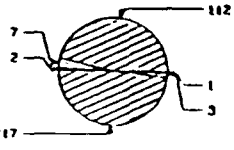

1. **C.F. Hester and D. Casasent**, "Multivariant Technique for Multiclass Pattern Recognition," Appl. Opt. 19, 1758 (1980).

2. **B.V.K. Vijaya Kumar**, "Optimality of Projection Synthetic Discriminant Functions," SPIE Vol. 579, Sept. (1985).

3. **Joseph L. Horner and Peter D. Gianino**, "Applying the phase only filter concept to the Synthetic Discriminant Function correlation filter," SPIE Vol 519 Analog Optical Processing and Computing (1984).

4. **D. Casasent and Wen-Thong Chang**, "Correlation synthetic discriminant functions," Appl. Opt. 25, 2343 (1986).

5. **E. Jenkins, J. Morris, S.R.F. Sims**, "Synthetic discriminant functions for target correlation," GOMAC Orlando,Florida (1987).

6. **B.V.K.V. Kumar**, "Minimum-variance synthetic discriminant functions," J. Opt. Soc. Am., Vol.3 No.10, Oct. (1986).

7. **A. Mahalanobis, V. Kumar, D. Casasent**, "Minimum average correlation energy filters," Appl. Opt. 26, 3633 (1987).

8. **L. Kennedy, B. Powell, and D. Gregory**, "Highly multiplexed optical correlation filters," SPIE Vol. 938 Digital and Opt. Shape Representation and Pattern Recognition (1988).

ABSTRACT

MONOPULSE ANGULAR ERROR REDUCTION
FOR COMPLEX TARGETS
USING HIGH RANGE RESOLUTION

by
Michael R. Christian
J. Blake Winter

Multipath causes unacceptable monopulse elevation angular errors when measuring a complex target's position. High range resolution can be used to measure angular position of individual scatterers on the target. Averaging high range resolution angle measurements of the scatterers provides a reduction of the standard deviation of the angular error. Scatterer heights can be derived from the complex angular measurements under specific circumstances.

## I. ADKEM DESCRIPTION

The Advanced Kinetic Energy Missile (ADKEM) is currently being developed by MICOM's RD&E Center to travel at hypervelocity speeds and deliver a kinetic energy kill against both ground and air targets. The missile will be inertially guided through the boost phase (or to short range targets) and command guided through the coast phase to the target. To ease the design burden for an inertial guidance unit, command guidance is also being considered for a portion of the boost phase. Since millimeter wave energy has been shown to propagate through various motor plumes with very little attenuation, millimeter wave radar was chosen as the primary approach in providing the command guidance for the missile with laser beamrider as an alternate approach. Subsequent error analysis has shown for either the ground target or air target scenerio, the primary error source for the millimeter guidance approach is multipath. This paper will describe multipath and its potential effects on tracking ground targets. This paper will also present various techniques that are being examined to reduce the target multipath effect.

The baseline ADKEM millimeter guidance approach has a monopulse radar on the launch platform that transmits a guidance command encoded in a variable PRF coded pulse to a receiver on the missile. The monopulse radar then measures the angle of the missile's CW transmitted signal in one set of delta and sum channels and the angle of the pulse returning from the target in another set of channels. Some of the system's operating characteristics are anticipated to be the following:

| | | |
|---|---|---|
| Center Frequency | 94.5 | GHz |
| Bandwidth | 1 | GHz |
| Frequency Steps | 1024 | steps |
| Antenna Diameter | 24 | inches |
| Antenna Height | 3 | meters AGL |
| Polarization | | vertical |
| Missile Transceiver | | |
| Frequency | 93.5 | GHz |
| Missile Receive | | |
| Antenna Aperture | 1 | inch |
| Missile Transmit | | |
| Antenna Aperture | 1 | inch |
| Missile Diameter | 2 | inches |
| Missile Speed | 2 | km/s |
| Missile Range | 5 | km |
| Target Height | .5-2.5 | meters AGL |

Table 1

## II. MULTIPATH

Multipath can be defined as being the propagation of energy from more than one path. For low angle radar applications, multipath is caused by the interference of the direct target energy with indirect target energy reflections from the terrain between the radar and the target. For smooth surfaces, the reflection from the terrain is termed specular and can be thought as emanating from a single spot on the ground between the target and the radar. For rough or irregular surfaces, the reflection from the terrain comes from multiple points and is termed diffuse reflection. For terrain surfaces which have a smooth mean contour but small scale irregularities, both specular and diffuse reflection will occur. Surface roughness not only induces diffuse scattering but it also attenuates the amount of specular scattering that will occur. A formula has been derived to describe this specular reflection coefficient attenuation factor and it is given in equation 1:

$$\Gamma s = \exp(-8(\pi * \sigma * \sin\epsilon / \text{lambda})) \qquad (1)$$

where $\sigma$= standard deviation of the surface height, $\epsilon$=grazing angle, and lambda= wavelength. As can be seen in equation 1, the specular reflection coefficient becomes smaller for decreasing wavelength. Therefore the higher the frequency of operation, the less the specular multipath effect.

As shown in Table 1, millimeter wave differential guidance has been chosen as the primary command guidance approach for the missile. The ADKEM operational scenerio involves ground to ground target engagement which will require accurate tracking of both the missile and the target in extreme low angle conditions. The frequency of operation for this approach was chosen to be 94 Ghz primarily because this is about the highest frequency attainable with relative component maturity. The high frequency of operation was desired in order to minimize antenna beamwidth thereby increasing the tracking accuracy resolution and to decrease possible multipath effects. An amplitude monopulse approach has been selected to achieve the angular displacement measurement. Multipath is a major source of error to low angle tracking systems and therefore one would expect it to be a major source of guidance error for the ADKEM guidance radar system. The easiest method to reduce the multipath effect would be to narrow antenna beamwidth such that none of the propagated energy would be reflecting off the terrain. For a ground target scenerio with the range of 5000 meters, the antenna would have to have a beamwidth of 400 microradians in order to achieve acceptable multipath

effects. The diameter of this antenna at 95 GHz operating frequency, would be approximately 8 meters. Clearly this would be impractical to implement on any ground weapon platforms. A 60 centimeter diameter antenna was chosen for the ADKEM radar since this size is probably the maximum size antenna that could be practically implemented on a launch platform. Since the antenna size is limited for our approach, other multipath reduction techniques must be investigated. Millimeter wave radar offers the opportunity to operate over a wide bandwidth of carrier frequency. Typical bandwidths of operation are 640 MHz (1 foot range resolution) while a bandwidth of 2 Ghz (4 inch range resolution) has recently been demonstrated in an instrumentation radar developed by MICOM (HIPCOR-95). This wide bandwidth capability will allow high range resolution to be used as a possible glint and multipath reduction technique.

The antenna height, target height, and maximum range all cause the grazing angle to be small for the ADKEM ground target scenerio. Because of the small grazing angle, multipath reflections of the target from the ground are going to have a major impact on missile guidance, particularly on the elevation channel. The radar antenna beamwidth is approximately 6 milliradians, whereas the angular separation between the highest target scatterer and its specular reflection over flat smooth terrain is about 1 milliradian -much less than the beamwidth. This lack of resolution between the target scatterers and their images causes errors in the monopulse angular measurement of the radar.

It is anticipated that the ground between the radar and the target will never be perfectly flat. Usually, the radar and the target will be slightly elevated above the reflecting surface. If the intervening ground between radar and target were concave, the target would be blocked and the radar would not detect the target. The target and multipath are still unresolved even if the target is as much as 15 meters above the reflecting surface. In addition, the radar and target heights are no longer known when the ground is not flat.

## III. COMPLEX ANGLE DERIVATION

Multipath can be examined as a two — scatterer interference problem with the two scatterers being the target and its image displaced in angular position in the elevation plane as shown in Figure 1. Following the derivation of Sherman [1], an amplitude monopulse radar operating in the linear portion of its error sensitivity curve can be

described by equation 2 where $\delta$ is the elevation difference channel response, S is the sum channel response, k is the slope of the monopulse response curve versus angle, and $\theta$ is the angle with respect to boresight of the target.

$$\delta/S = k*\theta \qquad (2)$$

or equivantly $$\theta = \frac{1*\delta}{k*S}$$

Let the target subscript be denoted by d and the image subscript by r, then $\theta d$ and $\theta r$ are the angular displacements of the target and its image respectively to the elevation boresight axis. Then

$$\delta d = k*\theta d*Sd \ , \quad \delta r = k*\theta r*Sr$$

and the resultant indicated angle is

$$\theta = \frac{\delta}{k*S} = \frac{\delta d+\delta r}{k*(Sd+Sr)} = \frac{\theta d(Sd)+\theta r(Sr)}{Sd + Sr} \qquad (3)$$

Now define

$$Sd/Sr = p* \exp(j\alpha) \qquad (4)$$

where p is the amplitude ratio of sum signal returns from the target and its image and $\alpha$ is the relative phase between the the target and image return. The amplitude ratio is equal to ratio of the sum pattern voltage gains (G) for the target and image mutiplied by the ratio of the backscatter coefficients (R) of the target multiplied by the reflection coefficient ($\Gamma$), that is $p=\Gamma*G*R$. Dividing equation 3 through by Sd and substituting in equation 4 we have:

$$\theta c = \frac{\theta d+(p*\exp(j*\alpha)*\theta r)}{1+(p*\exp(j*\alpha)} \qquad (5)$$

Equation 5 reveals that the indicated angle is complex and the indicated angle will be either somewhere in between the target and its image (since $p \leq 1$) or somewhere above the target, depending on the value of p and the value of $\alpha$. Most monopulse radars measure only the real part of the complex quantity given in equation 4 and this is given in equation 6 below:

$$Re(\theta) = \frac{\theta d+(p*\cos\alpha*(\theta d+\theta r))+(p^2*\theta r)}{1 +(2p*\cos\alpha) + p^2}$$

$$\text{or} \quad Re(\theta)-\theta d = \frac{(\theta d-\theta r)*((p*\cos\alpha)+p^2)}{1+2p\cos\alpha+p^2} \qquad (6)$$

The derivation above assumes the boresight was pointing at the target. A plot of equation 6 normalized to θd-θr is shown in Figure 2.

## IV. MULTIPATH EFFECTS

### IV A. SINGLE SCATTERER AND MULTIPATH

Another way of expressing Sherman's equation for a scatterer and its image is the following:

$$\theta c = \frac{(G(\theta d)*\theta d+\Gamma*G(\theta r)*\theta r*\exp(j*(\alpha+\pi)))}{(G(\theta d)+\Gamma*G(\theta r)*\exp(j*(\alpha+\pi)))} \qquad (7)$$

$$\alpha = 4*\pi*Ha*Hs/(R*lambda) \qquad (8)$$

$$\theta d = ATAN((Ha-Hs)/R)-\theta a \qquad (9)$$

$$\theta r = ATAN((Ha+Hs)/R)-\theta a \qquad (10)$$

where θa is the radar antenna angle with respect to the reflecting surface. G is the radar antenna gain in the direction of either the direct or reflected path. Ha is the radar antenna height above the reflecting surface, Hs is the height of a target scatterer, R is the range to a target scatterer, and lambda is the wavelength. The radar cross section has been assumed to be the same for the direct and indirect paths and has been divided out of the numerator and denominator. At low grazing angles, the specular reflection coefficient has a phase shift of 180 degrees for vertical polarization, which is the reason for the $\pi$ factor in the complex exponential term. At higher grazing angles the phase can have other values between 0 and 180 degrees.

The real part of θc in equation 7 is the measured indicated angle of the target after multiplying the voltage by a slope factor. In the absence of multipath, it is the actual angle of a single scatterer. When multipath is present, Real(θc) is the actual angle of the scatterer plus an error due to the multipath.

When a single scatterer's height was randomly chosen uniformly from .5 to 2.5 meters at a range of 5000 meters in 1000 Monte Carlo runs, the indicated angle varied non-uniformly. The probability density function of the indicated angle is shown in figure 3. The mean indicated

angle was 150 μradians and the standard deviation was 357 μradians.

The missile transmitter acts as a single scatterer, and the radar's measurement of missile position suffers angular error because of multipath.

## IV B. MULTIPLE SCATTERERS

A complex target can be thought of as consisting of multiple scatterers and their images, 5 for example, as shown in Figure 4. When more than one scatterer and its multipath is present, the linear superposition assumed in equation 7 can be expanded to include the effects of other scatterers on the complex indicated angle.

$$\theta c = \Sigma \frac{(Sdi*\theta di+Sri*\theta ri*\Gamma*\exp(j*(\alpha i+\pi)))}{\Sigma\ (Sdi+Sri*\Gamma*\exp(j*(\alpha i+\pi)))} \qquad (11)$$

where i is the scatterer summation index ranging from 1 to the number of scatterers .

If no multipath were present, Real(θc) would still have an error because of the presence of the other scatterers. This error is due to glint caused by the interference of the scatterers with one another.

When 5 scatterers' heights were randomly chosen uniformly from .5 to 2.5 meters at a range from 4999 to 5001 meters in 1000 Monte Carlo runs (a representation of 1000 different aspect angles), the indicated angle varied non-uniformly, but the probability density function was different from the single scatterer case. The probability density function of the indicated angle in this case is shown in figure 5. The mean indicated angle was 148 μradians and the standard deviation was 463 μradians. The simulation assumes a flat table top reflection surface with a specular reflection coefficient of .5 (from recent measurements over medium roughness asphault at 95 GHz) and no diffuse scattering.

When the radar antenna is aimed at the center of the scatterers, the desired error for all aspects of the target is 0 μradians mean error and 50 μradians standard deviation. The total error budget for the ADKEM system is 100 μradians for a target at 5 kilometers. If the root of the sum of the squares of the standard deviations of all the error sources (thermal noise, multipath, calibration error, servo error,

etc.), the largest any single error can be is 50 μradians. When a target has multiple scatterers, the angular error exceeds the desired level.

## IV C. HIGH RANGE RESOLUTION ANGLE AVERAGING

When high range resolution is used, the target is divided into many distinct scatterers. A complex indicated angle θc can be derived for the scatterers in each range cell. Although the scatterers in each range cell are probably composed of several unresolved scatterers, for the purposes of this report it is assumed the scatterers in each range cell are composed of only a scatterer and its multipath.

Averaging Real(θc) of the individual scatterers in each of 1000 Monte Carlo runs reduces the standard deviation to 164 μradians, and the mean is only 9 μradians. The probability density function is shown in figure 6.

When the radar antenna height was changed to 2 meters, the mean increased to 159 μradians, but the standard deviation was only 13 μradians.

Neither of these cases meets the criteria of 0 μradians mean and 50 μradians standard deviation, but there is a definite improvement over the non high range resolution case.

## IV D. HIGH RANGE RESOLUTION COMBINATORIAL AVERAGING

Another approach to reducing the angular error caused by multipath was to synthetically combine the complex high range resolution scatterers in different combinations:

$$\langle \mathrm{Real}(\theta c) \rangle = \frac{\mathrm{Real}(\delta 1/\Sigma 1+\delta 2/\Sigma 2+(\delta 1+\delta 2)/(\Sigma 1+\Sigma 2)\ldots)}{2\hat{}Ns-1} \qquad (12)$$

For 5 range cells there are 31 combinations of scatterers. This technique turned out to be slightly worse than the technique described in IV C. The mean was 110 μradians and the standard deviation was 140 μradians. The probability density function for 1000 Monte Carlo runs is shown in figure 7.

This technique does not meet the 0 μradians mean and 50 μradians standard deviation criteria, either, but there is still improvement over the non high range resolution case.

## V. DERIVATION OF SCATTERER HEIGHTS

In equation 7, the fact that the reflection coefficient is only real can be exploited to solve for some of the other parameters of equation 7. Solving for $\Gamma$ in equation 7:

$$\Gamma = \frac{\exp(-j*(\alpha+\pi))*G(\theta d)*(\theta d-\theta c)}{G(\theta r)*(\theta c-\theta r)} \qquad (13)$$

but the imaginary part of $\Gamma$=0. If Imag($\Gamma$)=0 then the following expression is true:

$$0 = 2*Hs/R*\theta cq*\cos(\alpha)+\sin(\alpha)*(\theta ci^2+\theta cq^2+2*\theta ci*\theta a+\theta a^2-2*Ha/R*(\theta ci+\theta a)+(Ha^2-Hs^2)/(R^2)) \qquad (14)$$

$\theta$ci is the in phase indicated angle obtained from measurement, $\theta$cq is the quadrature indicated angle obtained from measurement, and the range gate provides the measurement of R. When the earth is flat, $\theta$a and Ha can be measured, and Hs is the only unknown parameter in equation 14. Hs in equation 14 can be solved iteratively; however, equation 14 is pseudo-periodic as a function of Hs, and there is more than one solution for Hs. High range resolution is used to solve the ambiguities.

Assuming the multipath reflection coefficient $\Gamma$ is the same for all the scatterers in the range cells, the ambiguous values of Hs can be used in equations 8,9, and 10 to solve for $\Gamma$ in equation 13 (G in equation 13 can be found from a lookup table if $\theta$d and $\theta$r are estimated). Several values of $\Gamma$ are found for each scatterer, but only one value of $\Gamma$ is the same for all the scatterers. The Hs of each scatterer which provides the same $\Gamma$ common to all the other scatterers is the correct Hs for that scatterer.

In a more realistic scenario, $\theta$a and Ha with respect to the reflecting surface are not the same as the angle and height of the radar antenna with respect to ground below the radar. It is hypothesized that when $\theta$a and Ha are also stepped in small increments in equation 14, there is a particular set of values for $\theta$a, Ha, and Hs for each scatterer which provides only one common value of $\Gamma$ for all of the scatterers.

A more direct approach to solving for $\theta$a, Ha, and Hs is to perform a non linear least squares fit of some "measured" data.

## VI. EXAMPLES

A FORTRAN program was written to test the hypothesis. The following scenario was simulated.

| | | |
|---|---|---|
| Number of scatterers | = | 5 |
| Ha | = | 3 meters |
| Hs | = | .5 to 2.5 step .5 meters |
| Rs | = | 4999,5001 step .5 meters |
| RCS | = | 7.7,7.9,8.0,7.8,7.6 square meters |
| Ht | = | 1.5 meters |
| Rt | = | 5000 meters |
| θa | = | ATAN((Ha-Ht)/Rt) |
| Hae | = | .1 to 5.0 step .05 meters |
| Hse | = | .1 to 5.0 step .05 meters |
| θae | = | -500 to 500 uradians step 10 uradians |
| Frequency | = | 94 GHz |
| Reflectivity | = | .5 |
| Antenna aperture | = | .6096 meters |
| Angle noise | = | 0 |

Table 2.

In the program, θc was found for each of the scatterers using equation 7. These are the "measured" complex indicated angles for each scatterer. Then the θae, the estimated antenna angle with respect to the reflecting surface; Hae, the estimated antenna with respect to the reflecting surface; and Hse, the estimated scatterer height above the reflecting surface, were all varied over the expected limits in 3 nested DO loops. For each new value of θae and Hae, the values of Hse were found which made Imag(Γ)=0 for each scatterer. These values of Hse were then used in equation 13 to find estimated values of Γ. The estimated values of Γ were then compared. θae and Hae were then incremented until the minimum difference between the values of Γ for each scatterer was found. Table 3 shows the results when the program was executed using the conditions listed in Table 2.

| Estimated | | Actual | |
|---|---|---|---|
| Scatterer Height | Reflectivity | Scatterer Height | Reflectivity |
| 0.55 | .5000736 | .5 | .5 |
| 1.05 | .4770988 | 1 | .5 |
| 1.50 | .4991278 | 1.5 | .5 |
| 2.00 | .4984468 | 2 | .5 |
| 2.50 | .4975847 | 2.5 | .5 |
| Antenna Height | | | |
| 3.05 | | 3 | |
| Antenna Angle | | | |
| 309 uradians | | 300 uradians | |
| Target Angle | | | |
| -4.96 uradians | | 0 uradians | |

Table 3.

-4.96 μradians of error is within the acceptable limits. The computation time to find the standard deviation of the error is prohibitive.

If uniformly distributed angle noise of 50 microradians is added to the complex indicated angle, a rough approximation of thermal noise, the results change a little as shown in Table 4.

| Estimated | | Actual | |
|---|---|---|---|
| Scatterer Height | Reflectivity | Scatterer Height | Reflectivity |
| 0.50 | .5408928 | .5 | .5 |
| 0.85 | .5217696 | 1 | .5 |
| 1.25 | .5496593 | 1.5 | .5 |
| 1.55 | .5564616 | 2 | .5 |
| 2.00 | .5192856 | 2.5 | .5 |
| Antenna Height | | | |
| 3.70 | | 3 | |
| Antenna Angle | | | |
| 460 uradians | | 300 uradians | |
| Target Angle | | | |
| 30.0 uradians | | 0 uradians | |

Table 4.

30 μradians error is also within the acceptable limits.

If the scatterers vary only from 1 to 2 meters in .25 meter steps, the results are not as promising, as shown in Table 5.

| Estimated | | Actual | |
|---|---|---|---|
| Scatterer Height | Reflectivity | Scatterer Height | Reflectivity |
| 0.95 | .4996169 | 1 | .5 |
| 1.20 | .5064491 | 1.25 | .5 |
| 1.40 | .5067047 | 1.5 | .5 |
| 4.50 | .5235484 | 1.75 | .5 |
| 1.80 | .5162083 | 2 | .5 |
| Antenna Height | | | |
| 3.30 | | 3 | |
| Antenna Angle | | | |
| 380 uradians | | 300 uradians | |
| Target Angle | | | |
| -265 uradians | | 0 uradians | |

Table 5.

Table 5 shows that as the scatterers height difference lessens, the error of the estimated target angle increases. The error also increases as the increment size of Hae increases. The -265 μradians error is unacceptable.

## VII. ASSUMPTIONS AND CONSTRAINTS

Some significant assumptions and constraints were imposed on finding the solutions of the scatterer heights of a complex target. The most limiting constraint is that the reflections must be specular. Non-specular reflections (i.e., diffuse) cause the distance of a scatterer's image below the ground to be unknown deterministically. Also, the phase of the reflectivity from diffuse reflections is not 0 or 180 degrees, so the assumption that the reflectivity is real is no longer valid. This assumption is the key to the whole technique described in section V. Conceivably, there

are terrains on the earth that cause negligible diffuse multipath returns.

Another assumption is that the scatterers derived from high range resolution processing are composed only of a scatterer and its specular multipath. The effect of this assumption being false has not been tested.

The assumption was made that the reflection coefficient is the same for all scatterers. This is a likely assumption, but it needs to be measured.

It was assumed that Hs, Ha, and $\theta a$ varied over small limits. Larger limits may not result in only one minimum value of $\Gamma$.

The scatterers must span at least 2 meters in height extent. It was shown that height differences less than 2 meters cause appreciable errors in the results.

The number of scatterers has to be more than one but the minimum number required is unknown.

The complex indicated angles of the scatterers presumably derived from high range resolution were assumed to be exact. However, the limited bandwidth of the radar and the imperfection inherent in the FFT will cause small errors in the complex indicated angle derived for each range cell.

The increment of Hae, Hse, and $\theta ae$ must be small, but how small the increment must be is unknown. The smaller the increment, the more run time required. The examples shown in Tables 3 through 5 each took approximately 30 minutes to run on a DEC PDP 11/70. Obviously, the processing time is prohibitive to real time operations. Using non linear least squares fitting is not expected to improve the computation time. Further math analysis of equations 6 and 7 may reveal some mapping or transformation which would reveal a more efficient way to find the scatterer heights.

## VIII. SUMMARY

The millimeter guidance approach to the ADKEM scenerio requires the development of multipath reduction techniques to insure accurate guidance of missile to the target. This paper has examined various techniques to reduce the multipath error associated with the target in idealized cases (flat earth, specular multipath only). The high range resolution average and the scatterer height derivation technique show

some promise with the latter technique's performance degrading as the target cases become less than ideal. It should be pointed out that a worst case specular reflection coefficient (.5) was used in the analysis and that the occurence of such a reflection coefficient in typical battlefield terrains should be rare. It is probable that both specular and diffuse multipath will exist to some extent and it is hoped that target movement will help to decorrelate the diffuse error. Further multipath reduction technique analysis will continue on this rather challenging problem and it is hoped that in the FY 91 timeframe data can be collected to both support and verify reduction technique performance.

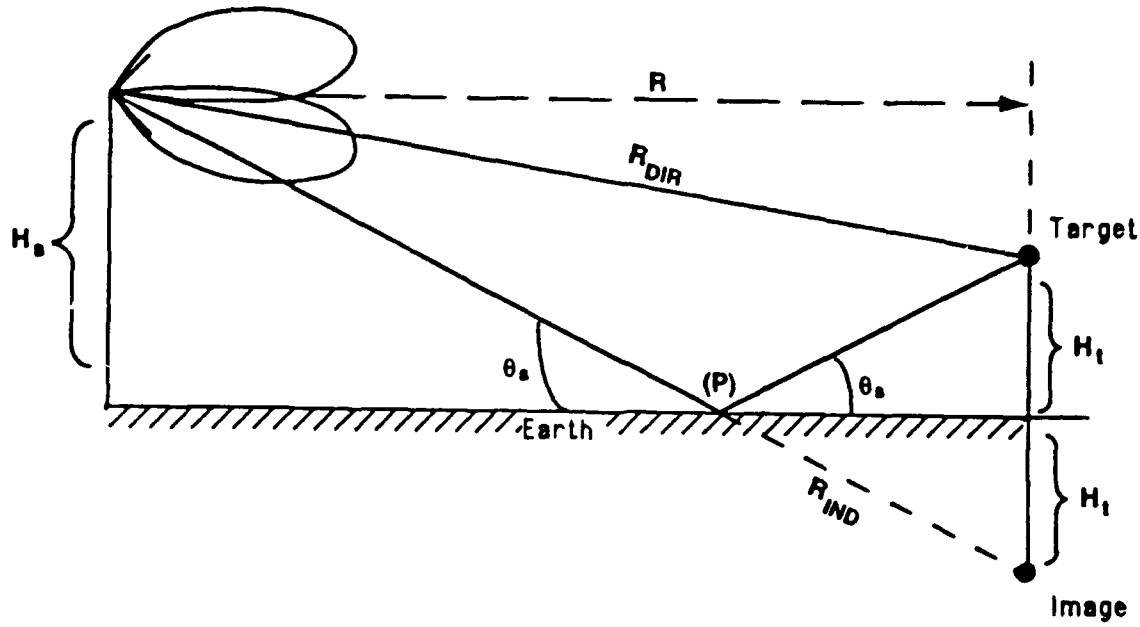


Figure 1. Generic specular multipath geometry.

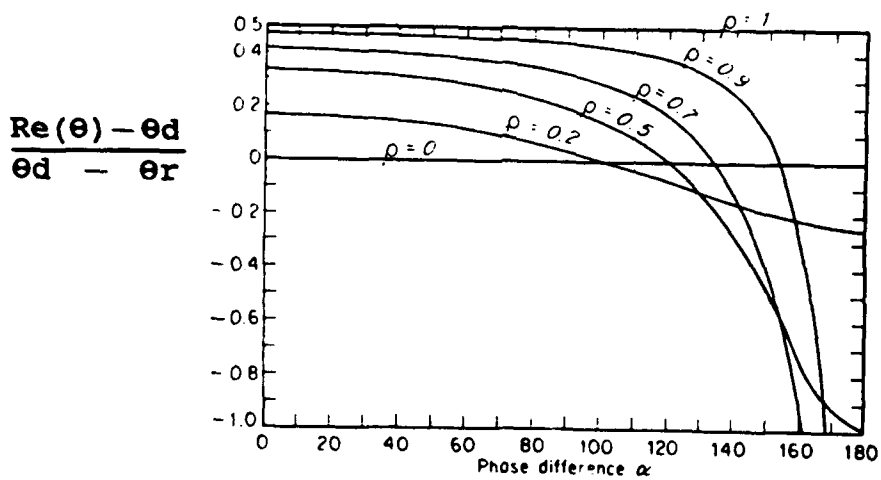


Figure 2. Angular error (normalized) as a FN. of phase difference and reflection coefficient.

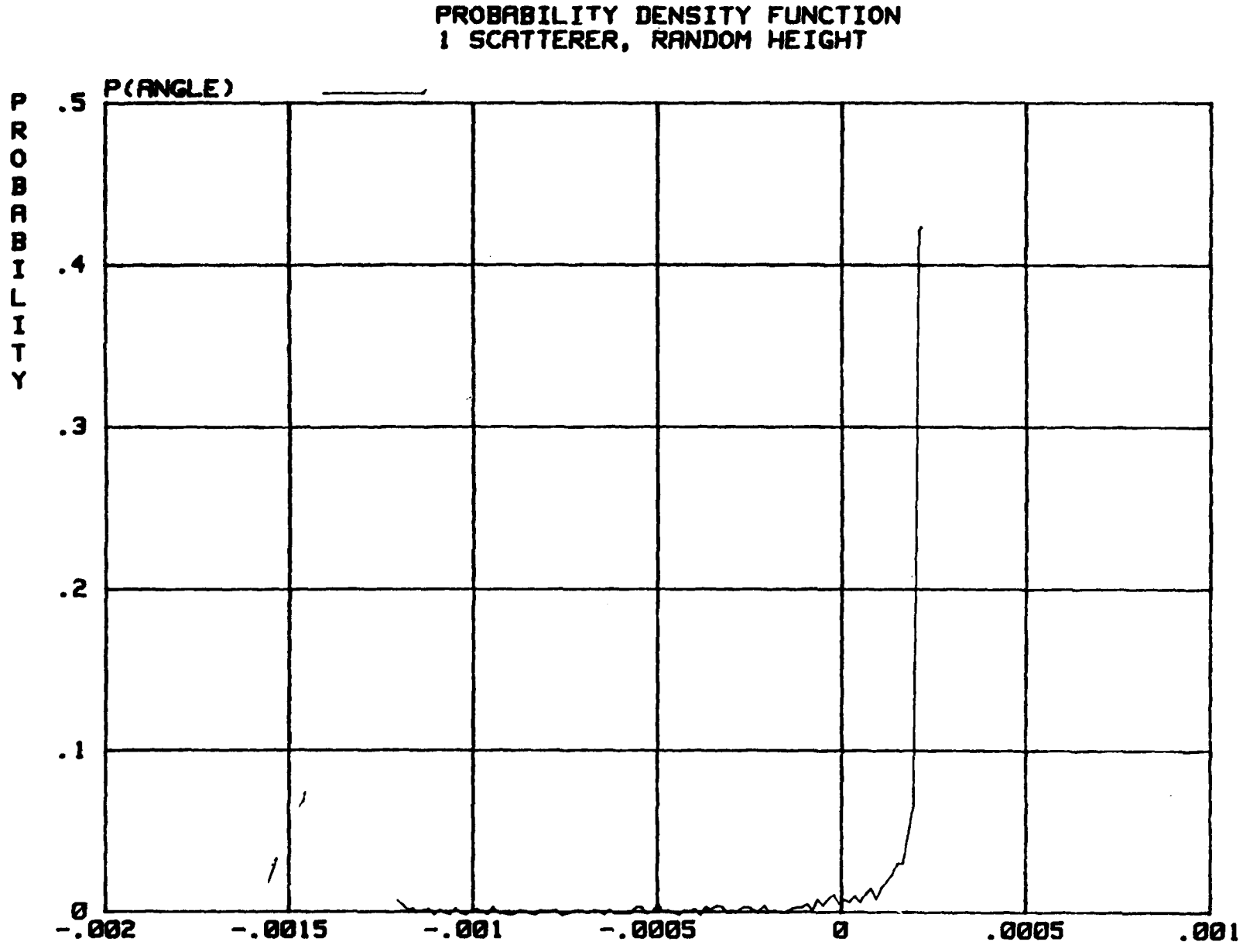


Figure 3. Measure angle (radians).

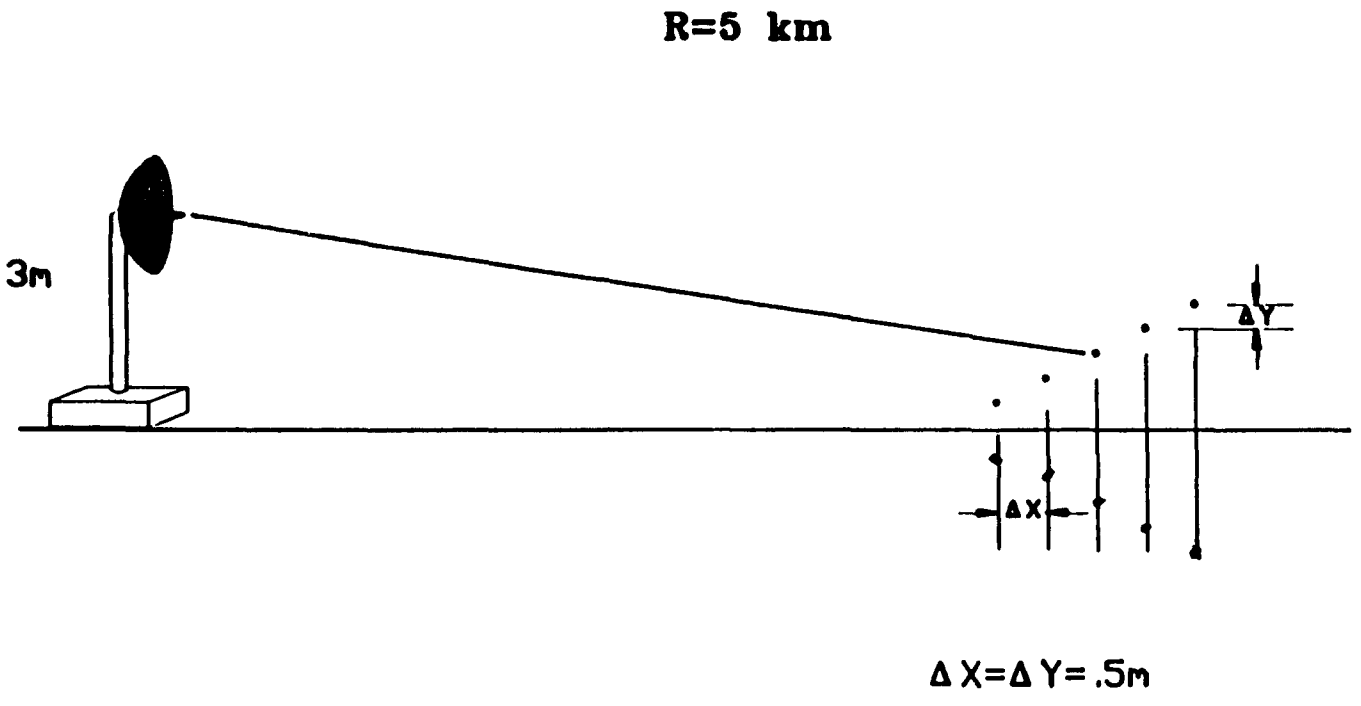


Figure 4. Specular multipath test case.

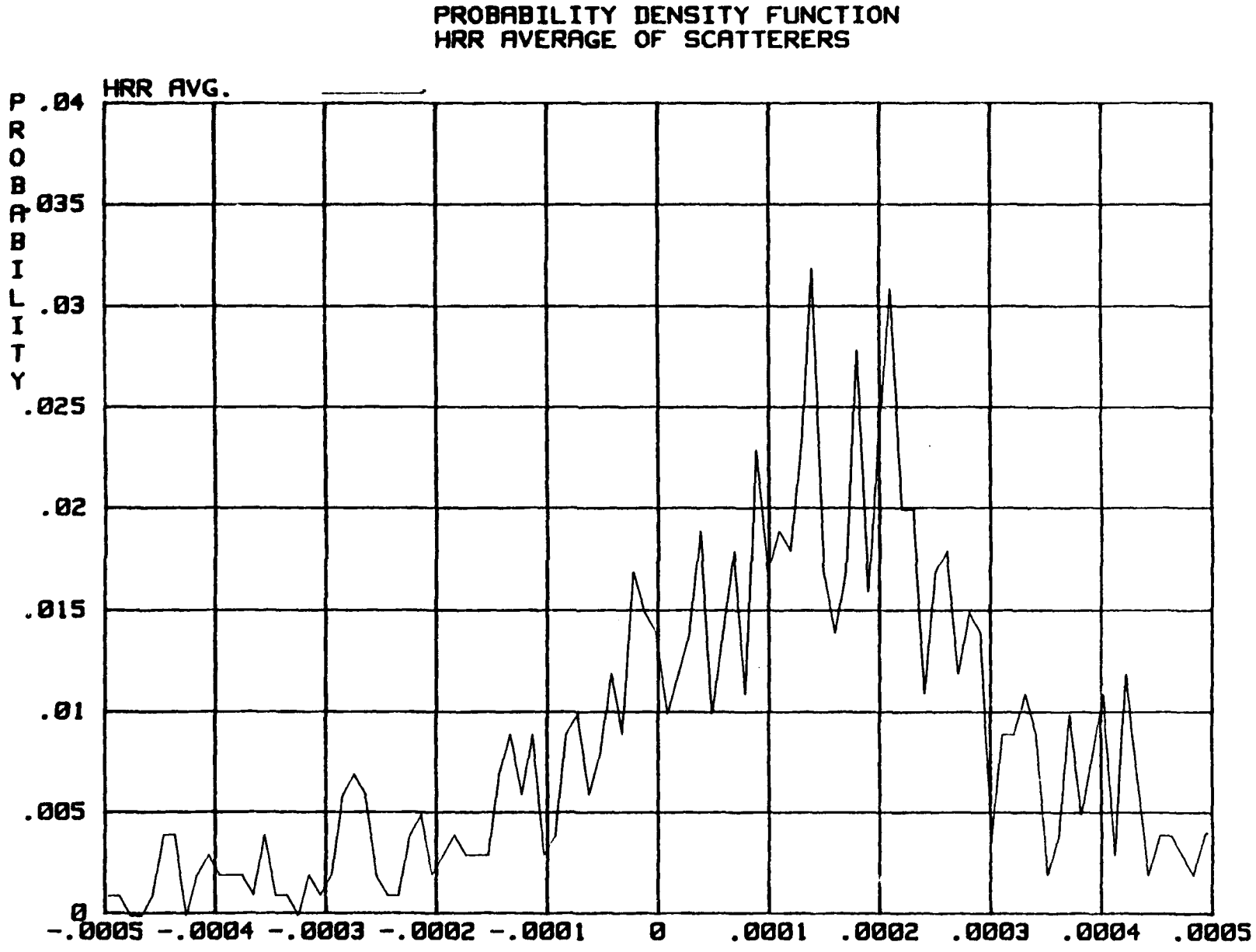


Figure 5. Angular error (radians).

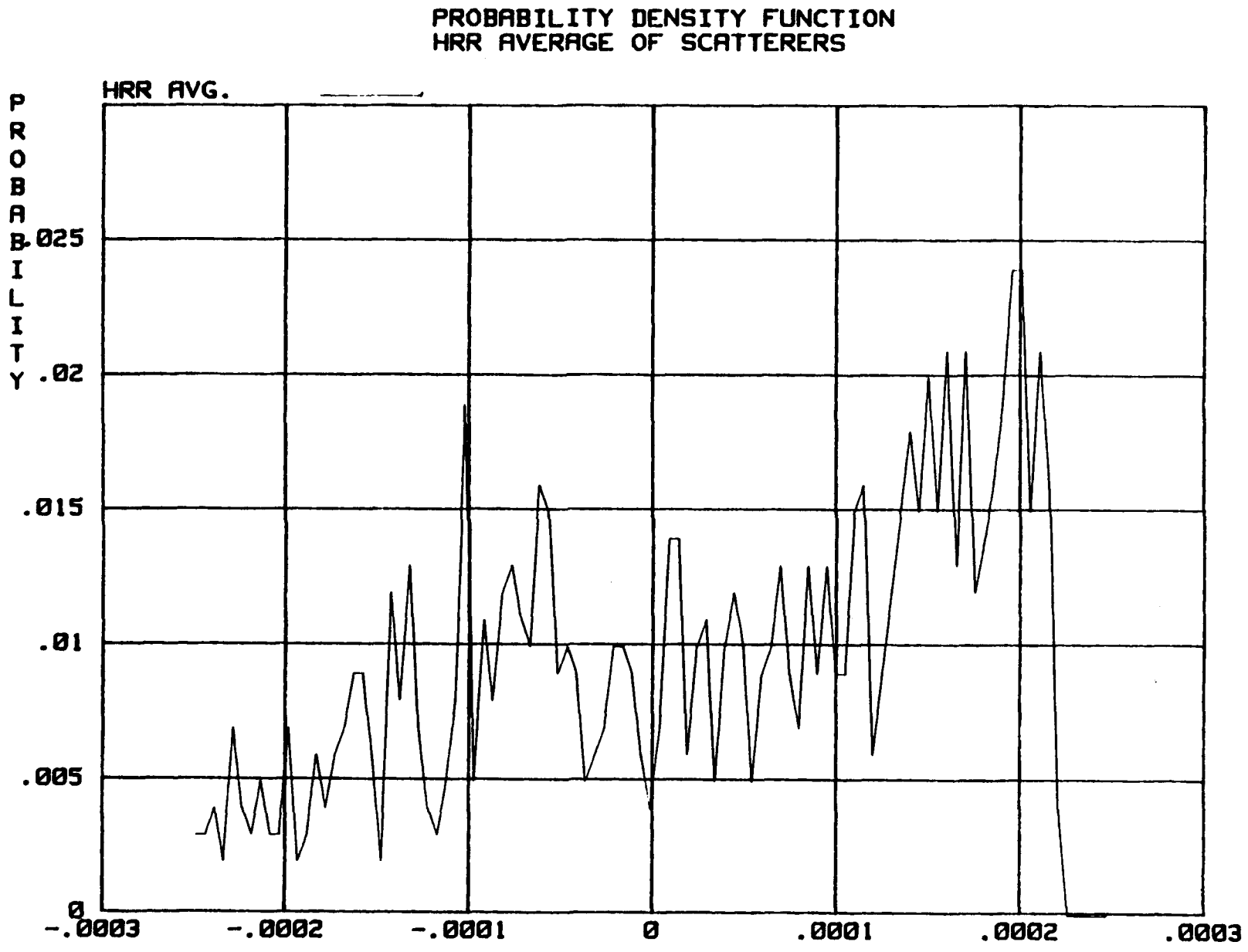


Figure 6. Angular error (radians).

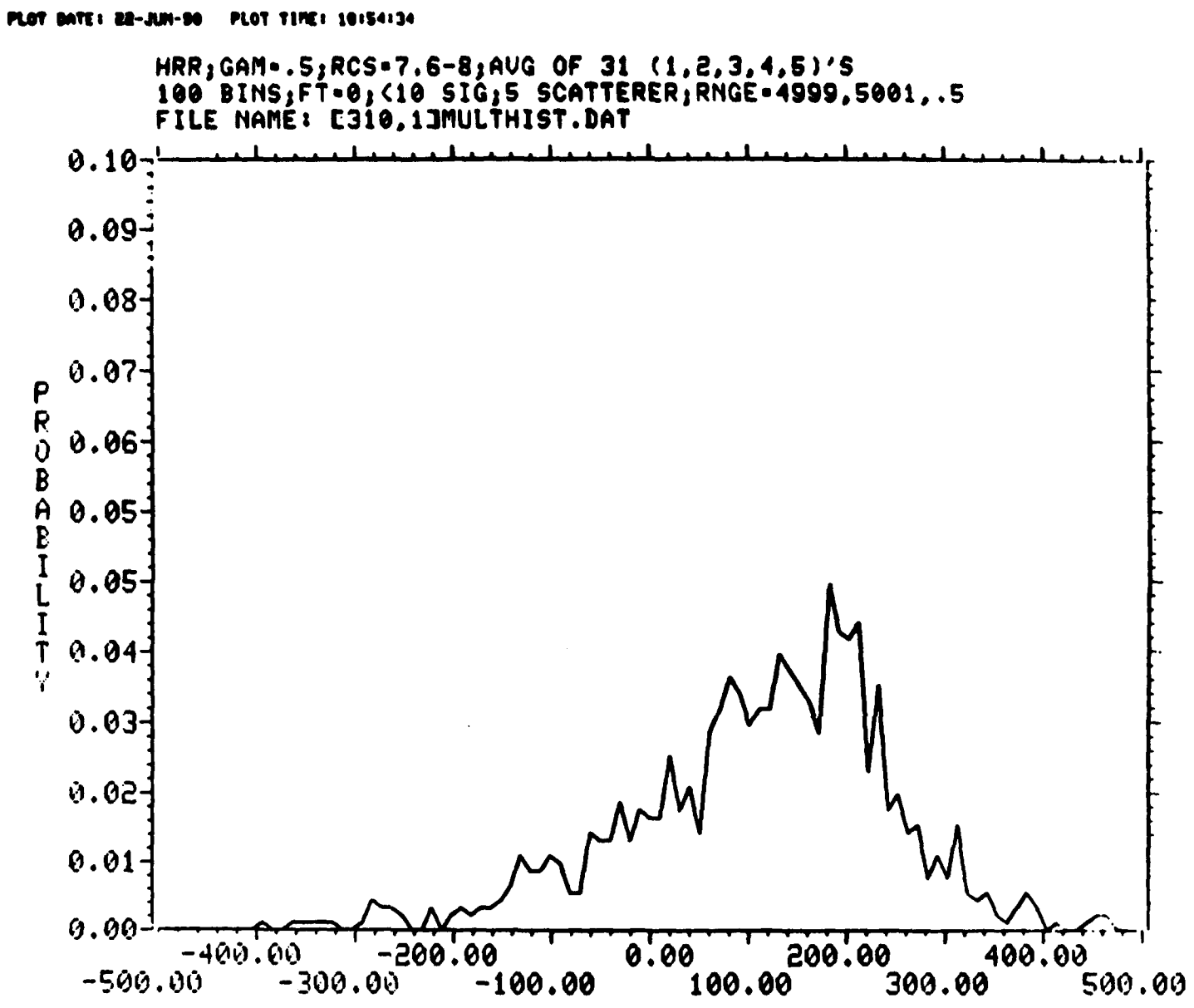


Figure 7. Angular error *μradians*.

REFERENCES

1. S.M. Sherman, Monopulse Principles and Techniques, Artech House, 1974.

# INFRARED SEEKER DEVELOPMENTS FOR INDIRECT FIRE APPLICATIONS

June 1990

Emily H. Vandiver and Ronald C. Passmore
Research, Development, and Engineering Center
US Army Missile Command, Redstone Arsenal, Alabama

## ABSTRACT

The U.S. Army has been developing an infrared seeker for application to the indirect fire role since the 1970's. The early attempts, which were successfully demonstrated in the ASSAULT BREAKER Program, resulted in seekers which were quite simplistic and did not address the challenges of target aimpoint selection or system availability in European weather. Target aimpoint selection was one of the areas addressed under the Two Color Infrared Seeker (TCIRS) Program, which considered both missile and projectile applications. The seekers were G hardened to withstand approximately 11,000 Gs during this program. Current efforts, which are being conducted under the Army Tactical Missile System (TACMS) Infrared Terminally Guided Submunition (IRTGSM) Proof of Principle (POP) Program are addressing some remaining technical challenges for this technology. In particular, this POP program will demonstrate the following: feasibility of the horizontal glide concept, sufficient lethality to kill the threat target, ability to package into the required size, and adequate seeker performance to achieve the required system effectiveness. The Army is also initiating technical investigations of utilizing infrared imaging seekers for the indirect fire engagement scenario. This paper compares the system requirements of the 1970's and today and how those requirements are reflected in the seeker technology. The utilization of staring focal plane array technology for future indirect fire systems will be discussed and the technical barriers which must be overcome will be delineated. Efforts to adapt the current technology to other applications will also be addressed.

## 1.0 THE ROLE OF ANTIARMOR INDIRECT FIRE FOR THE ARMY

Traditionally, the indirect fire mission in the deep battle was to attack nonmoving, area targets which could be located precisely and which could be engaged with high explosive warheads or bomblets. The engagement of armor in the deep battle presents a completely different set of problems; the targets are moving and are heavily armored. The lethal mechanism for defeating armored vehicles must be delivered on target, at an aimpoint which produces a kill. Fort Sill's Field Artillery School and Center has developed a draft Organization and Operation (O&O) Plan which describes how the recently developed Army Tactical Missile System (Army TACMS) will be utilized in the deep battle role. The plan outlines the roles of both the Army TACMS Block I (antimaterial/antipersonnel warhead) and the Block II (antiarmor smart submunition warhead). The stated purpose of the Block II is to disrupt and delay the enemy's course of action or prevent him from bringing up additional armor to the front. Obviously, killing the armored target delays that action indefinitely. Furthermore, the submunition must perform at the required effectiveness for a large percentage of the time in each season. It is important to note that the operations plan specifies that the TACMS missile will be fired into predefined firing zones which are selected based on many factors. It will not be fired at random targets but will be fired at pre-planned target arrays and therefore optimize the performance of the Infrared Terminally Guided Submunition (IRTGSM)(i.e. the Army TACMS is not likely to be fired at the threat target when it is in an urban area). The Block II is not intended for the attack of single targets but is designed and optimized for the attack of specific large target formations which are moving to the front. The targets are located by a separate, but integrated, target location system which specifies target location, direction of movement, and target velocity. This information is fed into a fire control system which sends firing orders to individual launchers. Crossrange firing and the maneuver capability of the Army TACMS missile allows a great degree of flexibility in the attitude at which the target can be engaged and should improve the IRTGSM performance. It is obvious that the operations plan can influence the overall system effectiveness. The Army has planned its operations to maximize the disruptive effects of Block II Army TACMS on the enemy's plan of action.

## 2.0 INFRARED TECHNOLOGY OF THE 1970'S

The infrared seekers that were developed by the Army in the mid 1970's for autonomous target acquisition and track were based on a system concept which optimized the probability of successful seeker operation. The original concept, which later was demonstrated in the ASSAULT BREAKER Program, dispensed the IRTGSMs from the "mother missile" at 2-3 kilometers above ground level. The submissiles were decelerated and oriented vertically with a parachute. The search scan pattern was an inwardly collapsing spiral. If a target was not detected on the first scan, the process was repeated until a legitimate target was acquired. Upon the acquisition of a target, the parachute was released and the submissile homed on the target to impact. The concept is shown in figure 1.

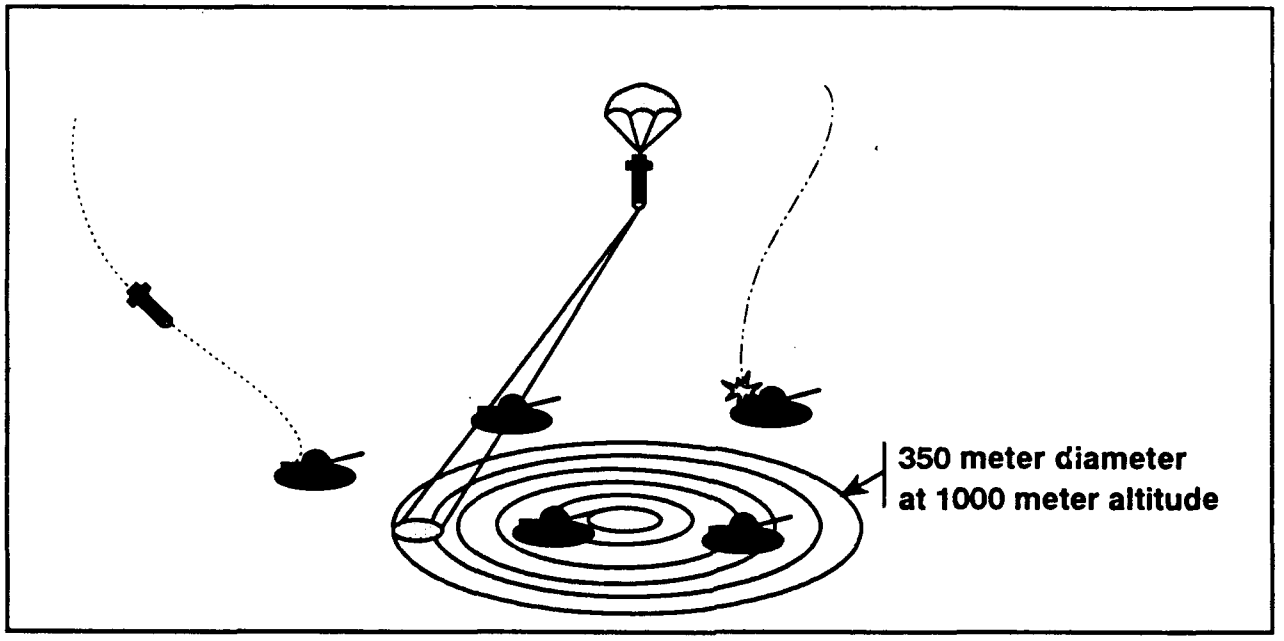


FIGURE 1. VERTICAL DESCENT IRTGSM CONCEPT

There were concerns that autonomous acquisition, indirect fire infrared seekers would suffer from high false alarm rates, would be easily countermeasured, and would not reliably acquire targets. Nearly a thousand hours of captive flight testing substantiated the performance capability of the seeker concept and all design goals were met or exceeded. The two color seekers utilize a relatively simplistic combination of spectral, spatial, and temporal processing to acquire valid targets and reject hot countermeasures. Figure 2 illustrates, in simple fashion, the use of thresholds in the seeker. The lower threshold is adaptive, and is determined as a multiple of the RMS value of the background. In order to be processed, a potential target pulse must exceed the target threshold. If it exceeds this threshold, the signal is examined in both spectral bands (colors) for a fixed number of samples to determine if it is a valid target. Also a countermeasure (CM) threshold is set to correspond to an excessively intense target such as flares, fires, etc. If a pulse exceeds this CM threshold, it is discarded as an obvious false target. Objects which produce too wide a pulse are also rejected as invalid. Once a target is declared valid, the seeker tracks it and develops guidance signals for terminal homing. In the 1970's seekers, there was no concerted attempt to investigate the possibility of "fine tuning" the aimpoint since any hit on the top interior profile of the target would produce a kill.

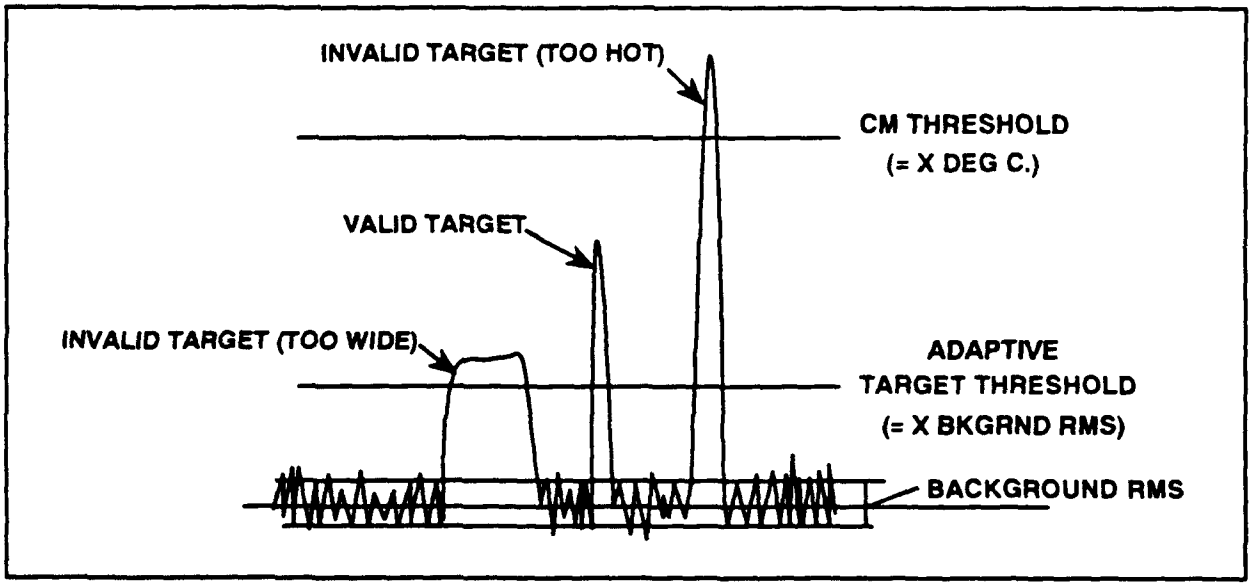


FIGURE 2.0 THRESHOLDS IN THE TWO COLOR SEEKERS

The two color seeker contractors were Raytheon Company and General Dynamics/Valley Systems Division. The two seeker inboard profiles are shown in figures 3 and 4. The General Dynamics two color seeker and the vertical approach IRTGSM were selected for the long range, ASSAULT BREAKER missile demonstration firings at White Sands Missile Range. The program culminated with an approximately 85 km shot in which five live IRTGSMs were dispensed successfully. They autonomously acquired five individual targets and guided to highly accurate hits on the hot area of the targets.

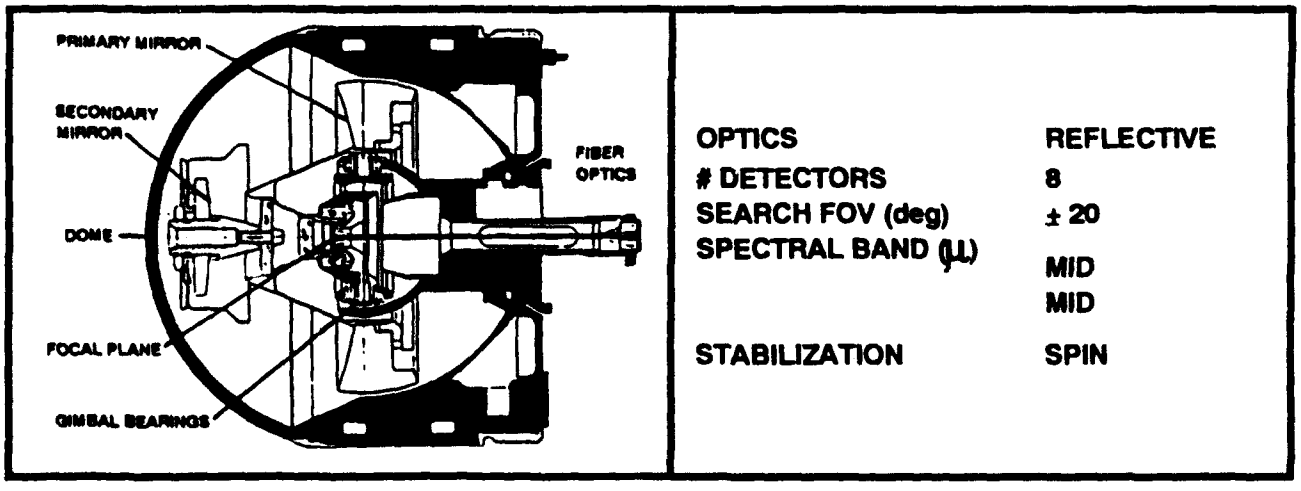


FIGURE 3.0 GENERAL DYNAMICS ASSAULT BREAKER TWO COLOR IR SEEKER

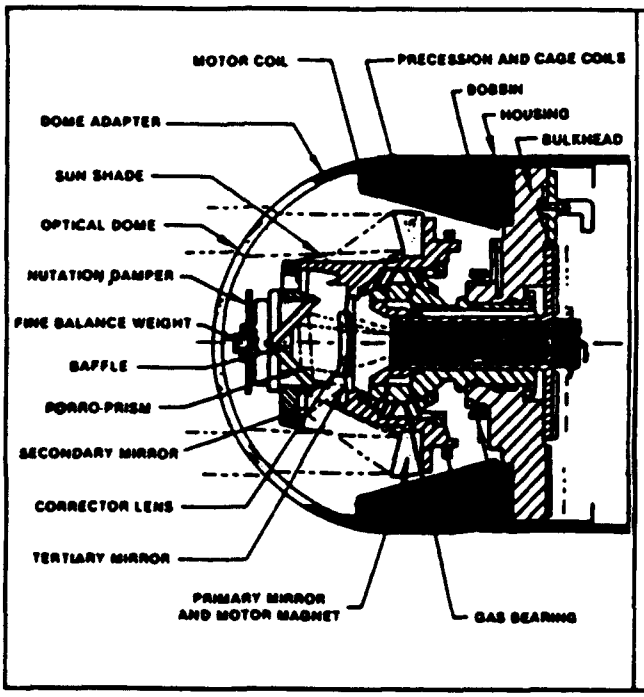


| | |
|---|---|
| OPTICS | REFLECTIVE |
| # DETECTORS | 14 |
| SEARCH FOV (deg) | ±20 |
| SPECTRAL BAND (μ) | MID<br>LONG |
| STABILIZATION | SPIN |

FIGURE 4.0 RAYTHEON ASSAULT BREAKER TWO COLOR IR SEEKER

## 3.0 TWO COLOR IR SEEKER (TCIRS) EFFORTS IN THE 1980'S

After the successful completion of the ASSAULT BREAKER Program, two color IR seeker technology efforts were put on hold by the Army. The technology was proposed for the MULTIPLE LAUNCH ROCKET SYSTEM Terminally Guided Warhead (MLRS TGW) but milllimeter wave technology was selected for the submissile guidance. In the mid 1980's the Army conducted a Smart Munitions study in an attempt to prioritize the development of smart weapon systems. As a result of that study the Armament Research, Development, and Engineering Center at Picatinny Arsenal, New Jersey was directed to include common seeker requirements for missiles and projectiles in the GUIDED ANTIARMOR MORTAR PROJECTILE (GAMP) Program. Because of a lack of a firm requirement, the GAMP Program was cancelled by the Army. However, the Army did fund TCIRS efforts to develop a seeker with maximum commonality of design for missiles and projectiles. The contracts to both General Dynamics and Raytheon were awarded by Picatinny Arsenal and transferred to the Army Smart Weapons Management Office (SWMO), located at MICOM.

The "common seeker" requirements had major impacts on the ASSAULT BREAKER seekers in two areas, gimbal limits and hardening the seekers to withstand launch shocks of approximately 11,000 Gs. In order to meet the requirements, General Dynamics settled on a design which had been proposed for the Navy five inch projectile. It utilizes refractive optics for the objective telescope

and has fiber optics to transfer the IR energy from the focal plane to the body-fixed detectors. Raytheon developed a completely new design which utilizes reflective optics and a linear array of detectors mounted on the inner gimbal. The scene is scanned by precessing the inner gimbal back and forth in the yaw direction. Both General Dynamics and Raytheon utilized a restraint mechanism ("gotcha") to hold the inner gimbal during the launch shock. Due to the difficulty in hardening the seekers to the design requirement, most of the efforts in the TCIRS Program were for G hardening as opposed to improvements in signal processing algorithms. Both seekers were fired in a canister from a howizter at MICOM and survived 11,000 Gs. The seeker concepts are shown in figure 5.

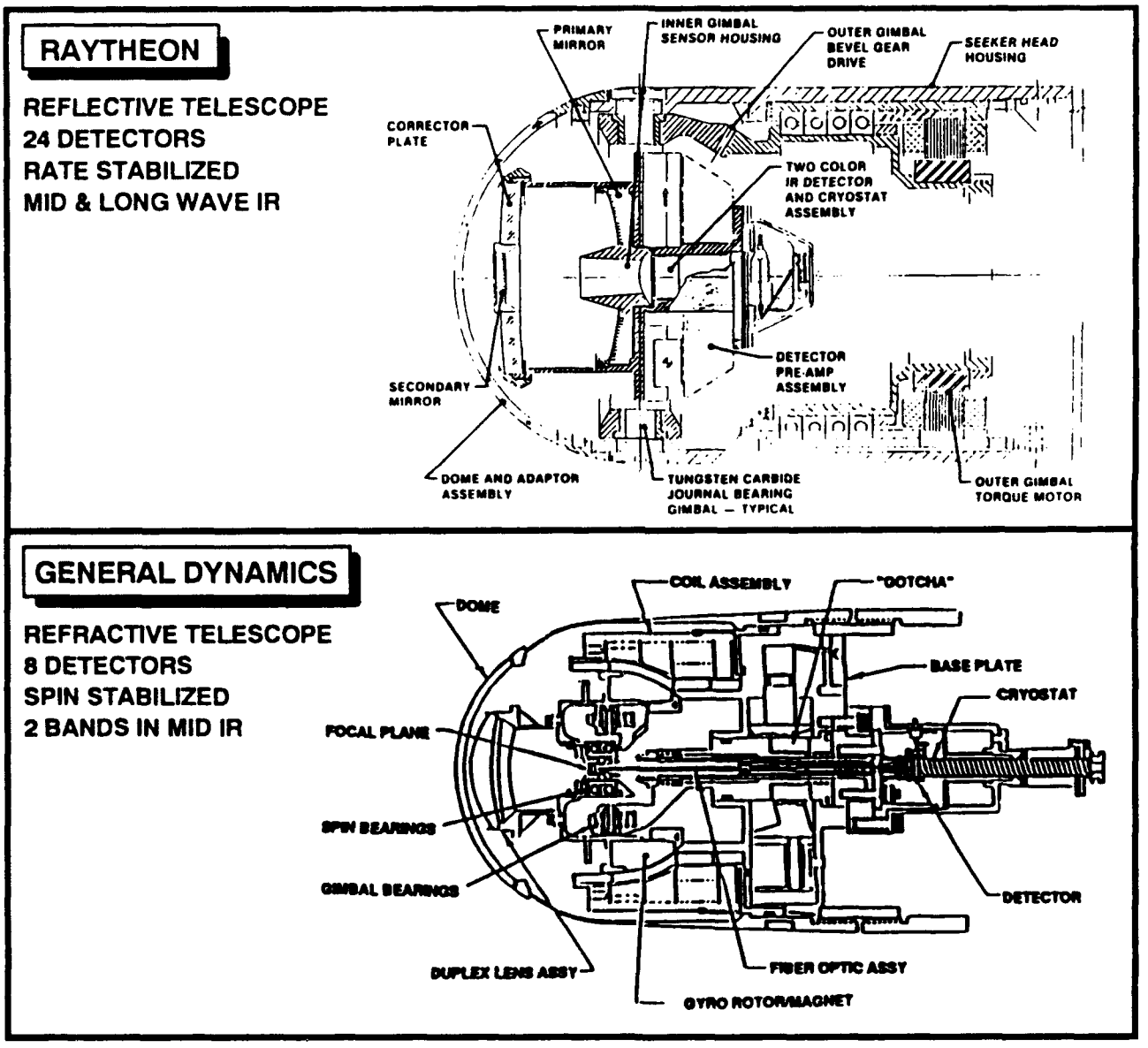


FIGURE 5.0 TCIRS SEEKERS

## 4.0 CURRENT INFRARED SEEKER TECHNOLOGY FOR INDIRECT FIRE

There were several changes that occurred in the 1980's that altered the way the two color seekers could be utilized in an indirect fire missile system. First, the threat was changed from a relatively circular array of targets to a linear array of targets that incorporated advanced armor on the top as well as on the sides and front of the vehicles. Secondly, the in-flight inertial up-date capability for the "mother missile" was eliminated, resulting in a larger projected miss distance for moving targets. Thirdly, the requirement was imposed for maintaining required submunition effectiveness for a large percentage of the time in each season of Central European weather. These changes forced a complete relook at the IRTGSM concept and how the two color seeker would be utilized. Basically, the changes forced the IRTGSM concept to a horizontal glide approach beneath the expected cloud ceilings of Central Europe and the addition of terminal aimpoint logic which produces the required lethality with a small diameter submunition. The threat target infrared signature also changed to present a much lower intensity target to the seeker, thus making it more difficult to acquire autonomously. The characteristics of the current IRTGSM concept are given in figure 6. It should be noted that there is a trade-off between system availability and search footprint. The means of trade-off is search altitude (i.e., the lower the search altitude, the greater the availability but narrower the search footprint).

- **INDIRECT FIRE WITH AUTONOMOUS TARGET ACQUISITION**
- **MANY-ON-MANY SCENARIO**
- **HORIZONTAL GLIDE SEARCH TRAJECTORY WITH GLIDE ALTITUDE UNDER SOFTWARE CONTROL AND LOADED BEFORE LAUNCH**
- **LARGE SEARCH AREA TO ACCOMMODATE SYSTEM ERRORS (TARGET LOCATION, DELIVERY, TARGET MOTION, ETC.)**
- **MODERATE $P_d$ REQUIRED**
- **TARGET SELECTION LOGIC EMPLOYED TO AVOID TARGET OVERKILL**
- **HIGH $P_{k/a}$**
- **LOW COST**

FIGURE 6.0 CHARACTERISTICS OF THE CURRENT IRTGSM CONCEPT

Although the current effort is a POP program, both Raytheon and General Dynamics, the competing prime submunition contractors, have studied the eventual tactical design which would meet all the system requirements. Figure 7 shows the inboard profiles of the tactical IRTGSM designs for both developers. The similarity in designs only indicates that certain non-tradable requirements force system design choices that are very limited.

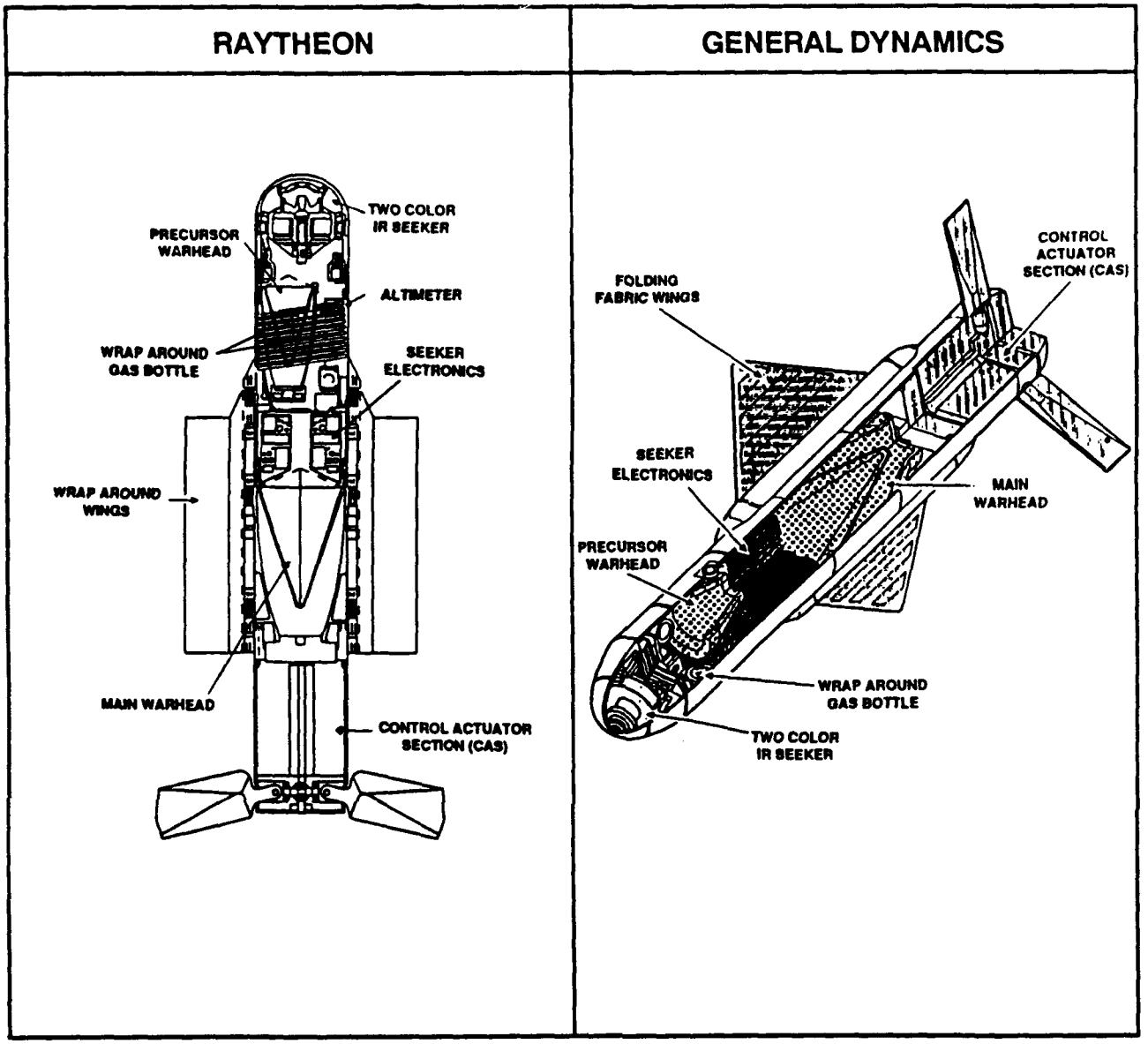


FIGURE 7.0 INBOARD PROFILES OF TACTICAL IRTGSMs

The seekers that each contractor is utilizing in the POP program is illustrated in figure 8. The General Dynamics design is almost mechanically identical to their ASSAULT BREAKER seeker. The Raytheon seeker is quite different from their ASSAULT BREAKER design in that it now employs a two-axis, rate stabilized gimbal with gimbal mounted detectors to maintain focus at the extremes of horizontal search. The General Dynamics seeker utilizes fiber optics to couple the gimballed focal plane to the body-mounted detectors to maintain focus. Both seekers incorporate aimpoint selection logic to bias the terminal aimpoint from the hot spot to a more vulnerable interior location. The ability of the seeker/airframe to hit at the

correct selected aimpoint is critical to the success of the IRTGSM POP program. There is no requirement for these seekers to be G hardened so both contractors are pursuing seeker designs which do not include hardening features. However, SWMO is conducting a commonality study for missile and projectile applications with the POP submunitions, including the seekers, being considered in that study.

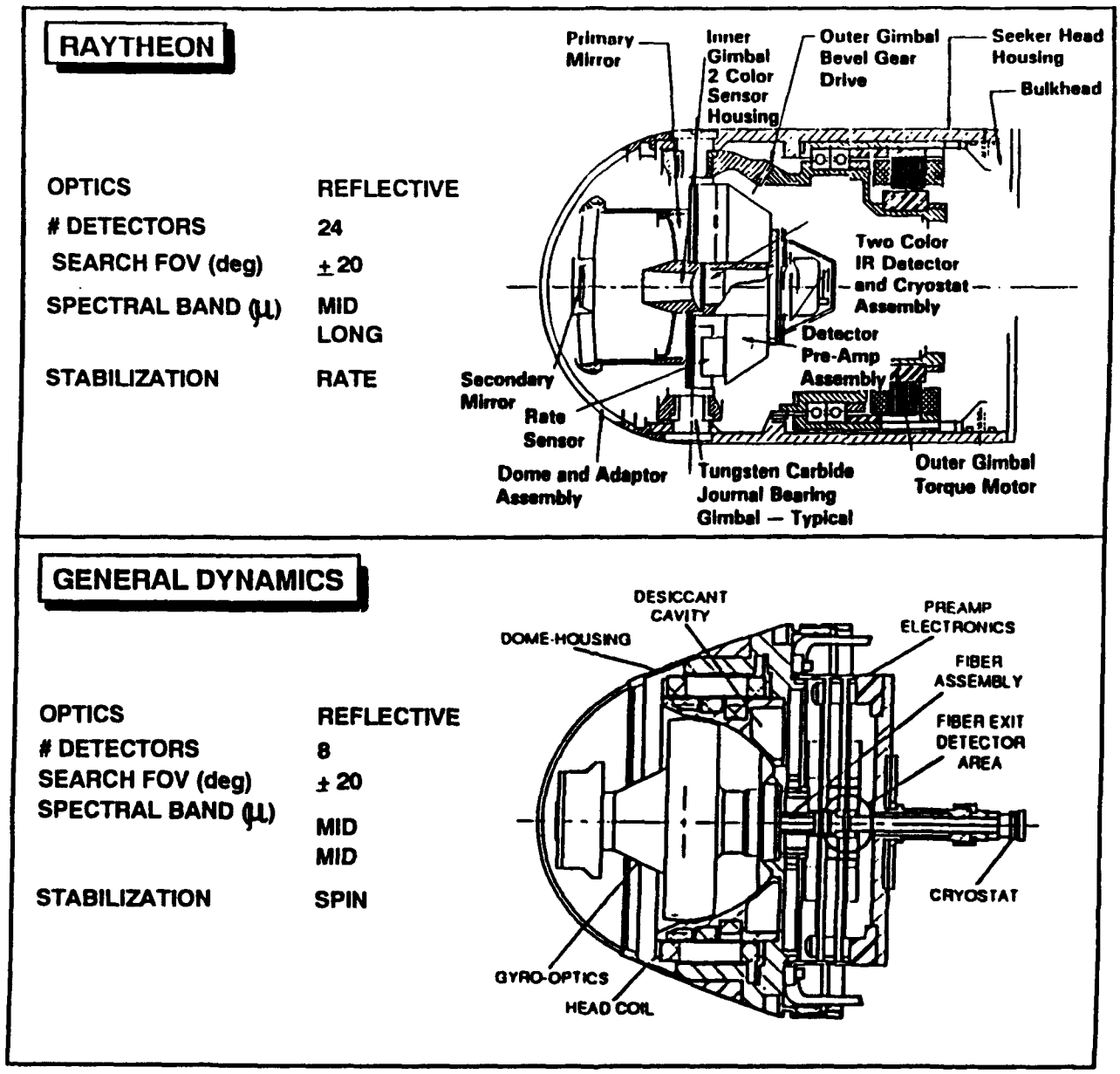


FIGURE 8.0 PROOF OF PRINCIPLE SEEKERS

The IRTGSM and the two color infrared seeker, in particular, are being considered for other indirect fire weapons systems applications. The IRTGSM can be packaged into the MLRS with a rocket load of five submunitions per MLRS with minor modification to the MLRS warhead. The Army Materiel Command's Smart Weapons Management Office is conducting a commonality study that addresses the utilization of indirect fire technology (including the IRTGSM) for rockets, missiles, and gun-launched projectiles. The study is scheduled to be completed by 30 October 1990.

The current state-of-the-art, two color infrared seeker technology has a place in the Army's indirect fire weapons family. It is mature, relatively low cost, reliable, and capable of being packaged into a 4 inch diameter by 26 inch long submunition.

## 5.0 INFRARED IMAGING IR SEEKERS FOR THE FUTURE

Although the two color seeker technology is a cost effective approach to destroying armor in the deep battle, it has shortcomings that cannot be overcome with the simplistic focal planes and algorithms that are characteristic of this class of seekers. Improvements are desired in counter-countermeasures, acquisition of low thermal contrast targets, aimpoint selection and hitpoint performance, and target selectivity (i.e., target recognition). One possible solution to solving the shortcomings of the present two color infrared seekers is to utilize imaging infrared seeker technology. To date, this alternative has not met with great favor by Army developers due to limitations in the technologies required to make imaging IR seekers feasible. However, advances in staring focal plane array sizes, development of high throughput processors, and refinement of autonomous acquisition algorithms now make the imaging infrared seeker for indirect fire quite attractive. Platinum Silicide Schottky Barrier focal planes are currently available in 512 X 512 element arrays and efforts are underway to expand the arrays to 1024 X 1024 elements. Indium Antimonide (InSb) and 3-5 μm Mercury Cadmium Telluride (HgCdTe) arrays are being made in larger sizes and should soon be available in sizes which are applicable for the indirect fire seeker concept. DARPA's ALADDIN processor, VHSIC, and application specific integrated circuits (ASIC) are just part of the advances in small volume, high throughput devices that are becoming available to process the vast amount of information outputted from large focal plane arrays. Finally, the government and industry supported efforts in autonomous acquisition and target recognition algorithm developments are maturing to the point that their utilization in indirect fire seekers appears feasible.

Figure 9 illustrates some of the benefits that might be expected from an imaging seeker as compared to the current two color seekers.

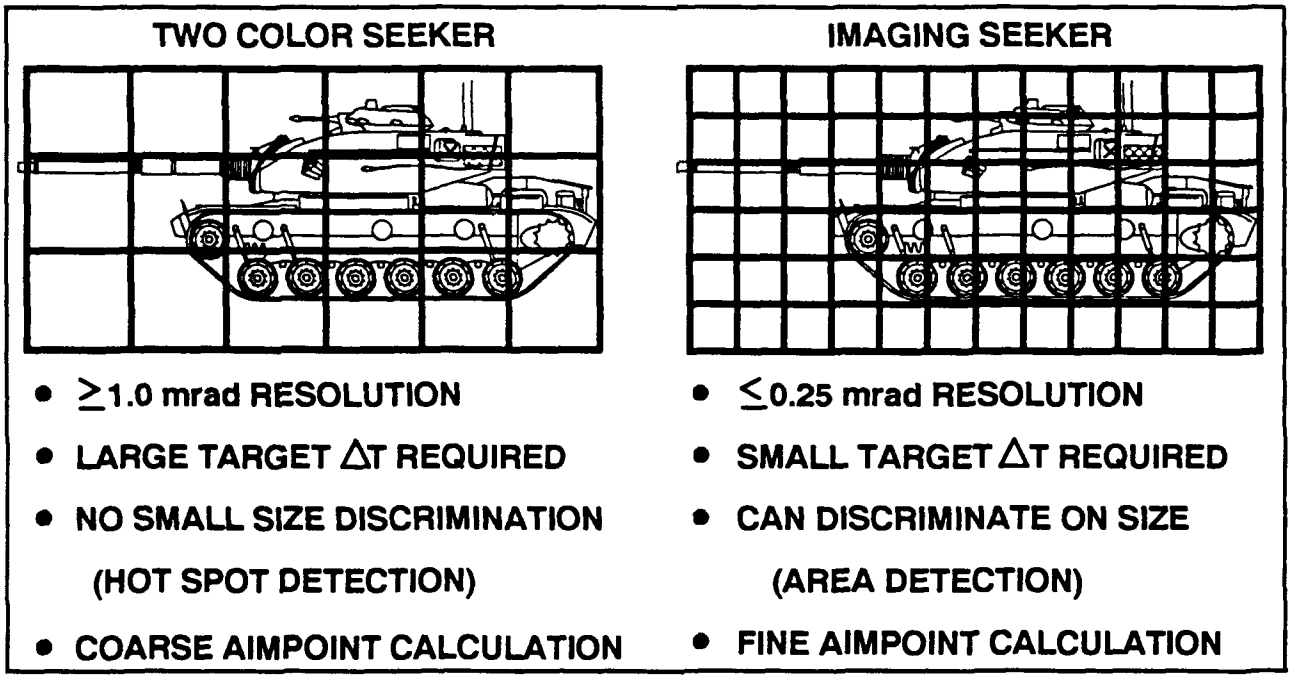


FIGURE 9.0 IMAGING AND TWO COLOR SEEKER COMPARISION

The transition to the imaging seeker concept for an IRTGSM is not a simple matter. There are still technologies which must be investigated and matured before the concept can be demonstrated. The focal plane arrays are one example of a technology which requires additional effort. The PtSi arrays, which are the only arrays that can presently be fabricated in large sizes, have small quantum efficiencies over the wavelengths of interest. In order to gain sensitivity, the integration time is allowed to be the frame time (1/30th sec.). With this long integration time, the problem with image smear arises. This is shown in figure 10 for a horizontal glide TGSM. The magnitude of the problem will be addressed in the ongoing exploratory development program. Obviously, one solution to the problem is to scene stabilize the seeker during the integration time so a pixel stares at a relatively constant area. This will add complexity (and therefore, cost) to the seeker. Another solution is to utilize a focal plane array which requires an extremely small integration time so the smear will be negligible during the integration time. Other FPAs (such as InSb which requires a very short integration time) are being investigated for use in the concept.

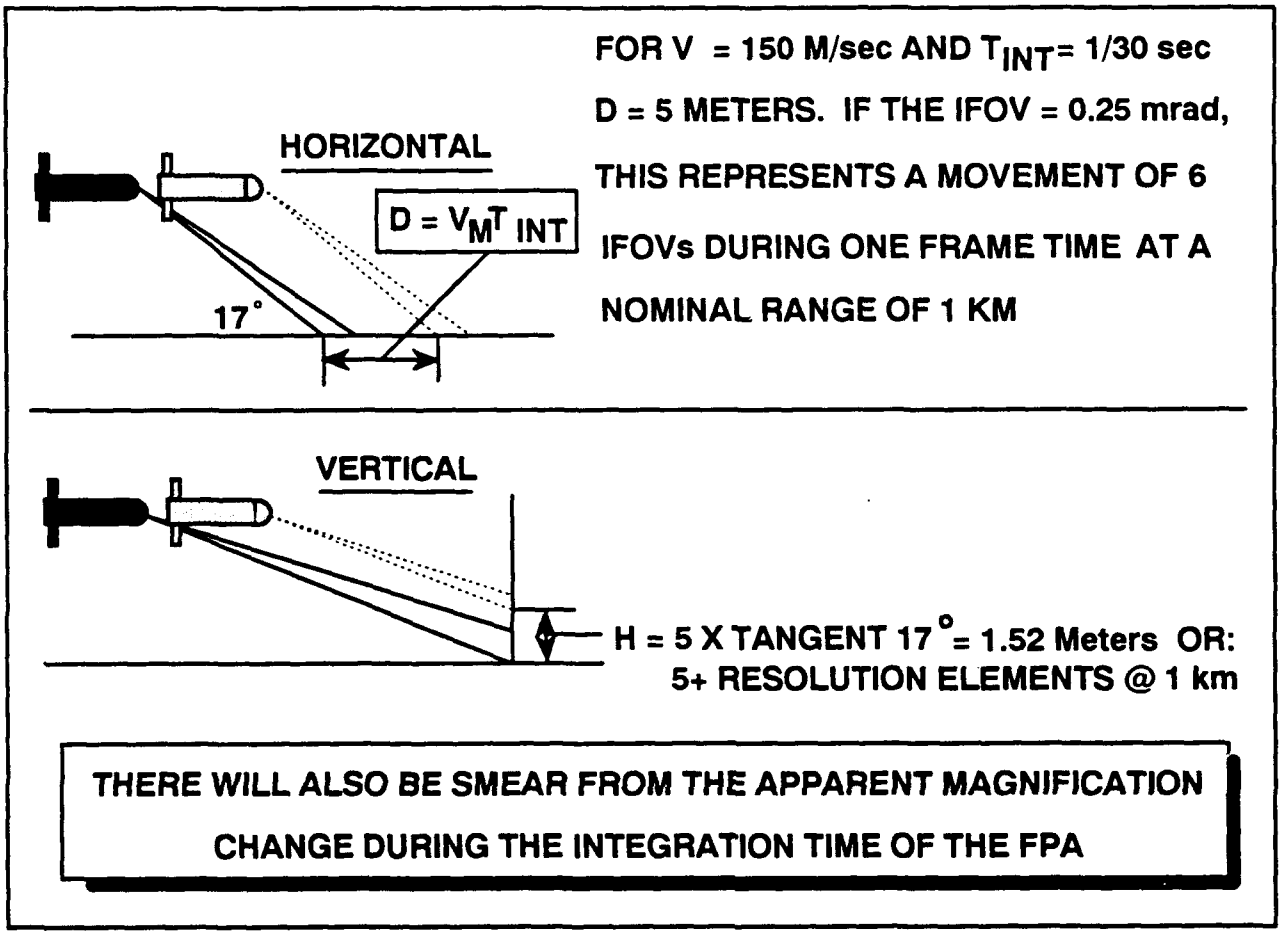


FIGURE 10.0 A POTENTIAL PROBLEM WITH IMAGE SMEAR.

The current exploratory development program being conducted in the MICOM Research, Development, and Engineering Center is investigating the effects of the relative motion between the seeker and the scene on contrast transfer function (CTF). Measurements will be made utilizing both PtSi and InSb FPA sensors and the CTFs will be measured in both the horizontal and vertical directions.. The CTF of the InSb sensor will be determined as a function of the frame rate. Figure 11 is a diagram of the experimental setup. It is a modified optical bench which is normally used to measure the minimum resolvable temperature (MRT) and noise equivalent temperature (NET) of imaging senors and seekers. The rotatable folding mirror has the capability of producing image angular rates of 0.5 to 5.0 degrees per second.

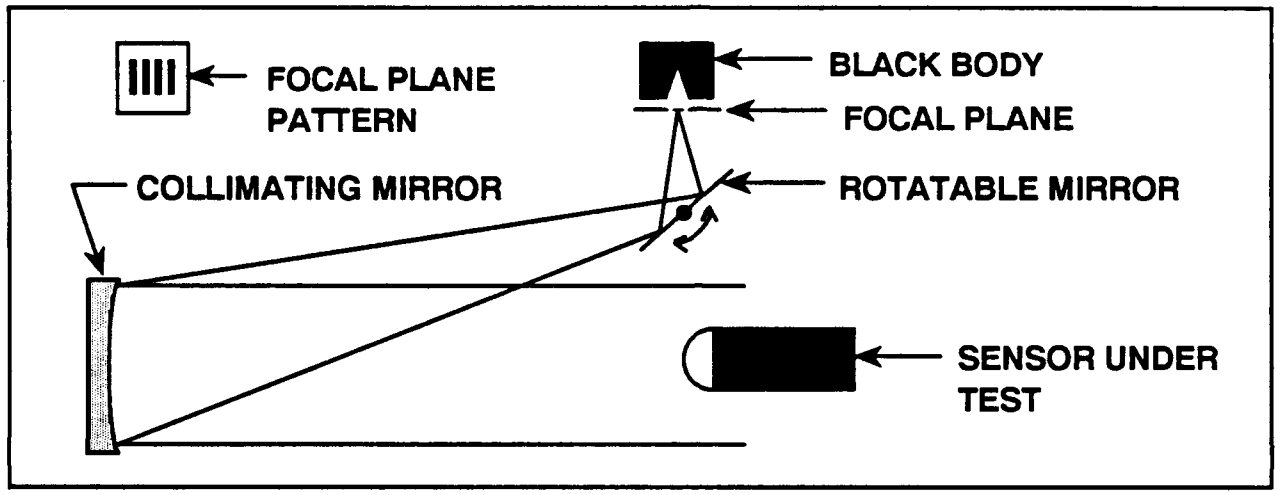


FIGURE 11.0 LABORATORY SETUP FOR CTF INVESTIGATIONS

If the short integration time requirement forces the Army from PtSi to a more exotic FPA material, the size (number of pixels in azimuth and elevation) may well become an issue. The FPA size relative to search field-of-view is pictured in a simplistic manner in figure 12. Even the 256 X 512 array, which is supportable with current PtSi technology, requires a three step-stare search scheme in order to cover the same search width as the present two color seekers. The step-stare technique has been demonstrated in the Army Non-Line-of-Sight (FOG-M) program but that system has a man-in-the-loop for detecting targets in clutter. Another approach might be to utilize smaller FPAs (i.e. 128 X 128 elements) as a one column (128 X 1 elements) in a gimbal scan search pattern. Once a valid target is detected, the full 2-dimensional array can be used for the validation, recognition, and tracking of the target. The trades between high and low density arrays must be addressed by the MICOM exploratory development program.

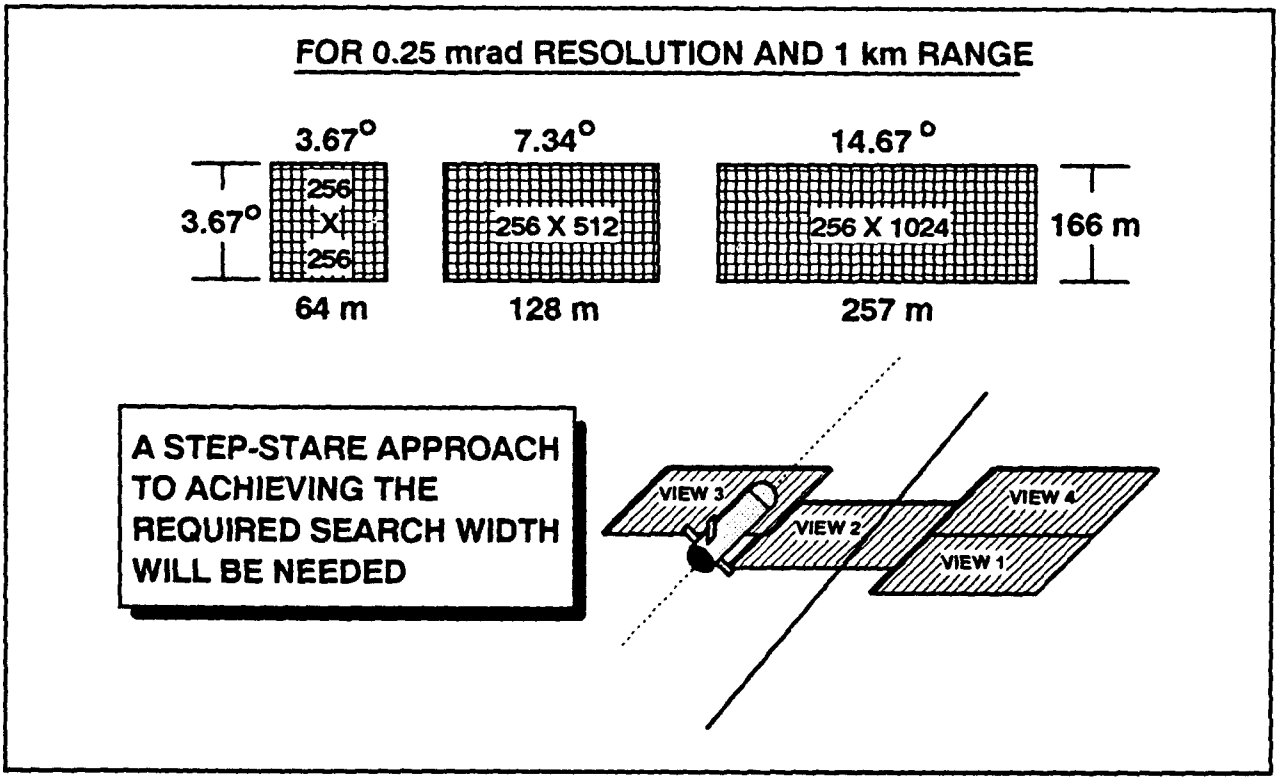


FIGURE 12.0 SEARCH FIELD OF VIEW COVERAGE

The technical challenges facing the autonomous imaging infrared seeker development are considerable. Only a few have been discussed above. The capability of the acquisition algorithms to detect and acquire low contrast targets must be demonstrated. In addition, there is a desire to implement target recognition capability as a growth option of the seeker. Aside from technical issues, the eventual cost of the imaging seeker must be addressed since an imaging IRTGSM must be cost effective for use in Army systems.

The MICOM exploratory development program schedule is shown in figure 13. The conduct of captive flight tests (CFT) has not been decided and will require further study to determine if they are technically and financially feasible. Tower tests are definitely planned if real time signal processing algorithms are available. Industry is encouraged to establish a dialogue with the program manager to make

the effort more meaningful. A Broad Agency Announcement (BAA) will be initiated that includes specific efforts that are of interest to this program. These include real time autonomous target acquisition signal processing, FPAs and FPA sensors/seekers, and real time automatic target recognizers.

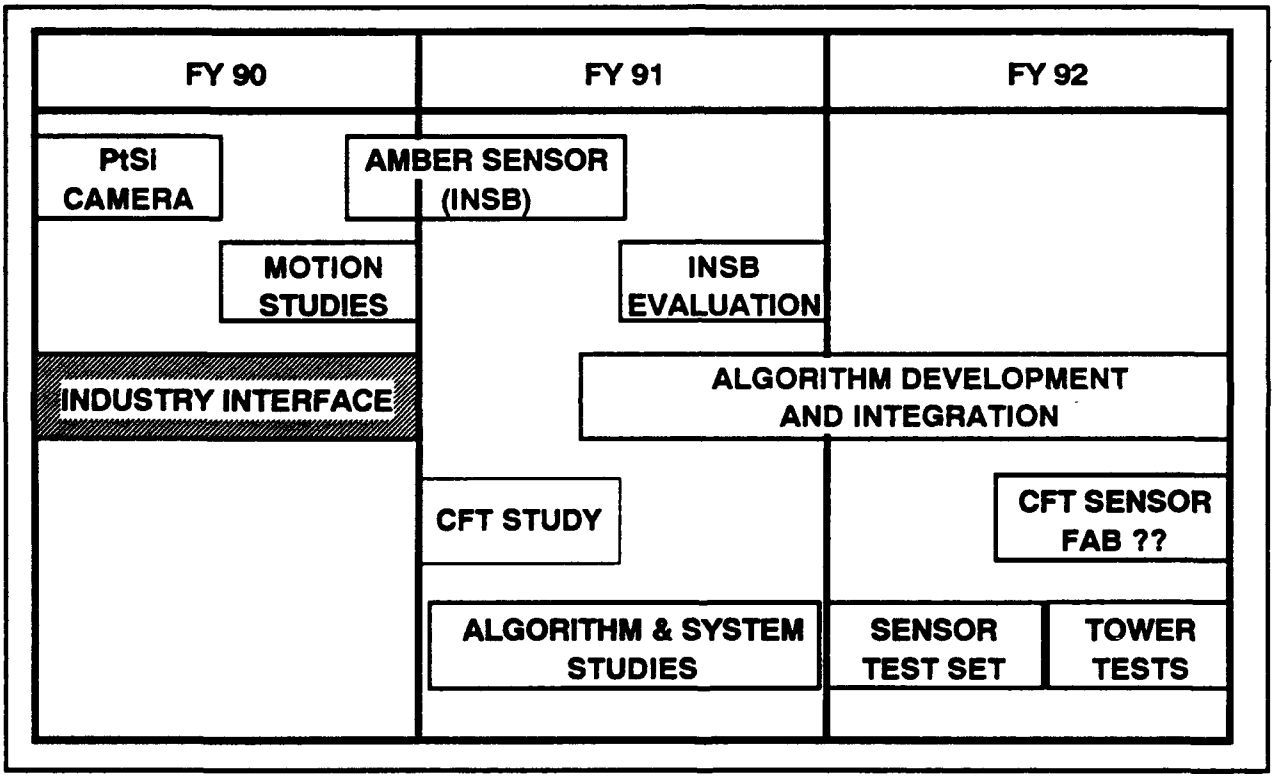


FIGURE 13.0 IMAGING IRTGSM EXPLORATORY DEVELOPMENT SCHEDULE

Given that no insurmountable technical barriers are uncovered and reasonable results are achieved in the exploratory development program, a follow-on, proof-of-principle effort is envisioned. The thrusts of the MICOM imaging IRTGSM are given in figure 14. The concerns with cost and real time processing need to be reiterated. The program is specifically oriented to getting the technology out of the laboratory and into a real-time and real-world environment. The cost issue is critical; every attempt will be made to select technological approaches which are affordable.

- RELIABLE ACQUISITION FOR LOW$\Delta$T TARGETS
  - STRESS SPATIAL PROCESSING
  - LESS RELIANCE ON TARGET INTENSITY
- IMPROVED TARGET AIMPOINT SELECTION CAPABILITY
- ENHANCED COUNTER-COUNTERMEASURES CAPABILITY
- REAL-TIME PROCESSING IN REAL-WORLD ENVIRONMENTS
- SMALL PACKAGING REQUIREMENTS
- COST CONSIOUS TECHNOLOGY SELECTION

FIGURE 14.0 IMAGING IRTGSM THRUSTS.

## 5.0 SUMMARY

Two infrared seeker approaches applicable to the Army's indirect fire, antiarmor, mission have been discussed. The two color seeker technology is mature, reliable, relatively inexpensive, and effective against the threat target. The horizontal glide concept maintains high system availability and the attendant lower probability of target acquisition does not seriously affect overall effectiveness performance. The imaging infrared seeker concept for indirect fire is being investigated under an exploratory development effort at MICOM. If the effort is successful, the seeker will have improved performance in several areas which are of interest to the Army. Emerging technologies are being exploited and a conscientious effort to utilize low cost approaches is being made. The Army will continue to monitor requirements, resources, and available technology to address the needs of Deep Fire Support.

# Laser Line of Sight Guidance

Kevin S. Lindley and Walter E. Miller
U.S. Army Missile Command
Redstone Arsenal, Alabama

## ABSTRACT

This paper is intended to be an interesting and informative top level tutorial of advanced laser-based missile technologies and systems. It will explain basic guidance techniques, capabilities, limitations, and alternatives. It will describe laser beamrider (LBR) methods, semi-active laser guidance, and the newest of all, laser updated self-simulation guidance.

Several different areas will be briefly discussed to give a concise understanding of laser guidance and its uses, including: performance advantages, such as accuracy/range, inherent countermeasure (CM) rejection, and simplicity and low cost; basic problem areas, such as the need to track the target and adverse effects of missile plumes and battlefield aerosols; laser technology alternatives, such as choice of laser, cooled or uncooled receivers, and various beam encoding methods; and developmental programs, such as LOS-F-H, LOSAT, ADKEM, CAMMS and several foreign systems.

## INTRODUCTION

The concept of laser guided missile systems has been around for many years, and several different approaches and methods have been conceived, designed, and successfully demonstrated. These guidance approaches can be divided into three major categories: semi-active, laser beamrider, and laser updated guidance. Each will be briefly described, and systems using the specific guidance technology will be highlighted, with emphasis being placed on laser beamrider guidance.

## LASER GUIDANCE DESCRIPTIONS

### SEMI-ACTIVE LASER GUIDANCE

This method uses a laser for target designation, which in turn provides guidance information to the missile by way of a seeker in the nose of the missile. A gunner selects a target using a day or night sight and then fires a laser at the target, illuminating a select area of the target with a laser spot. A missile containing a gimbaled seeker in its nose cone is fired at the target; most of the laser energy is reflected off the target and detected by the seeker, which homes in on it (see Fig. 1). The missile electronics determines the origin of the detected laser energy and guides the missile to this point.

This form of guidance is very accurate provided the laser is kept on the target until missile impact. Using more than one designator, such as a Ground/Vehicular Laser rangefinder Laser designator (G/VLLD) and helicopter based designators, multiple targets can be engaged as is Fig. 1. However, the technology

cannot yet be used on kinetic energy missiles (KEM) because of scan rate limitations of the seeker gimbal and the need for a transparent nose cone, which could not withstand the intense shock and friction of a KEM flight. It also requires constant target designation until missile impact, making the gunner more vulnerable to enemy response (not fire and forget).

LASER BEAMRIDER GUIDANCE

The guidance technique on which laser beamrider guidance is based is the Command to Line Of Sight or CLOS concept, the most widely known of which is the TOW system. With TOW, the missile and target are tracked by a common forward looking infrared (FLIR) system, and position information relative to the target is provided to the missile by means of a physical data link (thin wire). The TOW missile has been fielded successfully for over twenty years in various versions and was chosen as a testbed for beamrider because of its similarities to the beamrider guidance concept.

The TOW CLOS concept was modified to eliminate the need to track the missile and was provided a laser as the guidance link. The laser is aimed and fired at a selected line of sight target, and a missile is launched so as to enter the gunner-to-target line of sight and fly within the beam's guidance field (see Fig. 2). The missile has an aft looking receiver (ALR), which detects laser energy, and on-board electronics which decode position information provided by the laser.

The guidance field may actually be several meters in size depending on how the laser is scanned or dispersed; a balance must be achieved between optimum beam size, laser signal-to-noise ratio at the missile, and scan size/data rate. Guidance information is provided to the missile by spatially encoding the laser, a technique in which the laser is uniquely pulsed, scanned, or somehow coded, and the missile uses the laser energy received to calculate its position relative to the center of the beam. The two methods for spatial encoding are scan generated codes and reticle generated codes.

Scan Generated Codes. Three selected types of scan generated codes are shown in Fig. 3, all of which have been successfully flown. The four quadrant code uses four lasers modulated at different rates (pulse position modulation), each forming a quadrant of a circle as shown. This quadrant is moved in a nutation circle creating a guidance field, and the missile ALR detects the different laser frequencies as each quadrant passes over it. If the time spent in each quadrant is the same, the missile is in the center of the beam; as the missile flies off axis, one laser frequency (one quadrant) begins to dominate, and the missile makes adjustments to get back to center.

The bar scan works basically the same, but uses two lasers to project an azimuth bar and an elevation bar forming an L-shape in space. The bars are nutated, but here time between Az and El crossings is used to guide the missile. The missile's on board electronics decodes at what time

relative to a synch clock each bar was scanned across the ALR and the time between the azimuth and elevation bars, correcting its path to keep these times the same and fly in the center of the nutation circle.

With a raster scan, the missile clock is synchronized with a laser beam projector unit (BPU) clock before launch. The laser spot is scanned separately in azimuth and elevation by the BPU creating a guidance field, and pulses are received by the missile when the scans cross the missile's ALR. The missile uses time since launch, scan rate, and time between successive pulses to determine where it is within the guidance field. The missile makes guidance commands to keep the time between Az and El pulses the same, which only occurs in the guidance field center.

Reticle Generated Codes. The two main examples of reticle codes are the FM reticle and the Gray Code reticle, both shown in Fig. 4.

The FM reticle method employs a reticle with alternating transparent and opaque segments, which when rotated on axis in front of the laser effectively creates a fixed modulation frequency on the receiver of the missile anywhere within the guidance field. However, the reticle is also nutated within the guidance field creating a frequency modulated signal at the missile with greater depth of FM laser modulation at the center of the guidance field, and the lowest depth at the edge. When the frequency is synchronously detected with respect to the nutation angle, missile position relative to the line of sight is obtained in polar coordinates.

The Gray Code method encodes the laser beam using a series of reticles of diminishing width and spacing which are sequentially placed between the laser and the line of sight. Different areas of the beam are blocked as the reticles revolve, so the laser is intermittently received at the missile depending on missile position in the guidance field; the intermittent pulses are used on the missile to generate a code of ones and zeroes relating position in the guidance field. The missile electronics resolves position by comparing the pulse code to preprogrammed codes on the missile. This concept is being used to test multiple beamrider missile guidance, because the reticles can produce separate missile codes over the entire guidance field, and maintain a high data rate.

One of the best features of beamrider guidance is that the missile receiver looks back into friendly territory, providing excellent countermeasure rejection. It is also relatively simple technology (particularly on the missile), low cost, target signature independent (point and shoot), and highly accurate. However, it is not fire and forget and requires target illumination, making the gunner more vulnerable to detection and response by the enemy. These factors are minimized by the low energy levels associated with laser beamrider transmitters and the short flight time of supersonic missiles.

LASER UPDATED GUIDANCE

This method is the newest laser guidance technique and uses a self-simulating missile that flies a preprogrammed trajectory towards a target. Position updates are sent using a laser and are then compared to the nominal trajectory downloaded into the missile guidance computer before launch.

The testbed for this form of guidance has been a Kinetic Energy Missile which has a very large, hot plume trackable in a FLIR. A target is first selected by the gunner and ranged on with a laser, and the weapon system computer on the launcher calculates a nominal trajectory for target intercept based on this range and the known missile characteristics (thrust profile, etc). A laser guidance field defining the limits of the update range in space is boresighted to the FLIR as in Fig. 5; the guidance field size can be varied, but not during flight.

The nominal trajectory is downloaded to the missile and the missile is fired. The target and missile are differentially tracked by the FLIR during flight and a vertical and horizontal difference is calculated. The laser is positioned in the guidance field at the missile position provided by the FLIR tracker, and when commanded fires a pulse. The timing of the pulse provides true missile position relative to the target, based on time of flight and when the pulse was received. After comparing anticipated update time to actual pulse time of arrival, a change in the self-simulation states is made based on the difference (see Fig. 6). The missile then continues to be guided by this internal simulation which has now been updated.

This concept is well-suited for kinetic energy missiles, where a large amount of obscurants from the missile motor would make direct line of sight guidance difficult. The missile flies an arched, command-to-intercept type trajectory; however, because of its self-simulation capability, some loss of missile track and/or guidance updates can be accommodated for portions of the flight.

## SELECTED LASER GUIDANCE PERFORMANCE FACTORS

OPTICAL ACCURACY

The accuracy associated with laser systems has been proven to be limited principally by optical diffraction, a small error that provides extreme overall accuracy for missile guidance. This has been proven in a number of flight tests over the years. For example, in the late 1970's a series of approximately 15 laser beamrider guided flights yielded center hits each time through targets out to at least 3 Km; the average miss difference between missile impact and where the laser was aimed was less than six inches.

WAVELENGTH COMPARISON

There are obviously several alternatives to choose from as to which laser to use for missile guidance. Three have been quite

well investigated, and their advantages and drawbacks are known.

Gallium Arsenide (GaAs) is a very convenient laser. It is very small, lightweight, and low cost. It's ease of modulation and spatial array configuration make it a very versatile source. It is generally eyesafe in this use except at very short ranges. The principal disadvantage is lack of smoke penetration equal to the FLIR capability.

Neodymium YAG (Nd:YAG) and similar glass and crystal lasers possess a high peak power, which can somewhat compensate for poor smoke penetration but not completely. The laser technology is also mature, but size and complexity are disadvantages. It is generally not eyesafe in this application.

Carbon Dioxide ($CO_2$) is at present the laser of choice. It's size, weight, and complexity are between the above two, it is completely eye safe, and aerosol penetration exceeds the FLIR performance in all cases. The detectors must be cryogenically cooled, and while techniques are quite well developed this is a disadvantage.

Millimeter wave (MMW) is being considered as an alternative to these lasers in order to achieve even better aerosol performance, and some weather capability. Disadvantages are resolution vs. antenna size, target acquisition and track capability and complexity, and technological maturity. MMW is the source of choice for the in-house ADKEM system, which will be further discussed in the system section below.

## AEROSOL EFFECTS

Figure 7 shows attenuation curves for some tactical smokes at different laser wavelengths. Note the very large attenuation levels achievable. An attempt has been made to achieve full FLIR compatibility with a GaAs Laser Beamrider. This was achieved in the phosphor smokes (WP & PWP munitions) with an excess S/N of 25000:1 above minimum operational. However, as can be seen from these curves, a FLIR is essentially undisturbed by large quantities of HC smoke, while GaAs is seriously degraded with even a small amount. Thus full compatibility (ability to guide ANYTIME the FLIR can be used to acquire a target) requires the laser to operate within same the spectral band as the FLIR.

## DETECTABILITY

Figure 8 depicts the off-axis detectability of $CO_2$ (10.6 microns) and Nd:YAG (1.06 microns) laser wavelengths. The short wavelength laser detectability is higher by at least a factor of ten at any given range, so $CO_2$ is obviously the better of the two to avoid enemy detection. However, two targets even several hundred meters apart will likely both be in the gunner's field of view. Multiple or even rapid target engagement by the gunner would thus significantly reduce the chances of enemy response even if laser detection occurred.

## U.S. DEVELOPMENTAL SYSTEMS

There are several U.S. missile programs currently under development that plan to employ some type of laser guidance. The four to be mentioned here are in different stages of development; two are being developed by the MICOM RD&E Center in-house, while two are being developed by contractors and managed by project offices.

The Combined Arms Multipurpose Missile System (CAMMS) is an in-house program that will use a $CO_2$ laser beam projector and raster scan to guide a missile initially, then use a tv or infrared seeker for the latter stage of flight. A multi-guided missile such as this would provide fire and forget capability under the best conditions, but allow for engagement of longer range targets or partially obscured targets as well. If the seeker could not accurately lock on to a target, the gunner could use the beamrider mode to guide the missile until the seeker was within target detection range. It is noteworthy that the laser beamrider signals are used to point the seeker to aid in seeker target lock-on.

The Advanced Kinetic Energy Missile (ADKEM) is another in-house program, with competing guidance technologies ($CO_2$ laser beamrider and MMW). The missile will consist of a projectile which will be accelerated to supersonic speeds by a cluster of booster motors, which will fall away after expenditure. Though the concept is still in the early stages, several static motor tests and simulations have already shown that communication through the missile plume and smoke with a carbon dioxide laser is possible, providing an accurate, low cost guidance method. A beam projector and raster scan pattern are the planned guidance techniques if the laser concept is chosen. The MMW differential track approach is similarly promising, less affected by smoke, and has some adverse weather capability.

The Line Of Sight-Forward-Heavy (LOS-F-H) project office has chosen a $CO_2$ laser beamrider system as part of the Forward Area Air Defense (FAAD) initiative. The concept and technology is the same as the foreign Air Defense Anti-Tank System (ADATS, described below) developed by Switzerland in the U.S., but it will be integrated into a Bradley vehicle for the U.S. Army. LOS-F-H will use a $CO_2$ laser to create a digital position code utilizing phase shift keying (PSK). The missile will fly non-line of sight in the initial stages of flight for plume smoke avoidance, then converge back to a line of sight trajectory until target impact.

The Line Of Sight Anti-Tank (LOSAT) project office has selected a $CO_2$ laser commanded KEM system as its primary candidate. This system is the one described earlier; if successful as a guidance technique, it will provide a significant overmatch to current and future threat armor out to extended ranges. LOSAT is foreseen as a replacement for the TOW system.

## FOREIGN SYSTEMS

As mentioned, ADATS is a foreign system which has been purchased by Canada and other countries. It is mounted on a modified personnel carrier as a dedicated air defense and anti-tank weapon system.

RBS-70 uses GaAs laser diodes to create an azimuth and elevation bar scan for missile guidance. It is a ground-launched, portable air defense weapon system; the gunner's seat, sights, and the launcher and guidance system can be rotated 360 degrees by the gunner to allow full manual track of air targets.

Starstreak is a British supersonic, GaAs laser beamrider air defense weapon. The missile has a two-stage motor and is shoulder launched using the first motor, then when the missile has reached a predetermined safe distance from the gunner the second motor accelerates it beyond Mach 1. The first motor is dropped after expenditure for reduced drag. The gunner continues to sight the laser on the target until missile impact.

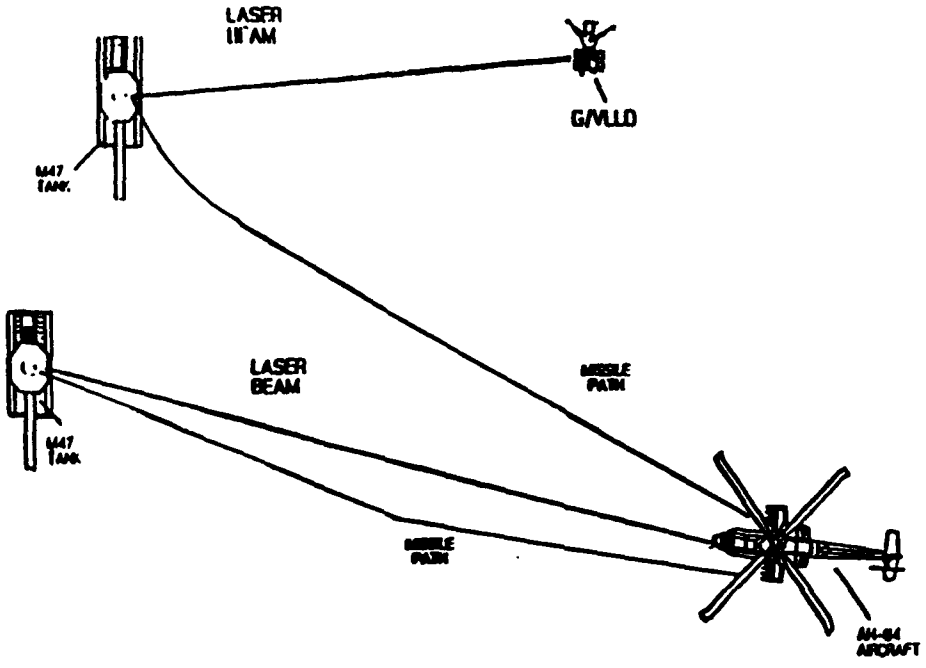


**FIGURE 1: SEMI-ACTIVE LASER GUIDANCE**

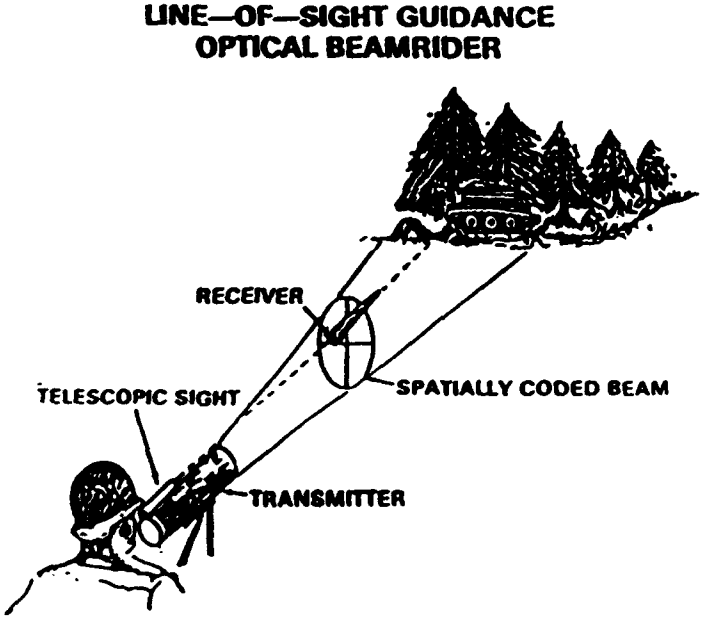


**FIGURE 2: LASER BEAMRIDER GUIDANCE**

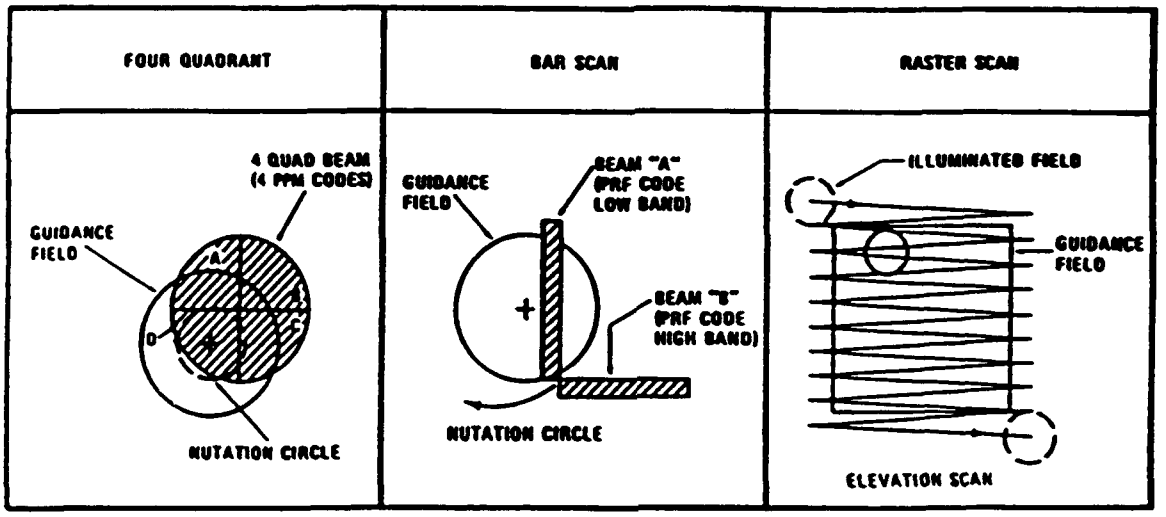


FIGURE 3: SCAN GENERATED CODES

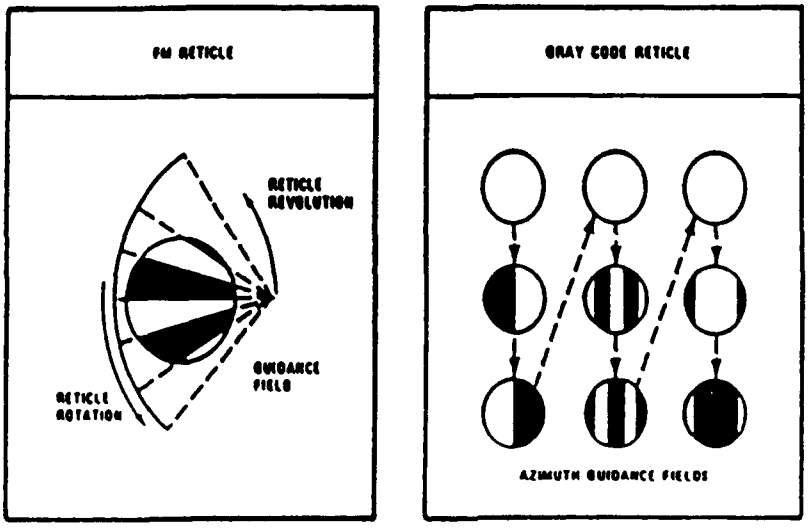


FIGURE 4: RETICLE GENERATED CODES

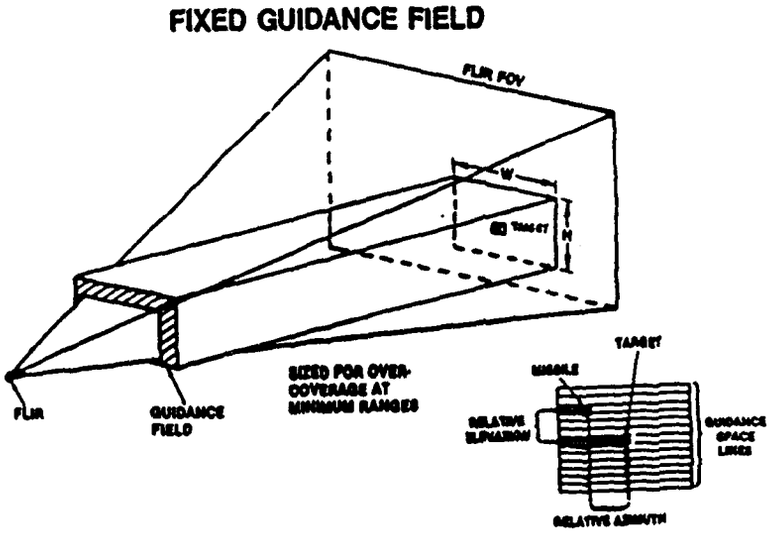


FIGURE 5: LASER UPDATED MISSILE GUIDANCE FIELD

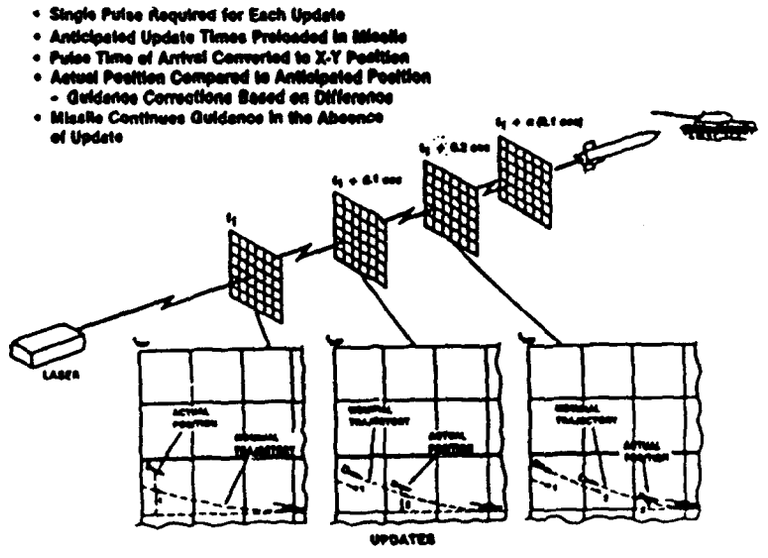


FIGURE 6: LASER UPDATE CONCEPT

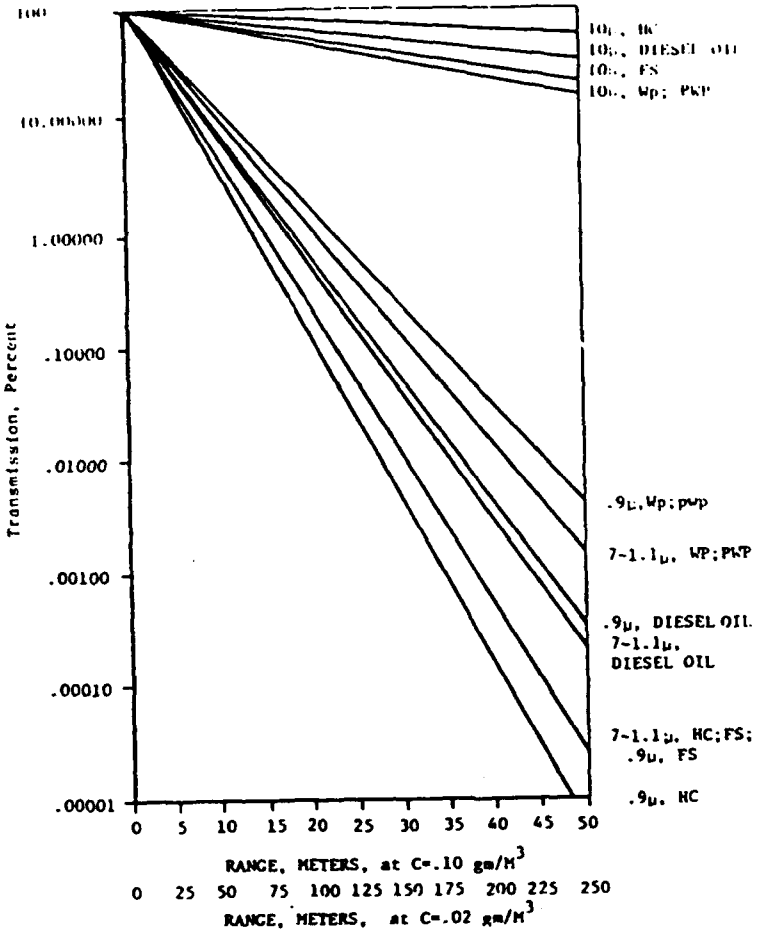


CO2 and FLIR Wavelengths

GaAs Wavelength

Broadband Silicon Detector Wavelength

***FIGURE 7: LASER TRANSMISSION THROUGH SELECTED AEROSOLS***

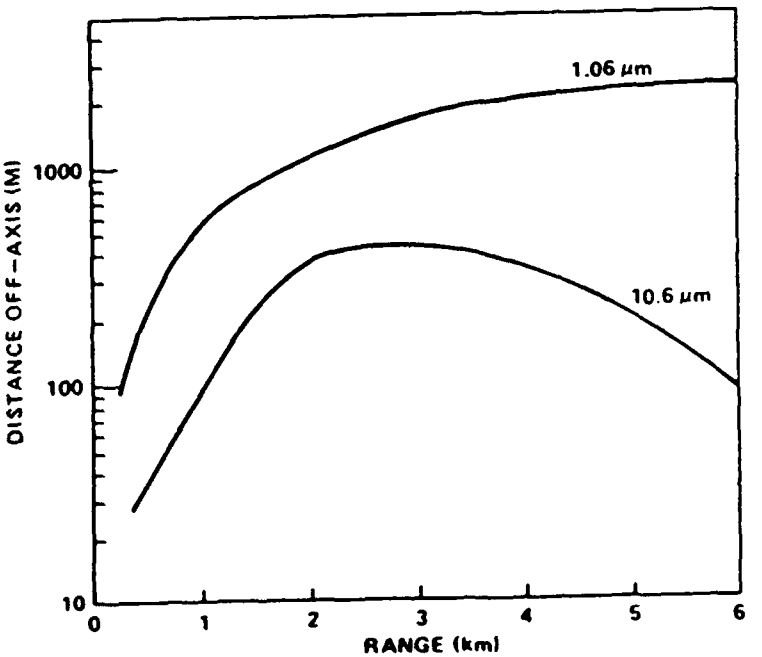


**FIGURE 8: OFF-AXIS LASER DETECTABILITY**

# Measuring Radar Cross Section Using a CW Track-While-Scan Radar

Will D Caraway III
Research, Development and
Engineering Center
Redstone Arsenal, Al

## ABSTRACT

Fielded radar systems offer a realistic means of measuring an airframe's radar cross section (RCS) and the effects of RCS reduction attempts. This paper presents a method for performing these measurements using a CW Track-While-Scan radar. RCS measurements of a target with a known cross section are presented to establish error boundaries.

## INTRODUCTION

Most airframes currently in use undergo extensive flight testing before their actual production begins. These flight tests are generally conducted on well instrumented test ranges equipped with a wide variety of instrumentation and threat simulation radars. This paper presents a method for calculating an airframe's radar cross section based on the detection data normally collected by the range radars during these tests. This allows the realistic evaluation of an airframe's RCS during its flight tests without the added time and expense of using an RCS measurement facility. In addition, this method can be used to measure the change in RCS that occurs when an airframe is modified, provided similar data exists for the original configuration.

During a 1985 tracking test, a technique was developed for estimating the RCS of a target from detection data collected by the Track-While-Scan Quiet Radar (QR) [1]. The QR is an exploratory development, short range, air defense radar capable of performing both track and search functions. As the number of tracking tests involving the QR grew, the technique was refined, generalized and implemented in modularized software. In its present form, the technique is an extremely flexible tool capable of being used with almost any well characterized radar.

This paper describes the basic theory behind the use of detection data for calculating a target's RCS and its specific application to the QR. A discussion on the issues involved in applying this technique to another radar is also provided. Finally, data collected with the QR on a static target of known cross section is provided to establish a minimum error boundary.

## RADAR CROSS SECTION COMPUTATIONAL METHOD

The basic equation from which to calculate RCS is the radar range equation: [2]

$$\frac{S}{N} = \frac{P_T G_T G_R \lambda^2 \sigma}{(4\pi)^3 R^4 KTB \cdot NF \cdot L} \tag{1}$$

where
- S/N = signal to noise ratio,
- $P_T$ = power transmitted,
- $G_T$ = gain of transmit antenna,
- $G_R$ = gain of receive antenna,
- $\lambda$ = wavelength of transmit frequency,
- $\sigma$ = target RCS,
- R = target range,
- KTB = thermal noise power in the processing bandwidth,
- NF = noise figure,
- L = losses.

Solving Eq. 1 for RCS yields:

$$\sigma = \frac{(4\pi)^3 R^4 KTB \cdot NF \cdot L \left(\frac{S}{N}\right)}{P_T G_T G_R \lambda^2} \tag{2}$$

Those readers accustomed to using RCS measurement systems may be more familiar with Eq. 2 in the following form:

$$\sigma = \frac{(4\pi)^3 R^4 P_R}{P_T G_T G_R \lambda^2} \tag{3}$$

where $P_R$ = power received at the antenna.

While this form of the equation is preferable for RCS work, most radars, including the QR, do not measure the received power at the antenna but rather the signal to noise ratio at the output of their signal processor, necessitating the use of Eq. 2. At first glance, Eq. 2 seems to provide a relatively simple and accurate means for calculating target RCS; however, several of the parameters can be difficult to quantify, injecting a proportional amount of inaccuracy into the result.

The parameters in Eq. 2 can be divided into two distinct classes: those parameters independent of target returns and parameters dependent on target returns. Target independent parameters include $P_T$, $G_T$, $G_R$, $\lambda$, $(4\pi)^3$, KTB, and NF and are all dependent on the radar in question. For the QR, these values have been well quantified by MICOM or Hughes Aircraft Co., the QR's manufacturer. Target dependent parameters are R, S/N, and L and are determined from the radar's detection data. Up to now, L (losses) has been treated as one unknown; however, in practice, it is made up of several unknowns. The determination of L is generally the most challenging aspect of the problem and the one most prone to error. In addition, the formulation of L is usually unique to the radar. The components of L for the QR are shown in Eq. 4.

$$L(\text{in dB's}) = L_{RNG} + L_{DOP} + L_{BPE} + L_{BPA} + L_{CAL} \qquad (4)$$

where
$L_{RNG}$ = range cell straddle loss,
$L_{DOP}$ = doppler filter straddle loss,
$L_{BPE}$ = beam pointing loss in elevation,
$L_{BPA}$ = beam pointing loss in azimuth,
$L_{CAL}$ = calibration determined losses.

The beam pointing losses will reduce the parameters $G_T$ and $G_R$ which are fixed to represent maximum antenna gains, and the processing losses, $L_{DOP}$ and $L_{RNG}$, will reduce the processing gain for the speed and range of the target. The $L_{CAL}$ term accounts for any bias found when calibrating the algorithm against a target of known RCS. This could result from unusual atmospheric conditions on the day of the test, aging degrading the target independent radar parameters, etc.

Since the target independent parameters are constants or previously determined quantities, the determination of a target's RCS is contingent upon accurately estimating the target dependent parameters. Range and S/N can, in general, be obtained directly from the radar detection reports. The various loss components are then calculated from differing combinations of detection reports and, if necessary, high accuracy target position data. The target position data is needed to calculate beam pointing losses for radars such as the QR that have no way of determining where in their beam the target is located. This is not the case for all radars. For instance, a staring, monopulse system would be able to determine where in its beam the target is located, and its reports should have sufficient information to calculate beam pointing losses without need of position data. This information is then processed and stored in a separate loss table for each track so that the RCS at each detection in the track can be calculated. For the interested reader, the specifics of the calculation of L for the QR are presented below.

Once the loss table for a track is complete, an RCS table can be calculated from it. For ease of calculation and convenience, RCS is usually calculated in dB's since most of the parameters are conventionally in dB's. In addition, Eq. 2 (in dB format) can be rearranged into the following form:

$$\sigma\,(dBsm) = L_2 + \frac{S}{N} + C \qquad (5)$$

where $L_2 = 40LOG_{10}(R) + L_{BPE} + L_{BPA} + L_{DOP} + L_{RNG} + L_{CAL}$
sum of target dependent parameters
S/N = signal to noise for current detection

$$C = 30\log(4\pi) + KTBNF - P_T - G_T - G_R - 20\log(\lambda)$$

sum of target independent parameters
= 177.6 dB for the QR

These RCS tables can then be analyzed as appropriate to determine either absolute RCS or difference RCS.

Eq. 5 can easily be applied to any standard radar. First, the quantities that compose C would need to be accurately determined so that C can be recalculated. Then, the equation for $L_2$ may need to be adjusted for any differences in the radar's loss mechanisms. Finally, if absolute RCS measurements will be made, the RCS of a target of known RCS needs to be measured in order to determine $L_{CAL}$.

## QR LOSS CALCULATION

### Range Cell Straddling Loss [1]

The QR is a CW radar and uses bi-phase codes to resolve range. A 31-bit maximal length code is implemented using two code repetition frequencies (CRF) providing thirty-one identical range cells, numbered 1 through 31. The range cell spacing is 62.5 and 59.4 meters for CRF1 and CRF2, respectively. As a result of the range cell spacing, the maximum unambiguous range for CRF1 and CRF2 is 1937.5 and 1840.6 m. The two CRFs are combined to extend the QR's maximum unambiguous range to 36.8 km.

The range cell straddling loss is determined by using a range cell interpolation algorithm. The data required by the algorithm is the detection range cell amplitude along with the highest adjacent filter amplitude. The difference in the amplitudes, in dB's, is determined by subtracting the adjacent amplitude from the detection amplitude. As can be seen in Fig. 1, this difference defines a unique point in the two range cells. This difference is then used as the interpolation point on a difference vs straddling loss table; a graph of which is shown in Fig. 2.

Doppler Filter Straddling Loss

The QR performs doppler processing via a digital Moving Target Indicator (MTI), for clutter rejection, and 32 digital doppler filters providing inbound and outbound velocity determination [2]. Generally, doppler filter straddling loss for the QR is calculated using a method virtually identical to the one described above for range cell straddling loss. Sometimes though, a target will not have sufficient airspeed to make this possible. For instance, a helicopter's average speed is 55 m/s, but the center of the QR's first doppler filter is approximately 75 m/s. Consequently, instead of appearing in the main lobes of two same sign, adjacent filters, the target appears in the main lobe of filter + or - 1 and the first sidelobe of the other. As can be seen from Fig. 3, small changes in the amplitude difference yield large changes in doppler frequency, and therefore doppler loss, for targets in this portion of the filters. This problem makes this technique too unstable to use to calculate doppler loss for low radial velocity targets.

The solution to this problem is to determine the target's doppler frequency from time tagged positional data. This requires calculating the velocity vector of the target, extracting its radial component relative to the QR, converting this component into frequency, and determining the doppler loss from a table based on normalized frequency. Reference radar data is generally used to calculate the target's velocity vector since their higher data rate makes it fairly simple to calculate a new velocity vector for each QR detection. The radial component of the velocity vector can then be found by forming the dot product of the velocity vector and the QR unit pointing vector. Finally, the normalized frequencies are calculated by converting the radial component into frequency and dividing by each pulse repetition frequency (PRF). The complete mathematical development of this method is shown below.

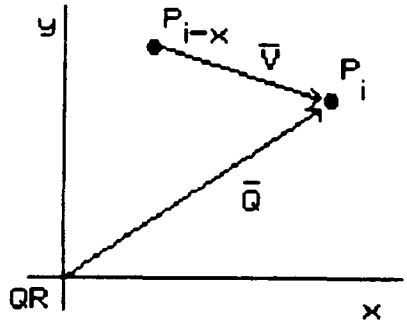


Given: Target positions i and i-x w.r.t. QR in (X,Y,Z) coordinates

Velocity Vector $$\bar{V} = \frac{X_i - X_{i-x}}{t_i - t_{i-x}}\bar{x} + \frac{Y_i - Y_{i-x}}{t_i - t_{i-x}}\bar{y} + \frac{Z_i - Z_{i-x}}{t_i - t_{i-x}}\bar{z}$$

QR Pointing Vector $$\bar{Q} = X_i\bar{x} + Y_i\bar{y} + Z_i\bar{z}$$

Unit Pointing Vector $$\bar{Q}' = \frac{\bar{Q}}{|\bar{Q}|}$$

Radial Component $$V_r = \bar{V} \cdot \bar{Q}'$$
$$= \frac{X_i(X_i - X_{i-x}) + Y_i(Y_i - Y_{i-x}) + Z_i(Z_i - Z_{i-x})}{t\sqrt{X_i^2 + Y_i^2 + Z_i^2}}$$

Doppler Frequency $$f_d = \frac{2V_r}{\lambda}$$

Normalized Frequency $$f_n = \frac{f_d}{PRF}$$

where the PRFs are 81494 and 77419 Hz and are related to the CRFs by multiplying by 31.

Beam Pointing Losses [1]

The QR uses a rectangular phased array antenna with electronic steering in elevation and azimuth scanning by mechanical rotation. Its radiation pattern is very closely approximated by the following equation:

$$G(\theta_e, \theta_a) = G(\theta_e)G(\theta_a)$$

where $G(\theta_e, \theta_a)$ = the radiation pattern as a function of elevation and azimuth
$G(\theta_e)$ = the elevation principle plane radiation pattern
$G(\theta_a)$ = the azimuth principle plane radiation pattern.

As indicated by the above equation, the radiation pattern can be separated into the elevation and azimuth principle plane patterns. Thus, the beam pointing losses can be determined independently for both elevation and azimuth. A Taylor illumination function is employed to produce the principle plane patterns in both elevation and azimuth.

Elevation Pointing Loss [1]

To determine either an elevation or azimuth pointing loss, the exact position of a detected target is required. Elevation "truth " data must be obtained from a reference radar with accuracy significantly greater than .25 deg. Using this data and the elevation of the detection beam's center during a target detection, an elevation offset with respect to the beam's center is determined. This offset is then used as the index into the elevation loss lookup table to find the elevation pointing loss. A plot of the elevation offset versus pointing loss is shown in Fig. 4. This plot was generated from the elevation loss lookup table. Note, Fig. 4 is normalized with respect to beam numbers and can be used for all beam positions. The following equation relates beam numbers to elevation angles:

$$BN = \frac{2^6 df}{c} \sin(\theta_T - 10.3)$$

where BN = beam number
f = frequency in Hz
d = element spacing = .0174 m
c = speed of light
$\theta_T$ = elevation angle of the target.

Azimuth Pointing Losses

Azimuth pointing losses are determined using exactly the same method as is used for elevation with one minor difference. The azimuth pointing error is calculated in degrees. Fig. 5 is a plot of azimuth offset versus pointing loss and was generated from the azimuth loss lookup table.

Calibration Determined Losses

It is rarely possible to account for all the losses and system aging effects associated with a radar; therefore, it is important to calibrate Eq. 5 when attempting to perform absolute RCS measurements. In the case where RCS differences are being tested, this calibration is unnecessary since these losses will affect each target equally and will be nulled out in the comparison. For the QR, this calibration is performed using a stationary target of known RCS located at a surveyed point. A statistically large sample of data is collected and the target's average RCS is calculated using Eq. 5 with $L_{CAL}=0$. This average is then compared to the target's known RCS and $L_{CAL}$ is set to the difference.

## ERROR ANALYSIS

The results from Eq. 5 are expected to vary because of two uncontrollable phenomenon: the unpredictable nature of complex target returns (category 1) and the variation in radar operating characteristics (category 2). The measurement variation caused by category 1 effects are the result of actual variations in a target's RCS and should not be counted as errors; however, the variation caused by category 2 effects are the result of errors in determining the target dependent and independent parameters and should be counted as errors. Determining the amount of variation caused by these random events would be a very complicated task since each target return received by the QR is affected by many parameters within these two categories. For instance, in the first category, target scintillation and aspect variation could cause significant fluctuation in a target's RCS; and the characteristics of these fluctuations are target dependent. RCS variation due to these variables should not be included in defining an error for Eq. 5. On the other hand, varying radar parameters, such as antenna beam pointing loss, doppler and range filter straddling loss, signal-to-noise ratio (S/N), multi-path, and equipment instability, contribute to some variation in the RCS results; and these parameters are considered responsible for the error associated with Eq. 5. The processes to determine losses and S/Ns are implemented as accurately as possible; but as with all estimated phenomenon, some error must exist. These category 2 parameters contribute some variation (error) to the results of Eq. 5; but as mentioned before, determining the amount of variation due to category 2 quantities is extremely complex in the presence of the category 1 quantities.

An additional complication is the filter rolloff associated with doppler and range filter losses. As can be seen from Fig. 2 and 3, any corruption of the filter amplitudes used to calculate losses will corrupt the loss calculation. In addition, the degradation will not be uniform. Targets in the center of a filter, where the response is flatter, will experience less degradation than targets beyond the filter knee, where the response is changing rapidly. Also, returns with low S/N ratios, where small noise changes may produce significant amplitude corruption, will be less reliable than returns with high S/N ratios, where small noise changes produce little amplitude corruption. Clearly, the worst possible case would be a target well into the filter rolloff region with a low S/N ratio, and the best case would be a target centered in the filter response with a high S/N ratio. Further complicating the situation is the fact that over the course of a test most moving targets will appear in a wide variety of filter locations at varying S/N ratios. Consequently, while the error for a single measurement could be calculated, determining the error for an entire test would be extremely complex.

As an achievable alternative, a method has been derived to estimate the error associated with Eq. 5 by determining the RCS of a stationary target with constant RCS. A target of this type exhibits no category 1 phenomenon in its RCS results, so the variation caused by the category 2 parameters can be directly observed; however, the error derived for Eq. 5 will only be valid for stationary, non-complex targets. Using this approach, a minimum error bound can be established (for various situations), and a small error will verify the validity of the approach.

A stationary target with known RCS was placed at four locations and detection data was collected with the QR. The S/N ratios for three of the sights were set to 20 dB, and the fourth was set to 16 dB. RCS estimates were generated for the calibrated target using Equation (5) with $L_{CAL}=0$. The mean and standard deviation of the RCS data was then calculated for each site. The difference between the mean and theoretical RCS was -2.5 dBsm for the 20 dB S/N sites and -4 dBsm for the 16 dB S/N site; therefore, a -2.5 dBsm bias for the 20 dB S/N sites and a -4 dBsm bias for the 16 dB S/N sites was defined as being present in the RCS data. They could be removed by adding 2.5 or 4 dBsm to the corresponding RCS results generated by Equation (5). The standard deviation of the four sites ranged from about 1.7 to 2.9 dBsm. The largest of these, approximately 3 dBsm, would be chosen as a conservative estimate of the error. Thus, the minimum error associated with Eq. 5 for measuring the RCS of a target would be 3 dBsm.

The standard deviation of the RCS data was used to represent the error associated with Eq. 5, because the RCS measurements were considered independent and Gaussian distributed. Independence was assumed because RCS estimates were determined from detection data that was collected on a beam to beam basis. Two measurements were made for each beam, one for CRF1 and one for CRF2, which would be correlated if one assumes a Swirling case 1 target; however, the category 2 parameters mentioned above were independent, so the RCS values varied enough between CRFs to safely assume independence between these measurements also. The RCS data was also assumed to be Gaussian distributed when properly normalized. The logarithmic results from Eq. 5 were shown to fit a log-normal distribution without having to normalize the magnitude of the data with respect to the mean and standard deviation, so the error was approximated in these units.

In summary, an error analysis was performed to validate the procedures used to estimate RCS. A worst case error of 3 dBsm was associated with Eq. 5 when measuring the RCS of a stationary target with constant RCS. The magnitude of this error indicated the methodology described earlier is sound, and the QR produced fairly accurate results for a system of its complexity. In addition, a marked increase in accuracy was noted for high S/N ratio returns. Also, it was noted that a -2.5 or -4 dBsm bias was present in the RCS data, and it could be removed by adding an equal amount to the respective RCS results generated by Eq. 5.

## CONCLUSION

In this paper, a method for determining an airframe's RCS from the radar detection data collected during its flight tests has been presented. The solution methodology for a generic radar has been formulated with the methodology for the QR being provided as a specific example. In addition, data collected with the QR on a static target of known RCS has been presented to validate the methodology and demonstrate the performance of the QR.

## REFERENCES

[1] McElroy, R. R., et al, "Measurement of FOG-M's Radar Cross Section Using the Track-While-Scan Quiet Radar," US Army Missile Command, Redstone Arsenal, AL, September 1987, TR-RD-AS-86-20

[2] Berkowitz, R.S., ed., Modern Radar Analysis, Evaluation, and System Design, John Wiley & Sons, Inc., New York, New York

[3] McElroy, R. R., et al, "Angular Interpolation Algorithms Implemented in the Track-While-Scan Quiet Radar," US Army Missile Command, Redstone Arsenal, AL, February 1989, TR-RD-AS-89-8

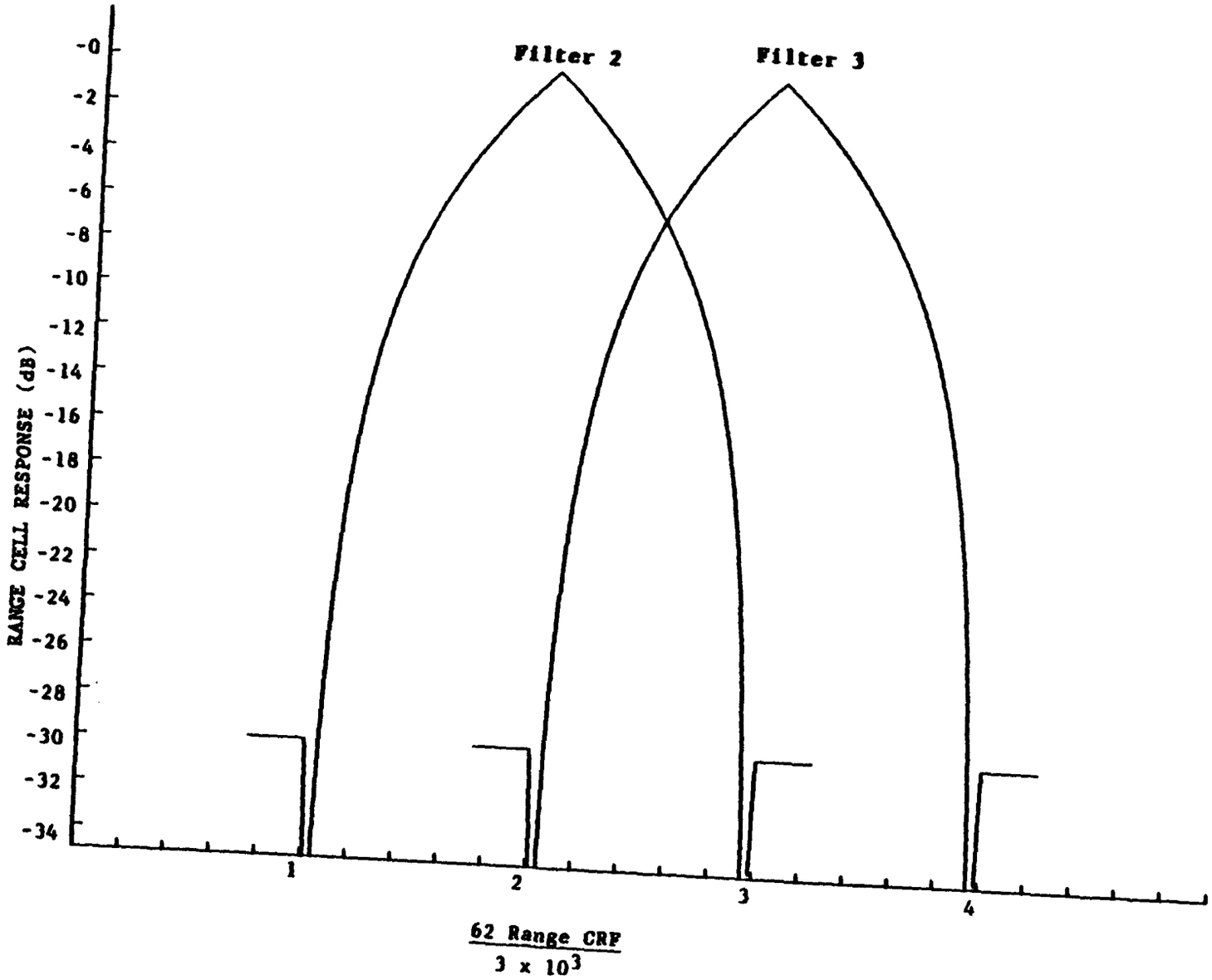


Figure 1 (U) Range cell response.

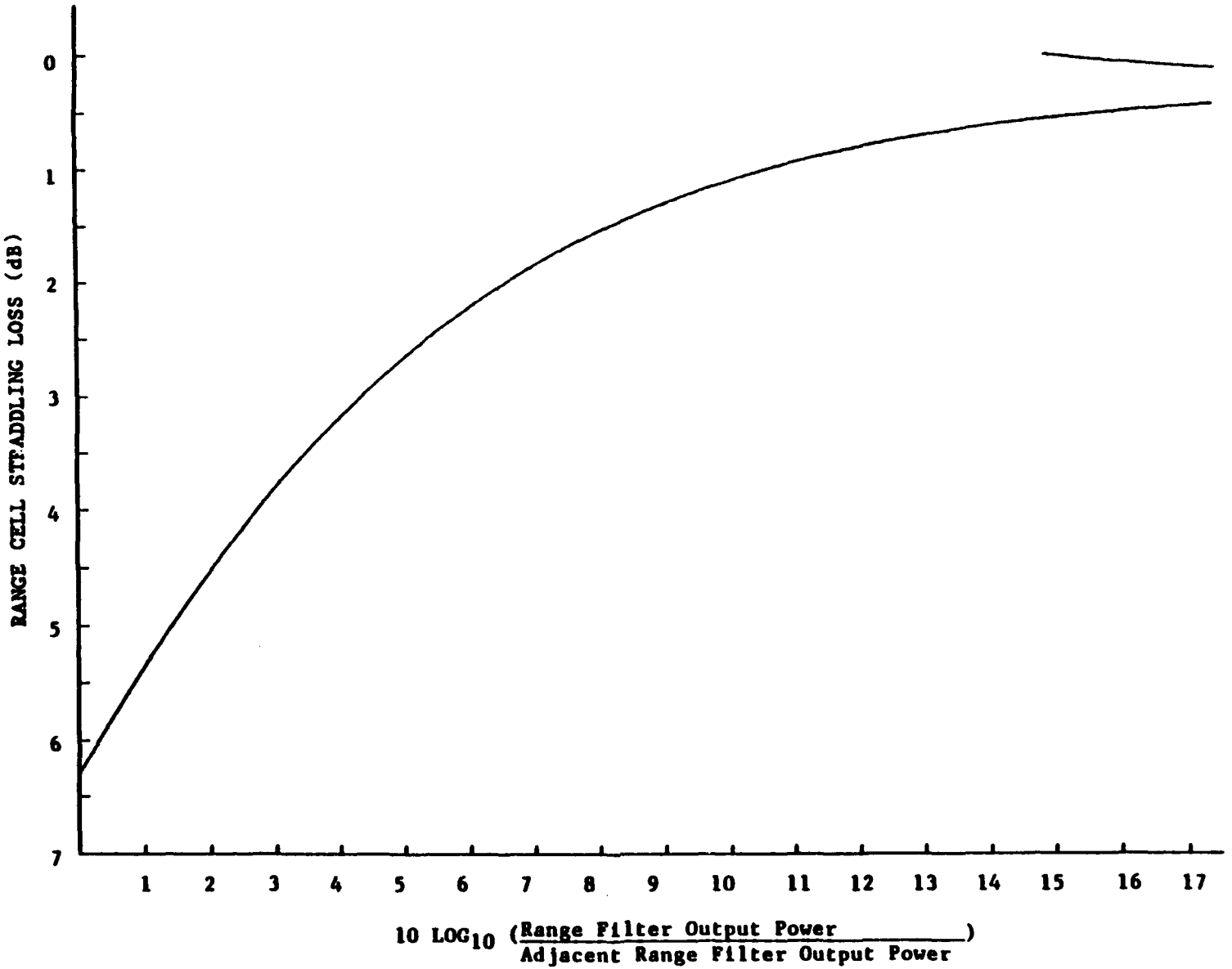


Figure 2 (U) Range cell straddling loss.

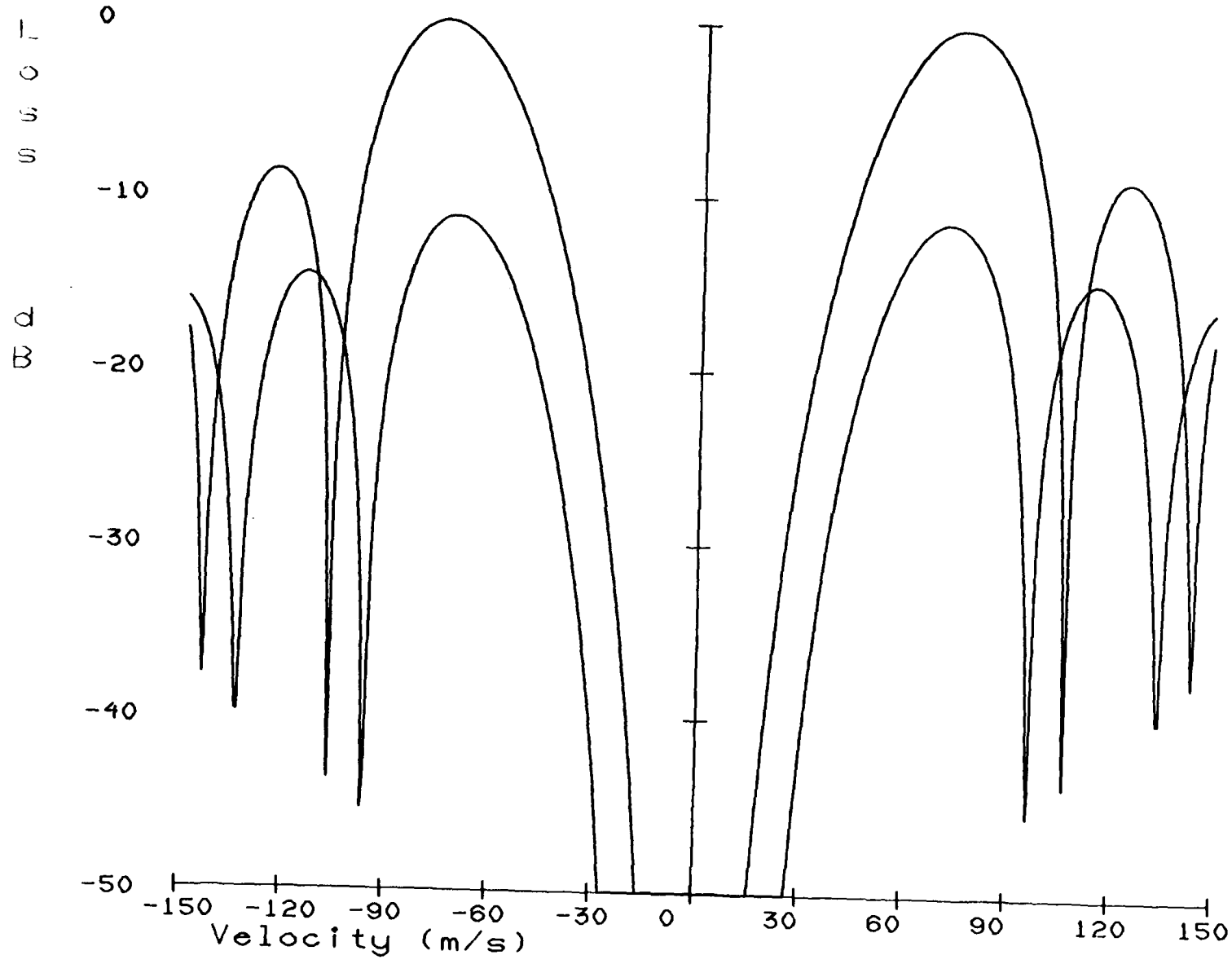


Figure 3. (U) Doppler Filters ±1 Loss v. Velocity

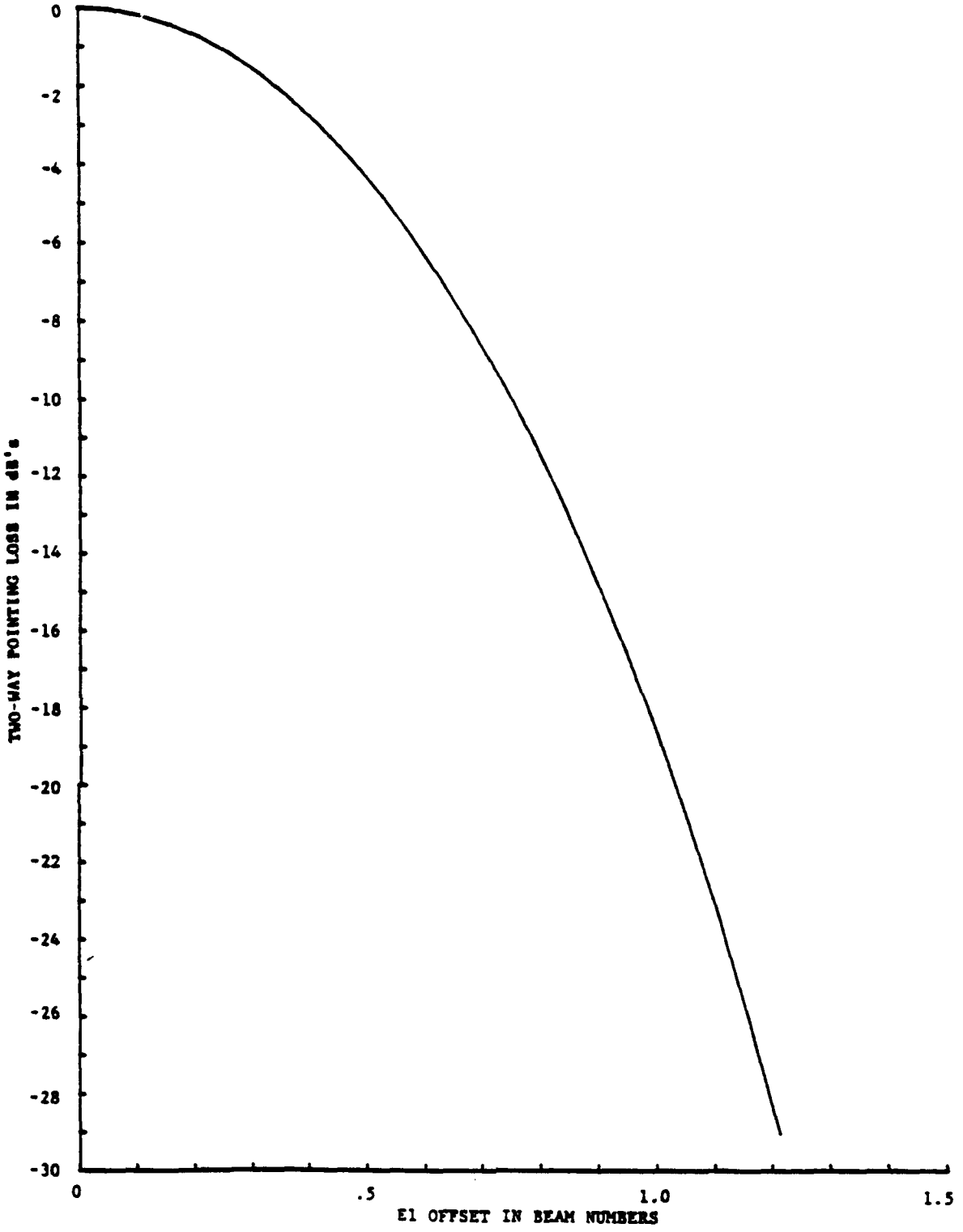


Figure 4 (U) **Elevation pointing loss vs elevation offset.**

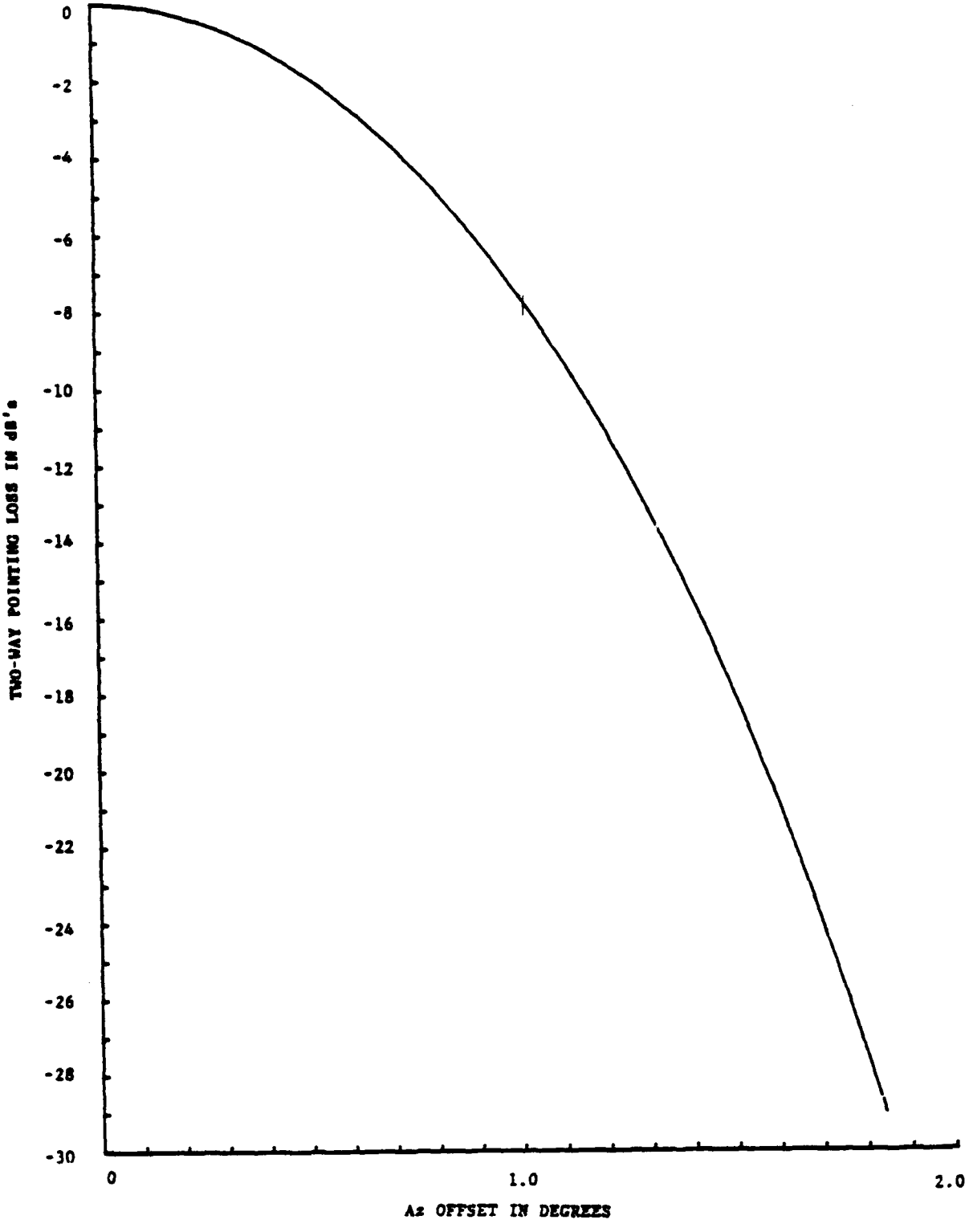


Figure 5 (U) Azimuth pointing loss vs azimuth offset.

## - SESSION III -

GUIDANCE AND CONTROL

# THE DEVELOPMENT AND APPLICATION OF AUTOMATIC TARGET CUEING TECHNOLOGY FOR MAN-IN-THE-LOOP FIRE CONTROL SYSTEMS

Traci K. Malone and Pat H. McIngvale
AMSMI-RD-GC-C

## ABSTRACT

The Control Systems Group, Guidance and Control (G&C) Directorate has been actively involved in the development of image processing techniques and hardware for automatic target cueing applicable to man-in-the-loop fire control systems. This effort has included development of a video data base, development of processing algorithms and implementation of the algorithms in prototype hardware. A major result of this program was the development of a brassboard automatic target cuer applicable to a FOG-M or unmanned aerial vehicle. This cuer processes video from the imaging sensor and produces cues around those objects that have a high probability of being targets. The operator makes the final decision of whether it is a target. This prototype cuer has been evaluated in a series of field and lab experiments at MICOM and White Sands Missile Range (WSMR). Although the design goals have not yet been achieved, the results are encouraging and planned system improvements are expected to allow achieving these goals.

## INTRODUCTION

One of the major challenges to be overcome in the application of man-in-the-loop fire control systems is the efficient, fast, and accurate acquisition of targets. The problem is compounded because the use of wide field-of-view sensors (necessary for midcourse guidance and to achieve a large search area) results in tank or helicopter targets subtending a very small angle when viewed a reasonable distance from the sensor. A missile technology program has been evaluating techniques and developing real-time, prototype hardware to demonstrate an automatic target cuer that can assist a system operator in locating these elusive targets.

The prototype target cuer was developed under a cooperative venture with Loral Defense Systems Division. The actual hardware, development, and much of the evaluation of the algorithms and processing techniques that defined the hardware were performed by Loral. The Control Systems Group had a very strong in-house effort in algorithm development and evaluation which contributed significantly to the cuer design. Some of the processing techniques were first developed/evaluated at MICOM and then given to the contractor for modification and implementation in hardware for real-time operation.

The target cuer was developed using a very limited set of recorded video data. In order to fully evaluate the potential of the cuer, it was subjected to more realistic testing during the Non-Line-of-Sight (NLOS) missile Initial Operational Evaluation (IOE) Captive Carry Test (CCT). The cuer was taken to WSMR in January-March 1989 and field tested as a side experiment during the NLOS CCT. Although the cuer performance was considered reasonably good, there was considerable room for improvement in the area of false alarms. LORAL developed and installed a series of shape screening algorithms that were intended to reject false targets without adversely impacting the classification of actual targets. The modified cuer was reevaluated in the laboratory using the same video data base as used before. The results of these evaluations were documented in MICOM technical reports[1,2]. This paper will generally describe the cuer process, hardware implementation, test and evaluation techniques, and results collected to date.

## DESCRIPTION OF THE AUTOMATIC TARGET CUER

The automatic target cuer design and operation has been well documented [3] but a brief summary of its operation will be given here. The cuer uses known parameters (altitude, field of view, and look-down angle) to calculate an estimate of range from the sensor to the ground at various places in the video image. This, in turn, allows using size as a discriminant. Thus, the operation of the automatic target cuer requires both the video to be searched and dynamic sensor parameters as just described.

Figure 1 is a block diagram of the improved automatic cuer discussed in this paper. Input video (to the cuer) is first digitized to six bits with an automatic gain control to obtain maximum dynamic range. The object detection process uses a modified contrast box with local adaptive thresholding. The adaptive thresholding is utilized to help overcome problems with low contrast (as caused by objects in a shadowed area, for example). Object detection scans the entire image and determines the locations of objects of about the right size and having a relative contrast exceeding a pre-set threshold. The locations and approximate sizes of the objects are passed to the object segmentation process. This process seeks to find the best outline of the objects. Two different segmentation processes can be used depending upon the object's size. For objects of 12 pixels or less in area, a segmentation process based on intensity data is used. Larger targets are segmented based upon gradient data. After the best outline of an object has been determined, gradient phase data is checked to determine if the object is the proper shape.

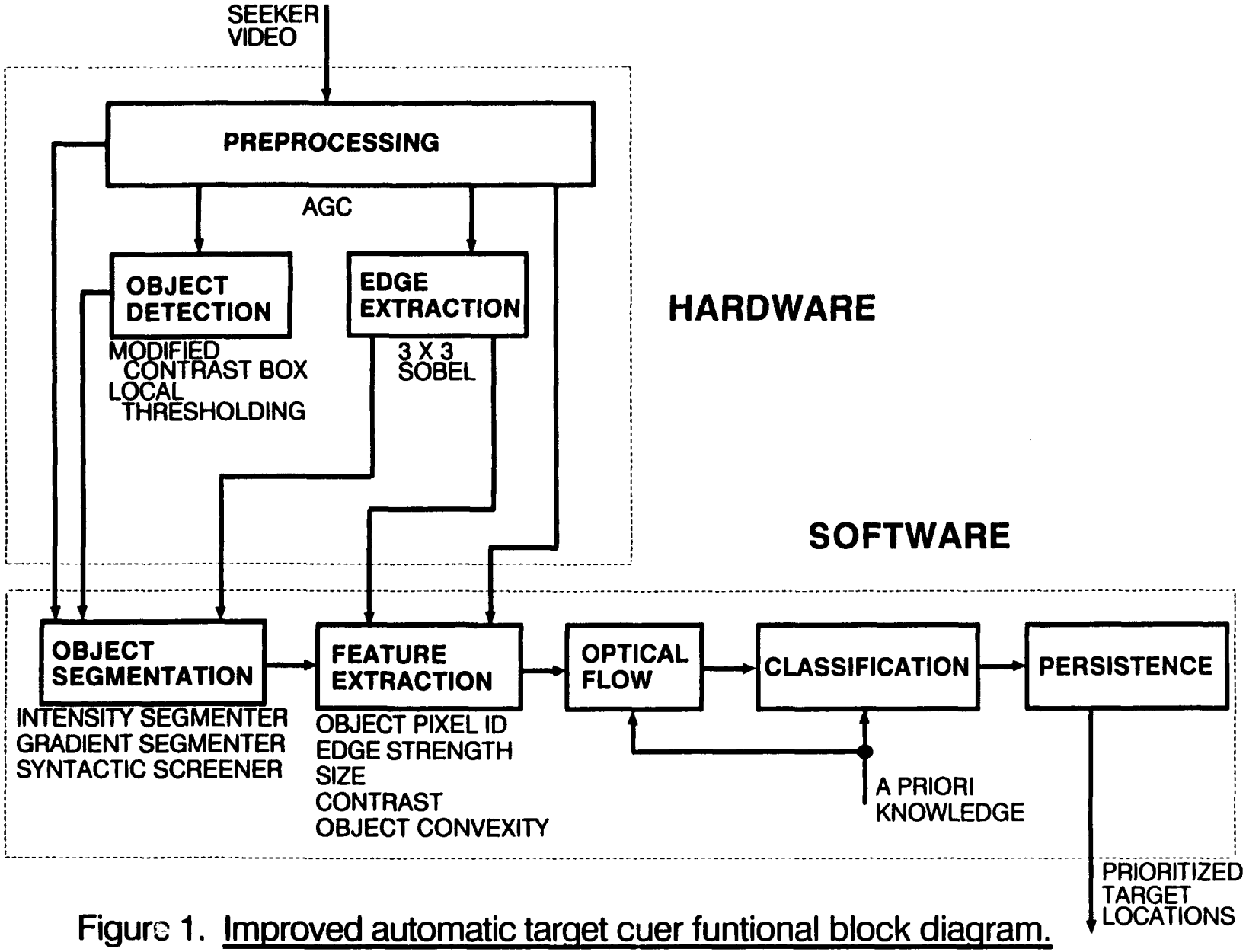


Figure 1. Improved automatic target cuer funtional block diagram.

The object outline is next passed to the feature extraction process. This process uses intensity, gradient, and contrast box data, along with size data to determine a series of features and screeners that provide maximum discrimination of targets from non-targets. Following this is the optical flow stage which serves as both a smoothing filter and a screener. This stage screens non-targets by requiring that a valid target be contained in at least 3 of 5 consecutive video fields and that it have a consistent feature set between images. This acts to smooth out problems in the object detection and segmentation stages. A modified Kalman filter is used to extract the velocity and positional information used to predict future locations of objects. Those objects passing this stage go to the classifier. The classifier examines the same parameters measured in the feature extractor (but uses more rigid threshold values) to make a final determination of whether an object is a target or not. In the total cuer software section (segmentation through classification), there are 140 screeners which typically screen out twenty or more false alarms per image. The persistence filter performs temporal smoothing to help reduce false alarms while helping eliminate occasional target detection dropouts. It does this by requiring that an object must have been classified a certain number of times in its recent past in order for it to be cued/highlighted. Once an object has been detected and highlighted, the feedback feature increases its constancy of being cued by reducing the severity of its screeners. These potential targets are then highlighted on the output video in real-time.

An example of cuer output video is illustrated in Figure 2. The cuer correctly cues the 2 helicopter targets located at the right and upper middle screen. The lower left cued object is a shadow in the terrain which is incorrectly cued (i.e., a false alarm).

In the field evaluation of the cuer, it was found that the false alarm rate was excessive. In an attempt to remedy this, a series of 8 shape screening algorithms were added to the "feature extraction" block of Figure 1. The basic idea behind the screeners was to find those shape related features that were not expected to be part of an actual target and eliminate objects containing them. For example, filter 2 (Box Filter) eliminates those rectangular objects that have square corners since neither helicopters nor tanks have such a characteristic. Although the reasoning behind some of the other filters is more obscure, Loral designed them to screen out those features which their research showed to be characteristic of false targets.

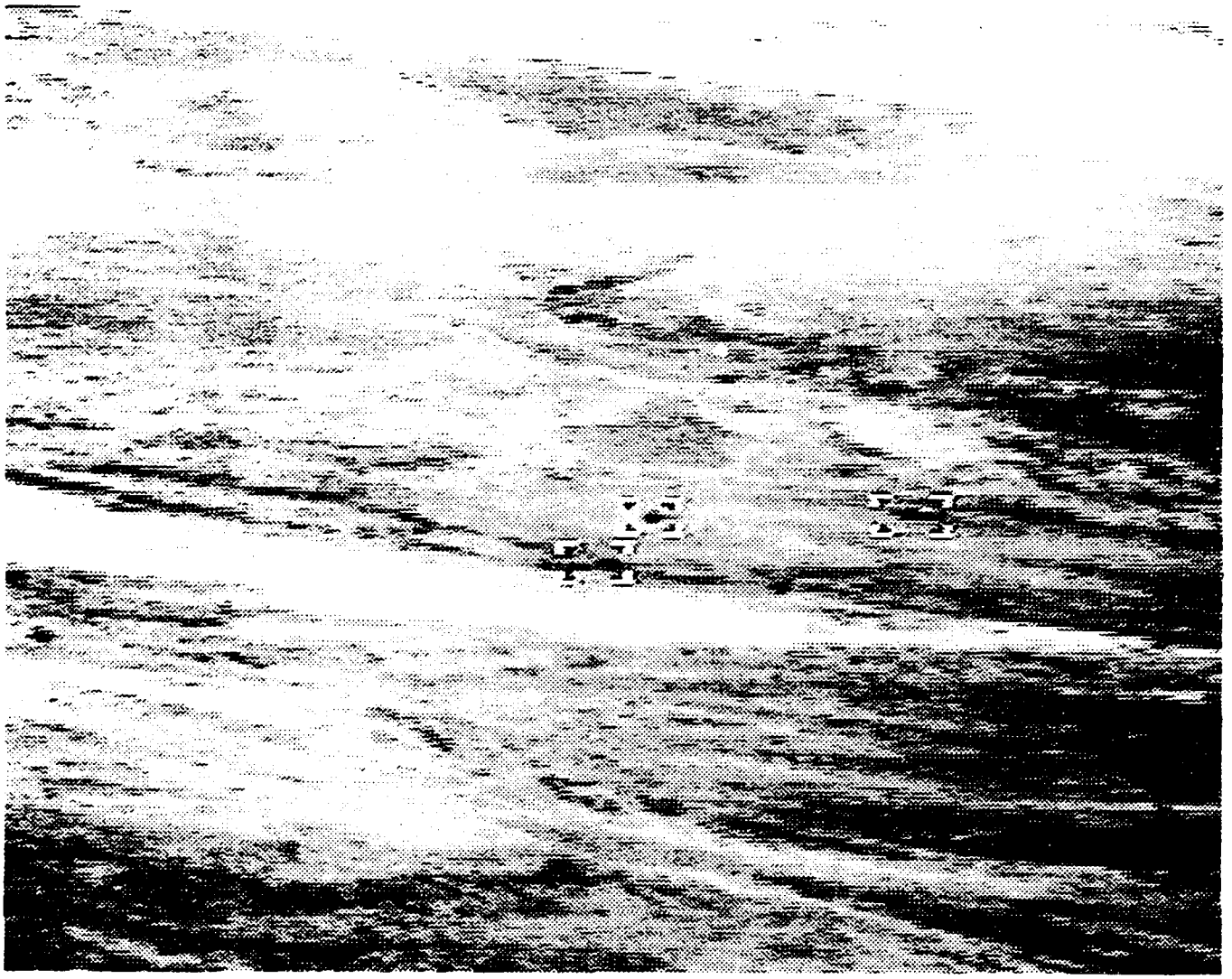

Figure 2. Example of cuer output.

## NON-LINE-OF-SIGHT CAPTIVE CARRY TEST DESCRIPTION

The NLOS CCT series was conducted to evaluate the ability of military operators to acquire targets under a variety of conditions. The test was implemented by carrying the NLOS seeker and related processing in a twin engine, propeller driven aircraft that could be flown at an airspeed approximating the normal velocity of the NLOS missile. A radio frequency data link was used to send video information to the gunner's station from the aircraft and to send control information back to the aircraft/seeker. The design of the cuer is such that it is intended to utilize certain data from the weapon or fire control system with which it is operated. This data (consisting of seeker altitude, down-look angle, and field of view (FOV)), was available in the gunner's station and therefore accessible to the cuer.

The raw seeker video (with encoded parameters contained on the audio channels) and the cuer output video (the video images with the highlights around potential targets) were both recorded during the CCT. The cuer video was used to evaluate its performance during these tests. The raw video was used to create a video data base which was used to evaluate the cuer after the shape screeners were added and will also be used for testing future improvements.

Because of the search technique employed, most test runs (or vectors) had a series of disconnected segments of video of 3 to 6 seconds duration. Some of the segments contain targets and some do not. Therefore, the test data was screened to determine which video was appropriate for evaluating the cuer. Video segments chosen as good test data had to meet the following criteria. It must contain at least one target (between 4 and 80 pixels in size) in its FOV for at least one second. Also, the cuer must be receiving parameters during the evaluation segment (an indicator on the video gave this information). If cuer parameters were withheld for any reason until after the target entered the FOV, the timing started when the parameters became available. The video data base thus created consisted of 86 selected runs and is documented in a MICOM letter report[4].

## EVALUATION PROCEDURE

After selecting the test data from all the video collected during the NLOS CCT, the cuer's performance was evaluated. When considered from a fundamental viewpoint, the most significant measures of performance for a target cuer are: how many real targets did it cue, how many real targets did it fail to cue, and how many false targets did it cue? These were the basic questions that the data analysis attempted to answer. As the evaluation evolved, additional questions were raised and some discussion will be given to those.

The evaluation process was as follows. First, all data analysis was performed by an analyst viewing the cuer output video on the monitor many times. Some of the test segments contained multiple targets so this data was collected for all targets in each video segment. For a cued object to be considered a false target it had to be cued for at least one second. Each false target was only counted once per repetition even if the cueing "box" blinked on and off several times during the time interval of the repetition. Also, it was noticed that some of the helicopters presented an extremely low contrast to the eye, so the contrast was calculated for several of the images by measuring the pixel gray levels at the target and background. The contrast was then calculated as:

$$Ct = 1 - Pt/Pb$$

Where Pt = target pixel value
Pb = background value

The above information was measured for each run and documented in raw data tables.

After the addition of the shape screener algorithms, the cuer was reevaluated in the laboratory using the previously described video data base and evaluation techniques.

## EVALUATION RESULTS

The information from the raw data tables of the first evaluation (without shape screeners) can be summarized as follows:

Correctly Cued Targets = 63.3%
False Alarms[1] = 7.7 per repetition or .66 per second

While the correctly cued target ratio was less than expected (63% instead of the predicted 85%), it was the false alarm rate that was of most concern. It was expected (from the process simulations with the limited data base) that a false alarm rate of one per scene would be experienced. Instead, an average of more than 7 false alarms per test repetition was measured. Of course, the repetitions lasted for a period of 2 to 40 seconds which gave a long time for false alarms to be triggered (they only had to last approximately one second to be scored a false alarm). For this reason the number of false alarms per second may be a more descriptive measure of this parameter. At any rate, the results of the first evaluation led to the development and installation of the shape screener algorithms in an attempt to improve false target rejection without adversely impacting the classification of actual targets.

There are several other points that need to be considered before the results of the shape screener evaluation are discussed. The first of these is target to background contrast. Obviously an object in a video image must have some contrast with the background to be detectable by any means (human eye or digital processing). There is a wide band of contrast that may be required based on the process to be followed. The automatic target cuer has a dynamic gain control that attempts to compensate for such occurrences as targets located in large shadowed areas. The cuer does not have a means of enhancing the contrast where the target and background both present the same (or nearly the same) gray level in the video signal. A situation like this occurred during the CCT when a faded olive drab (OD) helicopter (which actually appeared to be a light tan color) used for some of the tests was flown over a background of predominantly light colored soil. Nine runs were recorded with this helicopter and background. Three of these were cued although it appears that the shadow rather than the helicopter itself was cued on one of these. The contrast values for the normal olive drab and the faded or tan helicopter from these runs are presented in Table I along with whether the targets were cued.

---

[1]The false alarms were counted only during the test time when a valid target was in the FOV.

TABLE I. Contrast For Normal and Faded Helicopters

| RUN # | OD TARGET CONTRAST | "FADED" TGT CONTRAST | CUED |
|---|---|---|---|
| 7 | 40% | 12% | YES/NO |
| 9 | 53% | ~0 - 27% | YES/NO |
| 11 | 50% | 0 - 24% | YES/YES |
| 12 | 47% | 43% | YES/YES |
| 18 | 50% | 7% | YES/NO |
| 75 | 53% | 18% | YES/NO |
| 76 | 52% | 5% | YES/NO |
| 77 | 59% | 7% | YES/NO |
| 79 | 52% | 10% | YES/YES |

In run #9, the faded target so closely matched the color of the background that no contrast could be measured for most of the run; however, the contrast increased considerably near the end. The same situation occurred on run 11 and is attributed to the fact that the color of the helicopter only matched the color of certain portions of the background and when it flew over other background areas, the contrast increased. In the cases where the contrast was reported as approximately 0, the target could be detected only because it was moving when viewed in the dynamic video. Therefore, the contrast was recorded as approximately 0. In the other cases, the contrast was high enough to be measured but, as seen above, it was consistently much lower than the normal olive drab helicopters (except for run 12 where the contrast of both helicopters was nearly the same). Note that in runs 11 and 12 where the "faded" helicopter was cued, their contrasts were some of the higher values measured. In run 11, cueing did not occur until the contrast reached the 24% level. In run 75, the olive drab helicopter is visible and was correctly cued. The faded helicopter, which is extremely difficult to spot, was never cued.

Of the three runs where the "faded" target was cued, one appeared to actually be cueing the helicopter's shadow (run 79). In addition, there were two other cases (runs 4 and 5) where the cuer located the normal helicopter's shadow but failed to locate the actual target. At first, this was considered to be a false target (with the actual target missed) and was scored accordingly. However, upon reflection it appeared that this was not the proper way to

handle that occurrence. First, consider what a false target is and what its effect on the weapon system operation is. Obviously, a false target is an object which is not a target but which is marked as if it were. Its effect is to obscure the real target or to confuse the operator's search for the actual target. However, in the case of the helicopter's shadow, the situation does not often fit the false target scenario. Usually the shadow will be located close to the helicopter, particularly at reasonably long ranges. Therefore, if the operator's attention is directed to the helicopter's shadow, it is very likely he will also see the actual helicopter, particularly if there is any movement. As mentioned earlier, this was the only way to locate one of the tan helicopters.

Thus, it does not seem unreasonable to consider a cued shadow of a target as a correctly cued target when the two are located close together. Since the human operator is the final decision maker (real versus false target) it is very likely that finding the target's shadow is essentially the same as finding the target. Therefore, in some cases, the cued shadows of the targets were considered as correctly cued targets. If this rationale is unacceptable to some, the correctly cued targets on these three runs can be deleted which will slightly lower the success ratio of the cuer (by about 1%).

The evaluation of the cuer performance after shape screener modification provided the following results:

Correctly Cued Targets = 53.6%
False Alarms = 4.5 per repetition or .39 per second

The target classification performance was degraded some (as expected) by achieving better false target rejection. When compared with the results of the original evaluation, the false alarms were reduced by 41% while the amount of correctly cued targets was reduced by 15%. This indicates that the process is at least going in the right direction. The "cost" of reducing false targets is .37% reduction in correctly cued targets for each percent reduction in false targets/second.

## CONCLUSION

This paper has described the automatic target cuer developed under a missile technology program. It has documented the cuer's performance during two phases of its development. The overall performance of the cuer in the original field tests was not as good as had previously been predicted in simulations during process development. The major objection was the relatively high false alarm rate although the actual correct target classification was less than hoped for. The addition of the shape screeners were successful in reducing the false alarms significantly but the correct target classification was also reduced (although not as much as the false alarms). Unfortunately, it was known in advance that the likelihood of achieving significant false target reduction without some reduction in actual target classification was low. This is because of the small size of the targets and the type discriminants being used (essentially contrast and size with optical flow measurements between fields of video). On the positive side, it must be recognized that the addition of the shape screeners was a low cost, simple addition to the basic process which gives reasonably good results.

The shape screener addition to the automatic target cuer was but a single step to improve the performance based on the results of actual field testing in a realistic environment. Additional research is already in process. Some of the CCT data indicates that the fields of view likely to be utilized may allow cueing on larger targets than originally expected. The current cuer was designed to operate with targets that are between 4 and 64 pixels in size. If the fields of view are such that "typical" targets are larger than this, then the additional information available for the larger targets can be utilized to provide more accurate discrimination. An extensive re-evaluation of the screeners (including the shape screeners) has been conducted with the result that the weightings (and possibly the operation) of these screeners is being optimized. The primary research effort at this time is to develop the ability to detect motion. The emphasis is to enable the cuer to detect an object's motion with respect to its background as well as rotor motion from helicopter blades. An approach based on optical flow determination techniques proposed by Horn and Schunck [5] is showing considerable promise in simulation and the design of hardware for real time implementation should begin later this year. As indicated in the discussion on contrast, it is frequently possible to detect motion where there is essentially no measurable contrast between the target and background. As additional improvements are added to the processing, the cuer will be evaluated using the same captive carry video as used in the reported experiments.

## REFERENCES

1. McIngvale, Kilpatrick, and Cardno, "Field Evaluation of the Improved Automatic Target Cuer," TR-RD-GC-89-25, U.S. Army Missile Command, November 1989.

2. McIngvale and Kilpatrick, "Evaluation of Shape Screening Processes for Reducing False Alarm Rate in the Improved Automatic Target Cuer," TR-RD-GC-90-2, U.S. Army Missile Command, March 1990.

3. "Improved Automatic Target Cuer Function," ER-177446, Loral Defense Systems Division - Akron, August 1988.

4. McIngvale, Kilpatrick, and Carper, "A Wide Field-of-View, Small Target, TV Video Data Base for the Evaluation of Automatic Target Cuer/Recognizer Systems," LR-RD-GC-90-08-C, U.S. Army Missile Command, February 1990.

5. Horn and Schunck, "Determining Optical Flow," Artificial Intelligence, Volume 17, 1981, pages 185-203.

# LOCK-ON-AFTER LAUNCH (LOAL) TESTBED FACILITY

By

Charles L. Lewis and Heinz G. Sage
Guidance and Control Directorate
Research, Development, and Engineering Laboratory
U.S. Army Missile Command, Redstone Arsenal, Alabama

## ABSTRACT

This paper describes the Army Missile Command's dual-mode guidance, autonomous Lock-On-After-Launch (LOAL) Testbed Facility which resides in the Research, Development, and Engineering Laboratory's Guidance and Control Directorate. This real-time Hardware-In-The Loop (HWIL) Facility was developed to aid in the test and evaluation of low-cost dual-mode guidance mechanizations that are being considered for future weapon systems. The primary quantitative output of the LOAL Testbed Facility is probability of successful completion of in-flight handover from an inertial midcourse to a terminal seeker. A detailed description of the Facility mechanization is presented and results of verification tests to date are summarized.

## INTRODUCTION

The ability to LOAL is vital for modern Army missile systems when vertical launch, defilade, excessive target range, remotely tracked targets, and other conditions prevent terminal seeker lock-on before launch. Figure 1 shows a cartoon depicting one such dual mode application; that of a remotely launched air defense missile that employs an inertial midcourse flyout to some "acquisition basket" where an autonomous handover to the onboard terminal seeker is attempted. Once a successful, timely handover has occurred, some form of terminal homing guidance can be applied to achieve the desired final miss. The particular inertial flyout mode shown in Figure 1 utilizes an onboard computer and an inertial package to perform strapdown navigation for missile position; thereby removing the requirement for missile track by the ground sensor. Target state estimates are maintained in the missile computer by a target predictor periodically updated via uplink of the ground sensor track data. Onboard knowledge of missile and target states allows midcourse guidance to be performed, range to go to be estimated, and, when combined with missile angular information from the inertial components, where to command the seeker to point in order to acquire the target.

Efforts under the Guidance and Control Directorate's 6.2 Technology Line Item RG-3 have developed the analysis and evaluation tools required to design LOAL guidance concepts such as those shown in Figure 1, quantify hardware performance requirements for specific applications, implement breadboard mechanizations, and perform HWIL test and evaluation for simulation validation and laboratory demonstration. Although the simulation and design tools are applicable to any LOAL requirement, the supporting LOAL Testbed Facility presented in this paper is presently constructed to focus HWIL testing on low-cost small field-of-view (FOV) non-imaging infrared (IR) terminal seekers and medium accuracy strapdown inertial components.

## FACILITY CONCEPT

The real-time HWIL evaluation of various missile hardware components such as IR seekers, inertial packages, and flight computer mechanizations to determine their effect on the handover process is the primary application of the LOAL Facility. This scheme utilizes the probability of successful handover as the evaluation criteria for the candidate hardware components being tested. Figure 2 shows the requirements for a successful acquisition to occur. As can be seen from the figure, both missile and target uncertainties contribute to the seeker look-angle error at handover and these values must be sufficiently small so the target is contained within the seeker FOV.

In order to realistically measure acquisition probability, the LOAL Testbed Facility simulates the launch, midcourse flyout, and handover phases of a dual mode guided missile. Successful terminal homing is assumed if the handover is achieved within the time allowed for transition and is, therefore, not simulated. An estimate of probability of handover is obtained by running a set of simulated flyouts; with noisy, uplinked ground sensor target track data being the independent input variable, then dividing the number of successful in-flight handovers by the total number of runs.

The Facility is also used to perform open loop evaluation of the individual hardware components, such as determination of strapdown navigation accuracy with various gyros, and test results are used to validate the supporting all-digital six degree-of-freedom (6-DOF) Monte-Carlo inertial mid-course LOAL trade studies simulation.

## FACILITY DESCRIPTION

### OVERVIEW

The LOAL testbed facility consists of the major subsystems shown in Figure 3. The computer systems involved are located in one room, with the Moving Taget Simulator (MTS) and Carco flight motion table located in an adjacent room. The figure illustrates how these components are functionally configured into a flexible, modular HWIL simulation system. The missile dynamics, including autopilot and actuator models, are simulated in real-time on a special purpose AD-10 high speed digital processor being hosted by a VAX 11/780 digital computer. True target motion is modeled on the AD-10 to provide the data needed for intercept geometry calculations and MTS drive signals, while missile angular motions calculated by the AD-10 are used to drive the Carco table upon which the IR seeker and inertial measurement unit (IMU) hardware being tested are mounted. The ground control station, made up of a PDP 11/73 digital computer, performs the missile initialization and launch command fire control functions, simulates the ground sensor target track and uplink functions, and performs data logging and post processing on all the simulation data collected by the other computer. The final computer in the Facility is an in-house built flight computer (FC) breadboard constructed of two INTEL 86/14 processors and associated supporting software development, I/O, and power supply equipment. The FC utilizes either simulated or actual 3-axis missile angular rate data from the IMU being tested and simulated 3-axis missile translational acceleration data from the AD-10 simulation to perform strapdown inertial navigation for missile position and angles. This computer

also performs target estimation between target state uplinks, then utilizes this missile and target data to calculate autopilot angular rate feedback signals and midcourse guidance acceleration commands which are sent to the AD-10 missile simulation. Finally, the FC determines when to begin the in-flight handover and generates seeker pointing and scanning precession commands which are output to the seeker hardware being tested.

## TARGET GENERATION

The MTS is resident in the LOAL Facility to provide the proper dynamic missile/target line-of-sight geometric relationships to the seeker hardware during the handover phase of testing. The MTS is shown schematically in Figure 4. The target source is an IR temperature controlled black body coupled with a collimator to permit representation of a target focused at infinity. The collimation is accomplished by a ten-inch off-axis parabolic mirror and a beam director. The beam director utilizes precision closed loop position servos to rotate a flat 14" diameter pointing mirror in azimuth and elevation to present a moving point source target to the seeker hardware being tested. The beam director mirror gimbal order is illustrated in the figure. The mirror is mounted on the elevation servo. The mirror/elevation servo is, in turn, mounted on the azimuth servo, all of which is then mounted on the transverse linear servo. The AD-10 real-time simulator generates azimuth angle, elevation angle, and translation position commands to position the MTS optics such that the collimated target beam intersects the seeker receiving optics from the desired angular orientation. The installed MTS is shown interfaced with the Carco flight motion table in Figure 5, with specific performance characteristics as given in Table 1.

## FLIGHT MOTION SIMULATOR

A CARCO Model S-450 3-axis flight simulator is utilized in the LOAL Facility to provide simulated missile motion to the IR seeker and IMU hardware being evaluated. Under the present setup, missile roll stabilization is assumed and no roll gimbal is used. This electronically controlled, hydraulically driven fixture is shown in Figure 6 with representative seeker and IMU hardware mounted. Specific performance characteristics for the Carco simulator are given in Table 2.

## FACILITY INTERFACE STRUCTURE

The functional operation of the Facility is shown in Figure 7. Inertial data from either the multisensor IMU (MIMU) or the AD-10 is transmitted to the FC at 100 Hz. Using this data, the FC calculates missile attitudes at 100 Hz and missile position and velocity at 20 Hz. The FC receives target state updates from the ground control station every 1.33 seconds which it uses to update its 10 Hz target predictor. The missiel to target position and velocity vectors are then calculated at 20 Hz with the latest missile and target position information. These vectors are then used by the FC together with the proper missile attitudes to compute the missile guidance commands at 20 Hz. They are then sent to the AD-10. The FC also computes seeker precession commands at 50 Hz using seeker feedback angles in conjunction with the missile and target data.

Using the guidance commands from the FC, the AD-10 simulates the missile dynamics and stabilization with a 2.5 ms integration step size and a 2d order Adams-Bashforth integration scheme. Actual missile attitudes are generated at 400 Hz. Also, at 400 Hz, appropriate commands for the Carco table are calculated and output that will allow the Carco table to subject the seeker and MIMU to the actual missile attitudes. The Ad-10 also calculates commands necessary to properly position and orient the MTS every 2.5 ms so that an accurate presentation of the simulated target is produced.

## FACILITY ALIGNMENT

The Carco flight table, MTS (including each of the individual mirrors within the MTS), and the seeker hardware being tested needs to be aligned to the same boresight. A procedure has been developed that performs this alignment to within .05 degrees.

## LOAL FACILITY VERIFICATION

Proper operation of the LOAL Facility was verified by comparisons with an existing, well checked-out, 6-DOF simulation program. There were definite differences between the HWIL simulation and the 6-DOF and as many of these as possible were incorporated into a special version of the 6-DOF for comparison/verification purposes. Some differences could not be accounted for, however, such as the AD-10's 16-bit resolution limitation. The verification of the HWIL simulation was done in sections so that any differences found could be attributed to particular causes.

## NAVIGATION SOFTWARE VERIFICATION

The navigation portion of the HWIL FC code was verified by running the 6-DOF reference simulation to obtain true inertial information which was then stored in a table for use as input to the HWIL FC. Navigated positions calculated at 47 seconds into the flight were then compared between the HWIL FC and 6-DOF as shown in Section A of Table 3. The interface between the AD-10 and the FC was then verified by using the same inertial data previously used, but instead of the FC reading the data from a table in memory, it read the data from the AD-10. Navigated position results were again compared (see Section B of Table 3). Latency in the prototype FC was reduced by utilizing trigometric look-up tables and reducing the guidance update rate from 20 Hz to 16.67 Hz. Comparison of the FC navigation results with the trig look-ups and quidance update reduction were made with the 6-DOF and results were documented in Sections C and D respectively of Table 3. Finally, Section E of Table 3 lists the 6-DOF versus HWIL simulation comparisons with all the FC errors included.

## AD-10 SOFTWARE VERIFICATION

The missile positions calculated by the AD-10 were verified by storing the guidance acceleration commands generated by the 6-DOF into a file and feeding them to the AD-10 in place of the ones generated by the FC. The actual missile positions calculated by the AD-10 were then compared to those calculated by the 6-DOF as presented in Table 4. The reasons these values do not match exactly were attributed to the 16-bit resolution limitation of the AD-10 and

to the fact the AD-10 did not generate the inertial information the same as the 6-DOF (they were not generated the same because of the 16-bit resolution limitation) and therefore, would not produce identical guidance acceleration commands. The results were considered to be as close to the 6-DOF as was posible with the AD-10.

## GUIDANCE SOFTWARE VERIFICATION

The next step in the validation process was to integrate the FC and AD-10 to perform closed loop guidance and compare actual navigation error with the 6-DOF. This was done and the results given in Table 5. Section A of Table 5 shows the results running in nonreal-time with no FC latency optimizations included. Section B is with the FC latency optimizations included and Section C is with the FC latency optimizations and the simulation run in real-time. The navigation error shown in Section C equates to about a 0.6 degree pointing error at 3 km.

## SEEKER SEARCH AND ACQUISITION SOFTWARE VERIFICATION

The seeker software verification was a two part effort. The FC code that generates the seeker scan and is responsible for converting the seeker pointing and scan requirements into precession commands was checked out first using a seeker emulator. The emulator's outputs were compared to seeker feedbacks output by the 6-DOF. Once these matched, then the emulator was replaced by the actual seeker and its outputs compared to the 6-DOF. Figure 8 displays seeker scan patterns from the 6-DOF and the HWIL for a typical seeker scan about missile boresight with no pointing required.

# TEST RESULTS

## DEMONSTRATION HARDWARE DESCRIPTION

The dual-mode guidance LOAL Testbed Facility is designed to allow closed loop, real-time HWIL evaluation of various IR seeker, inertial angular measurement device, and flight computer hardware that has been configured to provide inflight handover from inertial midcourse to IR seeker terminal homing. A set of laboratory demonstration hardware has been configured that allows checkout of the LOAL Testbed. The demo hardware set is composed of the following individual stand-alone components:

Seeker - The seeker used for the LOAL Testbed demonstration is a CHAPARRAL ANDAW-1B IR seeker that has been extensively modified to have a pointing and scanning capability under computer control. Figure 9 shows this seeker mounted on the Carco flight table. The seeker's scan capability effectively increases its FOV from approximately 1.3 degrees radius to 4.8 degrees radius. During a LOAL Testbed HWIL run, the seeker is mounted on the Carco flight table and will be exposed to simulated missile angular motions. It will remain in a non-scanning, but pointed mode until it reaches the allowable acquisition range of the particular scenario being run. Then it will begin scanning and pointing, using commands sent from the FC at a 50 Hz rate. The seeker sends an acquisition/nonacquisition signal back to the FC, also at 50 Hz. Table 6 provides the seeker's performance characteristics.

Inertial Device - A Singer-Kearfott MIMU has been made available to the LOAL Testbed Facility for demonstration and evaluation. This solid state, strapdown inertial package is representative of the low cost, medium accuracy performance required in a short-to-medium range dual-mode air defense application. The MIMU is installed onto the Carco flight motion simulator table as shown in Figure 9. It will sense pitch and yaw angular rates during HWIL operation and send them to the FC at 100 Hz. It also supplies the master clock sync to the AD-10.

Flight Computer - As described earlier, the LOAL Testbed Facility demo FC hardware is an in-house built breadboard constructed of two INTEL 86/14 processors and associated supporting software development, I/O, and power supply equipment (see Figure 10). Major tasks performed are inertial navigation, target estimation, guidance, and seeker pointing.

## DEMONSTRATION TEST SETUP

The LOAL Testbed Facility's closed loop, real-time HWIL performance was evaluated by exercising the demonstration seeker and flight computer hardware through three simulation flight sets, with each set consisting of 25 individual simulation runs. Each successive flight set was designed to expose the hardware being tested to increasingly difficult scenarios. This was accomplished by first reducing the allowable missile-to-target acquisition range from 4 km to 3 km, then increasing the radar noise in the target state updates for the 3 km case. These parameters were first modified in the 6-DOF simulation program and reference simulation runs were then generated. The target update files which were generated by the 6-DOF during these runs were saved to be used in the HWIL simulation. The radar noise was increased in the third run set by decreasing the radar power paramenter in the 6-DOF. Table 7 details the parameter values used to run each of the 3 flight sets. All other parameters remained the same for the three flight sets. Selected key parameters are listed in Table 8.

## TEST RESULTS

The test results for the demo HWIL flight sets were recorded as acquistions or nonacquisitions and were compared to identically computed outputs of the 6-DOF. The performance of the simulation was related to its ability to match the 6-DOF results. The summary results of the three flight tests are given in Table 9. An example of the individual run comparisons for Flight Run Set #2 is given in Table 10. Look angle error values are given for each flight at 42.2 seconds and can be used as a measure of how well the HWIL simulation is correlating with the 6-DOF. Detailed plots in both pitch and yaw for total look angle error and also of target position, predicted target position, navigation error, and seeker feedback for runs #1 and #6 of Flight Run Set #2 are presented in Figures 11 and 12 respectively.

## TEST CONCLUSIONS

Based on the percentages of acquisitions/nonacquisitions that the HWIL facility matched the 6-DOF, and the corresponding general agreement of look angle error values, it was concluded that the HWIL facility is sufficiently robust to effectively evaluate candidate seeker hardware using simulated inertial data.

Aging and outdated hardware are major contributors to the errors encountered by the LOAL facility. The modified CHAPARRAL seeker has been undergoing severe HWIL testing for several years and its performance reliability is marginal at best. Seekers that would be brought in for evaluation would hopefully be less utilized.

The LOAL Testbed Facility itself is comprised of hardware components that are aging and have reached or surpassed their useful limit. New equipment has already been ordered and is in some cases being incorporated into the facility.

The AD-10 computer is the main component that is currently being phased out of the facility. Although a powerful machine, the AD-10 poses restrictions such as 16-bit resolution that impede the simulation's accuracy and performance. A modern microprocessor-based real-time controller driven by a 50 MHz Clipper chip is in the process of replacing the AD-10 computer. Better data resolution and easier programming of simulation modifications or new airframe models are examples of why the new real-time controller will be an excellent improvement to the facility.

An effort is also being made to replace the current FC with a new 386 based Intel 520 multi-bus II system. The additional speed of the Intel 520 will eliminate any latency that is present in the current flight computer and will simplify the two processor configuration currently required to perform I/O and calculations simultaneously.

An automated matrix I/O and operations control system is also being installed into the LOAL Testbed Facility. This will enable potential users to bring in their own test equipment and diagnostic tools and easily interface them to existing equipment.

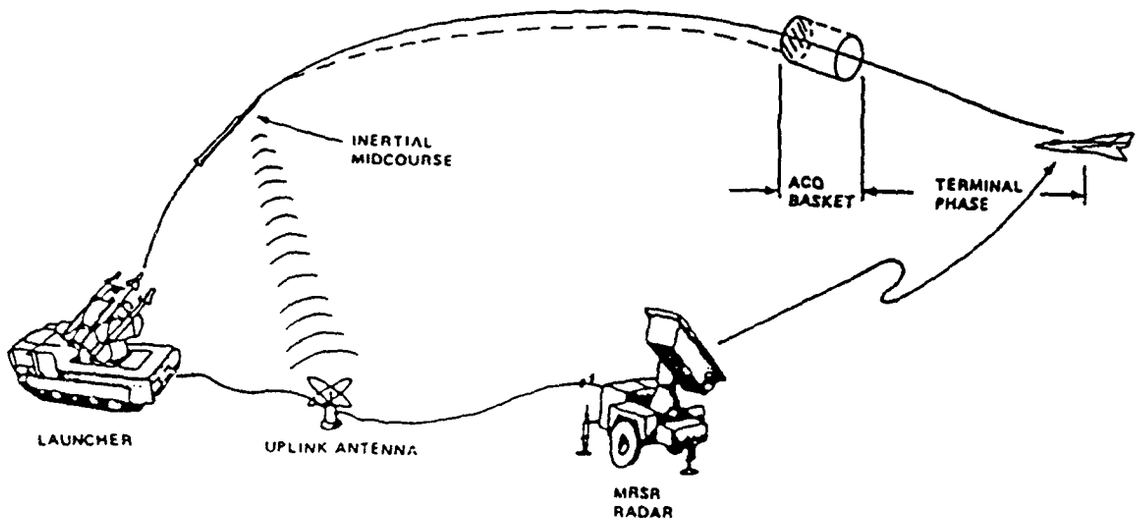


Figure 1. Dual Mode Guidance Scheme.

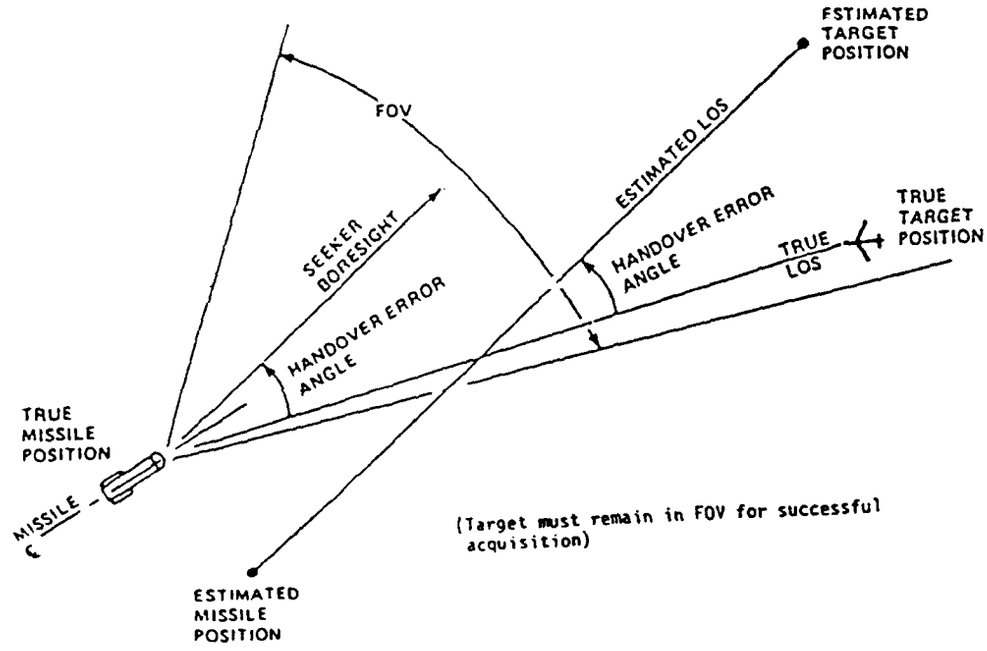


Figure 2. Acquisition at Handover Scenario.

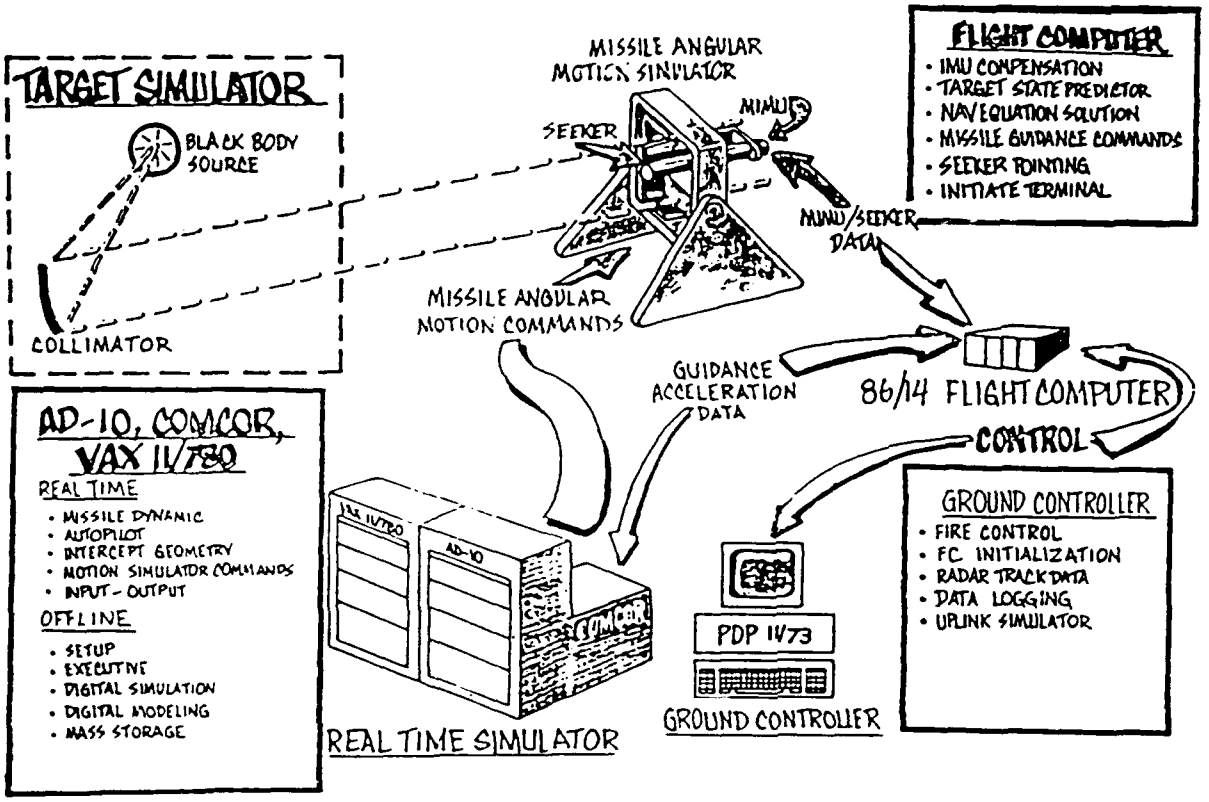


Figure 3. Lock-On-After-Launch (LOAL) Testbed Facility.

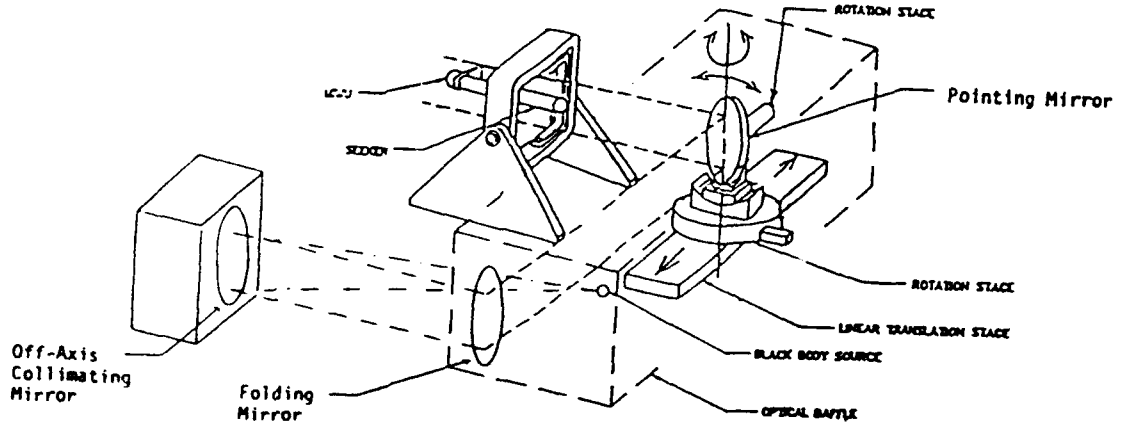


Figure 4. Moving Target Simulator Optical Schematic.

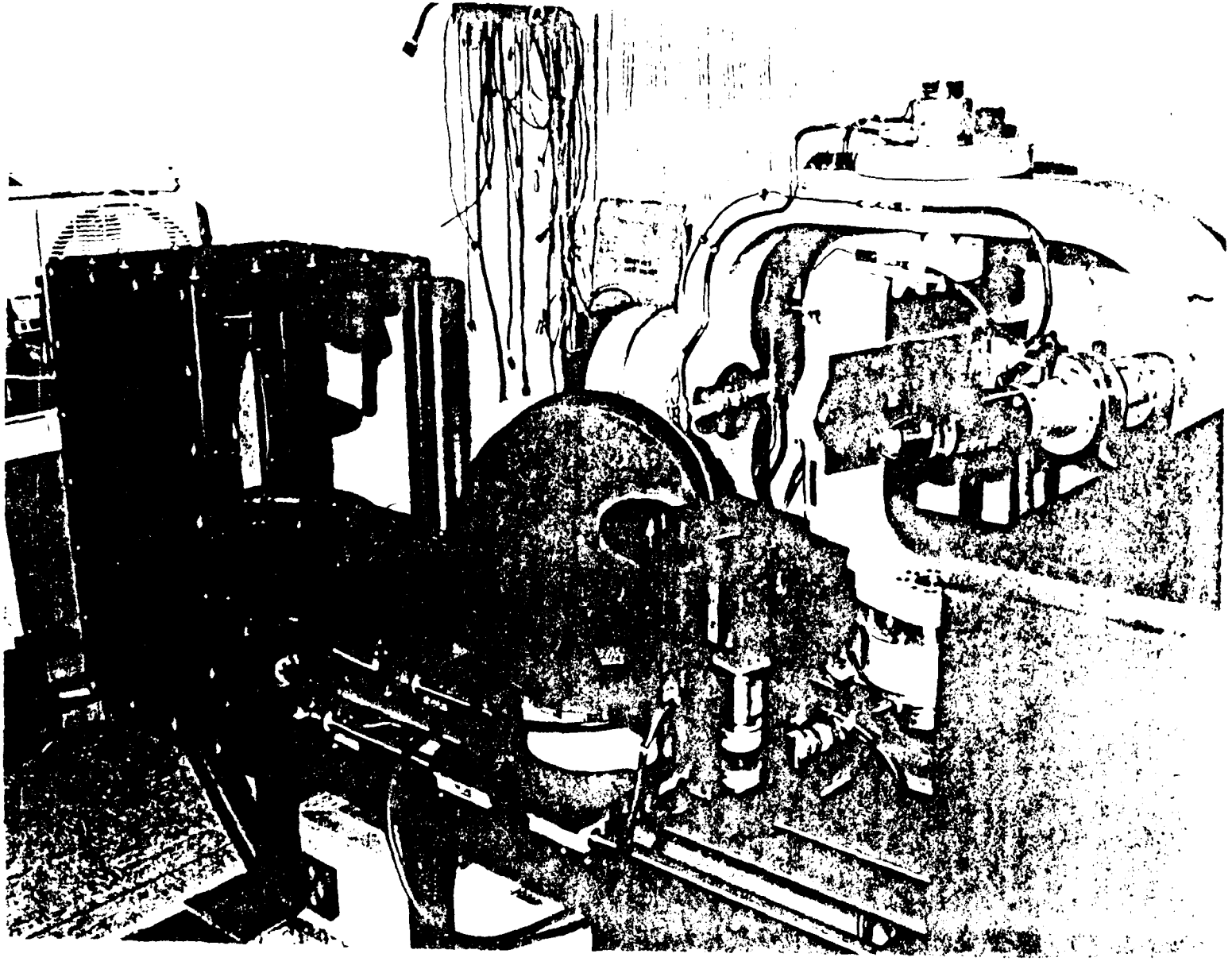

Figure 5. Moving target simulator.

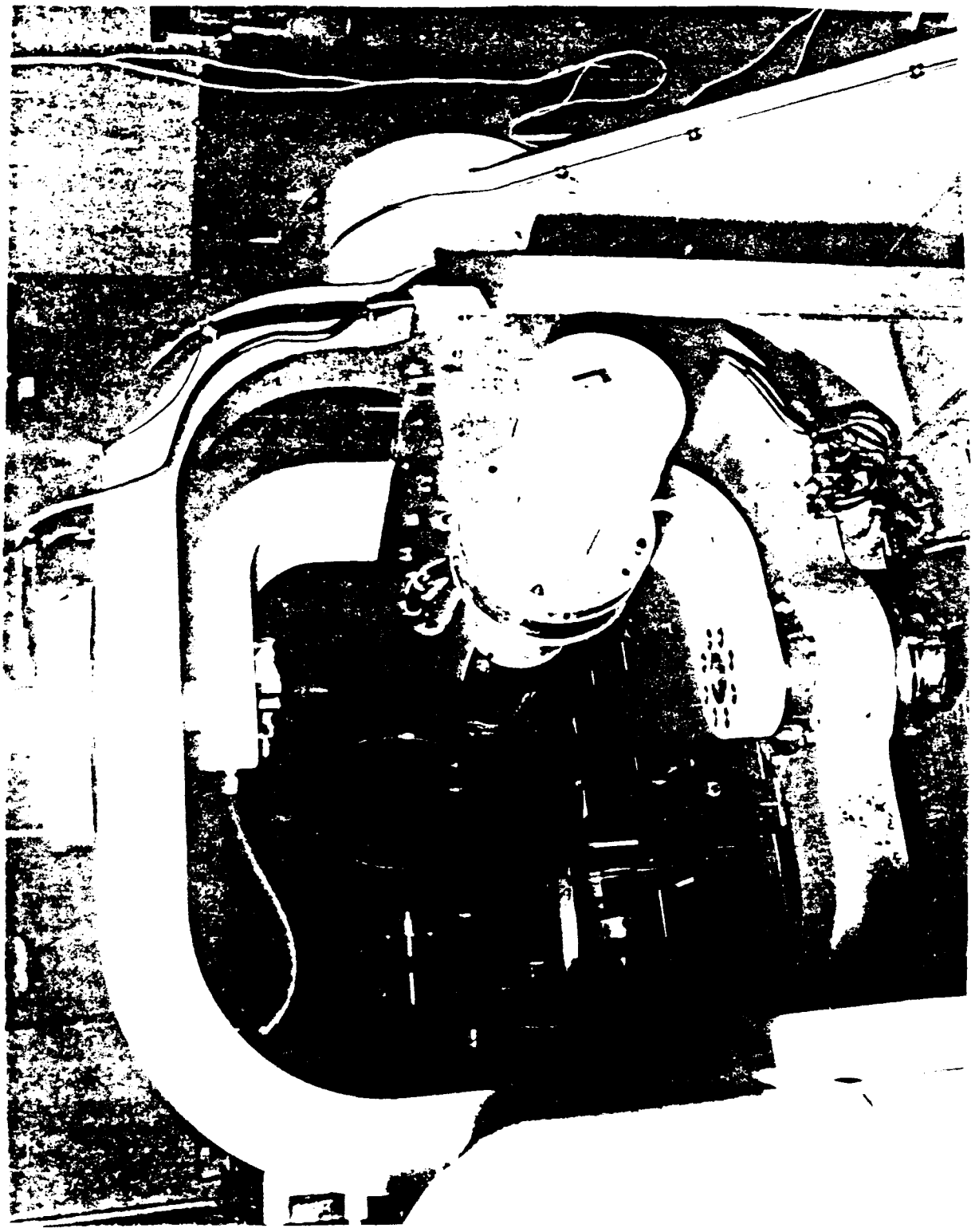

Figure 6. Flight motion simulator table.

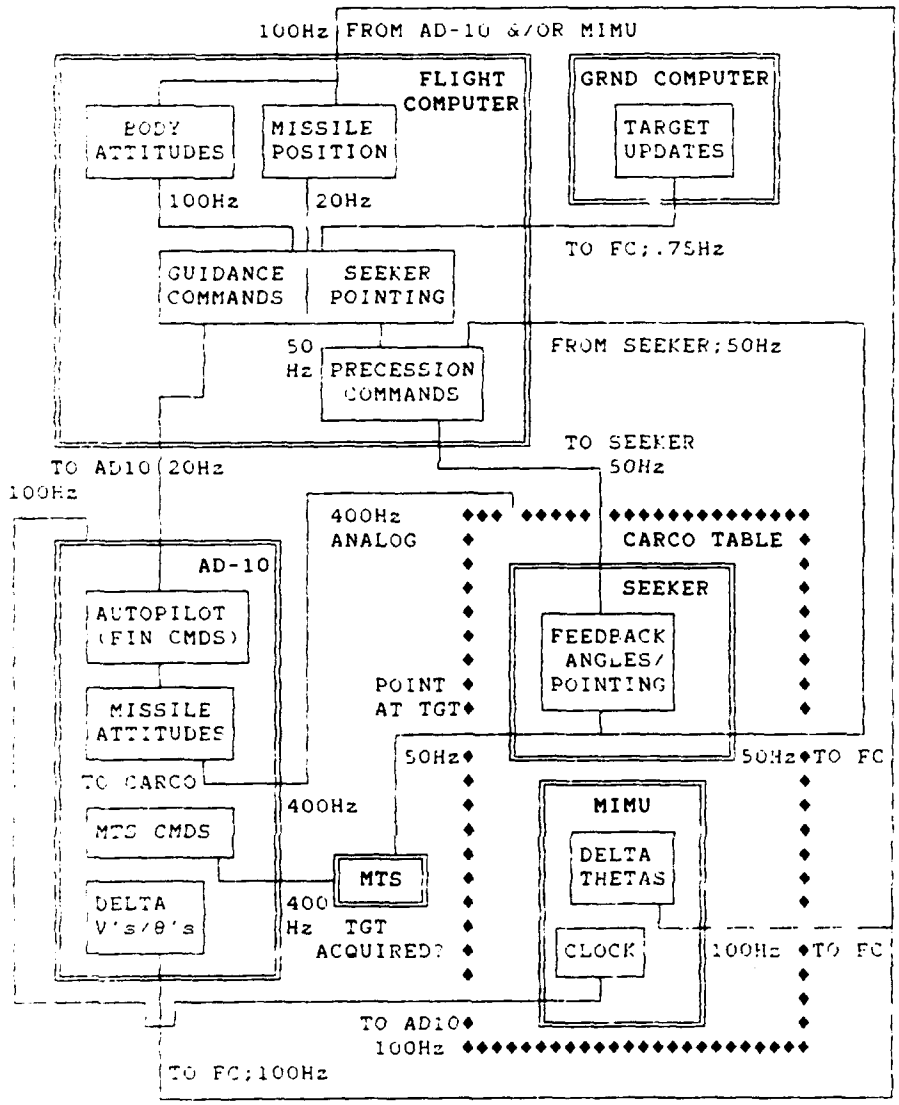


Figure 7. LOAL Facility Functional Flow Chart.

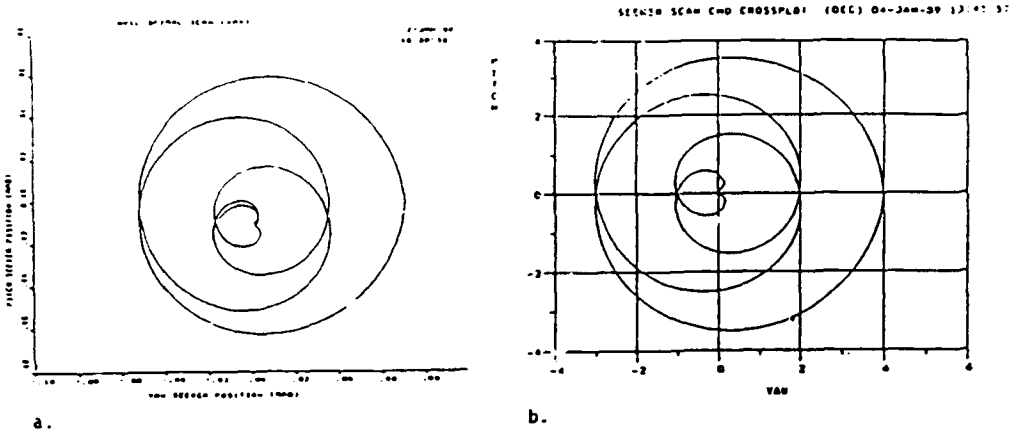

a.

b.

a. 6-DOF generated scan
b. HWIL generated scan position before feedback
c. Scan feedbacks from seeker emulator box
d. Scan feedbacks from actual seeker

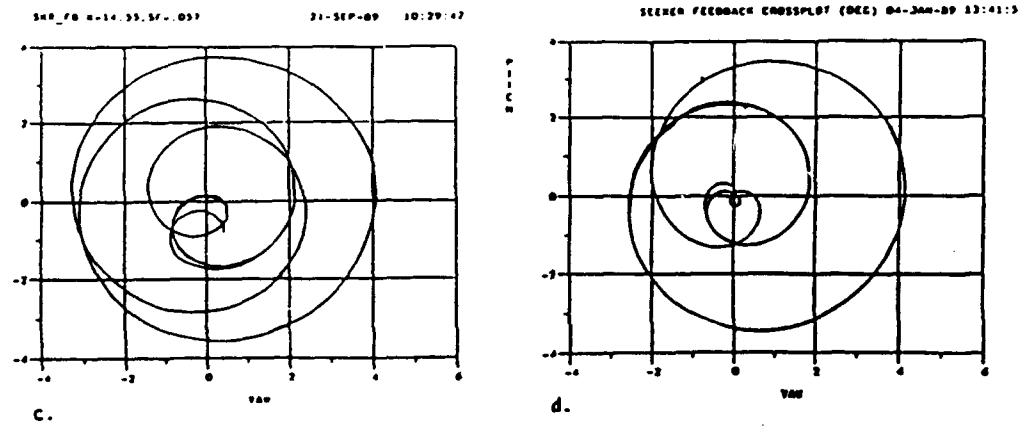

c.

d.

Figure 8. Seeker Scan Patterns About Boresight.

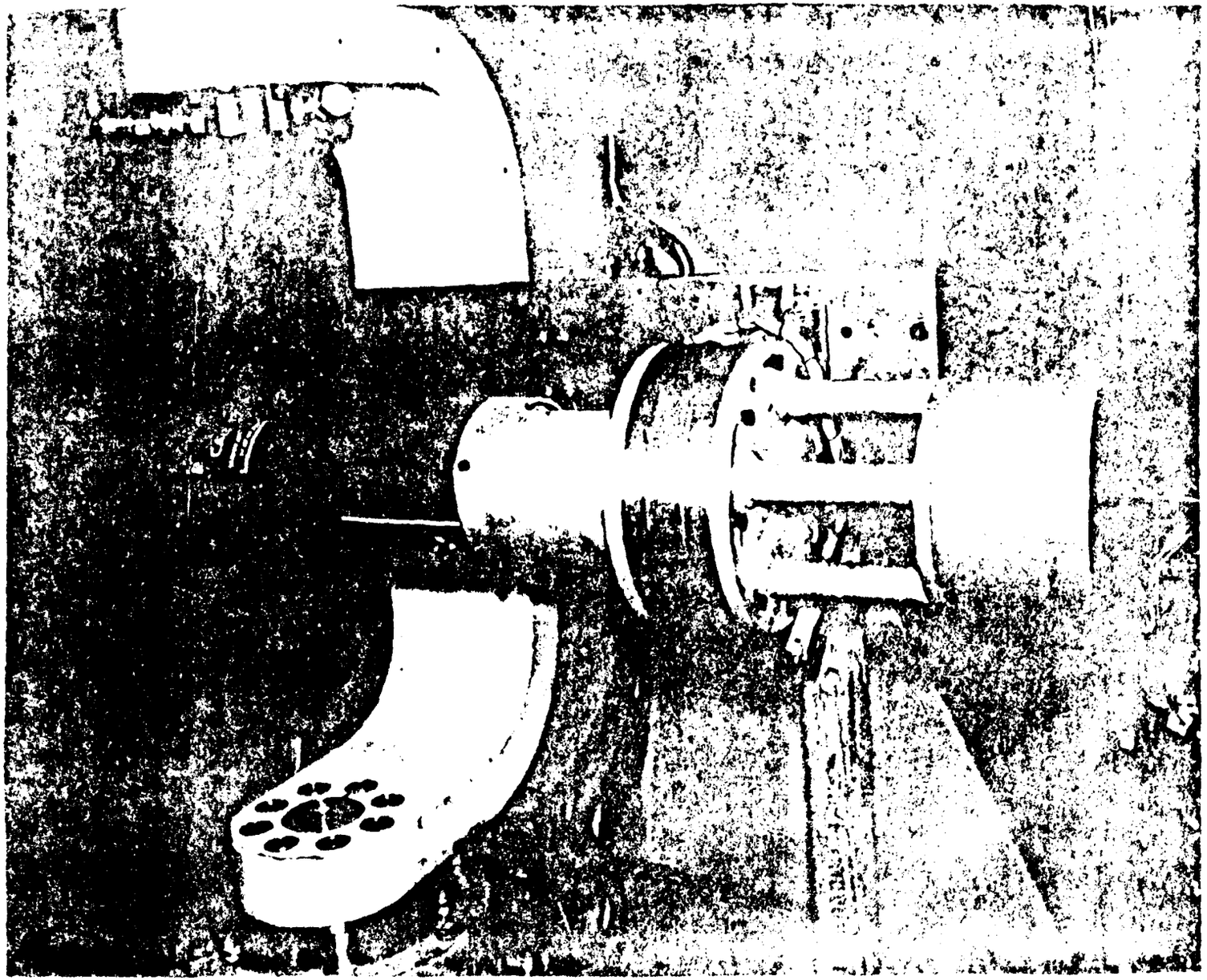

Figure 9. LOAL prototype hardware being tested.

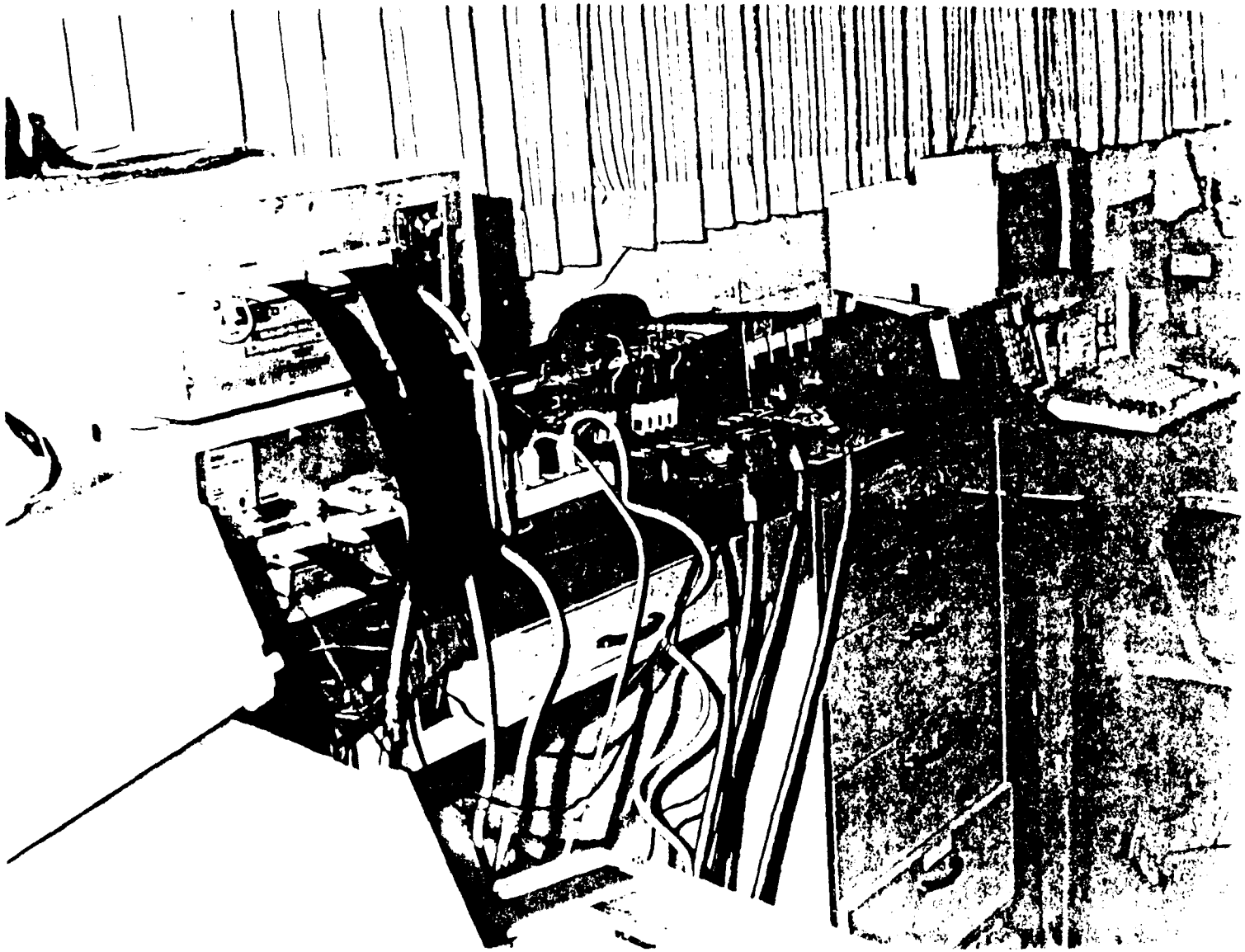

Figure 10. LOAL prototype flight computer.

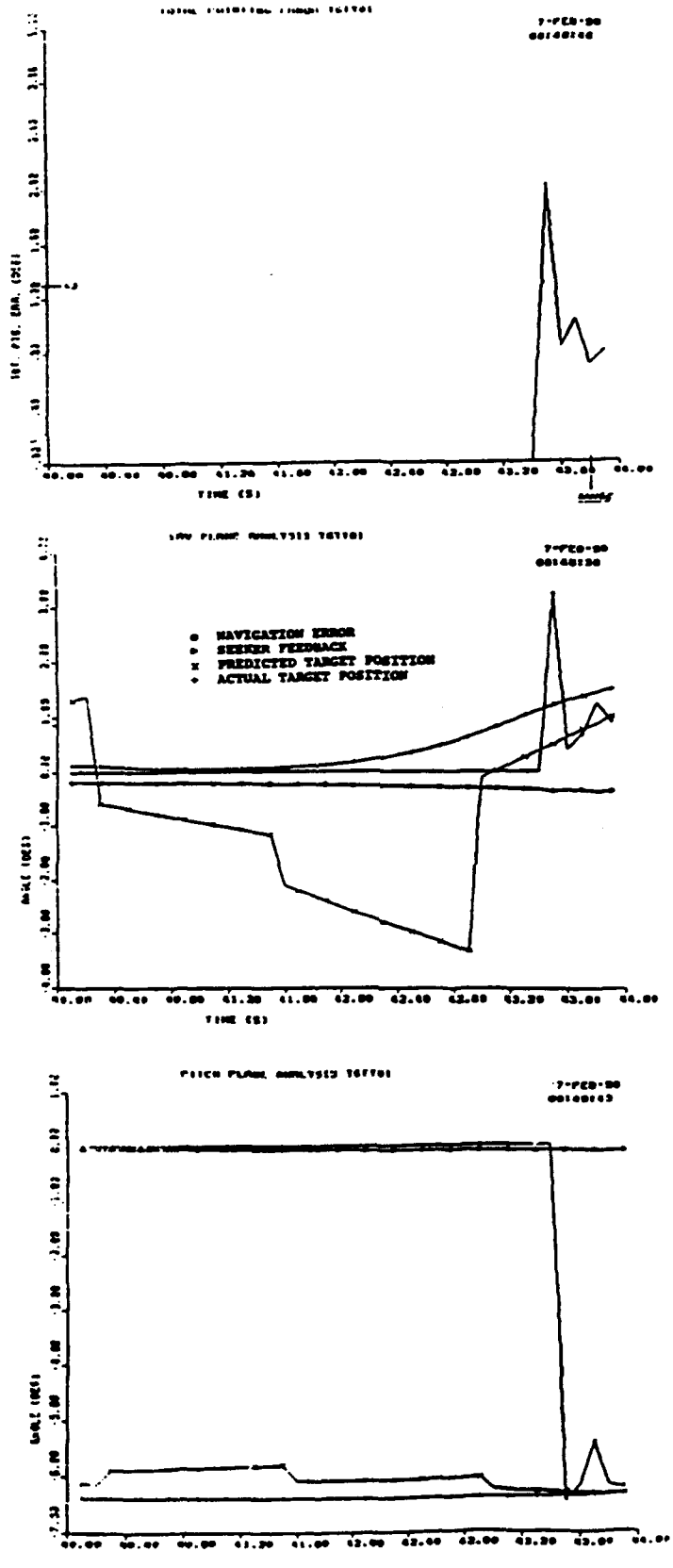


Figure 11. LOAL Testbed Run #1, Set #2.

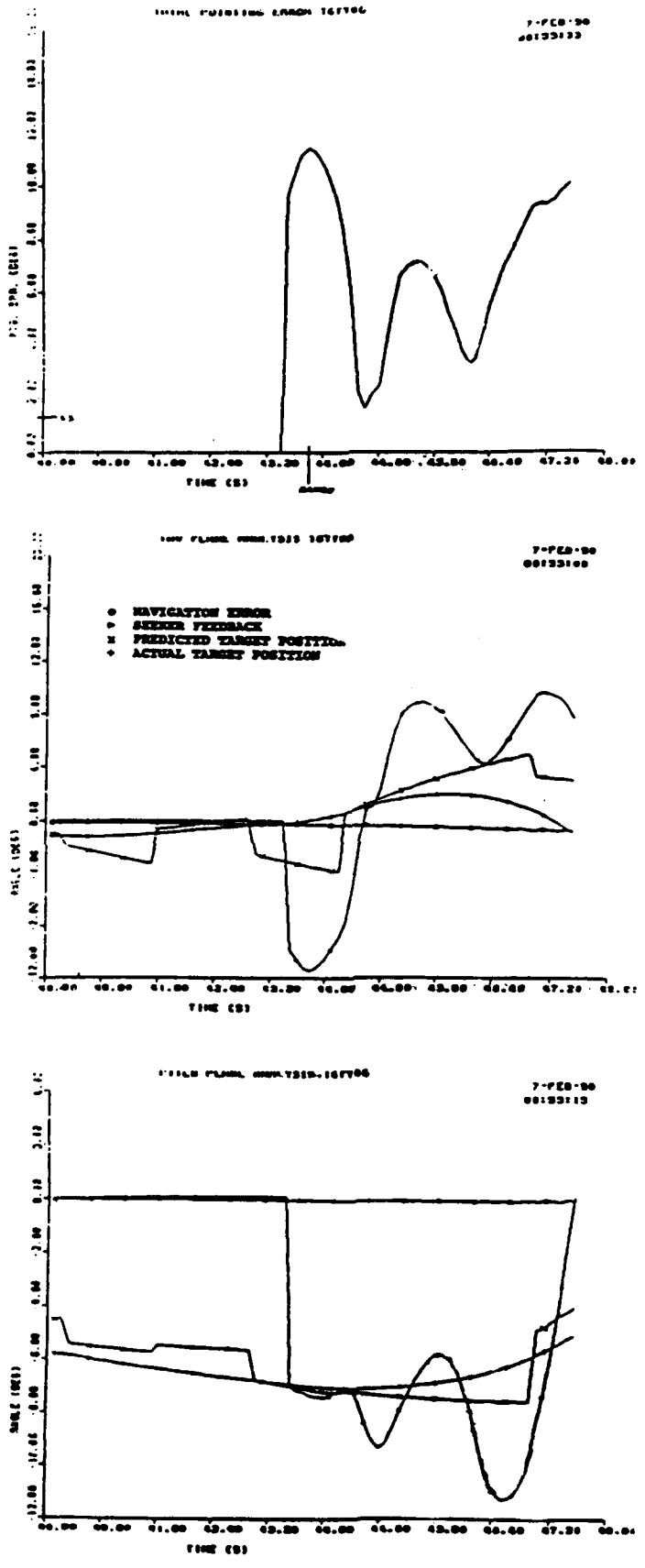


Figure 12. LOAL Testbed Run #6, Set #2.

TABLE 1. Moving Target Simulator (MTS) Performance Data

TARGET PHYSICAL CHARACTERISTICS:

- SOURCE WAVELENGTH - IR BLACK BODY RADIATION
- TEMPERATURE RANGE - 0 TO 950 DEGREES CELSIUS
- IMAGE - POINT SOURCE FOCUSED AT INFINITY

LINE OF SIGHT (LOS) MOTION CAPABILITIES:

| | AZIMUTH | ELEVATION |
|---|---|---|
| • TARGET LOS ANGLES SUPPORTED | (+/-) 26.5 DEG. | (+/-) 9.5 DEG. |
| • STATIC POSITION ACCURACY | (+/-) 0.01 DEG. | (+/-) 0.01 DEG. |
| • DYNAMIC POSITION ACCURACY | < 0.1 DEG. HANGOFF AT 20 DEG./SEC. LOS RATE | < 0.1 DEG. HANGOFF AT 20 DEG./SEC. LOS RATE |
| • ANGULAR RATE CAPABILITIES | 120 DEG./SEC. | 90. DEG./SEC. |
| • ANGULAR ACCELERATION CAPABILITIES | 1200 DEG./SEC.$^2$ | 900 DEG./SEC.$^2$ |

TABLE 2. Flight Motion Simulator Performance Data With 5.0 lb-in-sec.$^2$ Load

| | YAW AXIS | PITCH AXIS |
|---|---|---|
| MAXIMUM ACCELERATION | 25,000 DEG./SEC.$^2$ | 12,000 DEG./SEC.$^2$ |
| MAXIMUM VELOCITY | 250 DEG./SEC. | 200 DEG./SEC. |
| DISPLACEMENT | (+/-) 45 DEG. | (+/-) 120 DEG. |
| FREQUENCY RESPONSE, 90 DEG. | 23 HZ | 12.8 HZ |
| REPEATABILITY | (+/-) 0.005 DEG. | (+/-) 0.005 DEG. |
| POSITION ACCURACY | (+/-) 0.053 DEG. | (+/-) 0.053 DEG. |
| MAXIMUM DRIFT (ONE HOUR) | (+/-) 0.01 DEG. | (+/-) 0.01 DEG. |
| LOAD INERTIA | 5 in-lb-sec.$^2$ | 5 in-lb-sec.$^2$ |
| POSITION SCALE FACTOR | 1.0 DEG./VOLT | 1.0 DEG./VOLT |

TABLE 3. Navigation Position Comparisons

| AXIS | 6-DOF(ft) | FC(ft) | DIFFERENCE(ft) |
|---|---|---|---|
| A. FC Table Lookup Test Comparison | | | |
| X | -78002.4 | -78002.4 | 0.0 |
| Y | -32.4239 | -32.4242 | 0.0011 |
| Z | -3620.81 | -3620.81 | 0.0 |
| B. AD-10 to FC Interface Comparison | | | |
| X | -78002.4 | -78002 | 0 |
| Y | -32.4231 | -32.425 | 0.002 |
| Z | -3620.81 | -3620.8 | 0.0 |
| C. FC Trig. Lookup Comparison | | | |
| X | -78002.4 | -78002 | 0 |
| Y | -32.4231 | -39.569 | 7.146 |
| Z | -3620.81 | -3621.5 | 0.7 |
| D. FC to AD-10 Guidance Command Loop Comparison | | | |
| X | -78002.4 | -77986 | -16 |
| Y | -32.4231 | -30.908 | -1.515 |
| Z | -3620.81 | -3622.3 | 1.5 |
| E. TOTAL COMBINED NAVIGATION POSITION ERROR | | | |
| X | -78002.4 | -77985 | -15 |
| Y | -32.4231 | -38.050 | 5.526 |
| Z | -3620.81 | -3623.1 | 2.3 |

TABLE 4. Actual Missile Position Comparisons

| AXIS | 6-DOF(ft) | AD-10(ft) | DIFFERENCE(ft) |
|---|---|---|---|
| AD-10 Guidance Command Lookup Test Comparison | | | |
| X | -78058.4 | -77976 | -82 |
| Y | -38.3923 | -58.594 | 20.202 |
| Z | -3653.16 | -3593.4 | -59.8 |

TABLE 5. Navigation Error Comparison

| AXIS | 6-DOF(ft) | HWIL(ft) | DIFFERENCE(ft) |
|---|---|---|---|
| A. Navigation Error Comparison with No FC Errors | | | |
| X | -56.0 | -38 | -18 |
| Y | -5.9692 | 51.339 | -57.308 |
| Z | -32.35 | -7.1 | -25.3 |
| B. Navigation Error Comparison with FC Errors | | | |
| X | -56.0 | -54 | -2 |
| Y | -5.9692 | 57.167 | -63.136 |
| Z | -32.35 | -5.1 | -27.3 |
| C. Navigation Error Comparison with FC Errors and Latency | | | |
| X | -56.0 | -80 | 24 |
| Y | -5.9692 | 58.417 | -64.386 |
| Z | -32.35 | 51.7 | -84.1 |

TABLE 6. IR Scanning Seeker Performance Data

| | |
|---|---|
| INSTANTANEOUS FIELD-OF-VIEW (FOV) | 1.3 DEG. RADIUS |
| STATIC POSITIONING ACCURACY WITHIN 10 DEG. RADIUS ENVELOPE | (+/-) 0.10 DEG. |
| SCANNING MODES | CONICAL,SPIRAL |
| MAXIMUM SLEW RATE (VECTOR SUM) | 18 DEG./SEC. |
| MAXIMUM EFFECTIVE SCAN FOV | 4.8 DEG. RADIUS |
| SCAN TIME (SPIRAL 18 DEG./SEC.) | 2.86 SEC. |
| MAXIMUM POINTING ANGLE | 30 DEG. |

TABLE 7. Simulation Run Set Parameters

| RUN SET NO. | ACQUISITION RANGE | RADAR POWER |
|---|---|---|
| 1 | 4000m | 192dB |
| 2 | 3000m | 192dB |
| 3 | 3000m | 180dB |

TABLE 8. Selected Key Simulation Parameters

| | |
|---|---|
| Target Range | 25 km |
| Target Altitude | 1 km |
| Target Velocity | Stationary |
| MTS source temperature | 77° C |
| Seeker command gain | 43 |
| Seeker command scale factor | .01953 |
| Guidance loop frequency | 16.67 Hz |
| Seeker gimbal limits | ±25° |
| Flight table limits - pitch | ±30° |
| Flight table limits - yaw | ±25° |
| FC delta θ scale factor | .045 |
| FC delta V scale factor (X) | 10 |
| FC delta V scale factor (Y,Z) | 4.5 |

TABLE 9. LOAL Testbed Facility Preliminary Results

| Run Set # | % Acquisitions | | HWIL/6-DOF Correlation (%) |
|---|---|---|---|
| | 6-DOF | HWIL | |
| 1 | 88 | 88 | 92 |
| 2 | 72 | 64 | 76 |
| 3 | 48 | 16 | 68 |

TABLE 10. Run Set #2 Test Results

| RUN # | TARGET ACQUIRED 6-DOF | TARGET ACQUIRED HWIL | ACQUISITION TIME (sec.) 6-DOF | ACQUISITION TIME (sec.) HWIL | LOOK ANGLE (LA) ERROR @42.2sec. (deg.) 6-DOF | LOOK ANGLE (LA) ERROR @42.2sec. (deg.) HWIL | DELTA LA ERROR (deg.) |
|---|---|---|---|---|---|---|---|
| 1 | YES | YES | 43.835 | 43.093 | 2.661 | 2.911 | 0.250 |
| 2 | YES | YES | 43.885 | 43.953 | 0.398 | 0.572 | 0.174 |
| 3 | YES | YES | 44.035 | 44.304 | 1.660 | 1.409 | 0.251 |
| 4 | NO | NO | — | — | 2.980 | 2.639 | 0.341 |
| 5 | YES | YES | 45.310 | 44.884 | 2.637 | 3.117 | 0.480 |
| 6 | NO | NO | — | — | 1.069 | 1.035 | 0.034 |
| 7 | YES | YES | 43.885 | 43.944 | 0.037 | 0.122 | 0.085 |
| 8 | YES | YES | 44.245 | 45.033 | 0.886 | 1.035 | 0.149 |
| 9 | YES | NO | 43.885 | — | 3.771 | 4.006 | 0.235 |
| 10 | YES | YES | 43.885 | 44.003 | 1.302 | 1.298 | 0.004 |
| 11 | YES | NO | 45.125 | — | 2.297 | 2.242 | 0.055 |
| 12 | YES | NO | 44.455 | — | — | — | — |
| 13 | YES | NO | 45.275 | — | 3.756 | 3.647 | 0.109 |
| 14 | NO | NO | — | — | 1.163 | 1.215 | 0.052 |
| 15 | YES | YES | 45.030 | 44.463 | 1.943 | 1.884 | 0.059 |
| 16 | NO | NO | — | — | — | — | — |
| 17 | YES | YES | 43.985 | 44.113 | 2.313 | 2.012 | 0.301 |
| 18 | YES | YES | 43.795 | 44.014 | 1.966 | 1.773 | 0.193 |
| 19 | YES | YES | 44.665 | 44.733 | 2.261 | 2.009 | 0.252 |
| 20 | NO | NO | — | — | 2.627 | 2.311 | 0.316 |
| 21 | YES | NO | 45.120 | — | 4.528 | 4.155 | 0.373 |
| 22 | YES | NO | 45.360 | — | 0.056 | 0.275 | 0.219 |
| 23 | NO | NO | — | — | 0.527 | 0.603 | 0.076 |
| 24 | YES | NO | 45.040 | — | 0.048 | 0.306 | 0.258 |
| 25 | NO | NO | — | — | 2.691 | 2.788 | 0.097 |

# WINDING AND ENVIRONMENTAL TESTING OF POLARIZATION-MAINTAINING FIBERS

Paul B. Ruffin
US Army Missile Command, RD&E Center
ATTN: AMSMI-RD-GC-L
Redstone Arsenal, Alabama 35898-5254

## ABSTRACT

Winding and environmental effects on the state of polarization in optical fibers designed for Fiber Optic Gyroscopes (FOG) are addressed in this paper. An experimental setup for the measurement of the degradation of the state of polarization in polarization-maintaining (PM) fibers under external stresses (caused by small bends, lateral pressures and temperature changes) is discussed. An analytical fiber pack stress model, developed under the Fiber Optic Guided Missile (FOG-M) Inertial Operational Evaluation (IOE) program, is utilized in the development of novel winding techniques required to reduce the environmental effects caused by winding tensions, temperature and vibration. An arc fusion splice model, developed for high strength splicing under the FOG-M program, is also utilized in the development of techniques for coupling the fiber optic sensor coil to the fiber pigtail of the integrated optic chip. Some preliminary results from laboratory experiments conducted to evaluate the performance of commercially available PM fibers under realistic environmental conditions, in particular the wound coil configuration, are presented.

# 1. INTRODUCTION

The Fiber Optic Gyroscope (FOG) is emerging as a rugged, solid state device. Recent progress in the development of integrated optic components for the device suggests that the FOG is most likely to achieve a clear cost advantage and a significant weight, power, and size advantage over the corresponding conventional gyroscopes [1]. Present efforts in the development of integrated optic components for increased performance at reduced dimensions include the development efforts, to fully integrate the optics (phase/ frequency shifters, polarizers, beam splitters/directional couplers, modulators, single mode fiber optic guides/pigtails laser sources and detectors) onto a single chip to achieve a reliable low drift FOG of reduced dimensions [1,2,3].

It has been reported that the birefringence state of the fiber and integrated optic components for FOG can be altered in adverse environments, thus causing polarization state instabilities and optical losses [4]. The birefringence changes due to increased radial pressures and small radius bending can be significant [5,6]. Little has been reported on the problems associated with the winding of rate sensor coils that possess reduced environmental sensitivities and the demonstration of stable, low-loss fiber-to-fiber connections between the fiber pigtails and the fiber sensor coils.

The stresses that contribute to birefringence changes in polarization-maintaining (PM) fibers, that are wound under tension for FOG sensor coils, are investigated in this paper. The mechanisms that cause drift, noise and scale factor changes that limit the sensitivity and accuracy of the FOG are given prime consideration. The unique problems associated with the winding of PM fibers for FOG applications are discussed in the next section. The fiber optics and integrated optics measurement and test laboratory is discussed in the next section. A set of experiments for investigating the performance of PM fibers, fiber optic coils, and integrated-optic components under realistic environments is presented. A summary is given in the last section.

## 2. FIBER OPTIC COIL WINDING

The Guidance and Control Directorate brings a unique capability to the development of fiber and integrated optic components for the FOG. The Inertial Systems Development Group has gained more than seven (7) years experience in winding very small optical filaments/waveguides for the Fiber Optic Guided Missile (FOG-M) program. A picture of the fiber winding system is shown in Figure 1.

We have done extensive studies [7,8] on the subject of winding multiple layers of optical fibers, with crossover sites throughout the pack, for fiber optic payout systems. Lessons learned on winding of very small fibers on the Fiber Optic Guided Missile (FOG-M) program are applied to the FOG application. The bending (with tension) of the fiber, which cannot be avoided in the small fiber-optic coil, fiber crossovers in the presence of lateral pressures due to multiple layer winding, and temperature changes can introduce microbends and stresses in wound optical fiber and cause mode coupling. Coupling of the HE-vertical mode to the HE-horizontal mode, or vice versa, can cause fading of the detected signal and ultimately noise and drift in the FOG. Therefore, special winding techniques are required for the production of fiber optic rotation rate sensor coils for reduced sensitivity to environments.

Efforts are presently underway to modify the existing fiber winding system, which uses precision sensors and drives under computer control, to provide for more accurate tension control. A subsystem, unique to FOG coils, is presently being designed that will reduce the fiber optic coil's sensitivity to temperature and thermal gradients. An analytical fiber pack mechanics model, developed under the FOG-M program, is being utilized to optimize the winding parameters for the fiber optic coil.

## 3. ENVIRONMENTAL TESTING AND INTEGRATED OPTICS TECHNOLOGY

The G. & C. Directorate has been designing, developing and testing inertial systems and components for many years. The available equipment instrumentation include: Contraves Rate Table (0-1000 Deg/s), Thermotron Environmental Chamber (125 to 375 F), Contraves Indexing Table, MB Vibration Table (Random vibration, Sinusoidal vibration and Shock [up to 10g's, frequency range 5-3000 Hz]), etc. The tremendous progress in integrated optic components for the FOG has created a new thrust in the Inertial Systems Development Group.

A fiber/integrated optic component measurement and test laboratory is presently being developed to evaluate and test integrated optic components for the FOG. Several commercially available polarization-maintaining (PM) fibers are presently being evaluated. Schematics of the state-of-the-art PM fibers are shown in Figure 2. Geometry-induced and stress-induced birefringent fibers are prime candidates for optical fiber gyroscopes.

A set of experiments has been devised to ascertain some quantitative data on the effect of external stresses on the birefringence and state of polarization stability in PM fibers. A schematic of an experimental apparatus for the measurement of state of polarization, extinction ratio, and polarization-holding parameter is shown in Figure 3. Optical radiation from the source is linearly polarized and focused onto the end of the test via a microscope objective. The fiber output is collimated before encountering a polarized beam splitter cube that splits the single beam into two orthogonal polarized beams that are detected along two directions. The first and second half-wave plates are adjusted until the detected signal is at a minimum in one direction. Known stresses are applied to the PM fibers in various orientations to determine the environmental effects. Schematic representation of the approaches for applying periodic and random bends, uniform transverse pressure (with and without twist), randomtransverse pressure, and small radius bends (with and without tension) are illustrated in Figure 4.

Finally, an Arc Fusion Splicing Model, developed under the FOG-M program is presently being modified to evaluate the mode propagation characteristics of the PM fibers. A Fujikura Arc Fusion Splicer is also being utilized to investigate low loss coupling in the fiber-to-fiber pigtail fusion splice and the effects of azimuthal misalignment on fiber coupling losses.

## 4. SUMMARY

A brief overview has been given of the Fiber Optic Gyroscope (FOG) activities that are presently being conducted at MICOM. A set of experiments has been designed to evaluate the performance of PM fibers, fiber optic sensor coils, and integrated optic components for FOG. Some preliminary results from these experiments have verified that pure tension and bending ( > 1 inch-radii) does not have a significant effect on polarization degradation. However, temperature changes have a notable affect on the polarization state. The results from an extended matrix of experiments will be presented at a later date. The results of these efforts provide useful information required for designing PM fibers and integrated optic components for the FOG.

## 5. ACKNOWLEDGEMENTS

The author wishes to acknowledge the technical assistance and helpful consultation received from Dr. C. C. Sung. The author would like to thank Mr. Mark Smith for technical support in setting up the experimental apparatus. The assistance provided by Ms. Monica Jefferson in performing the extinction ratio measurements is greatly appreciated. Fiber samples for testing were provided by Corning Glass Works, AT&T, York Technologies, Andrew Corporation, and 3-M.

## 6. References


1. G. Pavlath, R. Carroll, G. Adams, J. L. Page, R. Swarts and D. Courtney, Fiber Optic Gyro Development, Paper presented at the DoD Fiber Optic Conference, McLean, VA, 20-23 March 1990.

2. V. Ramaswamy, R. H. Stolen, M. D. Divino and W. Pliebel, Applied Optics, 18, 4080, (1979).

3. A. Ourmazd, M. P. Varnham, R. D. Birch and D. N. Payne, Optical Waveguide Sciences, Martinus Nijhoff Publishers, Boston, MA, p. 87-90 (1983).

4. Ezekiel, S. and Arditty, H. J., Fiber-Optic Rotation Sensors and Related Technologies, Springer-Verlag Berlin Heidelberg New York, p. 65-68, (1982).

5. Ulrich, R., and Rashleigh, S. C., Opt. Lett., 5, 354-356 (1980).

6. Ulrich, R., and Rashleigh, S. C., IEEE J. Quantum Electron., QE-18, 2032-2039, (1982).

7. Ruffin, P. B. and Sung, C. C., SPIE Proceedings, Vol. 776, Metrology of Optoelectronic Systems (1987).

8. Ruffin, P. B. and Sung, C. C., SPIE Proceedings, Vol. 842, Fiber Optics Reliability: Benign and Adverse Environments (1987).

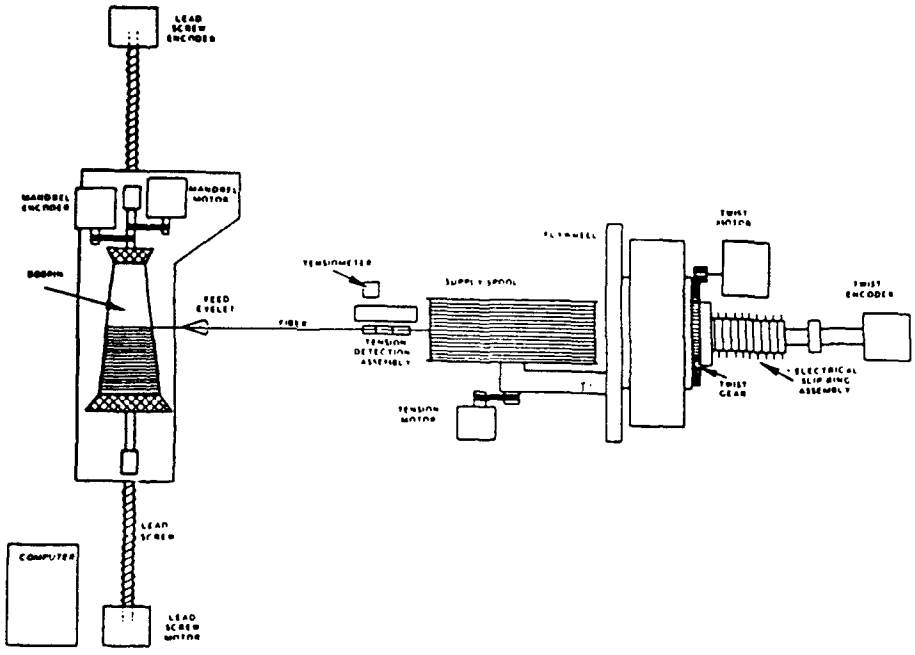

Figure 1. Fiber Winding System

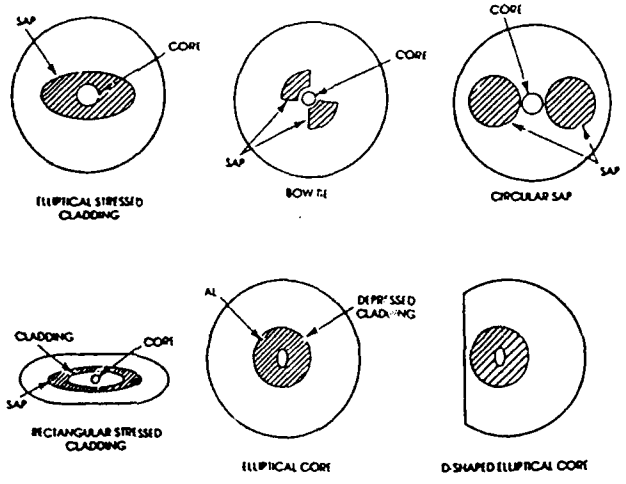


Figure 2. Schematics of State-of-the-Art PM Fibers

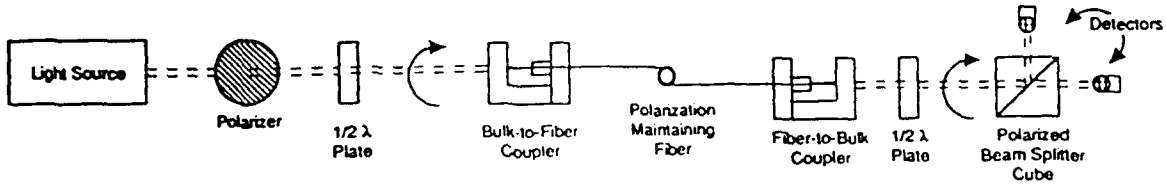


Figure 3. Experimental Apparatus for Measuring Extinction Ratio and the State of Polarization

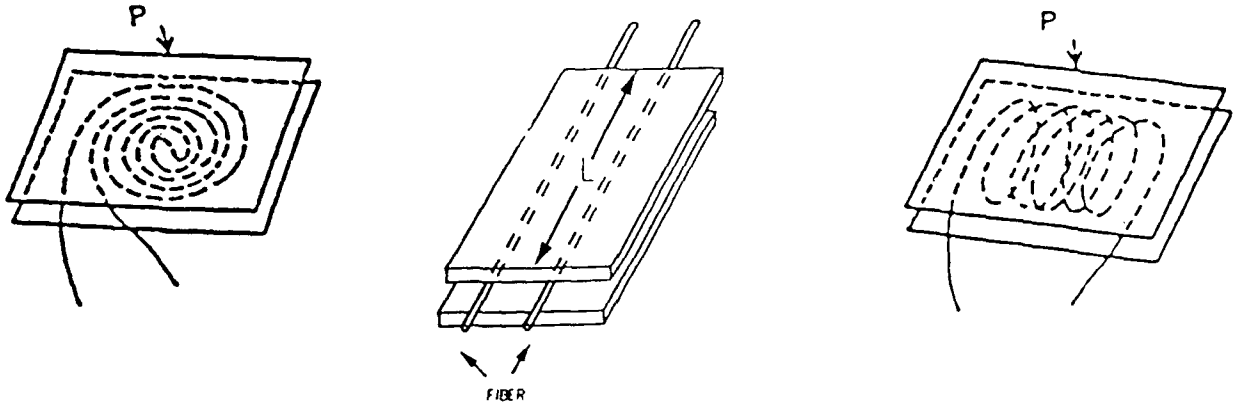


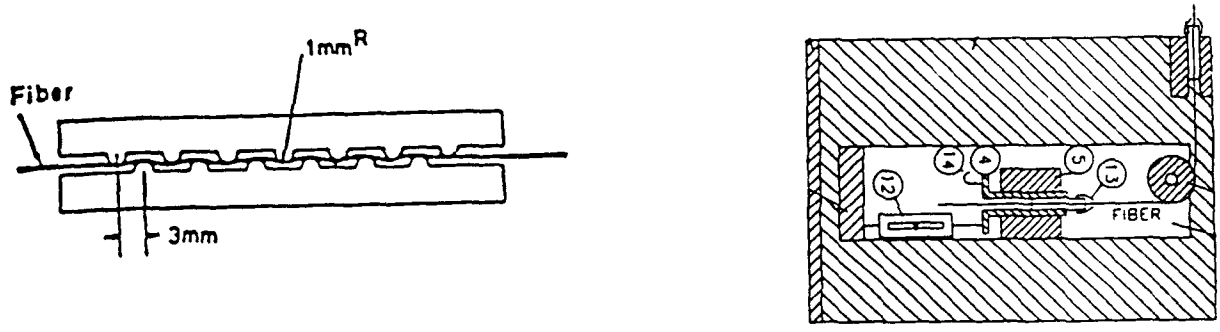


Figure 4. Schematic Representation of External Stresses Used in the Experiments

# CONTROL SYSTEMS DEVELOPMENT

Mark D. Dixon, Roger P. Berry, and Stephen C. Cayson
U.S. Army Missile Research, Development, and Engineering Center
Redstone Arsenal, AL

## ABSTRACT

The objective of the Control Systems Development program is to explore control technologies which support the development of missile actuation systems to meet the needs of current and future missile weapon systems. Current emphasis in missile system development is to increase the missile energy efficiency (ratio of energy delivered on the target to launch weight) in order to defeat advanced armor systems. Flexibility in launch and flight modes are required to provide the capability to launch these missiles from various platforms including armored vehicles, aircraft, and personnel. These system level requirements result in a need for control subsystems which are capable of providing effective control over a wide range of flight regimes including velocity up to Mach 6. Simultaneous to this need for increased performance is the conflicting requirement to decrease size, weight, and cost. This paper will discuss significant recent accomplishments in the Control Systems Development program including development and evaluation of a Dual Rate pneumatic actuator, a low cost, light weight Trolon pneumatic actuator, and the most recent work in developing a multi-mode control system for a hypervelocity guided missile. The discussion of the multi-mode control system development will illustrate the trade-offs between control system size, complexity, and performance.

## INTRODUCTION

The objective of the Control Systems Development program is to explore technologies which support the development of missile control actuation systems (CAS) to meet the needs of current and future missile weapon systems development. A high priority need in current missile systems development is to increase the missile energy efficiency, that is the ratio of energy delivered on the target to launch weight, in order to defeat advanced armor vehicles. To address this need a program has begun to develop a guided hypervelocity missile utilizing a solid rod penetrator to defeat both armored vehicles and aircraft. Also required is flexibility in missile launch and flight modes to provide the capability to launch these missiles from various weapons platforms including ground vehicles and aircraft and with 360 degree azimuth coverage.

These system level requirements result in a need for a control subsystem which is capable of providing effective control over a wide range of flight regimes including velocity up to Mach 6. Simultaneous to this need for increased performance is the conflicting requirement to decrease the CAS size, weight, and cost. These are the challenges which the Control Systems Development program has undertaken.

This paper will discuss significant recent accomplishments in the Control Systems Development program. These accomplishments include development and evaluation of a Dual Rate pneumatic actuator concept which has the potential to significantly reduce gas storage bottle size without degrading CAS small

signal performance. Also discussed is the development of a polymer (Torlon) pneumatic actuator which demonstrated a significant reduction in CAS weight and cost and finally, the most recent work in developing a multi-mode control system for the Advanced Kinetic Energy Missile (AdKEM) will be discussed.

## DUAL RATE PNEUMATIC ACTUATOR

The Dual Rate pneumatic actuator concept was conceived to tailor an open center valve actuator's pneumatic power consumption to fit system demand. This characteristic is particularly valuable to a system such as the Fiber Optic Guided Missile (FOG-M), because the fins are active during boost, relatively inactive during fly-out, and again active during terminal. If the actuator is tailored to this scenario, the required pneumatic power is minimized.

The Dual Rate pneumatic actuator concept is an open center valve actuator, with the capability to switch from a low vane rate to a high vane rate, based on position error. A schematic of the Dual Rate actuator design is shown in Fig. 1. This design uses a typical open center valve in series with a flow control valve. When the flow control solenoid is unenergized, flow is directed through the low flow orifice. The flow area of this orifice is sufficiently smaller than the upstream open center valve, such that, flow rate (vane rate) is controlled by the orifice. Since a single orifice sets the flow area for the charge and discharge cycles, the charge and discharge vane rates will differ in accordance with the regulated and control pressures. When the flow control solenoid is energized, the conical poppet valve opens. The conical poppet has a flow area which is sufficiently large such that flow rate is controlled by the open center valve's charge and discharge flow areas. As shown in Fig. 2, the error signal may be used to switch the actuator from the low to high rate mode.

A prototpye Dual Rate actuator was designed, fabricated, and tested. Results from testing the Dual Rate pneumatic actuator in the low and high rate modes are summarized in Table I. Comparing the low and high vane rates, one would expect a three fold difference in gas consumption, however it may be noted that only a 20% reduction in gas consumption was measured. To determine the cause for this unexpected behavior, the gas dynamics of the low rate mode was investigated. Analysis, combined with the experimental data shown in Fig. 3 revealed the cause.

Consider the fact that stored gas is only consumed during the charge cycle. The measured gas consumption is the flow rate during the charge cycle, averaged over the period of the pulse width modulation (PWM) frequency. Now, the rate of gas consumption during the charge cycle is determined by the pressure difference across the inlet valve and the inlet valve's flow area. Note from Fig. 3 that the pressure difference across the inlet valve is initially significant and exponentially approaches a small value as the intermediate volume is charged. Once this pressure difference becomes small, the rate of gas consumption will be dictated by the low flow orifice area and the difference between the intermediate pressure and control pressure. However, as seen in Fig. 3, the time required for the intermediate pressure to reach the supply pressure exceeds the charge cycle time. Therefore, the average rate of gas consumption in the low rate mode is driven by the inlet valve flow area, rather than the low flow orifice area. From this, it is obvious that improvement in gas consumption can be achieved by minimizing the intermediate volume.

## TORLON PNEUMATIC ACTUATOR

The design objective for the Torlon pneumatic actuator was to provide a low-cost, light-weight pneumatic actuator that meets the performance requirements for the FOG-M control actuator. To accomplish this objective, Torlon 4301, a polyamide-imide produced by Amoco Performance Products, Inc., was chosen as the primary component material. Torlon 4301 was chosen because of its excellent wear resistance qualities, low coefficient of friction, and high compressive strength. All of these characteristics are important in the design of actuator components such as pistons, piston chambers, and valve seats. The high compressive strength property is especially advantageous in the design of valve seats because the seat must be immune to the cyclic pounding administered by the ball. This results in virtually no increase in ball travel during operation, thus providing consistent actuator performance as operation continues. The room temperature tensile strength of Torlon 4301 is 28% less than that of annealed 7075 aluminum, but this strength is provided at 48% less weight. Because of these attributes, a 37% increase in material strength-to-weight ratio is realized.

The Torlon actuator pictured in Fig. 4 is a closed-center valve pneumatic actuator that meets the control actuator requirements for FOG-M. All components of the actuator, excluding the output shaft, were manufactured using Torlon 4301. However, during actuator testing the Torlon crank failed as a result of decreased strength caused by incorrect machining techniques. The faulty machining caused the crank to overheat and become brittle upon cooling. Consequently, a new crank fabricated from aluminum was used to replace the Torlon crank.

The Torlon actuator, weighing 205 grams (0.45 lb), compares to a weight of 391 grams (0.86 lb) for the original FOG-M pneumatic actuator made from aluminum and steel. The Torlon actuator offers this substantial weight reduction and also meets the performance requirements for FOG-M. It provides equal hinge moment capability and approximately the same bandwidth as the current FOG-M pneumatic actuator. A comparison of the closed-loop frequency responses is shown in Fig. 5.

A cost study was performed to determine the savings realized from fabricating an actuator with Torlon. This study showed that a Torlon actuator could be manufactured for 75% less than an actuator using conventional materials. This analysis was based on a production quantity of 200,000 actuators and assumed that most of the Torlon pieces could be injection molded to tolerance, eliminating the need for costly detailed machining work.

## HYPERVELOCITY MISSILE CONTROL ACTUATION SYSTEM

The development of a CAS for a hypervelocity missile, such as the AdKem, illustrates the conflicting requirements for improved CAS performance with reduced size and weight. The AdKEM is a command to line-of-sight guided, hypervelocity missile carrying a solid rod penetrator to defeat heavy armor and airborne threats. The AdKEM, as shown in Fig. 6, is comprised of a 5 cm (2 in) diameter airframe or centerbody and four discardable solid propellant boosters. The AdKEM concept is to launch the missile vertically from a ground

vehicle, orient the missile to a horizontal position, boost to Mach 6, and then coast to the target using beamrider guidance. With this concept the CAS must provide control during three distinct flight modes: vertical launch, boost, and coast.

As shown in Fig. 7, the AdKEM centerbody CAS includes three pneumatic actuators operating four control vanes for pitch, yaw, and roll missile control. During the boost phase these vanes act as jet tabs in the booster plumes and during coast (after booster separation) the same vanes act as aerodynamic control surfaces. Control during vertical launch is provided by a discardable orientation package which uses jet reaction thrusters and is attached to the rear of the missile. The orientation package thruster valves are also actuated by the centerbody CAS actuators. The AdKEM CAS is truly a multi-mode control system.

The AdKem CAS mechanical design is strongly driven by the need to minimize centerbody cross sectional area and weight and by the requirement to operate under the high acceleration and large forces of boost and control at Mach 6. The CAS dynamic performance is driven by the extremely fast missile response and resulting high autopilot bandwidth. The CAS performance requirements are given in Table II.

The AdKEM actuators must provide large hinge moment and lift force capabilities in a small package size. In order to meet the load requirements and stay within the designated package, it was necessary to overload the output shaft bearings. A prototype actuator was tested to determine the effect bearing overload has on actuator performance. The output shaft bearings were overloaded by 80% of their maximum static load rating and a frequency response curve was generated. A comparison of the actuator performance before and after the overloaded condition is shown in Fig. 8. As seen in Fig. 8, the reduction in actuator performance is not significant. Visual inspection after the series of tests showed no appreciable damage to the output shaft bearings.

Another result of the large hinge moment requirement and small package size was the necessity to utilize a high supply pressure in order for the actuators to develop the required output torque. Two cold gases, nitrogen and helium, were considered for the CAS power supply. Each actuator uses a solenoid driven ball poppet valve to control the gas flow through the actuator and the resulting motion of the vane. Each valve contains two orifices to limit gas flow into and out of the actuator control chamber. The flow control orifices each consist of a fixed-area orifice and a variable-area orifice arranged in series. The area of the variable-area orifice is a function of the ball travel and seat diameter. Typically, the use of nitrogen is advantageous because of its lower cost and lower leakage rates. The advantage of helium is that a smaller flow area can be used to achieve an equivalent volume flow rate (vane slew rate). Equating sonic velocity equations shows that 65% less area is required for a helium valve compared to a nitrogen valve with the same volume flow rate. This leads to a decrease in solenoid spring force requirements, resulting in a smaller solenoid package. Because of these qualities, the use of helium was found to be advantageous over nitrogen for the AdKEM actuators.

The thrust required to accelerate the AdKEM and the required maximum velocity results in the actuators being subjected to axial acceleration loads approaching 1400 g's and lateral and vertical accelerations of 50 g's. These acceleration loads cause the solenoid plunger inertia forces to be a significant part of the solenoid force requirements. If the solenoid is oriented so that its centerline is parallel to the missile centerline, a spring force of 70.7 Newtons (15.9 lbf) is required to push the ball off the discharge seat when the valve chamber is filled with gas at supply pressure. Of this force, 83% is required to overcome the plunger's inertia force. Conversely, when the solenoid centerline is oriented perpendicular to the missile centerline, as shown in Fig. 7, the required solenoid spring force drops to 16.5 Newtons (3.7 lbf), of which only 27% is required to overcome the plunger's inertia force. This simple change in solenoid orientation resulted in solenoid force requirements that were much lower and, more importantly, made it possible for a solenoid to be designed which would fit into the package space.

The AdKEM pneumatic power supply contains 143.1 $cm^3$ (8.73 $in^3$) of helium stored at 86.19 kilopascals (12,500 psig). The unit provides an average power of 84,000 watts (117 horsepower) for a duration of 6.9 seconds. Upon system activation an electro-explosive piston actuator pierces a burst disk. This releases the stored gas, which is regulated to 14.48 kilopascals (2,100 psig) and transferred to the control actuators. In the design process it was initially suspected that helium, due to its lower compressibility factor, would result in a smaller bottle volume than nitrogen. Isentropic blowdown analysis, which used the Benedict-Webb-Rubin state equation, revealed that nitrogen would provide pneumatic power 25% longer than helium, for an equivalent initial pressure and volume. Investigation into the cause of this revealed that, due to the higher specific heat ratio of helium, it cooled to a lower temperature during blowdown. This resulted in helium, on the average, having a higher compressibility factor than nitrogen during the blowdown process. Therefore, helium was not selected as the working fluid for this reason, but rather, was selected to reduce forces in the actuator valve as discussed above.

The design requirements for the CAS actuator control electronics are to achieve adequate CAS bandwidth and stability over the full range of vane deflections and load conditions. For the AdKEM, the relatively high bandwidth of the autopilot drives the CAS bandwidth to 30 Hz or better under full load. Actuator stability is specified somewhat qualitatively in that the CAS should not exhibit sustained oscillations under any flight condition.

A block diagram for the actuator controller is shown in Fig. 9. Control of the gas flow is accomplished by pulse width modulating (PWM) the bistate solenoid ball valve, with the pulse width proportional to the compensated position error signal. The PWM frequency is ideally selected to be much greater than the natural frequency of the actuator so that the actuator does not move in response to the PWM pressure fluctuations but only the average gas flow. The PWM frequency is limited on the high end by the response time of the solenoid. For the AdKEM actuator the natural frequency is 150 to 200 Hz and the solenoid response time is approximately 1.0 millisecond. The PWM frequency was selected at 250 Hz.

The compensation element shown in Fig 9 was designed to provide stable performance of the actuator with no hinge load (worse case). For the AdKEM actuator, the compensation is a first order lead network with a lead frequency at 20 to 30 Hz. The actuator controller including the compensation is implemented digitally with a 500 Hz basic update rate. A digitized version of the compensation element was obtained using the Tustin method with frequency pre-warping.

The actuator control equations are integrated with the AdKEM navigation, guidance, and autopilot equations in the on-board flight computer. This computer is based on the Texas Instruments TMS 320C30 32 bit Digital Signal Processor which has floating point math capabilities. A 10 bit A/D converter is utilized for the actuator position feedback. The pulse width modulation is implemented in software by comparison of the error signal with a 32 bit timer to set the pulse duration. The flight computer programming language is "C".

A detailed block diagram of the pneumatic actuator model and controller is shown in Fig. 10. A derivation of the equations of Fig. 10 is provided in the Reference. These equations were utilized to develop a detailed digital simulation of a complete AdKEM CAS (three actuators). The equations were coded in FORTRAN 77 on a VAX 11/785 computer. The actuator equations of motion were integrated using a Runge-Kutta routine with a 0.1 millisecond integration step size. This detailed simulation was utilized to verify performance of the CAS design and was also incorporated into a complete AdKEM system simulation for autopilot design and missile system performance evaluation.

Simulation results are shown in Fig. 11 and Fig. 12. A typical step response of the actuator with no hinge load is provided in Fig. 11. which illustrates the 1000 deg/sec rate capability of the actuator. Figure 12 shows the small signal bandwidth for the actuator with the maximum predicted hinge load of 12 in-lb/deg.

## SUMMARY AND CONCLUSIONS

The Control Systems Development program has made significant contributions in the development of missile control technologies which can meet the needs of current and future missile weapon system requirements. These contributions include developing and evaluating actuation system concepts for reducing CAS size, weight, and cost without sacrificing performance. These concepts include a Dual Rate pneumatic actuator which demonstrated a 20% reduction in gas consumption and thereby a proportional reduction in power supply volume and a Torlon actuator which was 48% lighter and could potentially cost 75% less to produce than a conventional metal unit. Finally, the Control Systems Development program has designed and is currently developing a multi-mode CAS for the AdKEM. The mechanical packaging and performance of this unit represents the limits of design and well illustrates the size/performance trade-offs for a tactical missile.

References:

(1) MICOM Technical Report RG-82-2, "Model For Pneumatic Control Systems", Gordon D. Welford, August 1982.

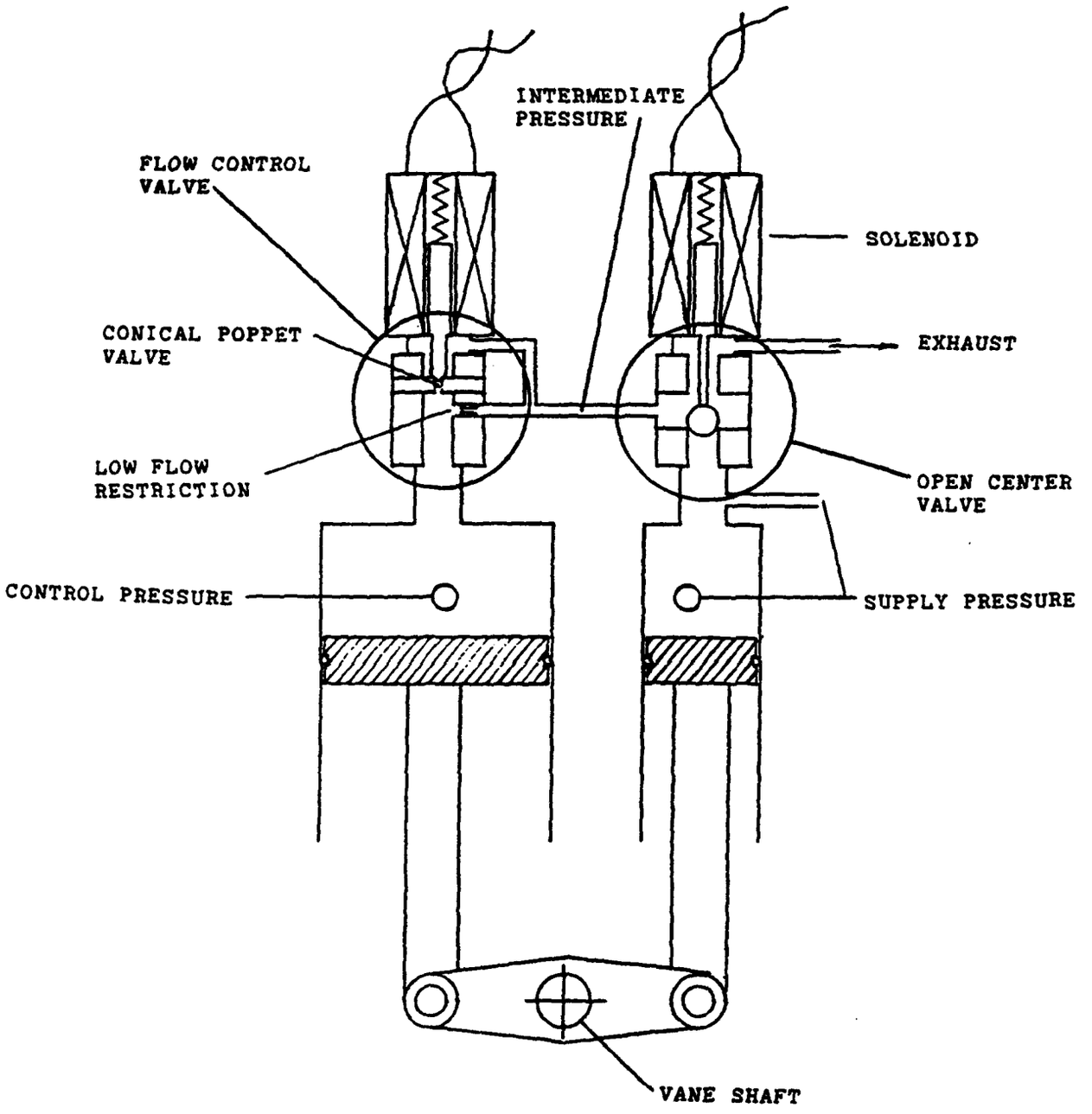


Figure 1. Dual Rate Pneumatic
ActuatorSchematic

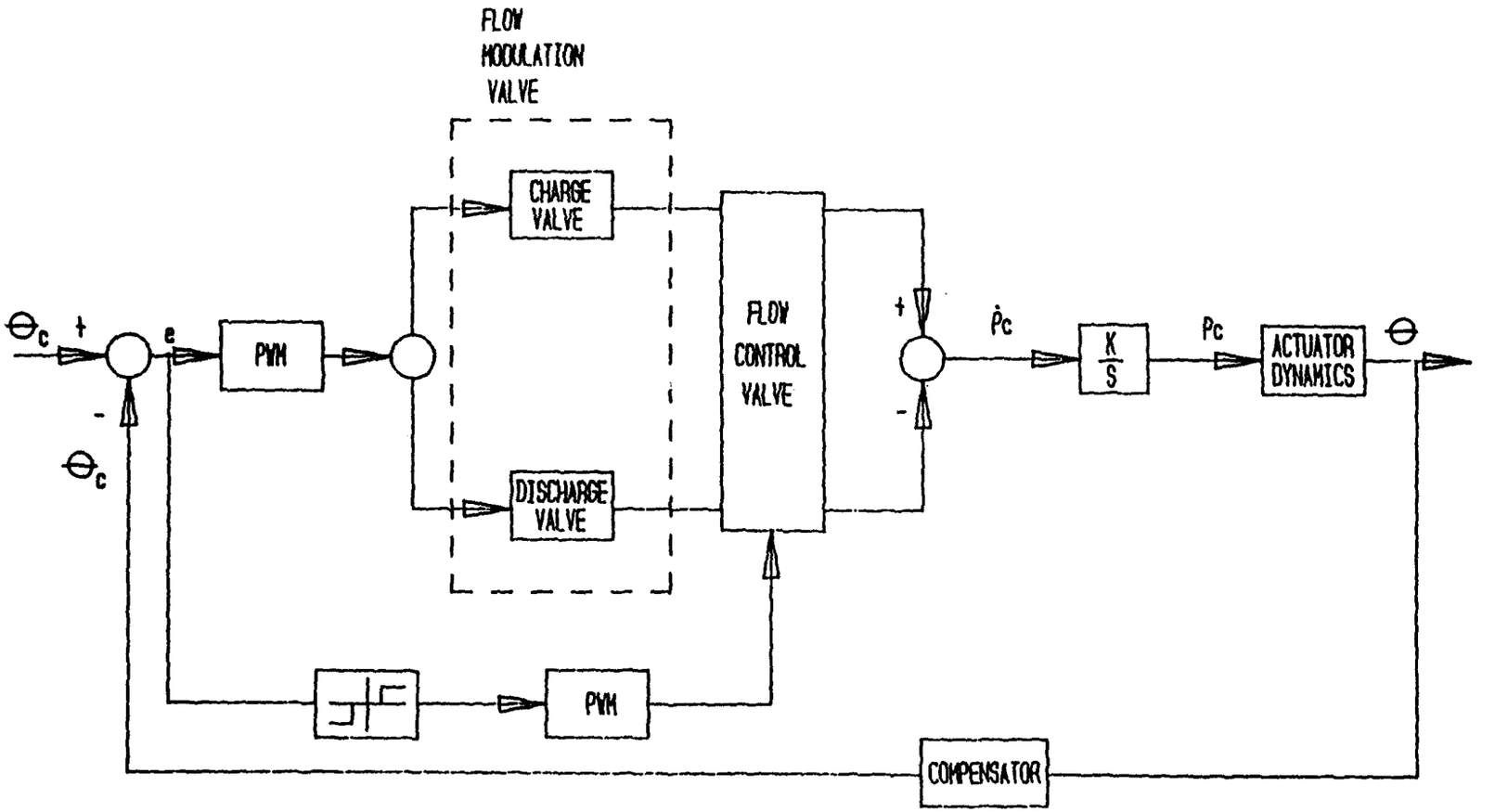


Figure 2. Dual Rate Pneumatic Actuator Control Loop

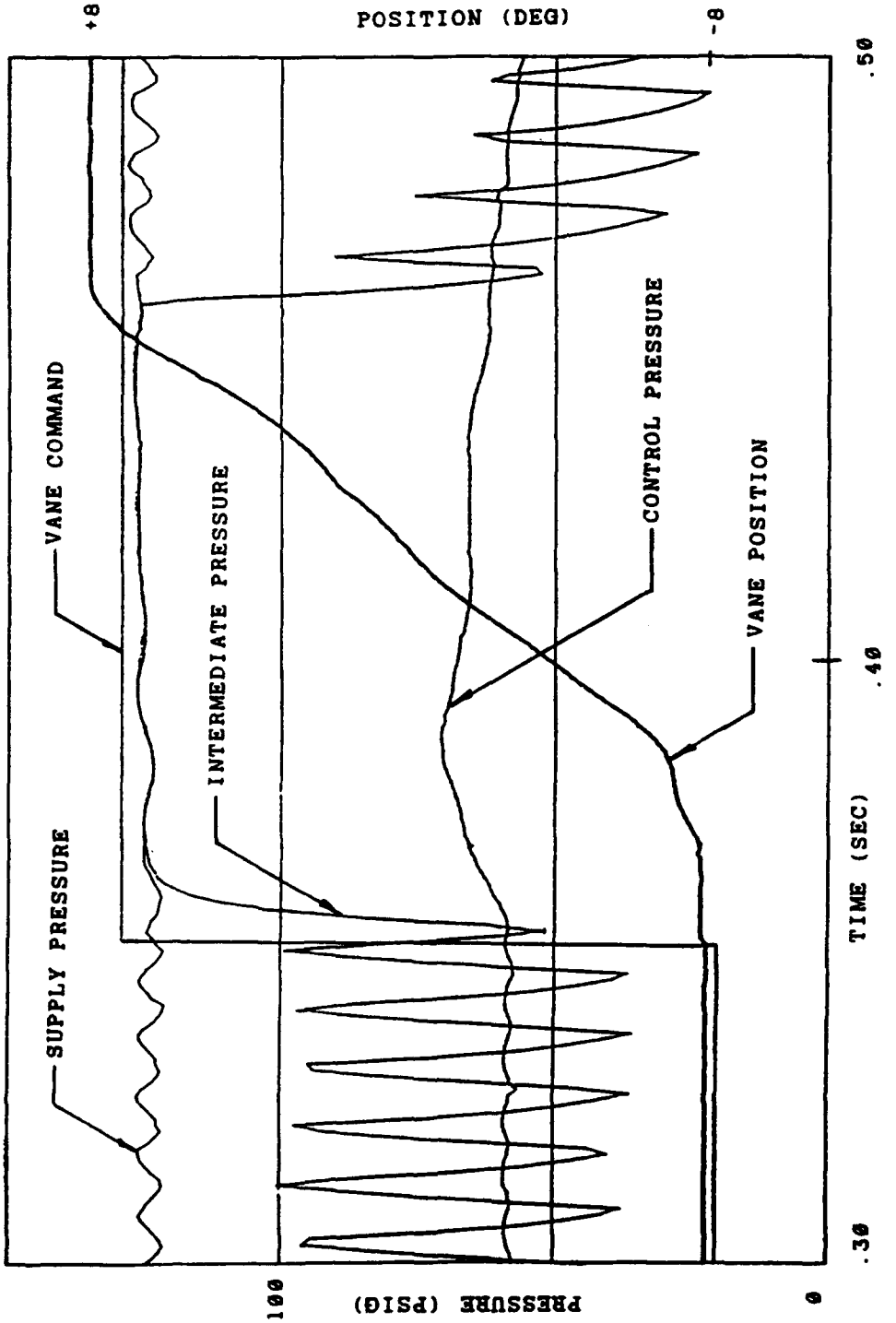


Figure 3. Dual Rate Pneumatic Actuator Test Results

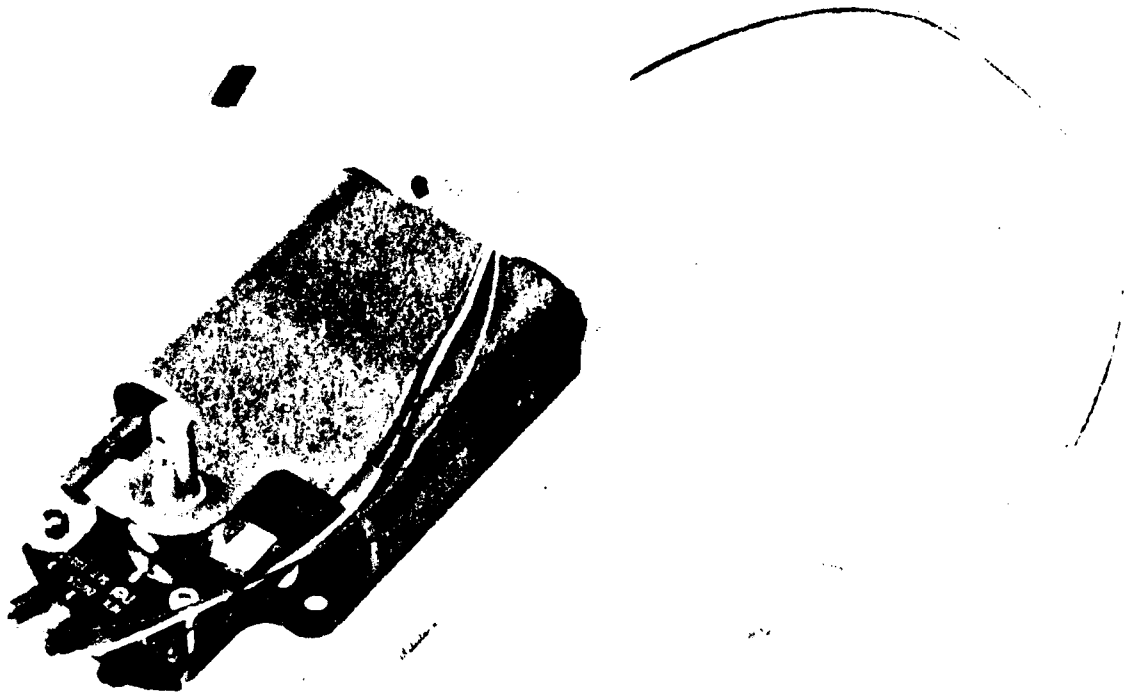

Figure 4. Intermediate Actuator

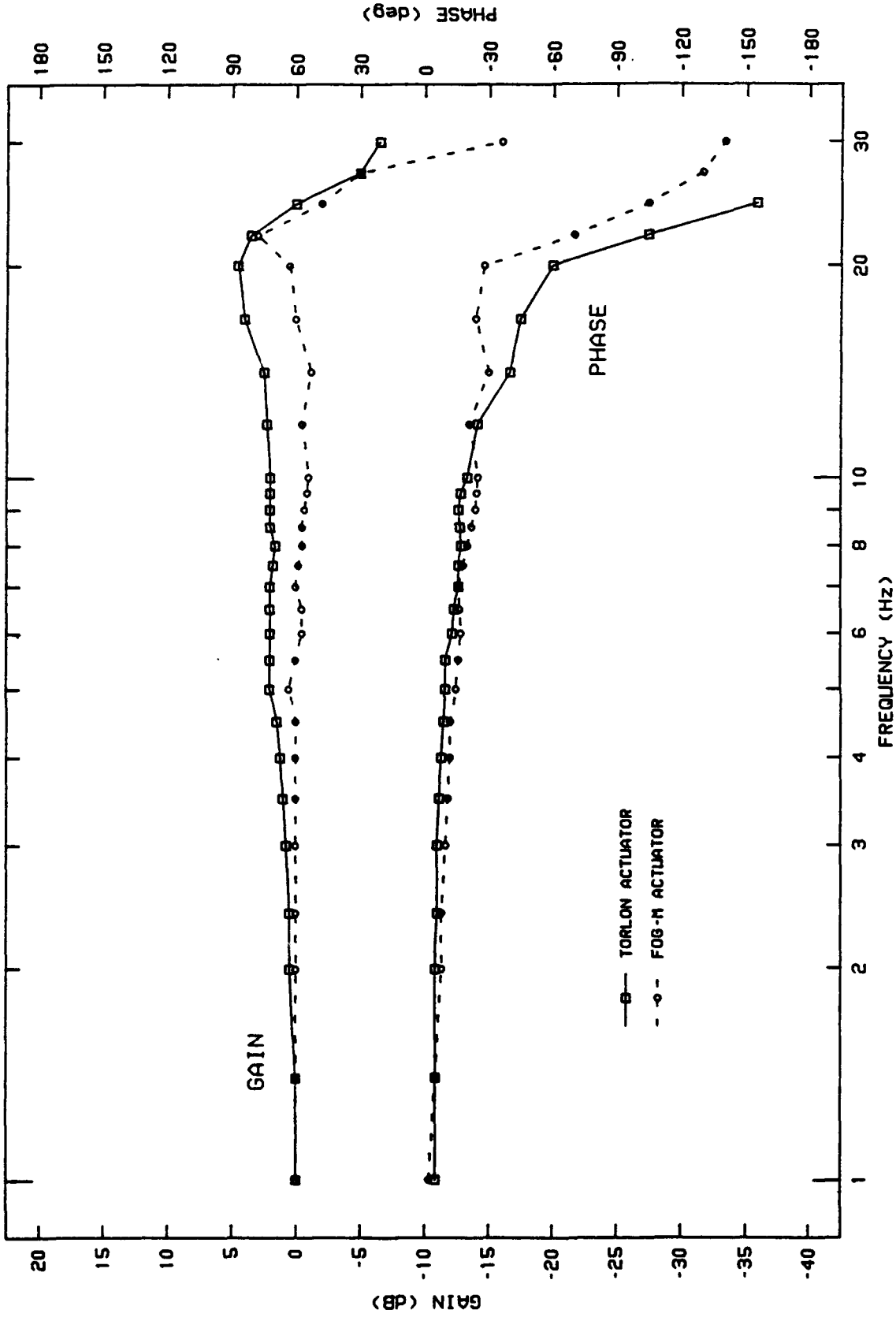


Figure 5. Intermediate Actuator Test Results

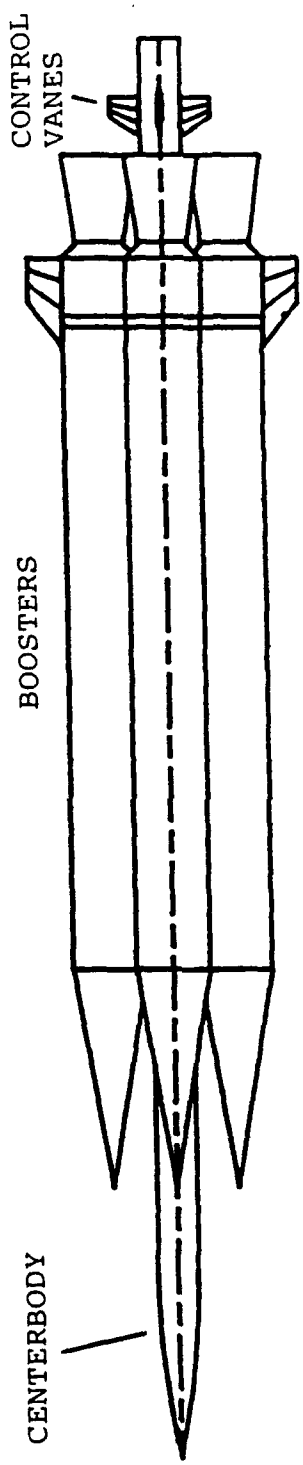


Figure 6. Advanced Kinetic Energy Missile

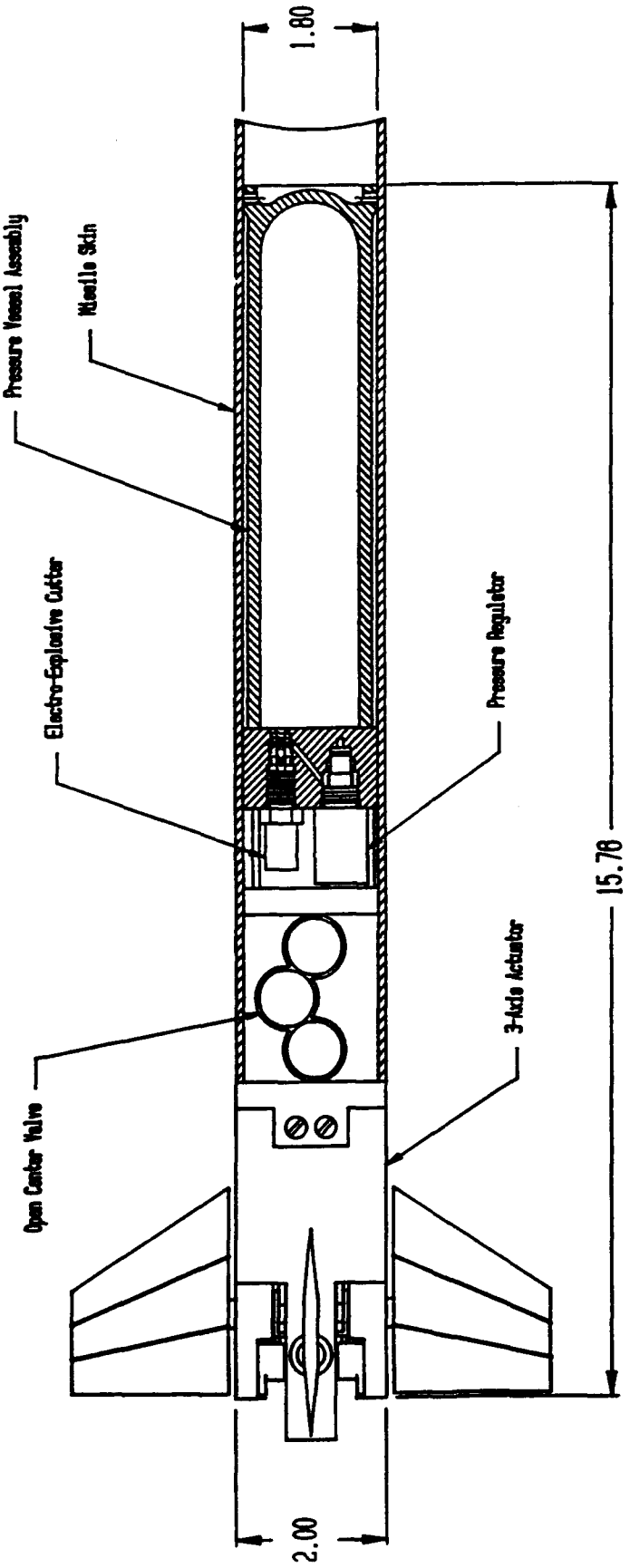


Figure 7. AdKEM Control Actuation System

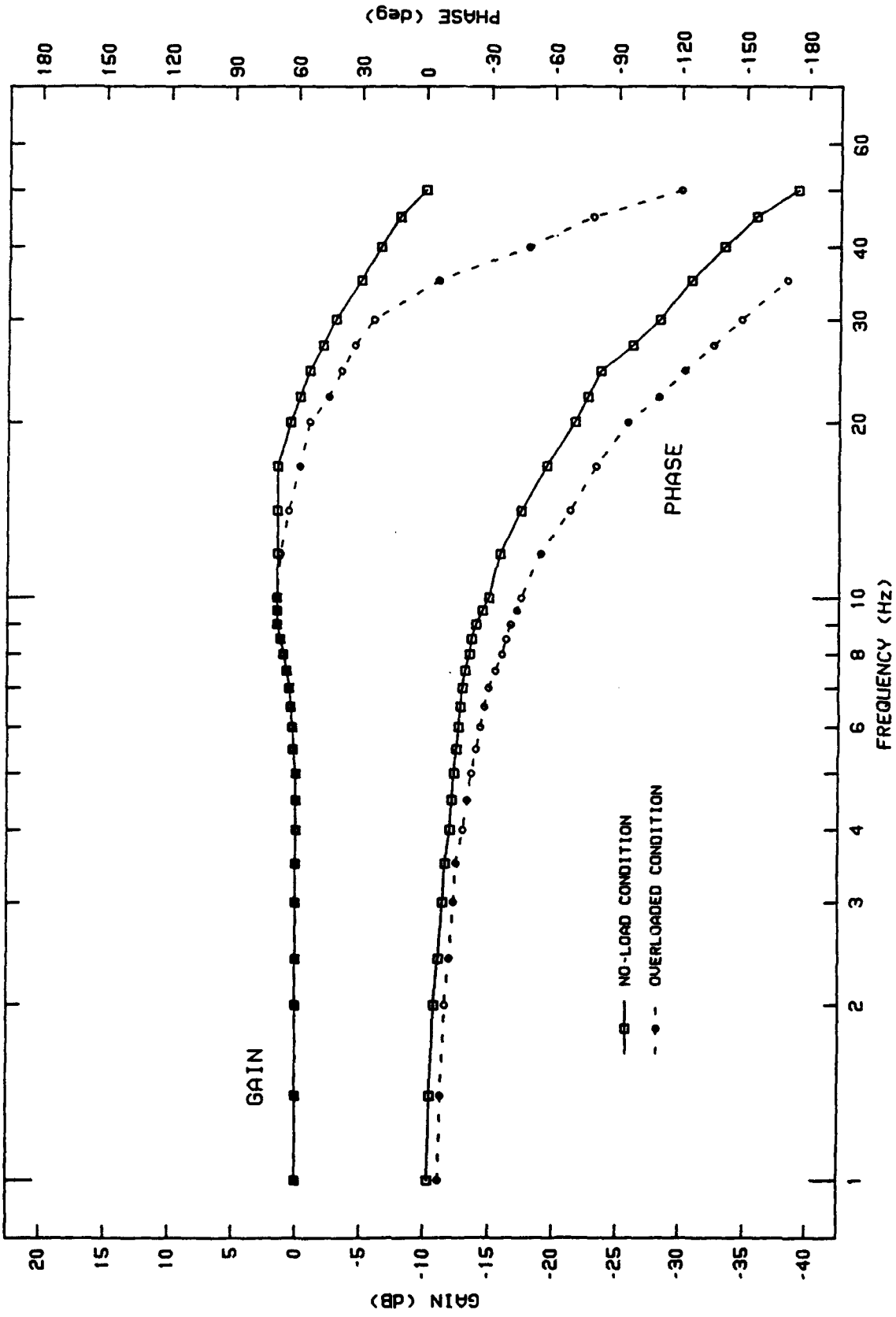


Figure 8. Frequency Response With Overload

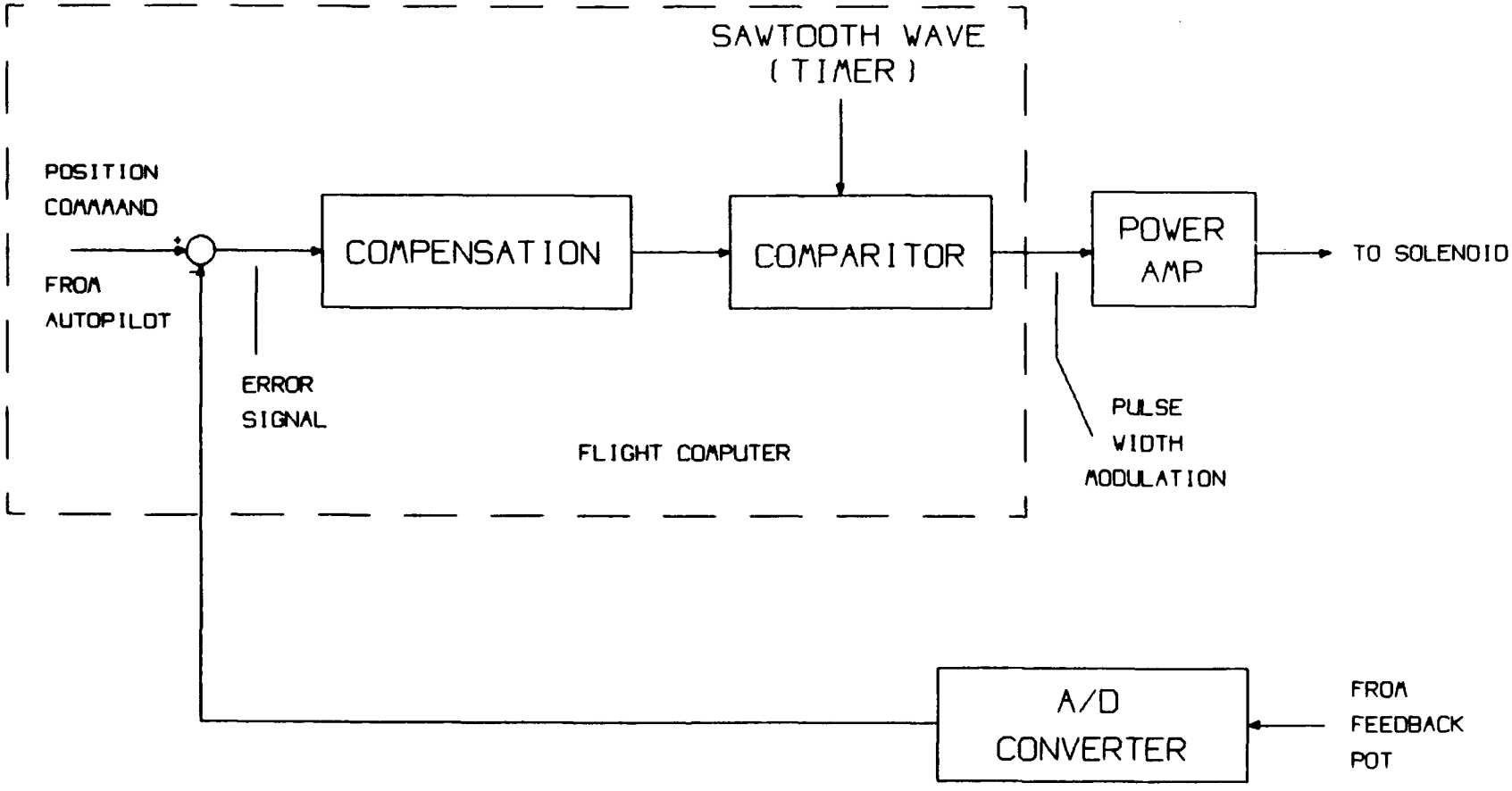


Figure 9. AdKEM Actuator Controller

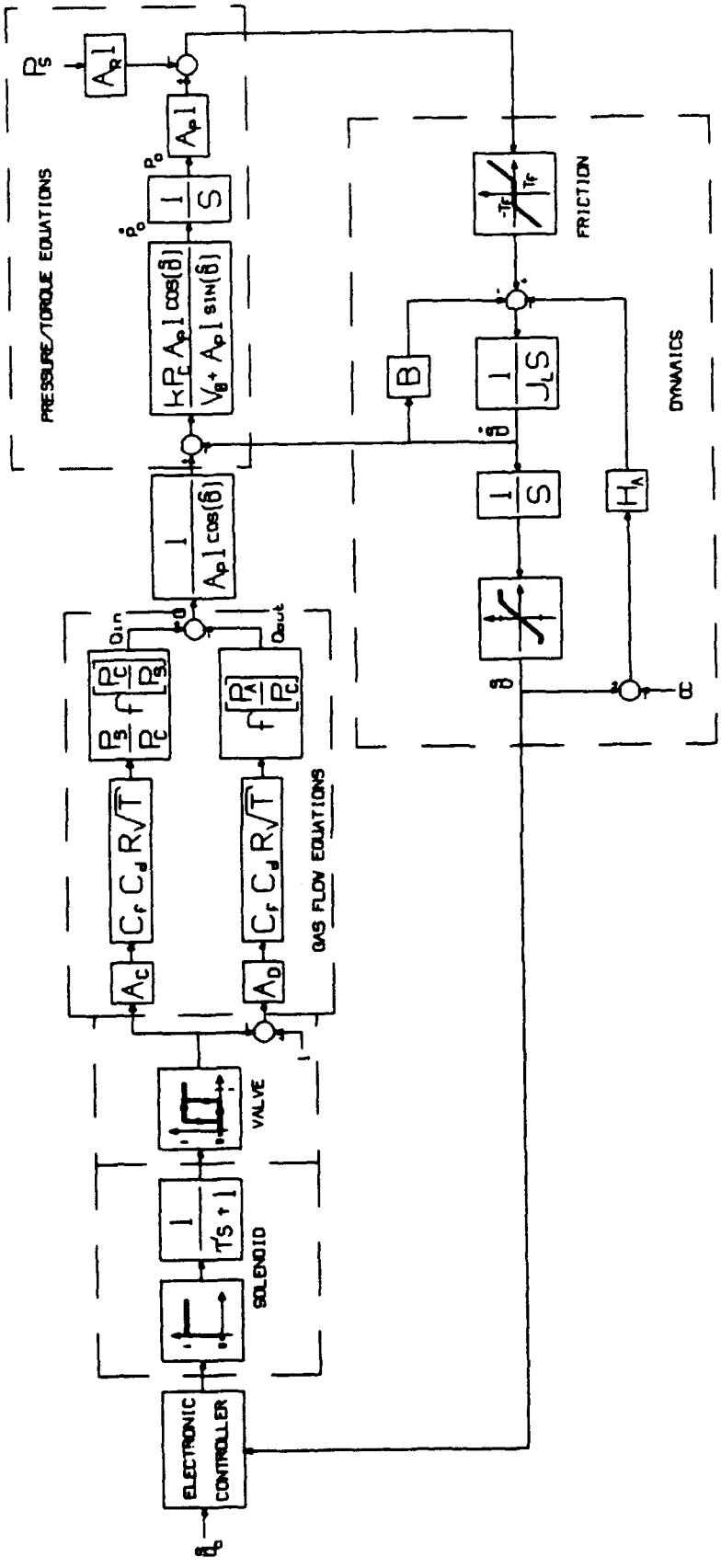


Figure 10. Actuator Model

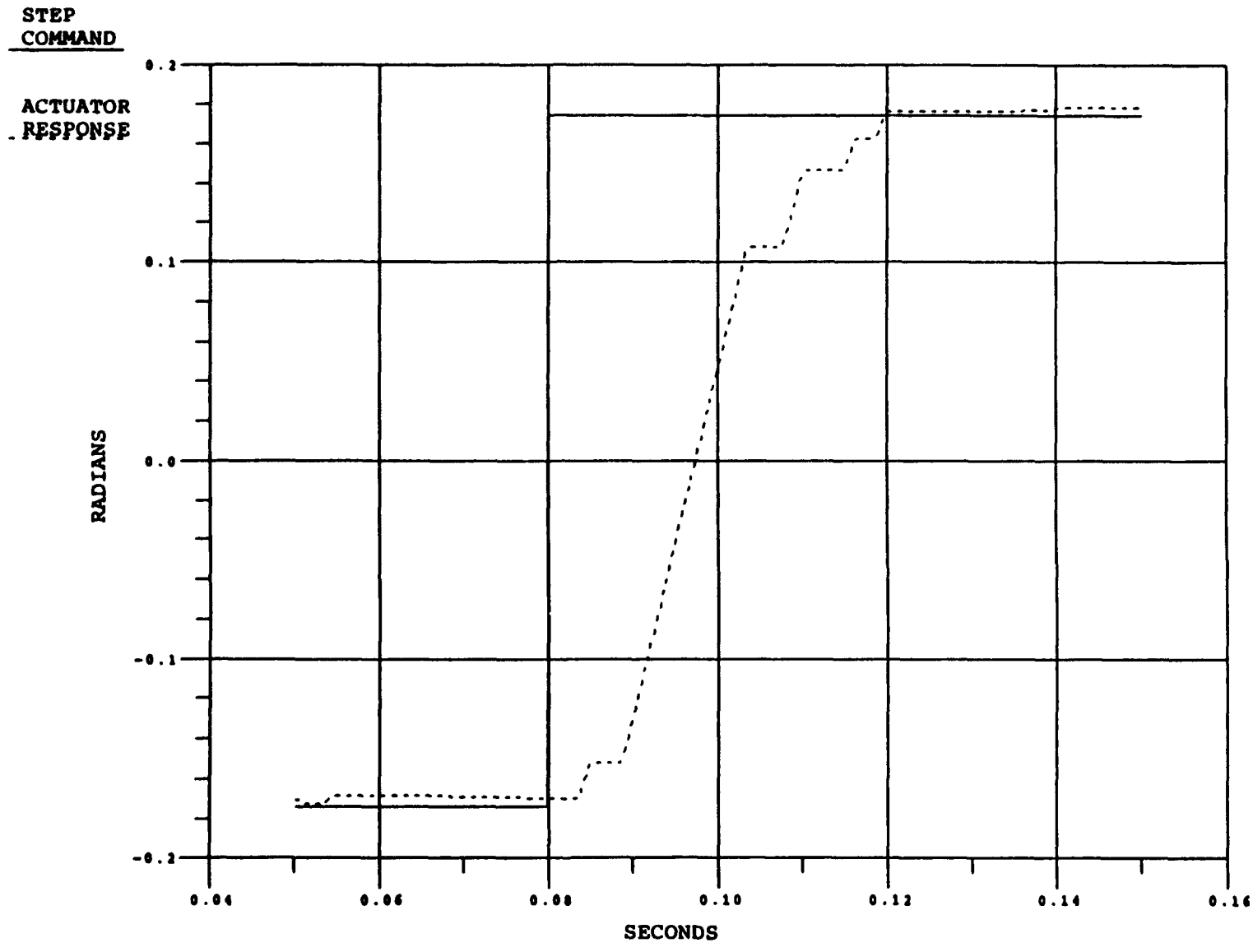


Figure 11. AdKEM Actuator Step Response

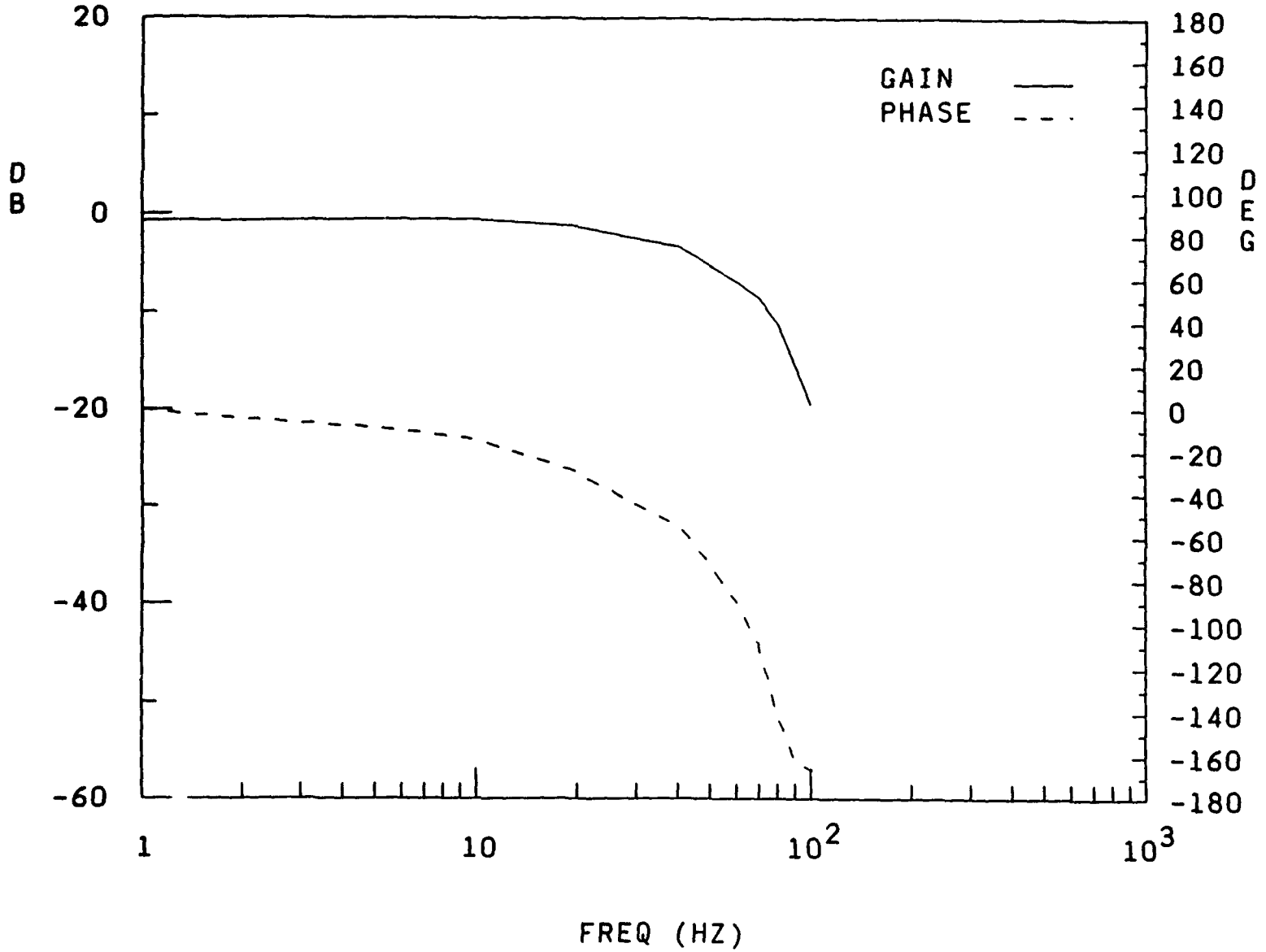


Figure 12. AdKEM Actuator Frequency Response

Stall Torque: 2.26 N-m (20 in-lbf)
Vane Travel: +/- 20°
Aerodynamic Loading: .034 N-m/deg (.30 in-lbf/deg)
Control Vane Inertia: $67.3(10)^{-6}$ $m^2$-kg (.23 $in^2$-lbm)

| | Low Rate | High Rate |
|---|---|---|
| Vane Rate: | | |
| Charge Cycle | 205°/s | 607°/s |
| Discharge Cycle | 157°/s | 516°/s |
| Frequency Response: | | |
| 1° P-P | 8.0 Hz @ -3 dB<br>6.5 Hz @ -90° | 20 Hz @ -3 dB<br>18 Hz @ -90° |
| 3° P-P | 6.7 Hz @ -3 dB<br>5.4 Hz @ -90° | |
| 6° P-P | 3.5 Hz @ -3 dB<br>3.6 Hz @ -90° | 20 Hz @ -3 dB<br>20 Hz @ -90° |
| Pneumatic Power: Consumption | | |
| 30 Hz PDM | 92 scc/s (.195 scfm) | 103 scc/s (.218 scfm) |
| Bang-Bang | 83 scc/s (.177 scfm) | 103 scc/s (.218 scfm) |

Table I

Dual Rate Actuator Performance

| | |
|---|---|
| Stall Torque: | 10.6 N-m (94 in-$lb_f$) (min) |
| Fin Aerodynamic Loads: | |
| Lift Force | 934 N (210 $lb_f$) |
| Root Bending Moment | 1005 N (226 in-$lb_f$) |
| Missile Acceleration: | |
| Axial | -150 to +1400 g's |
| Pitch | ±150 g's |
| Yaw | ±150 g's |
| Static Stiffness: | 147 N-m/r (1300 in-$lb_f$/r) |
| Vane Travel: | ±10° (min) |
| Frequency Response: | 50 Hertz with 1° P-P Input |
| Slew Rate: | 1000 degrees/second (min) |
| Hysteresis: | 0.05 degrees (max) |
| Operating Time: | 7 seconds (min) |
| Duty Cycle: | Continuous; ±2.5° 10 Hertz Input Signal |
| Storage Temperature: | -40° to +150°F |
| Operating Temperature: | -40° to +400°F |

Table II

AdKEM Control System Performance Requirements

# Microprocessor Technology Utilization Program (MICROTUP)

Michael C. Pitruzzello and Amy L. Pedigo
Guidance & Control Directorate
Research, Development, & Engineering Center
Redstone Arsenal, Alabama

## Abstract

The basis for this technology program is to demonstrate the utility of commercially-produced microprocessor technology for military applications. Two efforts undertaken in this program are described in this paper. The first, begun in FY88, was a study to determine the utility of high speed serial data bus technology for use in military systems. In order to investigate Local Area Network (LAN) technology, a "mini" FOG-M system was developed. The network consisted of several prototype military nodes and PCs emulating military nodes in a 10MB/s serial bus configuration. Several conclusions were derived from research and demonstration results. Token Passing Bus (IEEE 802.4) provides deterministic data throughput at high rates, decreases connectors and cabling, aids system debug, and allows not only data transfer but also audio and video data transfer. However, current protocols using the token passing scheme appear to cause delays significant enough to affect real time systems. This study demonstrates some clear performance advantages of LAN technology over military systems connected by MIL-STD-1553 type technology but also demonstrates some potential pitfalls. The second effort, begun in late FY89, investigated processors for a developmental missile system. Due to space constraints, floating point operation, and high throughput required, the Texas Instruments TMS 320C30 was chosen. Prototype missile computers are now being constructed using the TMS 320C30 and, with associated emulators, the processors will be examined against required performance criteria. Digital Signal Processors show significant promise for military applications requiring large numbers of repetitive mathematical operations, on-chip peripherals and on-chip memory. Guidance and Control Directorate engineers will produce six flight-capable autopilot computers to demonstrate the merit of state-of-the-art commercial microprocessor technology in military systems. Flight tests are scheduled to begin in early FY91.

## INTRODUCTION

The microprocessor is less than a quarter century old, but it has dramatically changed the way the world processes and uses information. This is just as true in the Department of Defense (DoD) as it is in the civilian world, for it has long been recognized that information processing is one of the keys to the development of force multiplying "smart" weapons. Microprocessors are and will continue to be the technology of choice for much information processing in the foreseeable future. The reason is that microprocessor performance continues to increase tremendously and at reasonable cost (see Figures 1 and 2). However, DoD does not hold a large share of the microprocessor market, so in general DoD has little influence on how products are designed and which are produced. This is especially true in the current environment of shrinking defense budgets. For this reason, DoD must be content to use the developments of the commercial microprocessor world where applicable.

The Guidance and Control Directorate of the US Army Missile Laboratory has long recognized the importance of microprocessors in missile guidance systems. To ensure incorporation of the latest technology into developmental systems, the directorate established the Microprocessor Technology Utilization Program (MICROTUP). The purpose of this paper is to describe two of the projects undertaken by MICROTUP. The first project, dealing with a previous effort using Local Area Network (LAN) technology, will be discussed briefly. The second project, dealing with the current MICROTUP effort, is concerned with the development of a complete missile flight computer for the developmental ADKEM missile and will be covered in more detail. The purpose in discussing two projects is to show the breadth of the MICROTUP program.

## LOCAL AREA NETWORK (LAN) PROJECT

A LAN is typically associated with a cable (usually coaxial or twisted pair) connecting together many computers or peripherals and over which the computers and peripherals can communicate with one another using a bit serial data stream. A two-conductor cable, which forces the bit serial method of communication, is used to keep wiring costs to a minimum and reliability of the cable high. Many years ago, the Air Force recognized the savings in cable weight which could be achieved by using bit serial communications between its avionics boxes. This resulted in the creation of the MIL-STD-1553 bus. In addition to saving weight, the establishment of such a bus reduced interface development costs, increased wiring reliability, and simplified troubleshooting and maintenance procedures to the Line Replaceable Unit (LRU) level. These desirable characteristics are as valid today as they were when the 1553 bus was created, but today LAN technology offers an order of magnitude greater throughput (from 1 Mbit/second to 10 Mbit/second) with no DoD development effort. It is certain that increased data needs of emerging systems (especially those utilizing artificial intelligence techniques) will benefit from the increased throughput. Indeed, at least one Army system (NLOS) has had to resort to a second 1553 bus in order to meet its information bandwidth needs.

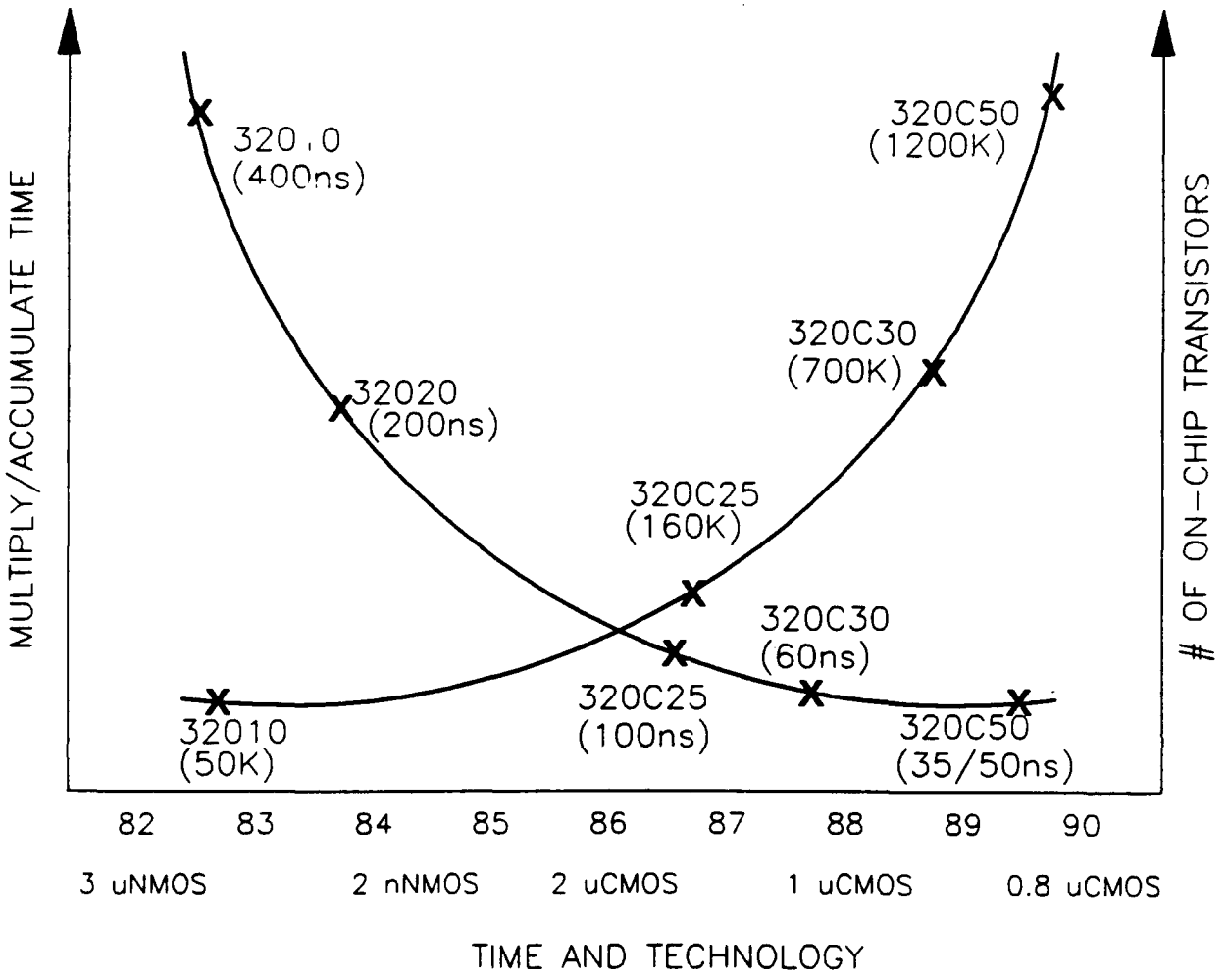


Figure 1. Performance and complexity of DSPs are typical of microprocessors in general. Both performance and complexity have increased dramatically over the past ten years.

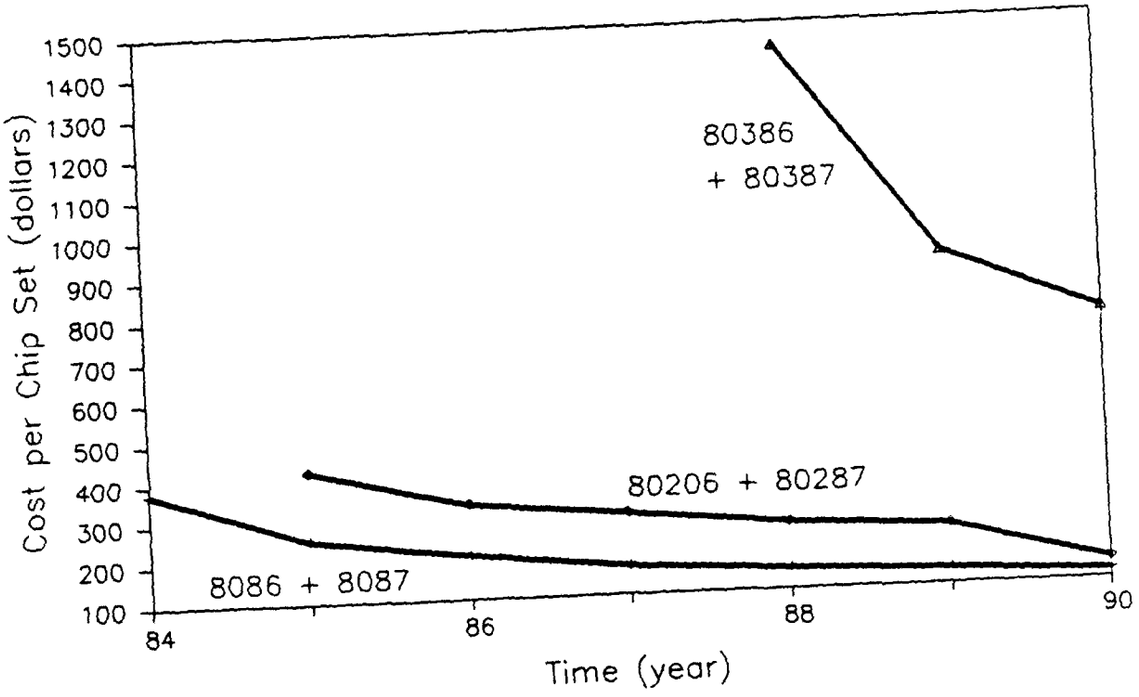


Figure 2a. Decressing costs of typical microprocessors with floating point numeric coprocessors.

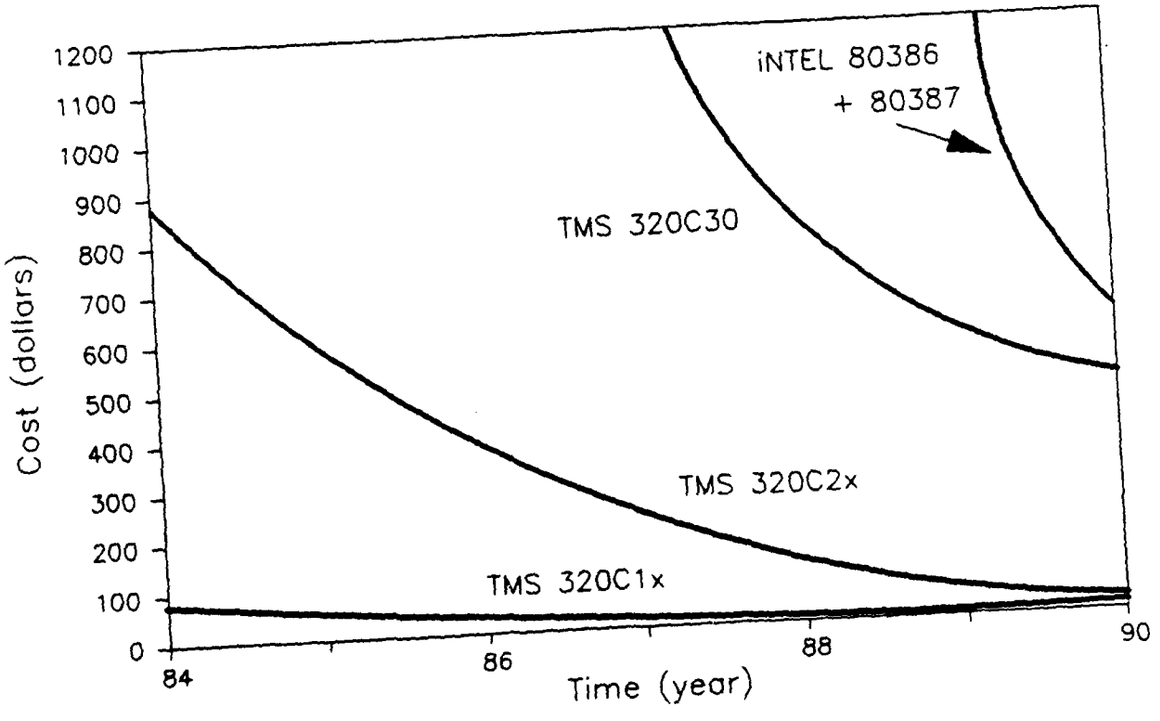


Figure 2b. Costs of typical DSPs and a high performance microprocessor with numeric coprocessor.

The purpose of the LAN project was to investigate the utility of modern LANs for use in military systems. To this end, a survey of the LAN market was made. The intent was to purchase equipment for several of the more promising LANs and demonstrate their utility. However, funding limitations limited the project to one LAN. In order to narrow the field, the following selection criteria was adopted:

1. The LAN must be nonproprietary and preferably based on an IEEE standard.
2. Implementation of the physical layer must require no more than five integrated circuits.
3. The data rate must be at least 10 Mbits/second.

Only two LANs met the selection criteria, that based on the IEEE 802.3 [1] specification (such as Ethernet) and IEEE 802.4 [2] specification (such as is used in the MAP/TOP specification). At this point, it was decided that the application would be used to discriminate between the two. Due to availability of existing peripherals, it was decided to create a "mini" Fiber Optic Guided Missile (FOG-M) system whose block diagram is shown in Figure 3. The IEEE 802.4 LAN was chosen as a better fit to the application. The basic reasons for this were:

1. The IEEE 802.4 LAN, being based on token passing, is deterministic. IEEE 802.3 is not. Further, the throughput during high network loading is greater for token passing LANs [3] (see Figure 4).
2. The IEEE 802.4 LAN, being a broadband system, would allow growth to having video transmission on the same cable as data transmission. This would support the video channels used in the FOG-M system.

## PROJECT RESULTS

The system shown in the block diagram of Figure 3 was constructed using hardware and software based on the MAP/TOP specification. This system was used because it was the only IEEE 802.4 compatible LAN available at the time. A photograph of the hardware is shown in Figure 5. A photograph of one of the Multibus LAN boards is shown in Figure 6. Note the single chip used to implement the IEEE 802.4 token passing scheme. The remainder of the board contains an Intel 80186 processor, wideband modem, memory, and Multibus interface logic as required to implement the MAP/TOP protocol and to interface to the host (master) on the Multibus. The Master Controller (see Figure 3) was loaded with actual FOG-M software which had been modified by deleting the existing multiple software drivers and inserting the single LAN driver.

During testing, the LAN communications worked as expected with one serious exception. The time required from transmission of a data packet to a LAN board and its reception by the receiving host was found to be approximately 26 milliseconds. This was too long to support the desired 60 Hz autopilot update rate (i.e. 16.67 millisecond autopilot cycle). The delay appeared to be in the LAN boards and it is surmised that most of the delay comes from processing the MAP/TOP protocol. The lesson learned, as is often the case in the computer world, is that the speed of the hardware was compromised by the software overhead used to process the protocol. For such a LAN to be effective in a real time system such as FOG-M a streamlined protocol would have to be developed.

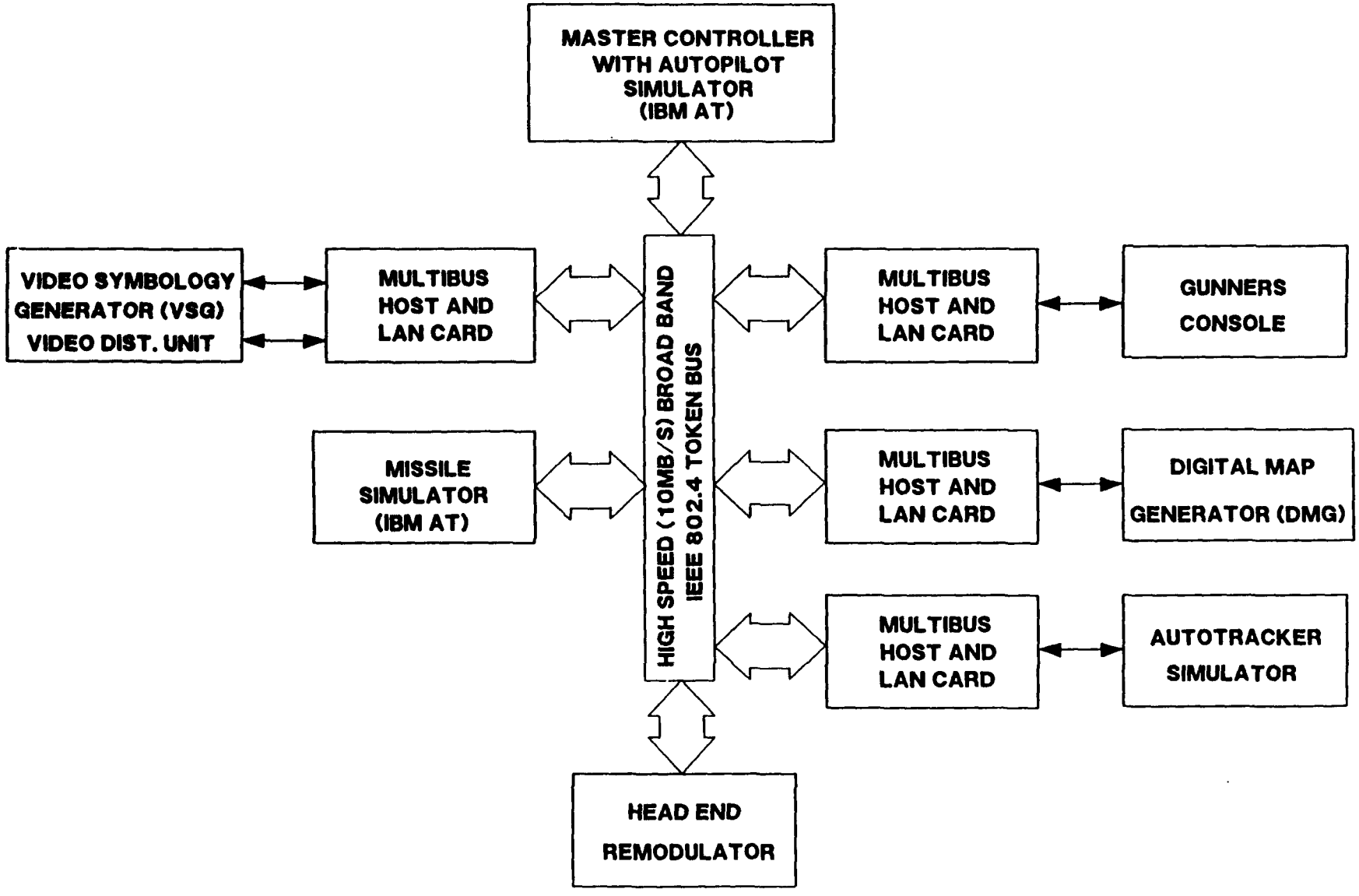


Figure 3. Block diagram of the LAN demonstration system.

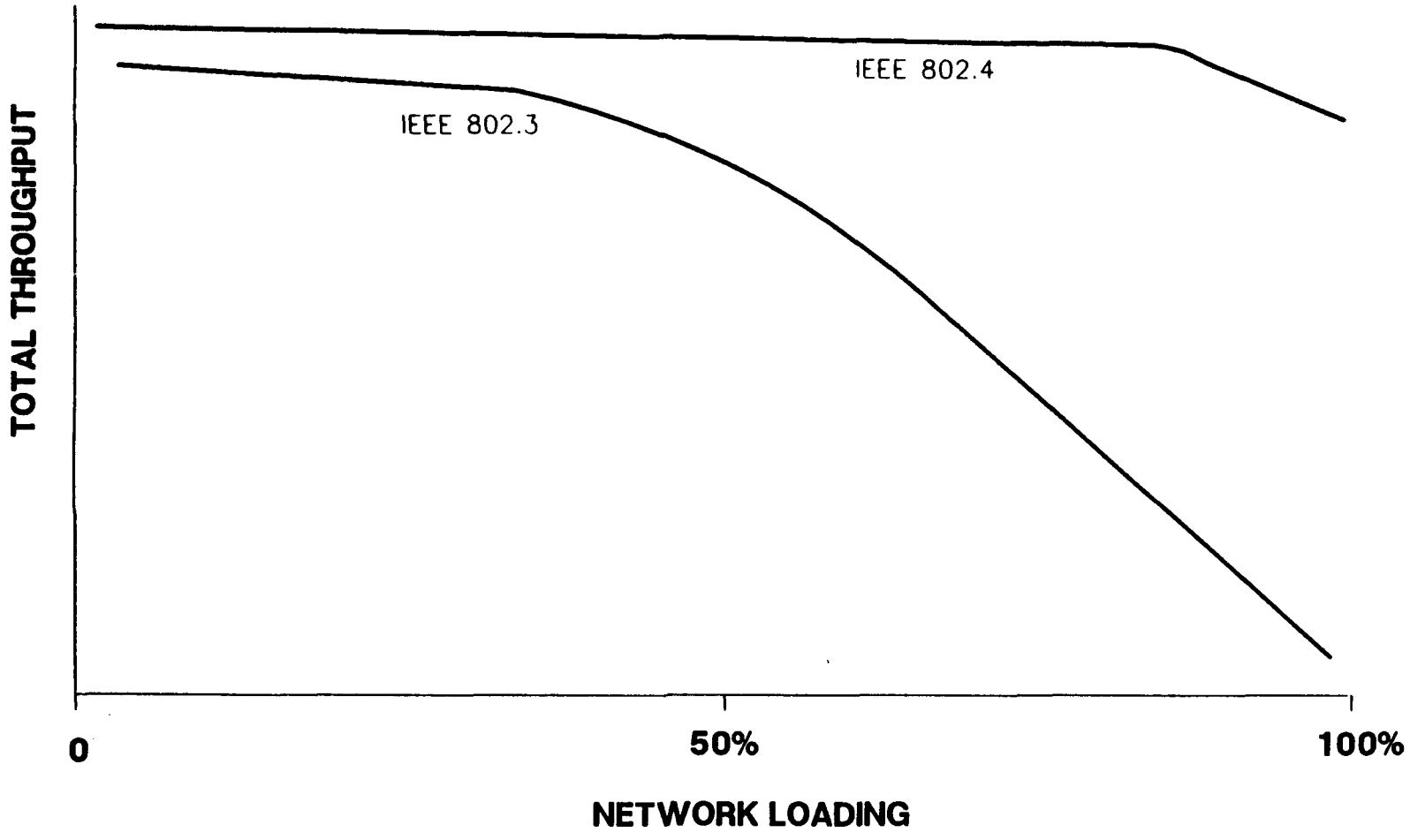


Figure 4. Throughput of IEEE 802.3 and 802.4 LANs.

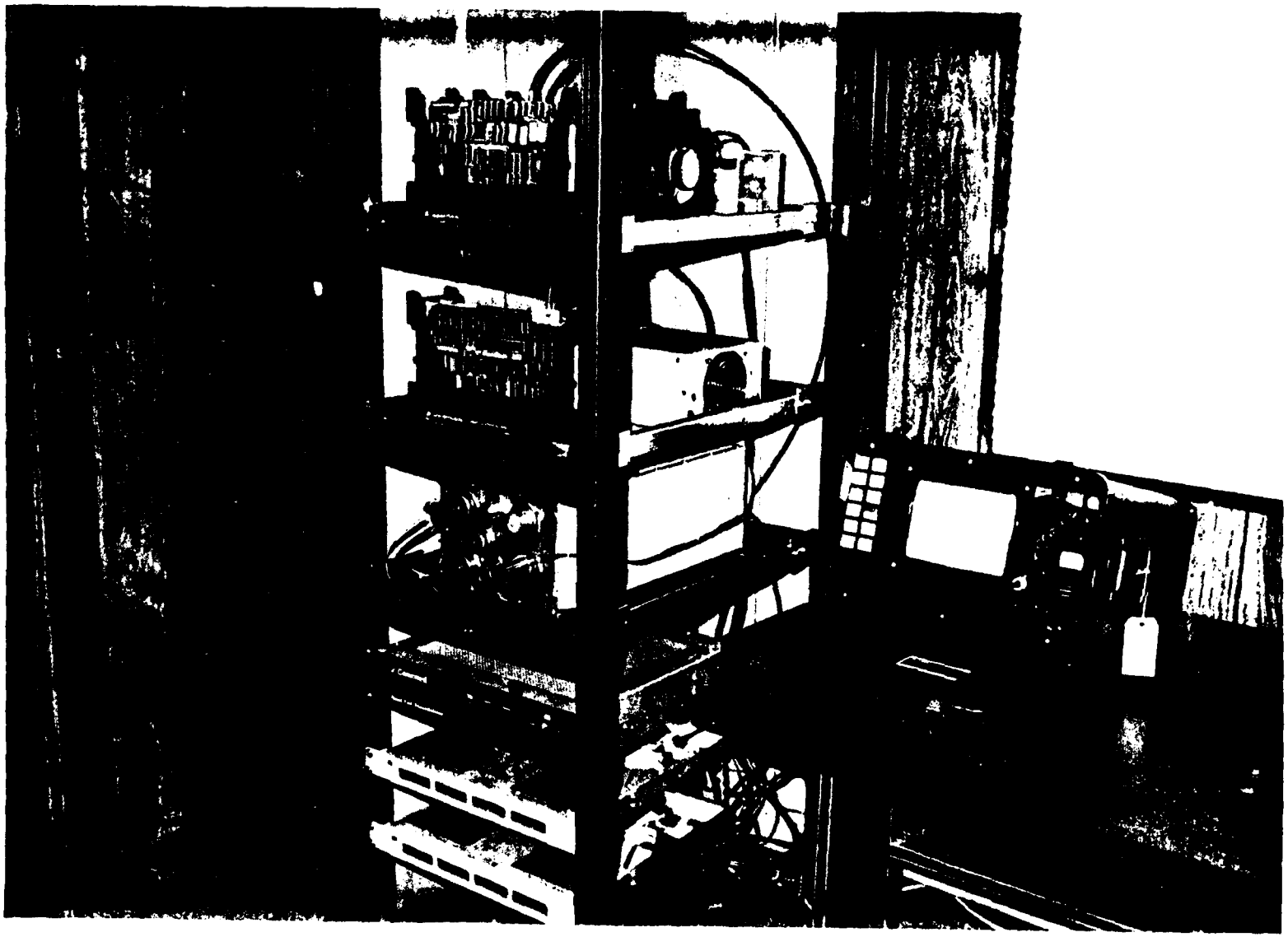

Figure 5. LAN project hardware.

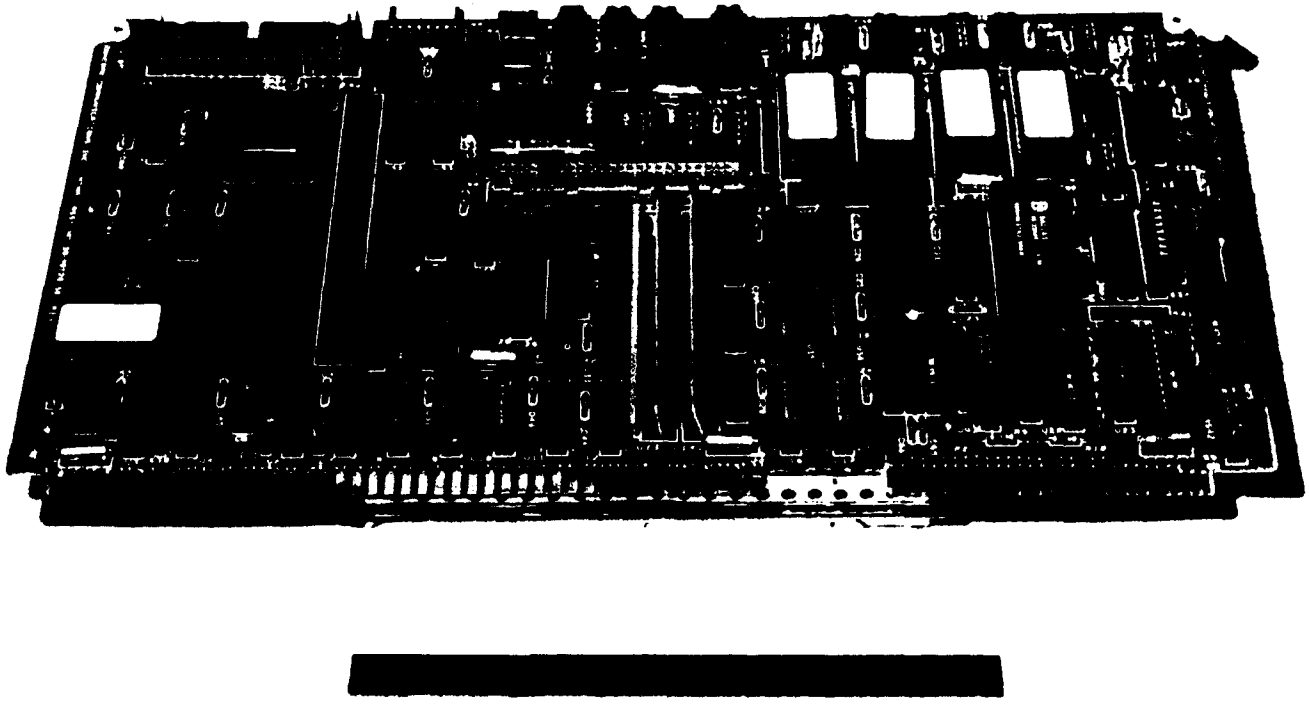

Figure 6. Multibus LAN board implementing IEEE 802.4 token passing bus and MAP/TOP protocol.

## DIGITAL SIGNAL PROCESSOR (DSP) PROJECT

As previously mentioned, the current MICROTUP effort is aimed at providing a Flight Computer (FC) for the ADKEM program. As in most guided missiles, the FC consists of one or more processors which generally provide the following functions:

1. An autopilot loop to keep the missile stable. This loop generally requires a suite of sensors (usually of the inertial variety as in ADKEM) to sense missile motion and a Control Actuator System (CAS) loop to control missile attitude.
2. A CAS loop which has missile attitude control devices (such as actuator driven fins as in AdKEM) with feedback mechanisms (such as potentiometers as in AdKEM).
3. A guidance loop which keeps the missile heading toward the target. This loop typically accepts the processed output of a target sensor (a radar in the AdKEM case) and uses this information to execute the appropriate guidance law.
4. Miscellaneous functions such as missile Built-in-Test (BIT), controlling of missile modes, firing squibs as required during flight, etc.

It is clear that any general purpose processor with sufficient speed, memory and Input/Output (I/O) facilities can perform the above functions. However, todays' DSPs provide significant advantages over typical general purpose machines in this application because they are optimized to provide the mathematical and I/O facilities required by the above listed functions. These on-chip facilities usually include:

1. Fast hardware multiply/accumulate, usually performed in a single machine cycle, and available in floating point from several manufacturers. The multiply/accumulate function is the basis for nearly all digital filter algorithms.
2. Integrated peripheral facilities such as serial ports, parallel ports, timers, and Direct Memory Access (DMA) controllers.
3. A small but significant amount of both Random Access Memory (RAM) and Read Only Memory (ROM). In some dedicated applications no external memory is required.
4. An optimized bus architecture usually containing more than one bus to get data into and out of the math unit quickly.

The net result of having these facilities on-chip in this application is lower FC cost, size and weight. As will be seen below, space is at a premium in the AdKEM missile. Having all these facilities on-chip was one of the keys which allowed the FC to fit within the allowable space without having to resort to expensive technologies such as hybrid circuits.

## THE ADKEM FC REQUIREMENTS

The ADKEM missile is a hypervelocity missile containing a penetrator rod. Its primary targets are armored ground vehicles and both fixed and rotary winged aircraft at moderate ranges. There is a strong desire to keep overall missile weight low. These requirements in essence dictate a missile with a small diameter (i.e., low drag) and as short a length as possible. These characteristics drove many of the ADKEM FC requirements as listed below:

1. The required processor throughput is estimated at 6 Million Floating Point Operations Per Second (MFLOPS). This estimate is based on the figures given in Table 1 which come from another developmental missile system. The actual estimated throughput requirement was multiplied by 2.5 in order to arrive at the throughput figure of 6 MFLOPS. This was done to allow for errors in the estimate and to meet Army requirements which require a processor to have at least 50% spare throughput for growth when initially fielded. Note that these figures are based on efficient high order languages such as C or PL-M. A not-so-efficient language such as Ada may require considerably more throughput than estimated.

2. The size constraints of the FC are shown in Figure 13. Note that most of the circuitry is packaged around the penetrator with only the processor board requiring the full missile inside diameter of 45.7mm (1.8"). In this way the FC contributes no more than 101.6mm (4.0") to the overall missile length.

3. The memory required is estimated to be 256 Kbytes. Again, this is based on another developmental missile program using an efficient high order language. At this time separate ROM and RAM requirements are not firm, so it was decided to provide at least 256 Kbytes of both.

4. The FC is required to have the circuitry necessary to interface to the Inertial Measurement Unit (IMU), CAS, telemetry unit, Millimeter Wave (MMW) receiver, ground computer, and booster separate squibs.

5. The FC must supply regulated power to all missile items which require such power.

6. The processor chosen must have good software development tools available including high order language and hardware emulator support.

7. The FC must of course operate in the AdKEM environment. To date, only the acceleration environment is defined, being 1000g's along the missile center line and 100g's in the other two orthogonal axes.

TABLE 1. Projected ADKEM Processing Load.

| | # of Instructions | | Execution Frequency | | Instructions per Second |
|---|---|---|---|---|---|
| Executive | 2700 | X | 250 | = | 675,000 |
| Attitude Reference | 550 | X | 500 | = | 275,000 |
| Coordinate Transform | 125 | X | 500 | = | 62,500 |
| Navigation | 1350 | X | 250 | = | 337,500 |
| Guidance | 1150 | X | 250 | = | 287,500 |
| Autopilot | 875 | X | 500 | = | 437,500 |
| Telemetry | 125 | X | 250 | = | 31,250 |
| Actuators | 309 | X | 500 | = | 154,500 |
| | | | | | 2,260,750 |
| | | | | | X 2.5 |
| Total Projected Processing Load | | | | | 6,038,125 |

## FIGURE 13: FLIGHT COMPUTER SIZE CONSTRAINTS

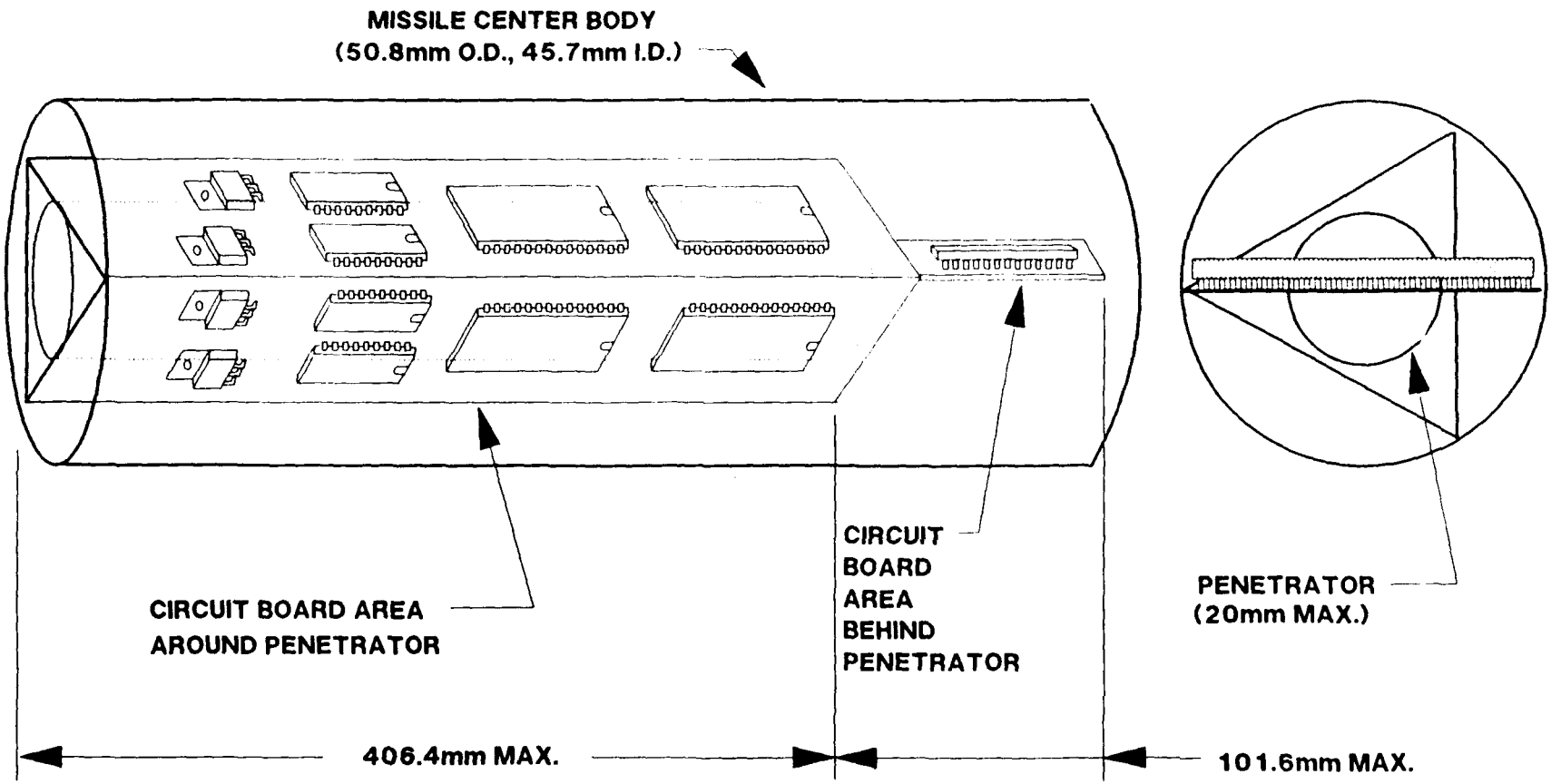

## DESIGN OF THE FC

Once requirements are known, the first step in most computer designs is the choice of the processor. A floating point processor was desired to ease the time consuming software development required when trying to provide floating point computations in software. Also, as many on-chip peripherals as possible were desired to keep space utilization to a minimum. The processor chosen for the ADKEM FC was the Texas Instruments TMS 320C30. At the time the processor decision was being made, only two DSPs were found which could meet the throughput requirements, contained floating point arithmetic units, were immediately available, and were being promised as military parts in the near future. These were the AT&T DSP32C and the Texas Instruments TMS 320C30. The DSP32C was initially chosen for its more convenient architecture and lower cost, but the VAX hosted C cross compiler was found to be seriously defective and the hardware emulator had a number of bugs which made software and hardware development less than efficient. Given the quality of the AT&T products received, it was decided that the Texas Instruments TMS 320C30 was more cost effective in the long run. Once the processor decision was made, a block diagram of the FC was derived and is shown in Figure 8. The design of the various subsystems are given below.

## MEMORY

As previously stated, the FC memory requirement was specified as 256 Kbytes. Because ADKEM is a developmental system, it was decided that a reprogrammable ROM technology would be used to hold the FC software. However, standard EPROM technology had two drawbacks. First, dense (256 Kbit or greater) parts were required to meet the severe FC space limitation, but no dense parts were available which would meet the FC throughput requirements (i.e., 25 ns access time). Second, EPROM technology required physical removal of the parts to reprogram and this required sockets. Not only was there no room for the sockets, there was also no vendor found which would guarantee that their socket would operate in the 1000 g operating environment. For these reasons it was decided that EEPROM technology would be used to hold the flight software and, on power up, would down load the flight program to fast RAM for execution. Flash EEPROMs were selected as they are more cost effective than standard EEPROMs and there is no requirement to change single memory locations in EEPROM during code execution. One slight problem with this architecture was that the TMS 320C30 keeps its start-up vector and interrupt vectors in low memory starting at location 0. This means that EEPROM must start at location 0, and whenever an interrupt occurs wait states must be inserted into the memory cycle to meet the EEPROM access time. Fortunately, the TMS 320C30 contains an on-chip, very flexible wait-state generator. By using a single inverter as shown in Figure 9, an address line is used to select between zero wait states (i.e., RAM access) and 4 wait states (i.e., EEPROM access). A block diagram of the memory system is shown in Figure 9. It is a conventional design and uses dense memory parts to keep size to a minimum while still using cost effective standard parts and mounting techniques. RAM access time was selected at 25ns since faster dense devices in a military temperature range could not be found. Although this limits the maximum processor clock frequency to 28 MHz (and the maximum throughput to 28 MFLOPS) this is still considerably faster than the estimated required throughput.

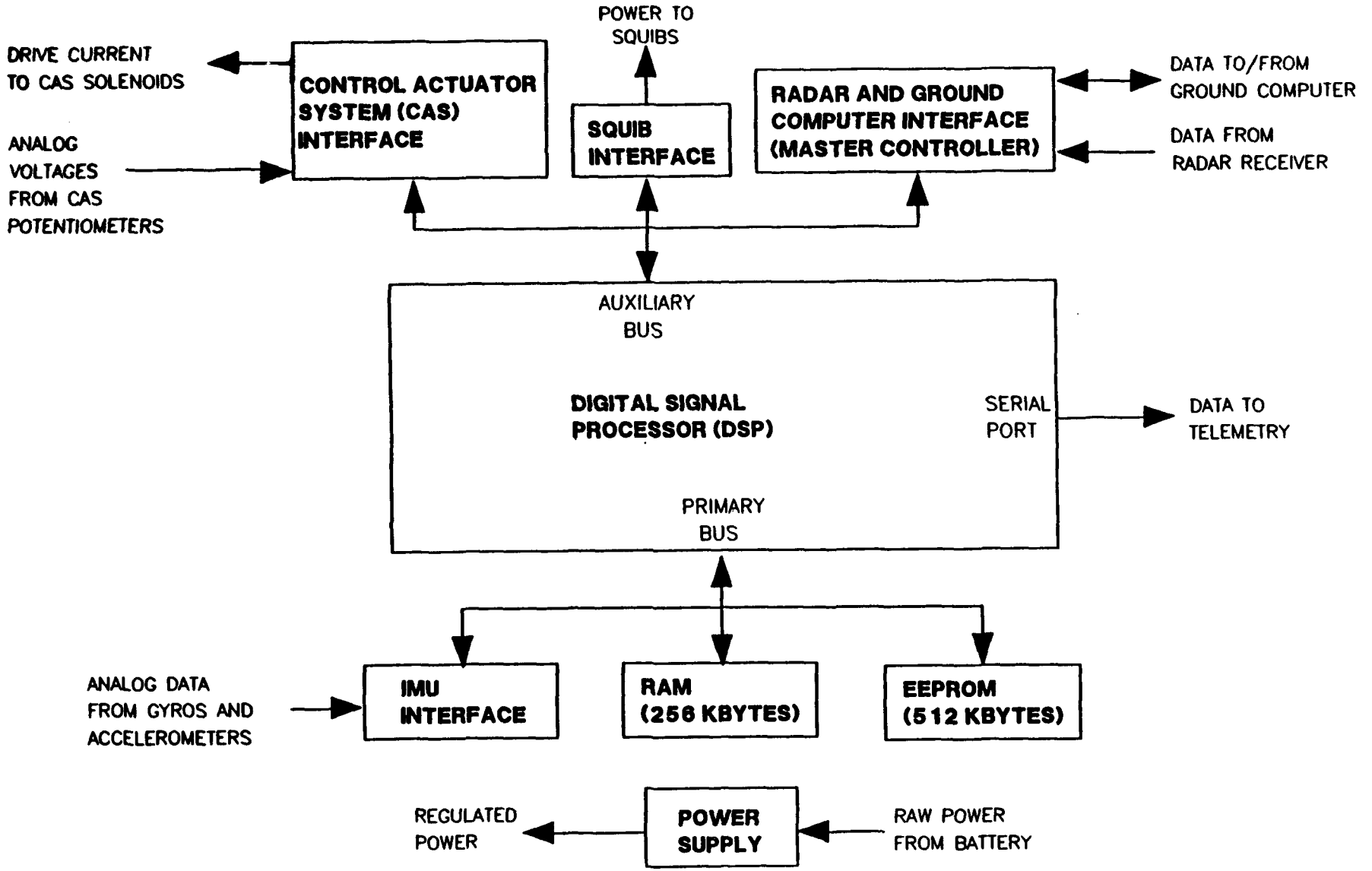


Figure 8. ADKEM flight computer block diagram.

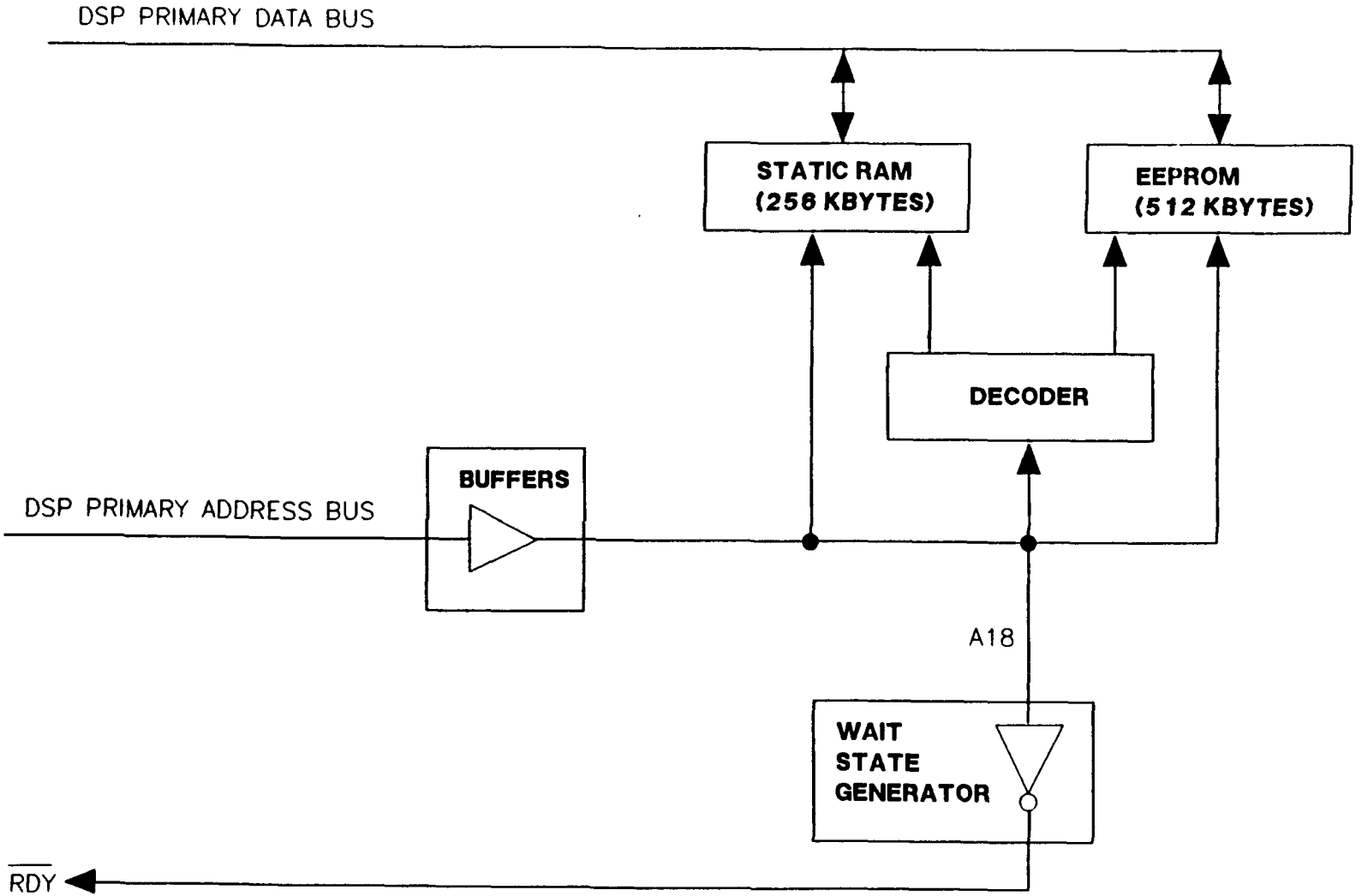


Figure 9. ADKEM memory block diagram.

## INTERFACES

The FC contains interfaces to the IMU (which consists of three gyros and three accelerometers), CAS, MMW receiver, the ground computer, missile squibs, and telemetry unit. The latter two are not well defined and will not be discussed in this paper. The others are discussed in more detail below.

The IMU interface consists of conventional analog filters, analog multiplexer, sample-and-hold (S/H) amplifier, 16 bit Analog-to-Digital (A/D) converter, a First-In-First-Out (FIFO) buffer, and miscellaneous timing and interface logic as shown in Figure 10. It is memory mapped into the primary bus of the DSP. In operation, the analog data from the IMU is sampled and converted to a digital format. As each conversion is completed, it is stored in the FIFO buffer. When all six signals have been converted, the control logic issues an interrupt to the DSP which then reads all of the data out of the FIFO. This interrupt marks the beginning of each autopilot cycle. The process repeats every two milliseconds (i.e., 500 Hz autopilot rate).

The CAS interface consists of analog input filters, a monolithic A/D converter chip (containing an analog multiplexer, S/H amplifier, and 10 bit converter), a reference voltage generator, control logic, and three bit latch with solenoid power drivers as shown in Figure 11. In operation, the DSP writes the analog channel number of the CAS potentiometer to be converted to the control logic which then starts the conversion. When the conversion is complete the DSP is interrupted to read the results of the conversion. This data, in conjunction with one of the DSP's on-chip timers, is used to compute the pulse width required to drive the appropriate CAS solenoid. The pulses are output through the three bit latch to the solenoid power drivers. The three bit latch and A/D converter are at different locations on the DSP's auxiliary bus so that their operations are independent. The reference voltage generator generates the reference voltages for both the potentiometers and the A/D converter.

The MMW receiver interface uses a single chip microcontroller (designated the Master Controller) to accept and decode pulses supplied by the MMW receiver. Data is encoded as a pulse stream, with the time between pulses signifying logic 0, logic 1, or sync. The chosen microcontroller contains a hardware timer circuit which captures the time between pulses. Its internal software then decodes each pulse time, packs the resulting bits into digital words, and then sends them to the DSP over a memory mapped parallel interface. A block diagram is shown in Figure 12. Note that the Master Controller also performs the ground computer interface function.

The ground computer interface is a serial, asynchronous, full duplex interface which is used for the following functions:

a. Allows the FC to communicate its BIT status to the ground computer prior to being committed to flight.

b. Allows the ground computer to give initial target position information to the FC so that it can navigate before being captured by the MMW radar beam.

c. Allows research and development personnel to upload flight software into EEPROM prior to missile assembly.

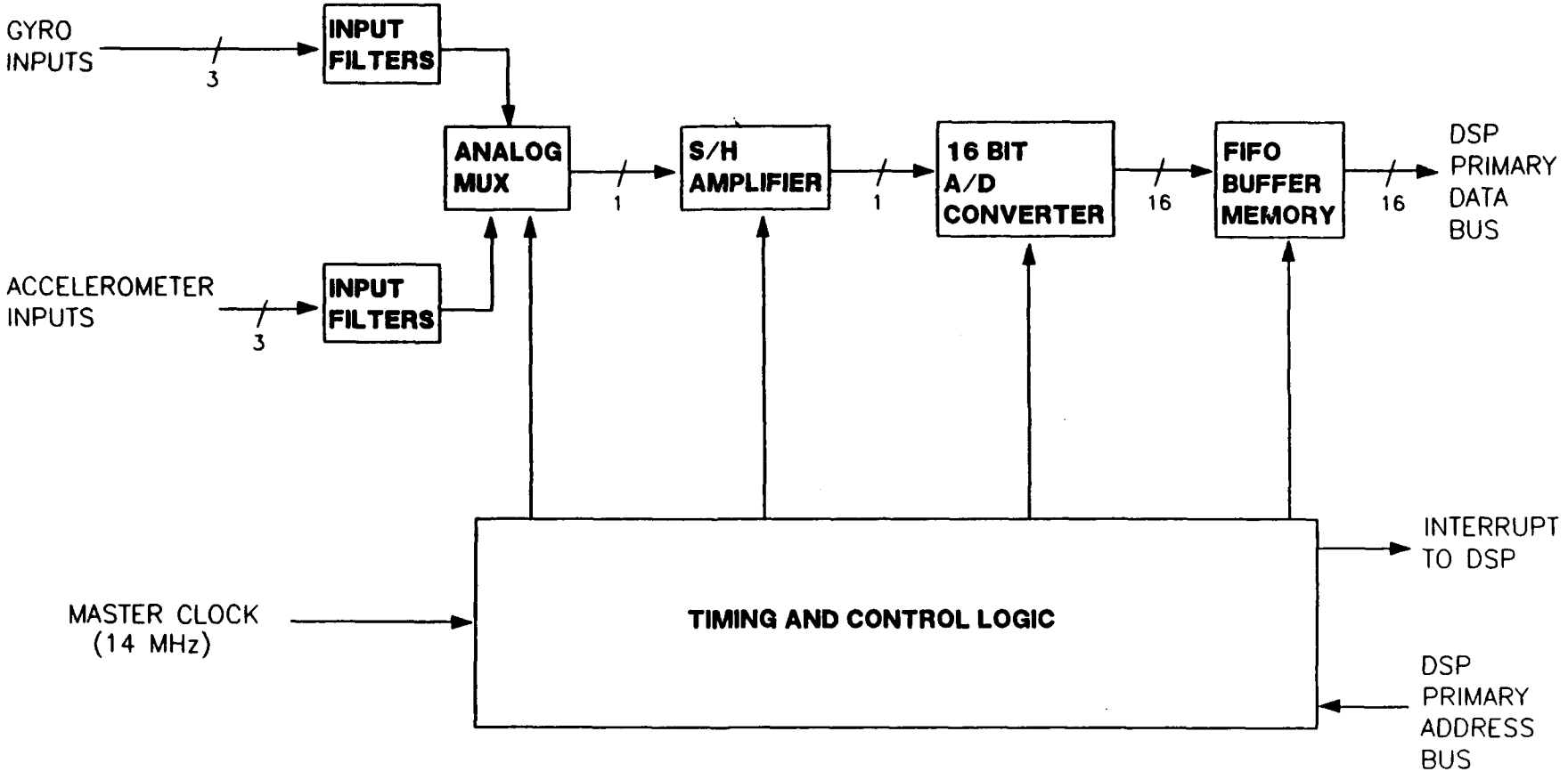


Figure 10. Block diagram of the IMU interface.

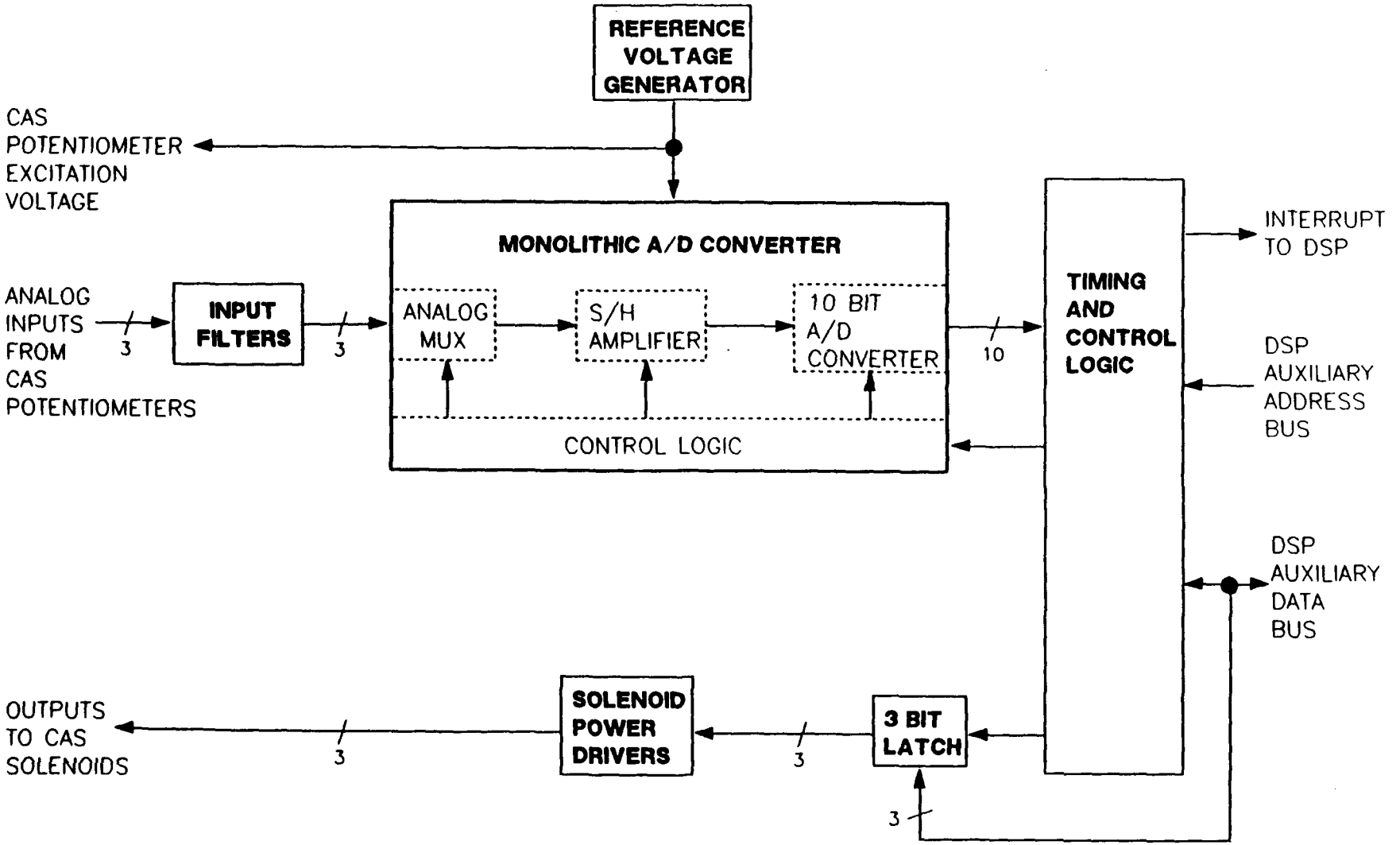


Figure 11. Block diagram of the CAS interface.

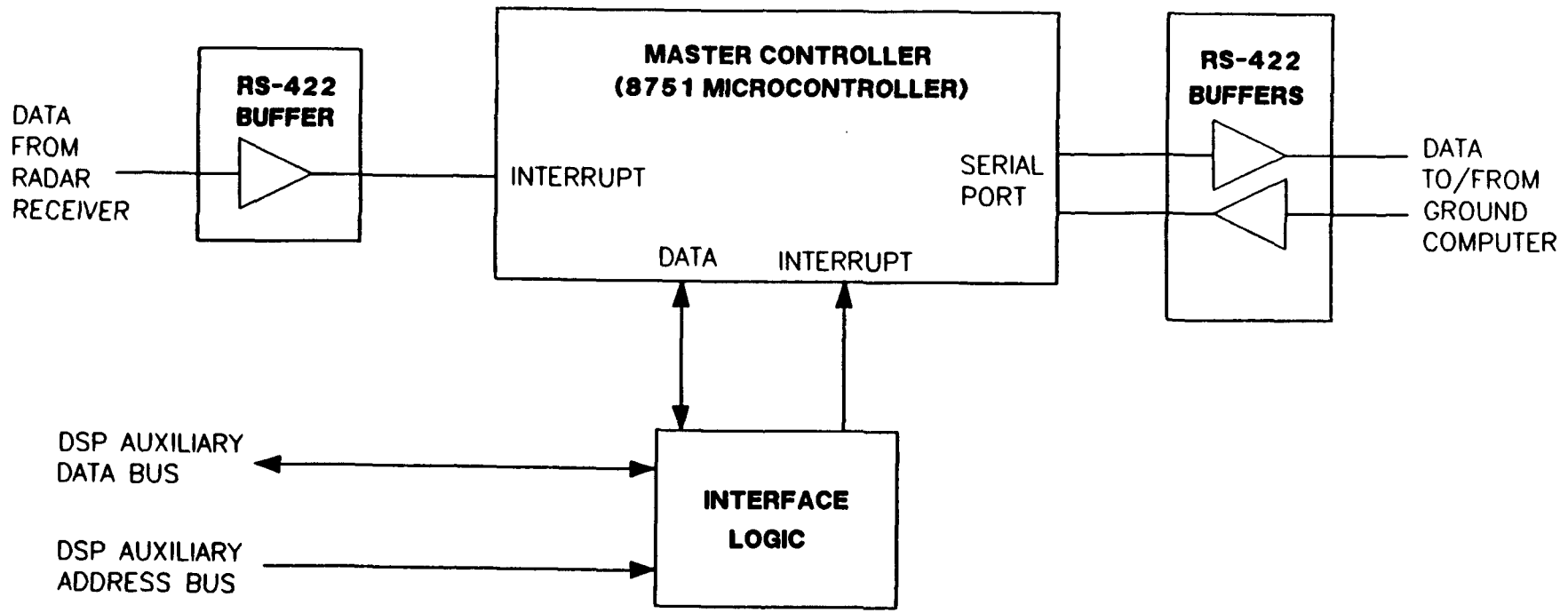


Figure 12. Ground computer and MMW receiver interface.

## PHYSICAL CONFIGURATION

As previously mentioned, and shown in Figure 13, the ADKEM FC must fit into a small space (about 706 cubic centimeters or 43 cubic inches) with a non-ideal form factor. After some debate, the mounting scheme shown in Figure 13 was chosen. The memory, interface, and power supply circuitry is mounted on the three boards surrounding the penetrator. The boards are connected together using flat printed circuit flex cabling. The DSP, with its associated clock, pull-up resistors, and decoupling capacitors is mounted on a small board behind the penetrator because of the size of the DSP chip. It is connected to the memory board with flat printed circuit flex cabling. Through judicious choice of components this scheme will accommodate all of the circuitry envisioned for the FC while using only standard through-hole parts and surface mounted (J-lead) parts.

During the design process there was concern over the 1000 g acceleration environment which exists when the ADKEM boost motors are fired. In order to gather preliminary data as to the mechanical integrity of standard through-hole and surface mounted parts, a set of test boards was constructed and sent through a series of centrifuge tests which subjected them to accelerations of up to 1000 g's for several seconds. A variety of parts, including 300 mil and 600 mil DIPs in both ceramic and plastic packages, J-lead parts, and miscellaneous discrete resistors and capacitors, was tested. Figures 14 and 15 are photographs of these boards after the tests. The only mechanical damage noted throughout the tests was that some of the RTV silicone rubber adhesive used to fasten the wire wrap wires to the back of the active board was thrown off the board (see Figure 15). The wires themselves remained intact throughout the tests.

Most of the test parts were not operated during the tests. However, two test circuits, one consisting of a crystal oscillator and the other consisting of an 87C51 microcontroller, were operational during the tests. The purpose of these two circuits was not only to confirm operation through the 1000g environment but also to check the stability of typical crystals in this environment. A plot of frequency versus acceleration for the two circuits is shown in Figures 16 and 17. There is reason to believe that much of the frequency variation seen in these plots is actually pickup noise contributed by the centrifuge drive motor. This is suggested by the fact that at particular g-levels the frequency counter readout was not constant (see HIGH and LOW RANGE levels in Figures 16 and 17), but when the centrifuge motor was turned off at an acceleration of 1000 g's (i.e., at the end of a test run) the frequency counter value remained constant throughout spindown. Regardless of the cause of the frequency variations noted, the readings demonstrated a maximum change of less than 0.02%.

## SUMMARY

In the current era of shrinking defense funding, DoD can greatly benefit from state-of-the-art technology found in the commercial market place. This is especially true in the microprocessor world where commercial demands and pressures have driven performance up dramatically and price/performance down just as dramatically. This paper has presented two projects using state-of-the-art microprocessor based technology. The

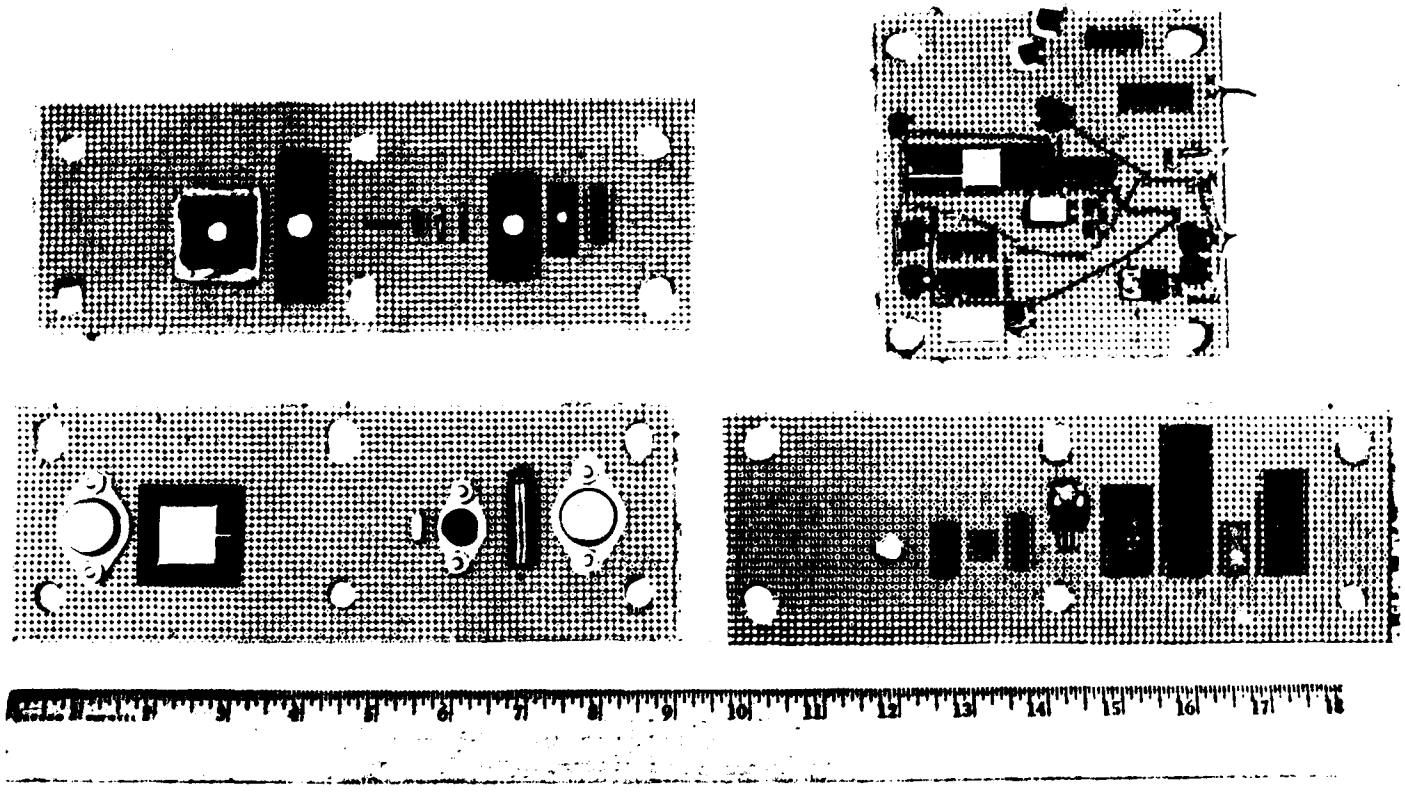

Figure 14. Photo of the centrifuge test boards. These were subject to an acceleration of 1000 g's with no apparent damage.

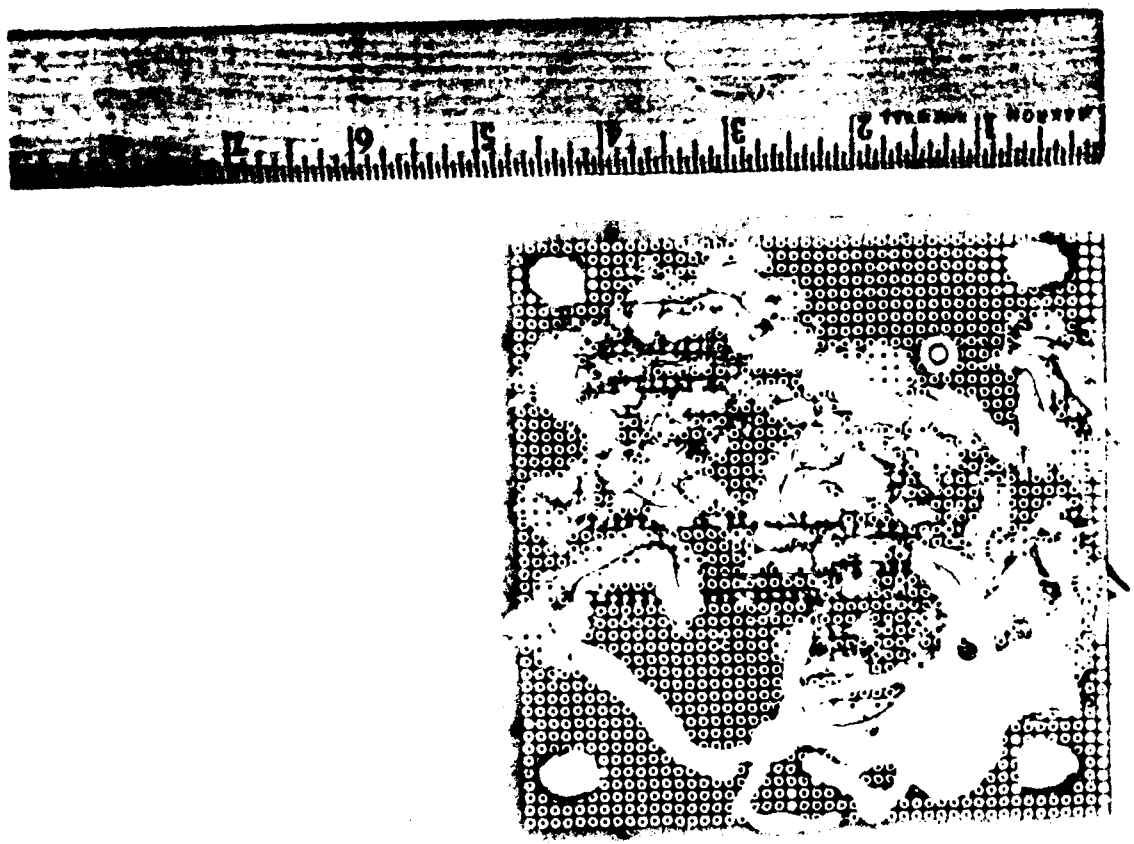

Figure 15. Back side of the active centrifuge test board, some of the RTV potting was thrown off the board, but all wiring and parts remained intact throughout the test.

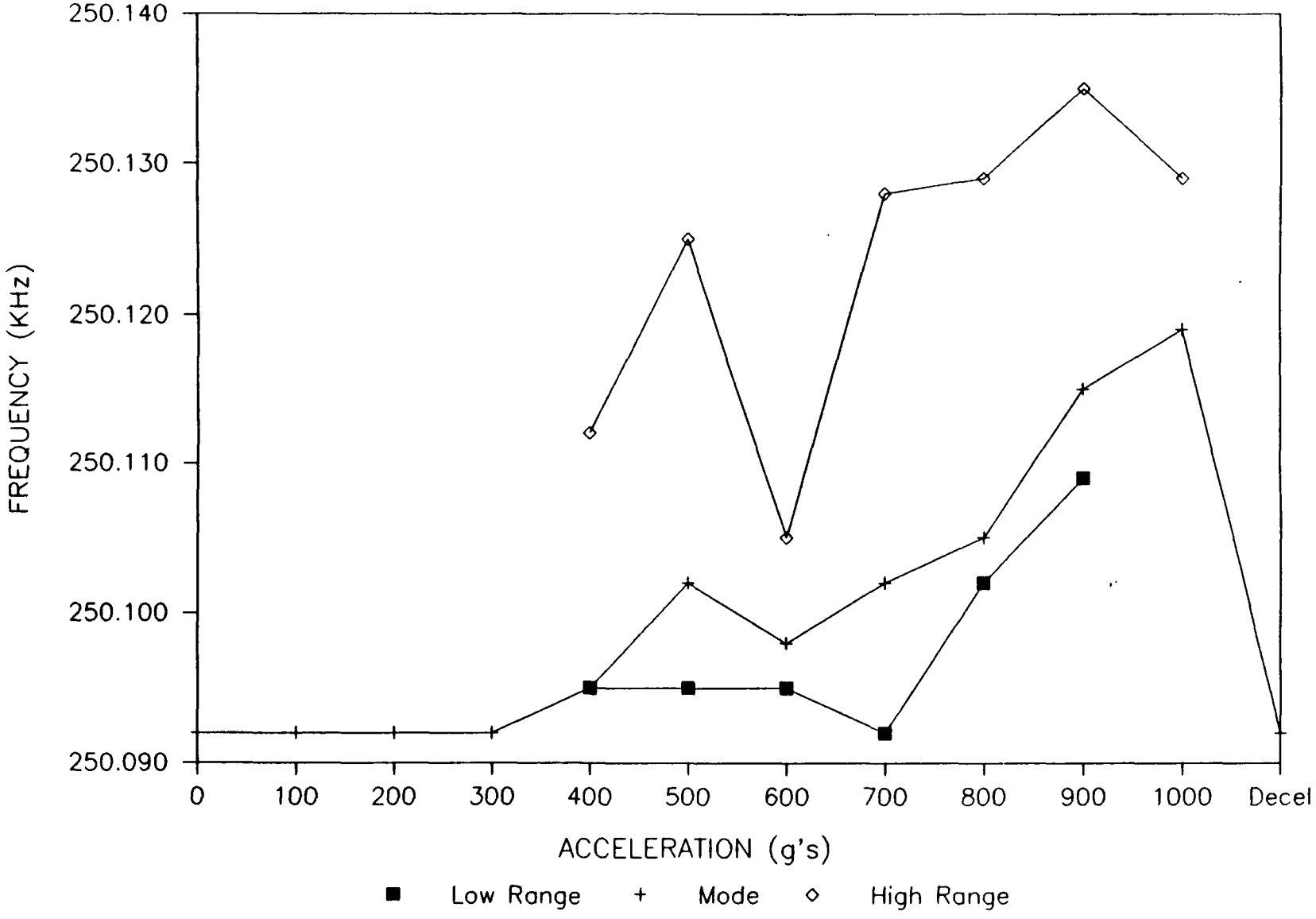


Figure 16. Changes in processor output pulse rate.

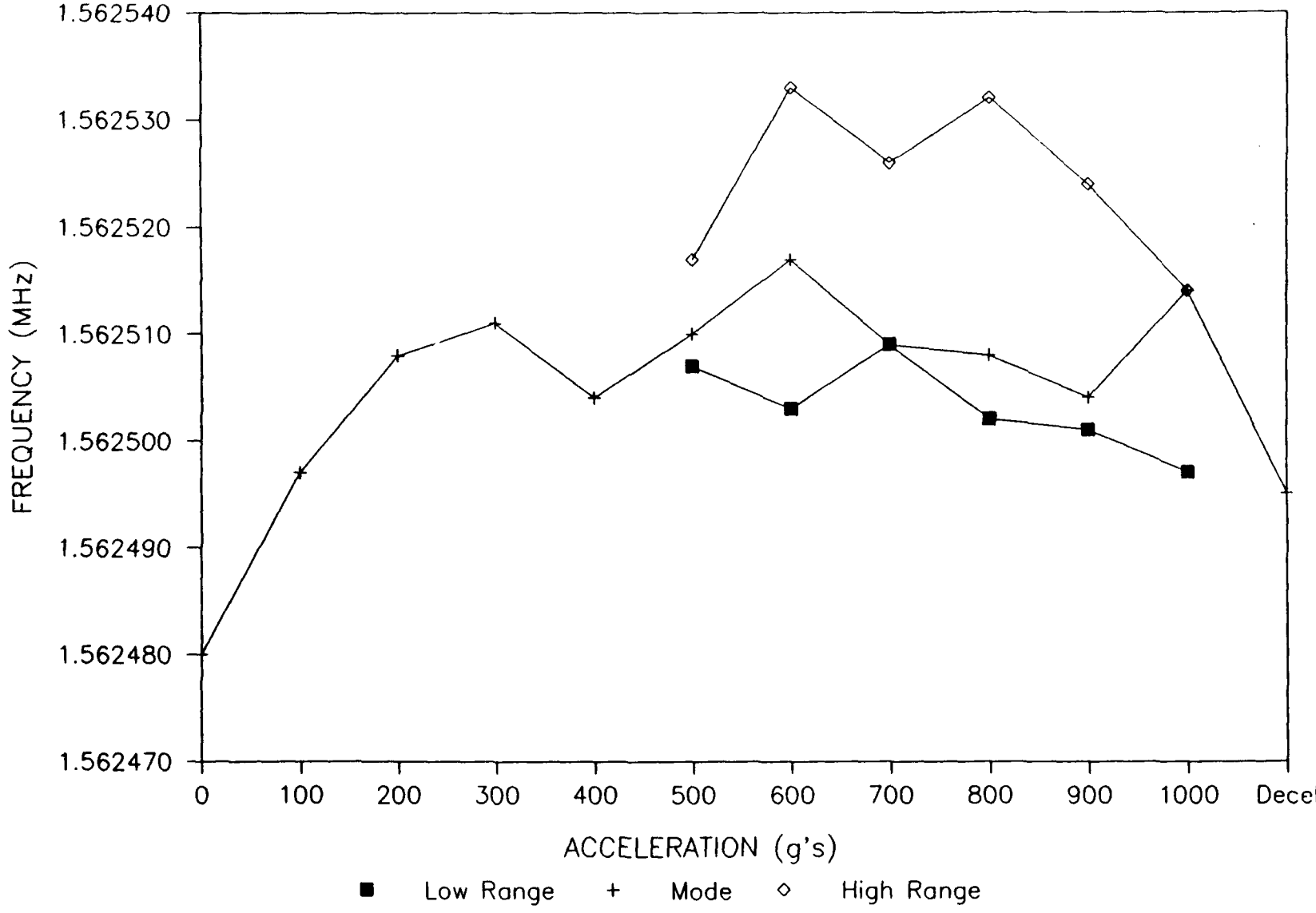


Figure 17. Frequency versus acceleration for a typical crystal oscillator.

LAN project, although not meeting its intended goals, revealed where the shortcomings in such technology existed and pointed to possible solutions. The ADKEM project uses the latest DSP technology to help solve the throughput and physical space problem aboard a small missile without resorting to expensive or nonstandard mounting technology. Such projects are crucial to the understanding and use of such technology in future missile systems.

## References


[1] Carrier Sense Multiple Access with Collision Detection IEEE Std 802.3-1985, The Institute of Electrical and Electronics Engineers, Inc., October 1985.

[2] Token-Passing Bus Access Method and Physical Layer Specifications. IEEE Std 802.4-1985, The Institute of Electrical and Electronics Engineers, Inc., October 1985.

[3] William Stallings. Local Networks: An Introduction, page 255, Macmillian Publishing Company, 1984.

# REAL TIME EXECUTIVE FOR MISSILE SYSTEMS (RTEMS)

Wanda M. Hughes and Phillip R. Acuff
Guidance & Control Directorate
Research, Development & Engineering Center
Redstone Arsenal, Alabama

## ABSTRACT

A study was completed in 1988 which compared the various aspects of the Ada programming language as they relate to the application of Ada code in distributed and/or multiple processing systems. Several critical conclusions, which have a major impact on the way the Government develops software, were derived from the study. The two major conclusions were that the Ada programming language does not fully support multiprocessing and the run time executives being delivered with the Ada compilers were too slow and inefficient to be used in modern missile systems. Because of these shortfalls in the implementation of the Ada programming language for embedded systems, software developers in Army Research and Development and missile system prime contractors are purchasing and utilizing specialized third party kernel code to fill the void where Ada is lacking. The contractor, and eventually the Government, must pay a licensing fee for each copy of the kernel code used in an embedded system. The main drawback to this development environment is that the Government does not own, nor has the right to modify code contained within the kernel. Techniques for Verification and Validation (V&V) of software in this situation are more difficult than if the complete source code were readily available and could be modified.

## INTRODUCTION

In 1974, the United States Department of Defense (DoD) realized that far too much money was being expended on software development and maintenance activities. As a result, a study was performed to determine how software costs were distributed over the various application areas. The study indicated that over half of all software expenditures were directly attributed to embedded systems [1]. In addition, the study concluded that two key factors were primarily responsible for these costs: an overabundance of programming languages and the "primitive" nature of those languages.

A proliferation of languages (more than 450) emerged as defense agencies and system project offices repeatedly spawned new languages from existing ones in an attempt to meet new project requirements. With numerous languages came numerous problems. For instance, languages were largely incompatible; They could not easily "talk" to each other. This computer "Tower of Babel" resulted in many costly mistakes. In one situation, an attempt was made to develop a tactical operations system that would use computers to assist battlefield commanders in making decisions. When this system was interfaced to other tactical systems (using different computer languages), translation was slow and error prone. The entire development program was halted after $100 million were expended. Another problem with numerous languages was that the software being developed was not portable. It could not be easily transported to different computers or projects. Similarly, software engineers could not transfer their skills across a broad spectrum of projects; rather, they had to become highly specialized. The use of so many languages also resulted in restricted competition in the maintenance and enhancement phases of projects as well as producing a minimal amount of software available in each language. Competition was restricted as competitors had to bear the initial investment associated with a new language, including the development and acquisition of both programmer training and support software. Obviously, the original developer of the software system would not incur these costs.

In addition to the overabundance of computer languages, the existing languages were inadequate because they were obsolete (they did not support modern software engineering principles). As a result, code generated in these languages was difficult to read and understand. In turn, these characteristics increased both design complexity and maintenance difficulty. The code lacked clear structure and contained low-level details that would have been hidden by a more modern language. These obsolete languages also resulted in software that was hard to reuse, because units of code were so interdependent. Modules often could not be extracted and used in different programs. This interdependency also made it difficult to modify code without introducing unwelcome and often "fatal" side effects.

All of these problems were especially severe in embedded systems. An embedded system is one in which a computer is part of a larger system, such as computerized radar used in aircraft. Embedded systems are typically complex real-time systems that contain many lines of code, are long lived, and are continually being modified. Because of the size, complexity, life-span, and volatility of these systems, they were responsible for 56% of DoD software costs in 1973.

The software issue, then, included such problems as software being excessively expensive, not portable, difficult to maintain, and not reusable. All of these problems were intensified in embedded systems. Clearly, something had to be done to help address this growing problem. The solution was the creation of a new standard software development language, Ada [2].

Ada was designed primarily for programming embedded computer systems. It is a real-time language and execution environment in that it not only contains a complete set of general purpose language features, but also provides facilities for multi-tasking, real-time synchronization, and direct programming of low level device hardware[3]. Ada offers many advantages over other programming languages. For instance, since no subsets or supersets are allowed, Ada source code may be ported between different Ada compiler systems, with minimal changes. In addition to code portability, people portability is enhanced. Programmers can move from project to project without having to learn new languages. Ada also helps manage the complexity and improve the maintainability of software by supporting modern software engineering principles [2]. This is accomplished by enforcing a strict programming discipline designed to make programs more readable, reliable, portable, modular, maintainable, and efficient – all qualities of good software [4].

It should be pointed out, however, that Ada is a large and complex language. The difficulties involved in learning how to use it effectively should not be underestimated [3]. In fact, the virtues of this language are still being tested within both the Government and in the private sector. In accordance with this, the study that was completed in 1988, comparing the various aspects of the Ada programming language as they related to the application of Ada code in distributed and/or multiple processing systems, brought to the forefront several critical conclusions which have a major impact on the way the Army develops application software for embedded systems. This impact applies to both in-house software development activities as well as contractor developed software. The MICOM/RDEC programs which have immediate impacts in this area include Non-Line Of Sight (NLOS/FOG-M), Army Unmanned Aerial Vehicle (AUAV), Multiple Launch Rocket System (MLRS), and Advanced Kinetic Energy Missile (AdKEM).

A conclusion of the analysis, which has been previously recognized by other agencies attempting to utilize Ada in a distributed or multiprocessing environment, is that the Ada programming language does not fully support multiprocessing (systems with more than 1 processor). Ada does provide a mechanism for multi-tasking, but this capability exists only for single processor systems. The language also does not have an inherent capability to access global named variables, flags or program code. These critical features are essential in order for data to be shared between processors. Although these drawbacks do have workarounds, they are sometimes awkward and defeat the real intent of a "self documenting" programming language, such as Ada.

However, the feature most essential for a distributed system is the capability to spawn tasks on another processor. This capability does not exist within the Ada language. Furthermore, there appears to be no suitable workaround within the language itself for this critical capability.

Another conclusion drawn from the analysis, was that the run time executives being delivered with the Ada compilers were too slow and inefficient to be used in modern missile systems. These run time executives are the core part of the Ada run time environment that provide operating systems functions such as task scheduling, input/output management and memory management.

## REAL TIME SOFTWARE DEVELOPMENT

To properly evaluate the impact of these problems with the Ada language a thorough understanding of the "art" of developing effective real-time software is essential. Real-time embedded software development differs from other software development in that two computers, one for development and one for fielding, are typically used instead of one. Because embedded systems perform clearly defined, limited sets of functions, they often lack features needed for software development. They frequently have limited memory and disk storage, and often have a specialized interface to the external world, such as buttons, gauges, sensors, or actuators. Developing software for them usually requires a different computer with the necessary software development tools. This software development computer is called the host, while the embedded computer is called the target.

The implementation phase for embedded systems software consists of developing software on the host, and then downloading the software to the target for testing. When software errors are found, they are corrected on the host before downloading again to the target for more testing. This cycle continues until all the bugs are worked out. The software may then be burned into PROMS, if desired, and installed on the target system. Figure 1 illustrates this process.

Although Ada was designed with real-time embedded applications in mind, such implementations depend heavily on the interaction between the compiler, interface library, and the embedded system's kernel, or executive.

## REAL-TIME EXECUTIVES

Real-time software development also differs from other software development by its very nature: in real-time, the right answer late is wrong. The system must respond to the unexpected events in the outside world rapidly enough to control ongoing processes. Special needs exist for an extensive set of support tools and technology to properly design and implement real-time software. Real-time design requires determinism, preemptive scheduling capabilities, real-time interrupt response with low interrupt latency, explicit tasking control, time-slicing, and prioritization of tasks to ensure reliability and predictability in a system's behavior [5].

Another key requirement is multitasking. Multitasking is the ability of the software to handle many tasks concurrently, because events in the real world usually overlap rather than occur in strict sequence.

The multitasking capability of a real-time operating system provides a framework that allows the design of very complex real-time software which has well-defined and controlled interactions among its various components. In addi-

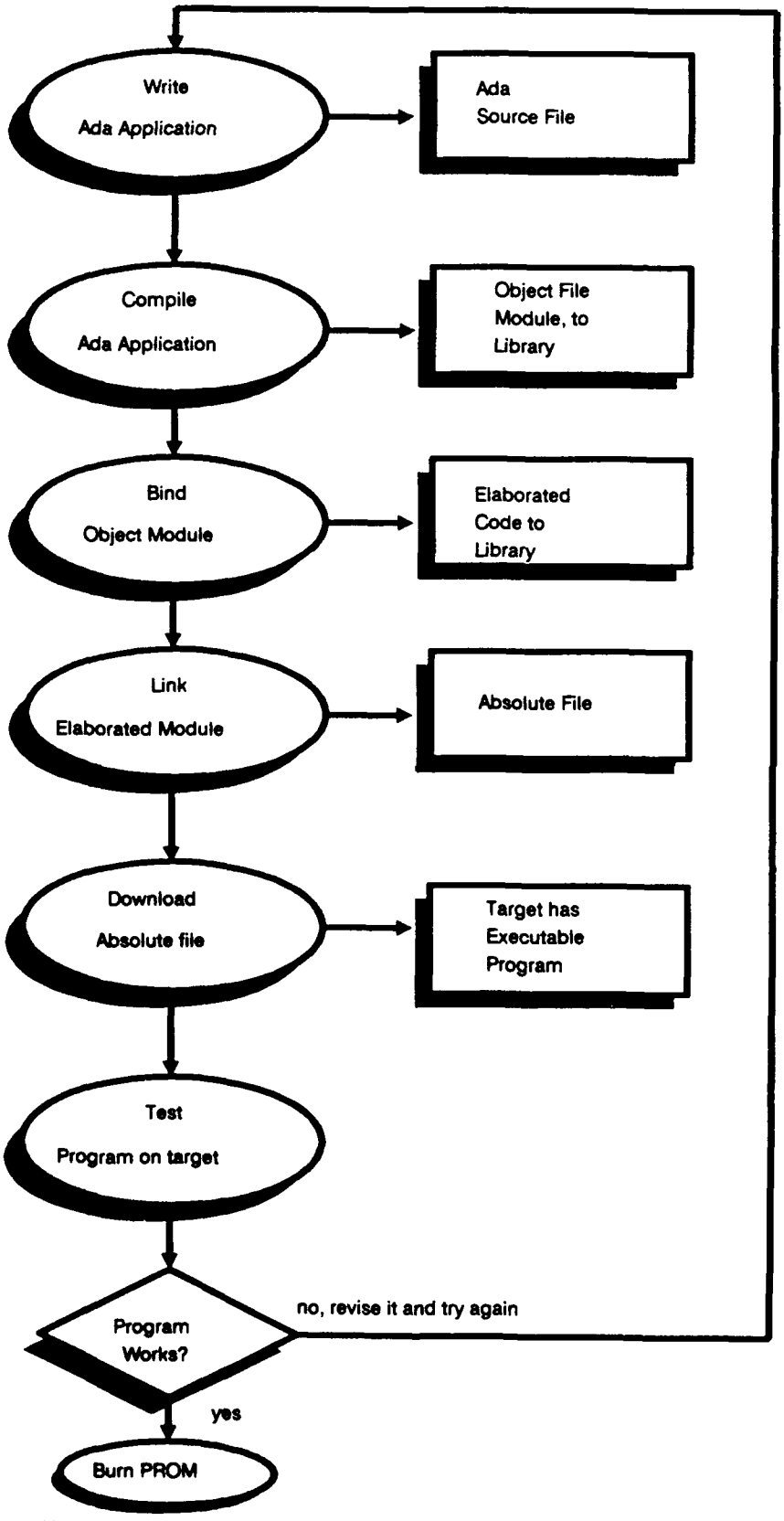


**Figure 1: Real Time Software Development Procedure.**

tion, the operating system supplies a number of prewritten and debugged software facilities such as interrupt handlers, data-transfer functions, real-time clocks, and I/O device drivers.

At the heart of a real-time executive is the concept of a task, or process. A task is an activity carried out by the computer. It consists of a program, data associated with the program, and computer resources such as memory space or I/O devices required to execute the program [6].

Programmers and designers of real-time systems frequently spend more time developing basic mechanisms such as intertask communications, synchronization, and memory management, than on the application program itself. In embedded applications, this set of mechanisms is called a real-time operating system or a real-time executive. Programmers build their applications using the real-time executive as the foundation.

It is important to note the difference between real-time multitasking operating systems and real-time executives. A real-time executive does not offer operating system commands and is not a replacement for an operating system such as UNIX. A real-time executive is used to create a single application on a target machine. Its sole purpose it to integrate a series of small programs into one real-time application [7]. A fullfledged real-time operating system adds a disk file system to the capabilities provided by a real-time executive.

A real-time operating system is distinguished from a normal multitasking operating system by its ability to schedule tasks on the basis of external events which are signaled to the computer by interrupts. Operating systems which are not intended for real-time applications usually do not give the user mechanisms to control how interrupt requests are handled and may actually disable interrupts for substantial periods while the operating system nucleus is executing. As a result, response to interrupts may be slow or interrupt requests may be missed entirely. Real-time operating systems are designed to provide fast response to interrupt requests. An interrupt latency time is often given in the specifications for a real-time operating system. This is the maximum amount of time it will take the operating system to recognize an interrupt request and begin servicing it.

Another distinguishing feature of real-time operating systems, or executives, is that their command interpreters are usually rather simple and they do not include many utility programs. The goal of a real-time executive is usually to serve the system it controls rather than human users.

The centralized multitasking capability offered by a real-time executive is not always required. In very simple real-time systems the application program can often be configured as a combination of a main program which executes sequentially and a set of interrupt service routines which respond to external events. However, as the system gets more complex and additional processors are added, it becomes more difficult to coordinate the interactions between the interrupt service routines and the main program. At some point, some well-organized means of coordination is required and multitasking becomes a necessity. This is the case for almost all DoD/military applications.

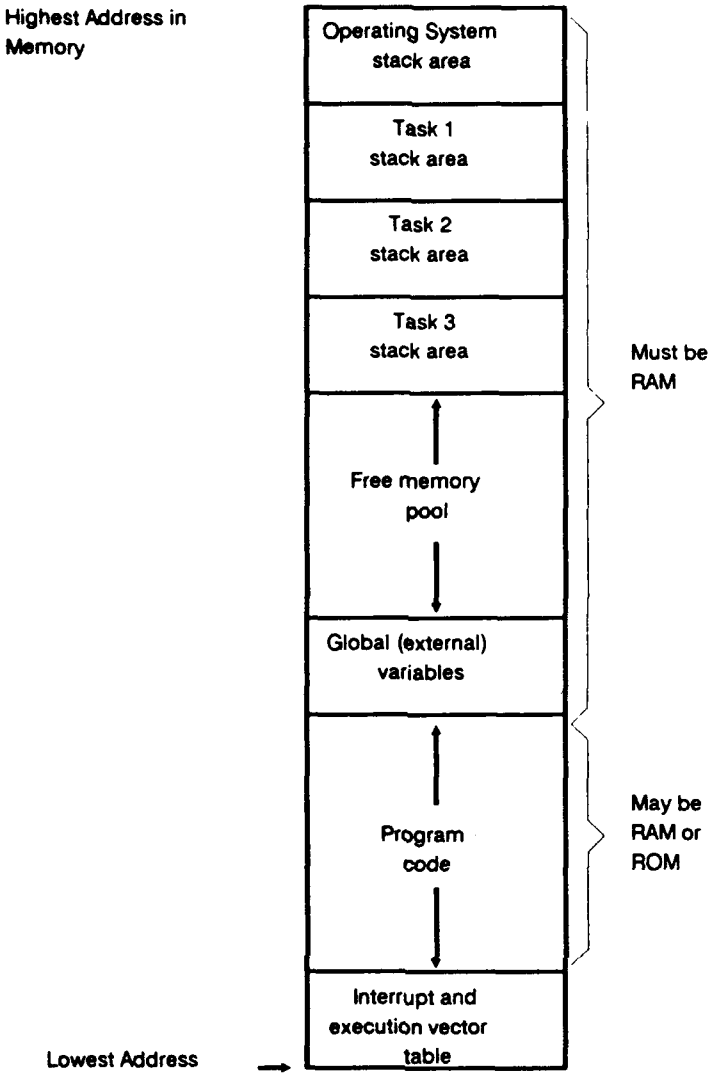


**Figure 2: Memory Map for a Multitasking System.**

A memory map for a multitasking system is shown in Figure 2. Each task and the operating system is assigned its own stack area in memory. This is used to store private data. A free memory pool is used by the operating system to create message channels or common data areas which allow tasks to exchange data. A certain number of global variables, accessible to all tasks and to the operating system, may also be required.

Two tasks can execute the same program but be distinct because they use different stack areas, message channels, and resources. For example, if a computer system contains three identical Analog/Digital (A/D) converters which provide input to the computer, three distinct tasks could be created to service the three devices. Each task will run the same code but will be assigned a different resource (A/D convertor), a different stack area, and a different message channel to transfer the incoming data to other tasks. The tasks will run independently (asynchronously) depending on when their A/D converter has data available. Since tasks can share program code, it is very important to use only reentrant programs in a real-time multitasking system.

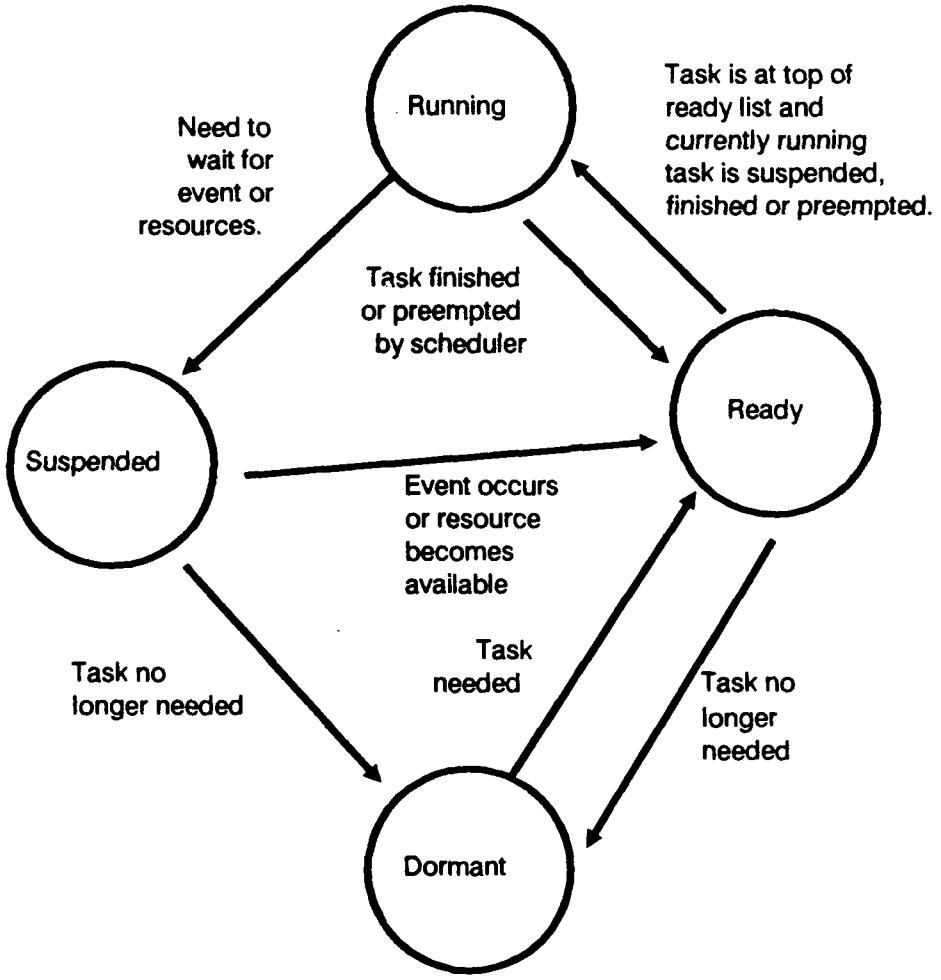


**Figure 3: Task State Transistion Diagram.**

Most real-time executives are designed so that a task can be in one of four states, as shown in the state transition diagram in Figure 3. If a task is in the running state, the computer is executing that task. If the task is ready to be executed but not actually executing, it is in the ready state. A task that is unable to execute because it is waiting for an event or a resource is in the suspended state or is said to be blocked. For instance, if a task is an interrupt service task, it must await the interrupt signal from the external device (an event) before it can execute. Similarly, a task which wishes to use a printer (a resource) may have to wait until another task has finished using the printer. Finally, if the task is not needed by the real-time system, it is in the dormant state.

The scheduler in a real-time operating system is responsible for controlling the transitions of the tasks among these states. The elements of a simple task scheduler are shown in Figure 4. The scheduler program receives interrupt requests from the computer's interrupt system. In addition, it receives messages from the running task in the form of system calls to the operating system. The scheduler maintains lists of ready, suspended, and dormant tasks. It also carries out the task switching function where the execution of the currently running task is stopped and a task on the ready list is started.

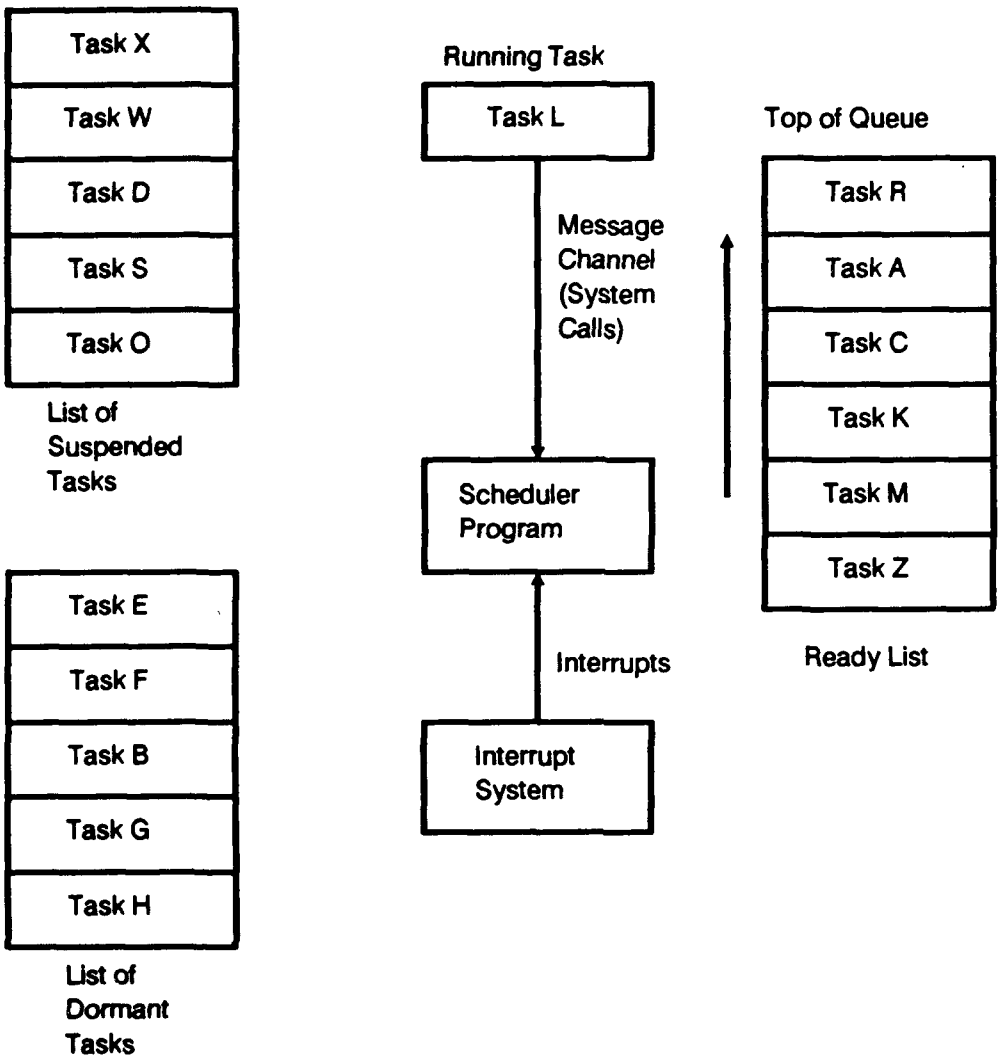


**Figure 4: Elements of a Task Scheduler.**

The scheduler's ability to control the execution of tasks is the key to the efficiency and speed of response of a real-time executive. A task which is waiting for an event to occur or a resource to become available does not execute and therefore does not take up any CPU time. When the event occurs or the resource becomes available (usually signaled by an interrupt or a message from the running task), the scheduler allows the task to continue execution. The amount of time that elapses between the occurence of an event and the execution of the task which was blocked on that event depends on the scheduling strategy used by the scheduler [6].

The actual scheduling method used to select the next task to run varies. In real-time operating systems, round-robin or priority-based preemptive scheduling techniques are typically implemented. In round-robin scheduling, all tasks have equal priority and the ready list is configured as a simple first-in-first-out (FIFO) queue. In priority-based preemptive scheduling, tasks are assigned different priorities. The highest priority task that is not in the suspended, or dormant, state is always running. In practice, a mixture of round-robin and priority-based scheduling is often used.

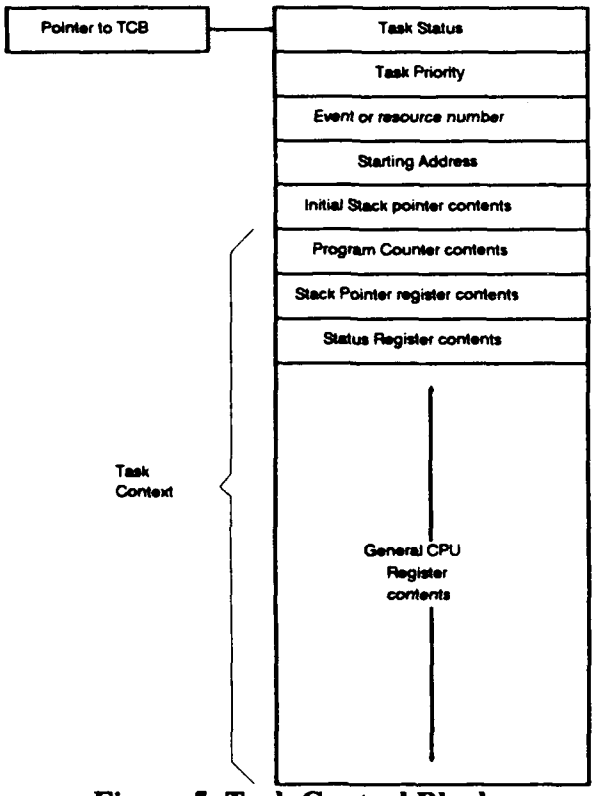


**Figure 5: Task Control Block.**

In order to carry out its scheduling functions, the scheduler makes use of task control blocks (TCB), or process descriptors. Each task is assigned one of these blocks, which is simply an array of data about the task. An example of a task control block is shown in Figure 5. The TCB contains data on the state of the task (i.e., dormant, suspended, ready, or running), the priority of the task, and events or resources for which the task is waiting. The starting address for the task's program code and the initial pointer value for the task's stack are also stored in the TCB. This information is used by the scheduler when a task is first activated and when a task is reactivated by moving it from the dormant to the ready state.

In addition, the task control block is used to store the task's context. The task context represents all the information that must be saved when the execution of a task is stopped and restored when task execution is resumed. In most real-time executives, this information is the contents of the computer's registers just prior to the moment when execution of the task was stopped. Note that this is the same information (the machine state) which must be saved and restored when the system responds to an interrupt.

In a simple system with more than one task, there is no inherent synchronization between the execution of tasks; each task executes independently. However, in most real-time systems, tasks must work closely together and may also have to perform their functions at defined times. Some synchronization mechanisms must be provided.

A common technique, used in real-time operating systems to synchronize two or more tasks, is to use the semaphore variable, s, and two system calls, Wait(s) and Signal(s), which act on the semaphore. A semaphore consists of a counter for signals that have not been received, and a queue for tasks that are waiting to receive the signals [6].

In addition, semaphores are used in the exchange of data between tasks. They prove quite useful in solving problems associated with the use of common data areas to transfer data between tasks. This process is also known as mutual-exclusion.

Most real-time operating systems provide a complete real-time clock facility. A task can make a system call to suspend itself for a time interval or until a certain time of day occurs. The scheduler suspends the task and places it back on the ready list only when the requested time interval has elapsed or the requested time of day has arrived. Thus, a task can ensure that it performs its functions at defined times [6].

To date, real-time executives have had their limitations. They must be custom designed for a given microprocessor. Therefore, the designer needs to choose a specific processor and hardware configuration before he/she can select an executive. Any executive chosen must meet certain performance criteria. It must be fast enough to allow the tasks under it to operate in real time. An executive's code should be small enough so that a large amount of program space does not have to be dedicated to it. Finally, the executive should not add a lot of unnecessary overhead to a task when that task needs to use executive utilities.

The ability to modify an executive can be important. Features can be modified or added to an executive as they are needed through the use of source code. Without the source code for an executive it is difficult, if not impossible, to alter it. Source code for some real-time executives cannot always be purchased. The cost of this code, when available, can easily cost up to $50,000 or more [7].

## MICOM CASE HISTORY

Traditionally, whenever efficient executive code was required by the application, the user developed in-house custom code, sometimes written in assembler language. The FOG-M gunner station code is an example of an in-house custom executive.

In 1982 the Research and Development Center (then known as Army Missile Laboratory), MICOM, began a technology demonstration program to prove out the use of fiber optic cable control in missiles. This successful program is now known by all in the MICOM community as the Fiber Optic Guided Missile (FOG-M) program. Personnel in the Guidance and Control organization were directly responsible for the computer hardware and software designs for FOG-M. The FOG-M multiprocessor configuration uses several microprocessors, communicating with each other on a common MultiBus. These processors are tightly coupled under software control to distribute the processor load. Since the hardware configuration contained global memory, this configuration was not distributed processing in the strictest since, but was a multiprocessing configuration.

At the initial development stage, the FOG-M computer software and hardware was the most complex multiprocessing architecture using the Intel 8086 family of processors in existence. This complexity was mandated by the complex functions required of the system. Due to this complexity the software had to be very efficient, thus the choice of a higher order language to develop the code, was a critical design decision. Since the requirements of the Gunner Station software dictated the software operate under a multitasking software architecture, engineers began looking at commercial off the shelf software to fulfill the needs of a real time executive.

After several trade studies were completed, an initial design choice was made. After the initial code development, debug and testing were completed, it was determined that this commercial real time executive was not suitable for the speeds required of the software (e.g.; trigonometric functions were derived by table lookup versus a math coprocessor because of the timing constraints.) Engineers working on the FOG-M software program began studying the feasibility of developing a custom in-house executive which met the needs of the FOG-M program, and only the FOG-M program.

As a result, a minimal executive was developed which contained specific functions required for the executive (i.e.; task scheduler, interrupt handler, global memory handler, exception handler, etc.). This executive was not contained in a single section of program code, but was distributed around the software as the need arose. Since the code was developed for the specific application, it is highly unlikely much of the code could be used in applications other than follow on work to FOG-M using the same processor family.

Although the FOG-M program was a success on most every front, the above example illustrates the way real time executives have been developed and used at MICOM in the past. Individual software developers "re-invent the wheel" each time an executive is needed for an application. With the primary push for software reusability in the Ada programming language, the software developers within the G&C Directorate realized that this programming practice must end. The development of RTEMS is an attempt to alleviate this redevelopment cycle.

## STANDARDS

The advent of Ada has created the need for efficient Ada-based development tools to augment the standard Ada runtime environment. This support must provide for efficient and flexible concurrent program execution that meets demanding real-time constraints. As we move from single to tightly-coupled to loosely-coupled multiple-CPU architectures, this support must be standardized to the extent practical. (Tightly-coupled system are generally characterized by the ability to communicate over a backplane. Loosely-coupled systems generally use some external communications media such as RS232 or network connection.) Existing Ada compiler runtime systems do not meet these needs.

Many real-time embedded computer systems require efficient, deterministic, and adaptable software concurrency, communication, and synchronization support. This support is needed for single processor systems and for distributed computer systems. The tasking model in Ada provides for concurrency, com-

munication, and synchronization and applies in principle to all computer architectures and applications. However, existing Ada compilers and their runtime support do not meet industry demands for efficiency, determinism, and adaptability in real-time embedded applications, and Ada implementations for distributed targets are only now becoming available.

The Ada language addresses a large application domain and offers many design features needed to promote reliable software; however, its intrinsic capability has not as yet been implemented with the efficiency and adaptability required to support many real-time computer system requirements. The need is the same for other languages used in real-time applications, but the power and formality of Ada dictate special emphasis on well-engineered execution environments that are integrated with Ada compilers.

Runtime support must be provided that allows embedded computer systems to be implemented with inherent runtime efficiency and with designed-in determinism. And, to increase reliability and reduce development cost and schedules, implementors must be able to tailor proven, available runtime support capabilities to their specific program needs. The Ada standard does not preclude any of those needs, nor does it overtly support them. Available implementations of the Ada tasking model do not meet either efficiency or determinism needs, and compiler vendor products and third-party products do not meet the system tailoring requirements of many DoD systems.

We have established that the run time executives being delivered with the Ada compilers are too slow and inefficient to be used in the increasingly complex modern missile systems of today. This code is purchased from compiler vendors who are not in the business of writing and properly testing and debugging real-time executive code. Indeed, their primary concern is in providing the customer (the Government) with a good compiler. The real-time executive is included as part of the run time environment in order to satisfy the underlying requirements of a run time support system and to attempt to overcome some of the shortfalls of the Ada programming language.

To date, software developers are purchasing and utilizing specialized third party kernel code. Problems imposed from purchasing third party kernel (executive) code is that the contractor, and eventually the Government, must pay a licensing (royality) fee for every copy of the kernel code used in an embedded system. This concept is similar to purchasing multiple copies of word processing software. In both cases, the original manufacturer of the software is the sole owner, while the end user pays a licensing fee for the right to use the code in a system design. This obligates the government on a per copy basis, every time the code is being utilized.

Another drawback to this development scenario is that the Government does not own, nor has the right to modify any code contained within the kernel. Techniques for Validation and Verification (V&V) of software in this situation are more difficult than if the complete source code were available. Most commercially available real-time executive manufacturers do not offer source code to the licensee. If they do, it is usually very expensive. Responsibility for system failures due to faulty software is yet another area to be resolved under this en-

vironment. The vendor will not accept any responsibility for a failure of any system containing its' code.

Typically, real-time software has been ignored by standardization and software engineering groups. Each system is almost an original, free-form expression of the development team. Unfortunately, real-time design is still in its infancy. This results in schedule overruns and maintenance problems. As a result, the cost of software continues to accelerate, even as the cost of hardware continues to decline [8].

To meet these challenges, the software industry must develop new and better tools for the design, analysis, development, and verification of real-time systems. Although research is constantly advancing the techniques of software development, the benefits of this research often take time to become available to the real-time software development community. As the results of real-time operating system research become accessible, the number of real-time operating systems and executives available to software developers will continue to grow. This fact makes it imperative that system developers recognize the common features and capabilities required to provide the needed support environment and incorporate them into an industry standard interface environment. This standard interface should allow the software developer to concentrate on the hardware dependencies and unique requirements of the application system being developed instead of learning to use yet another real-time executive.

## RTEID

One such standard interface, the Real Time Executive Interface Definition (RTEID) has been developed by Motorola, Inc. with technical input from Software Components Group. It has been submitted to the VMEbus International Trade Association (VITA) for adoption as a standard multiprocessor, real-time executive interface. RTEID defines a standard interface for the development of real-time software to facilitate the writing of real-time applications programs that are directly portable across multiple real-time executive implementations. This interface includes both the source code user interface and the run-time behavior as seen by a real-time application. It does not include the details of how a kernel implements these functions. Simply stated, the RTEID goal is to serve as a complete definition of external interfaces so that application code which conforms to these interfaces will execute properly in all real-time executive environments. With the use of an RTEID compliant executive, routines that acquire memory blocks, create and manage message queues, establish and use semaphores, and send and receive signals need not be redeveloped for a different real-time environment as long as the new environment is also RTEID compliant. Programmers need only concentrate on the hardware dependencies of the real-time system. Furthermore, most hardware dependencies for real-time applications can be localized to the device drivers [9,10].

An RTEID compliant executive provides simple and flexible real-time embedded multiprocessing. It easily lends itself to both tightly-coupled and loosely-coupled configurations (depending on the system hardware configuration). Both forms of multiprocessing, tightly-coupled and loosely-coupled, have unique advantages, disadvantages, and suitability for a specific application. RTEID does not favor one form over the other, but leaves this decision to the developer of an

RTEID compliant executive. Objects such as tasks, queues, events, signals, semaphores, and memory blocks can be designated as global objects and accessed by any task regardless on which processors the object and the accessing task reside. Each object may exist on a single processor configuration; or in a multiprocessor system. The system is defined as the collection of interconnected processors; including processors connected by network or other communications media [9].

## RTEMS

The Guidance and Control Directorate began a software development effort in 1989 to alleviate many of the problems discussed in this paper. A project to develop an experimental run time kernel was begun that will eliminate the two major drawbacks of the Ada programming language mentioned previously: that the Ada programming language does not fully support multiprocessing and that the run time executives being delivered with the Ada compilers are too slow and inefficient to be used in modern missile systems. The Real Time Executive for Missile Systems (RTEMS) is an implementation based on Draft 2.1 of the RTEID specification. RTEMS provides full capabilities for task management, interrupt management, time management, multiprocessing, and other managers typical of generic operating systems. The code will be Government owned, so no licensing fees need be paid. The executive was designed as a linkable, ROMable library with the Ada programming language. Initially the library code is being developed on the Motorola 68000 family of processors using the 'C' programming language as the development language. The 'C' programming language was chosen because of its portability and efficiency. However, other language and processor family interfaces are planned in the future.

The final RTEMS product will be capable of handling either homogeneous (processors of the same family type) or heterogeneous systems. The kernel will automatically compensate for architectural differences (byte swapping, etc.) between processors. This will allow a much easier transition from one processor family to another without a major system redesign.

RTEMS was designed to fulfill three fundamental design objectives: performance, reliability, and ease of integration. It provides a multitasking environment for single or multiprocessor real-time application systems. The RTEMS executive was developed by contractors for MICOM to perform research for multiprocessor based weapons systems. RTEMS is currently implemented on the Motorola MC68020 microprocessor [10].

The RTEMS executive provides a high performance real-time environment which include the following features: [10,11]

- *multitasking capabilities*
- *event-driven, priority-based, preemptive scheduling*
- *intertask communication*
- *semaphore, signal, and event synchronization mechanisms*
- *dynamic memory allocation*

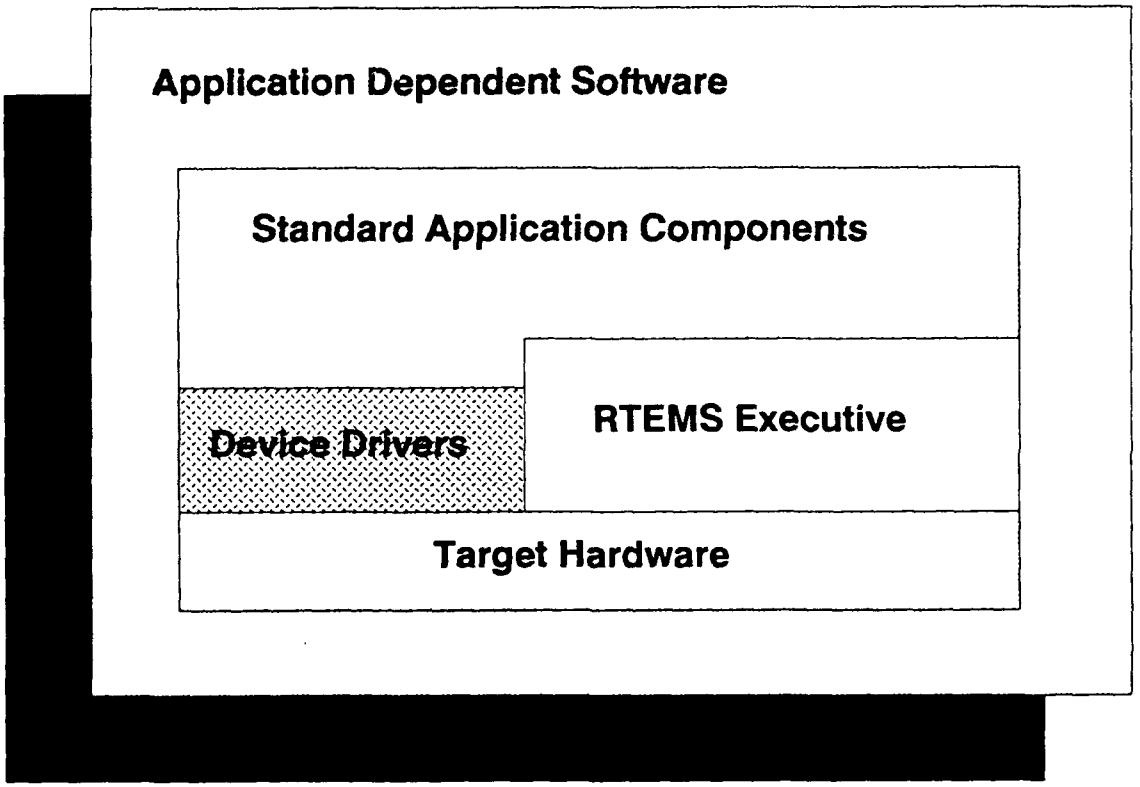


**Figure 6: Real-Time System Architecture.**

- *real-time clock management*
- *user-specified configurations*
- *user-extendable directives*

These features provide a robust set of cabability that allow system designers the flexibility to efficiently and cost effectively solve the complex problems associated wtih real-time systems.

Another important design goal of the RTEMS executive was to provide a bridge between two critical layers of typical real-time systems. It serves as a buffer between the project dependent application code and the target hardware. Standard software routines that acquire memory blocks, create and manage message queues, establish and use semaphores, and send and receive signals need not be redeveloped for a different real-time environment as long as the new environment is RTEMS/RTEID compliant. RTEMS provides efficient tools for incorporating these hardware dependencies into the system while simultaneously providing a general mechanism to the application code required to access them. A well designed real-time system, such as RTEMS should maximize these two concepts to build a rich library of standard application components which can be used repeatedly in other real-time projects [9,10,11].

The executive can be viewed as a set of components that work in harmony to provide a collection of services to a real-time application system. These com-

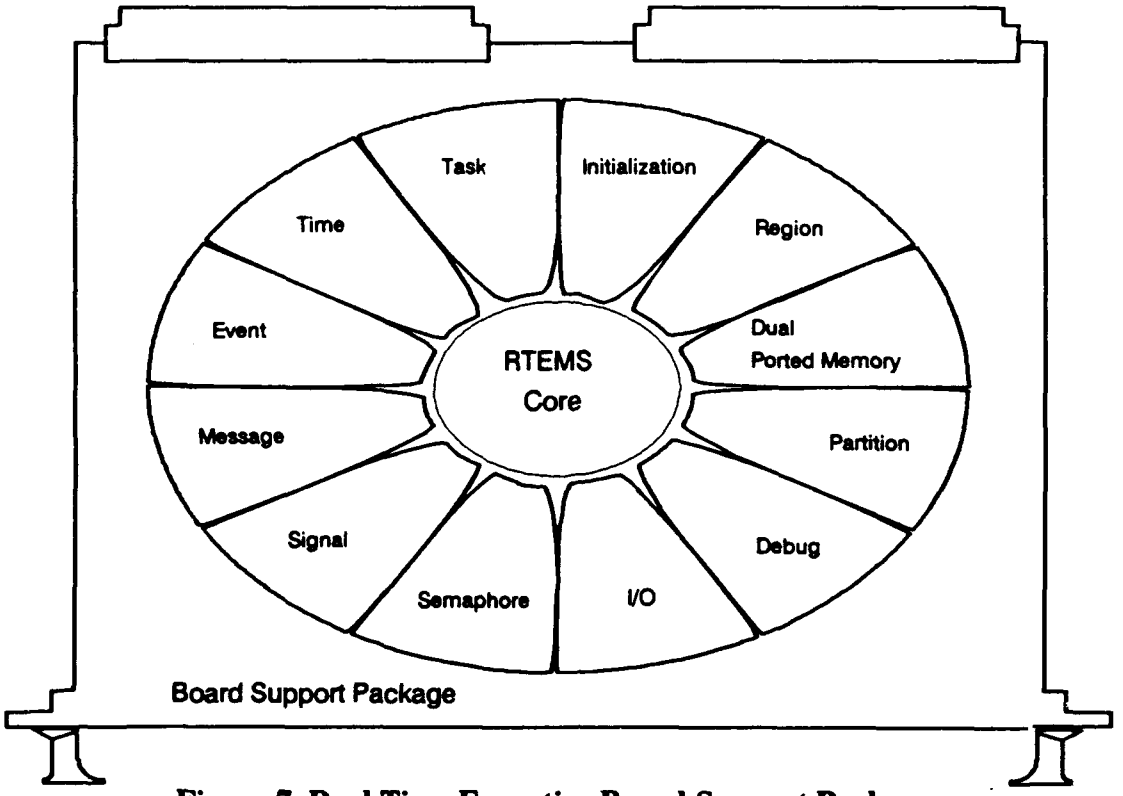


**Figure 7: Real Time Executive Board Support Package.**

ponents consist of a board support package, an executive core and a set of resource managers. Figure 7 shows this concept.

RTEMS makes minimal assumptions about its hardware environment. It does not depend on any particular implementation of interrupts, timers, buses, or I/O devices. This concept is necessary to allow the executive to be truly portable. To achieve this portability, the user must supply a small amount of code to interface RTEMS to those aspects of the surrounding hardware that it needs to know about. The **board support package** is a single piece of code that sets up the environment and controls the initialization process for the remainder of the software.

In every executive there exists a set of basic functions that must be performed, but do not naturally align themselves with any of the logical sets or groups of directives. Such things as scheduling, error processing, and data structure manipulation are very critical to insure the proper functioning of a real-time executive. The RTEMS design groups these functions together forming a component called the **executive core**.

The RTEMS core consists of the following components:

- *scheduler*
- *dispatcher*
- *chain handler*

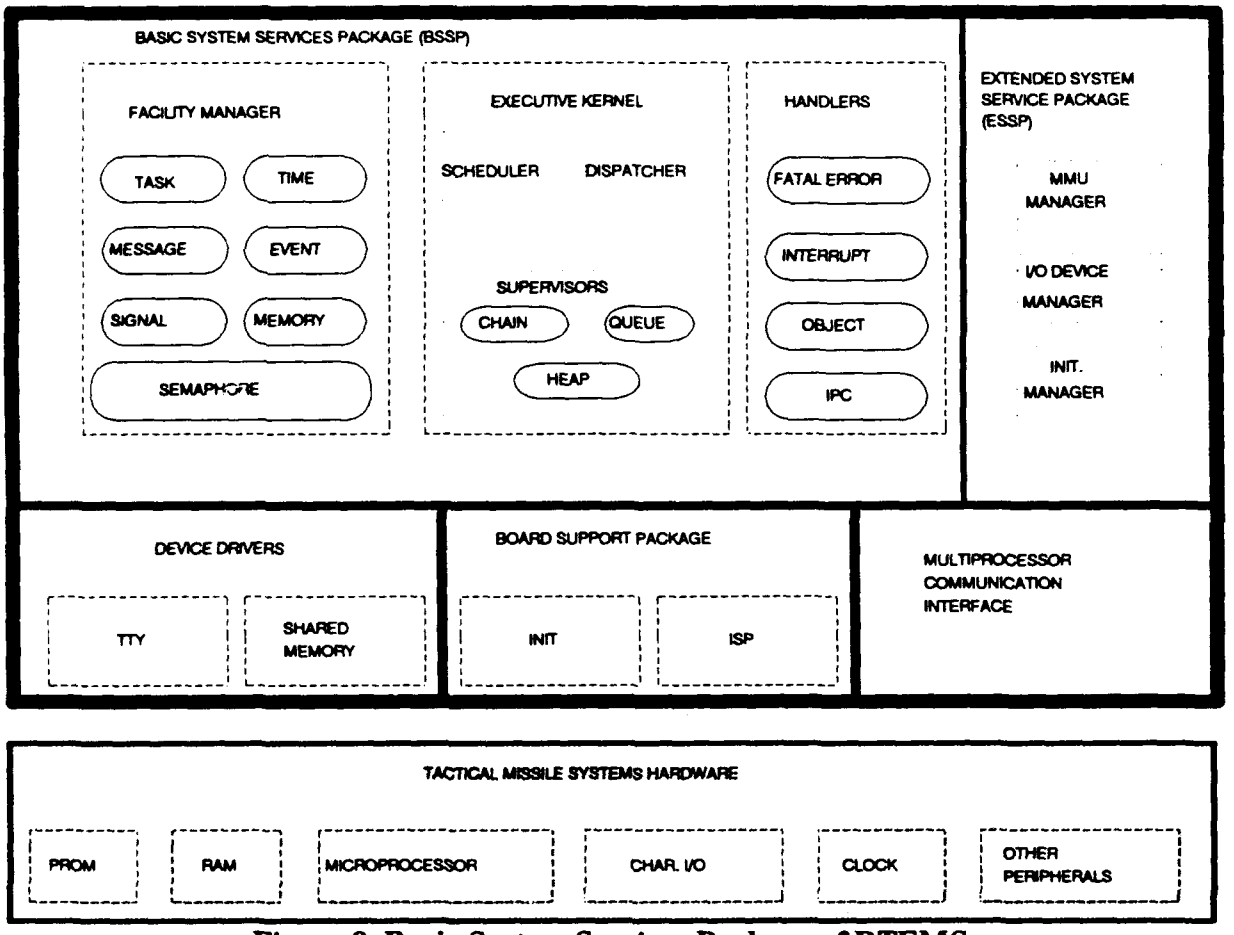


**Figure 8: Basic System Services Package of RTEMS.**

- *queue handler*
- *heap handler*
- *utilities*

Although no requirement exists for the RTEMS user to understand the details of the executive's implementation, it is important to be familiar with the basic concepts and algorithms used to control the real-time environment.

The RTEMS interface presented to the application is formed by grouping the RTEID specified directives into logical sets called **resource managers**. Together these components provide a powerful run time environment that promotes the development of efficient real-time application systems.

The following managers are included in an RTEMS compliant executive:

- *task manager*
- *message manager*
- *event manager*

- *signal manager*
- *semaphore manager*
- *time manager*
- *interrupt handler*
- *fatal error handler*
- *region manager*
- *partition manager*
- *initialization manager*
- *dual ported RAM manager*
- *I/O manager*
- *debug manager*

The **task manager** provides control features that act upon a task or a set of tasks as defined by the eleven task manager directives specified by the RTEID specification. A task is simply a sequence of closely related computations. A task may execute concurrently with or independent of other tasks.

In real-time multitasking applications, the ability for cooperating tasks/Interrupt Service Routines (ISRs) to communicate and synchronize with each other is imperative. A real-time executive should provide an application with the following capabilities:

- *Data transfer between cooperating tasks*
- *Data transfer between tasks and ISRs*
- *Synchronization of cooperating tasks*
- *Synchronization or tasks and ISRs*

RTEMS provides for communication and synchronization between tasks and between tasks and ISRs with the message, event, signal, and semaphore managers. The **message manager** supports one type of inter-task communication and synchronization as defined by the seven message manager RTEID directives. The message manager supports communication and synchronization between multiple tasks as well as tasks and ISRs using a basic support mechanism called a message queue. Messages are defined to be fixed length (16 bytes) blocks of information. The **event manager** provides a second, higher performance method of inter-task communication and synchronization as defined by the two event manager directives. The event manager will support communication and synchronization using a basic support mechanism called an event set. Event sets may only be directed at other tasks instead of queues. Events are defined to be bits encoded into an event mask. The **signal manager** supports a third type of inter-task communication and synchronization as defined by the three signal manager directives. The signal manager provides directives that allow asynchronous communication between tasks. The **semaphore manager**

supports a type of inter-task synchronization as defined by the five semaphore manager directives. These directives provide the ability to arbitrate access to a shared resource.

The **time manager** provides timing features based on both calendar and elapsed time as defined by the eight time manager directives. This manager requires a periodic timer interrupt to perform its required functions. The board support package will inform this manager that a clock tick has occured.

The **interrupt handler** provides the ability to preempt from an interrupt service routine while still maintaining a fast interrupt response and satisfies the basic design goals to provide a zero latency time to enter an interrupt and to insure that the highest priority ready task always executes. The **fatal error handler** also provides the ability to preempt from an interrupt service routine while still maintaining a fast interrupt response. Fatal errors can be detected from three sources: the executive (RTEMS), user system code, or user application code.

RTEMS provides two types of memory management: region management and partition management. The **region manager** deals with the allocation and deallocation of variable size segments in a specified region. Whereas, the **partition manager** deals with the allocation and deallocation of fixed (equal) size buffers in a specified partition.

The RTEID specification allows executive developers to define their own initialization mechanism. The RTEMS **initialization manager** provides for the initialization of RTEMS and the initiation of multitasking.

The **dual ported memory manager** provides a mechanism for converting addresses from internal to external representations. Dual ported memory can be accessed at two different address ranges. Typically, one of these ranges, the internal addresses, is used exclusively by the node which owns the memory. All other nodes in the system must use the external addresses to access the memory.

The **I/O device manager** provides a standard interface for accessing device drivers. This standard interface encourages the development of well-structured RTEID compliant device drivers.

The **debug manager** provides an interface between the executive and a debugger. This allows the development of debuggers that work efficiently and correctly with any implementation of an RTEID compliant executive. The debug manager provides three groups of features for: debugging tasks, debugging entire systems, and monitoring a running system.

To realize the goal of hardware independence, RTEMS makes no assumptions about the physical media connecting the nodes, or the topology of the connection. To perform interprocessor communication, RTEMS calls a user provided communication layer known as the Multiprocessor Communications Interface (MPCI). This MPCI routines enable the nodes in a multiprocessor system to communicate with one another.

**Remote procedure calls** (RPC) are used in RTEMS to transcend the physical boundaries of the set of processors included in the system. Conceptually an RPC can be viewed as a simple call to a procedure. The called procedure just happens to reside on another processor.

The software developer uses the set of directives provided by RTEMS to be free from the problems of controlling and synchronizing multiple tasks and processors. This freedom allows the programmer to concentrate all creative efforts on the application system.

The system calls, including optional managers provided by the executive are shown in the following figure [10,11].

| | |
|---|---|
| **Task Manager** | |
| t_create | Create a task |
| t_ident | Get id of task |
| t_start | Start a task |
| t_restart | Restart a task |
| t_delete | Delete a task |
| t_suspend | Suspend a task |
| t_resume | Resume a task |
| t_setpri | Set task priority |
| t_mode | Change task mode |
| t_getreg | Get value in tasks's register |
| t_setreg | Set task's register to value |
| **Message Manager** | |
| q_create | Create a message queue |
| q_ident | Get id of message queue |
| q_delete | Delete a message queue |
| q_send | Send message to message queue |
| q_urgent | Put message at front of message queue |
| q_broadcast | Broadcast N messages to queue |
| q_receive | Receive message from message queue |
| **Event Manager** | |
| ev_send | Send an event to a task |
| ev_receive | Receive an event |
| **Signal Manager** | |
| as_catch | Establish ASR |
| as_send | Send a signal to a task |
| as_return | Return from ASR |
| **Semaphore Manager** | |
| sm_create | Create a semaphore |
| sm_ident | Get id of semaphore |
| sm_delete | Delete a semaphore |
| sm_p | Get a semaphore |
| sm_v | Release a semaphore |
| **Time Manager** | |
| tm_set | Set system date and time |
| tm_get | Get system date and time |
| tm_wkafter | Wake up after specified interval |
| tm_wkwhen | Wake up at specified date and time |
| tm_evafter | Send event after specified interval |
| tm_evwhen | Send event at specified date and time |
| tm_cancel | Cancel timer event |
| tm_tick | Announce clock tick |
| **Interrupt Processing** | |
| i_return | Return (exit) from interrupt |
| **Fatal Error Processing** | |
| k_fatal | Invoke the fatal error handler |
| **Region Manager** | |
| rn_create | Create a region |
| rn_ident | Get id of region |
| rn_delete | Delete region |
| rn_getseg | Get segment from region |
| rn_retseg | Return segment from region |
| **Partition Manager** | |
| pt_create | Create a partition |
| pt_ident | Get id of partition |
| pt_delete | Delete a partition |
| pt_getbuf | Get buffer from partition |
| pt_retbuf | Retrun buffer to partition |
| **Initialization Manager** | |
| ex_init | Initialize RTEMS |
| ex_start | Initiate multasking |
| **Dual Ported RAM Manager** | |
| m_ext2int | Convert external address to internal address |
| *m_int2ext* | *Convert internal address to external address* |
| **I/O Manager** | |
| de_init | Initialize device driver |
| de_open | Open device for I/O |
| de_close | Close device |
| de_read | Read from device |
| de_wrtie | Write to device |
| de_cntrl | Special device services |
| **Debug Manager** | |
| db_control | Control a task |
| db_remote | Perform directive on remote cpu |
| db_block | Prevent a task from running |
| db_unblock | Run a task under control |
| db_getmem | Get a task's memory |
| db_setmem | Set a task's memory |
| db_getreg | Get a task's register |
| db_setreg | Set a task's register |
| db_system | Control a system |
| db_level | Set minimum proecssor mask level |
| db_get_id | Get identifier for an item |
| db_get_item | Get information about an item |
| **MPCI** | |
| mc_init | Initialize the MPCI |
| mc_getpkt | Obtain a packet buffer |
| mc_retpkt | Return a packet buffer |
| mc_send | Send a packet to another node |
| mc_broadcast | Send a packet to all other nodes |
| mc_receive | Called to get an arrived packet |

**Figure 9: RTEMS Directives.**

## CONCLUSION

The primary purpose of this paper is to summarize the impacts of Ada software development on current MICOM software development philosophies. The limitations of Ada in a distributed processing architecture and what the software development community was doing to complement the shortfalls of Ada was discussed. A brief discussion was given outlining how real-time software development is accomplished on Army missile systems. A detailed explanation of real-time executives in general was provided to give the reader an idea of the complexity of the task involved with developing an environment where Ada could be used in real-time systems. An example was then described showing how embedded computer software has been developed in the past at MICOM.

Many of the same events that lead to the development of the Ada programming language are also the same events that are mandating the development of a standardized real-time executive such as RTEMS. The need for developing a standard executive for use in embedded missile systems was then described. The Real Time Executive Interface Definition (RTEID) was introduced as the first attempt to develop a standard executive. And finally, the Real Time Executive for Missile Systems (RTEMS) was described as the MICOM solution for all the Ada shortfalls and standardization thrusts described in the previous sections.

It is hoped that this paper will spawn interests in real-time executives and standardization within the Army community.

## REFERENCES


[1] J.G.P. Barnes. Programming in Ada. Addison-Wesley Publishing Company. London, England. 1984.

[2] David Naiditch. Rendezvous With Ada: A Programmers Introduction. John Wiley & Sons. New York, NY. 1989.

[3] Stephen J. Young. An Introduction to Ada. Ellis Horwood Limited. Halsted Press. New York, NY. 1983.

[4] Narain Gehani. Ada: An Advanced Introduction. Prentice-Hall, Inc. Englewood Cliffs, NJ. 1983.

[5] Ready Systems, RTAda Real-Time Ada User's Guide for VAX/VMS-to-68020. Ready Systems. Sunnyvale, CA. 1989.

[6] Peter D. Lawrence and Konrad Mauch. Real-Time Microcomputer System Design: An Introduction. pages 482-489. McGraw-Hill Book Company. 1987.

[7] Gary Elfring. A Guide to Real-Time Executives. Computer Language. pages 65-70. June 1986.

[8] Transforming Software Design, From Art into Science. Software Components Group. Santa Clara, CA.

[9] R. Vanderlin, P. Raynoha, B. Hansche, and L. Dion, "RTIED: The Quest for Real Time Standards." Motorola Microcomputer Division. Tempe, AZ.

[10] RTEMS-68020/C User's Manual. G&C Internal Report. Redstone Arsenal, AL.

[11] Real Time Executive Interface Definitiaon, Motorola Microcomputer Division. Tempe, AZ. 22 January 1988.

- SESSION IV -

STRUCTURES

# AEROTHERMAL AND MATERIALS TESTING UTILIZING HYPERVELOCITY SLEDS

by R. W. Nourse, C. D. Perry,
and R. A. Reynolds
Structures Directorate
Research, Development, and Engineering Center
U. S. Army Missile Command

## ABSTRACT

The sled facility at Holloman Air Force Base, New Mexico, was utilized by MICOM to perform hypervelocity materials ablation tests and hypersonic aerothermal tests. Three Mach 5.5 sled tests were run to identify medium temperature ablative materials which can be used as thermal protection on current and future Army missile systems. Over 150 material candidates were screened using a plasma arc jet facility and 18 were were tested on the sleds. The heats of ablation vs. effective ablation temperature were determined and several materials recommended for further testing. Two hypersonic sled tests were performed to evaluate heating augmentation levels in the vicinity of simulated jet thruster ports or cavities on hypersonic missiles. Heating augmentation factors were measured and correlated with results from several analytical models. Models and treatment of the local flow fields were recommended for future predictions.

## INTRODUCTION

The primary mission of the Research, Development, and Engineering Center at MICOM is to perform applied research in support of the development of advanced missile systems. In the area of aerothermodynamics and heat transfer, the sled facility at Holloman Air Force Base, New Mexico, has been an invaluable tool in support of this type of research. As modern missile systems attain higher velocities at lower altitudes, the aerodynamic heating of missile structures becomes very severe. The hypersonic sled facility provides a unique capability to reproduce aerothermal environments associated with actual hypervelocity flight.

With this in mind, two test programs have recently been performed utilizing the sled facility. The first program, Hypervelocity Ablative Materials Tests, identified, tested, and

evaluated candidate materials for use as external thermal protection on hypervelocity missile systems. The second program, Thermal Augmentation Tests, evaluated the heating effects associated with the separation and reattachment of shear layers in the vicinity of cavities and ports. This paper summarizes the objectives, approach, and results of both of these test programs.

## HYPERVELOCITY ABLATIVE MATERIALS TESTS

### BACKGROUND

Missiles which fly at velocities exceeding Mach 3 require some form of thermal protection to insulate the load-bearing structures from high temperatures caused by the aerothermal heating effects. Materials such as Duroid, slip cast fused silica, quartz phenolic, and silica phenolic have been extensively studied and their aerothermal and erosion properties characterized. However, many medium-temperature ablators which are inexpensive and easily applied have not been studied or characterized. To be used in thermal protection schemes these materials should:

(1) be easily and quickly obtainable at reasonable cost,

(2) be easily and quickly applied and formed, preferably in-house,

(3). have effective ablation temperatures between 450 and 1088 K (350 and 1500 $^{o}$F),

(4) have known thermal properties, so their performance can be accurately predicted with confidence, and

(5) have densities less than 1360 kg/m$^3$ (85 lb/ft$^3$)

To fill this need and identify suitable medium-temperature ablators, a test program was developed and performed by the Structures Directorate, Research, Development, and Engineering Center, U.S. Army Missile Command, Redstone Arsenal, Alabama. This program consisted of an initial screening process using an 80kW plasma arc-jet at the Structures Directorate [1] and a more formal test process using the sled-track facility at Holloman Air Force Base, New Mexico [2,3]. The initial screening process identified potential candidates to be tested more completely and accurately using the sled facility. The sled tests provided a

means of correlating ablation depths with an aero-heating environment in the range of interest. This in turn allows the determination of an empirical relationship between heat of ablation and effective ablation temperature for each material tested.

## PLASMA TEST BED

The test bed [4] consists of a Metco 80kW dc power supply with type 7MC control unit which controls the gas flow rates, power levels and cooling water flow to the plasma gun. The gun is a Metco type 7MB. A shielded, cold wall calorimeter was used to measure and calibrate the heat flux impinging on the sample. The plasma gun was mounted in a fixture and the impingement angle set at 45 degrees. The gun-to-sample distance was set by adjusting the test bed and then clamping the test bed down using small mounting brackets. The optimum gun-to sample distance for these tests was found to be 31.75 mm (1.25 inches). The calorimeter and sample are mounted on a movable carriage. A piston slides the sample into the plasma stream for a predetermined amount of time and then slides the calorimeter back into the stream. The heat flux is then rechecked. Figure 1 shows the test bed and a sample in the plasma stream. Table I gives the standard operating conditions for the tests.

Table I. Plasma Operating Conditions

| | |
|---|---|
| Heat Flux | 2930 kcal/$m^2$-hr-K<br>(600 Btu/$ft^2$-sec-°F |
| Nozzle-to-sample distance | 31.75 mm<br>(1.25 inches) |
| Impingement angle | 45 degrees |
| Test duration | 5 seconds |
| Plasma gas | Nitrogen |

The materials were selected based on the requirements previously stated, and were obtained from commercial sources and by in-house formulations. The sample configuration used in these tests is illustrated in Figure 2. The materials were applied to the substrates and cured at room temperature. The coating thickess was 6.35 mm (0.25 inch). After the samples were completely cured, each sample was weighed, then measured with a point thickness gauge. The samples were tested at the conditions stated previously, unless otherwise noted, and the percent weight loss and erosion rate were calculated.

Of the 150 materials screened using the plasma arc-jet, the materials listed in Table II were identified as the more promising performers to be more thoroughly tested by the sled.

Table II. Materials Selected for Sled Testing

| Material | Description |
|---|---|
| Duroid 5667MAZ | ceramic fiber-reinforced teflon |
| Chartek 3 | fiber-reinforced intumescent-epoxy |
| Chartek 59 | fiber-reinforced intumescent-epoxy |
| Avco 8039CX | epoxy-polyimide w/5 percent cabosil |
| DC 93-104 | organo-silica elastomer |
| FMI 705 | ceramic fiber-reinforced polyimide |
| FMI 605 | ceramic fiber-reinforced polyimide |
| FMI CYC 5520.0 | epoxy-urethane w/7 percent cabosil |
| FMI CY 5520.0 | epoxy-urethane |
| FMI CZ 553.2 | epoxy-urethane |
| FMI CZ 3714.3 | epoxy-urethane w/3.2 percent quartz |
| FMI CT 7314.3 | epoxy-urethane |

It should be noted that the Duroid samples are included in all tests and analyses as a reference standard since it has been extensively tested in the past [5,6,7] and it's performance paramaters are well known.

## SLED TESTS

Test Facility. The sled tests were performed at the rocket sled track facility at Holloman Air Force Base, New Mexico [2,3]. The test vehicle was bolted to a two-stage sled system as shown in Figure 3. The rocket motors and stagings were selected such that peak velocities of approximately 1890 m/sec (6200 ft/sec) could be obtained. A series of three sled tests have been performed. The first sled of the series was not recovered and all data was lost; therefore only the results of Tests 2 and 3 [9] are presented.

Test Hardware. The MICOM seven-sting sled test vehicle, shown in Figure 4 was originally designed [6] for testing candidate radome materials on sleds at velocities up to 1980 m/sec (6500 ft/sec). For this series of tests, the test vehicle was used for evaluating candidate ablation materials. This vehicle permits the testing of cone frusta with different

semi-vertex angles on the same sled. The semi-vertex angles for the tests were limited to 15 and 22.5 degrees. The cone frusta have been designed to allow the testing of two samples per cone at each position, which allows a maximum of 14 samples to be tested on each sled run. Sketches of these cone frusta are shown in Figures 5 and 6. Sample thicknesses are measured before and after a test, giving an accurate measure of total depth ablated.

Aerothermal Test Environment. In order to evaluate ablation performance for these materials, it is necessary to determine the aero-heating environment, or test conditions. For the sake of simplicity and comparison, the aerothermal environments are presented with respect to the Duroid reference samples. The velocity profiles measured during Tests 2 and 3 are given in Figure 7. This figure shows that the peak velocity during Test 2 was approximately 1890 m/sec (6200 ft/sec) and for Test 3 was about 1920 m/sec (6300 ft/sec). The altitude was a constant 1219 m (4000 ft). These parameters allow one to calculate the recovery temperature, $T_r$, given in Figure 8 and the heat transfer coefficient, h, given in Figure 9 for Test 2. The peak recovery temperature was approximately 1672 K (2550 °F) and the maximHx local heat transfer coefficient was 6592 kcal/$m^2$-hr-K (1350 Btu/$ft^2$-hr-°F). These form the boundary conditions for the analyses and indicate the hot-wall heating rate, q, to the test cones:

$$q = h(T_r - T_s) \qquad (1)$$

where $T_s$ the heated surface temperature. During the interval where ablation occurs, the surface temperature of the Duroid reference sample was assumed to be represented by an effective ablation temperature, $T_m$, of 950 K (1250 °F). The maximum hot-wall heating rate for Test 2 was 1302 kcal/$m^2$-sec (480 Btu/$ft^2$-sec) as indicated in Figure 10. The $T_r$, h and q for Test 3 are approximately the same as those for Test 2 and are therefore omitted from this discussion.

Test Measurements. Tables IIIa and IIIb rank the tested materials from Tests 2 and 3 [9] according to ablation performance. Included in the table are typical measured surface recession depths, char-layer thicknesses (where applicable), and total ablation depths. Ablation depths were measured as the depth from the original, pre-test surface to the outer bounds of the virgin material (char layer scraped away). Examination of both the recovered test samples and the results given in

Tables IIIa and IIIb indicates Chartek 3 and 59 were the best performers of the group, other than the reference material (Duroid).

Table IIIa. Recession/Char/Ablation Depths Measured from Test 2

| Material | Surface Recession (mm) | Char Thickness (mm) | Total Ablation Depth (mm) |
|---|---|---|---|
| Duroid 5667MAZ | 0.584 | ----- | 0.584 |
| Chartek 3 | 1.016 | 0.508 | 1.524 |
| Chartek 59 | 1.092 | 0.635 | 1.727 |
| Avco 8039CX | 2.540 | ----- | 2.540 |
| DC 93-104 | 1.778 | 0.889 | 2.667 |
| FMI 705 | 2.540 | 1.397 | 3.937 |
| FMI 705 with Kaowool | 3.048 | 1.524 | 4.572 |
| Avco Resin with Kaowool | 4.572 | ----- | 4.572 |
| FMI 605 | partially removed (approx. 5.334 mm) | | |
| FMI 605 with Kaowool | partially removed (approx. 5.080 mm) | | |
| Korotherm 821 | completely removed (approx. 5.334 mm) | | |
| Epoxy Resin | Completely removed (approx. 6.350 mm) | | |

Table IIIb. Recession/Char/Ablation Depths Measured From Test 3

| Material | Surface Recession (mm) | Char Thickness (mm) | Total Ablation Depth (mm) |
|---|---|---|---|
| Duroid 5650MAZ | 0.711 | ----- | 0.711 |
| Chartek 3 | 0.965 | 0.406 | 1.372 |
| Chartek 59 | 0.813 | 0.457 | 1.270 |
| DC 93-104 | 1.219 | 0.279 | 1.500 |
| FMI CYC 5520.0 | 1.500 | ----- | 1.500 |
| Korotherm | completely removed (approx. 2.159 mm) | | |
| FMI CY 5520.0 | completely removed (approx. 6.350 mm) | | |
| FMI CZ 553.2 | completely removed (approx. 6.350 mm) | | |
| FMI CZ 3714.2 | completely removed (approx. 6.350 mm) | | |
| FMI CT 7314.3 | completely removed (approx. 6.350 mm) | | |

Analytical Approach. Knowing the parameters of recovery temperature, given in Figure 8 and the heat transfer coefficient, h, given in Figure 9, the heating rate (see Figure 11), q, to the test cones can be calculated from Equation (2), where $T_s$ is the

heated surface temperature. During the interval of the test where ablation occurs, the surface temperature is assumed to be represented by an effective ablation temperature, $T_m$, which is constant during this interval and is characteristic of the particular material being examined. Then, during this interval,

$$T_s = T_m \tag{2}$$

The relationship of ablation depth, a, to heat of ablation, $H_a$, is shown in the following equation

$$a = \int \dot{a} dt = \frac{\int q dt}{\rho H_a} \tag{3}$$

It is convenient to rearrange Equation (2) such that $H_a$ is defined as

$$H_a = \frac{\int q dt}{\rho \int \dot{a} dt} = \frac{1}{\rho a} \int h (T_r - T_m) dt \tag{4}$$

where $\rho$ is the density of the material being tested, $\dot{a}$ and a are the ablation rate and total ablation depth, and the integral is for the time interval during ablation. Since $\rho$ and a are known, measured values, and since h and $T_r$ have been calculated for the test environment (Figures 8 and 9), one can numerically determine $H_a$ as a function of $T_m$. This relation should be correct for any flight regime having an environment (heating and shear) similar to that of the sled test. Extrapolation to a sufficiently different flight regime may require re-testing in the new regime.

## RESULTS/CONCLUSIONS

Using the measured ablation depths from Tables IIIa and IIIb and numerical aero-heating/ablation/conduction analyses as discussed above, the relationship of $H_a$ to $T_m$ was determined for each of the materials after normalization with respect to the

Duroid standards. Typical results are shown in Figures 11 and 12. In general, the further the curve for a material is from the origin in the figure, the better its ablation performance.

While the curves in Figures 11 and 12 indicate only a relationship between effective $T_m$ and $H_a$ of the materials, single values of these parameters are needed for use in quantitative analyses to predict combined aero-heating, ablation, and conduction effects on the materials for thermal protection schemes on other flights. For this purpose, if $T_m$ was not previously known for a material, we quite arbitrarily picked a value for this parameter. These values were selected midway within the range of values possible for each material in an effort to minimize any errors which may result from the uncertainties in $T_m$. These choices are shown in Table IV along with the corresponding values of $H_a$ from Figures 11 and 12. These are considered the best values available for use in ablation analyses until further tests are performed for the purpose of more accurately establishing effective values of $T_m$.

Table IV. Recommended Effective Ablation Temperatures and Heats of Ablation

| Material | $T_m$ (°F) | $H_a$ (Btu/lb) |
|---|---|---|
| Duroid 5667MAZ | 1250 | 1500 |
| Duroid 5650MAZ | 1250 | 1250 |
| Chartek 3 | 1200* | 1450 |
| Chartek 59 | 1200* | 1600 |
| Avco 8039CX | 1000* | 1250 |
| DC 93-104 | 1150* | 1200 |
| FMI 705 | 750* | 950 |
| FMI CYC 5520.0 | 1000* | 1300 |

## THERMAL AUGMENTATION TESTS

### BACKGROUND

Currently, there is a need for being able to predict the heating effects in regions of reattachment of separated shear layers associated with cavities or ports. Significant increases in heat transfer are caused by the separation of the local

boundary layer as it passes over the cavity and reattaches on the downstream surface. This augmented heating will attain a maximum at the reattachment point and quickly decay along the flow for both the inside and outside cavity surfaces.

There are a variety of methods available for predicting heating augmentation. The predicted levels of heating augmentation associated with cavities varies significantly from one method to the next. This large variation in predicted values indicates the need for tests to determine the heating augmentation associated with the cavities and to identify methods that provide the best agreement with measured values.

A hypervelocity sled, utilizing the sled track facility at Holloman Air Force Base (HAFB), was chosen as the means to perform these tests. The heating augmentation levels were evaluated by comparing the ablation levels at various locations in and around the cavities to the ablation level at a location uninfluenced by the cavities. Since ablation depths (for a subliming material) can be directly related to the convective heat flux, the ratio of the ablation depths in the vicinity of the cavity to that of the unaugmented area will indicate the heating augmentation levels associated with the cavity.

## DISCUSSION

Heating Augmentation. The local boundary layer will separate from the wall upon reaching the cavity and reattach on a downstream surface, causing heating rates to attain a maximum at the reattachment point and quickly decay with distance from this point. For this reattachment, only the lower portion of the shear or boundary layer reattaches to the back wall of the cavity, while the upper portion reattaches to the downstream external surface aft of the cavity (see Figure 13). Several procedures were considered in analytically predicting these augmented heating distributions. These methods include a theoretical model presented by Nestler [10], two empirical methods presented by Kim and Parkinson [10] and Weatherford and Sayano [11,12], and an engineering method modeling the reattachment region as a blunt wedge or cylinder in crossflow.

The maximum heat transfer to the back wall of a cavity will depend on the properties of the limiting streamline as it reattaches to the back wall. For a cavity, the limiting

streamline corresponds to the dividing streamline of the separated shear layer (See Figure 13). Nestler assumes that the maximum heat flux (at the reattachment point) can be approximated by an expression for the stagnation point heat flux of an impinging jet on a flat plat, given by

$$q_r = \frac{0.5\lambda}{Pr^{2/3}}\left[\frac{\rho_D U_D \mu_{Do}}{\Delta_{eff}}\right]^{0.5}(H_D - H_w)\sin\beta \qquad (5)$$

where $\lambda$ is a free stream turbulence correction factor, Pr is the Prandtl number, $\Delta_{eff}$ is an effective shear layer width, $\rho_d$, $U_d$, and $H_d$ are the density, velocity and total enthalpy at the dividing streamline, $H_w$ is the total enthalpy at the wall temperature, $\mu_{do}$ is the viscosity at the dividing streamline total temperature, and sinß is a correction for angle of the step or cavity wall.

Nestler noted that maximum reattachment heating for turbulent separation was found to exceed the predictions of the jet impingement model given above. Additionally, he noted that a simple empirical expression based on the reattachment pressure ratio was found to yield more satisfactory predictions for the turbulent case. This alternate expression originally presented by Kim and Parkinson is given by

$$\frac{q_R}{q_\delta} = \left[\frac{P_R}{P_\delta}\right]^{0.8} \qquad (6)$$

where q is the heat flux, P is the pressure, and the subscripts R and $\delta$ refer to the reattachment zone and the undisturbed flow immediately upstream of the separation point, respectively.

Two methods are considered for calculating the turbulent reattachment pressure ratio. Nestler recommends the ratio of the stagnation pressure behind a normal shock for the dividing streamline Mach number, $M_D$, to the static pressure just upstream

of separation. Weatherford and Sayano recommend an alternate empirical method given by:

$$\frac{P_R}{P_\delta} = \frac{1 + 0.69M_\delta^2}{1 + 0.2M_\delta^2} \tag{7}$$

where $M_\delta$ is the local Mach number upstream of separation.

The heat flux distribution along the rear surface within the cavity as presented by Nestler is given by:

$$\frac{q}{q_R} = \left[\frac{X_2}{\Delta_{eff}}\right]^{-0.6} \tag{8}$$

where $X_2$ is the distance from the top of the cavity.

For the external surface aft of the cavity, the reattached flow can be modeled as a boundary layer having its origin at the reattachment point [10]. Therefore, the turbulent heat flux distribution is given as

$$\frac{q_3}{q_\delta} = \left[\frac{\rho_3 U_3}{\rho_\delta U_\delta}\right]^{0.8}\left[\frac{\mu_3 X_\delta}{\mu_\delta X_3}\right]^{0.2} \tag{9}$$

where subscripts $\delta$ and 3 represent conditions upstream and downstream of the cavity, respectively. Also, $X_\delta$ is the distance as measured from the forward tip of the test vehicle and $X_3$ is the distance downstream of the cavity as measured from the reattachment point.

An alternate approach, resulting from this effort, is to treat the reattachment region as the leading edge of a blunt wedge, with the maximum heat flux at the reattachment point being

approximated by an expression for the stagnation line heat flux of a cylinder in cross flow [13], given by

$$q_R = 0.54 \frac{k^* Pr^{0.4}}{D} \left[ \frac{\rho^* U_\delta DS}{\mu^*} \right]^{0.5} (T_r - T_w) \qquad (10)$$

where D is the diameter of the cylinder, $U_\delta$ is the local velocity, S is the velocity gradient, and $k^*$, $\rho^*$ and $\mu^*$ are thermal conductivity, density, and viscosity all evaluated at Eckert's reference temperature $T^*$ [14]. $T_r$ and $T_w$ are the recovery temperature and wall temperature, respectively.

The procedures outlined above provide a variety of methods for predicting peak augmentation levels and methods for predicting the decay of these augmentation levels with distance from the reattachment point both inside and outside the cavity.

Experimental Approach. The sled track facility at Holloman Air Force Base (HAFB), was chosen as the means to evaluate the heating augmentation levels in the vicinity of cavities. The augmentation can be evaluated by comparing the ablation levels at various locations in and around the cavities to the ablation level at a location just forward of a cavity. Since ablation depths can be directly related to the convective heat flux, the ratio of the ablation depths indicate the heating augmentation levels.

For a subliming material such as teflon, a simple ablation model can be used where the ablation depth is given by:

$$a = \int \dot{a} dt = \frac{\int q dt}{\rho H_a} \qquad (11)$$

where $\dot{a}$ is the ablation rate, $\rho$ and $H_a$ are the density and heat of ablation of the material, and the integrals are performed over the period of ablation.

Since the augmentation factor is defined as

$$F = \frac{q}{q_\delta} \tag{12}$$

Then the ratio of augmented ablation to unaugmented ablation yields an effective augmentation factor, F, for the sled flight given by:

$$F = \frac{a}{a_\delta} = \frac{\int q dt}{\int q_\delta dt} = \frac{\int F q_\delta dt}{\int q_\delta dt} \tag{13}$$

Post-test measurements of the ablation in and around the cavity are compared to the unaugmented ablation just upstream of the cavity, establishing effective augmentation factors. These measured augmentation factors are compared to those calculated using the analytical and empirical methods given above to establish the degree of confidence with which these methods can be used to predict augmentation factors for hypersonic flights.

In order to illustrate the coordinate system used in this report for presenting the ablation and augmentation profiles, Figure 14 shows an enlarged view of the pre- and post-test ablation profiles for the reattachment region of a cavity. As shown, the in-cavity coordinate axis lies along the original (pre-test) inside cavity surface, while the downstream coordinate axis lies along the original downstream surface. The origin for each of these coordinates moves as the reattachment point recedes and occurs at the intersection of the perpendicular projection of the reattachment point upon each of these axes.

Test Configuration and Materials. Figure 15 provides a sketch of the sled test model. It consists of a cone configuration with a nose radius of 6.35 mm (0.25 inch), a cone half-angle of 15 degrees, and a base radius of 120.7 mm (4.75 inches). Also, the test model contains three cavities equally spaced around the circumference. The nose tip is made of carbon-carbon, the main cone body is a silica-phenolic heat shield over a steel substructure; two of the three cavities are made of Teflon and the third of rubber-modified silica-phenolic. A sketch of the individual cavity geometry is provided in Figure

16. Figure 17 shows a picture of the sled test vehicle with an attached test cone and Figure 18 provides a close-up view of the a test cone.

Test Environments. Figure 19, which provides the actual flight trajectory attained during the tests, shows that the test cones reached approximately a 2057 m/sec (6750 ft/sec) peak velocity. Figure 20 shows a sled vehicle and test cone at peak velocity. Corresponding calculated boundary conditions (recovery temperature, $T_r$, and heat transfer coefficient, h), indicating the severity of the unaugmented aerothermal enivronment are shown in Figure 21. Local Mach numbers, calculated for a sharp-nosed cone using Hord's method [15], reach a maximum value of 4.4 and are shown in Figure 22. Predicted heating rates to Teflon (Figure 23) during the test peak at approximately 1167 kcal/$m^2$-sec (430 Btu/$ft^2$-sec). Given this thermal environment, the expected unaugmented ablation depth in Teflon (Figure 24) immediately forward of the port cavities was calculated to be 0.889 mm (0.035 inch) by the end of the ablation period.

## RESULTS/CONCLUSIONS

Port cavity ablation profile measurements were made at MICOM using a state-of-the-art profilometer. For each port, profiles were obtained along five different paths as shown in Figure 25, with each path lying in a plane parallel to the port plane of symmetry. Actual pre- and post-test profiles for the Teflon ports are shown in Figures 26 and 27. It should be noted that, within an estimated uncertainty of 0.127 mm (0.005 inch) in the measurments, the measured Teflon unaugmented recession depths, $a_\delta$, immediately upstream of the port cavities agrees with the pre-test calculations. Using Teflon recession depths measured versus location on each port, and the principles outlined above, an augmentation factor, F, was obtained for each port location by dividing the local augmented recession at that location by the unaugmented recession, $a_\delta$.

Figures 28 and 29 present measured recession depths for in-cavity and downstream locations along with "best-fit" curves which are considered to be representative of recession in each area. Recession depths on the side, bottom, and forward faces inside the cavities were small and are ignored in this report. Recession data from the fitted curves were then divided by the unaugmented value, $a_\delta$, to obtain overall effective augmentation

factor distributions for the tests. These results are shown in Figure 30 for both the in-cavity and downstream locations and hereafter are referred to as the measured results. It is seen that these augmentation factors peak at the rear lip of the cavity (the reattachment point) with values of approximately 2.4 and show most of their decay occuring within a distance of 2.5 mm (0.1 inch) from the reattachment point.

The measured results inside the cavity are shown again in Figure 31 along with analytical predictions which were made by the different methods presented in the Discussion. It is seen for the reattachment region, Nestler's method gives values (approximately 1.0) which are much too low. Nestler's alternate recommendation, using a relation advanced by Kim and Parkinson, gives values much higher (2.0) but still too low. The Weatherford and Sayano value (2.4) agrees very well with the measured value. This may be only coincidence, however, as we shall later see.

Lack of success and dissatisfaction with these correlations led to the realization that the reattachment point heating should be dependent on the "bluntness" of the reattachment region (i.e. near the rear lip of the cavity) and that this region should best be treated by modeling as one would the leading edge of a blunt wedge, by calculating heating to the stagnation line heating for a cylinder in crossflow. This leads to reasonable agreement with the test results; shows a variation which depends on bluntness of the rear lip; provides a more reasonable decay distance; and is good for both in-cavity and downstream predictions. Based on these tests, this is the recommended prediction model.

During the tests, the radius of curvature of the reattachment region varied due the recession caused by the ablation of the Teflon. The initial diamter, $D_i$, of the reattachment region was estimated to be approximately 0.762 mm (0.030 inch). The final diameter, $D_f$, was estimated to be about 5.33 mm (0.21 inch). The average effective diameter, D, was calculated to be 2.51 mm (0.099 inch), where $\bar{D}$ is defined as the diameter which gives average effective values of $F_R$ for the reattachment point.

It can be seen that the reattachment augmentation factor is proportional to the transformed reattachment point ablation depth:

$$F_R \propto a_R \propto h_R \propto \frac{1}{\sqrt{D}} \tag{14}$$

and the average augmentation factor is then dependent on $D_i$ and $D_f$ as:

$$\overline{F_R} = \frac{\int F_R dD}{\int dD} \propto \frac{\int_{D_i}^{D_f} \frac{dD}{\sqrt{D}}}{\int_{D_i}^{D_f} dD} = \frac{2(\sqrt{D_f} - \sqrt{D_i})}{D_f - D_i} = \frac{2}{\sqrt{D_f} + \sqrt{D_i}} \tag{15}$$

This then implies

$$\overline{D} = \left(\frac{\sqrt{D_f} + \sqrt{D_i}}{2}\right)^2 \tag{16}$$

and

$$\frac{F_{R_i}}{\overline{F_R}} = \frac{\sqrt{D_f} + \sqrt{D_i}}{2\sqrt{D_i}} \tag{17}$$

From these relations we can see that initially, or with a non-receeding rear lip rounded off to a representative tolerance of 0.762 mm (0.030 inch) diameter, the augmentation factor can be 1.8 times as large as the effective measured value. At the same time, the value at the end of ablation (when $D_f$ = 5.33 mm) could have been as low as 0.69 times the measured value. For convience, this is summarized in Table V.

Table V. Estimated Dependence of Reattachment Point $F_R$ on Rearlip Bluntness

| $D_i$ | $D_f$ | D | $F_R$ | $F_{Ri}$ | $F_{Rf}$ |
|---|---|---|---|---|---|
| 0.762 mm (0.030 in) | 5.33 mm (0.21 in) | 2.54 mm (0.099 in) | 2.4 | 4.4 | 1.6 |

Using this line of reasoning, the approaches put forth by Weatherford and Sayano and by Kim and Parkinson, since they are independent of geometry, should probably be considered strictly "ball-park" solutions. Calculations using a cylinder in cross flow model (Equation 9) are also presented in Figure 31 based on average effective diameter, D, so as to correlate with the overall average effects of the test. Upon plotting these results using Nestler's recommended properties for the reattachment streamline $M_R$ equal $M_D$, it was realized that this value (approximately 1.2) is probably much too low and that in reality $M_R$ probably lies somewhere between $M_D$ and $M_\delta$. Based on this, augmentation values are also shown for $M_R = M_\delta = 4.4$ and for a "best match" value of $M_R = M_{BM} = 3.3$, which was chosen to make the calculated value match the measured value. From this, we see that:

$$\frac{M_{BM}}{M_\delta} = \frac{3.3}{4.4} = 0.75 \qquad (18)$$

The decay of F as one moves away from the reattachment point is much faster for the measured data than for the data calculated with Nestler's methods. Using the coordinate system chosen, the decay of measured data can best be represented by Equation 19 and Table VI.

The measured results downstream of the cavity are shown again in Figure 32 along with analytical predictions made by Nestler's method as presented in the Discussion. It can be seen that Nestler's method again does not provide a good match with the measured data. The cylinder in cross flow approach shows good agreement using $M_R = M_{BM} = 3.3$ as was done for the inside cavity face. The decay predicted by Nestler is again much too

slow and the measured data is best approximated by Equation 19 and Table VI.

$$\frac{F_X}{\overline{F_R}} = \sum_{i=0}^{3} A_i \left(\frac{X}{D}\right)^i, \qquad \overline{F_R} = 2.4 \tag{19}$$

and

Table VI. Constants for Cubic Decay Curvefits

| | $A_0$ | $A_1$ | $A_2$ | $A_3$ |
|---|---|---|---|---|
| In-cavity | 1.005 | -1.31 | 0.812 | -0.169 |
| Downstream | 1.002 | -1.15 | 0.717 | -0.150 |

A second test was performed, with a trajectory almost identical to the that for the first, with the peak velocity being only slightly (1.5 percent) less. Ordinarily, this would lead to almost identical results for the two tests. However, the carbon-carbon nose-tip came off Test A2 at approximately the same time the Teflon inserts began ablating. This caused great interest, since the resulting bluntness of the test cone (see Figure 33) was expected to cause significant differences in the local unaugmented flow conditions. This is illustrated in Table VII, which compares several pertinent quantities as predicted for peak velocity using sharp-nosed cone (SNC) and blunt-nosed cone (BNC) analytical models.

Table VII. Some Pertinent Parameters for Test 2 as Calculated by SNC and BNC Models

| | $a_{tot}$ (mm) | $P_\delta$ (kg/cm$^2$) | $V_\delta$ (m/sec) | $M_\delta$ | $M_D$ | $q_\delta$ (kc/m$^2$-hr-K) | $F_R$ [11] |
|---|---|---|---|---|---|---|---|
| SNC | .889 | 4.36 | 1925 | 4.4 | 1.2 | 1050 | 2.4 |
| BNC | .711 | 4.43 | 1490 | 2.1 | 1.0 | 910 | 1.9 |

Since $M_\delta$ was assumed to exert a major influence on $F_R$ and since the bluntness effects were expected to cause major differences in $M_\delta$ for the two tests as seen in Table VII above, augmentation factors measured from the two tests were expected to be quite different. This expectation was reinforced by the fact that unaugmented Teflon ablation measurments indicated the

appropriate amount of decreased heating as expected from bluntness considerations. Augmentation factors, however, did not match any of the predicitons using BNC predictions and were only slightly different from Test A1. This leads to the conclusion that local Mach numbers were substaintially higher than those predicted from a BNC model and were probably transitioning back to higher SNC values in the region of interest.

Since many of the flight regimes of interest have peak velocities much greater than the peak sled velocity, it is of utmost importance to be able to extrapolate the test results to the more severe flight environments. For this purpose, calculated reattachment point augmentation factors (based on a cylinder in cross flow and a non-receeding reattachment surface with a radius of curvature of 0.381 mm) are shown in Figure 34 as a function of flight velocity. The reattachment point streamline Mach number is chosen as 3/4 of $M_\delta$. From this figure it is seen that, even for velocities up to 4570 m/sec (15,000 ft/sec), the augmentation factors are expected to be within 15 percent of values from the sled test results. It should be remembered that for a more blunt reattachment region or for a receeding surface, augmentation factors will be much less.

## REFERENCES


1. Ormsby, P.A., Simulated Thermal Environments for Missile Materials Evaluation, Technical Report RS-TR-66-3, U.S. Army Missile Command, Redstone Arsenal, AL 35898, 31 Mar 66.

2. Ehni, Friedrich P., Layout and Calibration of the Rain Simulation at the Holloman Test Track, 6585th Test Group (AFSC), Holloman Air Force Base, NM, ADTC-TR-75-83, 15 Nov 75.

3. "The Holloman Track, Facilities and Capabilities", Air Force Special Weapons Center, 6585th Test Group, Test Track Division, Holloman Air Force Base, NM, 1974.

4. Ingham, H.S., and Shepard, A.P., Flame Spray Handbook, Volume III, Plasma Flame Process, Metco Inc., Westbury, Long Island, New York, 1965.

5. Burleson, William G., Letson, K.N., and Reynolds, R.A., Thermal Performance and Rain Erosion Behavior of Duroid Radome Materials for Conical Models on Mach 5 Sleds, Technical Report RL-84-2, U.S. Army Missile Command, Redstone Arsenal, AL 35898, Jan 84.

6. Letson, K.N., "Behavior of Ablative Radome Materials in Single Impact Rain Erosion Tests, Proceedings of the Sixth International Conference on Erosion by Liquid and Solid Impact, Cambridge, England, pp. 25-1 to 25-6, 5-8 Sep 83.

7. McCord, B.N., Calculated Thermal Effects on Reinforced Teflon Radome Samples for Cones and Wedges at Mach 3.9, 4.6, 5.4, Technical Report RL-85-3, U.S. Army Missile Command, Redstone Arsenal, AL 35898, Aug 85.

8. Perry, C.D., Plasma Simulated Aerothermal Heating Effects on Selected Low Temperature Ablators, Technical Report RD-ST-89-1, U.S. Army Missile Command, Redstone Arsenal, AL 35898.

9. Nourse, R.W. and Reynolds, R.A., Aerothermal Ablation Performance of Candidate Materials on Conical Models for Mach 5.6 Sleds, Technical Report RD-ST-89-4, U.S. Army Missile Command, Redstone Arsenal, AL 35898.

10. Nestler, D.E., An Engineering Analysis of Reattaching Shear Layer Heat Transfer, AIAA Paper No. 72-717, AIAA 5th Fluid and Plasma Dynamics Conference, Boston, MA, June 26-28, 1972.

11. Weatherford, R.H. and Sayano, S., Techniques for Rapid Aerodynamic Heat Transfer Calculations, Douglas Missile and Space Systems Division, Report No. SM-45932, May, 1964.

12. Sherman, M.M., Heating Augmentation Levels Around Thruster Exhaust Port Frames, Technical Memorandum TM 1016-02, Aerothermal Systems and Structures, Mission Viejo, CA 92691, March 27, 1989

13. Kays, W.M., and Crawford, M.E., Convective Heat and Mass Transfer, McGraw-Hill Book Company, 1980.

14. Eckert, Ernest R.G., Survey on Heat Transfer at High Speeds, WADC Technical Report 54-70, Wright Patterson Air Development Center, April 1954.

15. Hord, R.A., An Approximate Solution for Axially Symmetric Flow Over a Cone with Attached Shock Wave, NACA TN 3485, October 1955.

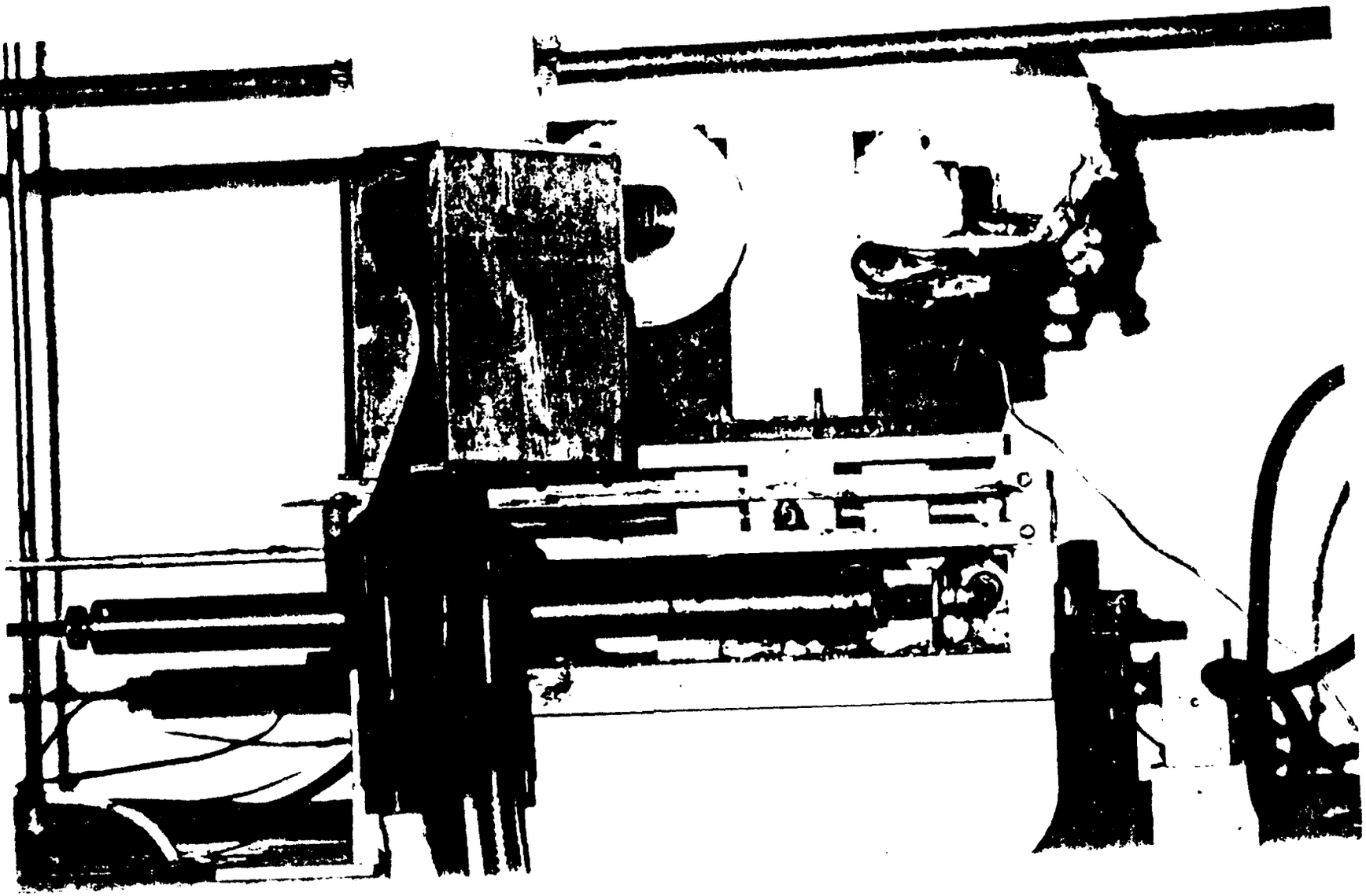

Figure 1. Test bed with sample in plasma stream.

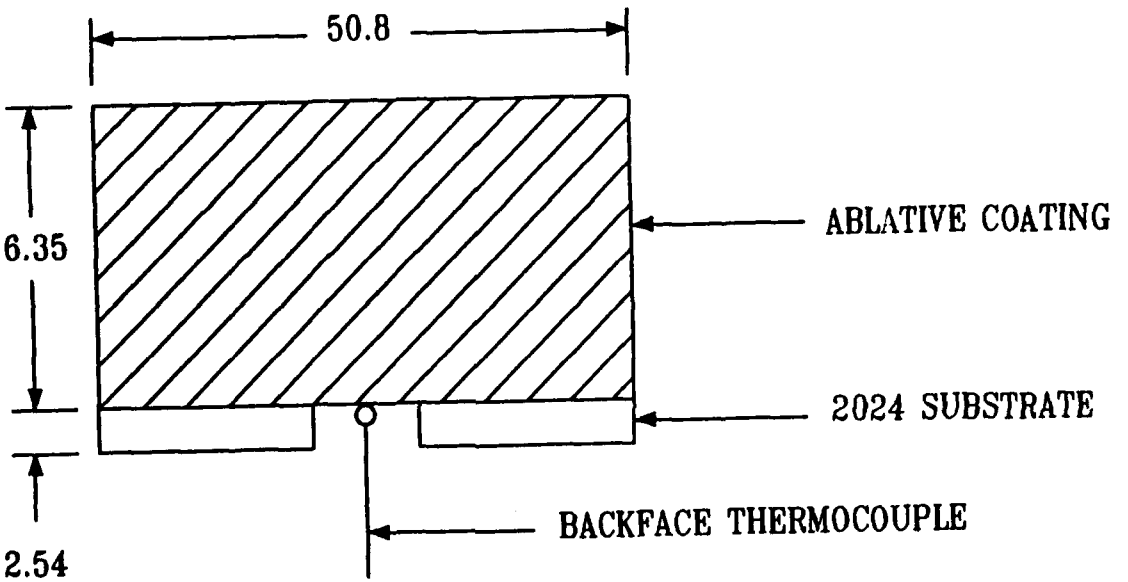


ALL DIMENSIONS IN MM

Figure 2. Sample configuration used in tests.

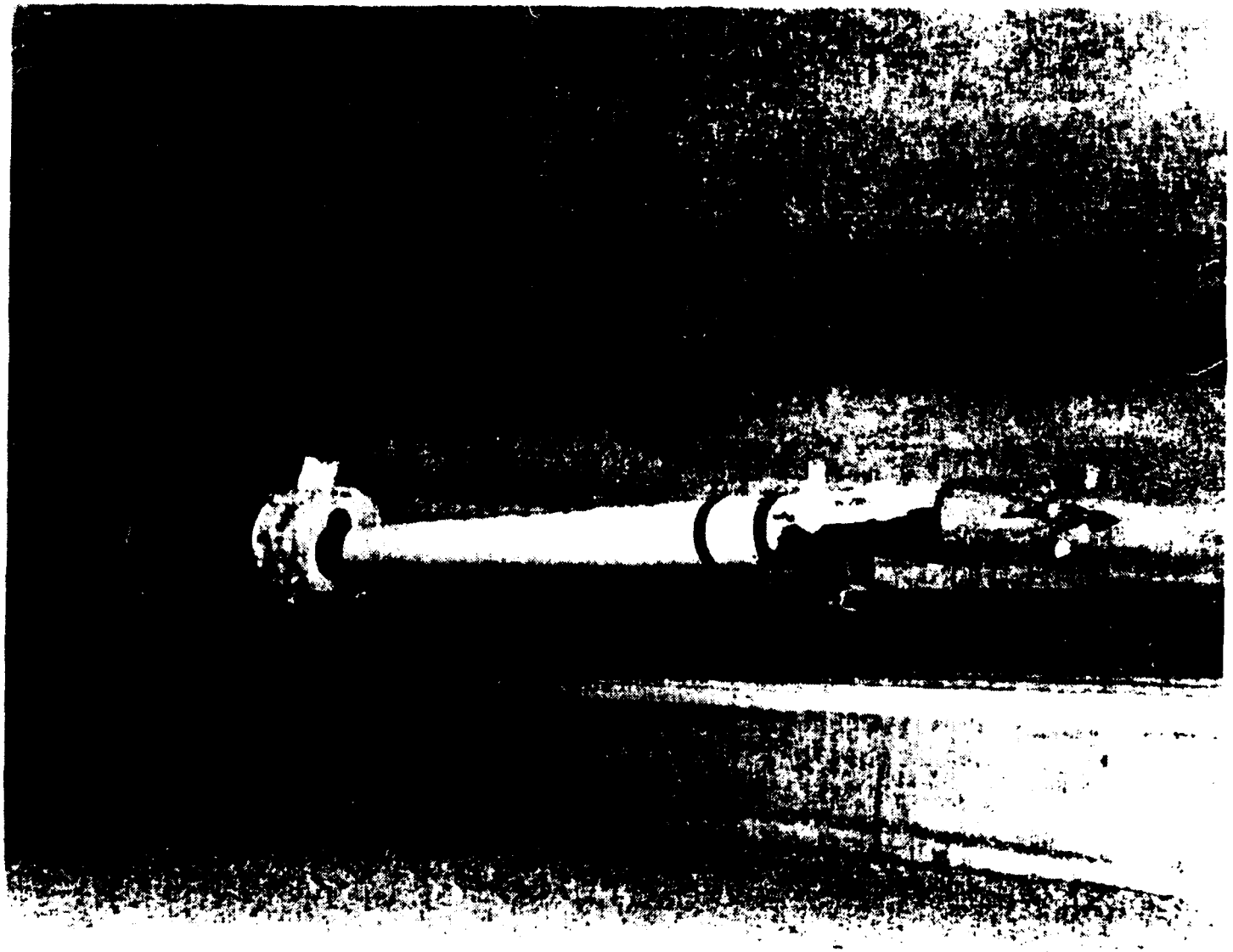

Figure 3. Test vehicle and sled system.

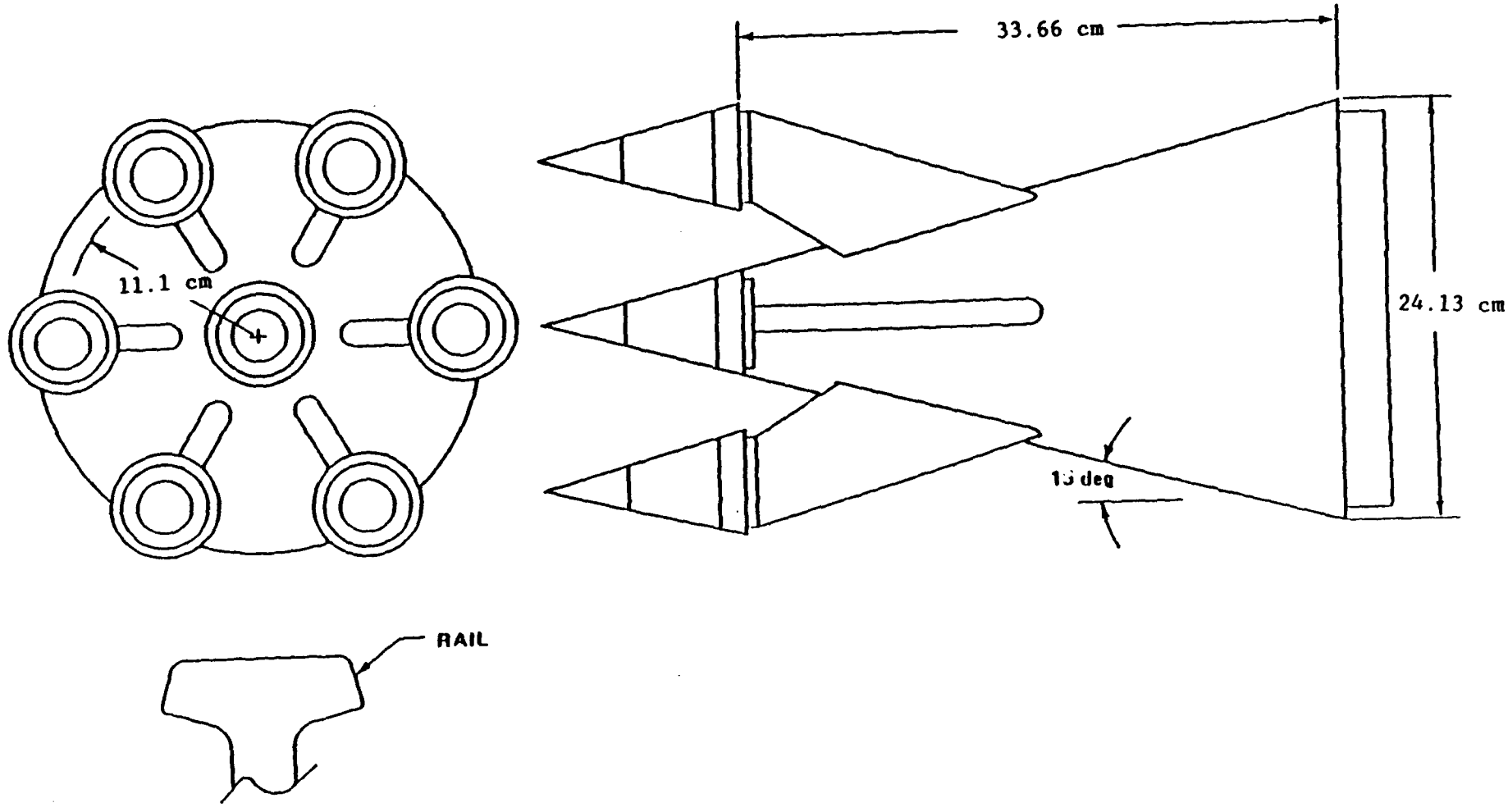


Figure 4. Seven sting test vehicle.

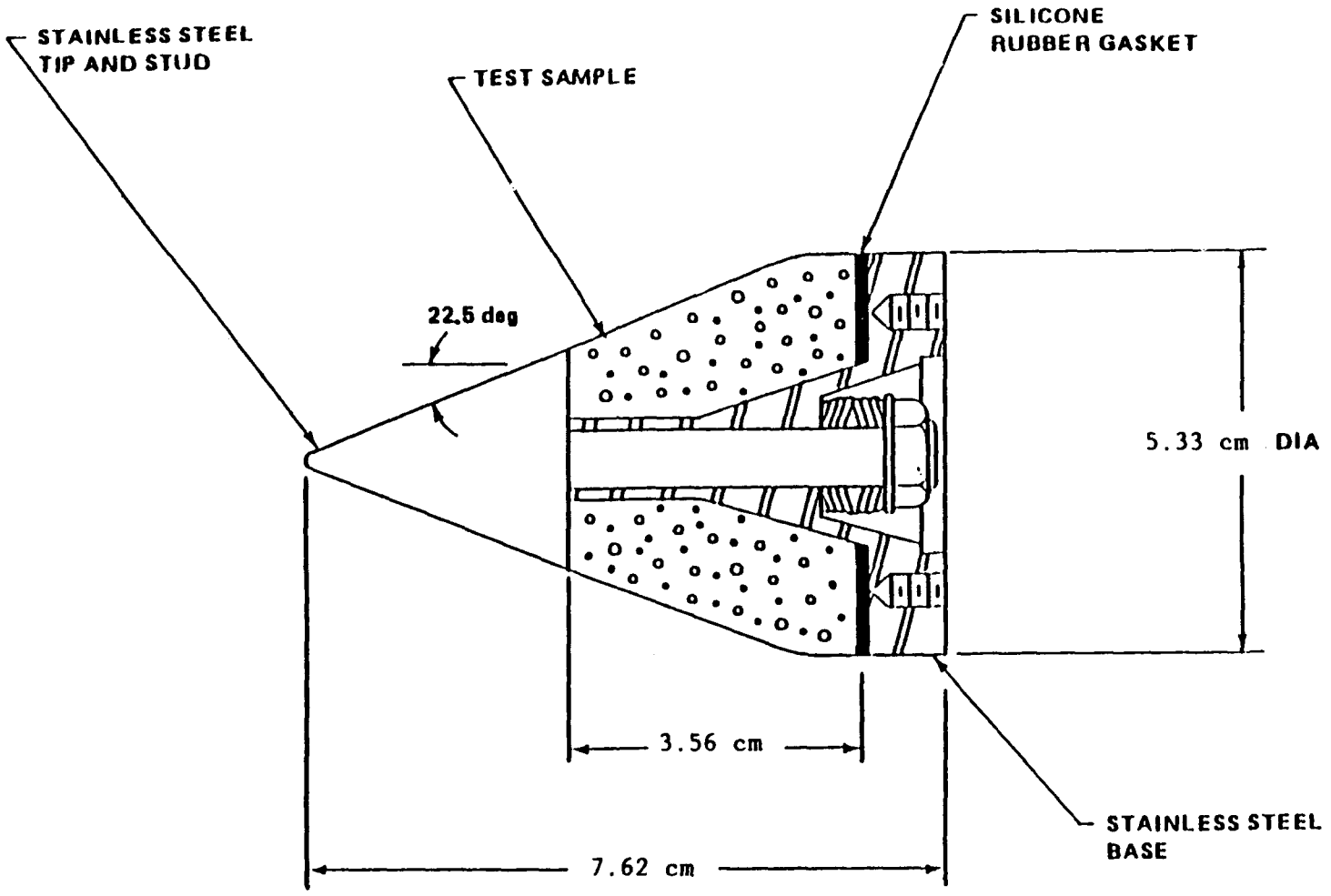


Figure 5. Sample subassembly, 22.5 degrees.

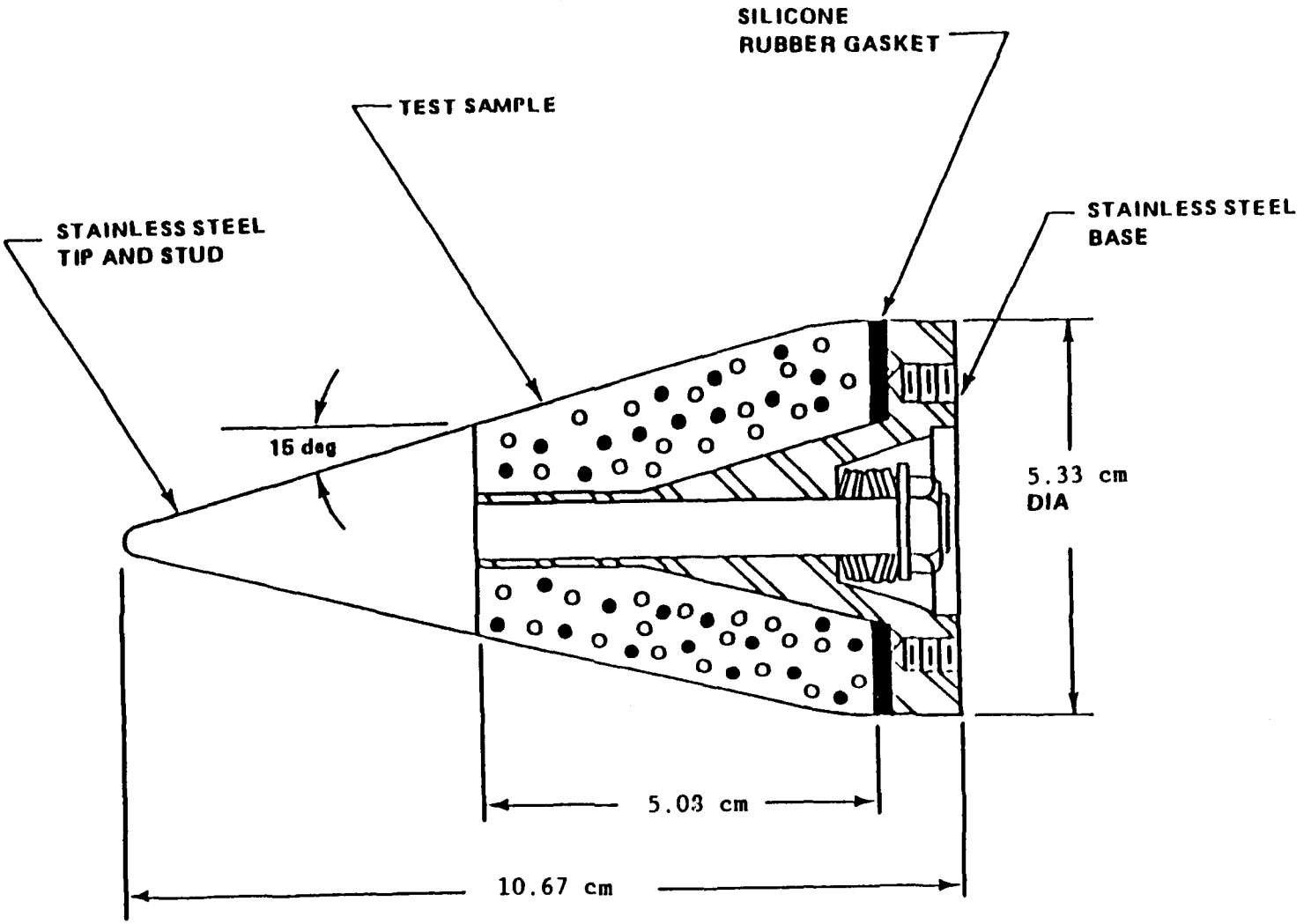


Figure 6. Sample Subassembly, 15 degrees.

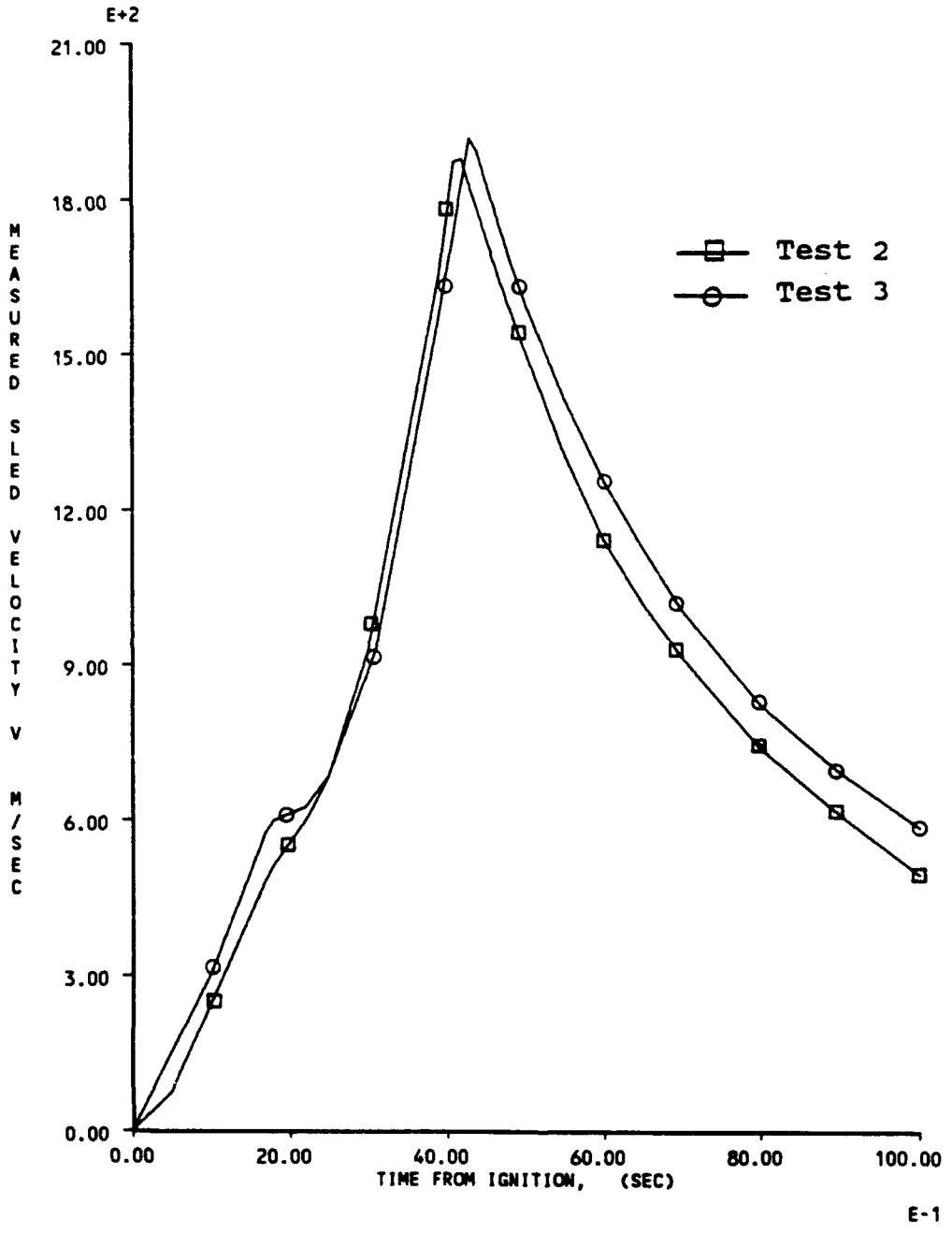


Figure 7. Measured sled velocities for Sled Tests 2 and 3 at Holloman AFB.

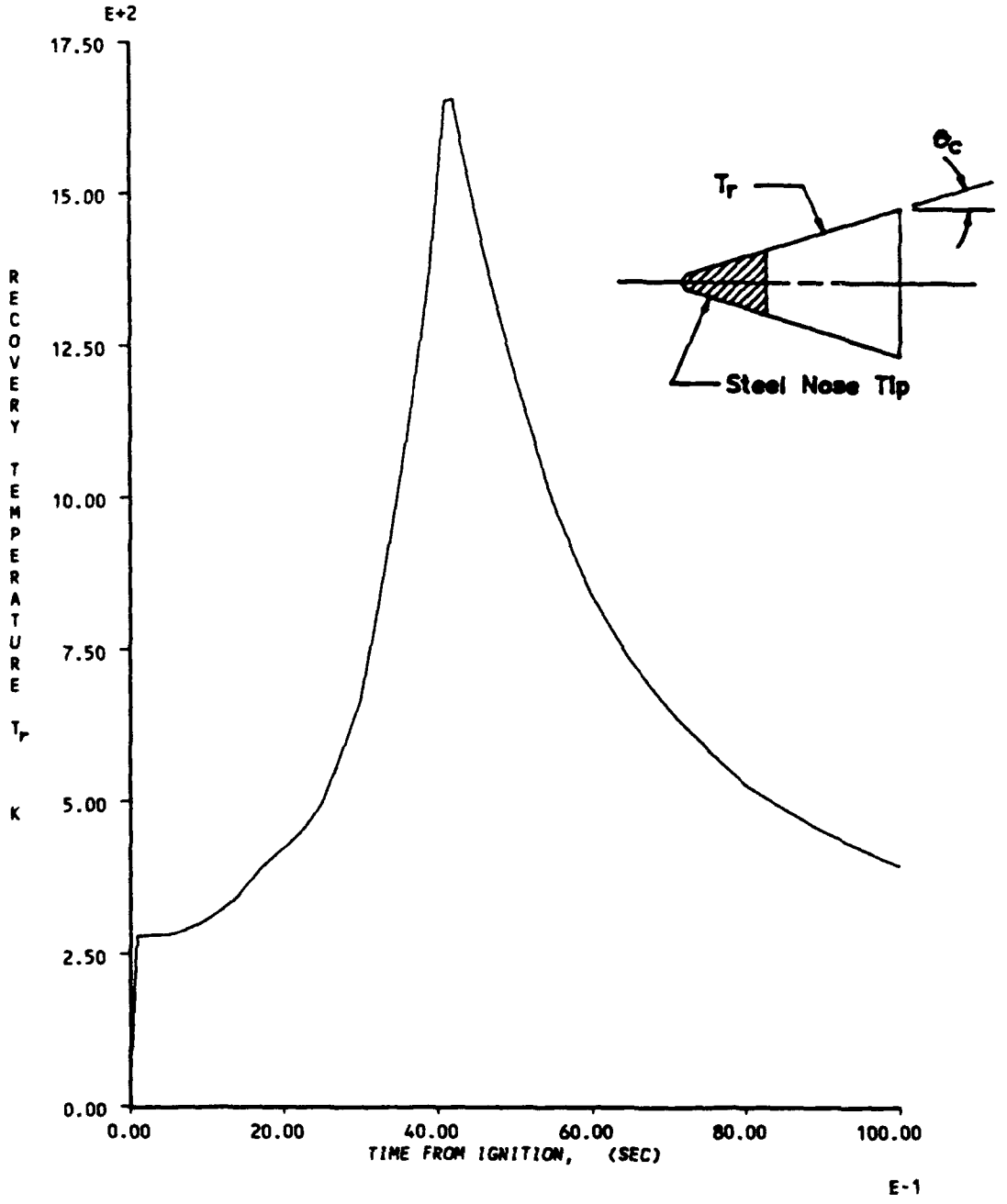


Figure 8. Calculated recovery temperature for Test 2.

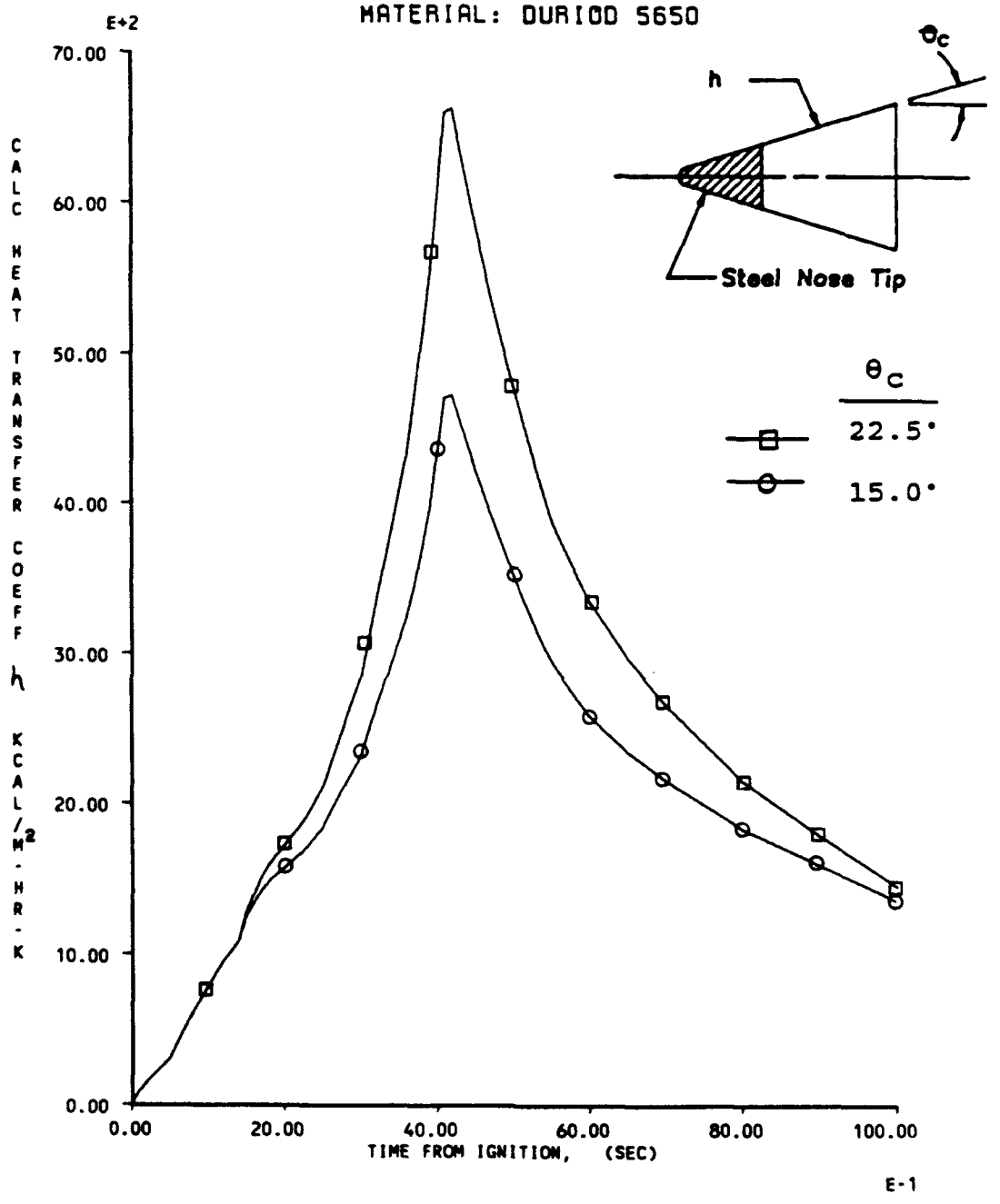


Figure 9. Calculated heat transfer coefficient for DUROID samples on Test 2.

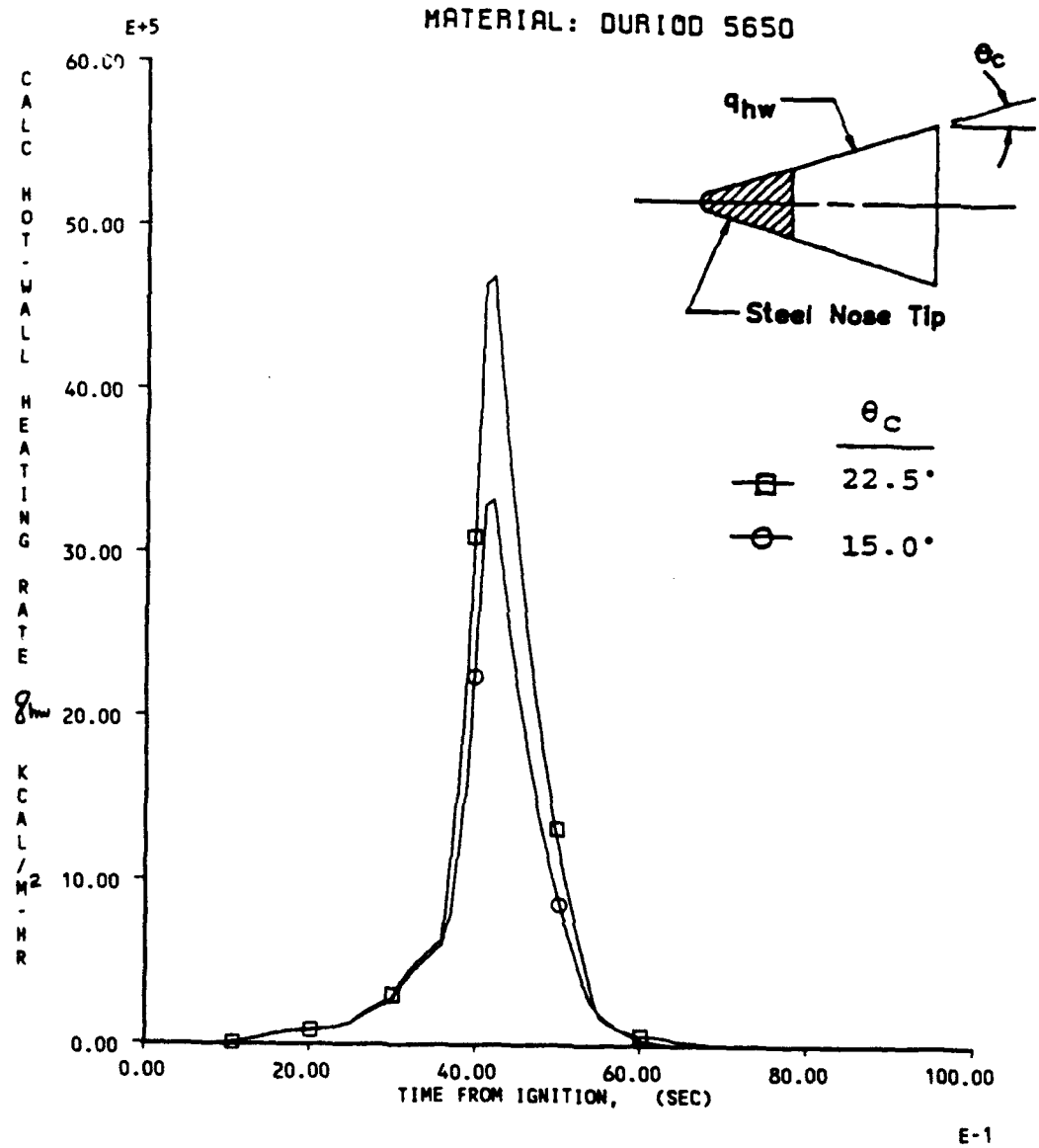


Figure 10. Calculated hot-wall heating rate for DUROID samples on Test 2.

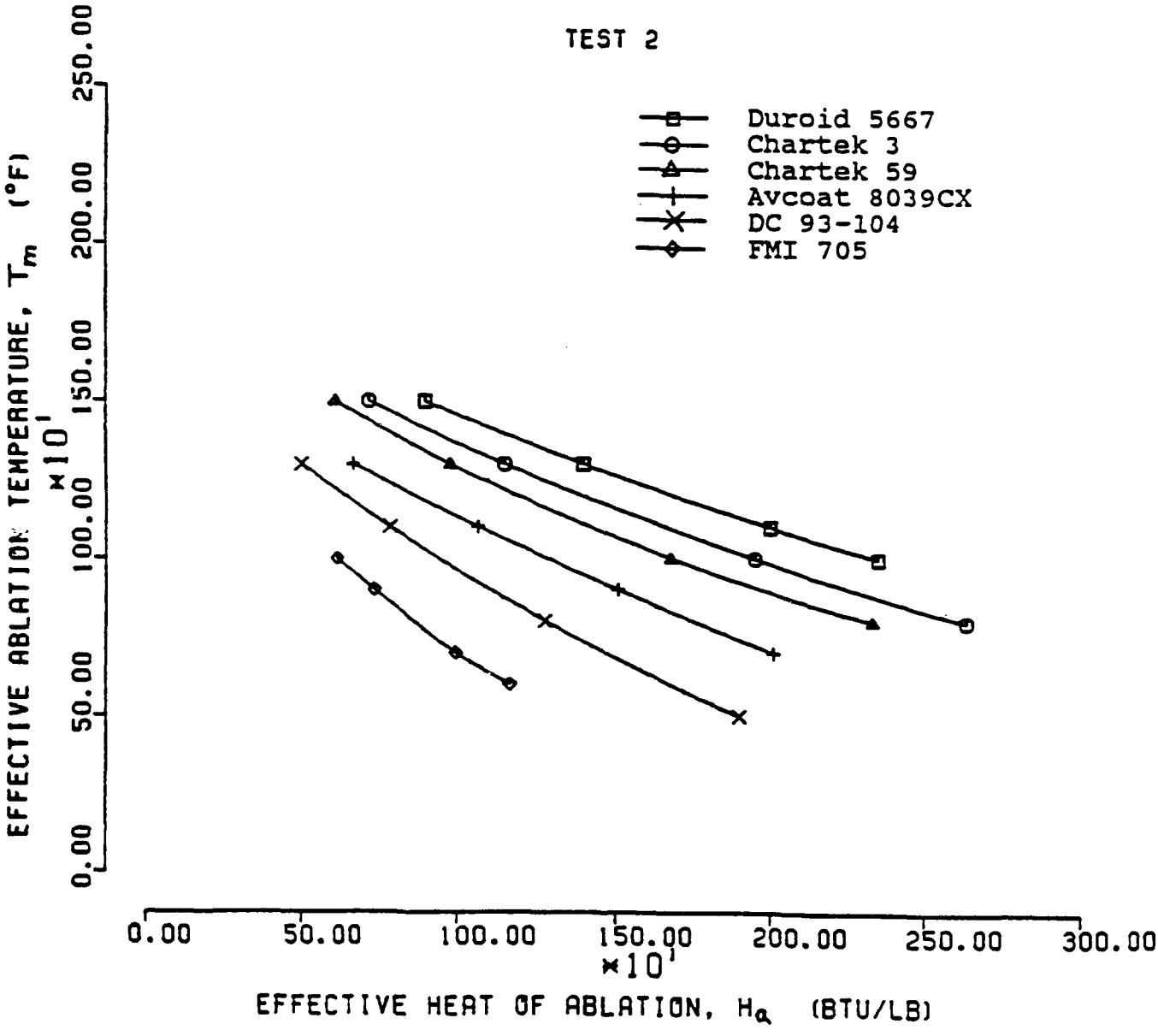


Figure 11. Effective ablation temperature vs. heat of ablation for selected materials on Test 2.

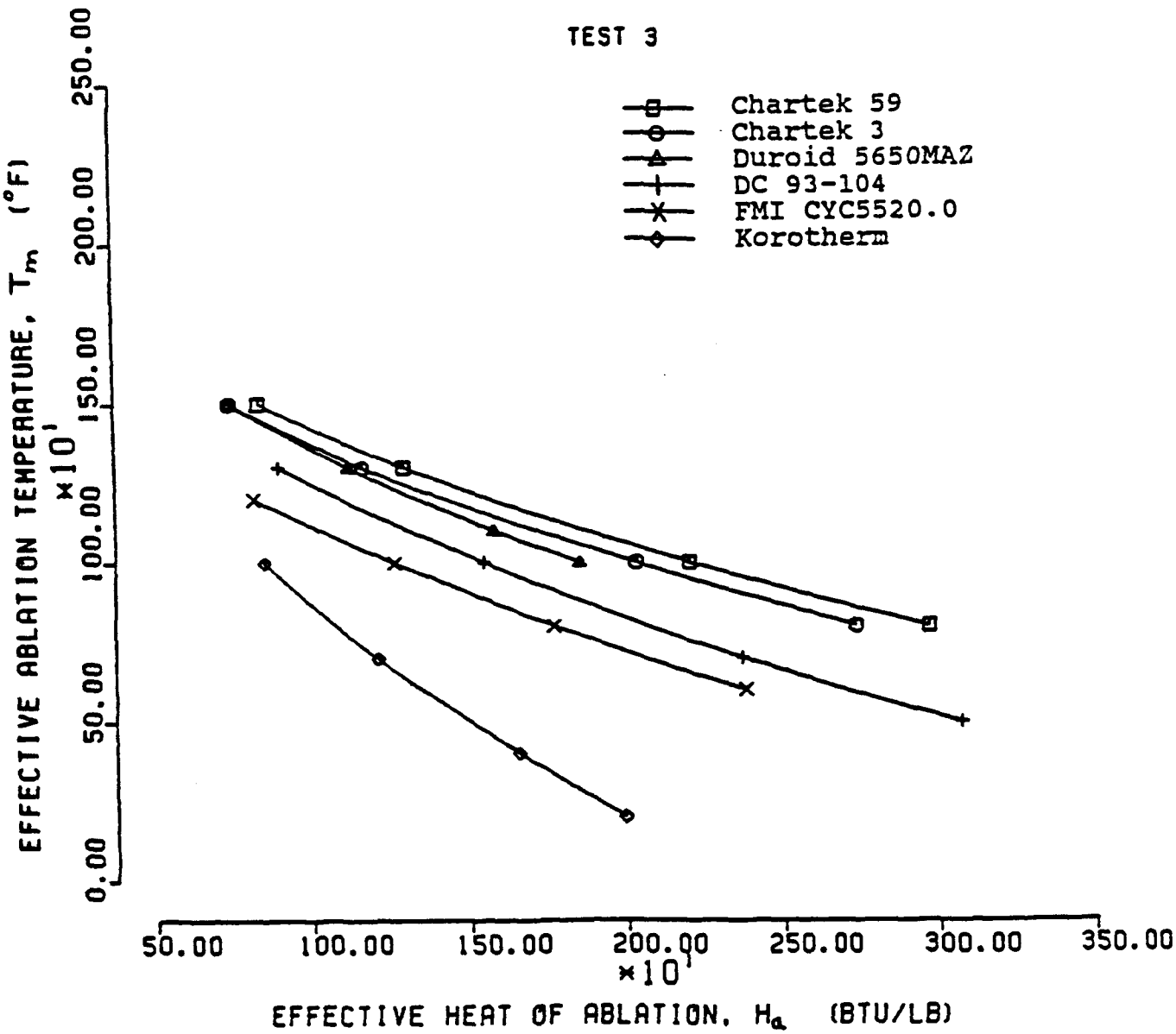


Figure 12. Effective ablation temperature vs. heat of ablation for selected materials on Test 3.

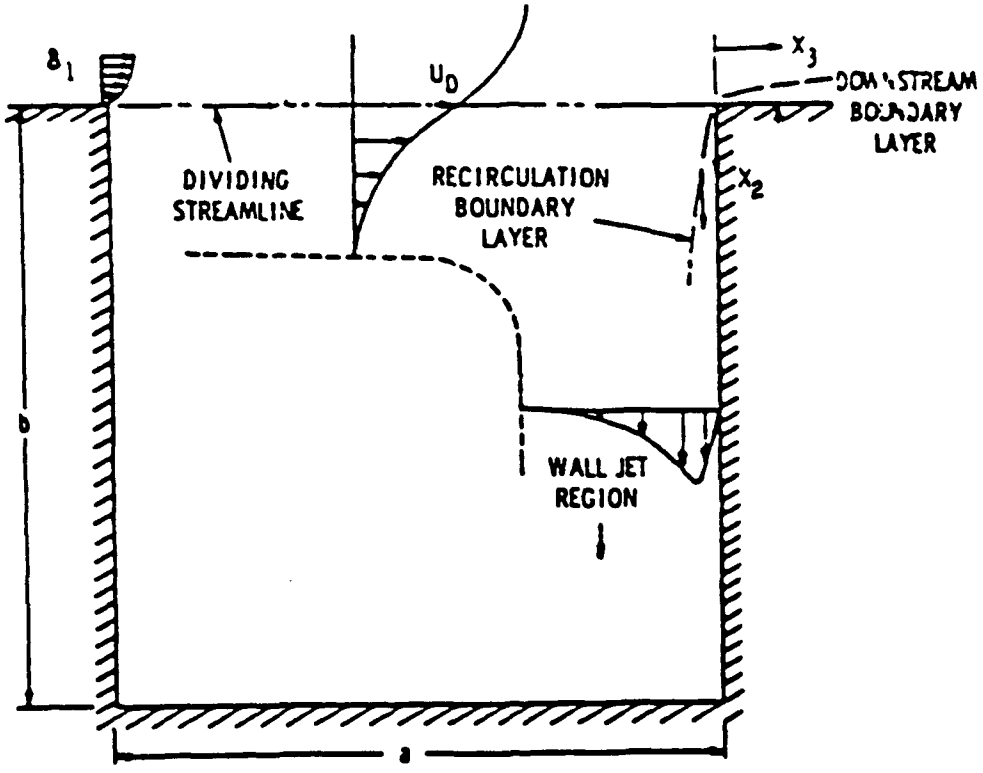


Figure 13. Shear layer separation and reattachment flow model for cavities [after Nestler].

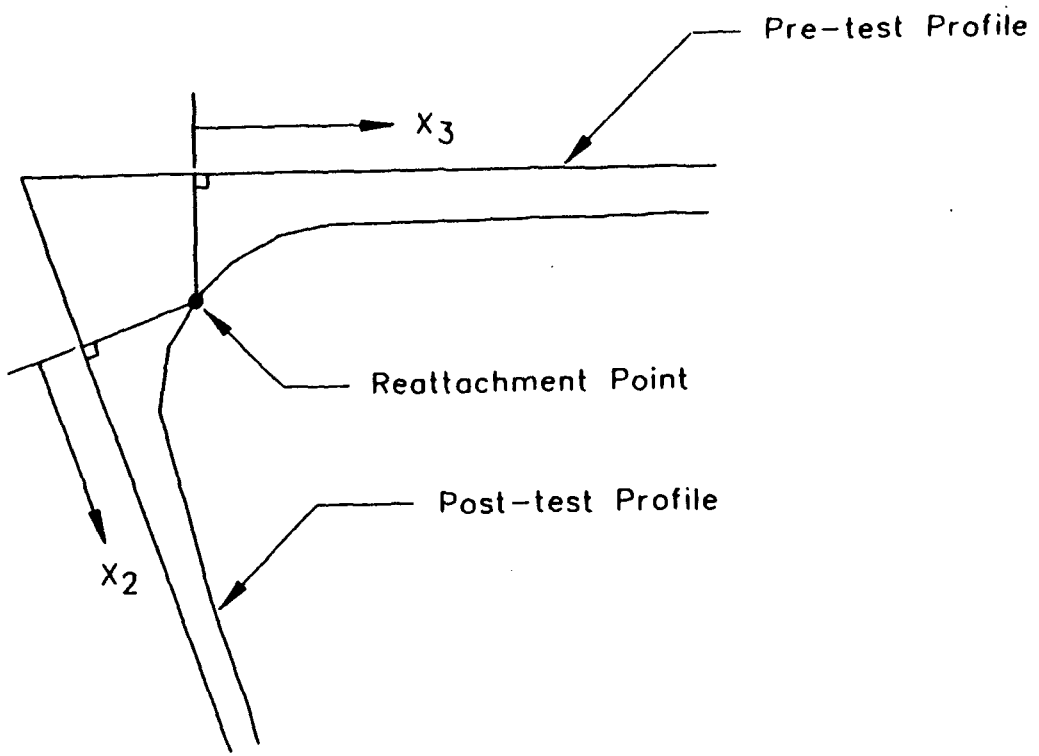


Figure 14. Coordinate system used for the reattachment region.

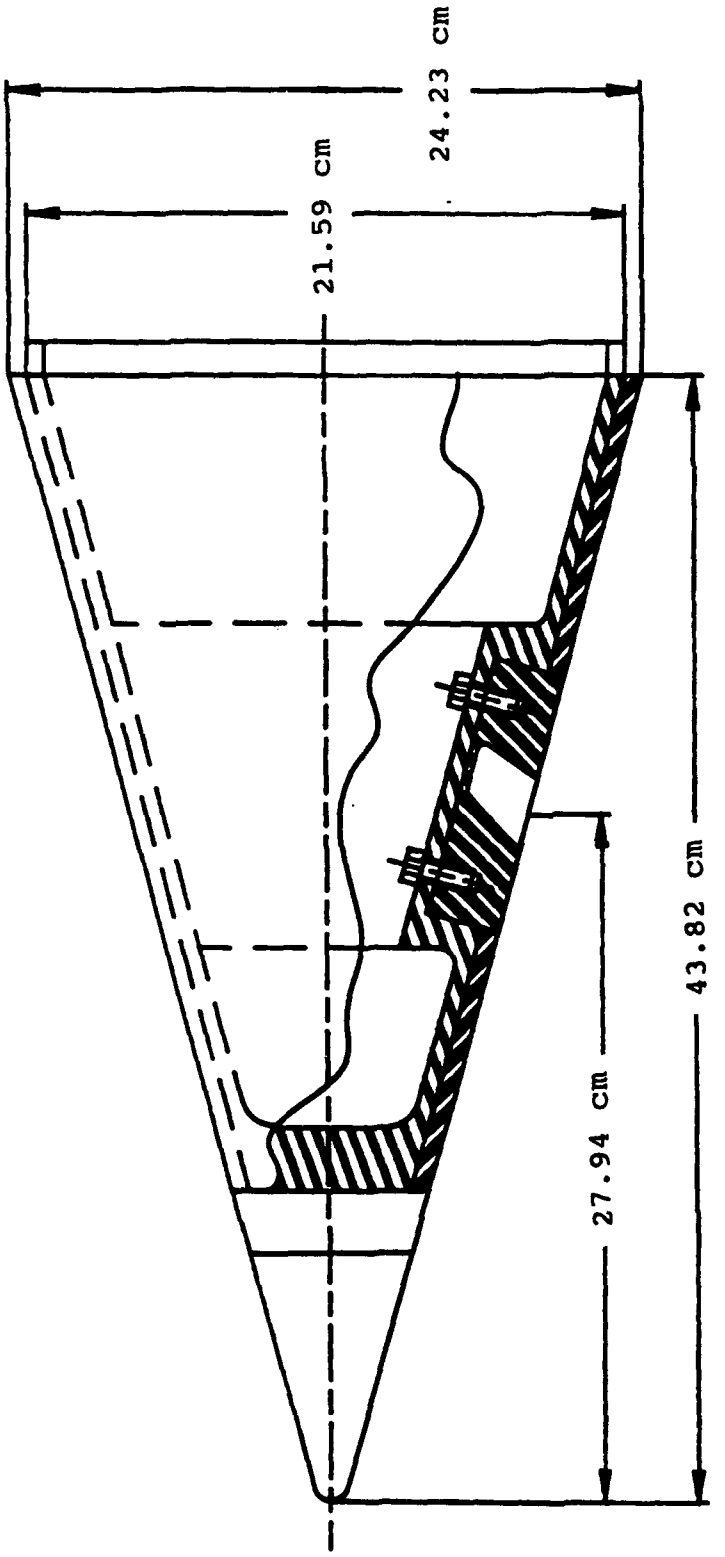


Figure 15. Sketch of sled test model.

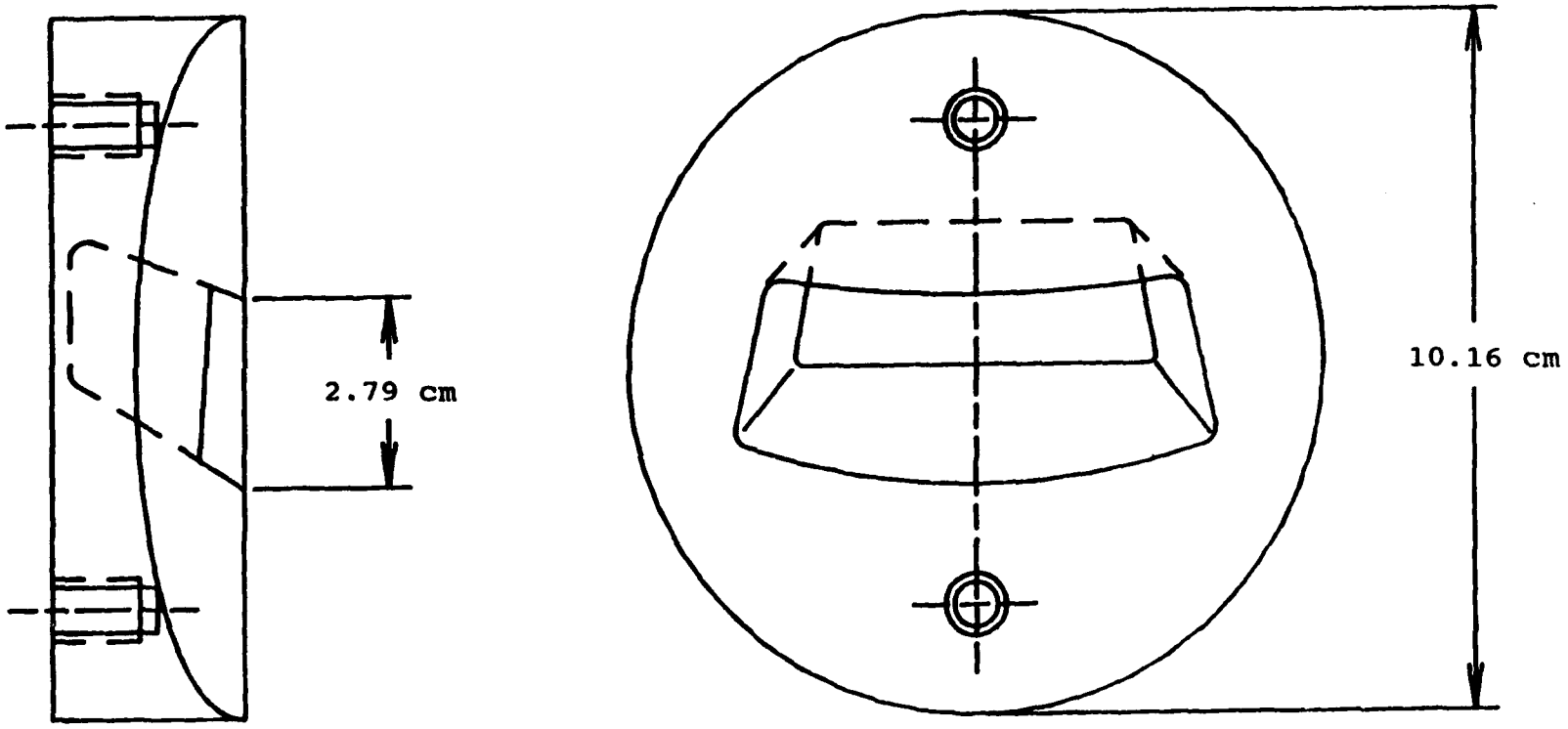


Figure 16. Sketch of the cavities tested.

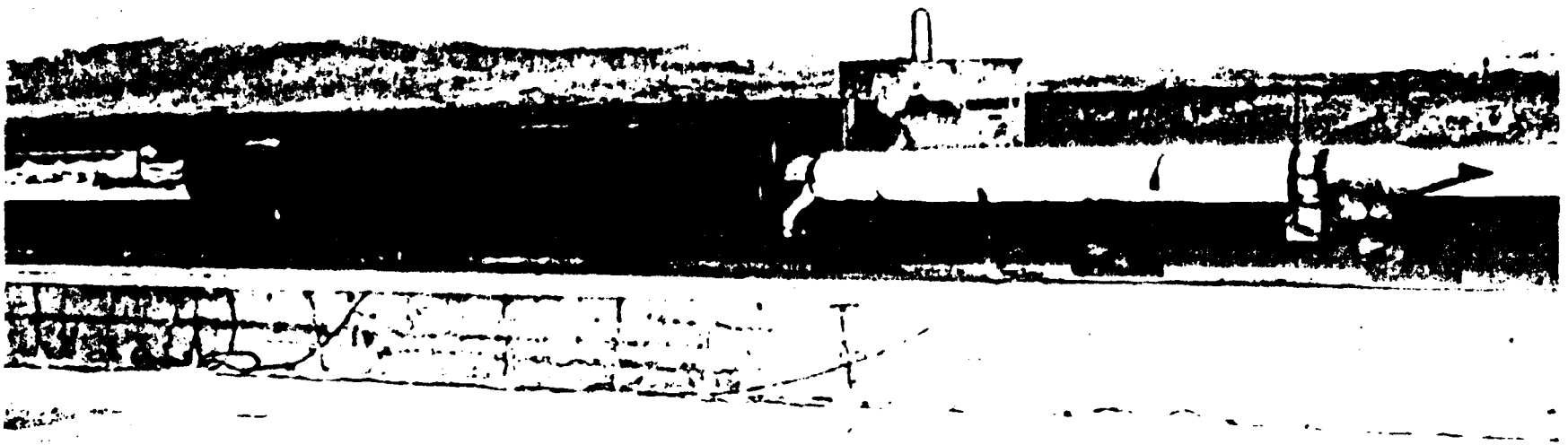

Figure 17. Sled vehicle with test cone.

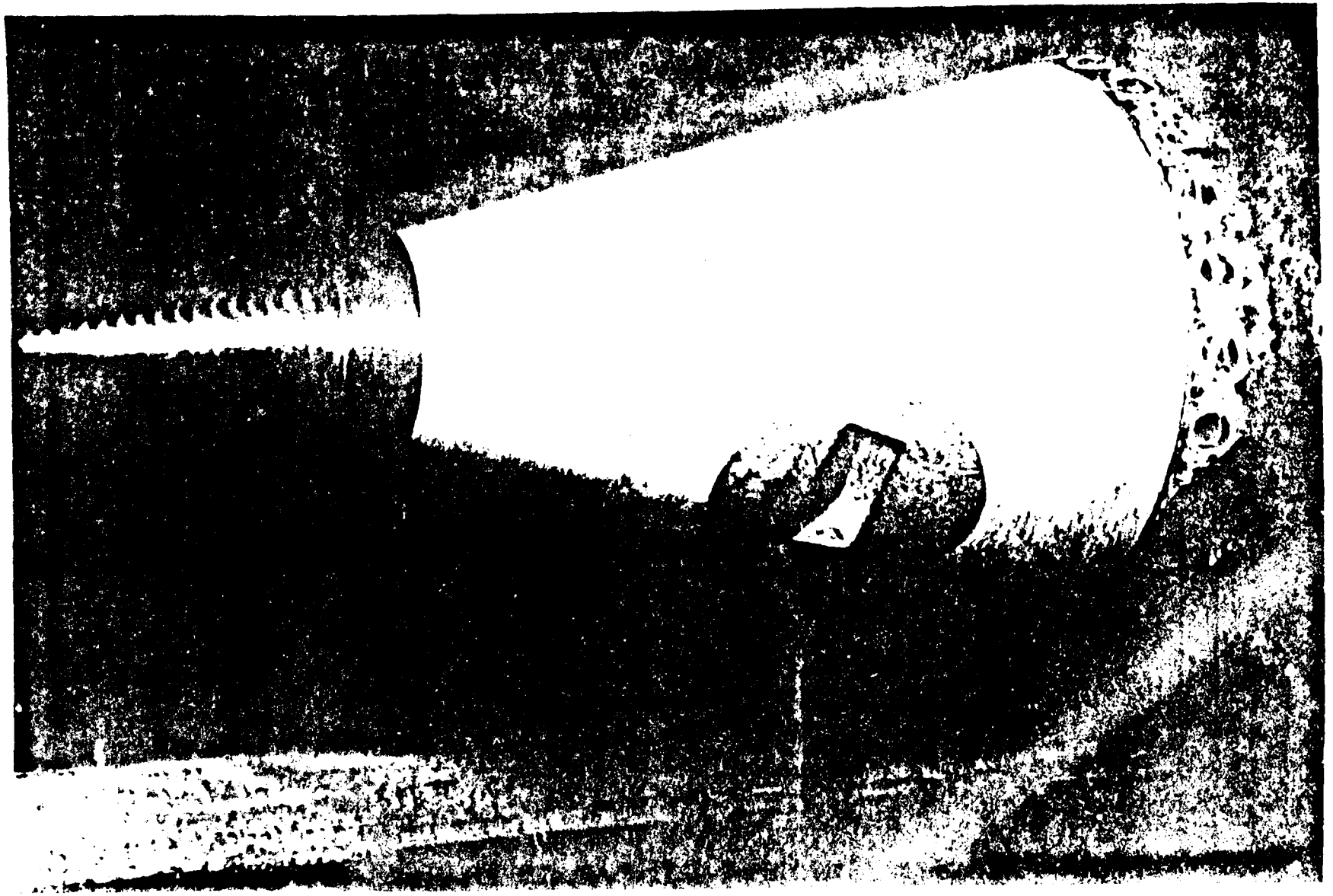

Figure 18. Close-up of test cone on sled vehicle.

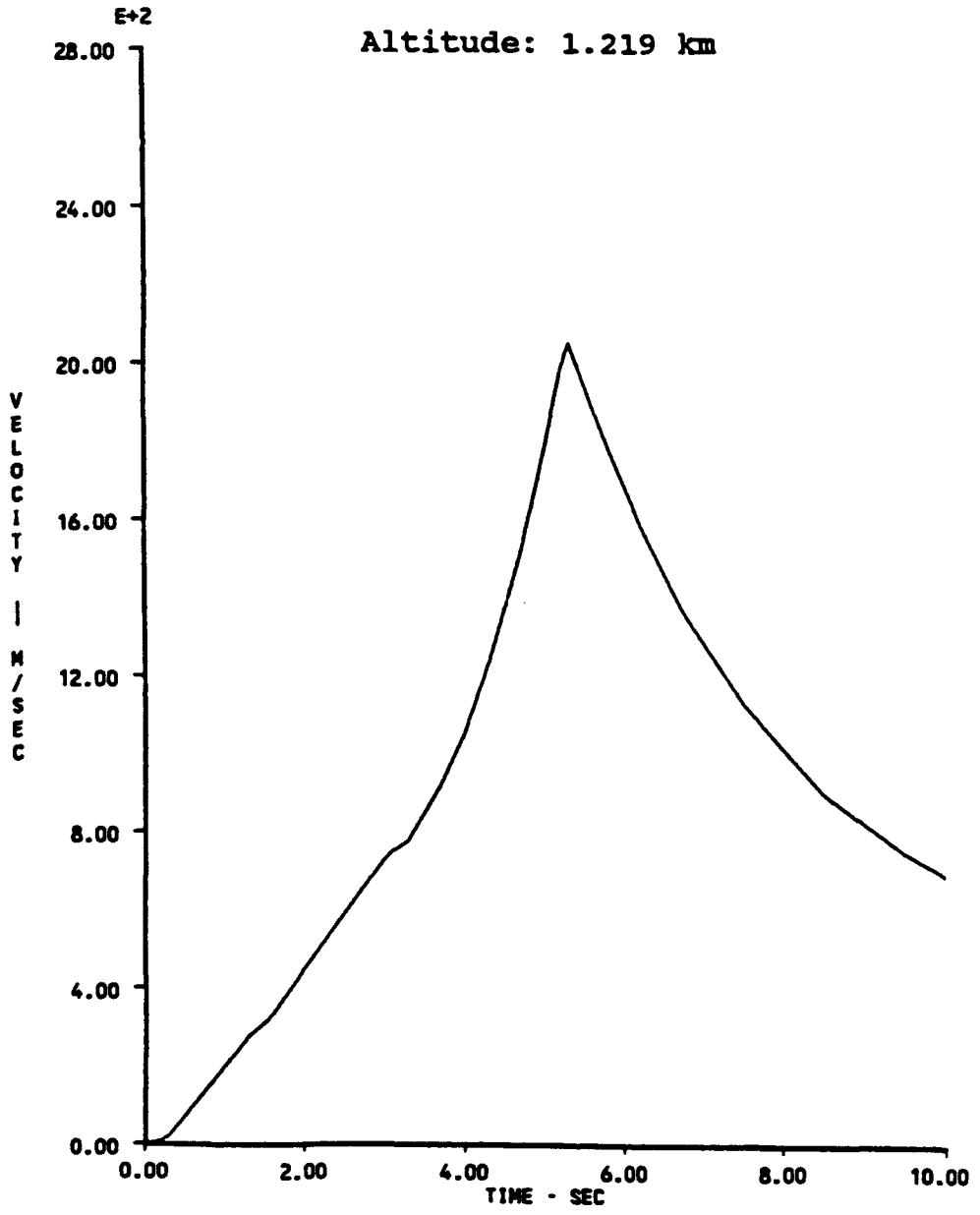


Figure 19. Measured sled velocity profile.

Figure 20. Sled vehicle and test cone at peak velocity.

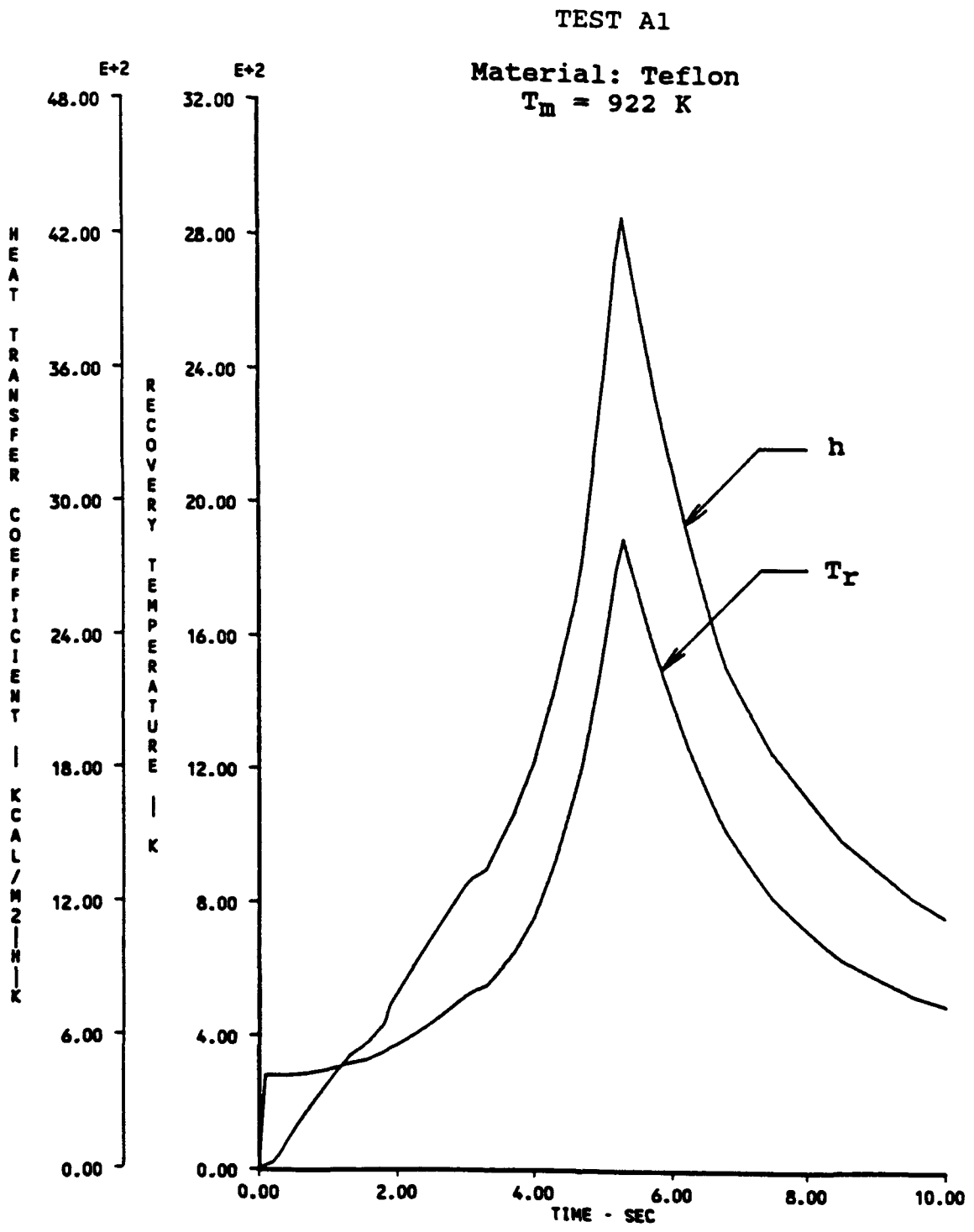


Figure 21. Calculated recovery temperature and unaugmented local heat transfer coefficient associated with Test A1.

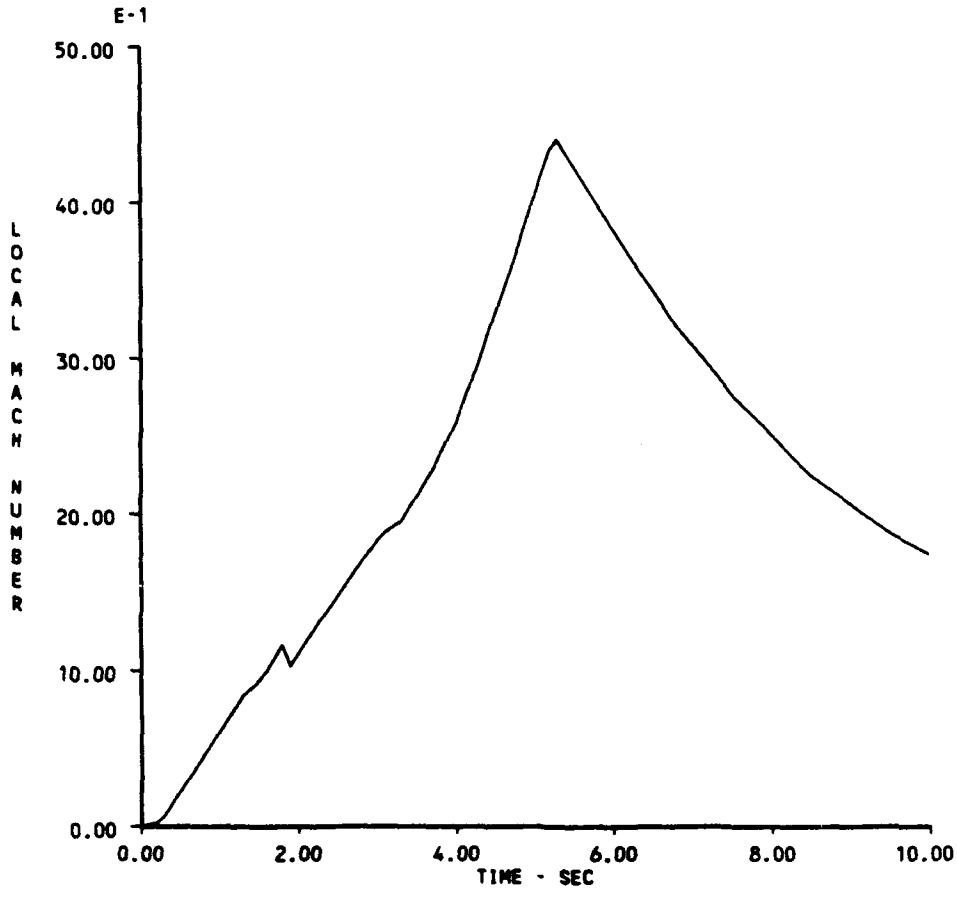


Figure 22. Calculated local Mach number vs. time for Test A1.

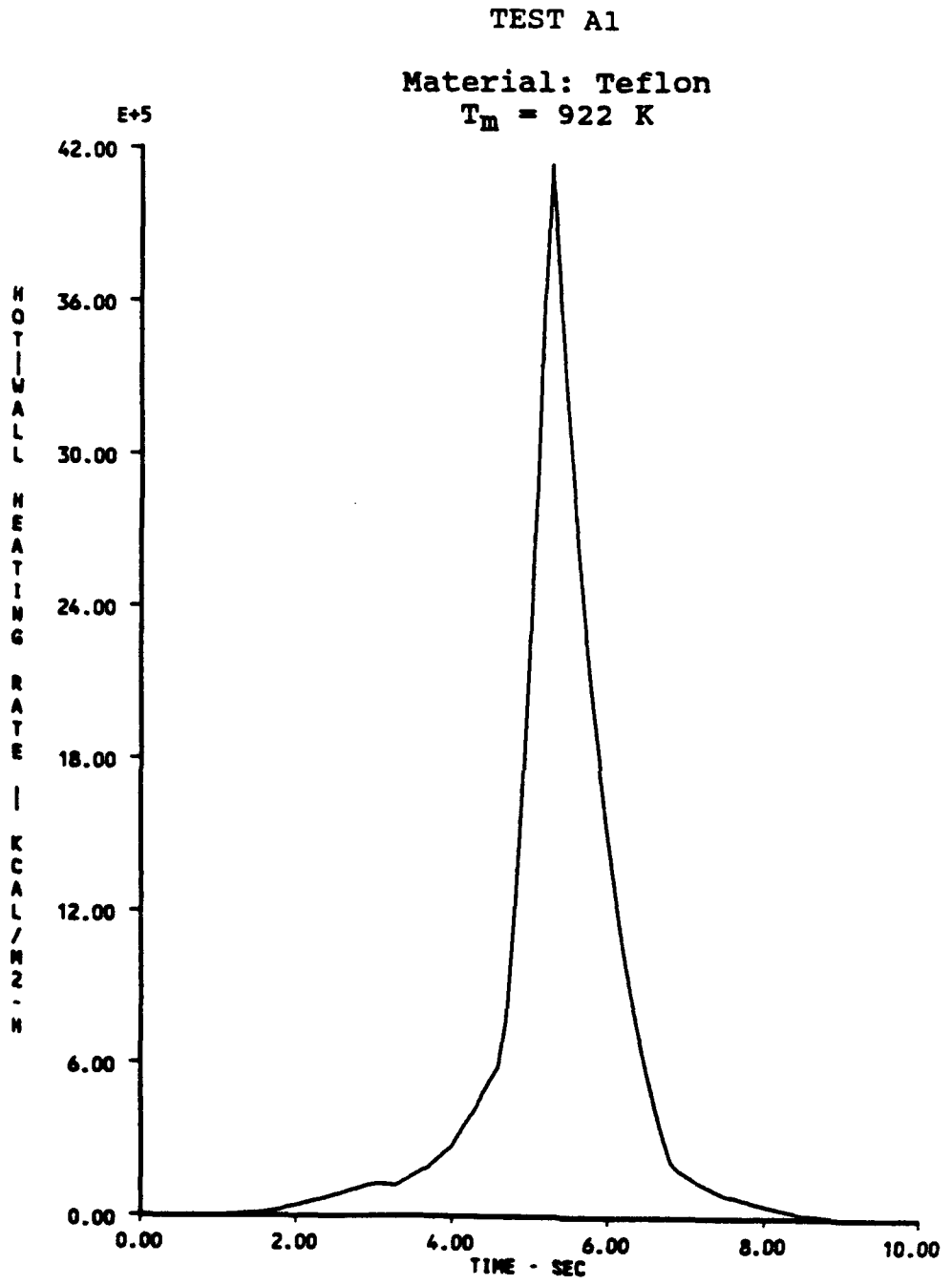


Figure 23. Calculated unaugmented hot-wall heating rate vs. time for Test A1.

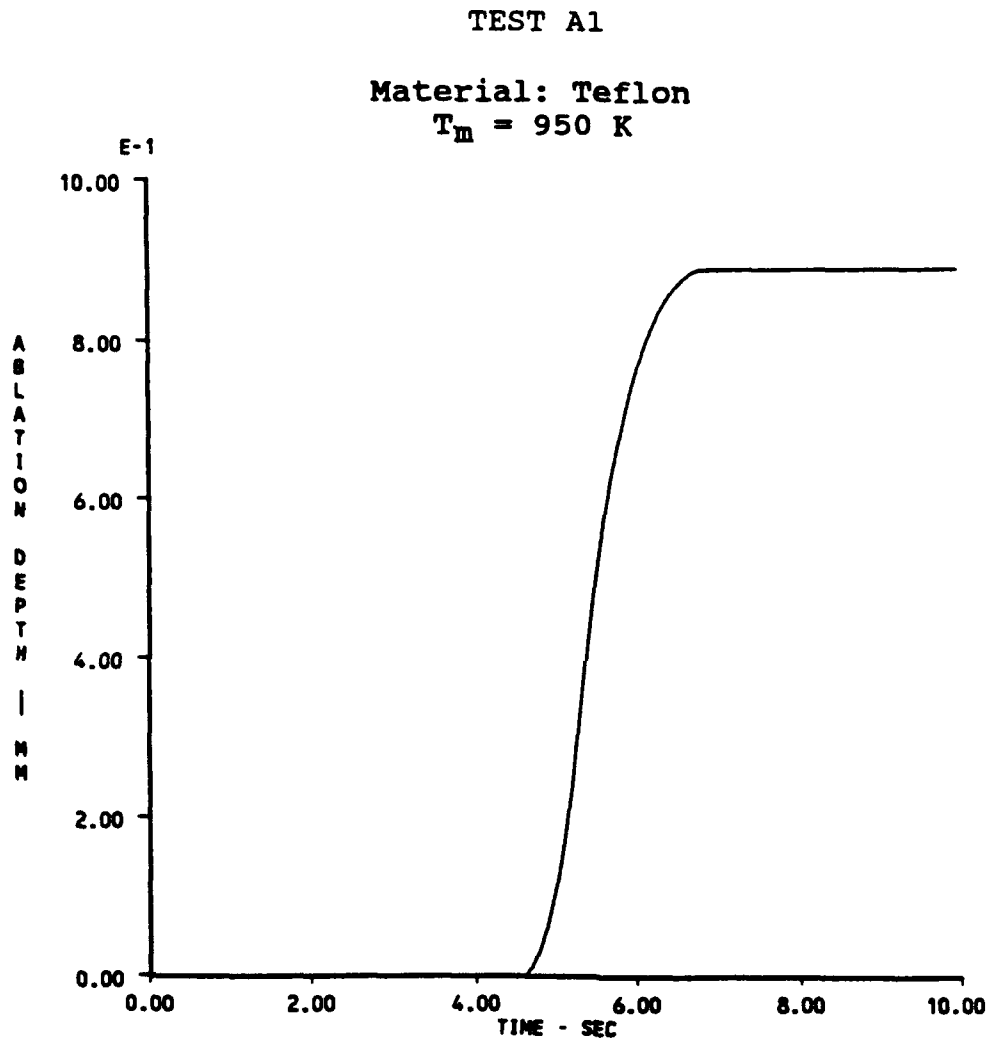


Figure 24. Calculated unaugmented ablation depth for Test A1.

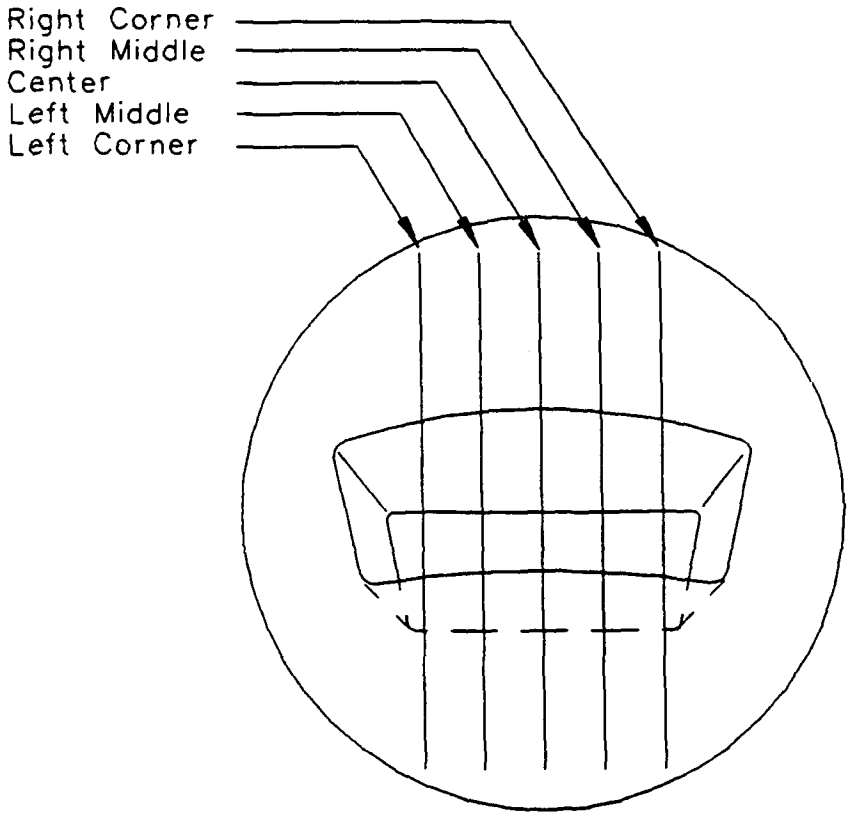


Figure 25. Measurement paths used for generating recession data.

TEST A1

Insert 2

Material: Teflon

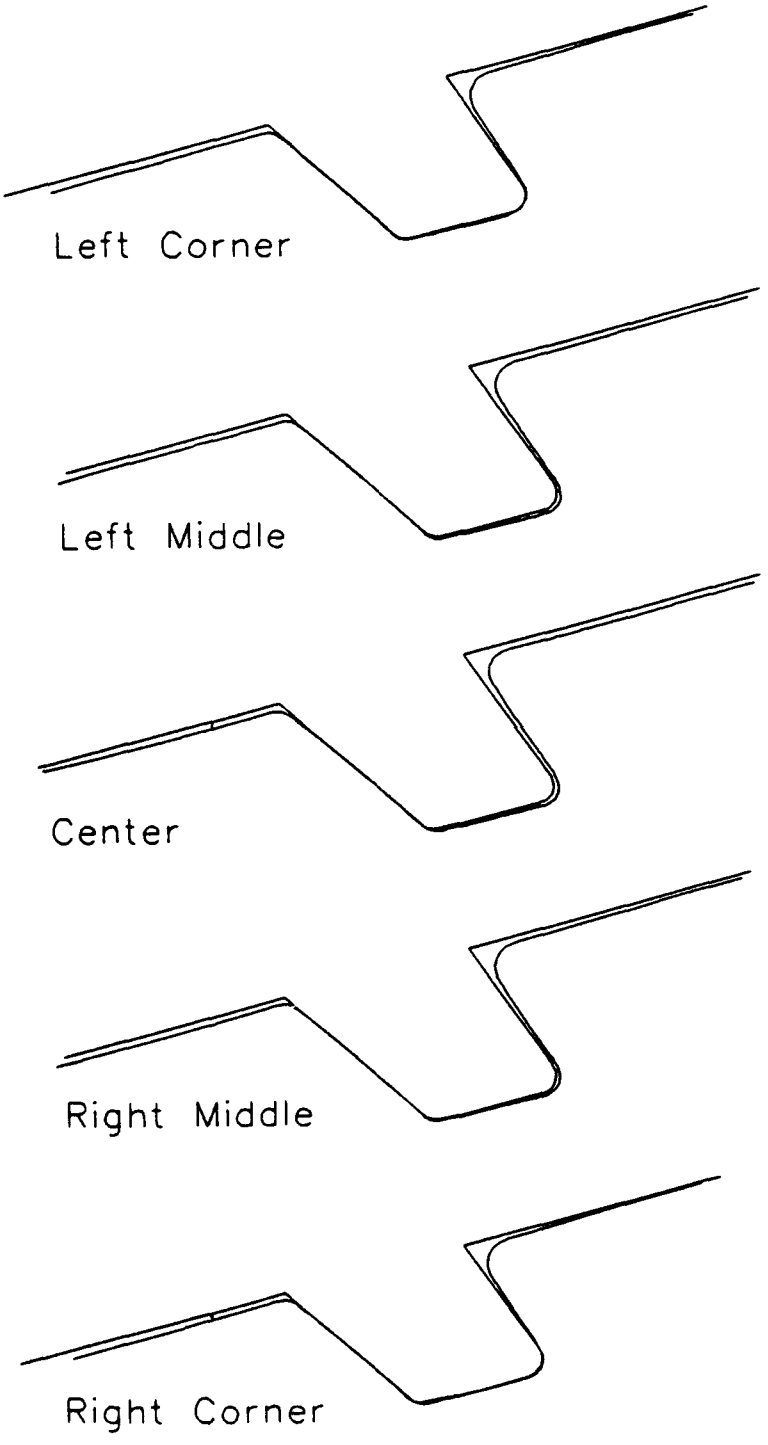


Figure 26. Pre- and post-test cavity profiles for Insert 2.

**Test A1**

Insert 3
Material: Teflon

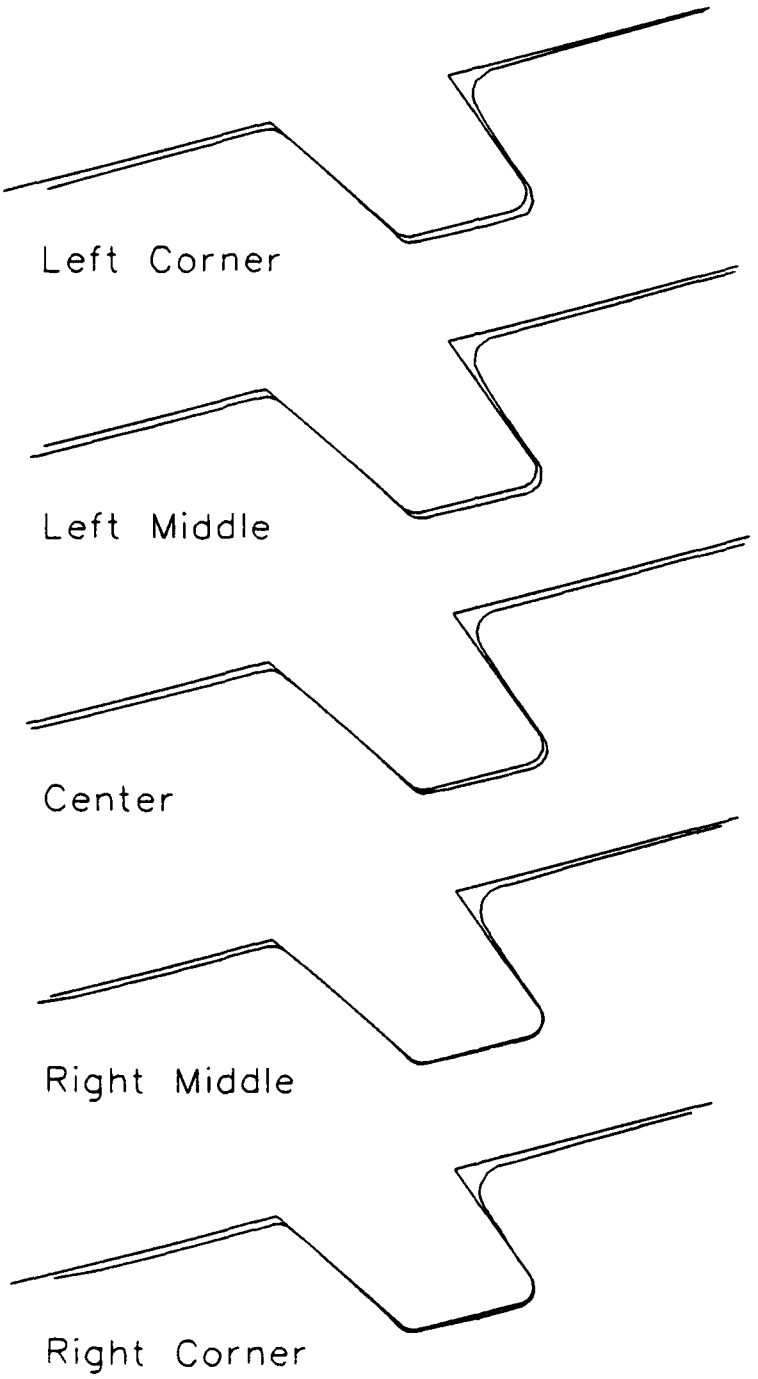


**Figure 27.** Pre- and post-test cavity profiles for Insert 3.

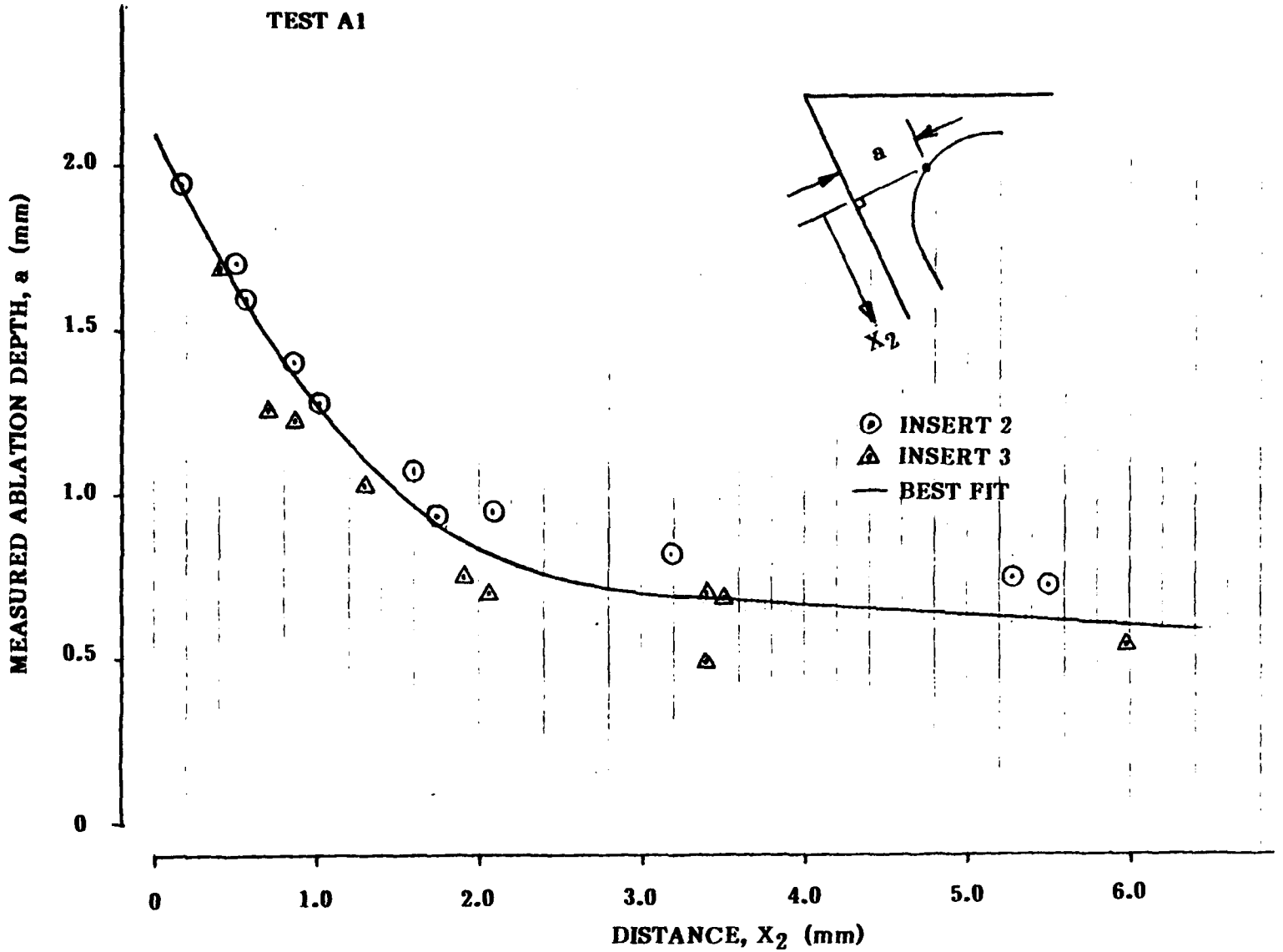


Figure 28. Measured in-cavity surface recession distributions for Test A1.

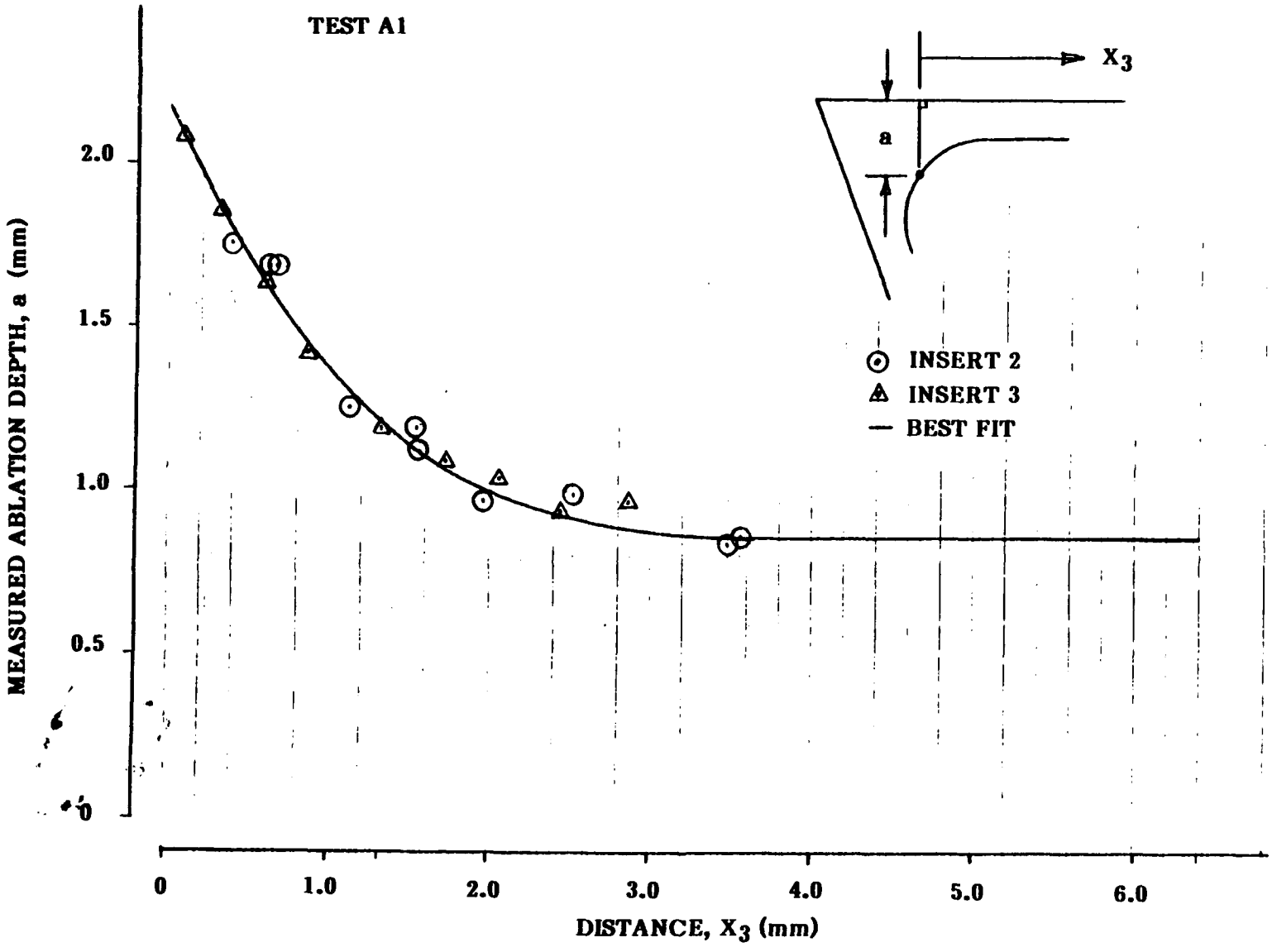


Figure 29. Measured downstream surface recession ditributions for Test A1.

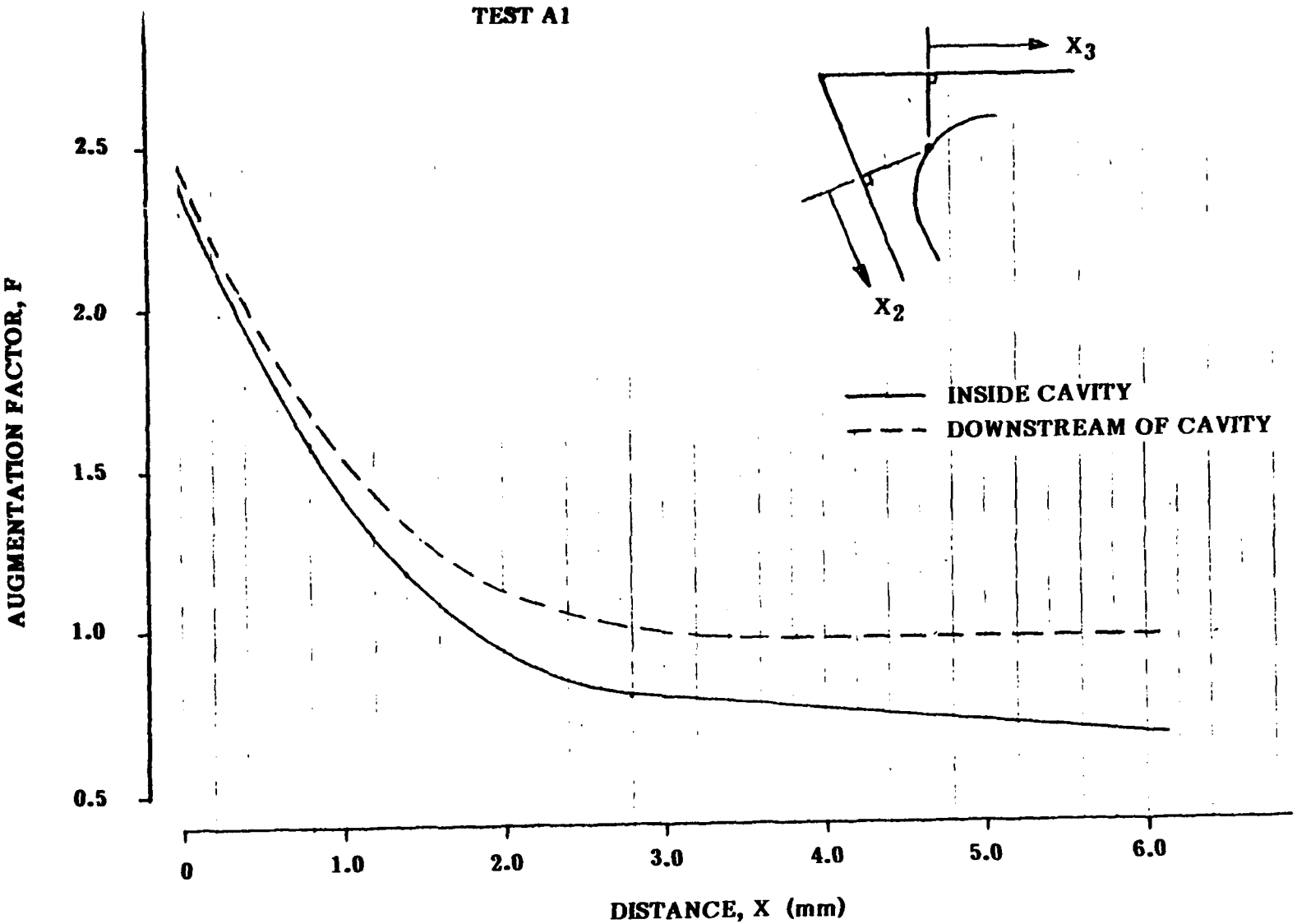


Figure 30. Measured in-cavity and downstream augmentation distributions for Test A1.

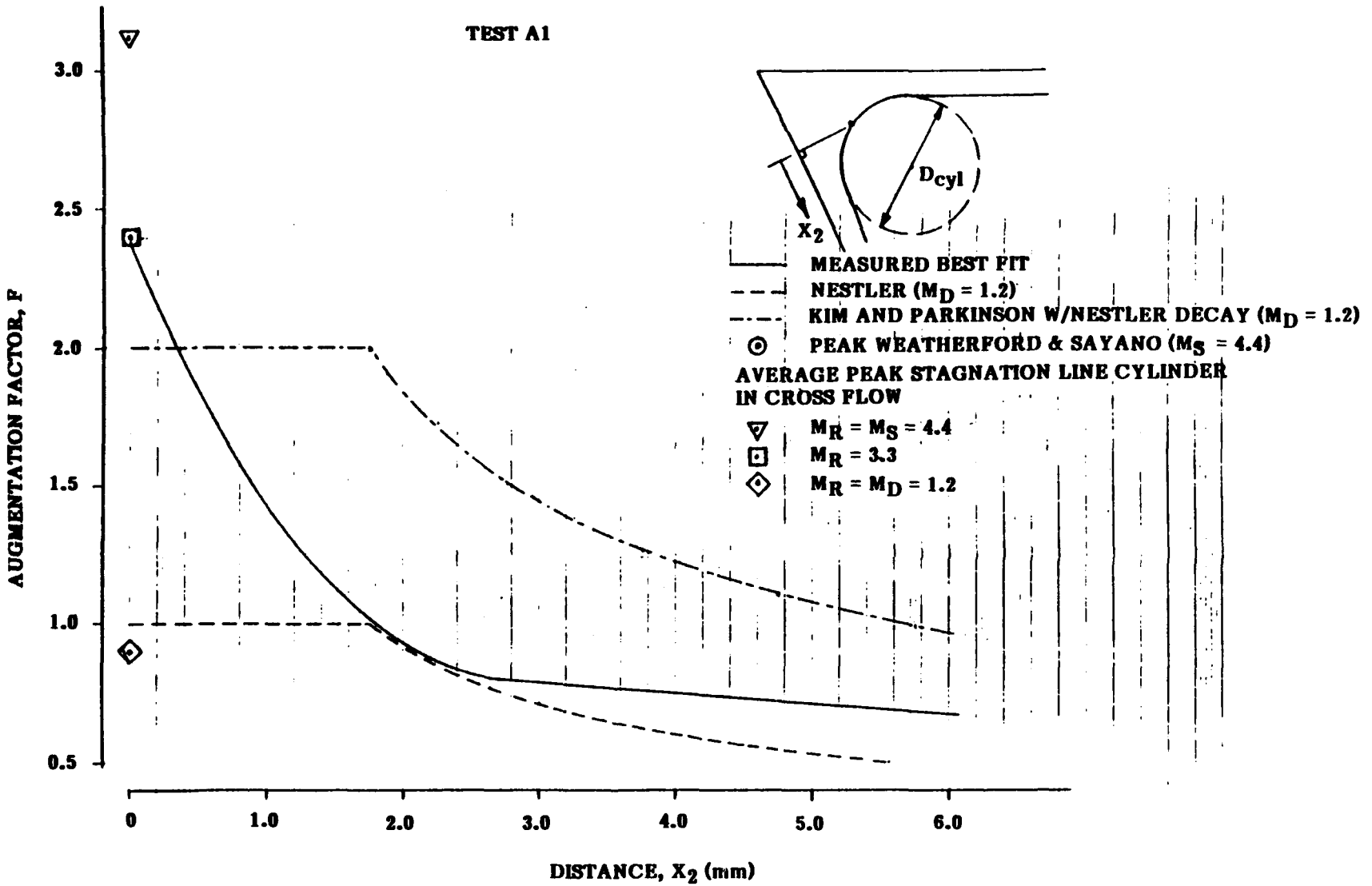


Figure 31. Measured in-cavity augmentation factors as compared to several analytical methods.

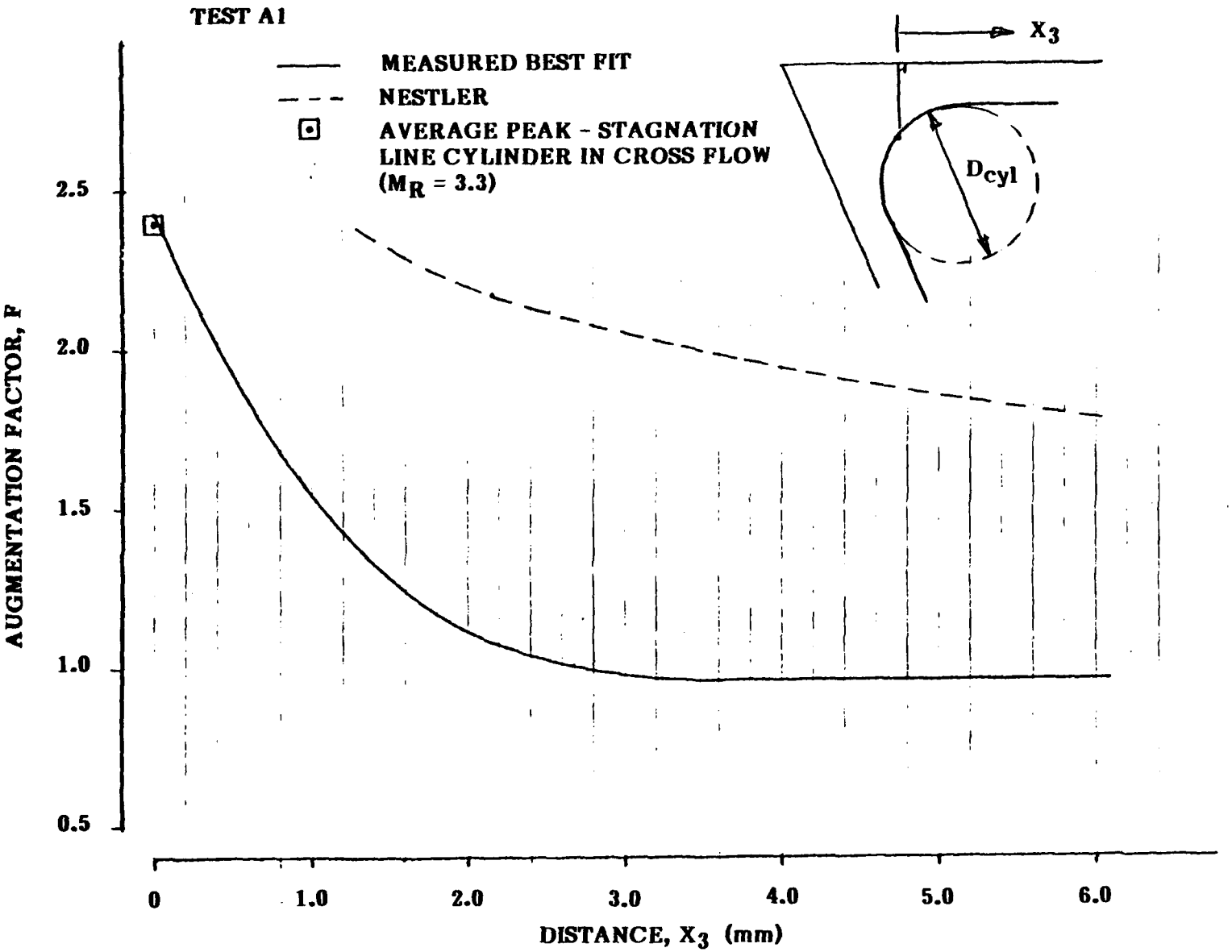


Figure 32. Measured downstream augmentation factors as compared several analytical methods.

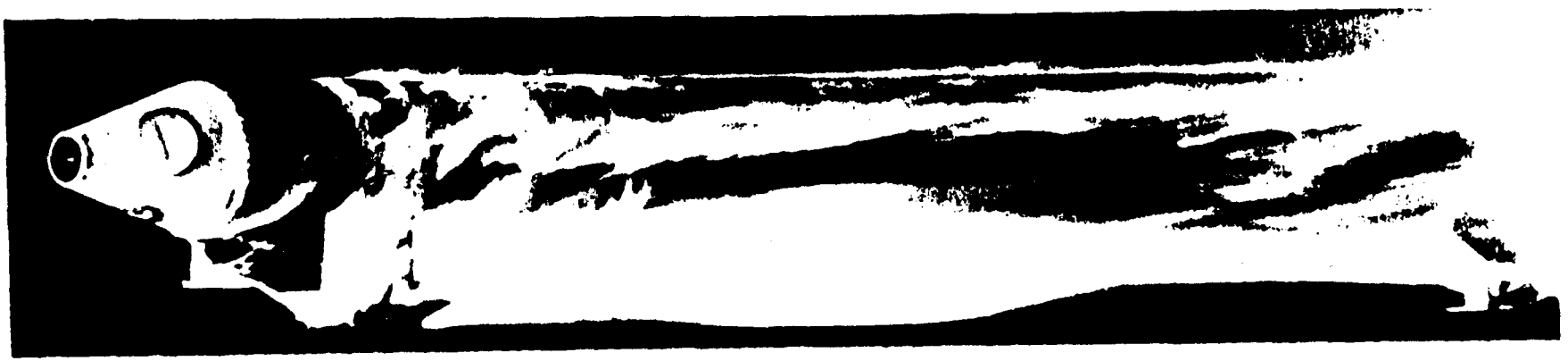

Figure 33. Test A2 at peak velocity showing nose-tip missing.

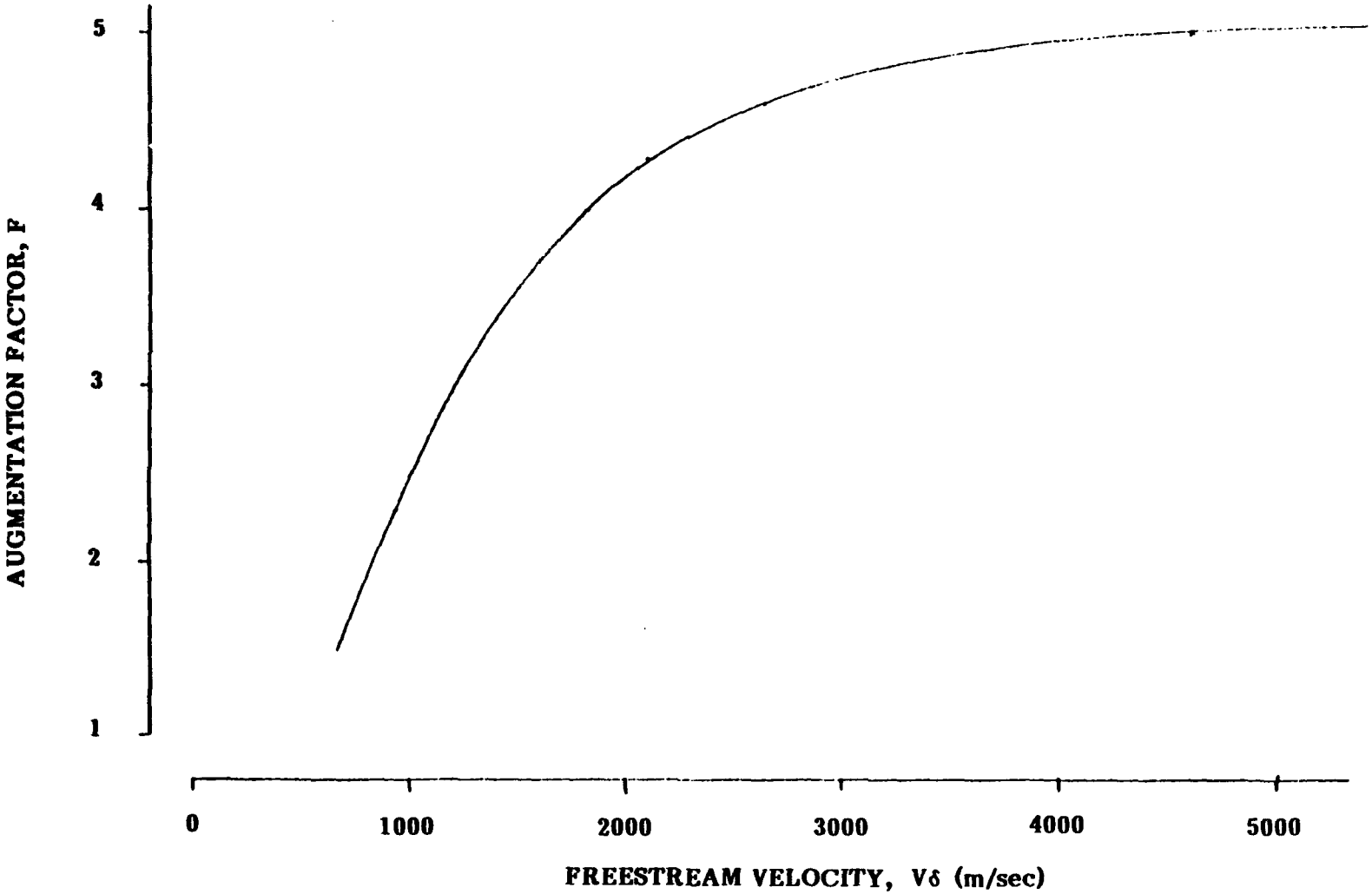


Figure 34. Maximum reattachment augmentation factors using cylinder in cross flow model as a function of freestream velocity.

# EVOLUTION OF HIGH PERFORMANCE SMALL ROCKET MOTORS

Robert N. Evans and David W. McNeill
U.S Army Missile Command
Redstone Arsenal, Alabama

## INTRODUCTION

This paper presents the in-house evolution of high performance composite rocket motorcases at the U.S. Army Missile Command. The rocket motors identified in this article will include SPIKE (Single Penetrator Kinetic Energy Missile), Improved SPIKE, Super SPIKE, Killer Bee, and the ADKEM (Advanced Kinetic Energy Missile) 3.75-inch diameter booster. All of the hypervelocity rocket motors listed above are high strength filament wound composite structures fabricated in-house at the U.S. Army Missile Command. Evolution of the rocket motors as evidenced primarily through substantial increases in propellant mass fraction ratios will be illustrated. Propellant mass fraction ratios are used in determining motorcase design efficiency. These increases were obtained through utilization of emerging fiber technology, integrally wound nozzles, and elimination of the forward head closure and pin joint. This paper will also discuss advantages of composite motorcase technology over conventional motorcase design techniques. These advantages include the ability to integrally wind the nozzle which permits highly accurate alignment of the throat with the centerline of the motor, installation of motorcase insulation prior to filament winding, and consistent motorcase geometry with minimum machining.

## THE SPIKE COMPOSITE MOTORCASE

The initial SPIKE motorcase design consisted of a maraging steel motorcase with a head closure and nozzle that were bonded to the case. This particular motorcase design had numerous problem areas. Approximately one-half of the maraging steel motorcases failed proof testing due to difficulties in machining the very thin 0.012-inch thick case wall. Variations in the wall thickness due to concentricity problems when machining resulted in missile curvature when the case was pressurized. The variations in thickness also caused critical flaw size issues to surface. Other problem areas included nozzle misalignment, application of motorcase insulation, and difficulties in obtaining a reliable bond between the head closure and nozzle with the motorcase.

The development of the SPIKE composite motorcase began in FY 82. The design requirements for the SPIKE motorcase are listed in table 1.

Table 1. SPIKE Motorcase Design Requirements

| | |
|---|---|
| Overall Length | 32.052 in |
| Inside Diameter | 1.754 in |
| Outside Diameter (Max) | 1.920 in |
| Propellant Grain Length | 28.500 in |
| Nozzle Throat Diameter | 1.000 in |
| MEOP | 2400 psi |
| Design Burst Pressure | 4000 psi |

Utilizing these design criteria, the Composite Structures/Materials Function of Structures Directorate developed a filament wound composite motorcase. The motorcase utilized an integrally wound glass phenolic nozzle insert which eliminated the nozzle misalignment problems. A full diameter opening on the forward end of the motor to facilitate propellant loading was also implemented. However, the full diameter opening required a head closure and pin joint to seal the forward end of the motorcase. The pin joint eliminated the bonding problems that were encountered with the maraging steel case. The winding mandrel was configured to allow the installation of insulation on the aft end of the case prior to filament winding. This eliminated a tedious hand operation required on the maraging steel case. The winding mandrel was also designed to allow the borerider surfaces to be machined between centers while the motorcase was still on the mandrel. This guaranteed nozzle alignment with the centerline of the motor.

The filament wound motorcase was fabricated with AS4 graphite and Kevlar 49 aramid fiber. The pin joint on the forward end of the case was reinforced with two layers of E-Glass cloth and AS4 graphite hoop windings. The pin joint build up area also served as the front borerider. Figure 1 shows the SPIKE composite motorcase along with the maraging steel counterpart. Table 2 lists the SPIKE composite motorcase physical characteristics.

Table 2. SPIKE Composite Motorcase Physical Characteristics

| | |
|---|---|
| Overall Length | 32.052 in |
| Borerider Diameter | 1.920 in |
| Inside Diameter | 1.754 in |
| Case Body Diameter | 1.830 in |
| Wall Thickness | 0.038 in |
| Composite Case Weight | 266.0 g |
| Head Closure Weight | 46.8 g |
| Propellant Weight | 1008.0 g |
| Propellant Mass Fraction | 0.76 |

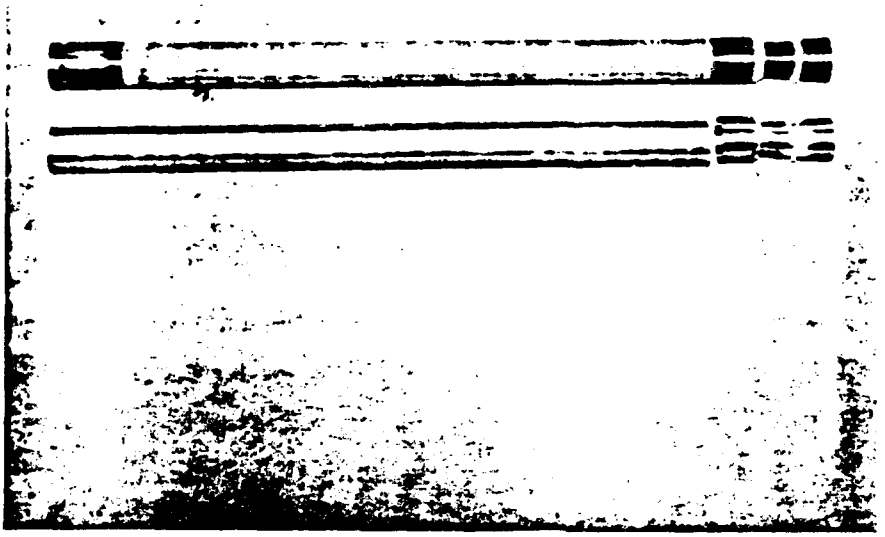

Figure 1. Composite and Maraging Steel SPIKE Motorcases

To verify structural integrity, all of the SPIKE motorcases fabricated were proof tested to 3000 psi. Figure 2 illustrates a pressure versus time curve for a SPIKE static test, and Figure 3 is the thrust versus time curve for the same test. Table 3 provides a summary of the SPIKE composite motorcase performance.

Table 3. SPIKE Composite Motorcase Performance Summary

| | |
|---|---|
| Design Burst Pressure | 4000 psi |
| MEOP | 2400 psi |
| Proof Test Pressure | 3000 psi |
| Thrust | 2200 lbs |
| Burn Time | 0.25 sec |
| Specific Impulse (Isp) | 228 sec |

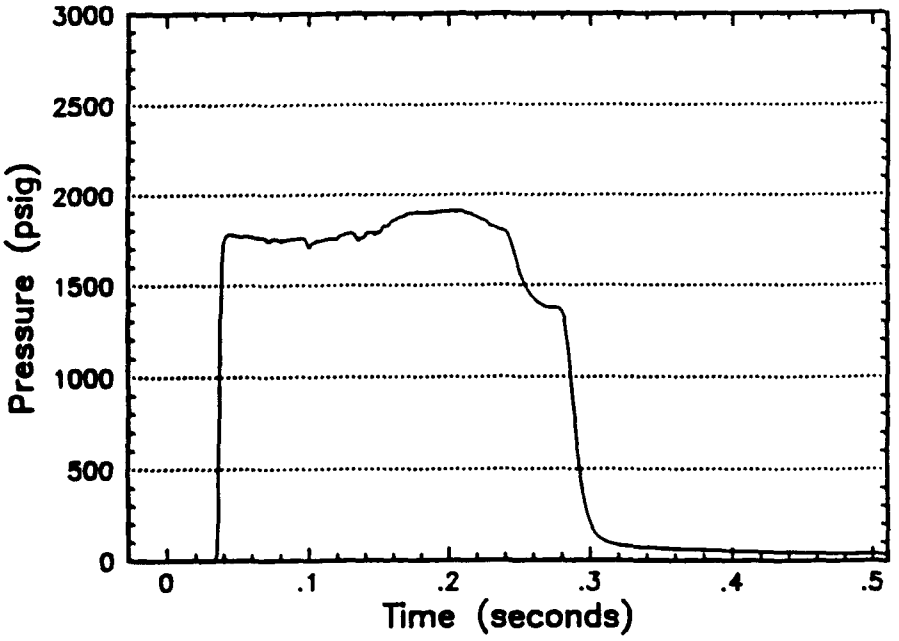


Figure 2. SPIKE Pressure versus Time Curve

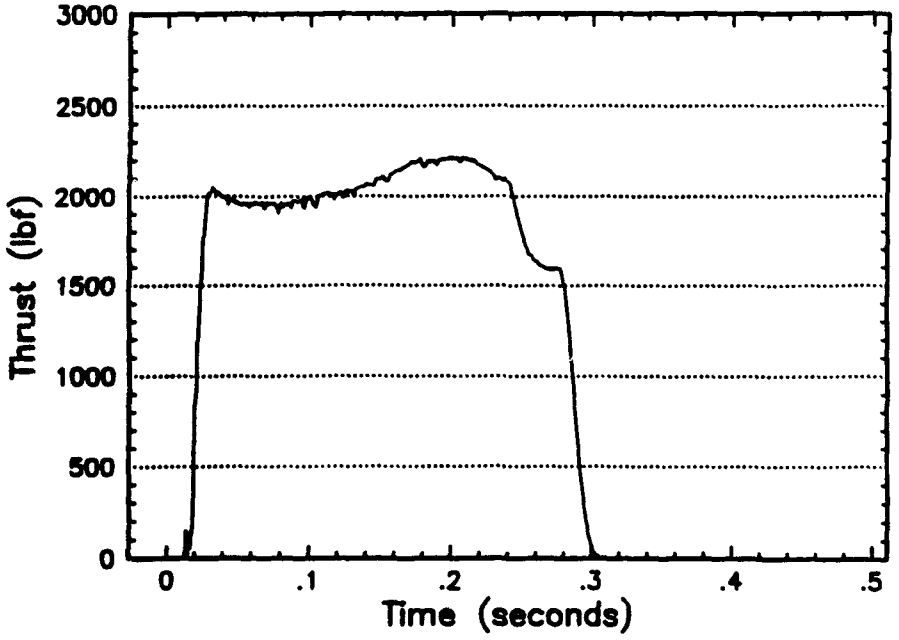


Figure 3. SPIKE Thrust versus Time Curve

The SPIKE composite motorcase performance was highly successful. The U.S. Army Missile Command has fabricated over 600 SPIKE motorcases. There has never been a failure during proof, static, or flight testing. The SPIKE composite motorcase program demonstrated the advantages of modern composite materials in future Army missile systems. The composite case proved to be lighter, stronger, stiffer, and more reliable than the maraging steel counterpart. Furthermore, it was demonstrated that the composite case was readily producible and substantially lower in cost than the maraging steel case.

## THE IMPROVED SPIKE MOTORCASE

The design criteria for the Improved SPIKE motorcase were identical to that of the original SPIKE motor. With the emergence of new high strength graphite fibers, MICOM performed a materials characterization program to find a new high performance fiber to use in the fabrication of the Improved SPIKE motorcase. AMOCO T-40 graphite was selected to replace the AS4 graphite fiber on the original SPIKE. The T-40 graphite is much stronger and stiffer than the AS4 fiber. The Kevlar 49 hoop layer was also replaced with the T-40 fiber. Utilizing the T-40 graphite fiber allowed the motorcase wall thickness to be reduced, thus reducing case weight.

Another improvement to the SPIKE motorcase was the nozzle insert. The SPIKE motorcase utilizes a machined glass phenolic throat insert. These inserts were complex in shape and were difficult and expensive to machine. The Improved SPIKE motorcase utilized a compression molded glass phenolic throat insert that is readily producible and has a consistent geometry between parts. These molded inserts not only performed as well as the machined inserts, but were less expensive to produce. Figure 4 shows the Improved SPIKE motorcase. Table 4 lists the Improved SPIKE motorcase physical characteristics.

Table 4. Improved SPIKE Motorcase Physical Characteristics

| | |
|---|---|
| Overall Length | 32.052 in |
| Borerider Diameter | 1.920 in |
| Inside Diameter | 1.754 in |
| Case Body Diameter | 1.812 in |
| Wall Thickness | 0.029 in |
| Composite Case Weight | 230.0 g |
| Head Closure Weight | 46.8 g |
| Propellant Weight | 1008.0 g |
| Propellant Mass Fraction | 0.78 |

Figure 4. Improved SPIKE Motorcase

The Improved SPIKE motorcase and the SPIKE motorcase had identical motor performance characteristics. The Improved SPIKE motorcase had a greater propellant mass fraction, was easier to fabricate, and lower in cost than the original SPIKE composite motorcase.

## THE SUPER SPIKE MOTORCASE

In an effort to increase the propellant mass fraction of the Improved SPIKE, the Super SPIKE motorcase was developed. Super SPIKE utilized a compression molded glass phenolic nozzle insert that had a throat diameter of 0.900 inches. The port of the propellant grain was also decreased to 0.900 inches. This allowed an additional 227 grams of propellant to be cast in the motor. The only other changes to the Improved SPIKE motorcase were the filament winding parameters.

The change in the throat diameter of the nozzle insert, and changes in the winding parameters resulted in an increase in weight of the Super SPIKE motorcase. However, this small increase in weight allowed an additional 227 grams of propellant to be added to the motor. This trade off increased the propellant mass fraction of Super SPIKE by 2.0% over that of Improved SPIKE. A summary of the Super SPIKE physical characteristics is listed in table 5.

Table 5. Super SPIKE Motorcase Physical Characteristics

| | |
|---|---|
| Overall Length | 32.052 in |
| Borerider Diameter | 1.920 in |
| Inside Diameter | 1.754 in |
| Case Body Diameter | 1.814 in |
| Wall Thickness | 0.030 in |
| Composite Case Weight | 260.0 g |
| Head Closure Weight | 46.8 g |
| Propellant Weight | 1235.0 g |
| Propellant Mass Fraction | 0.80 |

The pressure versus time and thrust versus time curves for a Super SPIKE motorcase static firing can be seen in figures 5 and 6, respectively. A summary of the Super SPIKE motorcase performance is listed in table 6.

Table 6. Super SPIKE Motorcase Performance Summary

| | |
|---|---|
| Design Burst Pressure | 4000 psi |
| MEOP | 2400 psi |
| Proof Test Pressure | 3000 psi |
| Thrust | 2400 lbs |
| Burn Time | 0.29 sec |
| Specific Impulse (Isp) | 238 sec |

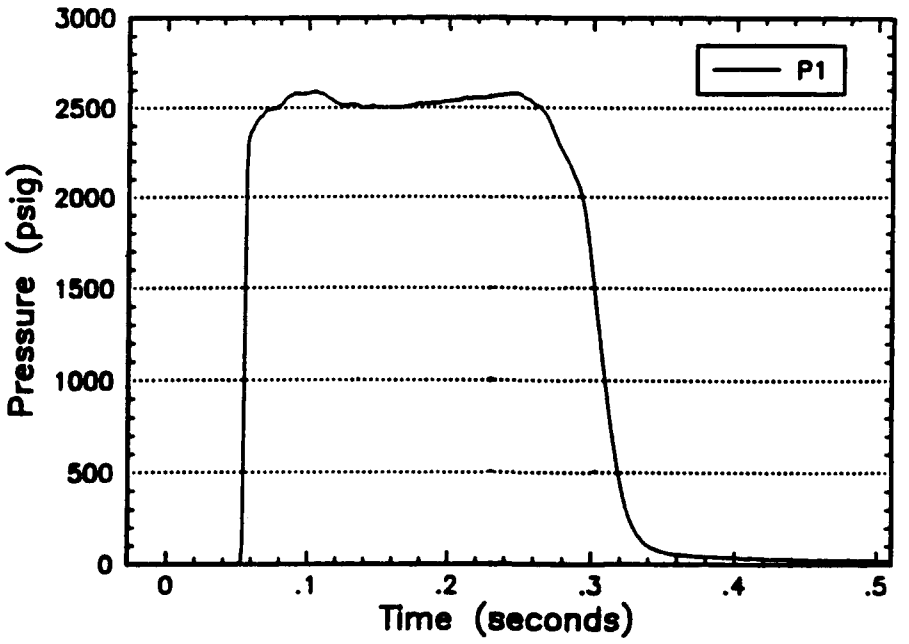


Figure 5. Super SPIKE Pressure versus Time Curve

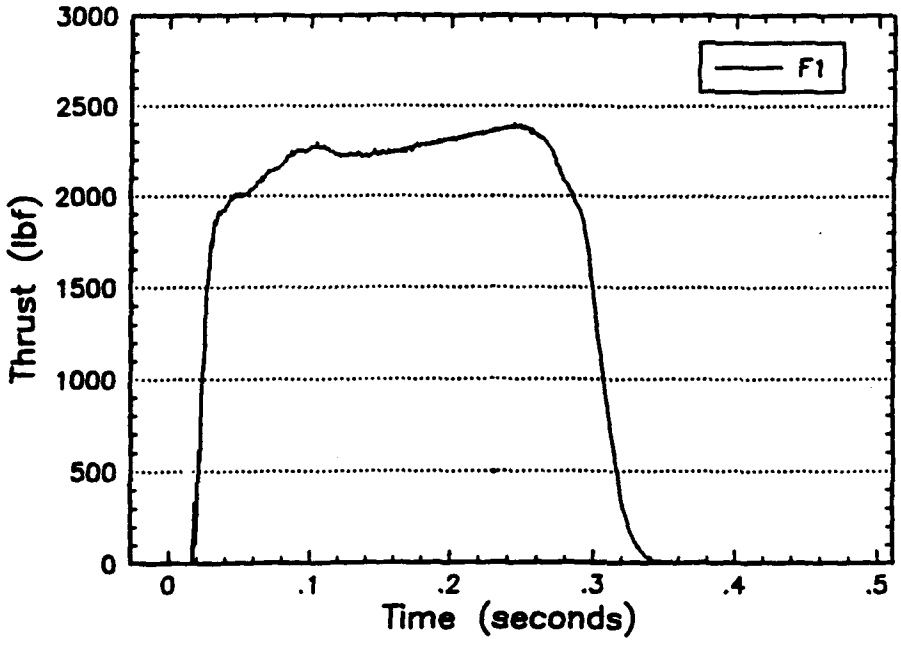


Figure 6. Super SPIKE Thrust versus Time Curve

The Super SPIKE program yielded a motor that had an increase in thrust, specific impulse, and propellant mass fraction over that found in SPIKE. As shown above, the propellant mass fraction was increased from 0.76 for SPIKE to 0.80 for Super SPIKE.

## THE KILLER BEE MOTORCASE

The objective of the Killer Bee composite motorcase development program was to fabricate a hypervelocity composite motorcase version of the 2.75 rocket. It was later determined that Killer Bee would be used as a 90% scale demonstration of the ADKEM (Advanced Kinetic Energy Missile).

The development of the Killer Bee motorcase began in the fourth quarter of FY 88. The design requirements for the Killer Bee motorcase is listed in table 7.

Table 7. Killer Bee Motorcase Design Requirements

| | |
|---|---|
| Overall Length | 45.000 in |
| Inside Diameter | 2.606 in |
| Outside Diameter (Max) | 2.885 in |
| Propellant Grain Length | 37.000 in |
| Nozzle Throat Diameter | 1.106 in |
| MEOP | 5000 psi |
| Design Burst Pressure | 7500 psi |

By utilizing these design criteria, the Composite Structures/Materials Function of Structures Directorate designed a motorcase very similar to that of SPIKE. Like SPIKE, Killer Bee utilized an integrally wound nozzle and a full diameter opening on the forward end of the motor. Once again the full diameter opening required a pin joint and head closure to seal the front end of the motorcase. Since Killer Bee was fabricated with the same techniques as SPIKE, the problems of nozzle misalignment and inconsistent bonding procedures were again avoided. One significant difference between SPIKE and Killer Bee is that Killer Bee required insulation over the entire length of the motorcase. However, it was applied directly to the winding mandrel before filament winding began.

The Killer Bee motorcase utilized a compression molded ceramic phenolic throat insert and was filament wound with AMOCO T-40 graphite fiber. The pin joint on the forward end of the case was reinforced with four layers of S-glass cloth and T-40 graphite hoop windings. The pin joint area also served as a front borerider. Figure 7 shows the Killer Bee and Improved SPIKE motorcases. Table 8 lists the Killer Bee motorcase physical characteristics.

Table 8. Killer Bee Motorcase Physical Characteristics

| | |
|---|---|
| Overall Length | 45.000 in |
| Borerider Diameter | 2.885 in |
| Inside Diameter | 2.606 in |
| Case Body Diameter | 2.764 in |
| Wall Thickness.(not including insulation) | 0.049 in |
| Composite Case Weight | 1050.0 g |
| Head Closure Weight | 180.0 g |
| Propellant Weight | 4313.0 g |
| Propellant Mass Fraction | 0.78 |

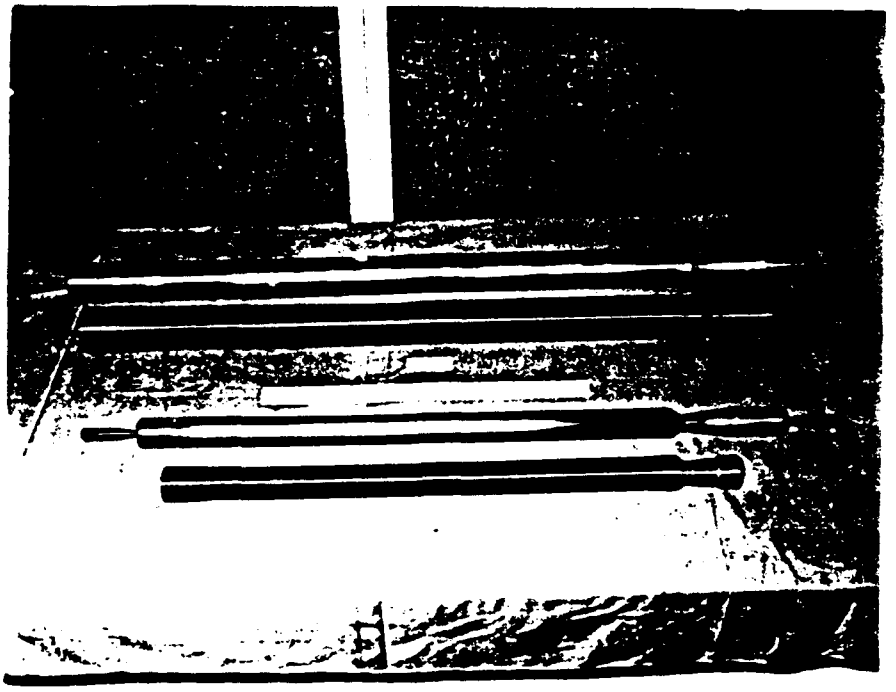

Figure 7. Killer Bee and Improved SPIKE Motorcases

The pressure versus time and thrust versus time curves for a Killer Bee motorcase static firing can be seen in Figures 8 and 9, respectively. A summary of the Killer Bee motorcase performance is listed in Table 9.

Table 9. Killer Bee Motorcase Performance Summary

| | |
|---|---|
| Design Burst Pressure | 7500 psi |
| MEOP | 5000 psi |
| Proof Test Pressure | 6250 psi |
| Thrust | 8900 lbs |
| Burn Time | 0.40 sec |
| Specific Impulse (Isp) | 251 sec |

The Killer Bee motorcase is virtually a scaled up SPIKE motorcase. Requirements for increased velocity with larger payloads have driven the size of these motors to become much larger. As mentioned before, Killer Bee was utilized as a 90% scale version of the ADKEM missile (see figure 10). The propellant mass fraction for Killer Bee is high, but future requirements (ADKEM) will need propellant mass fractions of greater than 0.80. In order to meet these requirements the ADKEM 3.75-inch diameter booster is in the process of being developed.

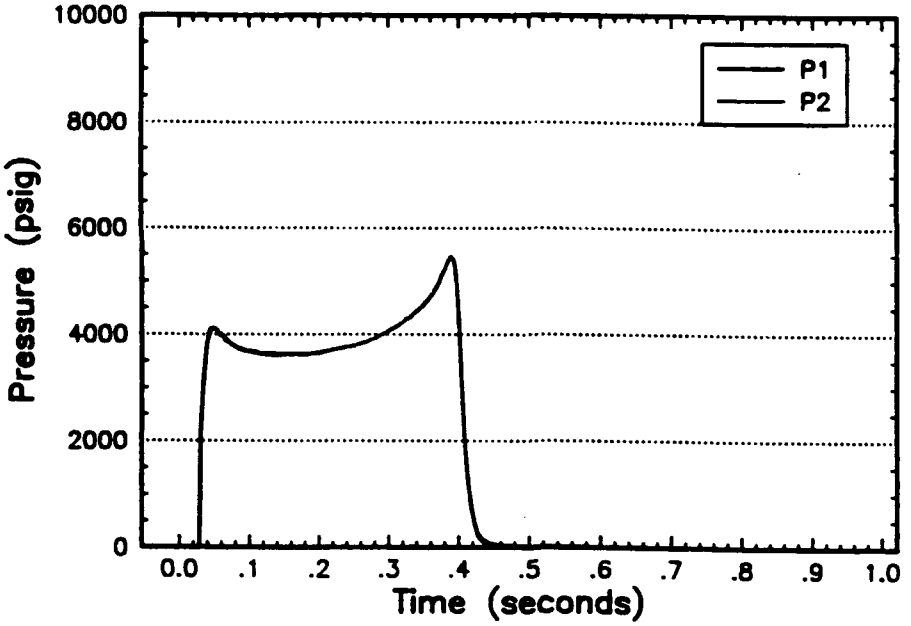


Figure 8. Killer Bee Pressure versus Time Curve

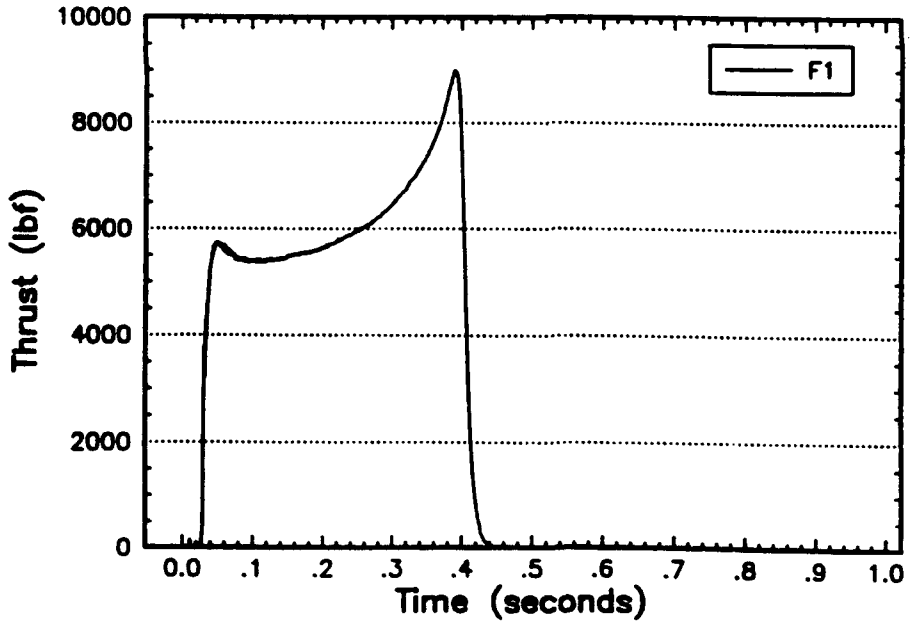


Figure 9. Killer Bee Thrust versus Time Curve

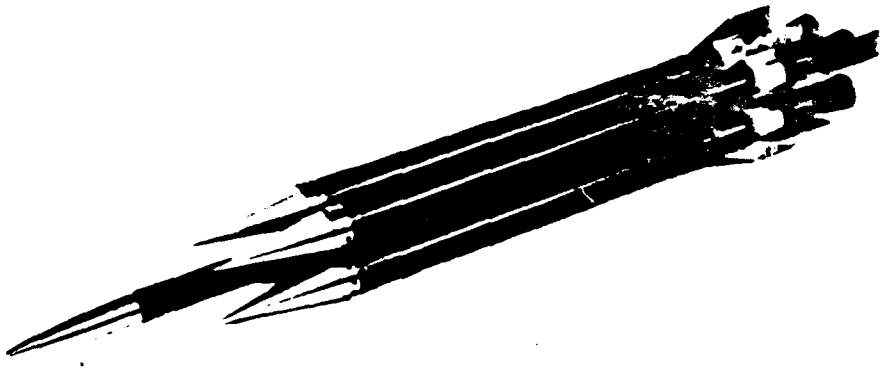

Figure 10. ADKEM Missile (90% Scale)

The ADKEM 3.75-Inch Diameter Booster

The Advanced Kinetic Energy Missile (ADKEM) is a U.S. Army Missile Command in-house missile design. The main objective of this missile system is to defeat the heavy armor threat of today. The requirements for this missile include an increase in penetration mass and velocity. In order to meet the velocity criteria, a lightweight, high performance, short action time booster is required. The ADKEM 3.75-inch diameter booster is being developed to meet these criteria.

The development of the ADKEM booster began in FY 89. The design requirements for the ADKEM booster is listed in table 10.

Table 10. ADKEM Booster Design Requirements

| | |
|---|---|
| Overall Length | 43.180 in |
| Inside Diameter | 3.600 in |
| Outside Diameter (Max) | 3.870 in |
| Propellant Grain Length | 37.500 in |
| Nozzle Throat Diameter | 1.660 in |
| MEOP | 4940 psi |
| Design Burst Pressure | 7400 psi |
| Propellant Mass Fraction | 0.85 |

By utilizing these design criteria, the Composite Structures/Materials Function of Structures Directorate has designed a motorcase similar to Killer Bee in the nozzle area. However, in order to meet the propellant mass

fraction requirement of 0.85, the head end configuration of the motorcase had to be modified. The SPIKE and Killer Bee motorcases utilized a full diameter opening on the head end of the case. This configuration requires a pin joint build-up area, and an aluminum head closure to seal the end of the motor. This design is very inefficient and only adds to the weight of the motorcase. The ADKEM booster is designed with an integrally wound dome and pole piece which will significantly reduce the weight of the motorcase. A drawing of the head end of the ADKEM booster with the integrally wound dome can be seen in figure 11. A parametric study to determine the motorcase weight savings was performed. A drawing of the head end of the ADKEM booster with a full diameter opening and head closure is listed in figure 12. Table 11 summarizes the component weights of the two ADKEM motor concepts.

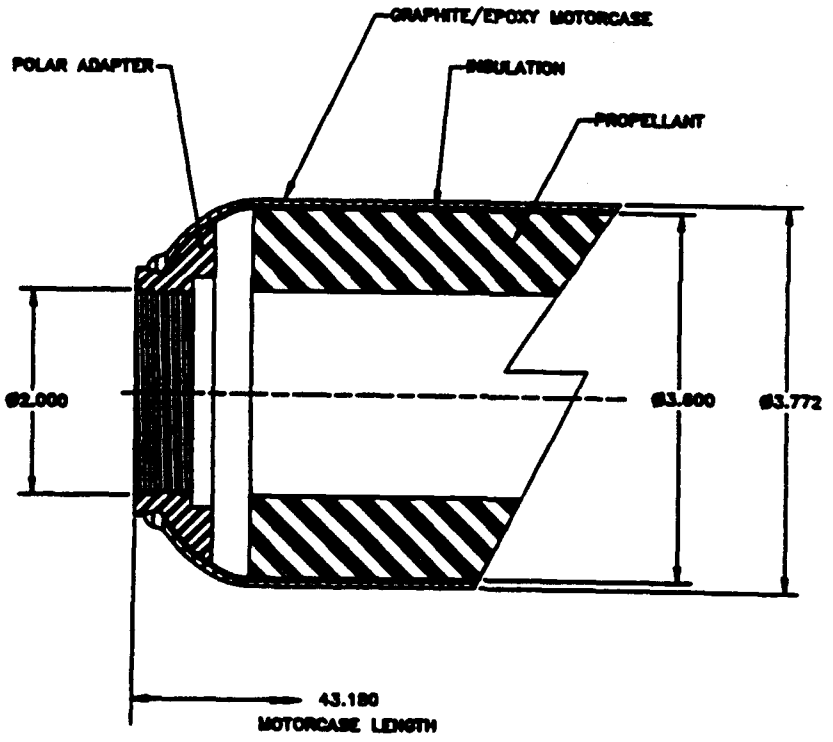


Figure 11. ADKEM Booster with Integrally Wound Dome

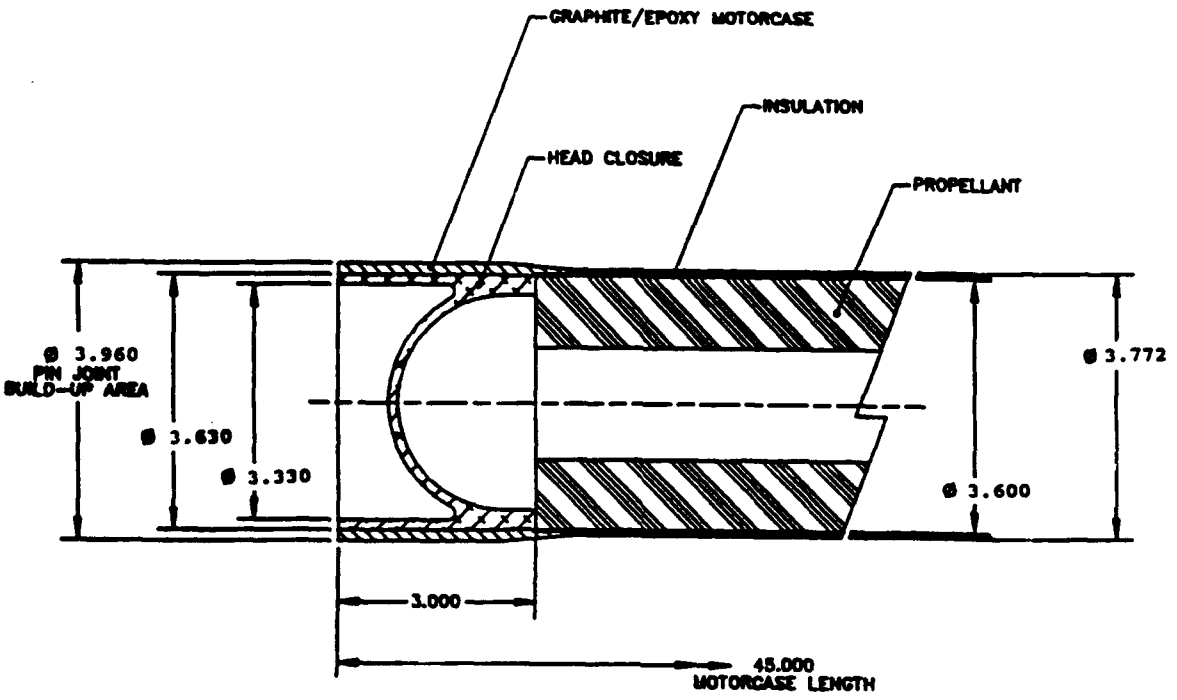


Figure 12. ADKEM Booster with Full Diameter Opening

Table 11. ADKEM Booster Component Weights

| Component | Full Opening | Integrally Wound Dome |
|---|---|---|
| Graphite/Epoxy Case | 971.6 g | 826.3 g |
| Rubber Insulation | 254.2 g | 254.2 g |
| Throat Insert | 263.3 g | 263.3 g |
| Head Closure/Pole Piece | 413.1 g | 109.0 g |
| Total Case Weight | 1902.2 g | 1452.8 g |

As can be seen in the above table, the integrally wound dome design saves 449.4 grams of weight. However, this design requires complex collapsible winding tooling and propellant casting tooling. The Composite Structures/Materials Function of Structures Directorate has designed the collapsible winding tooling, and fabrication of the tooling is in process.

The current motorcase design calls for AMOCO T-40 graphite fiber. The integrally wound throat insert is currently a compression molded glass phenolic. However, investigation into a non-eroding throat is currently in progress. Table 12 lists the predicted ADKEM booster physical characteristics.

Table 12. ADKEM Booster Physical Characteristics

| | |
|---|---|
| Overall Length | 43.180 in |
| Borerider Diameter | 3.870 in |
| Inside Diameter | 3.600 in |
| Case Body Diameter | 3.772 in |
| Wall Thickness (not including insulation) | 0.056 in |
| Composite Case Weight | 1343.8 g |
| Forward Pole Piece | 109.0 g |
| Propellant Weight | 7831.5 g |
| Propellant Mass Fraction | 0.84 |

Since fabrication of tooling and other hardware is in progress, there is no experimental data to present on the ADKEM booster. However, table 13 illustrates the predicted performance characteristics of the ADKEM booster.

Table 13. ADKEM Booster Predicted Performance

| | |
|---|---|
| Design Burst Pressure | 7400 psi |
| MEOP | 4940 psi |
| Proof Test Pressure | 6175 psi |
| Thrust | 14000 psi |
| Burn Time | 0.35 sec |
| Specific Impulse (Isp) | 251 sec |

Of the motorcases discussed in this report, the ADKEM booster is the most efficient. This is the result of improvements in manufacturing, fiber technology, and tooling design. The ADKEM booster's propellant mass fraction of 0.84 is very high. Improvements to this case could only come through the emergence of higher strength fiber and matrix technology.

## SUMMARY AND CONCLUSION

This paper has illustrated the evolution of high performance composite rocket motorcases at the U.S. Army Missile Command since FY 82. Systems requirements have driven these motorcases to produce more thrust, be lighter in weight, and develop an increase in the overall motorcase efficiency. A summary of propellant mass fraction and thrust for each motor discussed is listed in table 14.

Table 14. Propellant Mass Fraction And Thrust Summary

| Motorcase | Propellant Mass Fraction | Thrust |
|---|---|---|
| SPIKE | 0.76 | 2200 lbs |
| Improved SPIKE | 0.78 | 2200 lbs |
| Super SPIKE | 0.80 | 2400 lbs |
| Killer Bee | 0.78 | 8900 lbs |
| ADKEM | 0.84 | 14000 lbs |

A graphical representation of the thrust versus time curve for all of the motorcases can be seen in figure 13. All curves depict experimental data except the AdKEM booster which illustrates the predicted performance. Increases in propellant mass fraction have been obtained through utilization of emerging fiber technology, and integrally wound nozzles, and elimination of the forward head closure and pin joint.

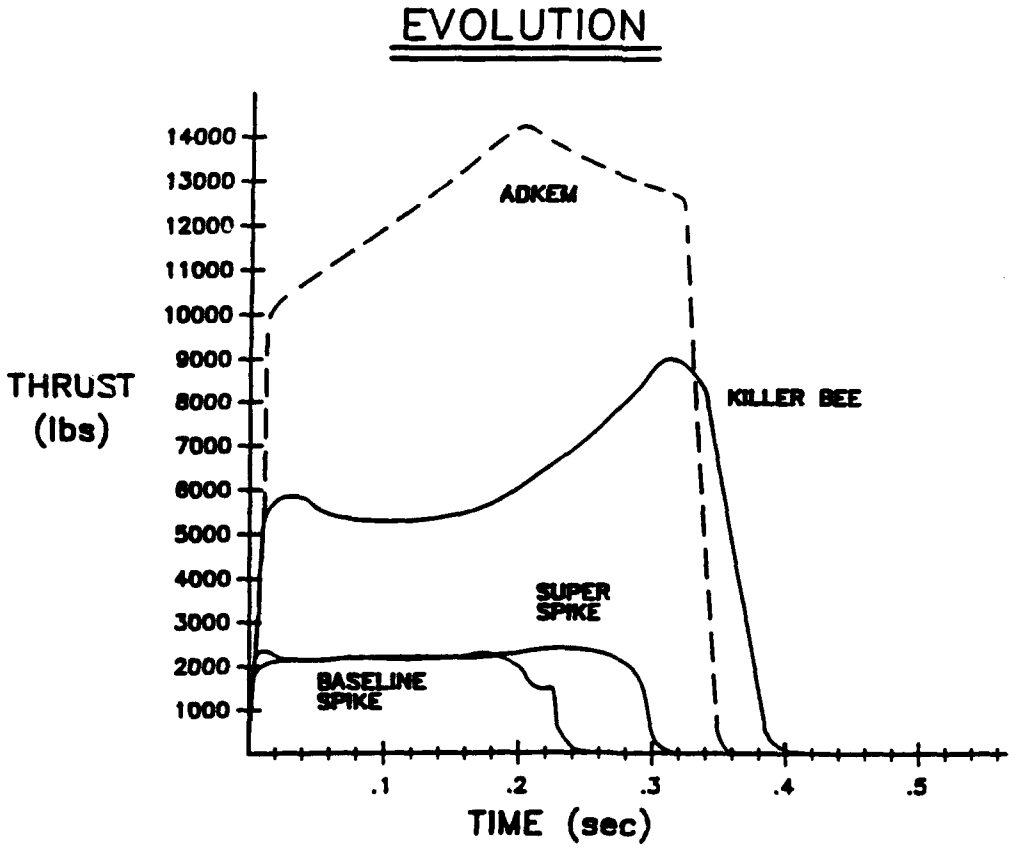


Figure 13. Motorcase Thrust versus Time Curve Summary

This paper has also discussed some of the advantages of composite motorcase technology over conventional motorcase design techniques. One of these advantages is the ability to integrally wind the nozzle which permits highly accurate alignment of the nozzle throat to the center line of the motor. Other advantages include installation of motorcase insulation prior to filament winding, reproducible motorcase geometry with minimum machining, low cost, and better performance. The high performance composite rocket motorcases discussed in this paper demonstrate the advantages of modern composite materials in future Army missile systems.

# CLUSTERED HIGH PERFORMANCE ROCKET MOTOR FLIGHT DEMONSTRATION

George W. Snyder
Robert N. Evans
David W. McNeill
*Gregory L. Johnson
U. S. Army Missile Command
Research, Development, and Engineering Center
Structures Directorate

## ABSTRACT

The Clustered High Performance Rocket Motor Flight Test Program was initiated to demonstrate the feasibility of flight testing a scaled model hypervelocity kinetic energy missile concept. Four Super SPIKE motors were clustered around a payload carrying centerbody to demonstrate the proof of principle to achieve a peak velocity of almost MACH 6. This velocity requirement is critical in the development of future advanced missile systems which may rely on a Kinetic Energy (KE) penetrator as the primary defeat mechanism. The flight demonstration program conducted at Redstone Arsenal, Alabama, validated the clustered booster concept to achieve a burnout velocity of 1950 meters per second in a distance of less than 300 meters. This achievement of the peak velocity will allow the implementation of an advanced KE penetrator design for the Advanced Kinetic Energy Missile (ADKEM) Technology Demonstration Program. Additionally, development of missile systems similar to the tested concept should allow for a shorter, lighter KE missile that will ease vehicle integration and increase stowed kills.

## INTRODUCTION

The primary purpose of the flight demonstration was to provide the initial technology thrust for the development of an advancement in hypersonic kinetic energy missile concepts. Performance goals in the development of a kinetic energy (KE) penetrator missile concept should require achieving peak impact velocities of greater than 2 kilometers per second (km/s), since theoretical and experimental analysis indicate the maximum penetration performance of continuous long rod KE penetrators occurs in the 2-2.2 km/s impact velocity regime. Other desirable weapon system features require the capabilities to achieve peak lethality characteristics against threat armors at a minimum range (<300 meters) for the close-in antiarmor application as well as up to a range of 5000 meters and also be effective at ranges of 6 to 10 kilometers (KM) for an air defense mission role. Previous hypervelocity missile concept studies indicate a clustered booster concept, which discards the boosters after burnout (min. range approx. 500 meters) and allows the penetrator carrying, low drag centerbody to be guided to the target during the coast phase is a viable hypervelocity antiarmor missile approach.

The flight test program provided early demonstration of the clustered booster configuration concept, demonstrated aerodynamic stability of the unguided clustered booster geometry, established boost error budget and narrowly missed the 2000 meter per second peak velocity objective. A lightweight graphite epoxy cylindrical shroud encased the previously proven SPIKE rocket motors propulsion system to provide a comparative rocket aerodynamic geometric shape. The four foot long Clustered Super SPIKE configuration launch weight was 18.4 pounds, including 11 pounds of propellant. The peak burnout velocity of 1950 m/s was achieved in less than 350 meters. Attempts have been made to achieve this goal in previous programs, but were never obtained. This is the first known success to achieve the 1950 m/s in the minimum range with an unguided missile of comparable payloads. The technology is essential in the development of future hypervelocity kinetic energy missile concepts.

The success of the unguided clustered booster flight test is only a portion of the effort to develop the next generation of technology for possible use by the Army in various mission roles and systems. Future required key technologies necessary to develop a clustered booster hypersonic kinetic energy missile include guidance system developments and integration, rocket motors development, design of time sensitive booster ignition and termination schemes, demonstration of separation technique, development of deployable aerodynamic stability devices, design of new launchers, and aerothermal protection material development.

The conduct of the near Mach 6 burnout velocity required advancements in the rocket motor propellant to achieve the required additional total impulse, use of ultra high strength composite technology for the booster motor design, use of high strength lightweight composites for the structural attachment hardware to achieve weight budget requirements, and modifications to an existing launcher to induce missile spin for aerodynamic stability. This paper addresses the design efforts to develop the Super SPIKE motors, the technical design issues associated with structurally clustering the configuration to withstand the launch environment, and the design requirements to conduct a stable free flight Mach 6 missile within the safety range boundaries of Redstone Arsenal.

## FLIGHT MISSILE CONFIGURATION DESIGN

### Missile

The flight demonstration program consisted of conducting two flight tests at Test Area #1, Test and Evaluation Directorate. The basic design of the clustered high performance rocket motor configuration consisted of four SPIKE motors tethered together and encased in a graphite/epoxy shroud with a penetrator simulate centerbody extending from the front of the missile as shown in Figure 1.

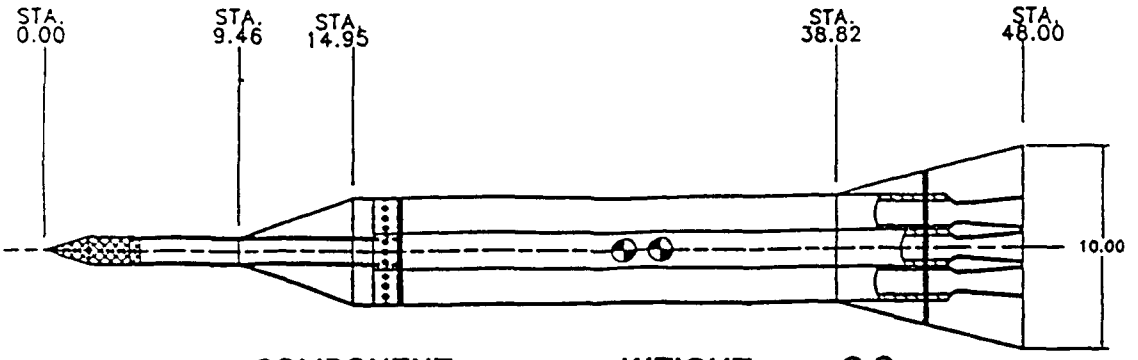


| COMPONENT | WEIGHT | C.G. |
|---|---|---|
| PENETRATOR | 1.316 lbs | 2.77 in |
| EXTENSION TUBE | 0.272 lbs | 10.70 in |
| FORWARD SPACER | 0.073 lbs | 17.27 in |
| NOSE CONE | 0.300 lbs | 12.52 in |
| SKIN WITH FLARE | 1.100 lbs | 32.87 in |
| AFT SPACER | 0.073 lbs | 43.24 in |
| SUPER SPIKE - LOADED | 4 x 3.353 lbs | 30.36 in |
| - INERT | 4 x 0.635 lbs | 28.20 in |
| CHARTEK | 2.054 lbs | 28.45 in |
| BEFORE BURNOUT | 18.600 lbs | 28.63 in |
| AFTER BURNOUT | 7.724 lbs | 21.89 in |

Figure 1. The clustered SPIKE configuration.

The graphite epoxy shroud encases the SPIKE rocket motors and has a 10" diameter base flare to provide aerodynamic stability. A chartec thermal ablative protective coating (0.005") was applied to the shroud to prevent aerothermal heating of the epoxy. Excessive heating would reduce the strength of the graphite/epoxy structure assembly and the aerodynamic geometry of the rocket would be destroyed, thus aerodynamic instability would occur.

The clustered SPIKE configuration (Figure 1) weighs approximately 16.4 pounds, is 48" in length, propellant weight is 8.87 pounds, major diameter is 5.4" (flare 10"), and the average thrust is approximately 8000 lbs. The second flight test configuration was identical with the exception of using Super SPIKE motors as the boost phase rather than the SPIKE motors. The Super SPIKE motors contain 25% more propellant and produce 25% more total impulse than the SPIKE motors. The 25% increase in propellant mass increased the launch weight to 18.4 pounds.

## Propulsion

The first four cluster high performance rocket motor flight test used the baseline SPIKE motors as the propulsion system boost phase. The second flight test used the Super SPIKE motors. The propellant formulation is identical for both the SPIKE and the Super SPIKE rocket motors. The single Super SPIKE motor simply has a lower port-to-throat ratio and 227 grams more propellant than the SPIKE. This provides for the 25% impulse

increase, which contributes to the approximate 15% velocity increase of the Clustered Super SPIKE over the Clustered SPIKE flight test.

The propellant used in the SPIKE and Super SPIKE is a HTPB ammonium perchlorate mix. The ammonium perchlorate is well characterized, provides high performance and good ballistics, as well as a short burn time. This is not a very good tactical propellant because of the contrail produced due to the sensitivity in the humidity and temperature conditions and by the highly erosive properties of the 15-16% aluminum present in the mix. The performance characteristics of the single SPIKE and Super SPIKE motors are provided in Table 2 and the single Super SPIKE thrust vs. time curve is shown in Figure 2.

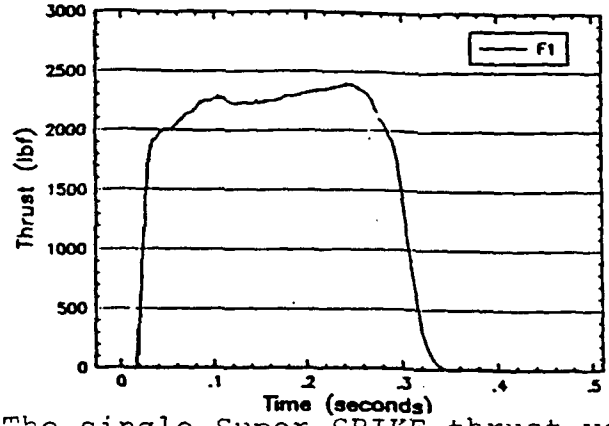


Figure 2. The single Super SPIKE thrust vs. time curve.

The squib used to ignite the motor propellent uses a 1W-1AMP-no fire detonator. To eliminate detrimental ignition delays between motors in the four cluster configuration the propellant was intentionally abraded. This was necessary to reduce thrust misalignment effects during the boost phase.

## Motorcase

The SPIKE motorcase is a high strength filament wound composite structure developed and fabricated in-house at the U.S. Army Missile Command. The filament wound SPIKE motorcase is fabricated with Amoco T-40 graphite and a 350°F cure epoxy resin.

| | |
|---|---|
| Length | 32.052 in |
| Inside Diameter | 1.754 in |
| Outside Diameter | 1.812 in |
| Borerider Diameter | 1.920 in |
| Nozzle Throat Diameter | 1.000 in |
| Propellant Grain Length | 28.000 in |
| Port-to-Throat Ratio | 1.1 |
| Motorcase Weight | 276.8 g |
| Propellant Weight | 1008.0 g |
| Propellant Mass Fraction Ratio | 0.78 |

Table 1. SPIKE Motorcase Physical Characteristics.

The motorcase utilizes a compression molded glass phenolic nozzle insert which is integrally wound with the case. The physical characteristics of the SPIKE motorcase are shown in Table 1.

The design and proof test performance capabilities for the SPIKE motorcase are provided in Table 2. The performance characteristics are based on numerous static and flight tests of the single SPIKE rocket motor.

| | |
|---|---|
| Design Burst Pressure | 4000 psi |
| MEOP | 2400 psi |
| Proof Test Pressure | 3000 psi |
| Ave. Thrust | 2200 lbs |
| Peak Thrust | 2350 lbs |
| Burn Time | 0.25 sec |
| Specific Impulse($I_{sp}$) | 228 sec |
| Total Impulse($I_t$) | 500 lbs-sec |

Table 2. SPIKE Motor/Motorcase Performance Summary.

In an effort to increase the SPIKE motor efficiency, total impulse and burnout velocity for the Four Cluster Demonstration, the Super SPIKE motorcase was developed. Super SPIKE utilizes a compression molded glass phenolic nozzle insert that has a throat diameter of 0.900 inches. The port diameter of the propellant grain was also decreased from 1.0" to 0.900". The smaller port diameter allows for an additional 227 grams of propellant to be cast into the motor. The approximate 25% increase in propellant mass and modification of the port-to-throat ratio to 1:1 provides the Super SPIKE motor with an approximate 25% increase in total impulse over the SPIKE motor, which in-turn produces an increase in velocity capability. The physical characteristics of the Super SPIKE motorcase are shown in Table 3.

| | |
|---|---|
| Length | 32.052 in |
| Inside Diameter | 1.754 in |
| Outside Diameter | 1.814 in |
| Borerider Diameter | 1.920 in |
| Nozzle Throat Diameter | 0.900 in |
| Propellant Grain Length | 28.500 in |
| Port-to-Throat Ratio | 1:1 |
| Motorcase Weight | 306.8 g |
| Propellant Weight | 1235.0 g |
| Propellant Mass Fraction Ratio | 0.80 |

Table 3. Super SPIKE Motorcase Physical Characteristics.

The performance characteristics of the Super SPIKE motorcase have been validated through burst tests, static tests and flight tests. The thrust vs. time curve shown in Figure 2 verified the predicted capability to achieve the 25% increase in total impulse, which is the area under the thrust vs. time curve.

The single Super SPIKE flight tests revealed a 21% increase in velocity over the single SPIKE motor and was obtained by the added propellant mass, reduced port-to-throat ratio, and increased total impulse. A summary of the performance capabilities of the Super SPIKE motor/motorcase burst and static tests are provided in Table 4.

| | |
|---|---|
| Design Burst Pressure | 4000 psi |
| MEOP | 2400 psi |
| Proof Test Pressure | 3000 psi |
| Ave. Thrust | 2400 psi |
| Peak Thrust | 2800 psi |
| Burn Time | 0.28 sec |
| Specific Impulse ($I_{sp}$) | 238 sec |
| Total Impulse ($I_t$) | 630 lb-sec |

Table 4. Super SPIKE Motor/Motorcase Performance Summary.

Attachment Hardware

The Four Cluster rocket was required to withstand 1600 g's of acceleration. In order to meet the velocity requirements of the Demonstration program, a very lightweight method for attaching the SPIKE motors was required to be within the weight budget and the performance capabilities of the propulsion system. The attachment hardware included a 7075-T6 aluminum forward spacer which also served as the kinetic energy penetrator load carrying structure. The aft spacer was fabricated from E-glass epoxy plate and also served as support for the shroud. The motors had grooves machined into the bore riders that interfaced with the forward and aft spacers.

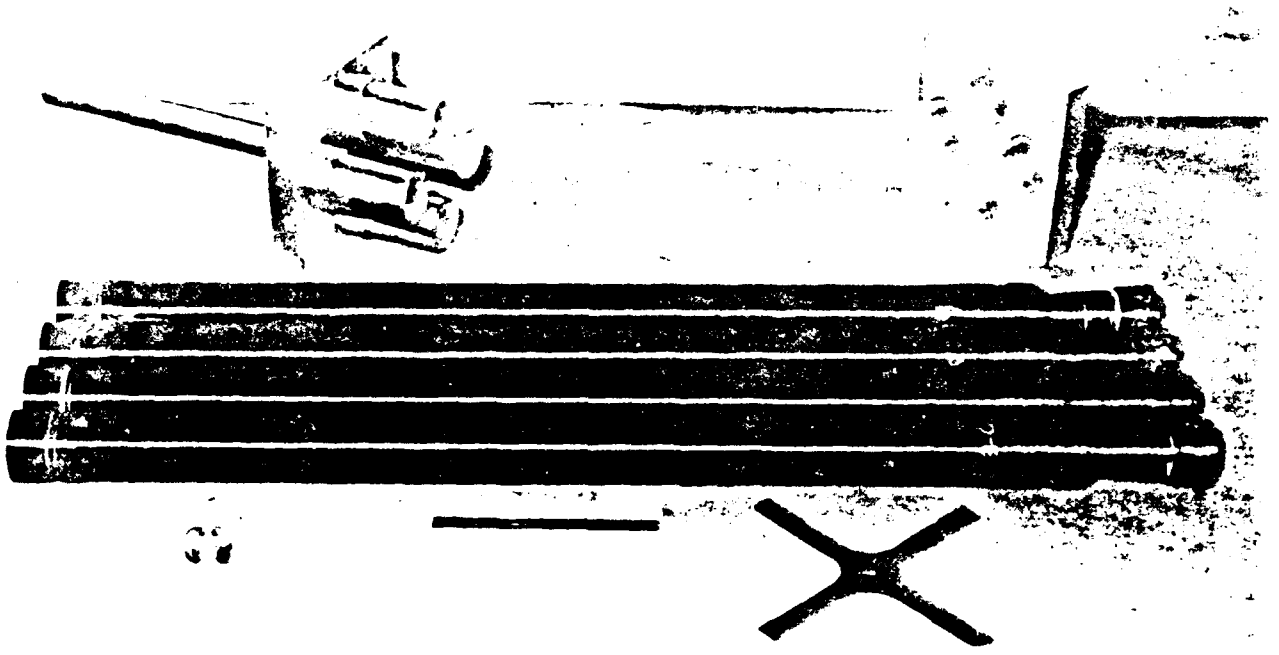

Figure 3. Motors, spacers, and fixture.

Figure 3 shows the four SPIKE motors, forward and aft spacers, and the fixture used to attach the motors. After assembly, the motors were strapped together with T-40 graphite hoop winding in the forward and aft borerider grooves.

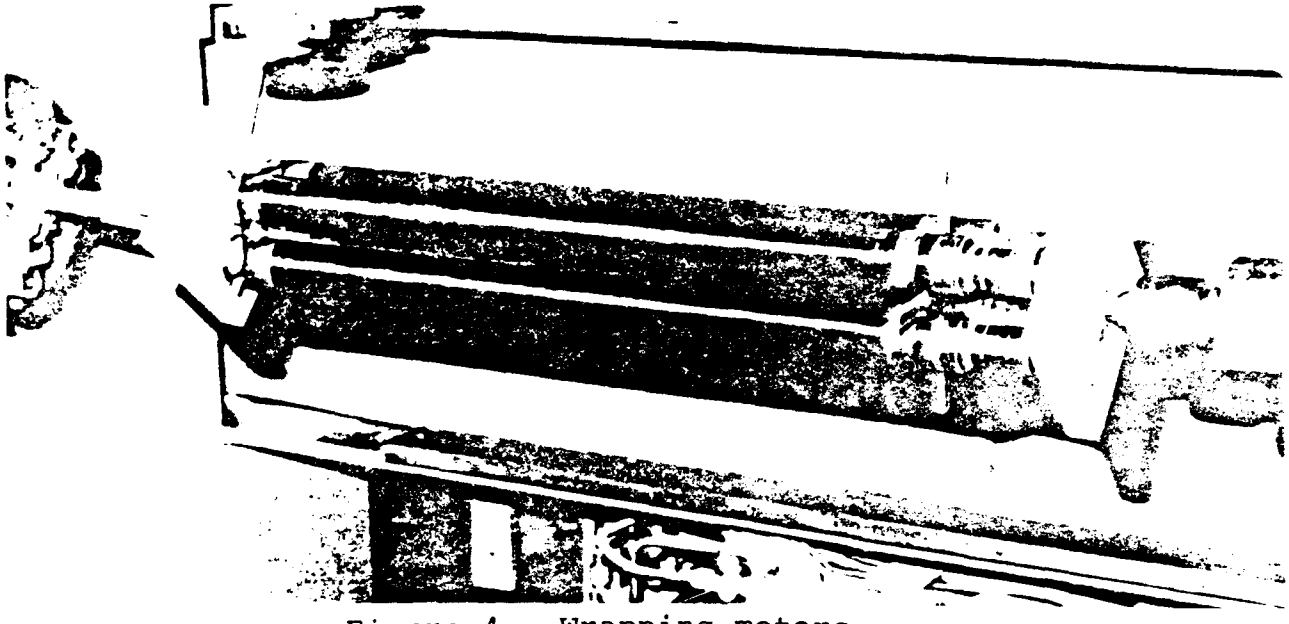

Figure 4. Wrapping motors.

Figure 4 illustrates the cluster being strapped together on a filament winding machine. Figure 5 is a closeup of the hoop windings being filament wound on the forward end of the motors.

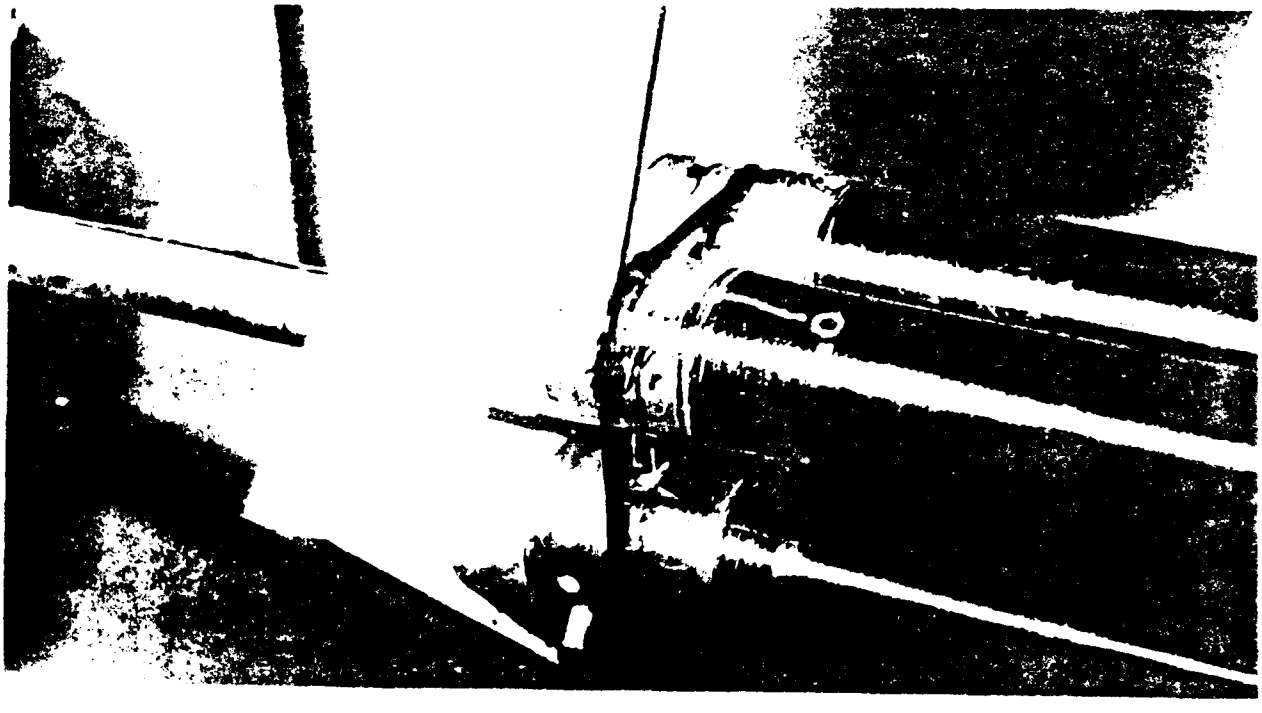

Figure 5. Closeup of Figure 4.

The centerbody/nonseparating penetrator consisted of a 15" long, 1.4" diameter 6061-T6 aluminum tube with a steel tip mass (Figure 6).

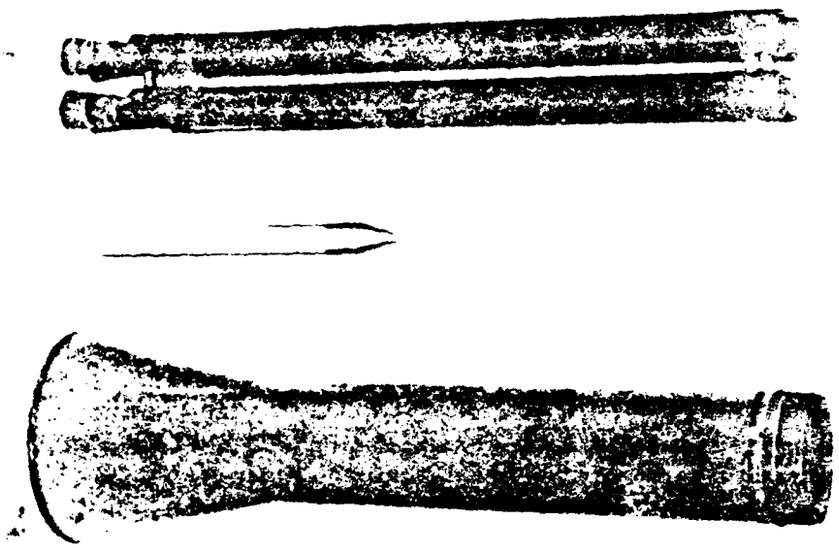

Figure 6. Disassembled missile.

The initial design of the centerbody and attachment hardware extended from the aft spacer plate to 15" forward of the front spacer plate. However, the aerodynamic stability margin was not sufficient and the total weight was above the weight budget to achieve the velocity performance goals. The reduced length of the payload/centerbody provided the required aerodynamic stability margin and also reduced the total rocket weight. The front spacer provided the aft attachment point of the aluminum centerbody and absorbed the launch environment acceleration loads.

Shroud

Stability requirements and the difficulties in analyzing the aerodynamic effects of a cluster motor configuration (non-circular) forced the clustered rocket to utilize an aerodynamic shroud in combination with a launcher induced spin rate of 12 RPS. The design requirements included the ability to withstand 1600 g's of acceleration and 3800 pounds of drag. The shroud was a filament wound graphite epoxy structure.

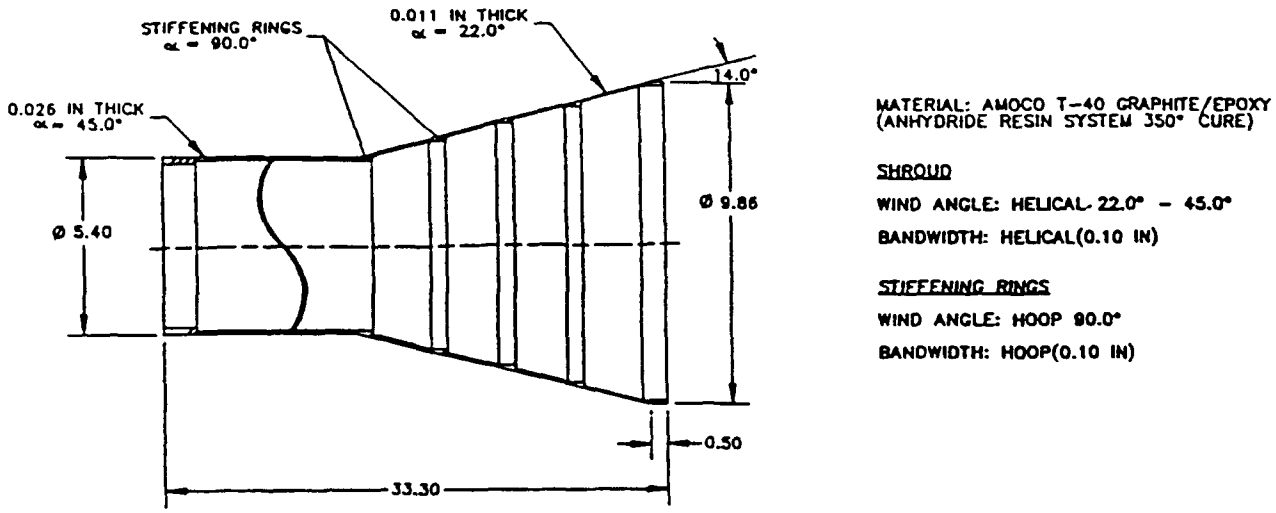


Figure 7. Shroud geometry with material selection and filament winding parameters.

Figure 7 illustrates the shroud geometry along with material selection and filament winding parameters. Figure 8 shows the shroud being filament wound.

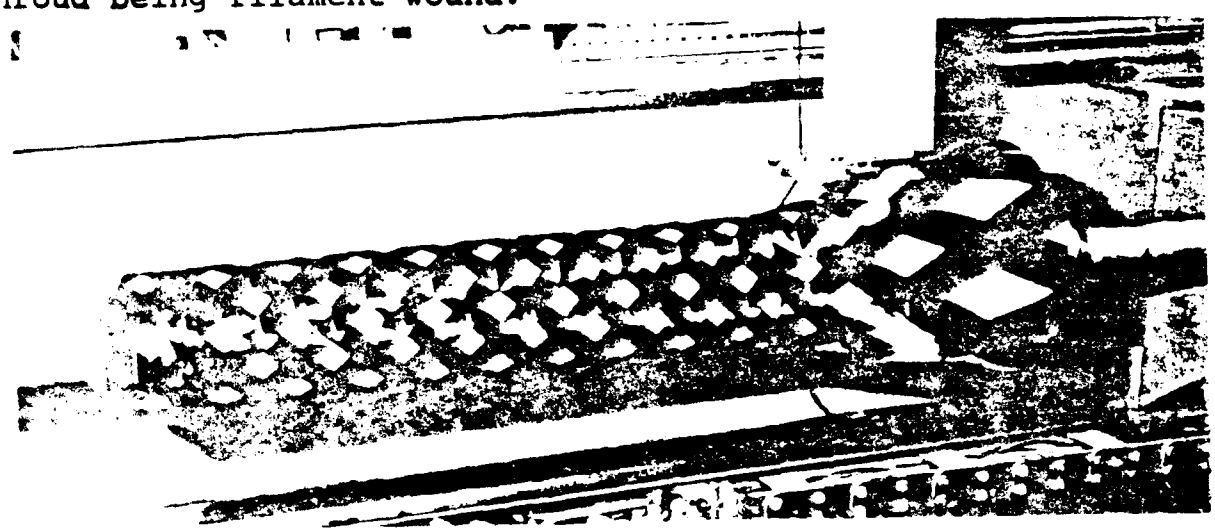

Figure 8. View of shroud being filament wound.

The requirement for the flare to withstand 3800 pounds of drag resulted in the requirement for stiffeners in the radial direction, since the 22° wrap angle was insufficient to withstand the loading conditions. A nose cone windshield that tapered from

the kinetic energy penetrator centerbody to the cylindrical section for the shroud was also required. The nose cone windshield was also a wound filament graphite epoxy structure.

Figure 9 illustrates the nose cone geometry along with material selection and filament winding parameters. The radial stiffeners in the nose cone were filament wound with the cone. An aluminum tip that interfaced with the composite nose cone windshield and centerbody was bonded into place during missile assembly.

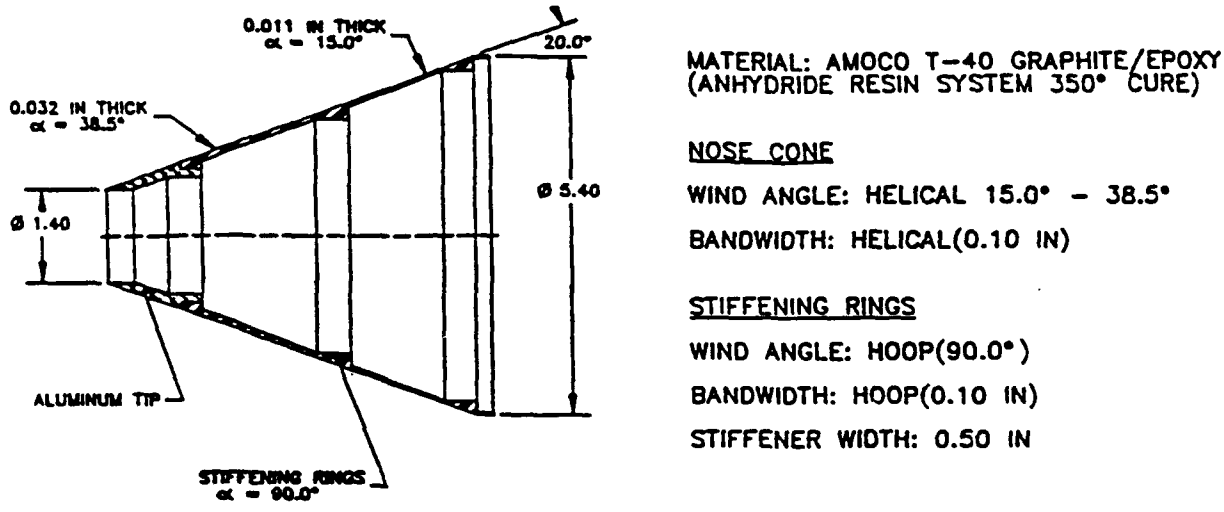


Figure 9. Nose cone geometry and materials.

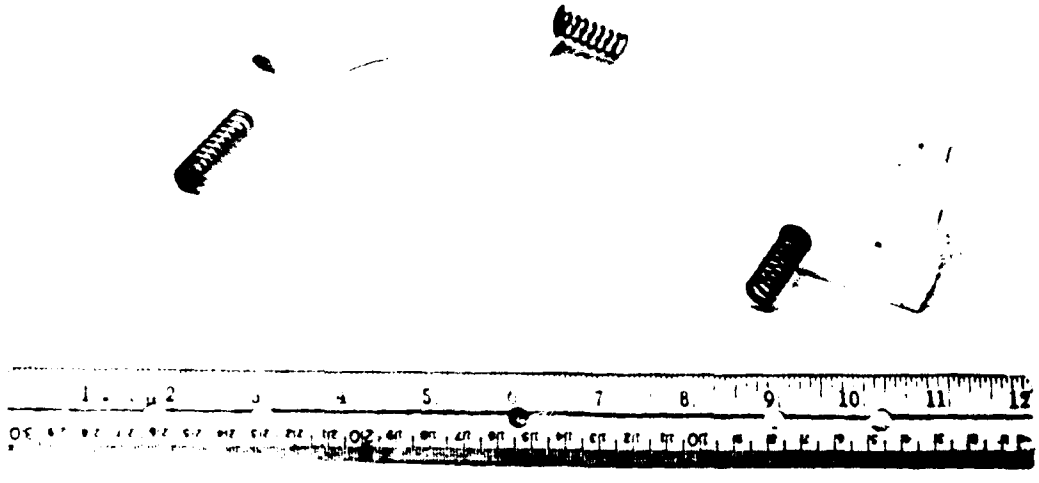

Figure 10. Sabot.

The 10" diameter stabilization flare on the aft end of the shroud forced the launch tube to a 10" inside diameter. The major diameter of the shroud was 5.4", thus a bore rider had to be designed to support the front of the rocket in the tube. The bore rider design relied on aerodynamics to 'lift' it from the rocket body after tube exit without striking the aft flare, similar to the technique used with sabots in gun launched projectiles.

Compression springs were installed between each quarter section to help release the bore rider (Figure 10) upon tube exit. The bore rider was machined from syntactic foam with Teflon strips on the tube contact surfaces to reduce sliding friction.

The launcher was a modified SPARK launcher, a platform which supports a rotating launch tube. The 10' long fiberglass launch tube is suspended between two bearing rings and rotated through twin belts attached to a side mounted electric motor (Figure 11). The launcher induced spin of 12 rps to the rocket provided aerodynamic flight stability and reduced the effects of thrust misalignment.

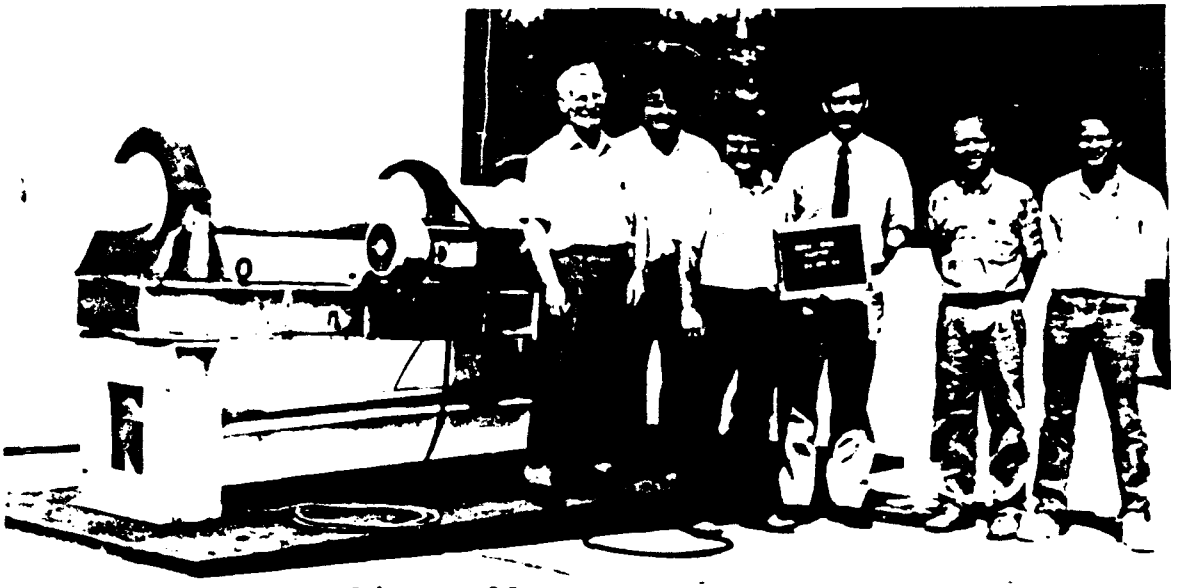

Figure 11. Launcher.

Connecting the squibs to the firing line was difficult because the spinning launch tube assembly would twist the squib firing wires, and cause a possible misfire of one or more of the motors. This problem was solved on the Clustered SPIKE flight by using a commercially available commutator. A commutator is a devise that allows the input (or output) wires to spin with respect to the mounting surface without twisting. Due to scheduling and delivery problems, no commercial commutators were available for the Clustered Super SPIKE test. Therefore, a new commutator design was engineered and fabricated to meet the specific requirements of this system. This design used a

rotating copper disk as one output pole and the attached shaft as the other.

## TEST SETUP & CONDUCTED TESTS

Full metrology data was recorded for each rocket before being transported to the flight range. This included weight (mass), center of gravity (from the nose), roll center of gravity, total length, roll moment of inertia, pitch moment of inertia, and yaw moment of inertia. This data is provided in Table 5 for both the Super SPIKE and SPIKE Clustered rocket configurations.

| | Clustered SPIKE | Clustered Super SPIKE |
|---|---|---|
| Weight | 16.4 lbs | 18.6 lbs |
| Cg (from nose) | 27.99 in | 28.63 in |
| Roll Cg | 0.005" @ $0^{o}$ | 0.009" @ $135^{o}$ |
| Length | 47.74 in | 47.80 in |
| Roll Moment | 69.8 lb $in^2$ | 73.984 lb $in^2$ |
| Pitch Moment | 2425.9 lb $in^2$ | 2608.2 lb $in^2$ |
| Yaw Moment | 2441.6 lb $in^2$ | 2615.1 lb $in^2$ |

Table 5. Metrology Data for Both Rockets.

The target consisted of a 12'x 12'x 2" steel plate located at 750' downrange for the Clustered SPIKE flight and 1150' downrange for the Clustered Super SPIKE flight. This target was used primarily as a backstop to terminate the flight, but it also provided accuracy data. According to the trajectory predictions, the aim point was chosen as 6' above the center of the target, approximately at the top of the target.

Flight data was recorded by several methods. An accelerometer was located on the launcher to provide first motion and launch tube exit data. An image motion compensation (IMC) camera was located 10' downrange of tube exit to provide tube exit spin rate, muzzle velocity, and verification of bore rider release. High speed (3000 frames per second) framing cameras were located approximately every 100' downrange to document the flight trajectory. A high speed framing camera was located behind the launcher to verify all four motors ignited and document plume size and plume interaction with surrounding structure. For the Clustered SPIKE flight, microphones were located at stations 100, 300, 500, and 700 feet downrange, one on the centerline and one 30' to each side of the centerline. The microphones were oriented in this fashion so the deviation of the rocket from the centerline could be calculated. For the Clustered Super SPIKE flight, the microphones were located at stations 100, 175, 350, 525, 700, 875, and 1000 feet downrange. At the first two stations, only one microphone was located on the centerline. On the subsequent stations, the microphones were located 15' to each side of the centerline to provide some data on the deviation of the missile from the centerline. The

Clustered Super Spike was also tracked with Doppler radar, which provided a velocity/time history for the flight.

Two flight tests were conducted between Oct 88 and Apr 89. The first test was with the Clustered SPIKE rocket motor configuration. This test was primarily a proof of concept demonstration, since this configuration could not provide the objective velocity of 2000 m/s. The Clustered Super SPIKE rocket motor configuration velocity goal was 1950 m/s. To provide the program objective goal of achieving 2000 m/s the development of larger rocket motors is required, since the additional weight (shroud) has been added to the configuration to insure flight safety in conducting the test at Redstone Arsenal.

## TEST RESULTS

The Clustered SPIKE rocket achieved a maximum velocity of 1700-1725 m/s, which was calculated from the microphone data. The initial predicted velocity was 1850 m/s, however an additional 2.4 pounds for the aerodynamic stabilization shroud and the chartec thermal protection material reduced the predicted velocity to 1700-1750 m/s.

In the Clustered SPIKE, the launcher frame mounted accelerometer provided a first motion reference point, an ignition delay of approximately 6 milliseconds, and approximately 57 milliseconds time in the tube. The framing camera behind the launcher verified that all four motors fired simultaneously. The IMC camera verified the 12 RPS spin rate and that the bore rider released without striking the aft flare. The high speed framing cameras provided coverage of the flight, showing a straight flight line and an extremely underexpanded nozzle condition. The microphones provided very good time of shock front arrival data, showing that the missile flew slightly off to the right of centerline (approximately 1′ at the target). This equates to an accuracy of approximately 1.33 mils.

The predicted peak velocity for the Super SPIKE configuration was approximately 2150 m/s at a burnout distance of 320 meters and an assumed burn time of 0.321 seconds. The Clustered Super SPIKE rocket achieved a maximum velocity of 1950 m/s, calculated from microphone data and Doppler data. The Doppler radar data is provided in Figure 12.

The achieved velocity is only 90 percent of the predicted velocity, however the predicted velocity calculation is ideal velocity, which is based on negligible drag effects and contains no mass imbalance calculations. Therefore, an obtained velocity of 90 percent of the predicted ideal velocity represents a very good data point and is within the rule of thumb predictions for loss of velocity due to drag.

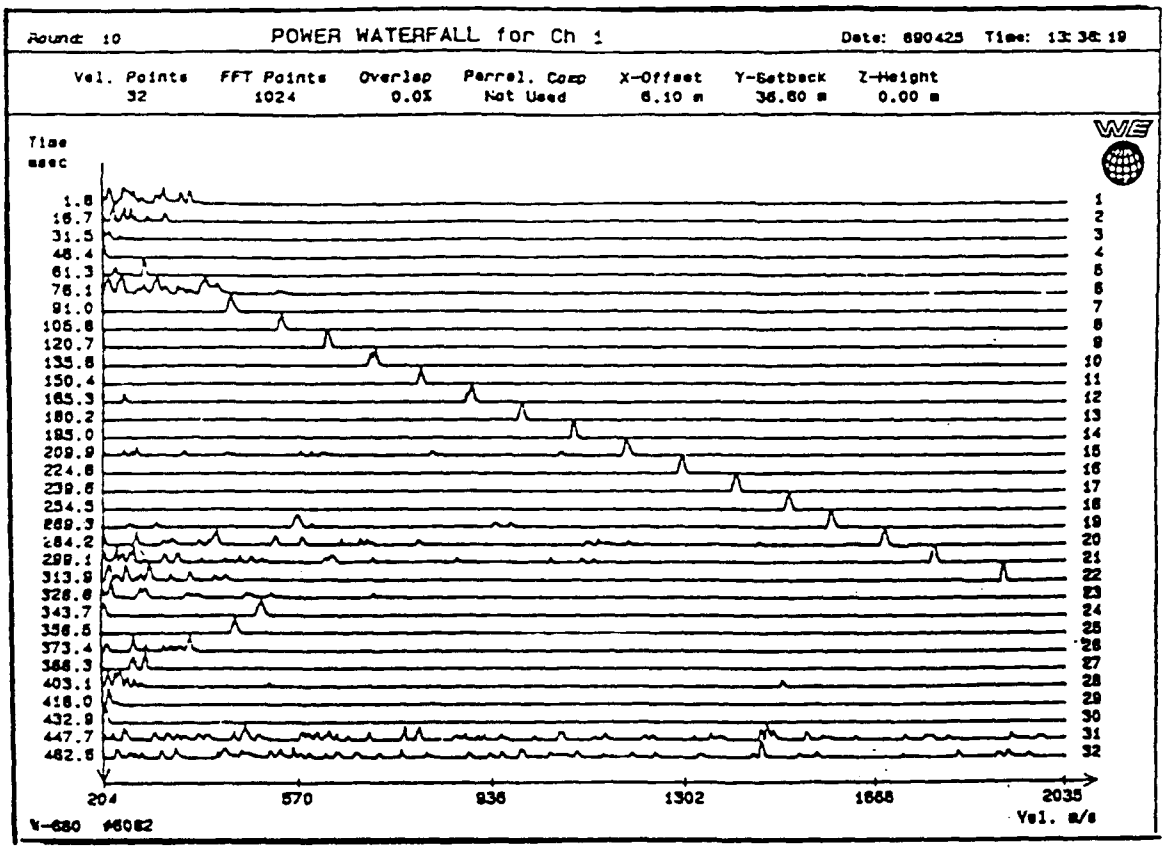


Figure 12. Doppler radar data.

The accelerometer received enough noise from the spinning launcher bearing rings in the Clustered Super SPIKE to wash-out the first motion and ignition delay data, but the firing signal was recorded, which gave a zero point to calculate velocities. Once again the framing camera behind the launcher verified that all four motors fired simultaneously.

The IMC camera located 10′ downrange provided verification of the 12RPS spin rate (Figure 14), the bore rider released without striking the aft flare, and the muzzle velocity was about 200 m/s. The firing sequence of photos in Figure 13 (following page) show this phenomena. The downrange IMC camera (at station 650′ - Figure 15) captured the rocket in flight, showing two very distinct shock waves extending from the tip and windshield. The velocity at this point was approximately 1300 m/s.

The high speed framing cameras provided coverage of the flight, showing a straight flight line and an extremely under expanded plume. The microphones provided very good time of shock front arrival data, showing the rocket flew slightly off to the left of centerline. The top of target impact point was once again within 1′ of the aim point, which is better than 1 mil accuracy at 1150′.

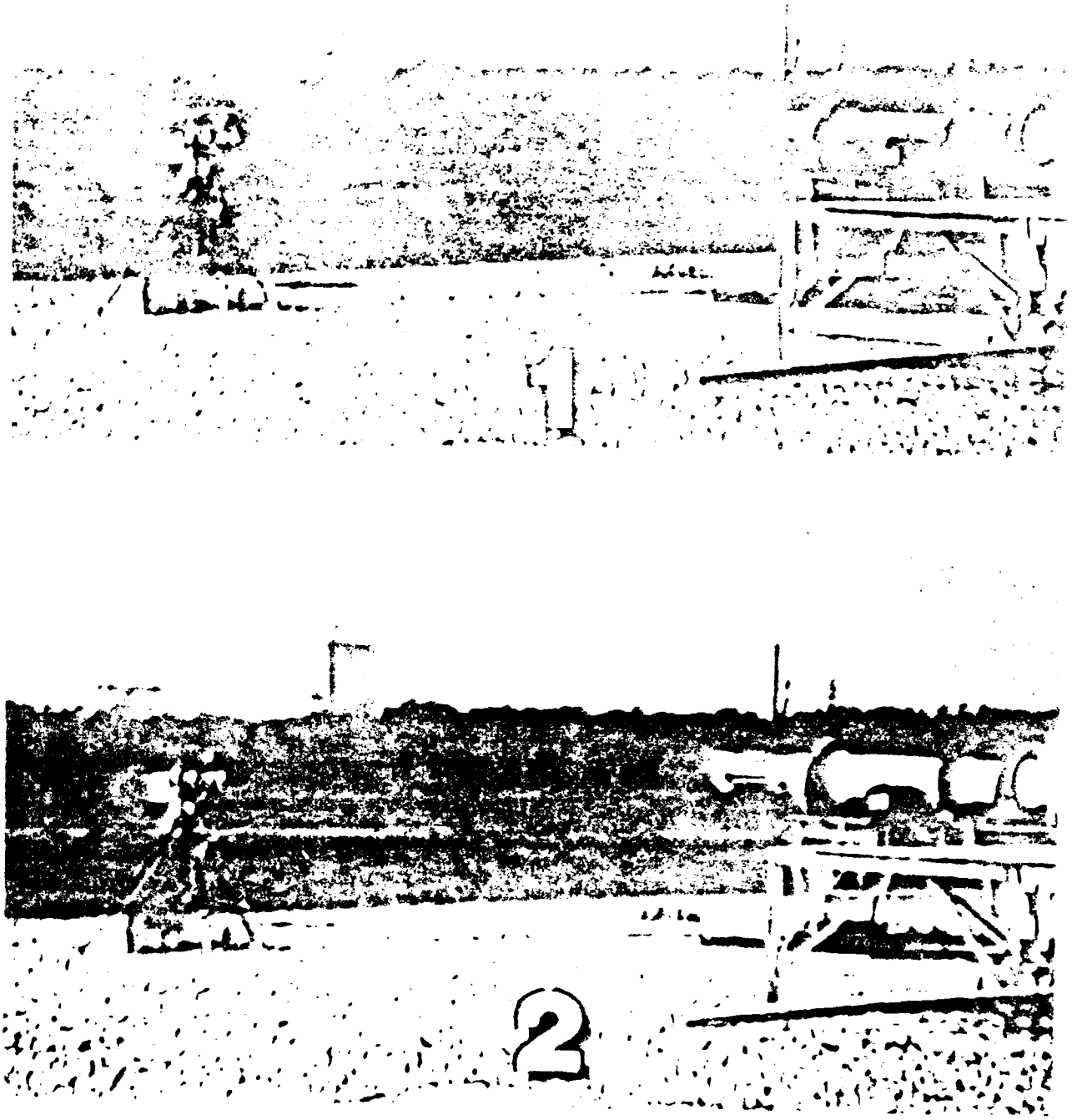

Figure 13. Firing sequence.

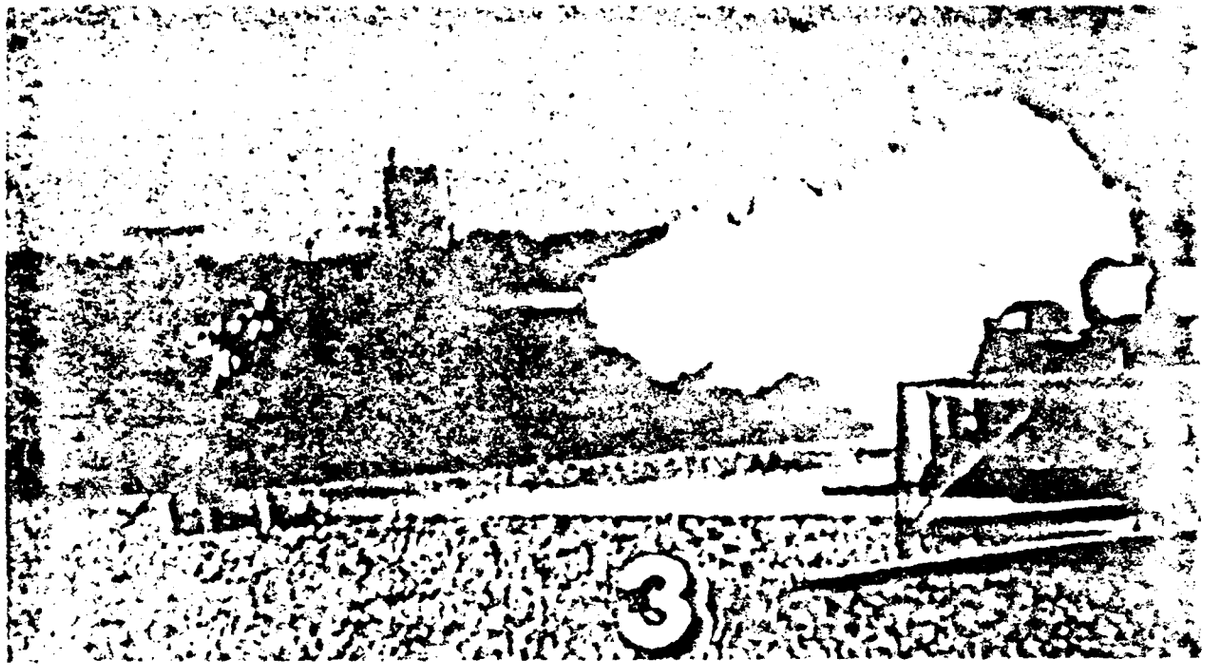


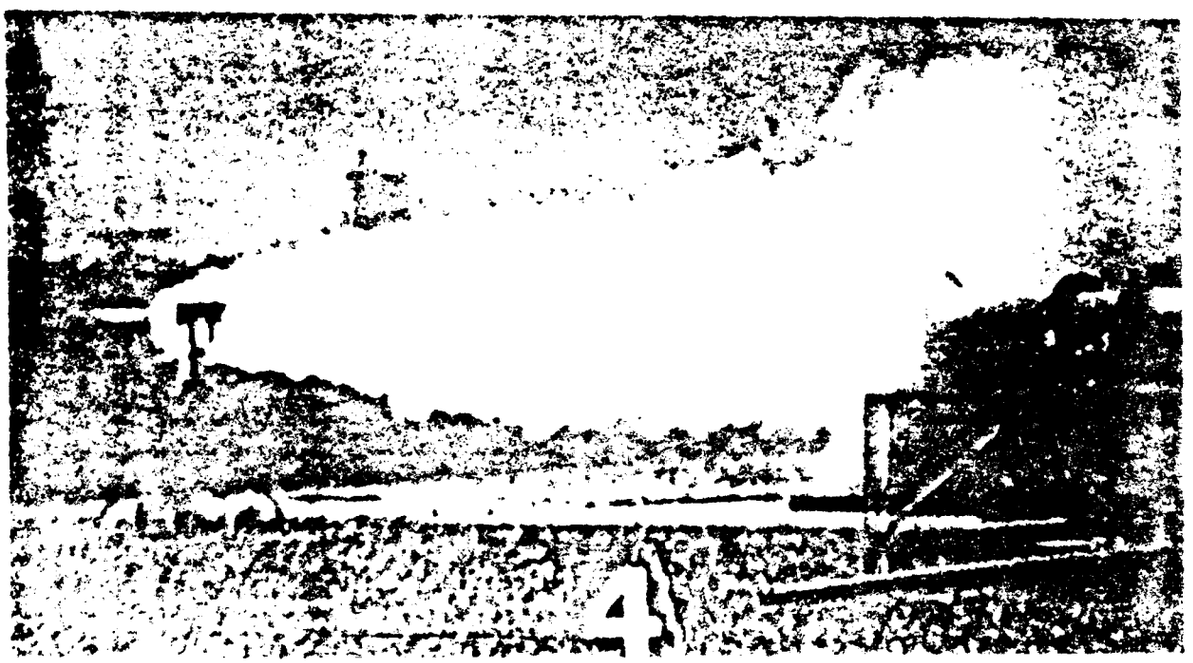


Figure 13. Firing sequence. (Continued)

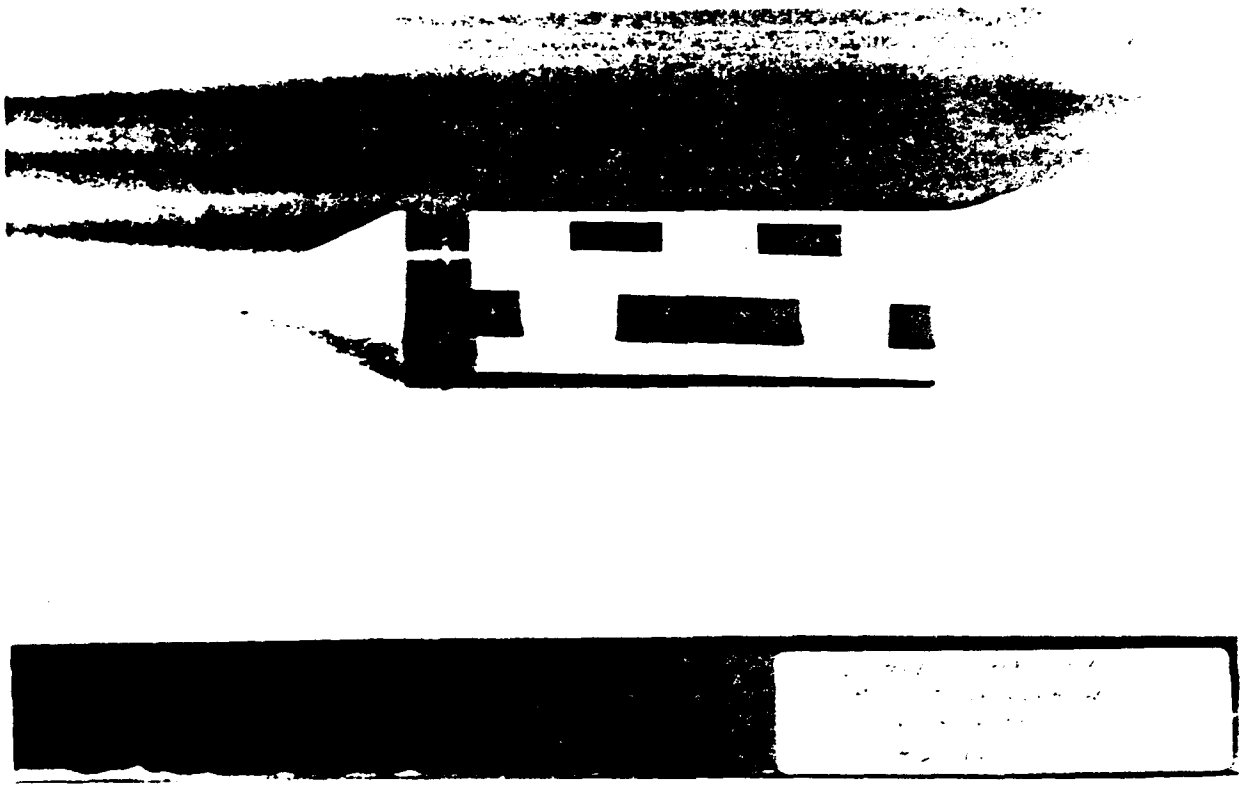

Figure 14. Ten feet IMC.

Figure 15. Six-hundred and fifty feet IMC.

## CONCLUSIONS

The effort required to coordinate these two tests, design and fabricate the hardware, and conduct the tests was performed in a relatively short period of time in comparison to similar efforts. The peak velocity goal of 1950 m/s was achieved in a burnout distance less than 1000' with better than 1 mil accuracy. This was possible because of revised rocket motor case and propellant designs to provide short burn times, and the combined thrust of four motors. These tests proved the clustered high performance rocket motor concept is a viable concept capable of leading technology into a full scale concept demonstration program.

The development of high performance rocket motors similar to the ones used in the Clustered Super SPIKE demonstration offers the capability to limit the accelerations to under 1600 g's which will permit the use of proven state-of-the-art guidance components. Mass fraction ratios of 0.8 to 0.9 can be achieved using the ultra high strength lightweight composite material technology. Additionally, maximum latitude is allowed for the missile configuration to optimally position KE penetrators within the airframe configuration to achieve maximum warhead lethality.

# Development of Full Scale Hypersonic Kinetic Energy Missile/Penetrator Sled Testing Techniques

George W. Snyder
*J. Frank Wlodarski
Gregory S. Parton
Donald W. Sandidge
U. S. Army Missile Command
Research, Development, and Engineering Center
Redstone Arsenal, Al 35898-5147

## ABSTRACT

This study involves the development of a hypersonic sled test technique to investigate the penetration performance of Kinetic Energy (KE) penetrator missile airframe configurations against monolithic rolled homogeneous armor (RHA) and full up-armored tank targets. Sled tests have been used to propel full scale KE penetrator missile airframe simulates to target impact velocities as high as MACH 5. This paper addresses the sled test techniques developed to determine penetration and total system lethality characteristics of full scale KE missile systems at velocities sufficient to duplicate hydrodynamic penetration theory.

Extensive impact dynamic analysis has been compared with the experimental data collected by MICOM and the Holloman Air Force Base, NM in an effort to validate hydrocode analysis for KE penetrator, guidance components, and total missile airframe configurations. This effort has helped optimize the design, attachment, and placement of KE penetrators within the missile airframe to provide a combined effect in providing the most efficient method of defeating advanced armors.

The benefit of developing these hypervelocity full scale missile sled testing techniques is to provide experimental data at lower costs than full scale flight tests and be performed in a more timely manner. Success in these testing techniques should significantly enhance the capability to predict total KE penetrator missile concept lethality characteristics against threat armor targets.

## INTRODUCTION

The interaction between Kinetic Energy (KE) penetrator missile systems and heavy advanced armor targets at impact velocities sufficient to duplicate hydrodynamic penetration theory is an area of great interest. Particular interest is in the military application of KE penetrators as the primary defeat mechanism of threat armors. The KE penetrator/missile terminal ballistic efficiency and lethality characteristics are measurable values associated with determining their effectiveness against specified threat armors. Adequate performance evaluation of the

KE penetrator and armor capabilities requires an understanding of the interaction to include total armor penetration, momentum transfer, and the effects of Behind Armor Debris (BAD). The challenge to test full-scale penetrator concepts as part of a hypersonic missile airframe, to determine the total terminal effects/impact interaction, is presently beyond current available technology without first developing the complete missile system (including guidance & tracking). Therefore, the total system lethality of a KE penetrator missile is not only uncertain but ignored in computer modeling lethality codes.

The high launch accelerations produced by guns and launch mass limitations have reduced the experimental testing capabilities of full-scale high L/D ratio KE penetrators and some novel penetrator concepts. These limitations have increased the value of conducting sub-scale and reverse ballistic tests to validate theoretical assumptions. However, sub-scale testing can create problems in completely validating (understanding) the terminal effects, especially against the advanced armor targets.

This paper describes the development of a full-scale KE missile concept lethality sled testing technique and provides the terminal effects results of the KE missile/airframe against heavy armor targets.

## SLED TEST DESIGN

The full-scale kinetic energy penetrator/missile airframe configuration lethality tests are being conducted by the U. S. Army Missile Command, Research, Development, and Engineering Center at Holloman Air Force Base, NM, High Speed Test Track Facility. The sled track consists of over 50,770 linear feet of continuous straight rail.

Two series of impact tests are being conducted to evaluate the lethality and penetration performance characteristics of candidate full-scale kinetic energy missile concepts against rolled homogeneous armor and advanced armor target arrays. The first technique, which is the concept addressed in this paper, was developed to provide the capability to test full-scale missile concepts with an integral KE penetrator and guidance components, and a total impact mass on the target of greater than 25 kilograms. The second approach provides the ability to test smaller missile configurations less than 3 in diameter. The latter technique can also be used to test full-scale alternate (novel) penetrator concepts within missile airframes.

A sled train (Figure 1) composed of several pusher sleds is used to accelerate the full-scale missile body to the required terminal velocity. After achieving peak velocity, the missile/sled (slipper) release mechanisms allow the missile to separate from the sled train and free flight until target impact. At the North end of the track, an 80 ft long - 1281 ft radius rail pulls down and/or diverts any pusher sled or carriage sled

debris away from the missile free-flight or target impact area. Photo-optics are used to record missile separation, free-flight and missile impact attitude (Figure 2).

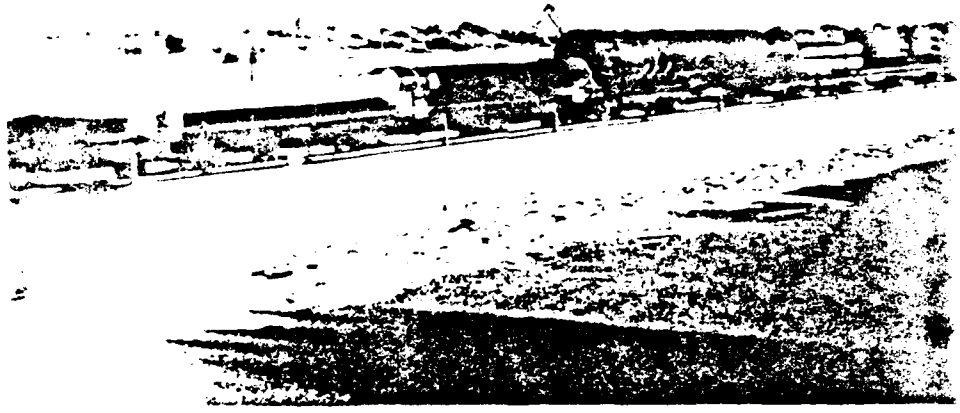

**Figure 1. Sled Train Assembled on the Rail**

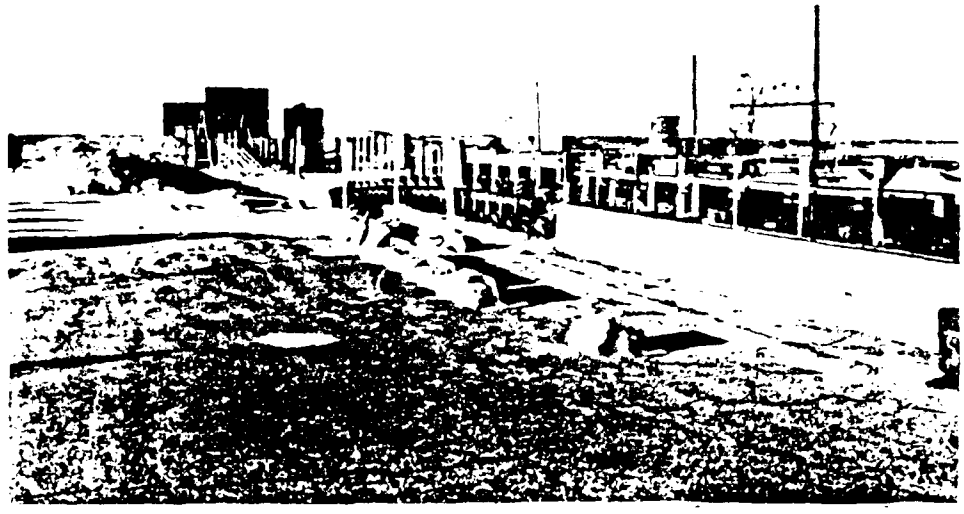

Figure 2. Rail Pull-Down Facility, IMC's, & Target Impact Area

The main program objective is to validate the penetration performance theory of the KE penetrator missile concepts against

specified armors. The other program objectives are associated with designing a test technique to provide the required missile/target impact conditions. Specific program requirements are to impact the target with only the KE penetrator missile at velocities ranging from MACH 4 to MACH 6, and impact the target with a pitch and yaw of less than ± 1°. This required: 1) the design of a release/launch mechanism to insure aerodynamically stable free flight of the missile to target impact, 2) designing missile structures representative of tactical missile concepts capable of withstanding the track induced dynamic loads and 3) designing the diverter mechanism to prevent pusher debris from entering the target area.

Missile Structure

After conducting several developmental sled tests, it was discovered that the engineering challenges of a missile sled train surviving the ride to peak velocity, achieving proper missile separation and free flight, and diverting sled train hardware away from the target area were as significant as the task of investigating the interaction of the KE penetrator at target impact. The missile sled train design requires allowing for the application of both quasi-steady state loads and dynamic loads. The quasi-steady state loads consist of aerodynamic lift and drag, thrust, braking and inertial loads in the down track direction. The vertical and lateral dynamic loads are comprised of inertial forces caused by the slippers slapping the rail. Figures 3 and 4 represent the load cases for 1700 ft/sec and 5000 ft/sec, respectively. The loads are based on analysis performed by Holloman Air Force Base and are dependent on the aerodynamic configuration of the missile, the sled train, stages in the sled train, velocity and acceleration profiles, and release mechanisms. The lower velocity has an aerodynamic uplift load that is not present at the higher velocity.

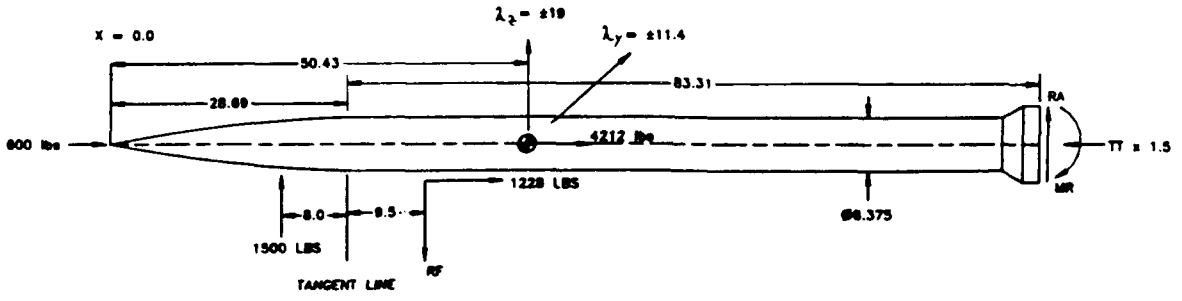


Figure 3. Applied Loads - Case 1 1700 ft/sec

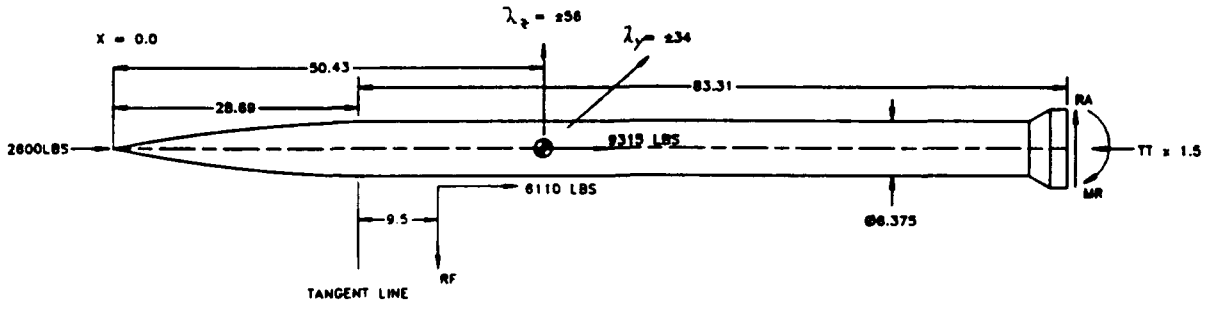


Figure 4. Applied Loads - Case 2 5000 ft/sec

The missile body is designed as part of the sled train with the front slipper just behind the ogive and the rear slipper bolted to the rear of the missile as depicted in Figure 5. The front slipper is attached to the missile with a band that secures the missile to the slipper, the rear slipper is attached by means of a chamfered surface to the rear face of the missile with an explosive bolt compressing the two together to prevent the bending moment at the interface from causing a gap to form between the two surfaces. The loads developed for this configuration are calculated in the missile body and the attachment points for each load case. The calculated loads were then used to design the missile body.

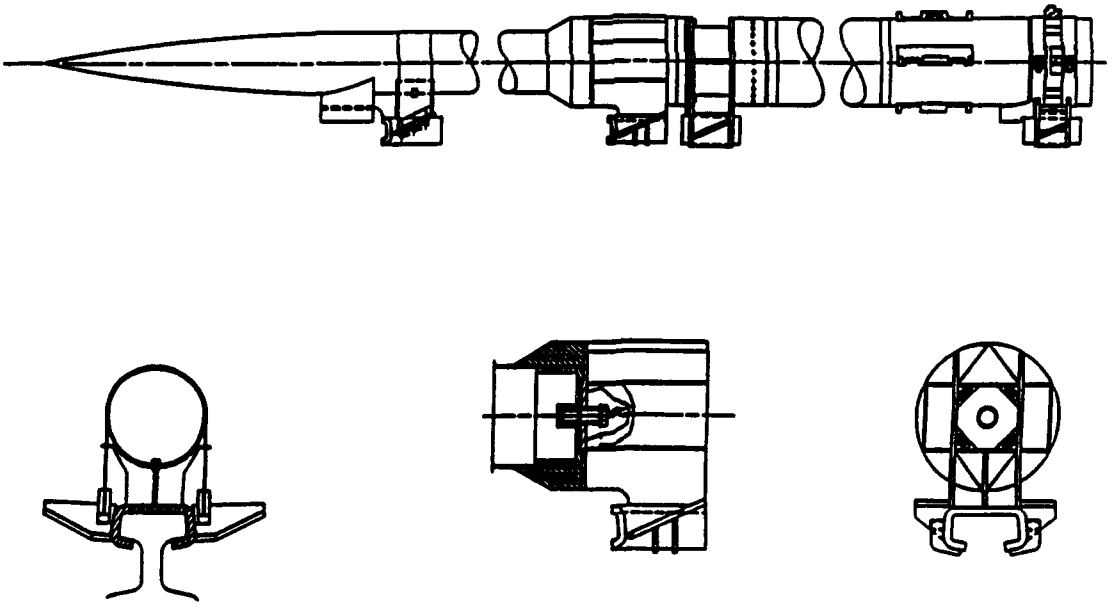

Figure 5. Sled Train Assembly, Front Attachment, Rear Attachment

The missile body was designed around several parameters in addition to loads such as weight, overall length, diameter, the KE penetrator it would have to carry, attachment points, loads, moments of inertia, center of gravity, and aerodynamic stability.

Internal simulants had to simulate the flight missile components as close as possible with the same materials and configurations as state-of-the-art guidance packages, nozzles, etc. The simulants served several purposes such as providing the same configuration as missile flight hardware, holding the KE penetrator, and providing attachment points for the slippers. The internal simulants were designed so that they could be bonded inside the missile skin without any mechanical fasteners, which may may penetrate the skin and break the fiberglass fibers thus reducing the strength of the missile airframe. Bonding the internal simulants is a key element in providing a strong and rigid missile body capable of surviving the sled track environment. The design also allows for the internal simulants to be assembled from the rear of the missile skin and house the KE penetrator as an integral part of the internal missile structure. Figure 6 shows a schematic of the overall configuration with the simulants installed.

The missile skin was fabricated by filament winding with fiberglass over an aluminum mandrel. The skin lay-up consists of low angle helical windings which provide bending and axial strength plus stiffness to the structure while the material has a high degree of toughness and fatigue resistance suitable for a sled test. After filament winding the missile, it was cured and machined to the final outside contour. Removal from the mandrel and bonding of internal simulants are the final steps to prepare the structure for the sled test. The missile is shipped as a complete assembly to HAFB, NM where it is ready for attachment to the sled train hardware.

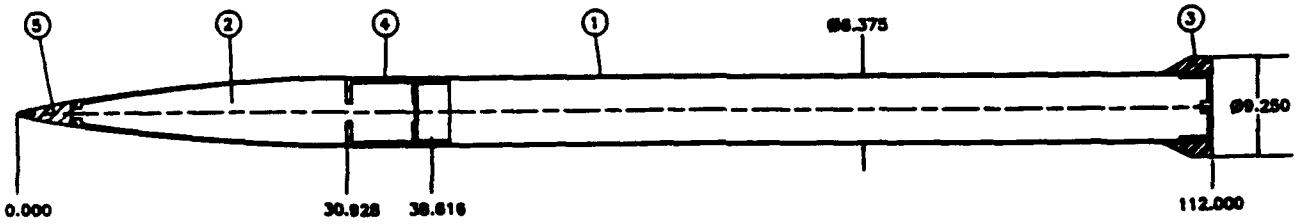


| NO. | NOMENCLATURE | QTY. | DWG.NO. | REMARKS/MATERIALS | WEIGHT(LBS) |
|---|---|---|---|---|---|
| 5 | AERO TIP | 1 | STC-1608 | 4130 STEEL TO 150 KPSI | 1.6 |
| 4 | ASM SIMULANT | 1 | STC-1607 | 4130 STEEL TO 150 KPSI | 18.1 |
| 3 | REAR BODY PLATE | 1 | STC-1618 | 4130 STEEL TO 150 KPSI | 8.0 |
| 2 | PAYLOAD | 1 | STC-1601 | | |
| 1 | COMPOSITE SKIN | 1 | STC-1609 | S-2 GLASS & EPOXY RESIN | 23.4 |

Figure 6. Composite Missile Simulant

Front Attachment Band

The front slipper attachment band design is based on loads analysis and has a 1.5 safety factor to yield or 2.25 safety factor to ultimate strength, whichever is greater. The front attachment band has to transfer inertial loads, vertical and horizontal, drag loads, and up lift loads due to aerodynamics between the front slipper and missile. A shear pin is on the top of the slipper and interfaces with the bottom of the missile skin to carry the down track inertia loads. Bending moments are transferred by the attachment band between the front slipper and missile skin. This is in addition to the tension loads placed in the band by the slipper slapping the rail. Because of the combined loading, a triangular load distribution is present in the band instead of the pure tension condition that is desirable for a band of this type. The original band was stainless steel .060 in thick and 3.5 in wide and long enough to wrap over the top of the missile and attach to the canards on the slipper. This band was later increased to .125 in thick with the same length and width but made out of 4130 steel due to better heat resistance. A block of steel with a slit cut wide enough for the band to fit in was welded to the band with three tapped holes in the underside for screws to attach the band to the canards (Figure 7).

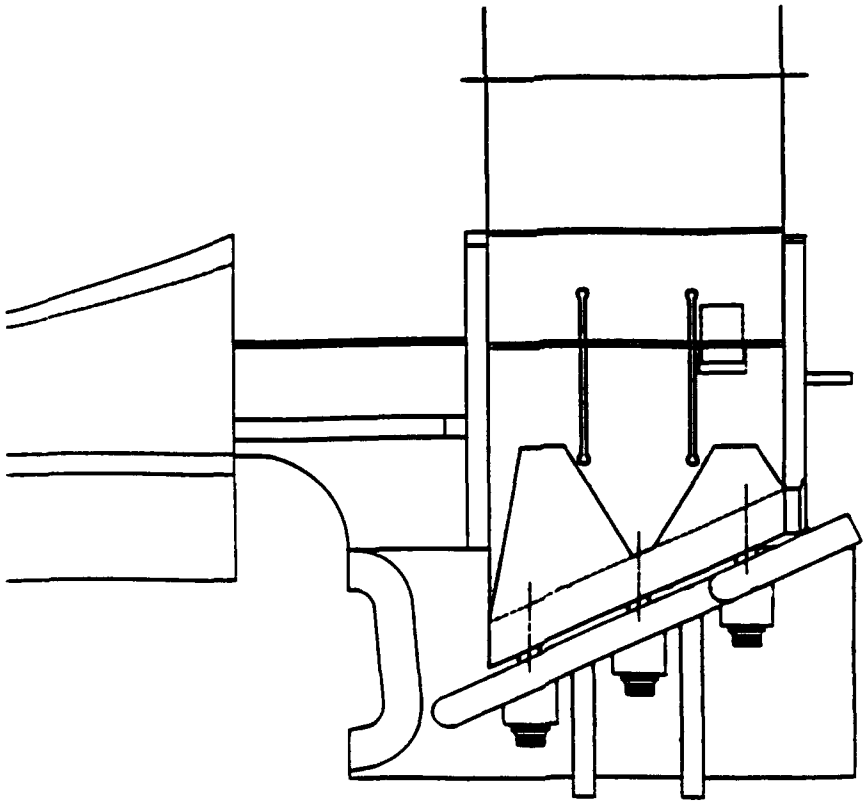

Figure 7. Front Slipper Assembly - Band Attachment

The front slipper and missile were assembled with calibrated strain gages on the band and the screws tightened to clamp the missile to the slipper with a predetermined amount of pre-tension equal to the uplift inertial loads placed on the slipper by the missile. Once the correct amount of pre-tension is in the band the screws and band assembly are welded to the canards to prevent track vibration from loosening the screws and thereby reducing the pre-tension. A loads analysis was performed on the missile structure, internal simulants and slipper attachment hardware before loads validation tests were performed (Figure 8) at Holloman Air Force Base.

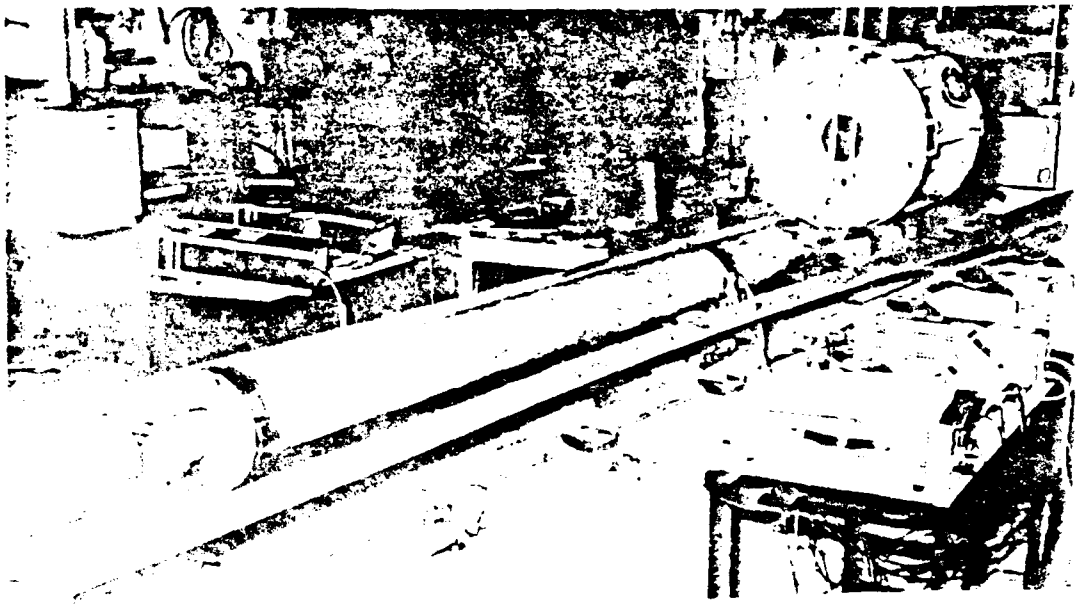

Figure 8. Loads Validation Static Test Set-up

Rear Slipper Attachment/Explosive Bolt

The rear slipper is attached to the rear of the missile by means of an explosive bolt. A nozzle simulant is bonded to the rear of the missile and interfaces to the slipper face with a chamfer to take out shear loads between the missile and slipper, the bolt takes out the bending loads in the structure through tension (Figure 9). The explosive bolt is pre-tensioned to an amount equal to the maximum bending load expected during test. Load validation tests were performed on the interface by lifting up on the front of the missile to generate a bending moment at the missile-rear slipper interface.

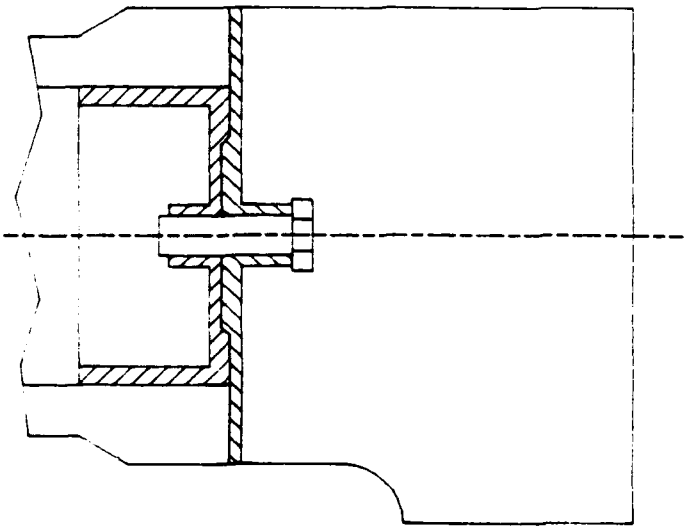

Figure 9. Missile/Rear Slipper Interface - Explosive Bolt

The explosive bolt is initiated with the proper current provided by trackside screen boxes. The trackside screen boxes are strategically located to insure the rear knife blades simultaneously contact the screen boxes at the instant the front attachment band contacts the trackside cutter bars. This timing is critical to provide a clean release of the missile body from the sled train assembly.

Static Load Tests

Complete loads validation static tests were performed on the missile/slipper assembly. The combined loading conditions are represented along with the applied loads and measured deflections in Figure 10. No failures were recorded in any of the loads validation tests and the static load deflection measurements were in agreement with the theoretical analysis values. Therefore, the load conditions and stress distribution within the missile structure and attachment hardware were calculated and the design assumed to be adequate for the missile to survive the sled environment loading conditions.

## CONDUCTED TESTS

The release mechanism for this full-scale missile test technique consists of severing (hydrodynamic penetration) the front attachment band with trackside cutter bars (Figure 11) and simultaneously initiating the aft slipper explosive bolt (Figure 12). The aft slipper is bolted behind the missile to prevent shock waves from impinging excessive pitch and yaw on the free flight missile. In the sled train design, the pull-down facility is used to divert any pusher sled debris or carriage sled hardware away from the target. All the pusher sleds can withstand the forces while travelling down the rail. However the loads induced by the 1281 ft radius rail at greater than 4800 ft/sec, will gouge or fail the rail itself.

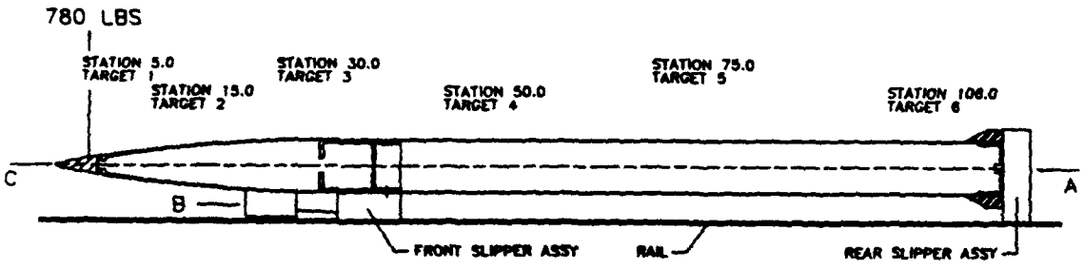


SLIPPER TO RAIL CLEARANCE= 0.14"
SLIPPER ASSEMBLIES FREE

| | DEFLECTION AXIAL (IN) | DEFLECTION RADIAL (IN) | |
|---|---|---|---|
| TARGET 1 | 0.0000 | 0.3688 | B= 54.17%(A) |
| TARGET 2 | 0.0050 | 0.3818 | |
| TARGET 3 | 0.0077 | 0.1688 | |
| TARGET 4 | 0.0137 | 0.0601 | A= 3910 LBS. |
| TARGET 5 | 0.0325 | 0.0043 | |
| TARGET 6 | 0.0471 | 0.0286 | |
| TARGET 1 | 0.0000 | 0.3286 | |
| TARGET 2 | 0.0626 | 0.2521 | |
| TARGET 3 | 0.0701 | 0.1617 | A= 8080 LBS. |
| TARGET 4 | 0.0766 | 0.0897 | |
| TARGET 5 | 0.1002 | 0.0478 | |
| TARGET 6 | 0.1267 | 0.0539 | |
| TARGET 1 | 0.0000 | 0.2818 | |
| TARGET 2 | 0.0731 | 0.2157 | |
| TARGET 3 | 0.0783 | 0.1469 | A= 12,000 LBS. |
| TARGET 4 | 0.0904 | 0.1056 | |
| TARGET 5 | 0.1154 | 0.0804 | |
| TARGET 6 | 0.1503 | 0.0788 | |

FRONT SLIPPER ASSY WEDGED

| VERTICAL TIP LOAD ONLY LOAD 780 LBS. | DEFLECTION (IN) |
|---|---|
| TARGET 1 | 0.2214 |
| TARGET 2 | 0.1378 |
| TARGET 3 | 0.0689 |
| TARGET 4 | -0.0411 |

Figure 10. Combined Loads Test

Figure 11. Trackside - Front Slipper Band Cutter Bars

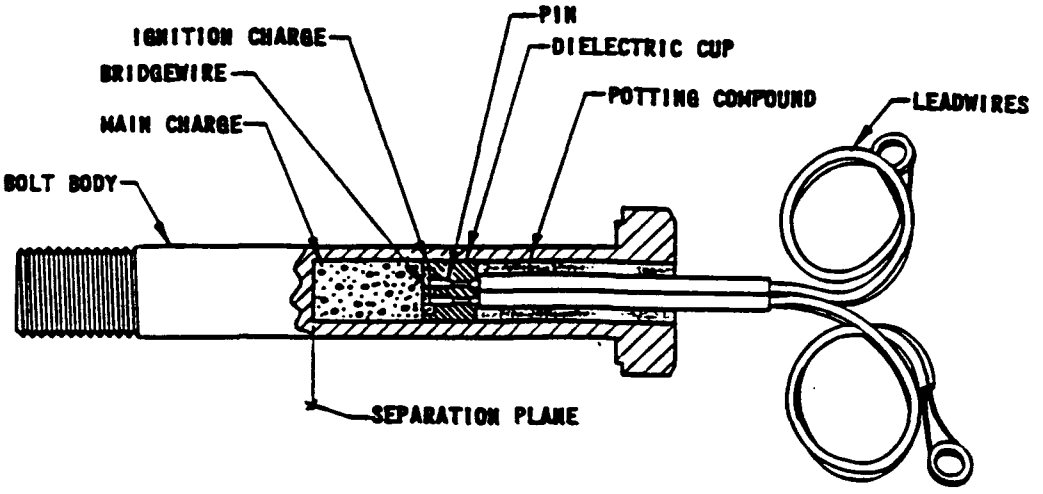


Figure 12. Explosive Bolt

The significance of developing the sled test techniques to propel the full-scale kinetic energy missile configurations to target impact, at the required impact velocity and pitch attitude, includes addressing the associated technical design issues of the test configuration and set-up. The missile forebody carriage sled concept identified various design areas which may have contributed to early failures. The carriage sled concept for the missile centerbody (penetrator) also identified several critical design areas. These unpredicted failures indicated the sled track environment induced quasi-steady state and dynamic loads much more severe than predicted in the original designs.

Front Band Modifications/Failure

The stress distribution in the front attachment band, the fixity condition of the joint, and the load distribution of the quasi-steady state and dynamic loads through the missile body were determined through extensive analysis and experiment. The initial analysis considered the front band attachment as a classical pre-stressed bolted connection. This assumed the band prestress load was greater than the combination of the aerodynamic uplift loads and the sled dynamic loads. As long as a gap did not occur between the slipper cradle and the missile ogive this phenomena would remain true; however, once the sled loads overcome the joint prestress load the band is no longer uniformly loaded and is subject to failure. Fortunately, the Image Motion Camera (IMC) photo-optical coverage for one calibration run captured a view of the missile at 4300 ft/sec just milliseconds prior to the band failure (Figure 13).

The combination of the extreme loading conditions induced by the sled environment and the assembly procedure prevent achieving a totally pretensioned joint connection between the missile and front slipper cradle. Therefore, the band does not remain in uniform tension and accepts a bending moment. The sled

environment induces two types of fixity conditions on the joint during a sled test. The clearance between the slipper and the rail allows the missile/slipper to bounce while riding the rail. At the instance the slipper bottoms out on the rail the front of the missile represents a cantilever beam fixed joint. In this case the connection does not represent the pretensioned bolted joint and carries a non-linear load distribution and moment into the slipper. Also, once a gap occurs between the ogive and slipper cradle the sled induced dynamic lambda loads can increase by an order of magnitude and fail the band. Figure 13 is a prime example of the development of a gap, which occurred prior to the band failure.

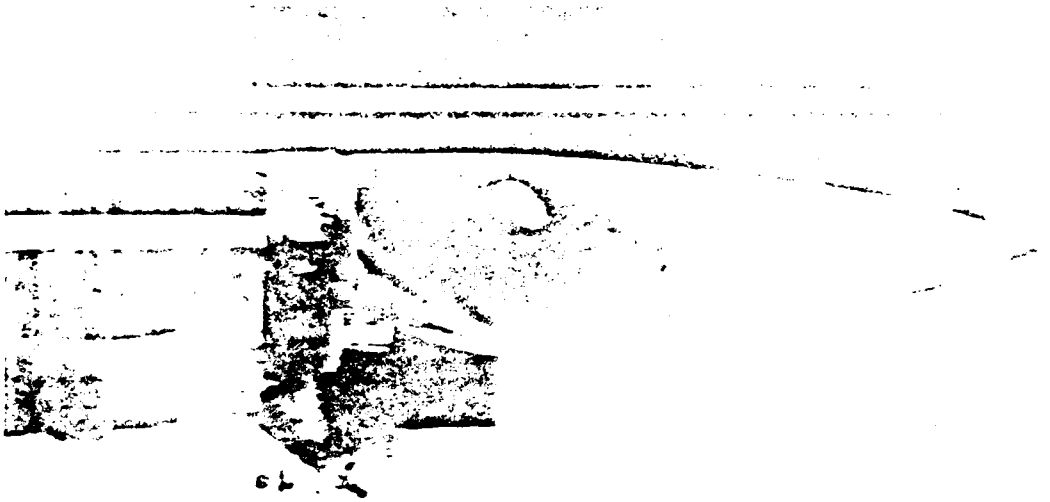

Figure 13. IMC Capturing Gap between Missile & Front Slipper

When the slipper is not bottomed out on the rail, the joint between the missile, slipper cradle, and attachment band represents a pinned connection. The moment load will be carried by the missile and not the band. Static load tests to represent both the pinned and fixed joint conditions verified adequate strength of the missile and attachment band redesign as mentioned previously.

Checkout Tests

The first checkout run investigated the performance of the foam braking technique to slow down the pusher sled and prevent interference with the free-flight missile. Other checkout runs were conducted to validate the band "cutting" technique and initiation of the explosive bolt at velocities in excess of 5000 ft/sec. These events were then combined and a calibration test was conducted to observe the interaction of the braking, band cutting, initiation of the explosive bolt, functioning of the

pull-down/diverter assembly, and to record the free-flight trajectory of the missile after release from the sled assembly.

Preliminary band cutting tests were performed at 5000 ft/sec to determine whether or not it was possible to cut a band at the high velocity, previously bands had only been cut at velocities up to 1500 ft/sec. Image Motion Cameras (IMC) positioned at the event location captured and verified the capability to cleanly cut the front attachment band (Figure 14). Even though for this test the missile body was bolted to the front slipper assembly, the cutting technique was proven adequate to release the front slipper from the missile.

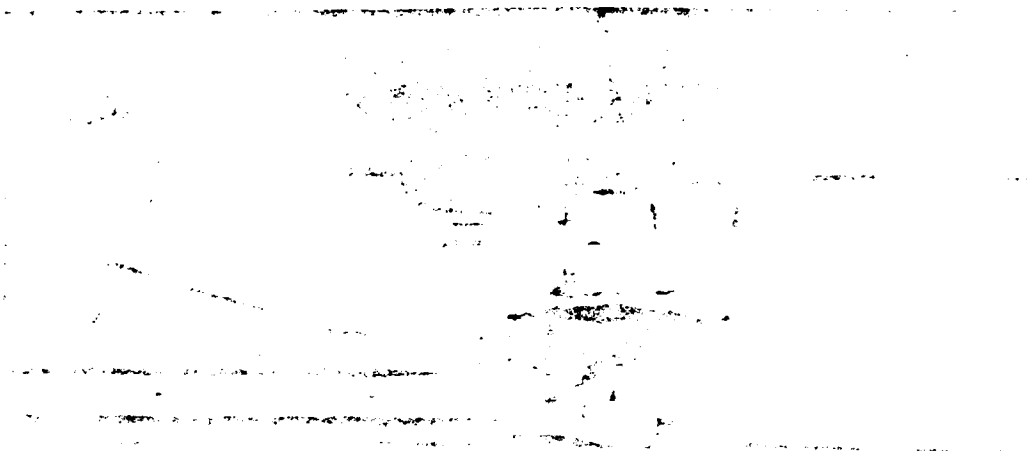

Figure 14. Band Cutting Verification

Approximately 26 ft after the band cutting and the explosive bolt initiation the sled train enters the pull-down and the missile begins separation from the front and rear slipper assemblies. The band and front slipper assembly cleanly separate from the missile and begin to follow the pull-down as shown in Figure 15, which is 20 ft after entering the pull-down. Separation is also evident between the rear of the missile and the rear slipper assembly, due to foam braking slowing down the rear slipper. The missile is now flying cleanly away from the sled train assembly and not subject to any induced loads causing excessive tip off.

Figure 16 records the missile and sled train at the end of the 80 ft long pull-down facility just before the slipper assembly goes into a pit. The pit insures that no sled train debris/hardware impacts the target area. A slight upward pitch is in the missile at this point, however the missile has aerodynamically stabilized itself over the $300^{+}$ ft free flight distance just prior to target impact and has negligible pitch and yaw (Figure 17). The yaw measurements were made by placing a mirror at 45° to the cameras thereby getting both pitch and yaw recordings in one frame.

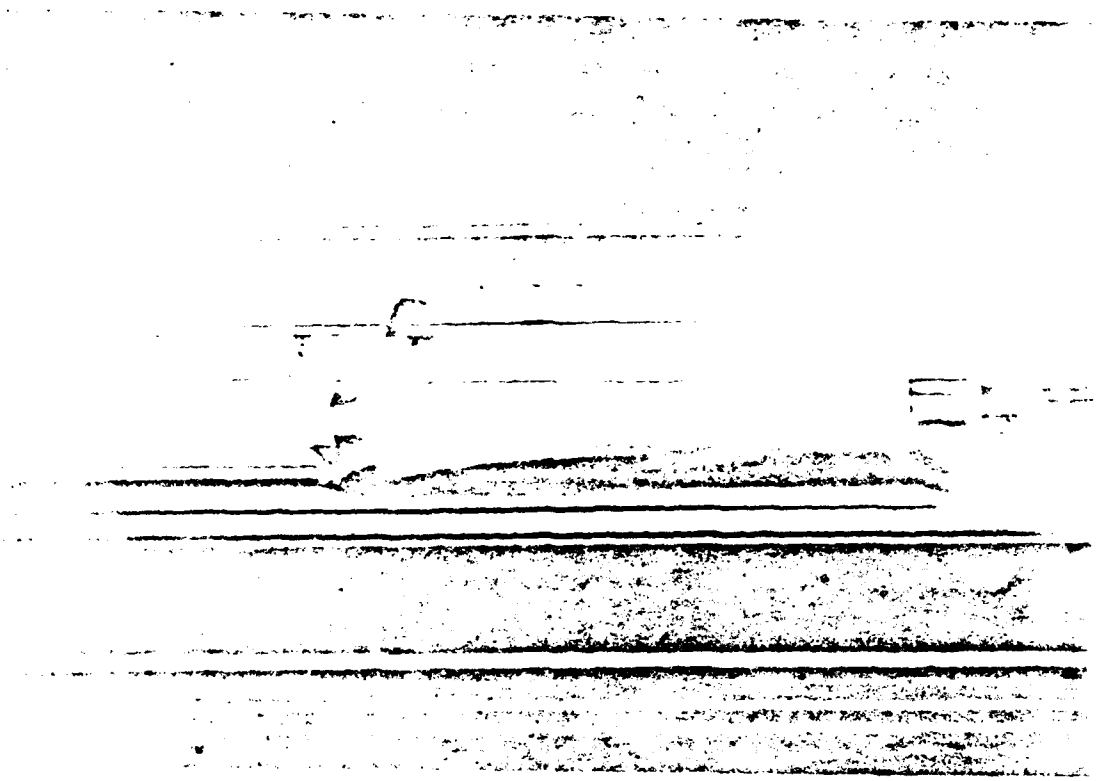

Figure 15. Missile/Sled Train Separation - 20′ into Pull-Down

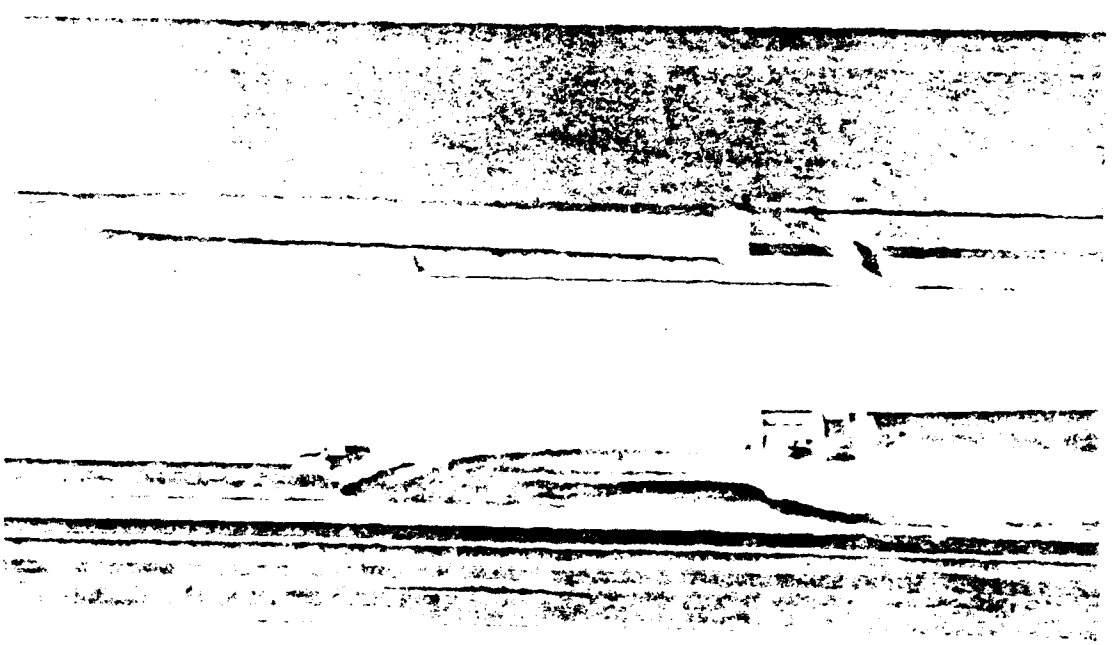

Figure 16. Missile/Sled Train at End of 80′ Pull-Down

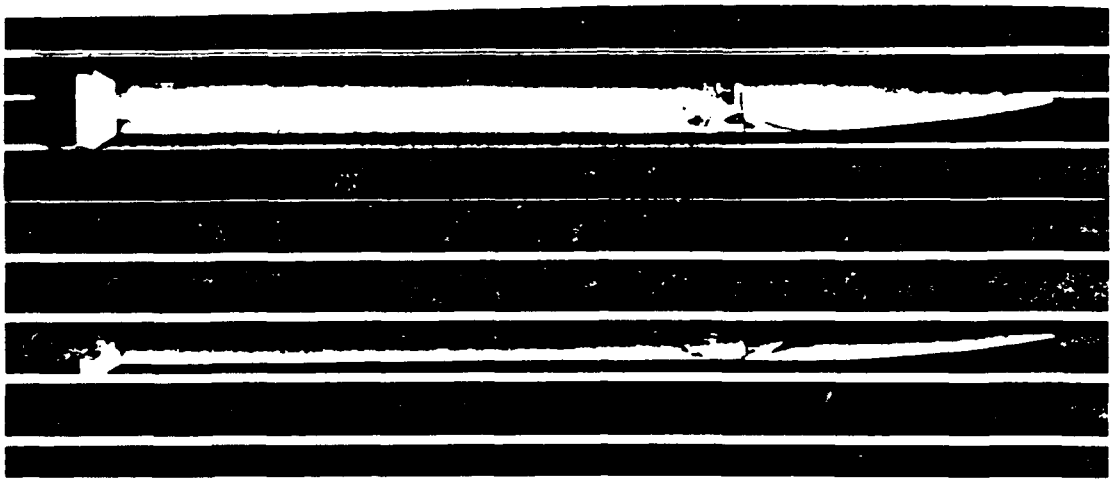

Figure 17. IMC Recorded Pitch & Yaw

Cameras and witness screens were placed at 25 ft intervals over the free flight distance before target impact to record the free flight trajectory (Figure 18). This data provides the information on aerodynamic damping frequency of the missile and its associated pitch and yaw and is plotted in Figure 19 to fit a sinusoidal curve. The damping frequency cycle should be repetitive between tests which provides the capability to accurately position the target to insure less than the ± 1° impact angle requirement.

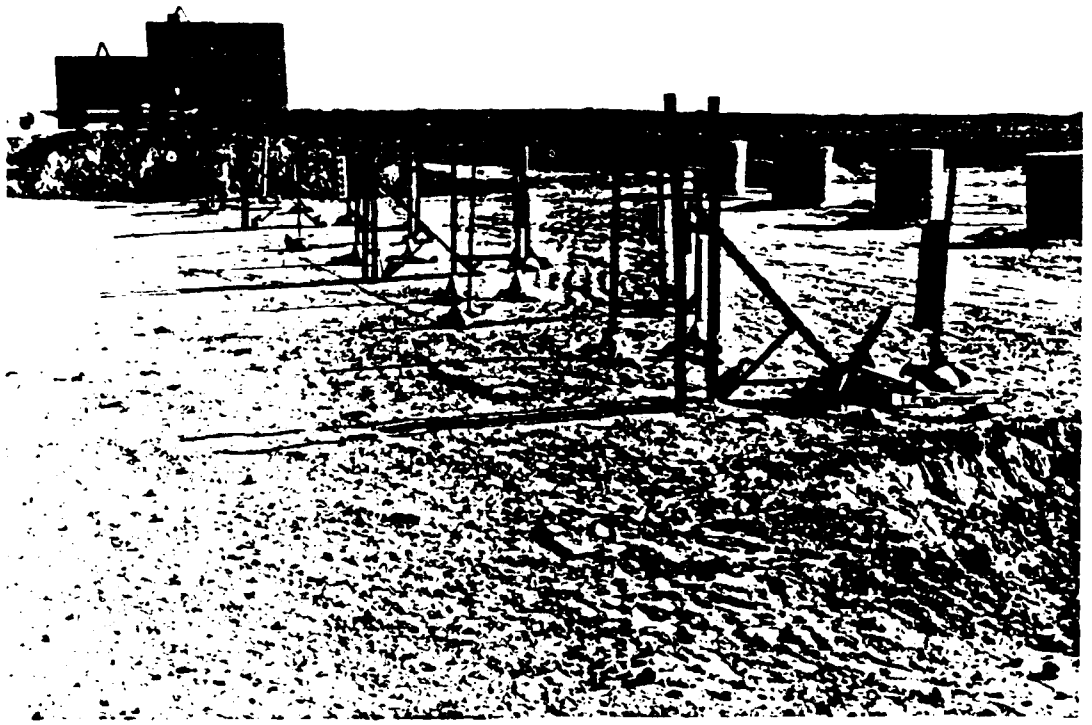

Figure 18. Cameras & Witness Screens

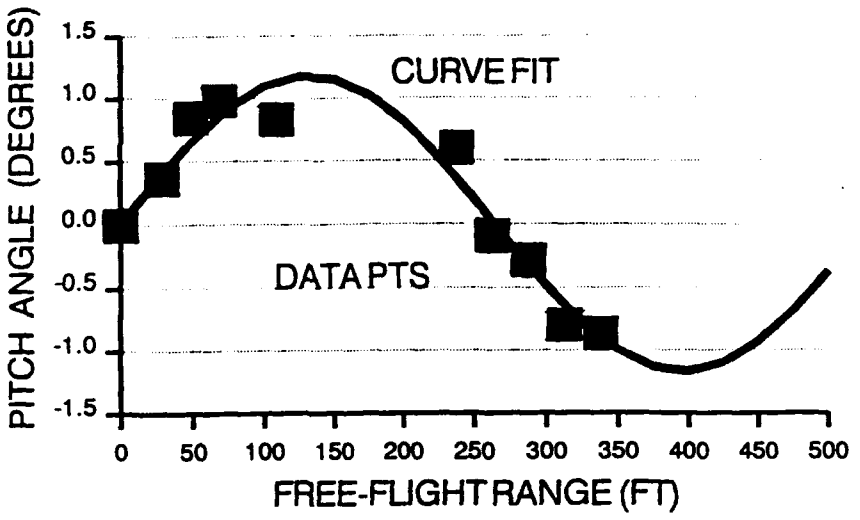


Figure 19. Flight Trajectory Curve Fit

## CONCLUSIONS

The full-scale kinetic energy missile sled testing techniques developed provide the only capability to experimentally determine the significance of missile airframe configurations, internal guidance components, integral KE penetrator, and other missile support structures in contributing to the defeat of rolled homogeneous armor (RHA) and advanced threat armor targets. The full-scale KE missile concept can achieve the required velocity for optimum KE penetrator performance, and impact the target at a controlled angle of less than ± 1°. The tests have helped optimize the design, attachment, and placement of KE penetrators within the missile airframe to provide a combined effect to defeat threat armor concepts as well as provide a method for testing future penetrator materials, geometries and designs. The sled test costs have proven to be one-tenth to one-twentieth the cost of a full-up missile flight test.

These test results should improve hydrocode modelling capabilities for predicting KE penetration and supporting missile system lethality. Presently, hydrocodes primarily rely on the KE penetration and the associated spall effects and neglect other structural damage. These tests verified that the additional missile kinetic energy delivered on the target may enhance the system lethality.

The results allow direct comparisons between full-scale single KE penetrator theoretical performance predictions and full-scale KE missile/airframe configurations. Comparisons between total penetration, total energy on target, hole profile and spallation verify an obvious difference in the terminal effects of a KE penetrator and a KE penetrator/missile airframe configuration.

# Metallurgical Failure Analyses of Maraging Steel Missile Motorcases

Albert S. Ingram
Structures Directorate
Composite Structures and Materials Function
U.S. Army Missile Command
Redstone Arsenal, Alabama

## Abstract

The U.S. Army Missile Command is using 18% nickel maraging steels in critical applications such as pressure vessels and motorcases. Investigations into past failures of missile motorcases have shown that stress corrosion susceptibility of C-300 and T-250 maraging steel is dramatically influenced by fabrication method and heat treatment. In particular, the shear forming method has been shown to impart lower stress corrosion properties to TOW motorcases when compared to motorcases fabricated using the deep draw method. Also, a moderate underaging heat treatment of STINGER motorcases has been shown to impart lower stress corrosion properties with no degradation of tensile properties.

## Introduction

Maraging steels are a unique group of iron alloys which combine high mechanical properties with relatively easy fabrication and heat treatment characteristics as compared to many other high strength steels. For this reason, maraging steels are being utilized for many missile structure and substructure applications. In particular, maraging steel is being used for several MICOM motorcases including the TOW launch motorcase and the STINGER flight motorcases (see figures 1 and 2). These motorcases are fabricated by using either the deep draw or the shear form methods, both of which increase the mechanical properties of the steel further due to cold work strengthening. Initially, both of these motorcases were fabricated by using C-300 grade maraging steel but this was later changed to T-250 grade due to cost and availability concerns.

The use of these high strength steels has not been without problems. The TOW launch motorcase has suffered four failures, the two latest failures occurring in 1986. The STINGER flight motorcase has suffered no flight failures but cracking has recently occurred on several motorcases during manufacturing which caused considerable production delays and cost until the problem was corrected. In both cases, the primary cause of failure was concluded to be motorcase deterioration due to stress corrosion.

## Failure Analysis

Only shear formed TOW motorcases which were fabricated from C-300 maraging steel have suffered failures attributed to stress corrosion damage. The most recent failures occurred from two separate incidents during firing exercises at Yakima, Washington, and Oahu, Hawaii. During such dynamic events, some of the motorcase is lost or damaged beyond usefulness. Approximately 75 to 80 percent (by weight) of the motorcases were recovered (figure 3). An intensive analysis of the size and number of the recovered motorcase pieces showed that both failures occurred from low pressure rupture (6,000 to 8,000 psi) (ref 1). Since an analysis of the manufacturing quality control showed these motorcases had been inspected and proof tested at a pressure of 18,250 psi, material deterioration had obviously occurred during field storage of the launch tube assembly.

Analysis of the failed TOW missiles did not result in the location of the failure initiation site. It is believed that the motorcase fragment(s) containing the initiation site was either not recovered or the failure event and following atmospheric corrosion attack had damaged the site beyond recognition. Elemental composition, mechanical properties and Rockwell hardness of motorcase fragments are shown in Tables 1 and 2. No material anomalies were found in either failed motorcase though evidence of stress corrosion cracking was found (Figure 4). Other unique fracture features (which are characteristic of shear formed TOW motorcases) included delaminations, shear bands and fracture splitting (Figures 5-6).

As part of the root cause investigation into these failures (ref 2), several failure scenarios of low pressure motorcase failure were examined. During one such test, the motorcase ruptured at 4,000 psi. Subsequent analysis of the motorcase fragments positively identified the cause of failure as being a pre-existing through-thickness stress corrosion crack (figure 7). The fracture, which had initiated on the inner diameter surface near the aft end threads, was completely intergranular. Several cracks were found in this area which had heavy pitting corrosion. Contamination from a sulfur/carbon compound had evidently initiated the pitting corrosion which in turn initiated the stress corrosion cracks.

## Stress Corrosion Susceptibility Tests

Immediately after the most probable cause of the TOW failure was established, questions had to be answered regarding the stress corrosion resistance of all configurations of TOW launch

motorcases, particularly with regard to newer motorcases which were being fabricated from T-250 maraging steel. A C-ring stress corrosion test (per ASTM G-38) was performed on the following groups of motorcases;

| Group | Alloy | Forming Method | Manufacturer |
|---|---|---|---|
| 1 | C-300 | shear form | Marquardt |
| 2 | T-250 | shear form | Marquardt |
| 3 | T-250 | deep draw | NI Industries |
| 4 | T-250 | shear form | Dynamic Tool |

The results of the tests are shown in Table 3. Conclusions regarding the test data are;

a. The T-250 alloy has a significant advantage over the C-300 alloy with regard to the stress corrosion resistance of the TOW launch motorcase.

b. The fabrication method employed has a strong influence on a component's stress corrosion resistance. Deep drawn TOW motorcases have far superior stress corrosion resistance over the shear formed motorcases. Even variations in the shear form method have a significant influence on stress corrosion resistance. The higher amounts of residual stress which the shear form method imparts into the motorcase is believed to be a major cause of the lower stress corrosion properties.

c. The change from C-300 to T-250 maraging steel has significantly decreased the probability of future stress corrosion failures of the TOW launch motorcase.

## STINGER Flight Motorcase Failure Analysis

### Failure Analysis

From 1979 though 1987, the STINGER flight motorcase was fabricated from C-300 maraging steel without any significant cracking problem attributed to stress corrosion (approx. 29,000 motorcases). After an extensive qualification test program, production of T-250 motorcases began in 1987. After the production of approximately 5,000 motorcases without any significant problems, a production rate increase was required to meet delivery schedules of other contractors. To meet this production increase, the motorcase manufacturer (NI Industries) increased the size of the heat treat load from 15 to 40 motorcases. Shortly thereafter, cracking was discovered in the "boat tail" section of the motorcase during x-ray or magnetic particle inspection. During the investigation, of 44 motorcases (out of approx. 11,300) were found cracked.

The majority of the cracks emanated from the Ortman key slot and propagated forward, while several motorcases had cracks at various locations around the aft section (figures 8 and 9). All cracks extended in the axial direction. The fracture morphology of all cracks was intergranular, which is typical of stress corrosion or hydrogen embrittlement (figure 10). The majority of the cracks had an organic contaminant high in sulfur over most of its surface which is attributed to lubricants and coolants used during motorcase fabrication (figure 11). Hydrogen embrittlement testing (bolt loaded aft end C-rings at 75 percent of ultimate tensile strength for 1,000 hours) resulted in no failures. Electron microscopy of fractures from over-loaded test samples showed a ductile (dimpled) morphology which also indicates that embrittlement from hydrogen did not take place. It was concluded that the motorcases had cracked from stress corrosion. Unfortunately, the attacking corrosive material was never isolated, although it is believed that simple contamination from moisture was the most likely cause.

Even though the basic manufacturing process had not changed, the stress corrosion resistance of the motorcase had decreased. The most obvious difference in the motorcase fabrication process was the increase in heat treat load from 15 to 40 motorcases. All other manufacturing processes were essentially the same. A comparison of the mechanical properties between motorcases from 15 and 40 piece heat lots showed little difference although the 40 piece heat lot usually was slightly higher (Table 4). This increase in heat lot size had a significant effect on the "time at temperature" for the motorcases. The heat treat process consisted of placing the motorcases (with fixtures) into the furnace (at 900 °F) and removing them 4 hours later. As seen in figure 12, some 40 piece heat lots were at 900 °F for less than 30 minutes and some heat loads did not reach 900 °F at all. The increased mass of metal (motorcases and fixtures) had simply overloaded the heat-up capacity of the furnace and resulted in an underaged heat treatment. The motorcase is required to be heat treated at
900 °F for 3 hours (per Mil-H-6875H). A comparison of the mechanical properties among tensile samples from underaged motorcases and samples with a 482 °C (900 °F) or 510 °C (950 °F) aging treatment is shown in Table 5. A stress corrosion test program was performed to investigate the effect of the underaging heat treatment.

Stress Corrosion Susceptibility Tests

The stress corrosion tests were performed using bolt loaded C-ring (per ASTM G-38) from the boat tail (aft end) section and from the thin wall section of the motorcase. The test consisted of three groups: the base line samples (underaged), samples aged at 900 °F for 4 hours, and samples aged at 950 °F for 4 hours.

The results of the tests (Table 6) clearly show the detrimental effect of the underaging heat treatment on the stress corrosion properties of the STINGER motorcase. Conclusions regarding the STINGER test data:

a. The underaging of T-250 maraging steel (STINGER motorcases) significantly reduces the materials resistance to stress corrosion cracking. This can occur even if the heat treatment has produced the required mechanical properties.

b. An aging temperature of 950 °F improves the stress corrosion resistance of T-250 maraging steel. There is an accompanying small decrease in tensile properties.

c. Tensile coupons from heat treated STINGER motorcases apparently have slightly higher strength than heat treated tensile coupons. It is believed that the inherent residual stress in an unsectioned motorcase aids in driving the precipitation strengthening reaction to produce higher properties.

Overall Conclusions

The total influence of mechanical working and an underaging heat treatment on the stress corrosion behavior of maraging steels is not very well understood. In particular, the precipitation hardening reactions occurring during aging requires further extended study to understand which phases and/or alloying elements are affecting the strength/stress corrosion relationship which was observed during these analyses.

Reference 1: Technical Report RD-PR-87-7, Investigation of 1986 Yakima and Oahu TOW Launch Motor Failures, Volumes 1 and 2, U.S. Army Missile Command, 27 Jun 90.

Reference 2: Unreported data, courtesy of NI Industries and Atlantic Research Corporation.

Figure 1. TOW launch motorcase. Nominal dimensions; length- 406 mm (16 inches), outer diameter- 53 mm (2.1 inches), wall thickness- 1.8 mm (0.072 inch)

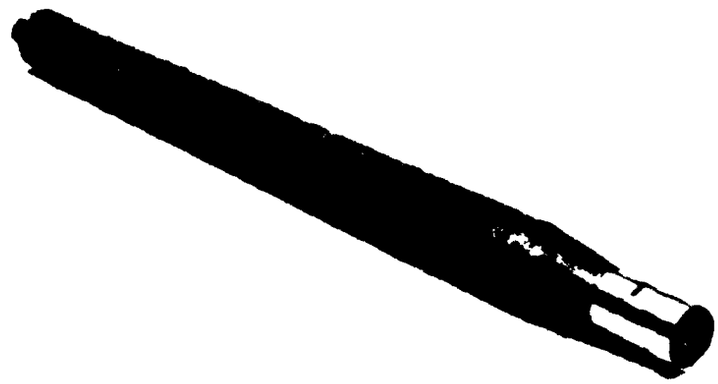

Figure 2. STINGER flight motorcase. Nominal dimensions; length- 990 mm (39 inches), outer diameter- 69.8 mm (2.75 inches), wall thickness- 0.58 mm (0.023 inch). Aft end outer diameter- 46.2 mm (1.82 inches)

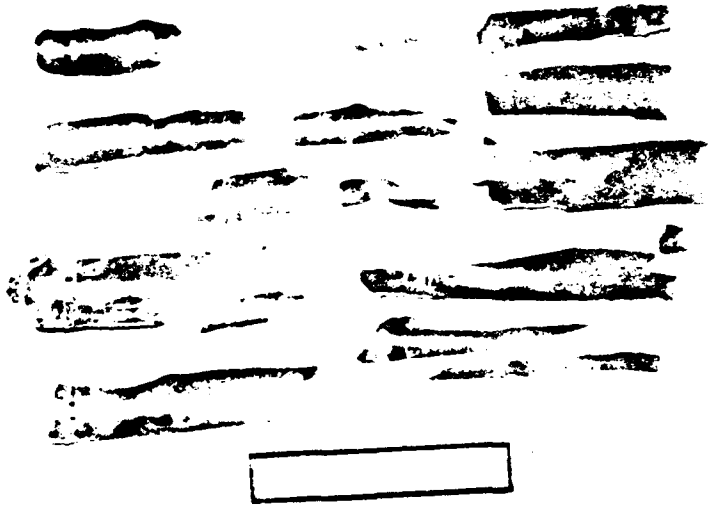

Figure 3. Photograph showing the typical fracture of a low pressure failure of a TOW launch motorcase.

Figure 4. Stress corrosion cracking found on the inner diameter wall of the Oahu motorcase failure (TOW). 300x

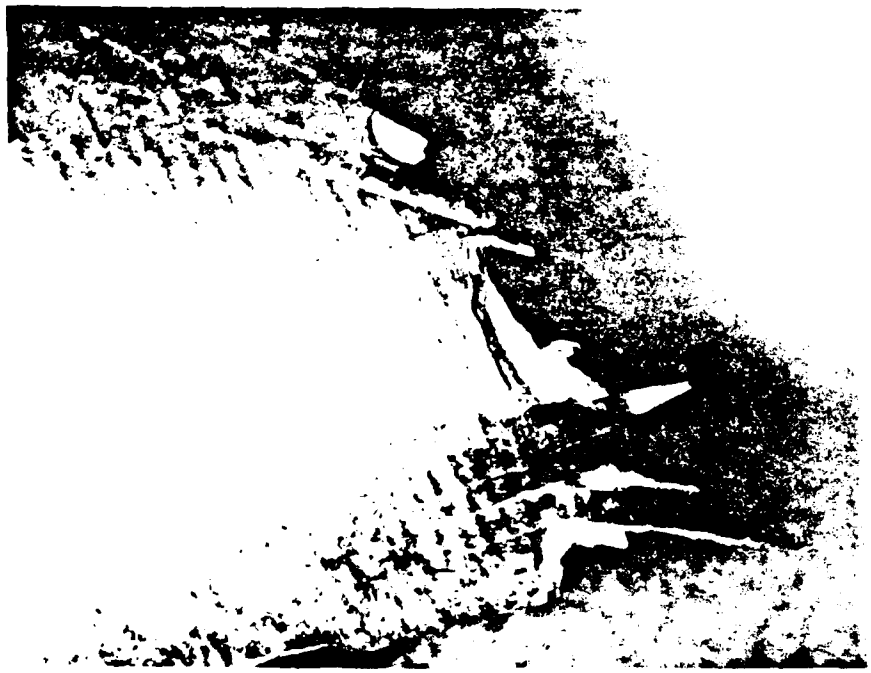

Figure 5. Photograph showing typical delaminations and secondary cracking found on shear formed motorcase fractures. 3x

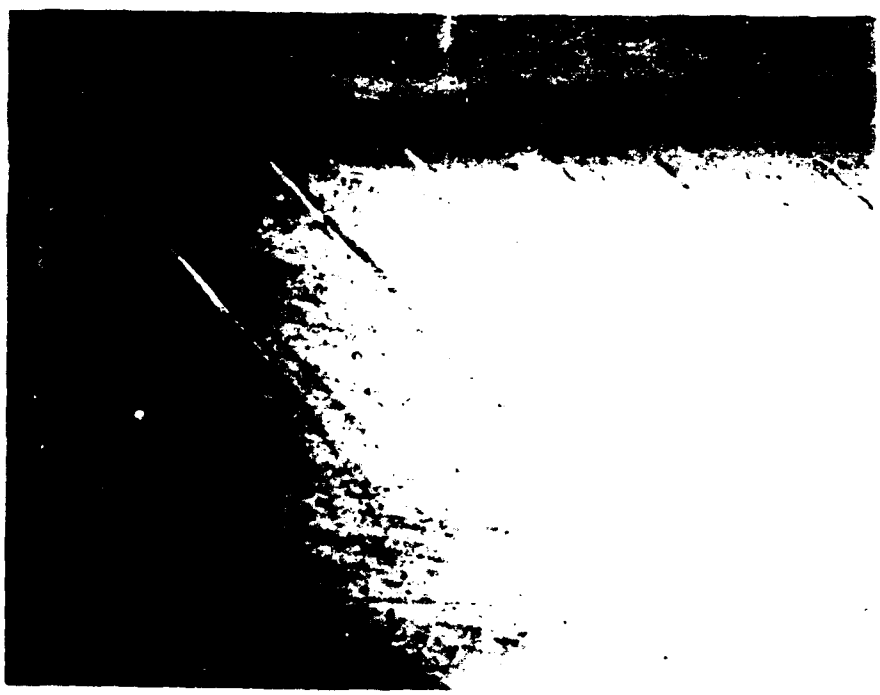

Figure 6. Shear bands found on TOW launch motorcase fracture. Transverse section. 140x

Figure 7. Electron micrograph of through thickness stress corrosion crack which caused low pressure failure of TOW launch motorcase.

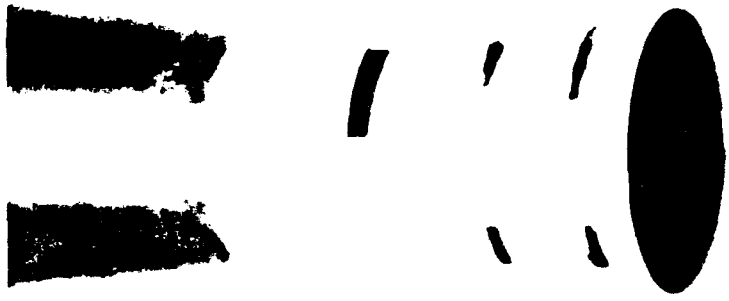

Figure 8. Aft end section of STINGER flight motorcase. Note Ortman key slot. Black radial lines mark the location of axial cracks. approx. 0.8x

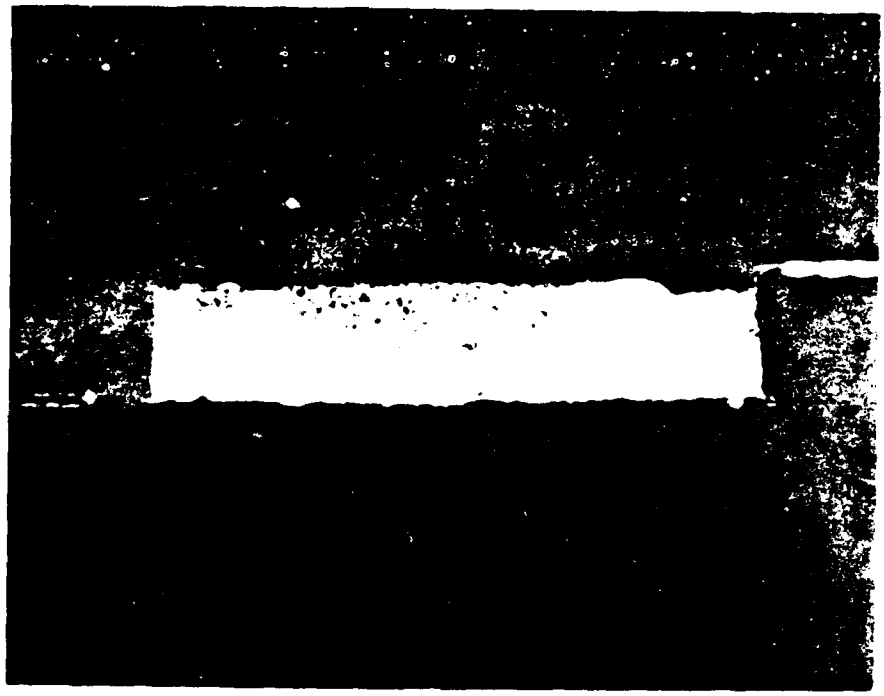

Figure 9. Elliptical surface crack found on the aft end section of a T-250 maraging steel motorcase (STINGER). 17x

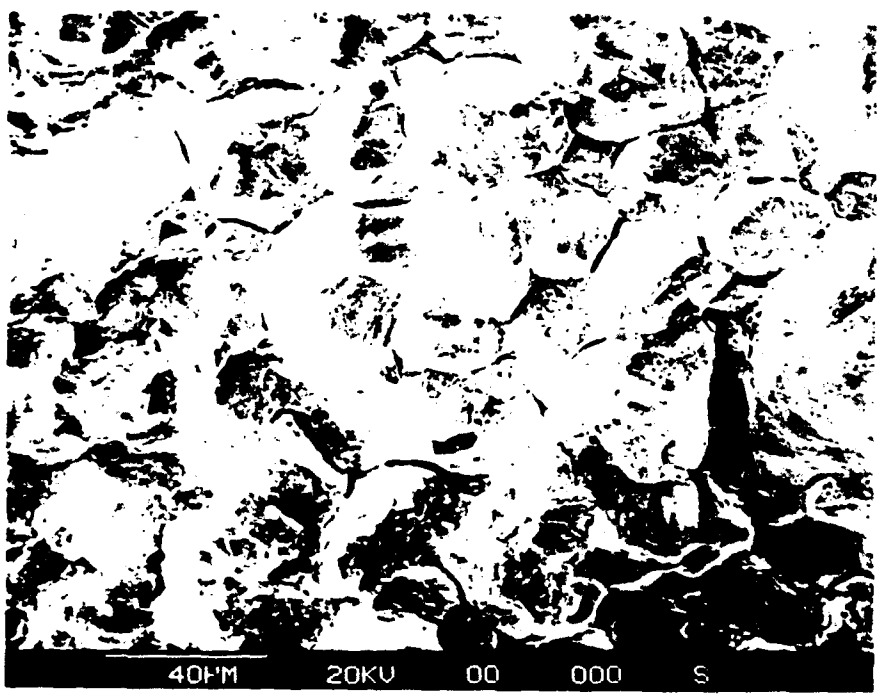


Figure 10. Electron micrograph of intergranular fracture found on a STINGER flight motorcase in the elliptical crack area (see figure 9). 500x

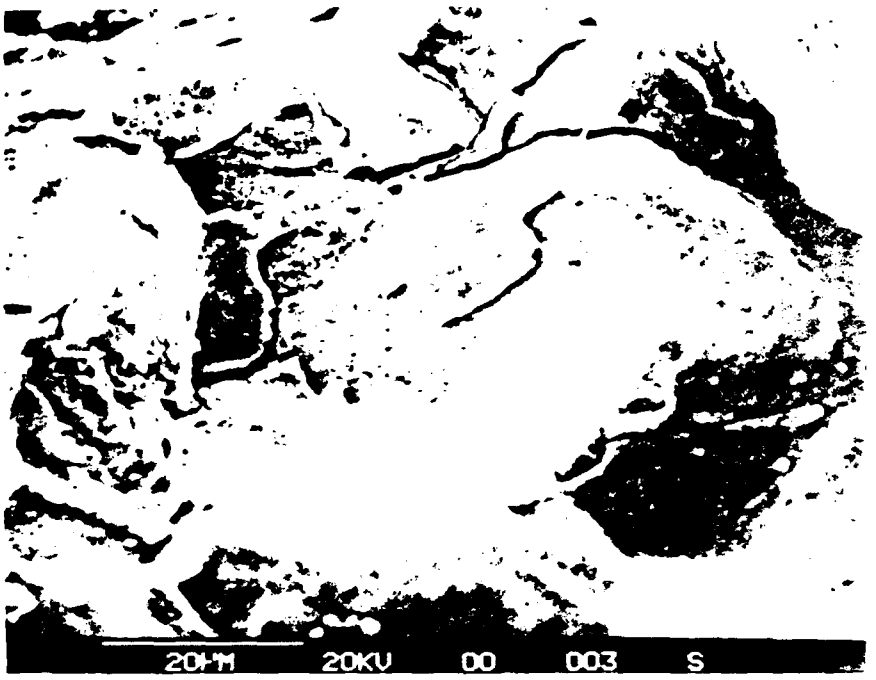


Figure 11. Electron micrograph of stress corrosion fracture showing intergranular fracture. Note the contamination (thin coating) which contained high concentrations of sulfur. approx. 1.25 kx

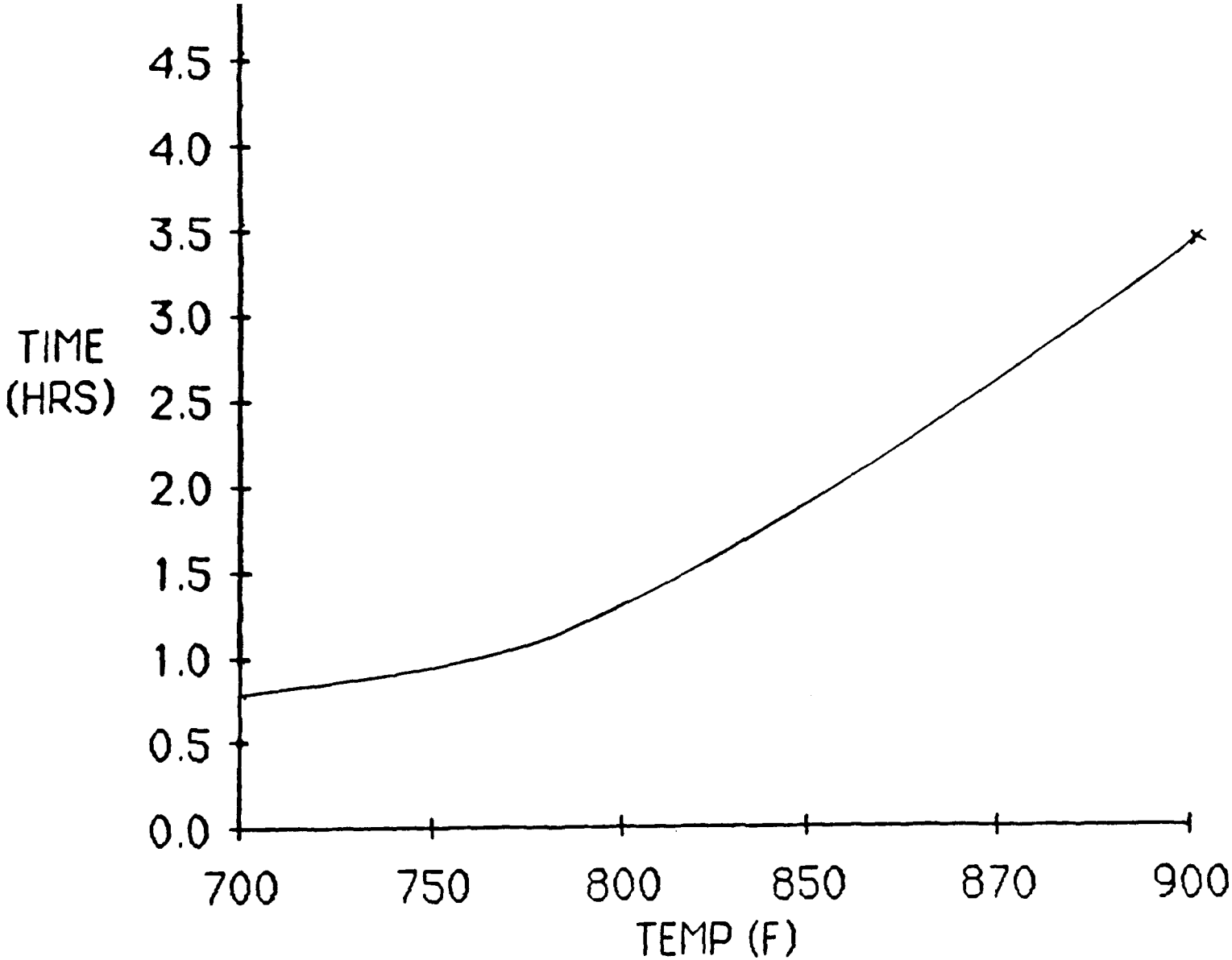


Figure 12. Typical (time vs temperature) heat treatment curve which produced T-250 maraging steel motorcases (STINGER) with reduced stress corrosion resistance. ref. 2

# Table 1
# TOW Launch Motorcase
# Elemental Analysis

| Element | % Required * | Oahu | Yakima | Test Case | T-250 @ |
|---|---|---|---|---|---|
| Nickel | 18-19 | 18.7 | 19.2 | 19.0 | 18-20 |
| Cobalt | 8.5-9.5 | 9.1 | 9.1 | 8.7 | 0.50 max |
| Molybdenum | 4.6-5.2 | 5.1 | 4.9 | 4.7 | 2.75-3.25 |
| Titanium | 0.5-0.80 | 0.82 | 0.84 | 0.86 | 1.20-1.60 |
| Aluminum | 0.05-0.15 | 0.12 | 0.10 | 0.15 | 0.05-0.15 |
| Carbon | 0.03 max | 0.016 | 0.013 | 0.033 | 0.03 max |
| Sulfur | 0.01 max | 0.002 | 0.003 | 0.006 | 0.010 max |
| Phosphorous | 0.01 max | 0.01 | 0.011 | 0.008 | 0.010 max |
| Iron | balance | balance | balance | balance | balance |

* C-300 per MIL-S-47139, Type II, Class 1
@ T-250 per AMS 6518

# Table 2
# TOW Launch Motorcase
# Tensile Tests

| Sample | Yield Strength MPa (ksi) | Ultimate Strength MPa (ksi) | % Elongation * |
|---|---|---|---|
| Yakima 1 | @ | 2,292 (332.4) | 1.0 |
| Oahu 1 | 2,184 (316.6) | 2,221 (322.2) | 1.6 |
| Oahu 2 | 2,311 (335.2) | 2,311 (335.2) | 1.0 |
| Test 1 | 2,313 (335.5) | 2,343 (339.8) | 1.7 |
| Test 2 | 2,356 (341.7) | 2,363 (342.8) | 1.5 |
| T-250 | 2,054 (297.9) | 2,090 (303.2) | 3.0 |

* 25.4 mm (1 inch ) gage length. Nominal thickness was 1.803 mm (0.071 inch) Nominal sample width was 3.17 mm (0.125 inch)

@ 0.2% yield offset requirement was not satisfied.

Rockwell hardness of C-300 samples: 52-55 HRC
Rockwell hardness of T-250 sample: 50-53 HRC

Tests 1&2 are comparitive samples from an unfailed C-300 motorcase

Table 3
TOW C RING SALT SPRAY DATA
Method-ASTM G-38
Average Time to Failure in Hours

| GROUP 1 | | | | GROUP 2 | | | |
|---|---|---|---|---|---|---|---|
| SAMPLE | 50ksi | 75ksi | 100ksi | SAMPLE | 50ksi | 75ksi | 100ksi |
| 1 | 3117 | 403 | 240 | 1 | 6094 * | 4500 | 1032 |
| 2 | 913 | 187 | 179 | 2 | 6094 * | 4124 | 1428 |
| 3 | 941 | 641 | 227 | 3 | 6094 * | 2015 | 323 |
| 4 | 3816 | 575 | 227 | 4 | 6094 * | 3584 | 384 |
| 5 | 4520 | 355 | 192 | 5 | 6094 * | 1267 | 704 |
| 6 | 2901 | 571 | 179 | 6 | 6094 * | 2015 | 2220 |
| 7 | 3117 | 713 | 168 | 7 | 4885 | 1023 | 1296 |
| 8 | 2811 | 669 | 132 | 8 | 6094 * | 2111 | 740 |
| 9 | 5136 | 427 | 132 | 9 | 6094 * | 2901 | 1152 |
| 10 | 4572 | 499 | 132 | 10 | 6094 * | 2283 | 344 |
| -- | ---- | ---- | ---- | -- | ---- | ---- | ---- |
| AVG | 3184 | 504 | 181 | AVG > | 5973 | 2582 | 962 |
| STD | 1354.2 | 154.3 | 39.0 | STD | 363 | 1108.0 | 565.0 |

| GROUP 3 | | | | GROUP 4 | | | |
|---|---|---|---|---|---|---|---|
| SAMPLE | 50ksi | 75ksi | 100ksi | SAMPLE | 50ksi | 75ksi | 100ksi |
| 1 | 6094 * | 6114 * | 2733 ** | 1 | 6094 * | 2916 | 323 |
| 2 | 6094 * | 6114 * | 704 | 2 | 4712 | 885 | 132 |
| 3 | 6094 * | 6114 * | 2733 ** | 3 | 6094 * | 1895 | 179 |
| 4 | 6094 * | 6114 * | 280 | 4 | 6094 * | 933 | 323 |
| 5 | 6094 * | 5160 | 1719 | 5 | 5800 | 1363 | 227 |
| 6 | 6094 * | 4500 | 2440 | 6 | 6094 * | 1703 | 280 |
| 7 | 6094 * | 6114 * | 1733 | 7 | 6094 * | 1009 | 280 |
| 8 | 6094 * | 4968 | 972 | 8 | 4572 | 1363 | 560 |
| 9 | 6094 * | 6114 * | 2592 | 9 | 6094 * | 785 | 368 |
| 10 | 6094 * | 6114 * | 2124 | 10 | 6094 * | 2425 | 280 |
| -- | ---- | ---- | ---- | -- | ---- | ---- | ---- |
| AVG > | 6094 > | 5743 | 1803 | AVG > | 5774 | 1528 | 295 |
| STD | 0 | 587 | 842 | STD | 574 | 674 | 111 |

Group 1 = Marquardt C-300
Group 2 = Marquardt T-250
Group 3 = Norris T-250
Group 4 = Dynamic T-250
* = No Failure
** = No Failure. Samples removed early.

# Table 4
# Tensile Properties
# STINGER Flight Motorcase

| Heat Lot Size | Yield Strength, mean Mpa (ksi) | Ultimate Strength, mean Mpa (ksi) | % Elongation mean | Yield Stregth, range Mpa (ksi) | Ultimate Strength, range Mpa (ksi) | % Elongation, range |
|---|---|---|---|---|---|---|
| 40 | 2,019 (292.8) | 2,032 (294.7) | 2.5 | 1,978-2,047 (286.9-296.9) | 1,989-2,068 (288.5-300) | 2.3-3.2 |
| 15 | 1,972 (286) | 2,006 (291.2) | 2.4 | 1,808-2,106 (262.3-305.5) | 1,840-2,136 (266.9-309.8) | 2.0-3.0 |
| required | 1,655 (240) min. | 1,724 (250) min. | 2.0 min. | | | |

All samples had a 25.4 mm (1 inch) gage length.
Nominal sample (wall) thickness was 0.58 mm (0.023 inch)
ref. 2

# Table 5
# Affect of Aging Temperature on Tensile Properties STINGER Flight Motorcase

| Aging Temperature, Centigrade (Fahrenheit) | Yield Strength, MPA (ksi) | Ultimate Strength, MPa (ksi) | % Elongation, 25.4 mm (1 inch) gage length |
|---|---|---|---|
| base line (figure 12) | 2,004 (290.6) | 2,024 (293.6) | 3.0 |
| 482 (900) * | 1,904 (276.1) | 1,933 (280.3) | 2.7 |
| 510 (950) * | 1,864 (270.4) | 1,888 (273.8) | 2.8 |
| 510 (950) @ | NA | 1,926 (279.4) | NA |

* Tensile coupons were removed from motorcase before heat treatment.

@ ref. 2 ; Tensile coupons removed from heat treated motorcase.
Yield strength and % elongation not available.

# Table 6
# Stress Corrosion Tests
# T-250 Maraging Steel
# STINGER Flight Motorcase

| Sample Location | Aging Temperature & Time Centigrade (Fahrenheit) | Failure Time, hours (average) |
|---|---|---|
| Aft end | base line (figure 12) | 9 * |
| Aft end | 482 (900) 4 hrs. | 287 * |
| Aft end | 510 (950) 4 hrs. | >762 * |
| Barrel Section | base line (figure 12) | 165 |
| Barrel Section | 482 (900) 4 hrs. | 1298 |
| Barrel section | 510 (950) 4 hrs. | 2695 |

* ref. 2: C-rings stressed to 414 MPa (60 ksi)
Nominal thickness of aft end sections was 1.52 mm (0.062 inch)

Nominal thickness of barrel section was 0.58 mm (0.023 inch). Barrel section samples were stressed to 689 MPa (100 ksi).

## - SESSION V -

SYSTEM SIMULATION AND AEROBALLISTICS

# MISSION AUGMENTED AIRBORNE PLATFORM: APPLICATION OF ARTIFICIAL INTELLIGENCE TO AIR DEFENSE SYSTEMS

Dr. Willard M. Holmes
US Army Missile Command
Research, Development, and Engineering Center
Redstone Arsenal AL 35898

## ABSTRACT

A need exist to develop methods and techniques for enhancing the survivability rate of Autonomous Airborne Platforms (AAP) traversing a high density threat battlefield en–route to achieving mission objectives. The Mission Augmented Airborne Platform (MAAP) program is a research and development effort in response to this identified need. An autonomous vehicle operating on a programmed route or table driven mode of operation has advantages in less intense environments. Operating in a more complex environment requires the use of intelligent threat avoidance tactics to increase survivability rates. Typically, more intelligent decision making requires an increase in both the quality and quantity of knowledge.

The autonomous nature of the platform restricts the options available for knowledge acquisition and time dependent decisions involving changing situational data and temporal knowledge bases. For unmanned autonomous systems this provides limited options: specifically, data and expert knowledge must be installed in the platform prior to initiating the mission; second, on board passive sensors must provide current situational data during mission operation; third, the up dated knowledge base must be used by a "Reasoning System" to accomplish situational assessment and generate intelligent actions to achieve threat avoidance.

## INTRODUCTION

### OVERVIEW

New and emerging mission requirements in the modern tactical battlefield dictates that new and emerging technologies be re–examined in context of finding new solutions to traditional problem areas. The MAAP program is a research and development effort to examine the application of knowledge based expert systems to the operation of an autonomous airborne platform. The effective application of the knowledge based system is context sensitive or domain dependent due to the knowledge base requirements for expert system operation.

Establishing a degree of bounds on the scenario used in this research, some basic assumption were made about the platform operation and the related battlefield environment: the first priority in achieving mission objectives is to survive battlefield threats through threat avoidance operations; second, for autonomous system operation there will be no ground based or operational environment signals generated specifically for the airborne platform; third, the platform will have a number of practical sensors on board for sensing the operating environment; and fourth, some knowledge about threat signatures are known prior to vehicle launch, but very limited knowledge about threat locations is available to the system prior to launch.

## FUNCTIONAL OPERATION

For purposes of concept explanation, a functional diagram of the MAAP system operation is shown in Figure 1. The Global Positioning System (GPS) satellite constellation is available to provide location in space, time and velocity information of the platform. This information is available through on board GPS receivers. More details on this information will be provided in a later section. As indicated in Figure 1, direction of data flow to the GPS is bidirectional for the battlefield environment. This is to indicate that the GPS signal is broadcast to the battlefield environment, but the battlefield can have the effect of jamming the GPS receivers on the platform.

Bidirectional data flow is shown between the platform and the expert system. This indicates the state of the platform is sent to the expert system knowledge base. With inputs from the battlefield environment through inboard sensors, the expert system reasons about collective status of the threat environment, platform states, and mission objectives. The results are appropriate maneuver commands to the platform for avoidance of the perceived threat. The platform inboard sensors include a five channel GPS receiver, a threat detector, and an inertial system that can stand alone or augment GPS operation. The MAAP system has an operationally degraded capability without GPS operation. The system can also operate in a basic mission mode without benefit of expert system operations.

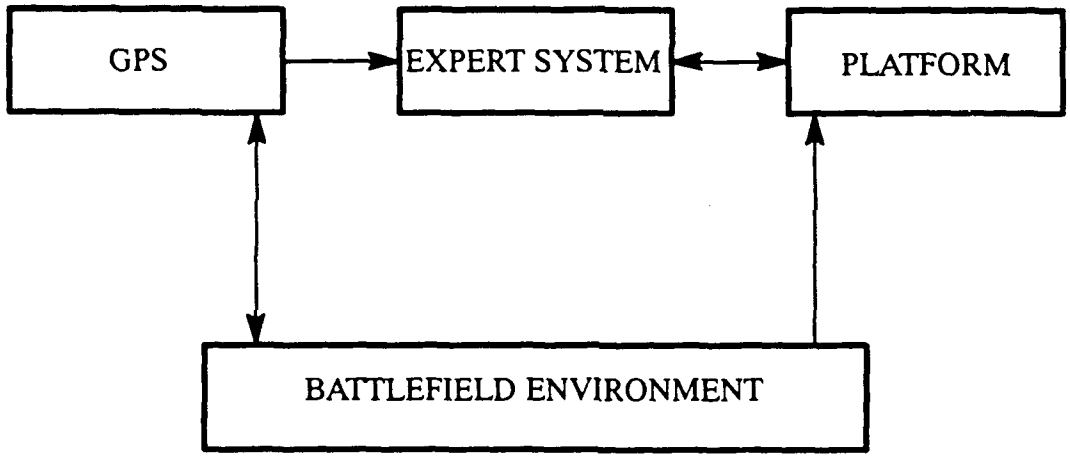


Figure 1. Functional Operation of MAAP.

# SYSTEM DESCRIPTION

## MAAP SYSTEM OPERATION

Before providing specifics on knowledge based system development and operation, it is necessary to provide an overview of the context of the MAAP system operations. One objective of the MAAP task is to develop a concept that will enhance the survival rate of an AAP while traversing a high density threat battlefield environment. As used here the term "autonomous" is defined to include the ability to sense the environment surrounding the platform but not radiating any electronic signals. This also excludes receiving any signal specifically generated and directed toward the platform for purposes of guidance or command.

The concept model developed here is defined in terms of two entities: an operating environment; and an AAP. Each of these entities is modularly structured and will be discussed in a later

section in terms of the associated major modules. In general the environment entity includes models of the GPS satellite constellation, battlefield threat lay down with associated terrain of interest, and the mission objective targets. The platform entity includes models of the platform structure, threat detectors/ sensors, an inertial measuring unit, a digital terrain map, and a knowledge based reasoning unit.

A representative MAAP operation is depicted in Figure 2. Typical operation would include the platform having certain information installed on board prior to launch. An example would be, in addition to mission target location, signatures of expected threats and related information. As the platform enters the threat environment, the threat detector senses signals to determine the nature of the threat–ground based signal jammer, surface–to–air–missile (SAM) target detection or engagement radars. After assessing the situation, one tactic might be to go into a terrain following mode to avoid missile engagement or fly up with minimum maneuvers to avoid jammers signal coupling into the GPS antenna on top of the platform.

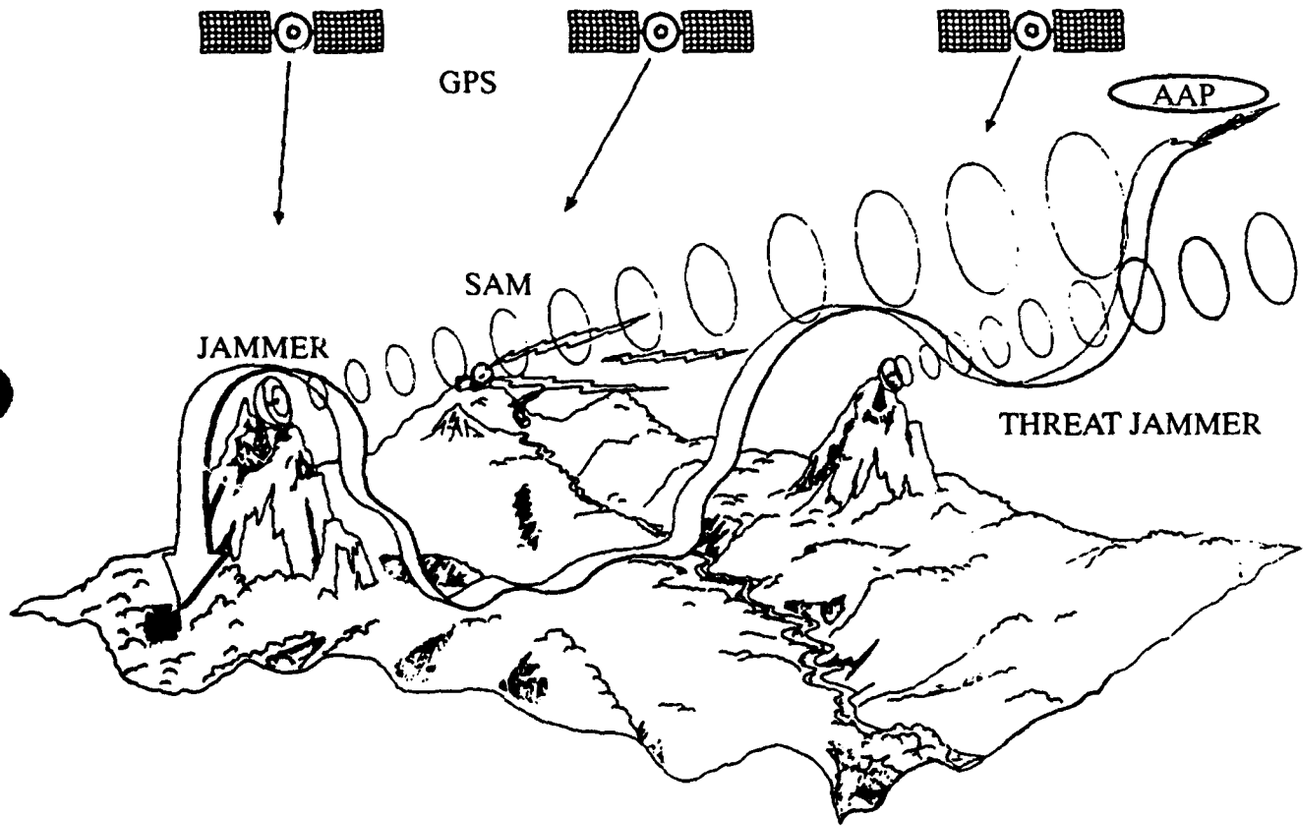


Figure 2. AAP Performance Environment.

## ENVIRONMENT OF PLATFORM OPERATION

### GLOBAL POSITIONING SYSTEM

The Navstar Global Positioning System (GPS) is a high–precision, worldwide network of orbiting navigation satellites. The final baseline constellation of 21 satellites (18 operational satellites with three spares) will operate in 12–hour orbits at an altitude of 20,183km (10,989nmi). It will provide visibility of 6 to 12 satellites at 5 degrees or more above the horizon to users any-

where in the world at any time. Typical orbits of the satellites are shown in Figure 3. With a four satellite constellation, highly accurate position, velocity and time is available to users equipped with suitable GPS receivers. Typical accuracies quoted for user equipment operating in P code are: positioning to 10 meters PMS in each axis; velocity to 0.1 meters/second in each axis; and time to 0.1 microseconds. Even more accurate positioning information has been reported using differential techniques[1]. The GPS system has been under development and operational verification by the Defense Department since the early 1960s.

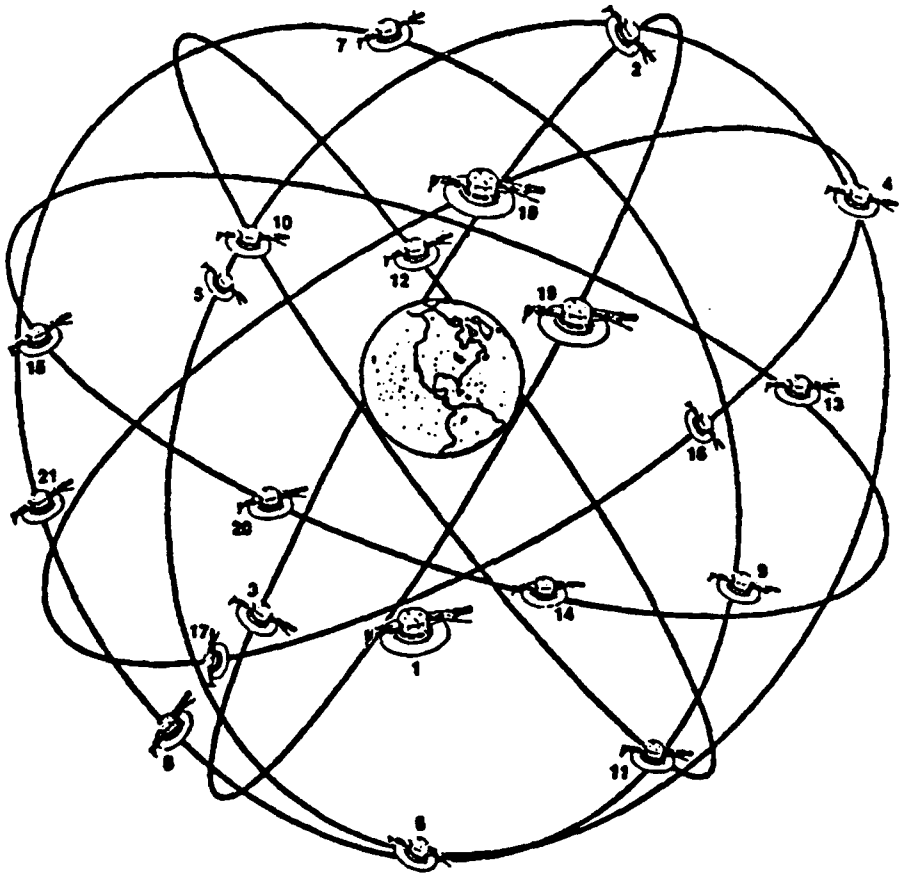

Figure 3. Navstar Global Positioning System.

## EARTH AND TERRAIN MODELS

Single and multi–channel GPS signal receivers process and display position solution in World Geodetic System coordinates. Developing a GPS model for simulation and analysis would offer advantages using an earth centered coordinate reference system with geodetic coordinates of longitude, latitude and altitude. This approach requires special consideration in forms of additional matrix transformation for displaying information in local coordinates at user

[1] Blackwell, Earl G.,"Overview of Differential GPS Methods", Navigation Journal of The Institute of Navigation, Vol. 32, No. 2, Summer 1985, pp 114 – 125.

locations[2]. The terrain model along with the earth centered geodetic coordinates system is used in accomplishing terrain following maneuvers for specific threat avoidance. The missile position is defined in geodetic coordinates (longitude, latitude, altitude) while velocity and acceleration are defined in local (north, east, down) coordinates.

## THREATS

Two types of threats are assumed for the MAAP conceptual model development: jammers and SAM systems. The jammers are wide band and have beams that can be directed toward sectors of the battlefield. The SAMs have two radars with different frequencies to accomplish tracking and engagement functions. These factors plus other related information will be instrumental in identifying the threat capability associated with a particular site. While the SAMs are ground based, the jammers may be located at different altitudes but are not mobile or moving during the scenario operation. The location and activation of the threats in the battlefield will be a random event. specifically, the platform will have no knowledge of the threat location in advance of detection. The major function of the jammers is to block or or cause a degraded operation of the GPS receiver on the platform.

# PLATFORM OPERATION

## PLATFORM MODEL

The platform operation is simulated with a six–degree–of–freedom model. The vehicle velocity profile is that of a typical slow flying craft with low level thrust capabilities. This assumption is included as part of the model to provide worst case condition for the reasoning module to develop avoidance tactics and minimize the critical time response required for real–time operation. Platform guidance can be accomplished in one of three modes: way point guidance, closed loop guidance, or a combination of both modes. The mode of operation can be controlled internally. The platform subsystems include: a five channel GPS receiver, a threat detector, and an inertial measuring unit.

## GPS RECEIVERS

The above quoted accuracies in position and time requires the use of a five channel receiver system. Four of the channels are dedicated to tracking on a continuous basis the four satellite frequency signals. The fifth channel sequences amount the different frequency transmissions from the four satellites to provide ionospheric delay compensations. Receiving data from four satellites simultaneously, the process is essentially to solve four unknowns with four equations. Early version of GPS receiver stations were complex and to bulky to put on board of only large platforms. With advances in digital circuity and microminiaturization, presently five channel receivers occupy a few cubic inches and weigh less than five pounds. This new weight and volume allows GPS receivers to be used for operation not feasible before, i.e., high performance aircraft, missile guidance systems and infantry patrols[3]. This new development in size and weight makes it possible to include GPS in the MAAP system.

---

[2] The Analytical Sciences Corporation, "Autonomous Platform Operation Phase II Software Users Manual", Prepared for US Army Missile Command, Huntsville, AL, Purchase Order No. 701603, 22 May 1989.

[3] Boutacoff, David A., "Navstar Forecast: Cloudy Now, Clearing Later", Defense Electronics, May 1986, pp 90 – 100.

Included in the GPS satellite models are representations of the random noise associated with the actual signals at the location of interest. To achieve improved operation using the GPS noisy signals and improved signal–to–noise ratios, Kalman filters are included as part of the signal processing on board the platform.

## INERTIAL MEASURING UNIT

An inertial strapdown measuring unit is modeled in the platform operations. The model is modular structured such that parameters of different quality gyros and accelerometers can be included for GPS aided operation or platform operation without GPS.

## THREAT DETECTOR

The sensor or threat detector monitors the RF environment of the platform and reports the results to the knowledge base for use in the expert system operations. The detected threat signatures can be resolved into specific information about the threat operation: Assumptions about the threat detector's capabilities include:

- A wide band receiver and signal processing to identify SAM sites and jammers from the detected signal;
- An approximate direction of the threat site from the platform;
- An approximate range from the platform to the threat site;
- An estimation of the power radiated from the jammers and SAM system radars.

For purposes of providing threat reference knowledge to the expert system, the angular section in front of the platform is divided into angular sectors. Each sector is assigned a weighting function. As threats enter different sectors, appropriate weighting functions are added to indicate the nature of the threat. Typical sector designations are depicted in Figure 4.

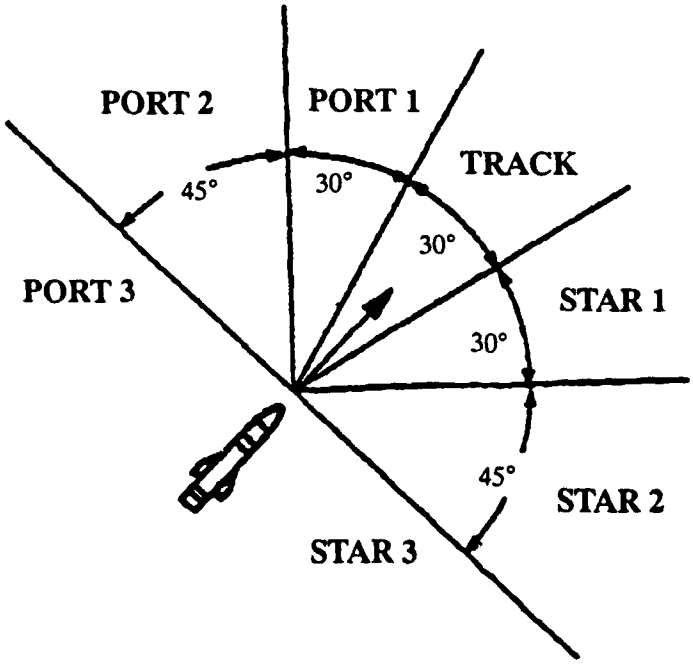


Figure 4. Threat Detector Sector Designations.

## BAROALTIMETER

In those instances where the GPS constellation shows degraded operation for a short period of time then the instrument of interest for GPS aiding is the altimeter. Degraded GPS operations are caused by poor geometry of satellites visible at locations of concern or the satellites are co-planar and cannot provide sufficient independent information to yield a meaningful position and time fix. This same type degraded operation occurs when a satellite fails, or when a satellite is shadowed by local terrain or by the vehicle carrying the GPS antenna. Since autonomous operation is the mode of MAAP operation, active devices such as radar altimeters are eliminated. The Baroaltimeter is the instrument of choice for this analysis. Reported results show that it is possible to use the Baroaltimeter as a source of information, i.e., altitude, when combined with signals from three satellites to yield successful navigation solutions. A model of a Baroaltimeter is included in the platform simulation model.

# KNOWLEDGE BASED SYSTEM

## REASONING MODULE

The MAAP reasoning module contains rules and an associated knowledge base to reason about the threats and best tactics to avoid the identified threats and produce guidance maneuver commands to execute the specific tactics. In general the rules are divided into five classes:

- Waypoint Sector Rules
- Jammer Response Rules
- SAM Response Rules
- Sector Cost Evaluation Rules
- Data I/0 Rules.

The Waypoint Sector Rules fire when facts pertaining to the location of the next Waypoint/target are asserted. These facts take the form:

way–sector SECTOR

where sector is one of the sector designations in Figure 4, indicating the sector in which the next Waypoint/target lies. The action taken by the Waypoint Sector Rules 5 is assign cost to each sector directly proportional to their displacement from the Waypoint/target sector. In the absence of any threats, this rule effectively results in the expert system recommending that the platform proceed directly to the Waypoint/target.

Jammer Response Rules fire when facts pertaining to the presence of jamming are asserted. These facts take the form:

jammer LEVEL

where LEVEL is either "high," "medium," "low," or "clear" indicating the amount of jammer power entering the GPS receiver. The action taken by the Jammer Response Rules is to return a message to the platform guidance indicating the set clearance to be used for terrain following. The set clearances specified are designated as low, medium, and high, according to jammer level. No message to commence terrain–following flight is issued – only a set clearance to assume in the event that the platform enters that mode. Here the platform is assumed to be autonomous, with no active sensor to aid in terrain following flight, terrain elevation in advance of the flight

path is determined from knowledge of position and heading from the navigation system, and an on–board digital map of terrain elevations. This concept is known as "passive terrain following[4]." In the presence of jamming, GPS accuracy will degrade and disrupt terrain following. In this instance, it is necessary to increase the set clearances to avoid crashing.

SAM response rules fire when facts pertaining to the report of SAM threats are asserted. These facts take the form:

sam RANGE SECTOR

where RANGE is either "near or "far" and SECTOR is as described above. The near/far field indicates whether the platform is within/outside the operating range of the SAM site. The SAM site is assumed to have detection and/or ranging radar that detects targets that are beyond the engagement range of the missiles. It is also assumed that a second radar is used to engage a target when within specified bounds. The threat detector can discriminate between the different frequencies. The "far" range indicates the platform has been detected but not engaged. Any evasive action taken at this point will be influenced by other threats either active or known to exist by previous encounters.

The "near" range indicates the platform in engageable by a SAM and has a fixed amount of time to take evasive action. One tactic available to the reasoning module when the "near" message is received is to immediately transmit to the platform to commence terrain–following flight, if not already in that mode.

Sector Cost Evaluation Rules fire when sector costs are revised, either due to threat reports or a change in the target/waypoint heading. These rules determine the sector of minimum cost and advises the platform if a change of heading is indicated. The Data 1/0 Rules control the external functions which monitor the serial port for incoming data, assert facts into the CLIPS fact–list, and transmit data to the platform when appropriate.

## SAMPLE RULES

A sample of the type rules used in the reasoning module is shown in Table 1. In addition, the module accomplishes the mission planning necessary to achieve the original mission objectives after completing threat avoidance maneuvers. The general concept followed in acquiring knowledge and developing rules for tactical maneuvers is to project action on the ground to action on the platform. Specifically, if a pilot on the ground or in an aircraft with the identified data and knowledge contained in the knowledge base, what would be his decisions and actions?

---

[4] Roberts, I. P., Ferguson, T. J., "GPS–Aided Passive Terrain Following", The Analytic Sciences Corporation, 55 Walkers Brook Drive, Reading, Mass 01867, Technical Report TR–4185–4–1, June 1985.

TABLE 1. Expert System Rules for Threat Detection.

## Rules

IF
the target is in the sector directly ahead
THEN
assign sector cost for Port–2 to 3.0
assign sector cost for Port–1 to 1.0
assign sector cost for Track to 0.0
assign sector cost for Star–1 to 2.0
assign sector cost for Star–2 to 4.0

IF
SAM is detected at *distant* range and
SAM is located in sector Port–2
THEN
modify sector cost for Port–2 by +10.0
modify sector cost for Port–1 by +10.0

IF
SAM is detected at *near* range and
SAM is located in sector Star–1
THEN
modify sector cost for Track by +10.0
modify sector cost for Star–1 by +10.0
modify sector cost for Star–2 by +10.0

## EXPERT SYSTEM INTERFACE

The early prototype expert system contained approximately 30 rules for situational assessment and guidance maneuver commands. Commands to the guidance system consisted of the limited set: up, down, left and right, and a restricted acceleration response. The information exchanged between the expert system and the platform required the implementation of an interface module. The module functionality includes:

- Performing a numerical–to–symbolic transformation of data to be sent to the expert system
- Performing a symbolic–to–numerical transformation of data received from the expert system
- Sending and receiving messages to and from the expert system via the host computer serial ports.

The above operations are identified as the mission manager and the resource manager in Figure 5. The sensor monitor operation is the exchange of data between the sensor system and resulting expert system based commands to the platform guidance system via the interface.

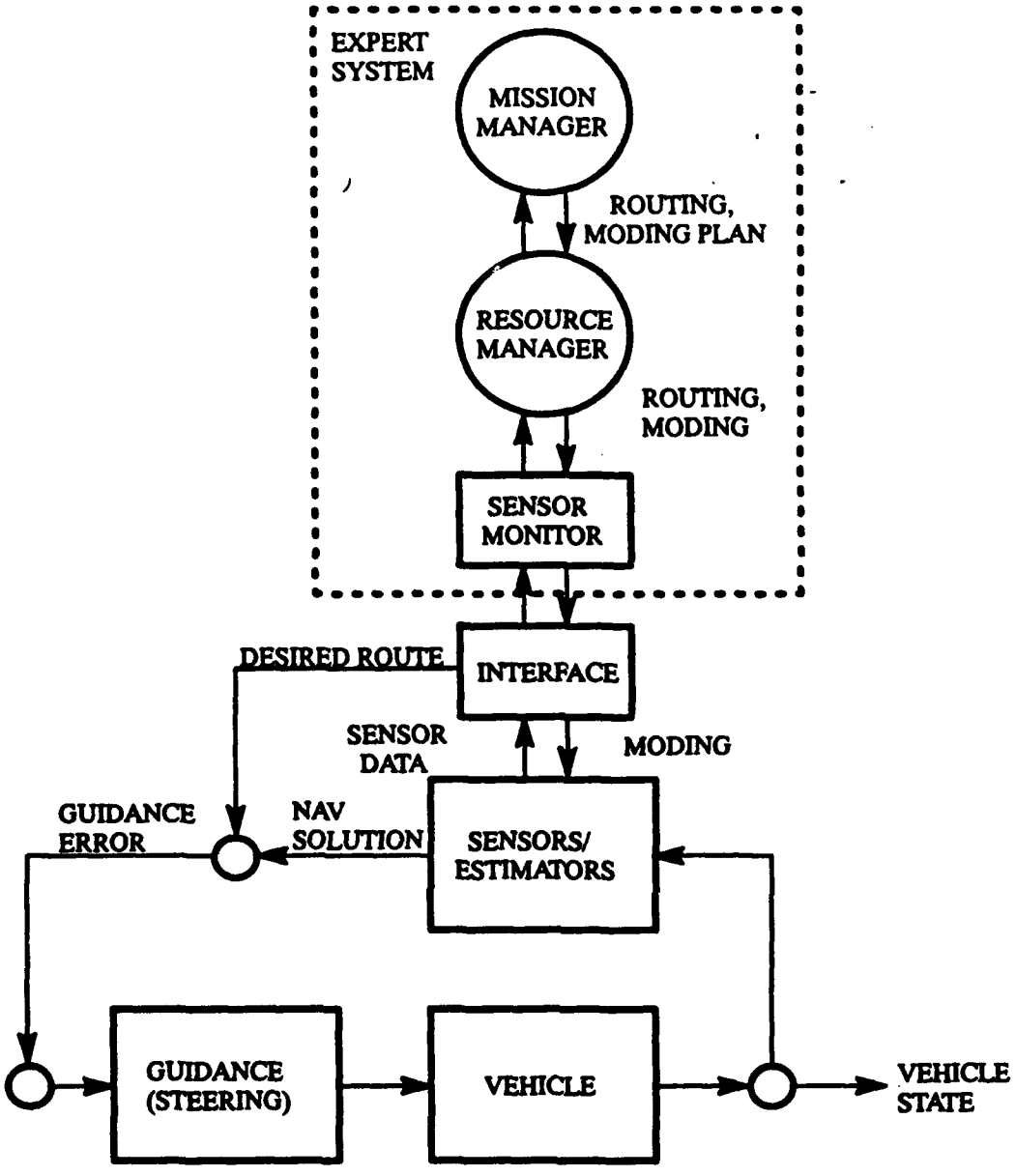


Figure 5. Expert System Integration with Autonomous Platform.

## SYSTEM SIMULATION

### SIMULATION MODEL IMPLEMENTATION ISSUES

The MAAP simulation operation consists of a numeric processing element and a symbolic processing element. Interaction and data transfer between these elements requires a special interface protocol be available for numeric–to–symbolic and symbolic–to–numeric conversion as described in the previous section. The numeric processing operation includes the environment, i.e., GPS satellites, threats, terrain models and the platform modules, excluding the reasoning system. The reasoning module is executed in the symbolic computation environment. The host computer configuration and the problem partitioning were selected to approximate actual real–world configuration for either hardware–in–the–loop operation or real–time laboratory testing. This configuration was of particular significance to investigate the operation of the reasoning

module on a portable processor,i.e., as a minimum, a 80286 based system supporting a C compiler.

## SIMULATION OPERATING ENVIRONMENT

The MAAP simulation was designed to operate on two parallel PC based processors. The numeric based algorithms are written in FORTRAN and operate on a 80386–based PC. The symbolic processing is a CLIPS (C Language Integrated Production System)[5] based operating system and executes on a 80286 PC environment. Embedded software is used to handle the asynchronous serial data communications and rule–based threat avoidance maneuver commands. The basic AAP as part of the MAAP simulation architecture is shown in Figure 6.

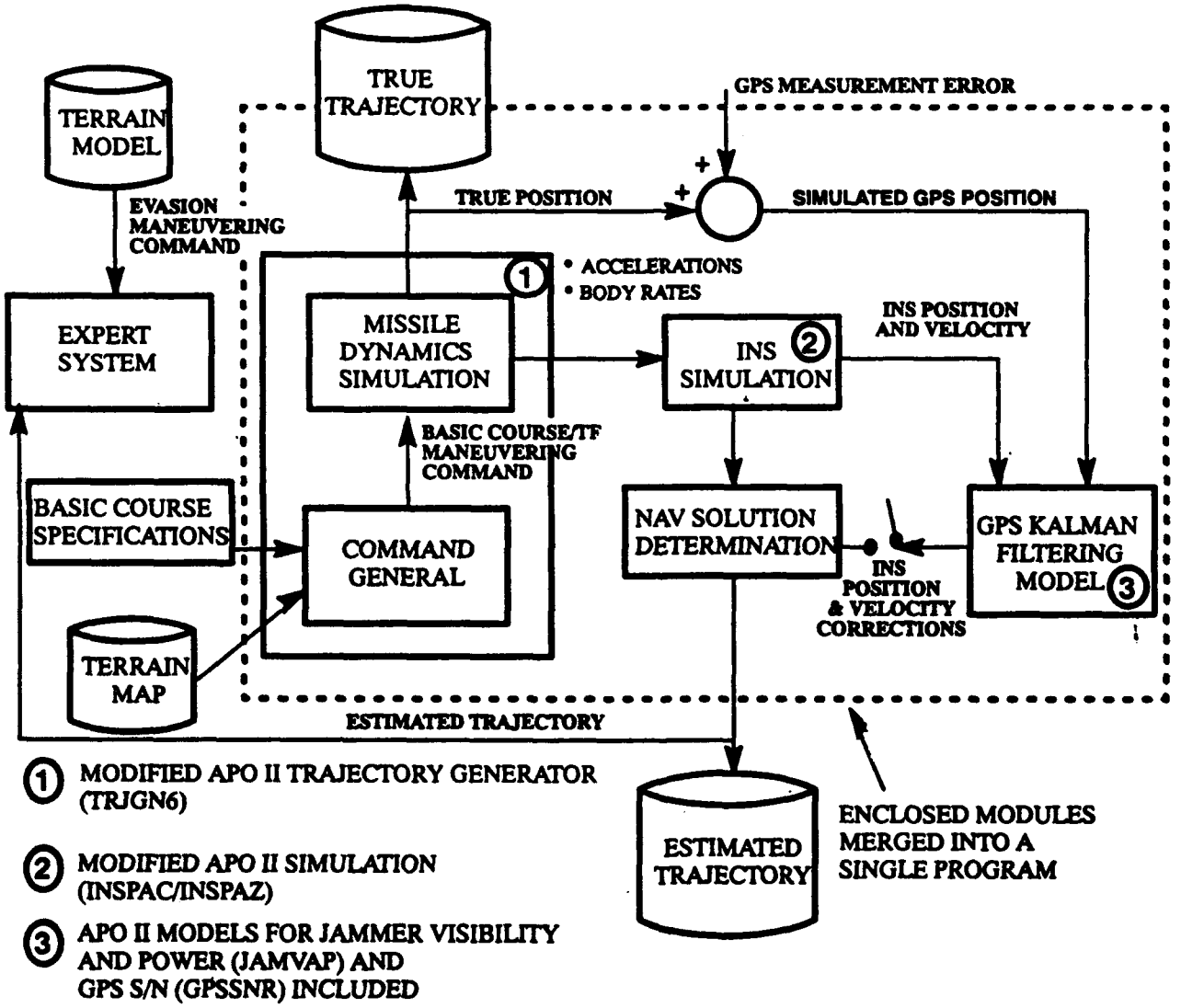


Figure 6. AAP Simulation Architecture.

[5] CLIPS is a C based expert system shell developed by NASA/Johnson Space Center's Artificial Intelligence Section.

## RESULTS

As stated previously, one objective of the MAAP program effort is to develop method and techniques to enhance the survivability rate of AAP operation in a high density battlefield threat. For purposes of demonstrating the the prototype operation of the MAAP, a simplified threat scenario was selected. Figures 7, 8, and 9 are snap shots (screen dumps) recorded at selected instance during a platform trajectory with MAAP operation against a specified threat scenario.

As indicated in Figure 7, the threat environment consist of two SAM sites and two jammer sites. The SAM sites are indicated with missile symbols at the center of two range rings. The outer ring of each site is the target detection/track boundary and the inner ring is the engagement boundary of the respective SAM site. The jammers are indicated as radiators with different beam widths. The jammer located in the lower part of the scenario, with a wide beam, is placed at ground level, the second jammer is located 500 meters above ground level. The platform has no knowledge about the location of the threats prior to initiating the mission. The threat scenario is shown as imposed on a terrain map. The beginning of the platform trajectory and the target objective are indicated by two crosses.

Figure 7 depicts the platform 103 seconds into the mission at an altitude slightly less than 1800 meters. The position of the platform is such that it is being illuminated by the ground based jammer and tracked by a SAM radar. While the ground based jammer is a minimal threat to jamming the GPS antenna, which is located on top of the platform, it is considered to be a higher threat than the SAM tracking radar. Threat avoidance maneuvers are executed to avoid the jammer beam.

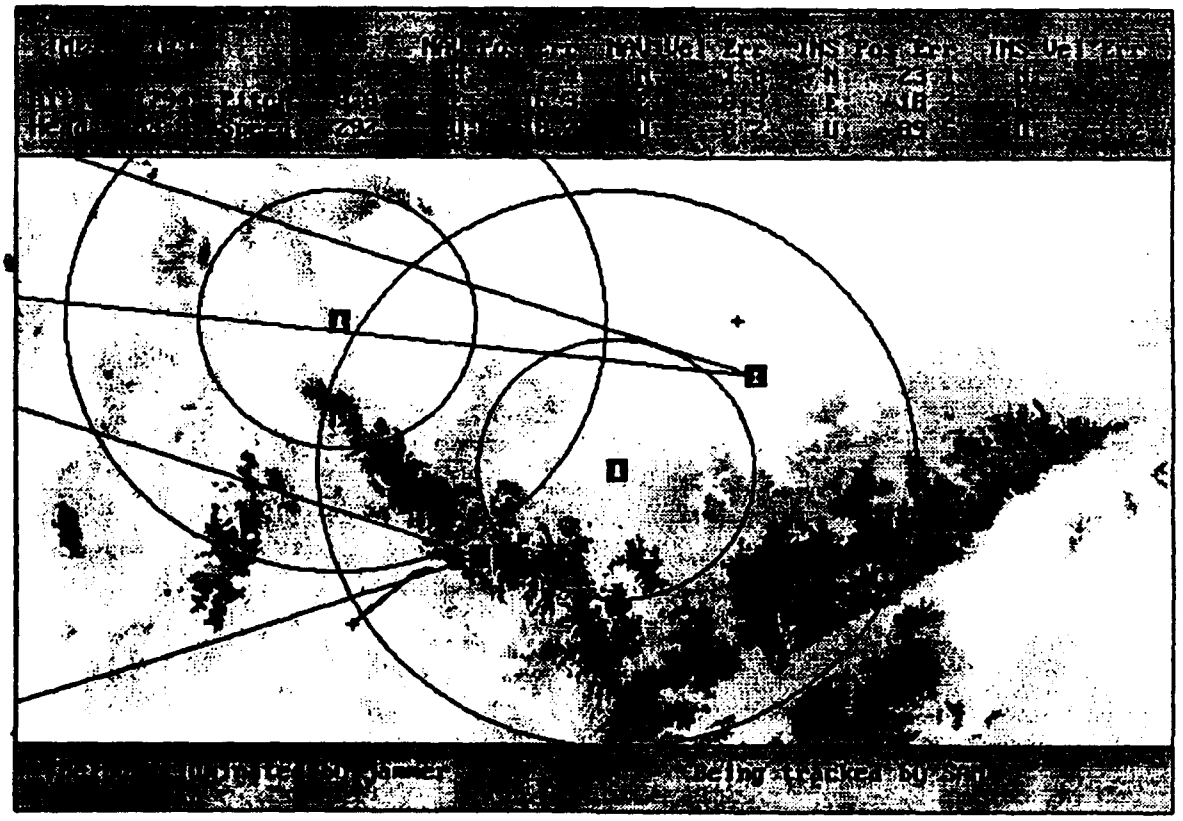

**Figure 7. Threat Scenerio Showing Platform Being Illuminated by Jammer and Tracked by SAM.**

As indicated in Figure 8, the platform is 230 seconds into the mission and with a status of clear at 273 meters for terrain following. The platform, while avoiding the jammer, has crossed the engagement boundary of the SAM system. A missile has been launched and the platform has initiated a maneuver to go into the terrain following mode. If the SAM site engagement radar is interrupted for three seconds or more, the missile launch exercise will be a failure. Threat avoidance commands maneuver the platform into a terrain following mode to provide terrain masking between the SAM site and the platform. An operational feature of the reasoning module is that once a threat has been detected, the approximate direction and estimated power levels are remembered for determining future avoidance maneuvers. With knowledge about the threat as depicted in Figure 8, the trajectory continues toward the mission objective in the terrain following mode.

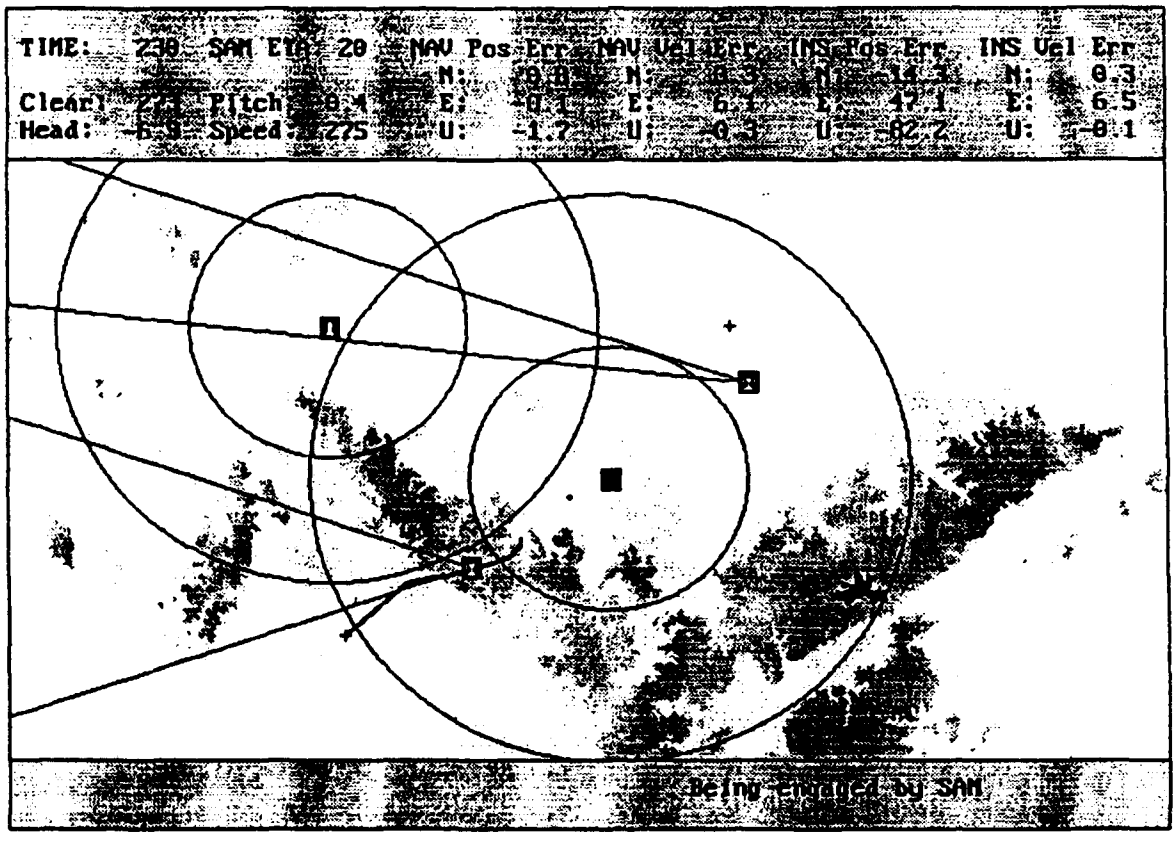


Figure 8. Platform Avoids Ground Based Jammer and is Engaged by SAM.

The platform trajectory extending through the SAM engagement range is shown in Figure 9. As the platform approaches the engagement boundary in the terrain following mode, the jammer beam located at 500 meters altitude is encountered. Since the jammer is above the platform, a high priority threat is present in terms of being able to jam the GPS antenna. The immediate command sent to the platform from the reasoning module is maneuvers command attempting to shield the antenna from the jammer with the body of the platform and climb to an altitude above the jammer. This operation is shown in Figure 9 with a final time of 567 seconds to engage the mission target at an altitude of 206 meters after descending from a higher altitude after avoiding the last jammer.

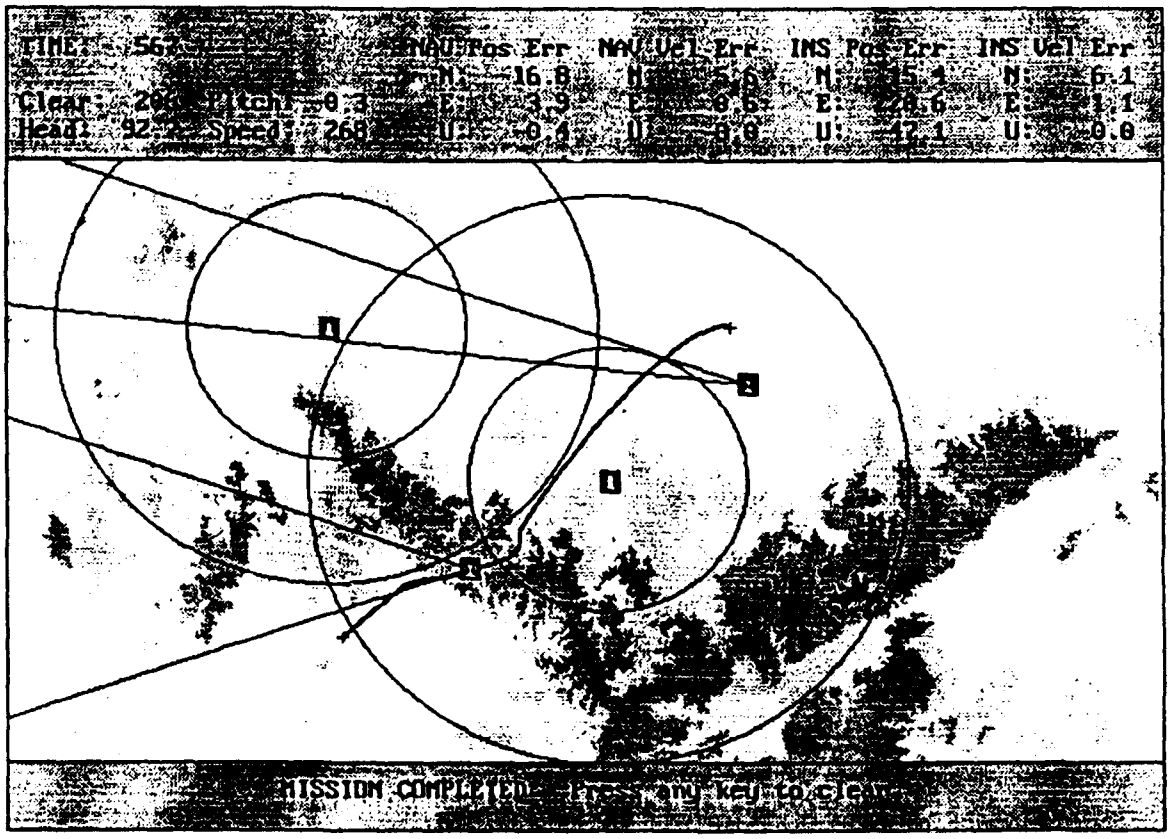


Figure 9. Platform Avoids High Altitude Jammer and Engages Target.

## CONCLUSION

The presentation is a very brief description of the major components and operation of the MAAP. This program is part of ongoing investigative efforts to identify techniques that can improve weapon system performance in a battlefield environment. Initial results provided by this effort clearly indicated that applying an emerging technology to traditional problem areas requires an examination of the traditional task and the new technology with a new set of questions. While the MAAP program described here is an early prototype, it does demonstrate the application of the emerging technology of Artificial Intelligence and related knowledge based system concepts can be cost effective when applied to traditional problem areas, i.e., air defense and more specifically operational survivability in a battlefield environment.

The question could be asked "Why the discussion about the items not directly related to the knowledge based system development and operation"? The use of knowledge based expert systems have proven to be very cost effective in certain areas of applications, particularly in areas such as an expert advisor, banking systems operations, reasoning over large data bases, etc. In most of these application the availability of additional information for the knowledge base was available to the expert system by interacting with the environment with mostly human inputs. Operating in domains where direct input is not feasible, alternatives must be considered. For the typical airborne autonomous system operation the cost effective use of a knowledge based system is difficult to establish with out demonstrating an extensive advantage.

The question was asked "What can be added to the autonomous system such that the advantages of expert system technology can be realized?" One answer – GPS. The GPS receivers

were added to the platform to provide additional information to achieve effective knowledge based system operation, i.e., improved threat avoidance. The answer to the initial question "Why the discussion...", the major factor is to give an emphasis on the need to review traditional problem areas with a new perspective in order to achieve new solutions.

# TARGET AND SCENARIO SIGNAL GENERATION FOR MICROWAVE AND MILLIMETER WAVE HWIL MISSILE GUIDANCE SIMULATION

Alexander C. Jolly
U.S. Army Missile Command
Redstone Arsenal, AL 35898-5252

## ABSTRACT

Evaluation of tactical missile guidance mechanisms and hardware components by means of hardware-in-the-loop (HWIL) simulation is extensively used by the U.S. Army Missile Command for the purposes of system development, integration and checkout and for detailed performance assessment. Experience has shown that HWIL simulation is a powerful tool which can be used to minimize the amount of flight testing required throughout the missile system total life cycle, from technology development through to field upgrades and product improvements.

In order to perform the realistic HWIL simulations that are needed to support missile system development and deployment it is necessary to provide realistic target and background scenarios which are received by the guidance sensor(s), including field-of-view dynamics and the effects of countermeasures and weather conditions. The required degree of target and background realism is governed by the sophistication and performance capability of the sensor(s). This paper provides an overview of the mechanisms and techniques used at the Research, Development and Engineering Center of the U.S. Army Missile Command to provide target and background scenarios for HWIL simulation of missiles guided by microwave and millimeter wave radar signals.

## INTRODUCTION

The Research, Development and Engineering Center (RD&EC) of the U.S Army Missile Command (MICOM) provides technical support to the Project Executive Officers and Project Managers charged with the development and fielding of tactical missile systems for deployment by the U.S Army. An essential element of this support is the evaluation of tactical missile hardware by means of hardware-in-the-loop (HWIL) simulations. The inclusion of missile hardware components, sub-systems and/or systems in a simulation implies the necessity of operating the simulation in real-time and, if the hardware includes external environment sensors, then a means of providing a realistic real-time input to the sensors is also required.

In order to meet the requirements for HWIL simulation of closed guided loop target engagements by tactical missile systems for the U.S. Army, MICOM RD&EC performs HWIL simulation in a number of HWIL target scenario simulators at its Advanced Simulation Center located at Redstone Arsenal, Alabama. These

simulators contain extensive real-time computer processing capability and are interfaced to the appropriate missile hardware via purpose-built interfaces. This paper reviews the target and scenario signature modeling and signal generation capabilities for the microwave and millimeter wave radar guidance simulation facilities (respectively known as the Radio Frequency Simulation System - RFSS, and the Millimeter Simulation system - MSS) and indicates planned developments for the future.

## SIMULATOR CONFIGURATIONS

### Microwave

The simulation facility in which microwave radar guided missiles are evaluated consists of a radio frequency (RF) shielded, anechoic room of dimensions 48x48x40 feet (width, height, length). Microwave signals in the frequency range 2-18 GHz are radiated from a set of 550 horn antennas located on a vertical wall of the room and are received by a missile antenna projecting into the room through the opposite wall. The circular array of antennas subtends an angle of 42 degrees at the missile receiving antenna which is positioned at the intersection of the flight table axes of rotation. RF signal generation equipment permits waveforms of almost any desired degree of complexity to be generated under computer control and to be radiated from an appropriate triad of antennas such that the real-world signal directionality is dynamically maintained at the receiving element.

The RFSS signal generation capability includes four independent channels with full polarization capability and continuous position control across the array. In addition, there are two channels available for the simulation of stand-off jammers on a sparse array of 16 antennas interspersed among the elements of the main array. A block diagram of the RFSS is shown in figure 1.

### Millimeter Wave

The MICOM Millimeter wave Simulation System (MSS) parallels the microwave simulation facility in that modulated signals representing radar returns from a target and clutter scenario are radiated into a shielded, anechoic room for receipt by the missile receiving antenna, followed by processing into guidance commands by the missile receiver and signal processor. Guidance commands are fed into a simulation of missile flight dynamics which provides missile-target relative motion for use in generating the target and scenario signals. This facility operates in frequency bands centered on 35 and 94 GHz.

At the present time, two independent channels are available for representation of targets and background signals. A third

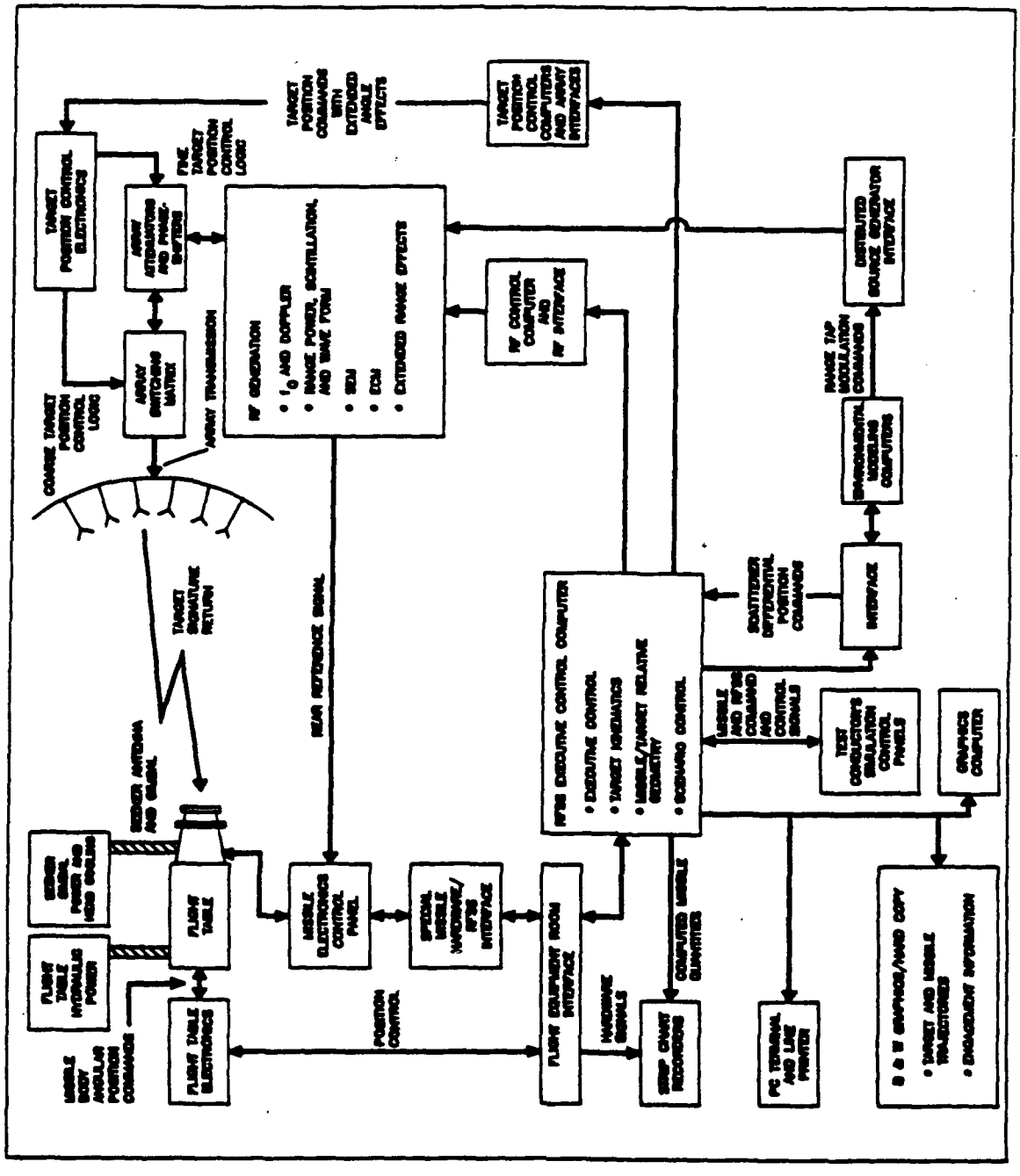


FIGURE 1. SEMIACTIVE MISSILE SIMULATION CONFIGURATION

channel is being added to expand the signal generation capability. The array of radiating antennas is of hexagonal shape flanked by a horizontal line of antennas extending on each side of the central hexagon. At 35 Ghz, the angular extent of the antenna array is 7.4 degrees maximum, and at 94 GHz it is 5.6 degrees. Obviously, for typical missile engagement trajectories these line of sight angular dynamic ranges are limited and synthetic line-of-sight angle control are necessary. A block diagram of the signal generation chain, from the missile transmitter to the radiated modulated target and background returns is shown in figure 2.

## GUIDANCE SENSOR CHARACTERISTICS

Target and background signature modeling requirements are heavily dependent on the characteristics of the missile guidance sensor for which the signatures are generated. Sensor parameters which govern the level of modeling detail include: resolution, dynamic range, angle measurement technique, field of view (antenna pattern and scan limits), coherence, frequency bandwidth, signal processing characteristics, update rates and synchronization methods.

Predominant use of the RFSS over its existence since 1975 has been to perform HWIL simulations of tactical missiles guided by semi-active or passive techniques. For these simulations, missile seeker antennas have been linearly or circularly polarized; angle tracking of targets has been based on monopulse direction finding; CW guided missiles have used Doppler signal processing. Consequently, target and background signature modeling for RFSS applications has required the realistic representation of signature frequency, signal power (i.e., amplitude) and Doppler frequency content. The single application of the RFSS to open loop tests of a coherent active RF seeker required the development of accurate range delay representation and phase control of the re-radiated signal.

In the MSS, HWIL simulations have been performed exclusively for active millimeter wave guidance units in which signal processing discriminants were: signal power, frequency, phase (coherence), time and signal polarization. Because of the larger number of signal discriminants and the consequent greater sophistication of receiver signal processing, millimeter wave target and background signatures modeling and signal generation is more demanding than that for the microwave regime.

## TARGET AND BACKGROUND SIGNATURE MODELING

### RFSS (Microwave)

For semi-active CW doppler processing seekers, target signatures are defined by their Radar Cross Section (RCS),

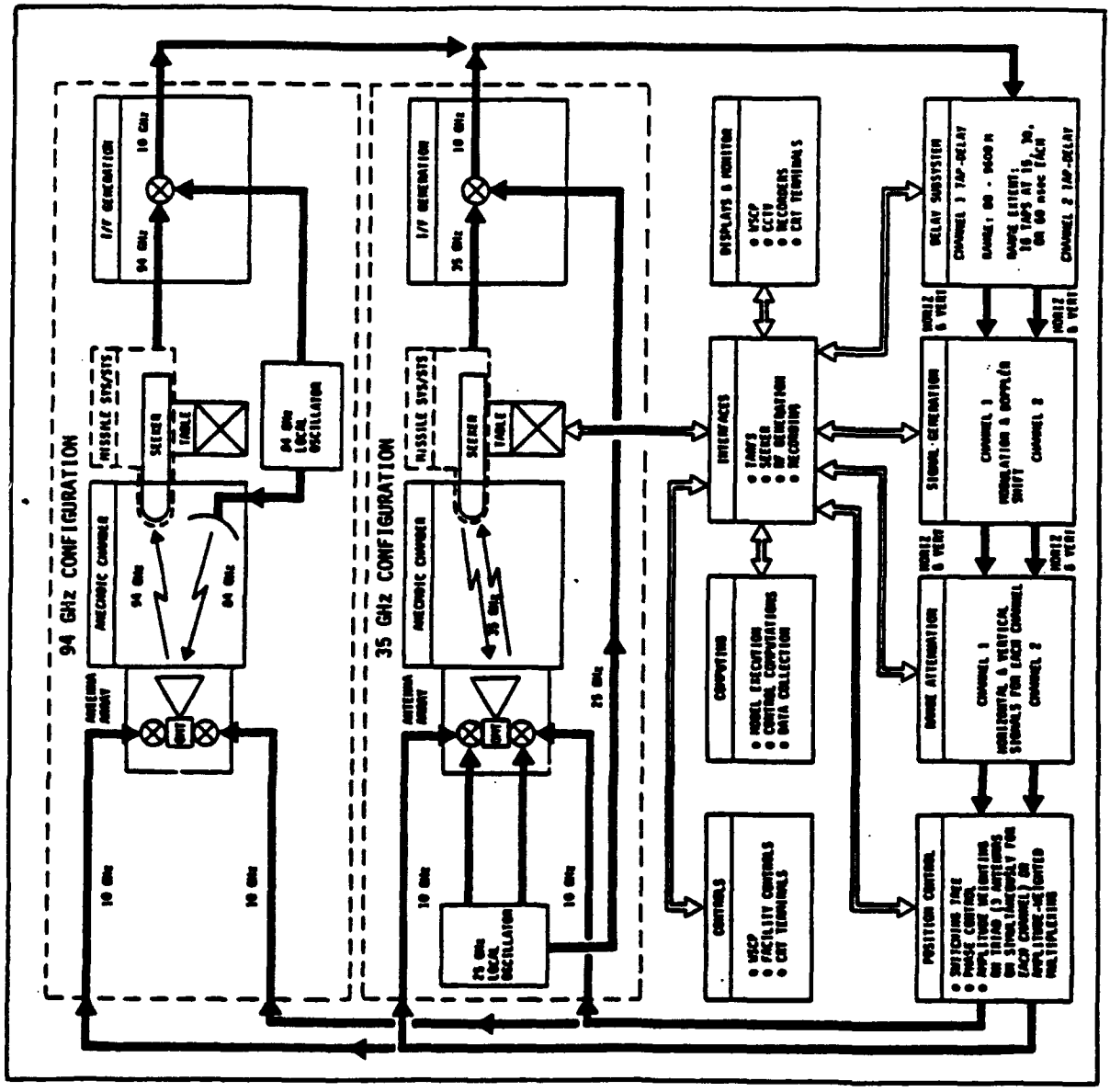


FIGURE 2. MSS SIGNAL GENERATION CONFIGURATION

doppler frequency shift and angle glint (the latter representing the short term angular variation of reflection centroid about a mean position). For passive RF seekers, doppler frequency shift is not necessary unless the receiver is extremely narrow-band; for active coherent seekers, signal phase and time delays are required to be represented. A summary of early developments of target signature modeling for the RFSS is given by Baird, et al (1981).

In the development of models for specific HWIL simulations it is necessary to decide at the outset whether the models are to be deterministic or statistically based. Historically, initial approaches to characterizing RCS have been statistical, as presented by Swerling (1960). Modern developments in radar design and signal processing have led to the need for target signatures to be represented as a set of range and angle extended discrete scatterers with the reflections obtained by coherent summation of scattered signals in each of the seeker monopulse channels.

Over the course of the last several years, an hierarchical sequence of target signature models has been developed for HWIL simulation in the RFSS of microwave guided missiles (that is, for the frequency range 2-18 GHz). This sequence has progressed from an isotropic point source target at a single frequency with range dependent amplitude, through statistically varying RCS and angle glint models to the range extended distributed scattering source models mentioned above.

Statistical Target Models Statistical target models offer the advantages of simplicity and speed of execution, the latter being an important consideration for real-time simulation. Selection and development of the model, however, must be made with care and good judgement, taking into consideration the signal processing characteristics of the seeker used in the simulation. In general, monopulse target signal statistics are obtained in non-real-time from a baseline model selected from available analytical models or from measurement data. Parameters representing the probability distributions, means, variances and covariances of RCS scintillation and angle glint are obtained from extensive analysis of available data. Attention must be given to joint probability distributions since although target RCS and angle glint are uncorrelated, they are not independent (Sandhu and Saylor, 1985). Figure 3 contains an illustration of the modeling process.

Models of air-breathing targets used in the RFSS during the past several years have ranged from simple Swerling scintillation and Gaussian glint versions with no interdependence between the two distributions to complex monopulse models incorporating statistical dependence among the I and Q components, leading to the faithful reproduction of the true joint probability distributions between scintillation and glint.

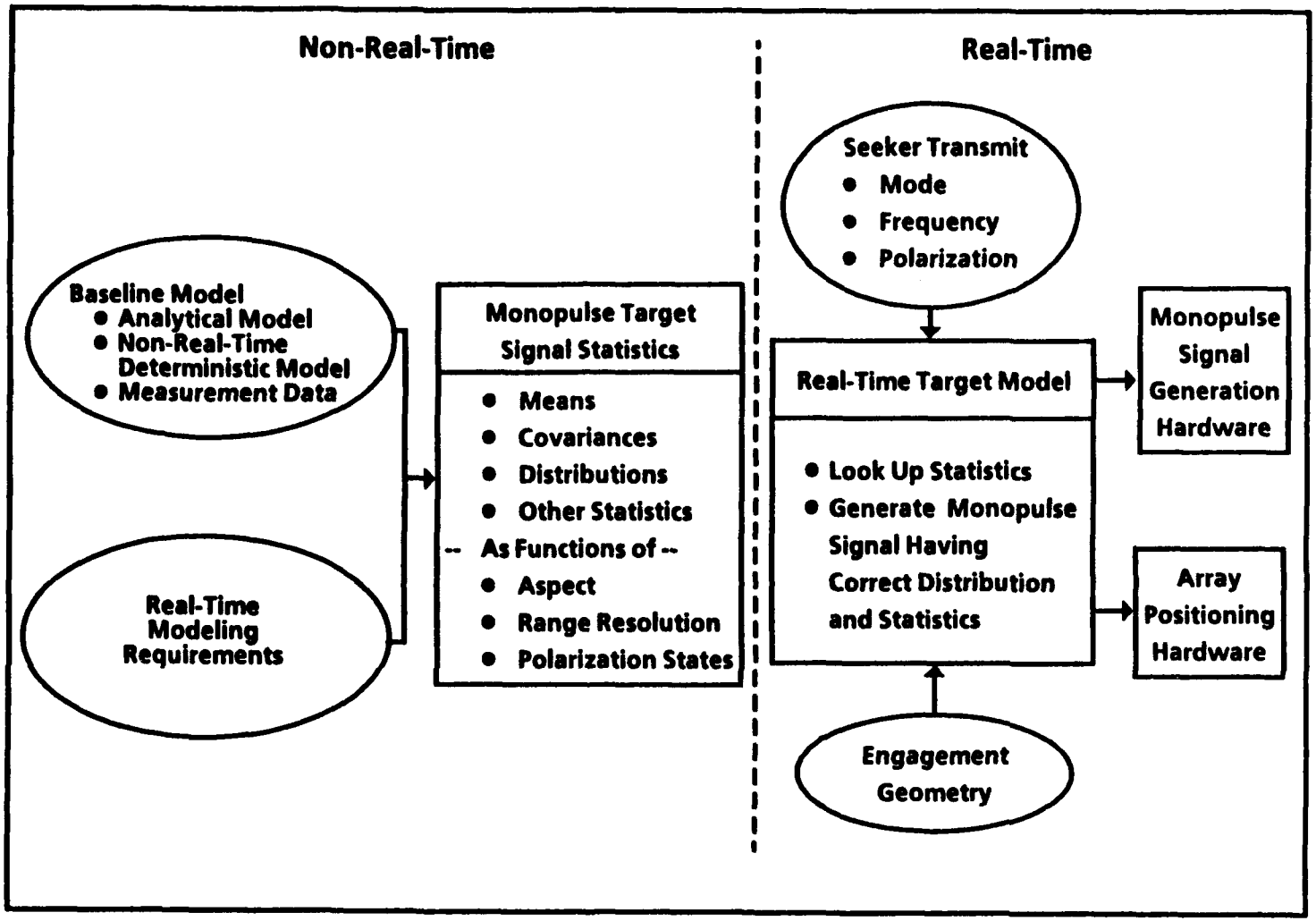


FIGURE 3. STATISTICAL TARGET MODELING: GENERAL APPROACH

Figures 4 and 5 illustrate comparisons of results achieved for measurements and models for a particular example of the latter type of model.

Deterministic Target Models Deterministic target models are represented by aspect-dependent, polarimetric scatterer lists containing relative amplitude and geometric position. During real-time simulation, missile-target relative geometry is used to compute target aspect at any instant; appropriate scatterer lists are obtained from look-up tables and transformed to line-of-sight coordinates. Seeker transmit frequency and polarization are used to compute a monopulse signal for each scatterer. Coherent summation of these signals results in a monopulse target signature (amplitude, phase, azimuth and elevation for each polarization) for transmission to the seeker from the RFSS antenna array. The response of a coherent monopulse seeker to a distributed scatterer target model has been analyzed by McPherson (1986).

While the real-time model is relatively simple to implement, the non-real-time derivation of scatterer lists is more difficult. One method of deriving scatterer lists is by making laser scans of a physical geometric model of the target and measuring reflections in various directions, although this is a costly and time consuming process. Other sources of radar signature data are the specialized facilities such as those provide by the U.S. Air Force at RATSCAT or the U.S. Navy at PMTC. A diagrammatic representation of the modeling process is contained in figure 6.

Jet Engine Modulation Jet engine modulation (JEM) and the related modulation phenomena of helicopter blades and propellers are all members of the "reciprocating machinery" class of radar scattering problems wherein one or more primary scatterers undergo a deterministic, oscillatory amplitude variation. This results in a strongly defined spectral structure which affects missile guidance performance, especially in an ECM environment. JEM and blade modulation simulation is based upon modeling the correct frequency domain signature of the modulation and converting to the time domain by means of Fourier transformation.

JEM spectral structure (Gardner, 1970) is characterized by lines whose amplitude and spacing are determined by the number, size and rotational speed of blades on the engine compressor and turbine. Amplitude dependence with aspect angle is an exponential function of the cosine of the off-axis aspect. Amplitude fluctuations of the individual JEM lines is log-normally distributed and generally uncorrelated with fluctuations of other lines. Non-real-time modulation parameters are obtained by detailed analysis of measured data or from engine parameters; real-time models generate aspect dependence and statistical fluctuation of the power spectrum envelope.

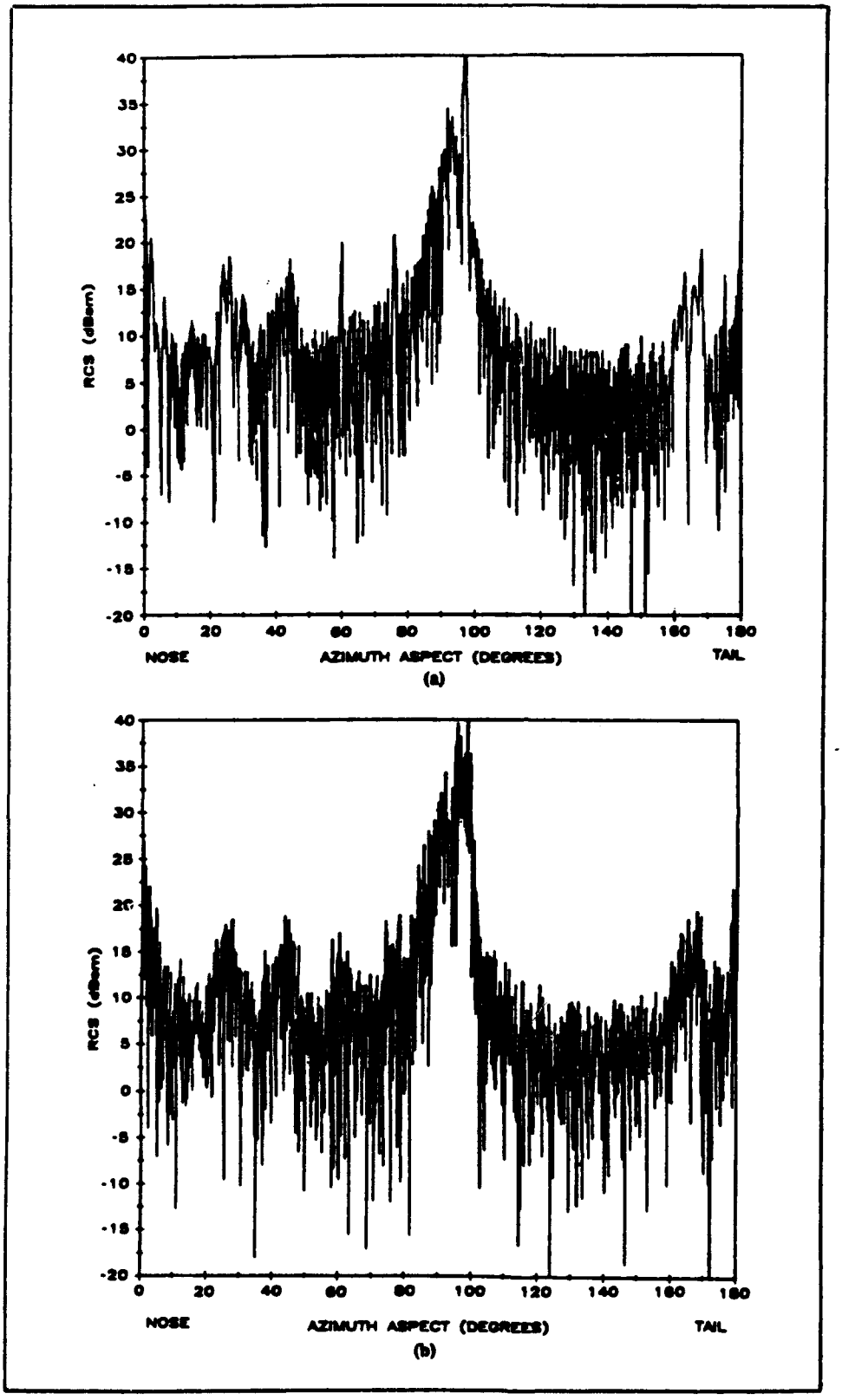


**FIGURE 4. STATISTICAL MODEL TARGET RCS COMPARISON WITH MEASURED DATA**

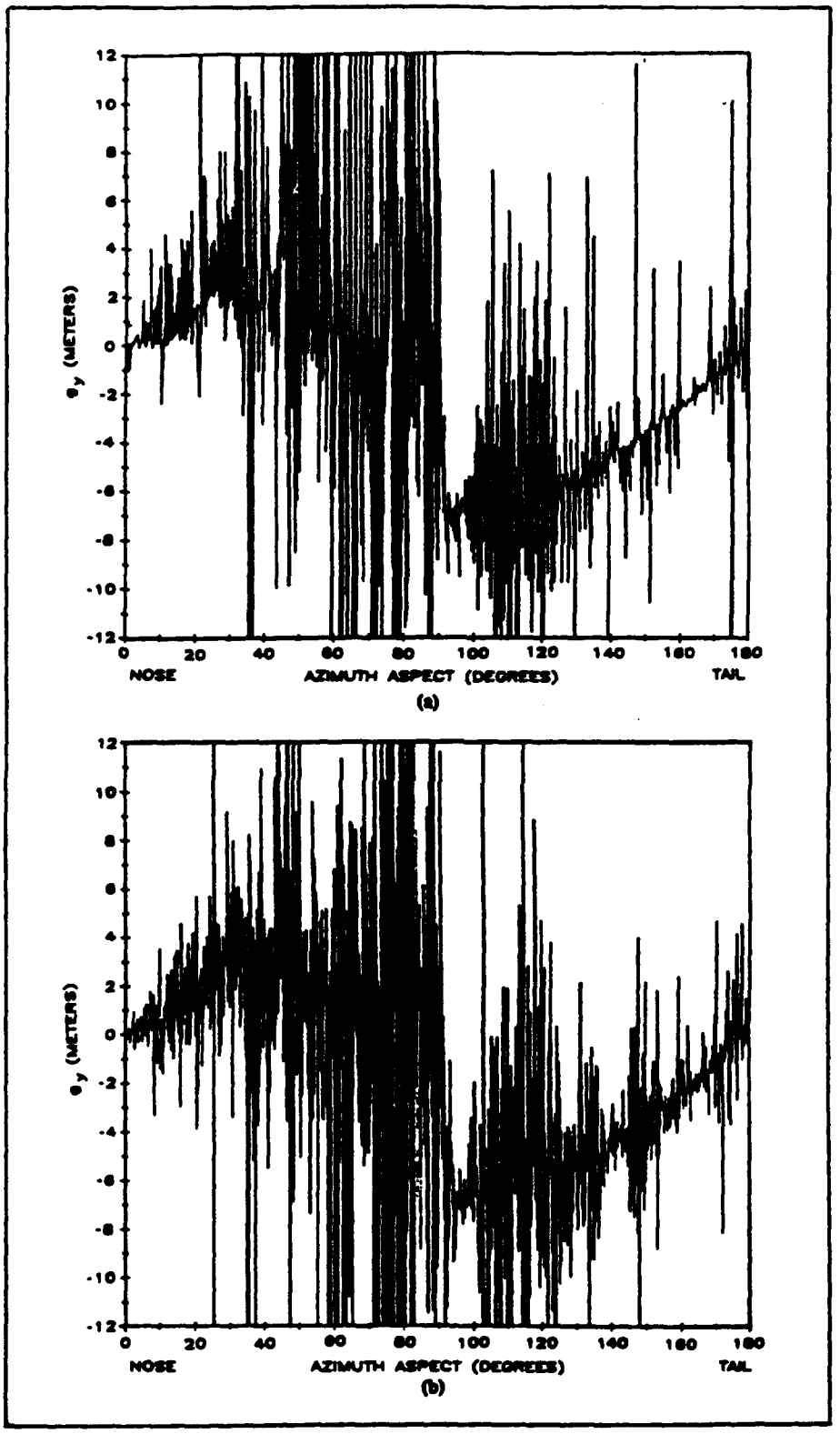


FIGURE 5. STATISTICAL MODEL TARGET GLINT COMPARISON WITH MEASURED DATA

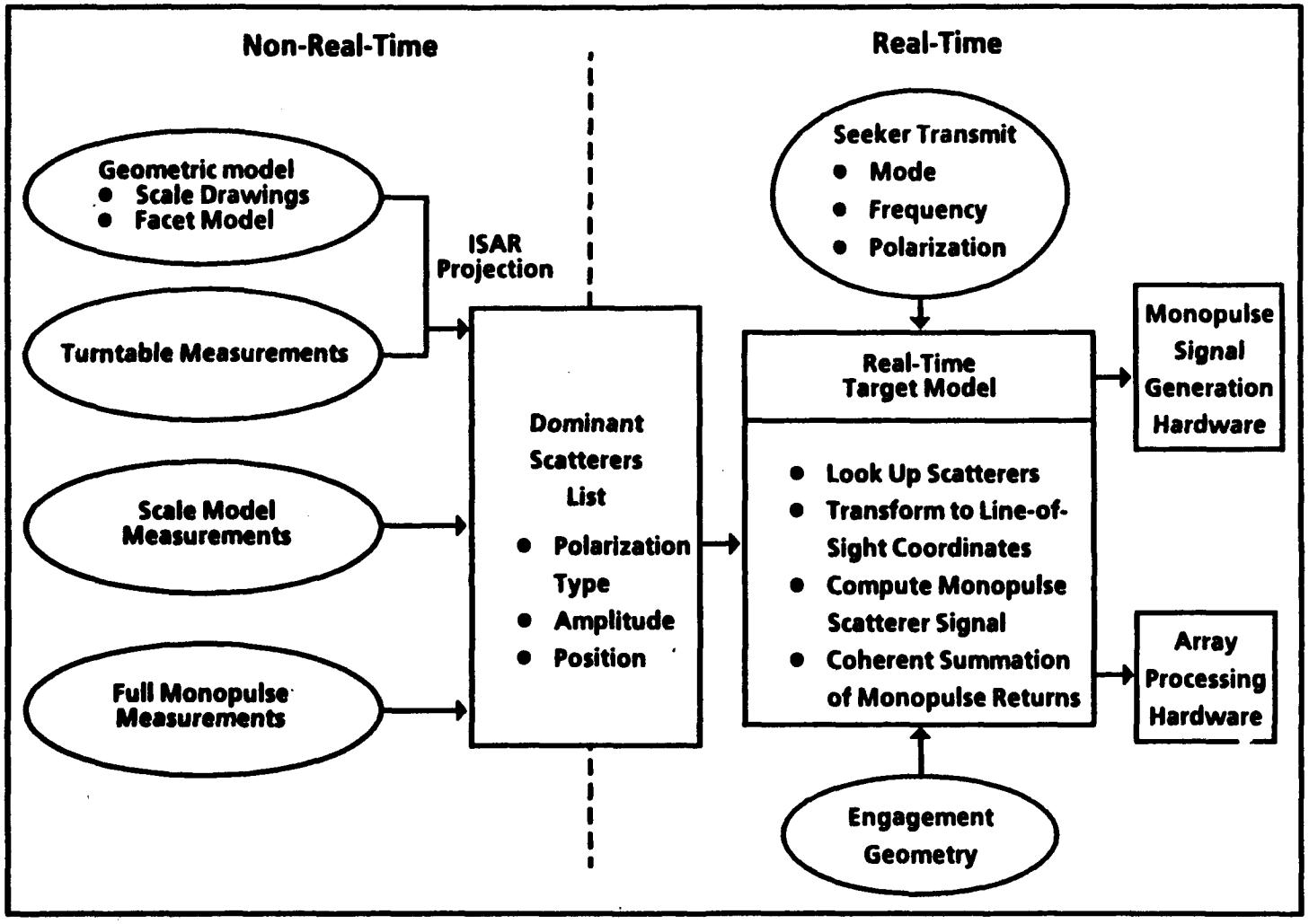


FIGURE 6. DETERMINISTIC TARGET MODELING

Ground Return Models Ground return modeling requires data representing: transmit and receive antenna characteristics, seeker signal processing details, terrain model, and electromagnetic scattering model. During real-time simulations, the ground return model incorporates scattering coefficients, antenna gain patterns and engagement geometry to compute model outputs such as: total reflected power, power spectrum, and direction of arrival. These outputs control the signal generation hardware to provide the ground return signals which are radiated or injected to the seeker.

Terrain model inputs may be deterministic or statistical in nature and represent terrain elevation and slope of the ground over which the simulated missile target engagement takes place. A source of these data is the Defense Mapping Agency. Other ground truth information such as type, extent, size and dimensions of ground cover, soil type and state, dielectric properties of ground cover are also necessary for an accurate estimate of backscatter coefficients. Analytical electromagnetic scattering models make use of the terrain model data, but are used in an off-line, non-real-time mode to generate tables of backscatter coefficients which are looked up in the real-time models.

Clutter modeling is a specific example of ground return and is modeled using the techniques described above, applied in a method known as "integration-along-isodops", that is, along curves of constant doppler shift as illustrated in figure 7. The process involves transformation of engagement geometry data (position and velocity) to inertial, velocity and transmitter and receiver boresight frames of reference and defining clutter patches along isodops which are sub-divided into range cells. A scattering coefficient table is indexed using clutter patch position transformed into the inertial reference frame. Antenna patterns in the direction of the clutter patch are determined and all the data are entered into the radar range equation to yield clutter patch reflected power. The power spectrum is completed by summing all clutter patches over range cell steps and then stepping along the doppler spectrum. The process is shown in block diagram form in figure 8. Clutter signal generation consists of generating a time domain clutter signal from the spectrum by means of inverse Fourier transformation, and modulating the transmitter carrier frequency with the clutter signal.

MSS (Millimeter Wave)

Modern active seekers operating in the millimeter wave spectrum perform far more extensive signal processing than the typical microwave guidance sensor. Millimeter wave seekers measure the amplitude and phase (or in-phase and quadrature components) of the monopulse sum, elevation delta and azimuth

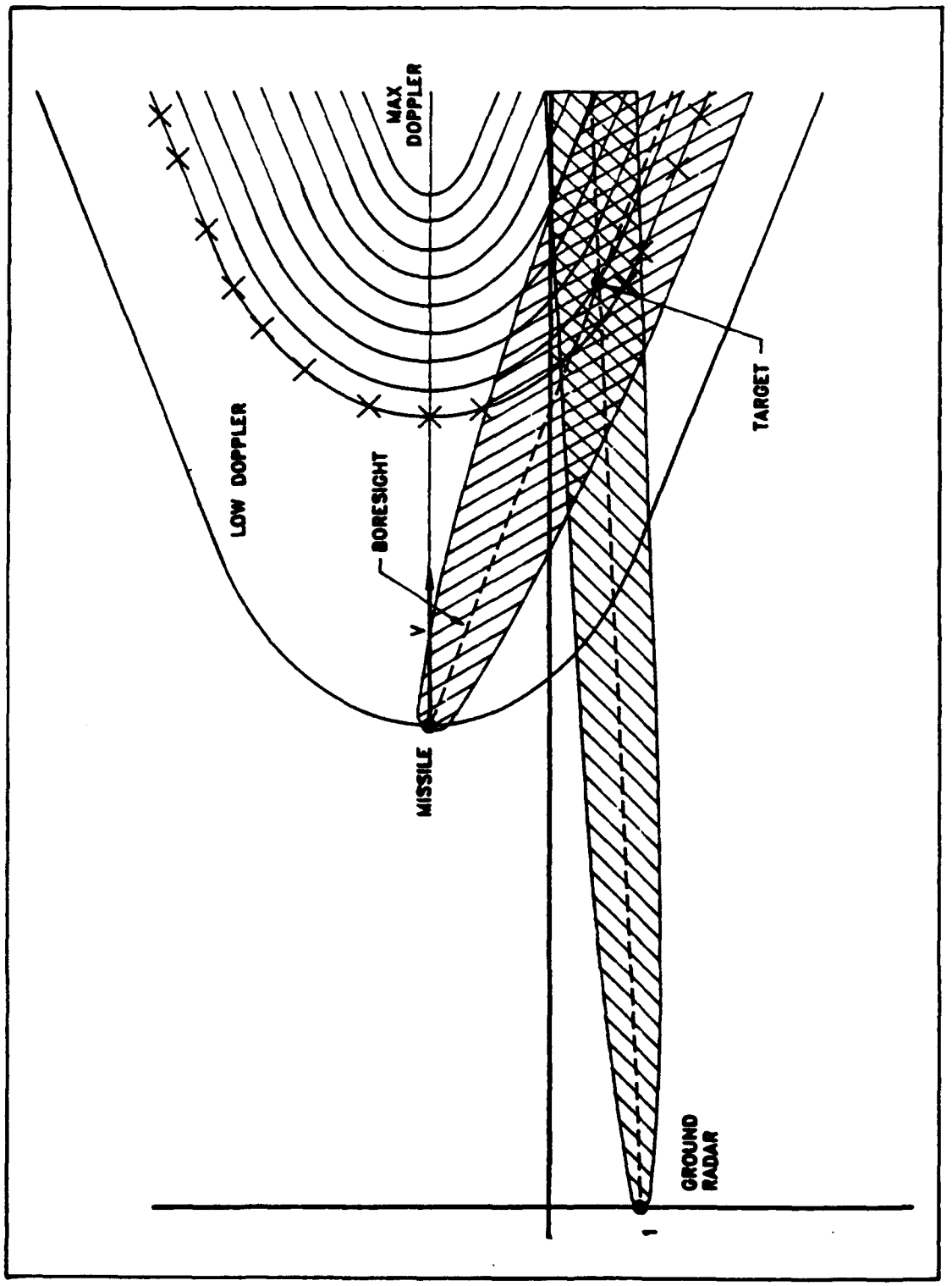


FIGURE 7. INTEGRATION ALONG ISODOPS BISTATIC CW CLUTTER MODEL - CONCEPT

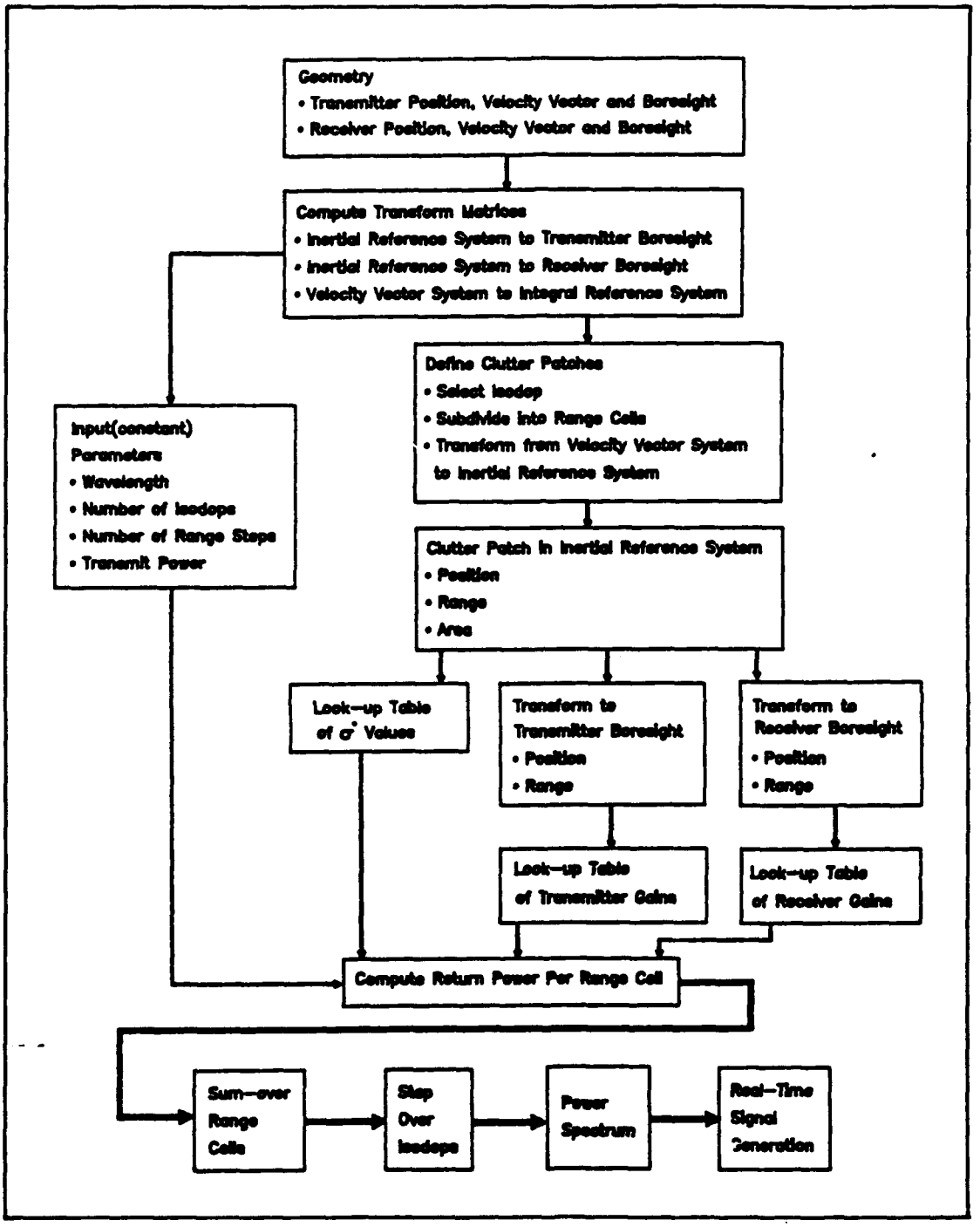


FIGURE 8. INTEGRATION ALONG ISODOPS CLUTTER MODEL

delta channel signals for the co- and cross-polarization components for each pulse transmitted. The measurements are made in each cell of a relatively coarse range gate for every pulse processed. A set of pulses using a "template" of discretely stepped or continuously scanned frequencies provides sets of data as functions of frequency and polarization in each coarse range cell which can be Fourier transformed to yield a fine-grained range profile corresponding to each coarse range cell. A map of the dominant scatterers in each fine range cell is then available for monopulse angle determination (ratio of delta/sum) and polarimetric processing for target discrimination and classification. Use of the three monopulse measurement channels permits the development of a three dimensional representation of the target and clutter returns.

Polarimetric processing is facilitated if the transmitted polarization is circular. In this case the return signals are independent of the missile antenna rotational attitude and return signals may be classified into even-bounce and odd-bounce scatterers (reflected polarizations changed by either an even or odd number of 180 degree units from the transmitted polarization). Measured signature effects with respect to reflected signal polarization may then be used as the basis of target and clutter classification algorithms.

Target Models Based on the brief discussion above of the typical requirements for millimeter wave signal processing, it is clear that simulation models for targets must contain realistic coherent range, angle, polarization and Doppler frequency shift information for all transmit frequencies and polarizations used by the seeker. It is sufficient to produce the correct amplitude and phase response in each of the three monopulse channels as the seeker changes transmitted frequency and polarization. For both clutter and targets, the signatures are deterministically dependent on the illumination and observation aspect relative to an earth-fixed or target-fixed coordinate system, respectively. Conceptually, the simplest model for a target is a deterministic discrete scatterer model in which the most significant scattering points on the target are identified over a window of aspect angles. Each scattering point is characterized by its location in target coordinates, its amplitude and its polarization characteristics (i.e. even- or odd-bounce for circular polarization or, more generally, a scatterer is characterized by its polarization scattering matrix). For each combination of transmitted frequency and polarization, the target scatterer returns are weighted by the transmit and receive antenna patterns and range gate function, and coherently summed, resulting in a total amplitude and phase for the co- and cross-polarized returns for the current transmitter state. A different coherent sum is computed for each possible transmitter state and for each monopulse receive channel. Simplifications normally employed in real-time models are a) the use of the far-field approximation,

b) equal sum channel pattern weighting for all target scatterers, c) a delta channel weighting which is proportional to the angle offset of the scatterer from a reference point on the target, d) equal range gate weighting for all target scatterers, e) equal range attenuation for all target scatterers, f) no change in aspect over a complete sequence of transmitter states. The input data for this multiscatterer model can be derived either from coherent measurement data or from a mathematical electromagnetic scattering model. Methods of reducing coherent sum channel data obtained by Inverse Synthetic Aperture Radar (ISAR) measurements of returns from a target rotating on a turntable, in combinination with geometric facet data, have been developed to produce the scatterer lists (Saylor, 1987). The output of such an analysis is shown in figure 9.

When the number of significant target scatterers is too large to permit real time computations, a statistical model can be employed to reduce the computational load and data storage. The statistical model consists of replacing all the scatterers in a fine range cell by a statistically equivalent scatterer. This scatterer is characterized by the statistics of the scattering amplitude within an aspect angle cell. The size of the angle cell is chosen small enough so that the scatterer statistics are stationary within the cell and independent from one range cell to another, and large enough so that the data storage available in the simulation computer is not exceeded. The statistical parameters chosen to describe the equivalent scatterers are the mean and variance of the in-phase and quadrature (I&Q) components of the complex scattering amplitude. By the central limit theorem of statistics, the I&Q components are expected to be gaussian distributed and are thus completely described by their means and variances. More details of the method are given by Saylor, McPherson and Henry, 1988.

Individual statistical range profiles are developed for the monopulse sum and delta channels. The statistical scattering amplitudes in corresponding range cells in each monopulse channel are related by correlation coefficients. That is, the scattering amplitudes for the monopulse channels (for a given fine range cell) are jointly gaussian. The means and variances characterize the marginal densities for each channel. In the simulation, independent gaussian variables can be generated and transformed to achieve the desired covariance. Maintaining the proper correlation among the monopulse channels is essential for seekers which compute multidimensional scatterer maps for tracking. Failure to achieve the correct correlations will generally result in forcing the seeker to track the amplitude centroid of the target rather than the geometric centroid.

Ground Return Models The number of clutter scatterers present in the seeker's beam is generally too large to permit a real-time deterministic model to be used. Thus, a statistical

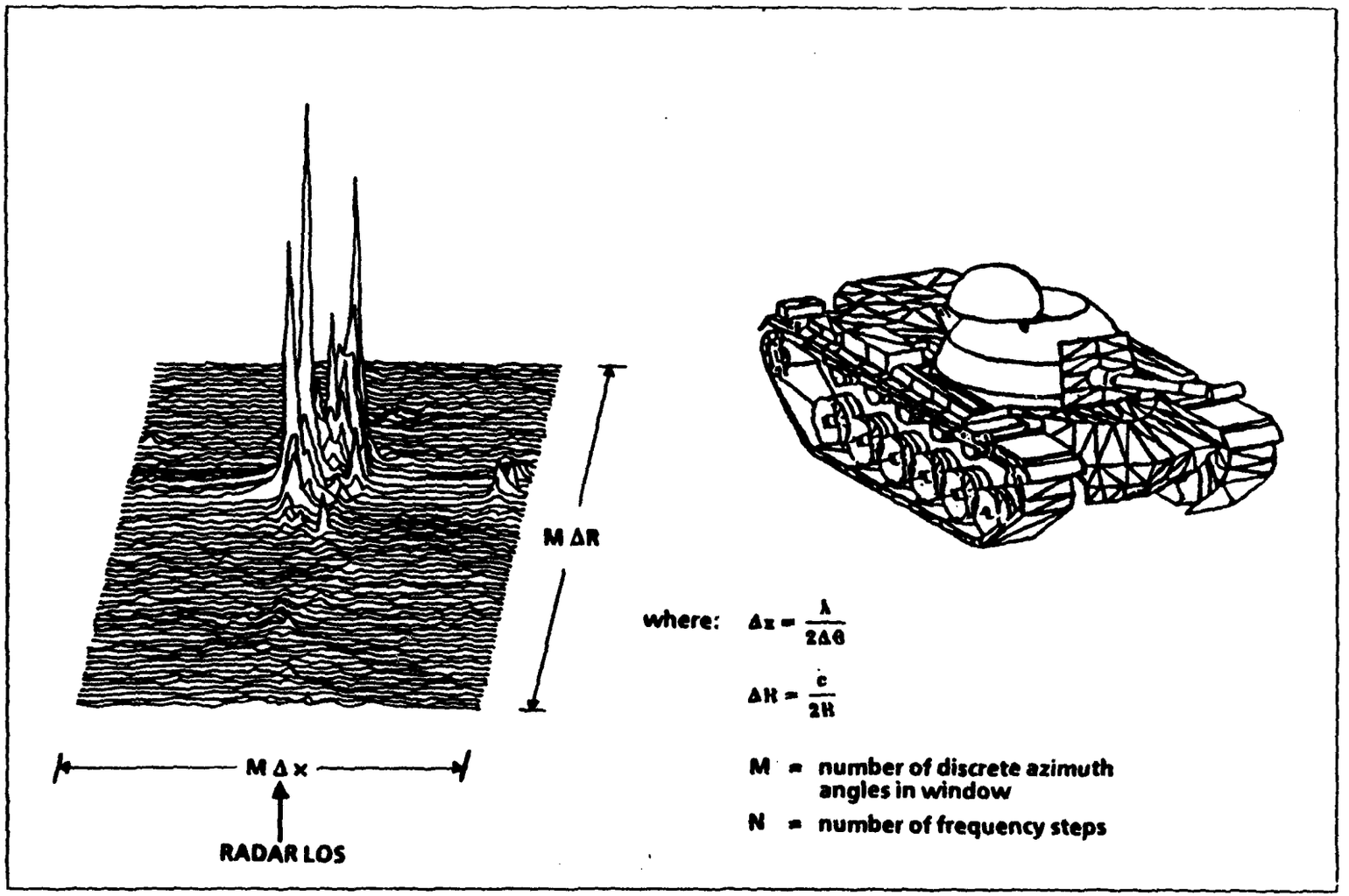


FIGURE 9. ISAR/TARGET MEASUREMENTS AND REGISTRATION

range profile model is usually the best choice for modeling MMW clutter for high range resolution seekers. The statistics for the I&Q components are the same from fine range cell to fine range cell for uniform clutter. Clutter is usually assumed to be uniform within a coarse range cell but is allowed to vary (i.e. have different statistics) from one coarse range cell to another.

The frequency response for a statistical range profile model is generated by coherently summing the equivalent scatterer signals for each transmit frequency. Separate sums are performed for even and odd range profiles and for each monopulse channel. Under the usual conditions of equally spaced seeker transmit frequencies (or the simulation quantizes the continuous FM sweep into equally-spaced steps), and the number of frequency samples being an integral power of 2, the coherent sums may be generated by using the FFT. The input to the complex FFT routine is a random sample of the uniformly sampled range profile for the sum and two delta channels. The output is the amplitude and phase (or I&Q) modulation which the target (or clutter) applies to each transmit frequency as measured in each monopulse channel. Line-by-line ratios of the delta to sum sequences can be performed to generate the signal glints in azimuth and elevation as functions of transmit frequency. The use of the FFT optimizes the phasor sum computation time for real-time operation. The FFT sum, however, is not as general as the direct phasor summation of the equivalent scatterer amplitudes at each transmit frequency. For example, near-field effects are not included and changes in aspect due to angular rotation of the missile-target line of sight during a seeker transmit sequence do not occur. These effects would result in a slight smearing of the seeker's range profile measurements and a small degradation in detection performance.

## SIGNAL GENERATION

### RFSS

A primary objective of the seeker signal processor is to enhance the target-to-clutter ratio sufficiently to effectively eliminate the corrupting influence of clutter on missile guidance. A monopulse doppler processing seeker accomplishes this by filtering sum and delta channel interfering clutter doppler components displaced from the target doppler before forming the delta/sum ratio used for angle tracking. This process is shown in figure 10. A high fidelity simulation must therefore produce the correct dynamic target and clutter spectral distributions in the radar receiver sum and delta channels simultaneously. It is theoretically straightforward, although in practice a little more difficult, to generate the desired spectral response in the receiver sum channel.

The clutter sum and delta channel power spectra are

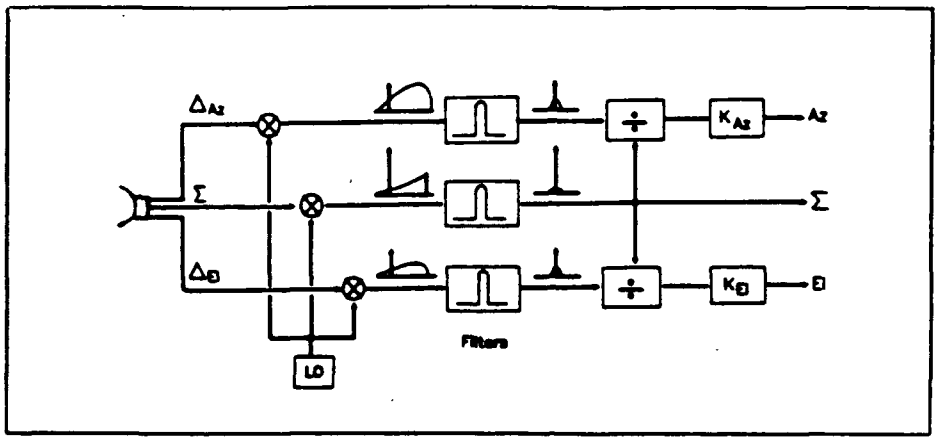


FIGURE 10. MONOPULSE ANGLE PROCESSING

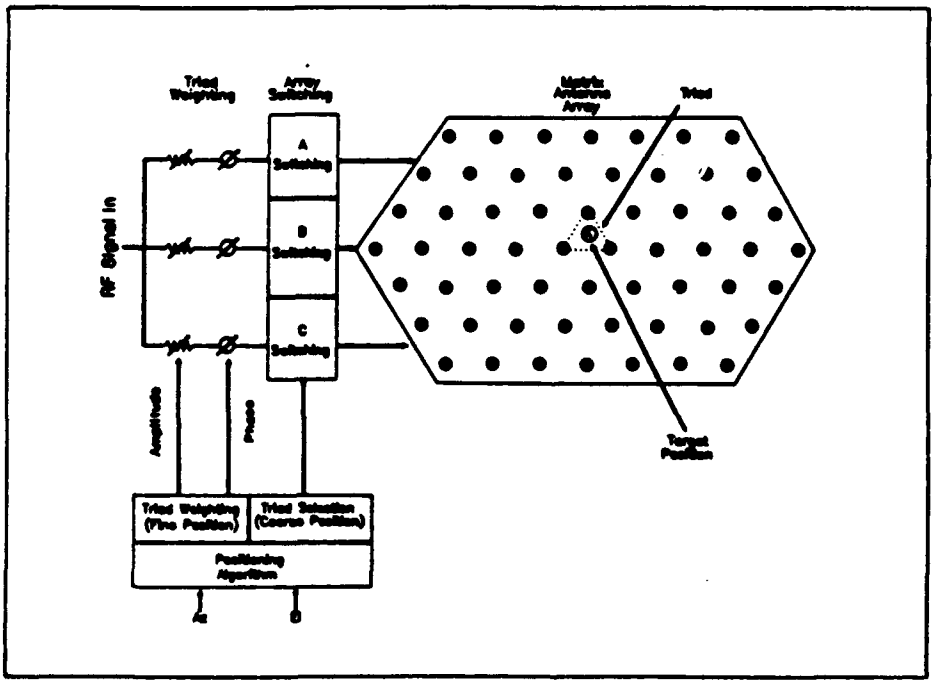


FIGURE 11. HWIL TARGET POSITIONING HARDWARE

constructed at each missile position update by the "integration along isodops" method described above. These discrete power spectra are converted to complex voltage spectra by applying random phase angles to each spectral line amplitude. Conversion to the time domain occurs via discrete Fourier transformation. The resulting complex modulation sequence is combined with the simulated target signature and the sum channel signal is transmitted from the RFSS antenna array position corresponding to the seeker antenna beam peak.

The target signature is computed either by forming the phasor sum of the discrete target scatterers or from the statistical model described above. Sum and delta channel components are weighted by the appropriate sum and delta antenna patterns in the direction of the target for that particular simulation time interval.

Signal radiation from the antenna array for both the RFSS and MSS is based the weighted triad method of signal positioning, as illustrated in figure 11. The algorithm for determining the amplitude weights is shown in figure 12. This algorithm is derived by computing the response of the three weighted triad signals in an ideal linear monopulse receiver, setting this response equal to the desired response and then solving for the required weight values. For a geometrical point-source target (no spatial extent), the resulting weights are real (i.e. not complex) and therefore amplitude weighting is sufficient (no phase weighting is required).

The amplitude weights for an isotropic point source target are implemented with attenuators as shown in Figure 11. The phase shifters are used only to ensure that all three triad signals are transmitted in-phase. When it is desired to simultaneously produce desired spectral and spatial distributions of target and clutter signals in all three monopulse channels of a seeker receiver, the additional degrees of freedom for such control is obtained by deriving phase shifter weighting values. This permits the combined target and clutter signals to be generated by a single RFSS or MSS signal generation channel.

A procedure using triad position modulation to create the desired monopulse signals is shown in figure 13. The first step is to scale the delta channel signals relative to the sum channel to obtain the proper conversion of delta channel voltage to angle relative to boresight. The next step is to convert the delta channel complex voltage sequences to complex angle sequences by doing a sample-by-sample normalization of the delta channel to the sum channel (this normalization is a sample-by-sample complex division process). The results will be to associate with each sum channel complex modulation sample, complex azimuth and elevation angles which are equal to the complex delta-to-sum ratio. The complex angles are used to generate a set of complex

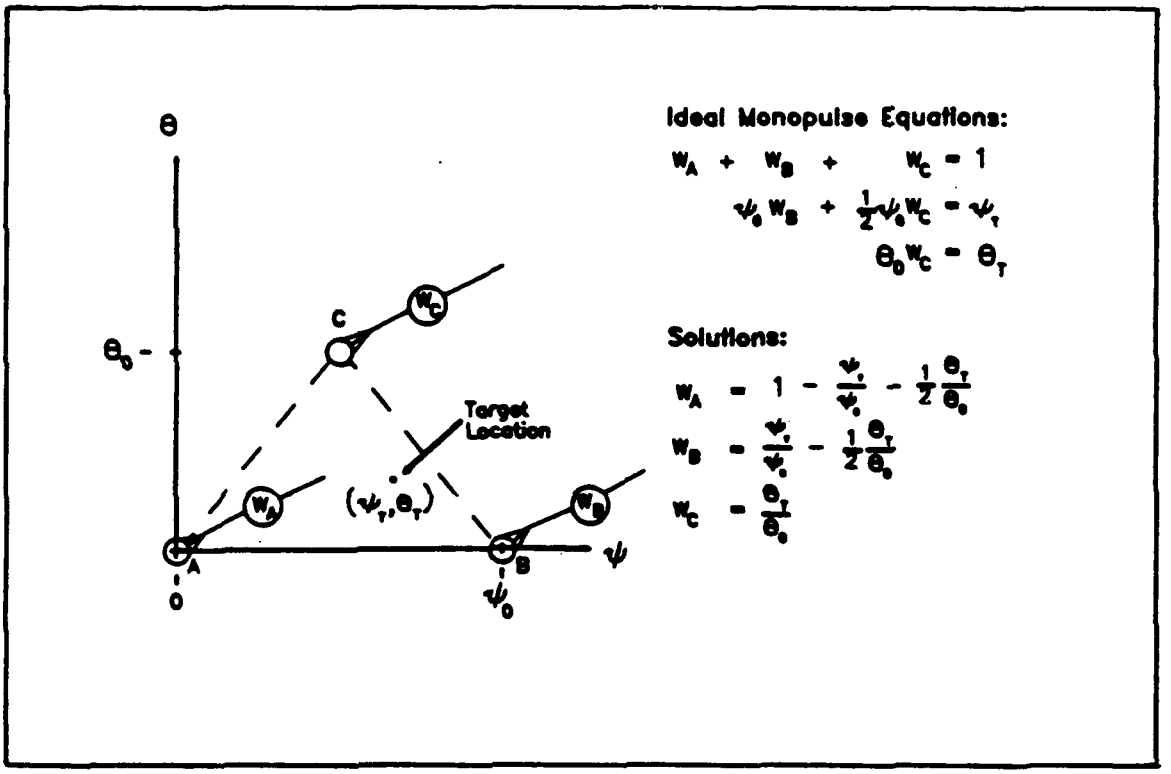


FIGURE 12. HWIL TARGET POSITIONING ALGORITHMS

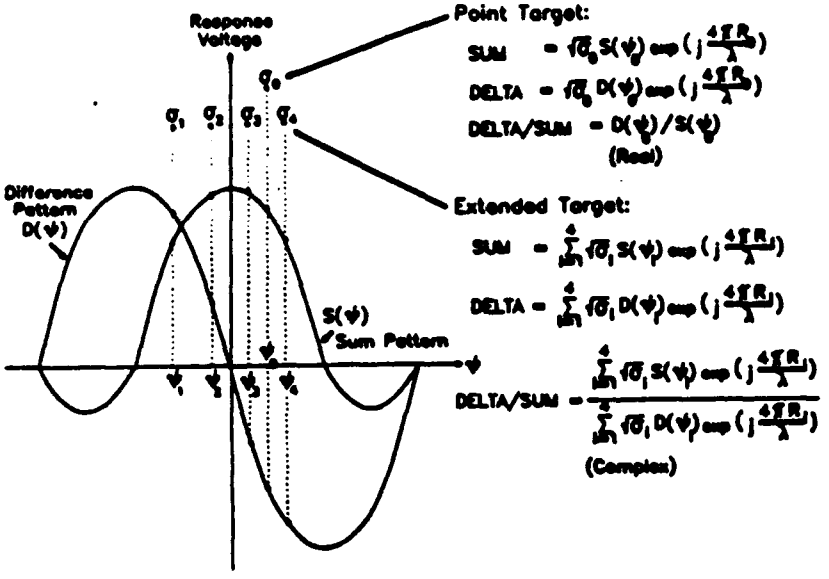


MONOPULSE RESPONSE TO POINT TARGETS AND EXTENDED TARGETS

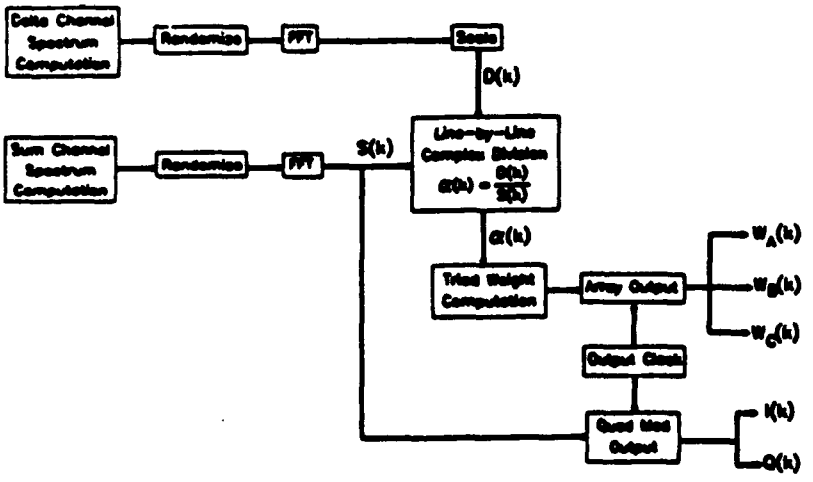


FIGURE 13. COMPLEX TRIAD POSITIONING CONCEPT

triad weights. The algorithm used to compute the triad weights is the same as the conventional algorithm. The essential difference in the triad weights resulting from this procedure and those resulting from the conventional approach is that the complex angle inputs to the algorithm yield complex (phase as well as amplitude) weights. As usual, the amplitudes are adjusted with attenuators. The phase shifters, however, are no longer used to level the phase among the triad signals, but to provide a sequence of controlled phase differences. The amplitude and phase modulation provided by this sequence of relative attenuations and phase shifts among the triad signals creates an independent amplitude and phase sequence in each of the three receiver monopulse channels. Each monopulse channel sequence has a different doppler frequency spectrum, reflecting the different illumination of target scatterers and clutter patches by the three monopulse antenna patterns.

MSS

Simulation of active seeker radar returns in the MSS require the coherent modulation of replicas of the seeker's transmit waveform to produce the correct instantaneous amplitude and phase in each of the seeker's three monopulse channels. The capability should exist to coherently delay replicas of the seeker's waveform to produce energy in each of the coarse range cells. The ability to produce a complex fine range cell distribution is required to produce the correct range profile signature. An independent fine range cell distribution is required for each monopulse channel to produce the correct angle signature. Independent copolarized and cross polarized range profile and angle signatures are required. These basic simulation requirements, in turn, require that the delayed seeker waveforms transmitted to the seeker in the simulation must be modulated in amplitude, phase, polarization and direction of arrival with a modulation sequence which changes at every step in the seeker transmit frequency and at every change in seeker transmit polarization. To date, the fastest modulation rate required has been on the order of 100 KHz, although future systems may require higher rates. Coherent range delay, signature generation and directions of arrival control systems are required for coherent signal processing seekers. A fully coherent simulation will satisfy the requirements of both coherent and noncoherent seekers.

The requirement to produce an independently controlled, complex, coherent range profile in each of the three seeker monopulse channels can only be achieved by independently modulating the amplitude and phase of a triad of sources on the simulator array, as discussed above. Generally these sources transmit simultaneously and their location on the array may change at each change in seeker transmit state. This is one significant departure from standard narrowband monopulse seeker

simulations in which only the amplitude of the triad signals are controlled to provide direction of arrival information to the seeker. In general, amplitude-only control (with leveled phase) is the minimum requirement when amplitude-centroiding within a coarse range cell is used by the seeker to develop aimpoints on the target. When scatterer mapping techniques are employed, both amplitude and phase control are required for the simulator sources which determine direction of arrival. The basic target positiion algorithms used in the simulator change significantly when phase control is added. The form of the algorithms has been described in the previous subsection (see figure 13).

## FUTURE DEVELOPMENTS

It is anticipated that the capabilities of new generations of guided missiles and "smart weapons" will impose a higher burden than hitherto on required target and background modeling fidelity because of the increased signal processing power associated with such missile developments. Because of these requirements, RD&EC is continuing an active program of research into target and scenario modeling techniques for all regions of the electromagnetic spectrum, and into the use of new signal generation technologies. Examples of new technologies in the RF world include digital RF memories (DRFM) and numerically controlled modulated oscillators (NCMO); both of these devices give promise of much improved signal generation capability, but entail considerable expenditures in their applications.

In addition, the MICOM Advanced Simulation Center has instituted a construction program which will, when complete, provide additional HWIL simulation facilities to complement the existing facilities. The new simulation facilities include:

- o a MMW simulator for the frequency range 20-220 GHz
- o an RF simulator for the the frequency range 2-12 GHz
- o an RF simulator for the frequency range 6-18 Ghz
- o an imaging infrared (IIR) simulation laboratory
- o a 3 chamber weapon systems simulator for inclusion of full scale ground equipment in battlefield simulations

An illustrative layout of the facilities under construction in the High Bay of building 5400, Redstone Arsenal is shown in figure 14.

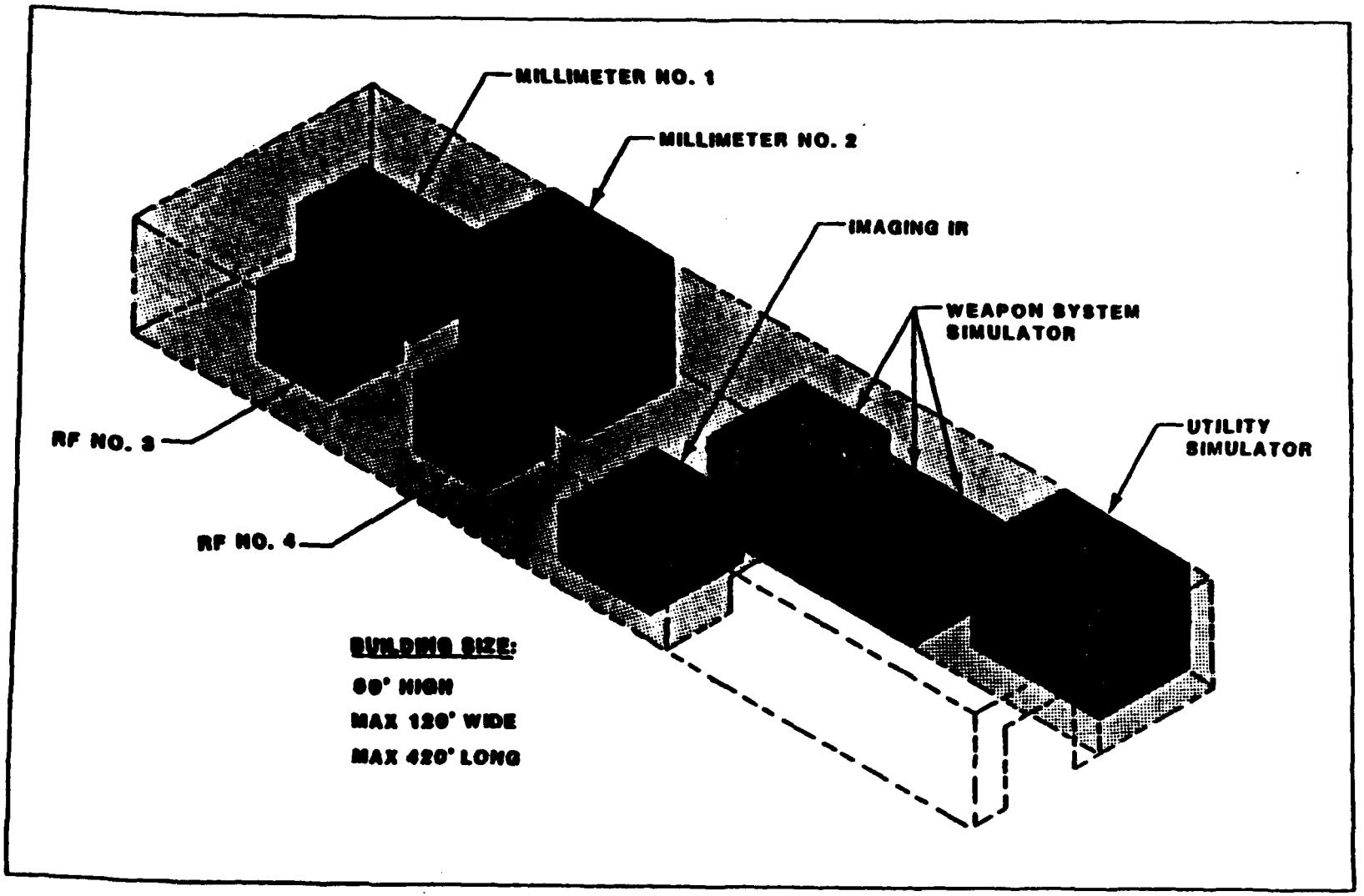


FIGURE 14. MMSF SIMULATION CHAMBERS

## CONCLUSIONS

This paper has described the methods used to model and generate target and scenario background signatures for HWIL simulations of missiles guided by microwave and millimeter wave frequencies in the MICOM Advanced Simulation Center. The subject of the paper is extremely extensive and space constraints have permitted only the essentials to be addressed. Other topics associated with the subjects of this paper include the validation of models by comparison and correlation with measured data; this is an important area of simulation model development which has not been discussed but which is a topic of great interest and activity at RD&EC. Furthermore, the topic of computer requirements and capability, on which the degree of fidelity of signature modeling ultimately depends, has also been neglected for reasons of lack of space.

Research into improved techniques of signature modeling and signal generation are continuing. Clearly, the introduction of "smart/brilliant weapons" in which signal processing capabilities exploit developments in processor technology will require corresponding advances in both target and scenario modeling techniques and in the basic need for HWIL simulation as a means of evaluating the hardware and software performance of the new generations of munitions in an efficient and cost-effective manner. MICOM RD&EC has long recognized the value of the role of HWIL simulation in missile system development and has positioned itself to provide the very advanced simulation capabilities which new generations of tactical guided missiles will require.

## REFERENCES


Swerling, P., "Probability of Detection of Fluctuating Targets", IRE Transactions on Information Theory, IT-6 pp 269-308, April 1960.

Gardner, R.E., "Target Signature Study (U)", Naval Research Laboratory Report 7156, 15 September 1970 (Classified SECRET).

Baird, A.M., N.C. Randall, D.A. McPherson, "RF Environmental Modeling in the Radio Frequency Simulation System", U.S. Army Missile Command Technical report RD-CR-81-3, 6 May 1981.

Sandhu, G.S. and A.V. Saylor, "A Real-Time Statistical Radar Model", IEEE Transactions on Aerospace and Electronic Systems Vol AES-21, No. 4, July 1985.

McPherson, D.A., "Multiscatterer Target Response for a Coherent Monopulse Tracker", Simulation Technologies Inc, Tech Note 131-013, 10 December 1986.

Saylor, A.V., "Derivation of Target Scatterer Lists from ISAR Target Images", Simulation Technologies Inc, Tech Note 131-026, 27 July 1987.

Saylor, A.V., D.A. McPherson, and S.C. Henry, "MMW Statistical Range Profiles Model for Real-Time Seeker-in-the-Loop Target and Clutter Simulations", Simulation Technologies Inc, Tech Note 131-032, 16 July 1988.

# DYNAMIC INFRARED SCENE PROJECTION TECHNOLOGY

Scottie B. Mobley
U.S. Army Missile Command
Redstone Arsenal, Alabama

## ABSTRACT

This paper will provide an overview of the critical Infrared (IR) projector requirements and specifications for Hardware-in-the-Loop (HWIL) simulations of imaging IR systems and will review the most prominent technologies associated with IR scene projection. Each method will be briefly discussed in terms of physical operaton with all revelant advantages and disadvantages being highlighted. A comparison will be provided of the different categories of projection devices for applicability to HWIL simulation.

## INTRODUCTION

The use of and benefits of HWIL simulations in the evaluation of weapon system performance is well established throughout all branches of the Department of Defense. For example, such simulations have provided substantial payoffs to radio frequency (RF) and millimeter wave (MMW) guided weapon system research and development. For "Hot Spot" IR guided weapons this statement also applies to some extent. However, unlike the RF and MMW guided systems, no technique has been developed which can provide a complete evaluation of the new sophisticated imaging IR guided weapons. Accordingly, other simulation techniques have been utilitzed for their evaluation. These techniques are most often referred to as "signal injection" or "tracker-in-the-loop" simulations. The system's optical and imaging characteristics are modelled using a special purpose computer image generation device which then injects the appropriate digital data into the tracker electronics thus bypassing all the system optics. Despite the success of these types of simulations, there are inherent weapon system characteristics which can not be evaluated in this manner. For their accurate evaluation, the complete seeker optics and IR detector device must be included in the HWIL simulation. This type of simulation is referred to as "in-band" or "seeker-in-the-loop" to denote the fact that IR images are produced and projected to the entrance aperture of the weapon's seeker.

Figure 1 provides a simple block diagram of a typical inband HWIL simulation involving imaging IR guided weapon systems. Currently, all major components shown are available with the exception of an IR projector capable of producing the realistic, radiometrically correct IR images required for complete system seeker and tracker evaluation.

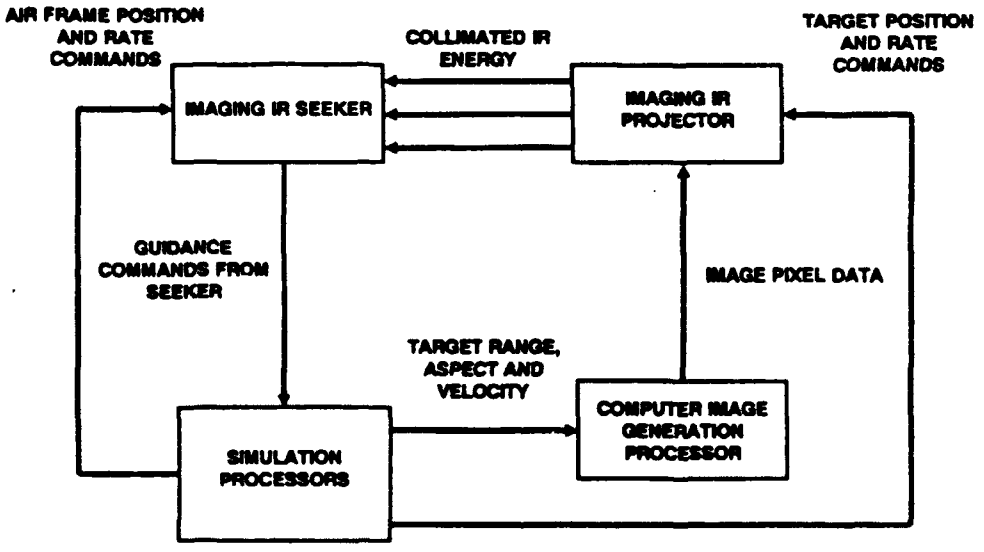


Figure 1. Imaging IR HWIL Simulation Block Diagram

## REQUIREMENTS

In general, imaging IR guided weapon systems can be classified as scanners or starers. Both sample the IR radiance over some wavelength range of interest and process this information to establish the appropriate airframe guidance commands for target intercept. Scanners typically consist of a linear array of detectors which are sampled by the missile's image processing electronics as different IR components of the scene are reflected onto the detector elements by a moving mirror. Starers typically consist of a two dimensional matrix of detector elements called a Focal Plane Array (FPA). This FPA is usually monolithic in construction and resides at the focal point of the collection optics. In the staring systems, each detector element samples the IR radiance from a different, adjacent component of the missile's Field of View (FOV). As was the case with the scanning systems, the image processing electronics samples the FPA at the appropriate time interval. Both techniques are utilized in the design of seekers for the modern imaging IR guided weapons. Accordingly, the requirements placed upon the IR projector are dependent on the type of system which is used in the weapon system being tested in HWIL. To a large extent, these differences in requirements are a function of the IR projection technique proposed.

Despite their inherent differences, certain IR projector performance specifications are required by both types of systems. Examples of these are spatial resolution, frame rate, dynamic range, temperature resolution and flicker. Table I shows an expanded set of requirements for the projector. These are based on the available or proposed IR sensors in the two time periods shown. The spatial resolution of the projector would ideally be greater than the resolution of the missile's imager by a factor of two. This would provide satisfaction of the Nyquist criterion. However, the performance of the imaging system is complex and useful results might be attainable with only equivalent resolution. Typically, as is indicated in Tab. I, the spatial resolution required is greater in the 3 to 5 micron band than in the 8 to 12. This is primarily the result of the requirement for larger arrays in the 3 to 5 to counter detector quantum efficiency problems and of the difficulty in the manufacture of larger arrays in the 8 to 12 region. The frame rate required varies according to the type of detector material which is used and according to the type of scenario being simulated. Longer integration times require slower frame rates. In general $10^3$ represents an acceptable dynamic range, but the simulation of some scenarios requires a dynamic range on the order of $10^5$.

Table I. Imaging IR Projector Requirements

| Characteristic | 1990 | 1995 |
|---|---|---|
| Spatial Resolution (Pixels) | | |
| 8 to 12 microns | 128 x 128 | 256 x 256 |
| 3 to 5 microns | 512 x 512 | 1024 x 1024 |
| Frame Rate (Hz) | | |
| 8 to 12 microns | 200 | 500 |
| 3 to 5 microns | 60 | 200 |
| Dynamic Range | $10^3$ | $10^5$ |
| Target Temperature Simulated (°C) | 0 to 120 | 0 to 700 |
| Target Temperature Resolution (°C) | | |
| 8 to 12 microns | 0.1 | 0.1 |
| 3 to 5 microns | 0.5 | 0.5 |
| Countermeasure Simulation | yes | yes |
| Pixel Addressing | vector | vector |
| Simultaneous Wavebands | one | two |
| Flicker (%) | 1 | 0.1 |

## TECHNOLOGIES

The technologies currently being developed for IR projector applications can be categorized into three groups. These are resistor arrays, light modulation devices and other approaches. The principal characteristics of the various techniques are described below.

### RESISTOR ARRAYS

The basic operational principle of the resistor arrays is relatively simple. Electric current is passed through the individual resistor elements which heat up and emit IR energy in accordance with Planck's Law. The amount of energy produced is dependent on the resistor temperature, the ratio of active to total pixel area (i.e. fill factor) and emissivity. Two distinct types of devices are currently under development in the United States, United Kingdom and Australia. These are the "bridge" and isolated thin film techniques. Both are generally addressed a line at a time through the use of a diode or transistor drive system. The diode approach relies on the thermal mass of the resistor to maintain IR energy output until it is readdressed. The transistor network approach uses the gate capacitance of the transistor to maintain a voltage accross the resistor until it is readdressed.

In the resistor bridge devices two approaches have been considered for there fabrication. One uses a raised bridge element over a flat substrate. The other consists of a bridge element over a cavity. The raised bridge concept has not reached the status of development of the cavity backed devices and there is little data available on its characteristics at this time. Accordingly, only the cavity backed structures will be further discussed.

The cavity backed devices are monolithic in construction and are fabricated on standard silicon wafers. They typically have very small active areas and poor emissivity characteristics. Resistor temperatures of 1000 K have been demonstrated. However, fill factors less than 10% and emissivities less than 0.20 degrade the temperature performance substantially. The bridge elements are small and frame rates on the order of 200 Hz are readily achievable when the substrate is cooled. Crosstalk between adjacent resistors is minimal because of the thermally isolated cavity structure of the resistor. Arrays of 128 x 128 elements have been fabricated and are currently being integrated into a projection system. The fabrication of larger structures is possible, but yield problems could limit the development of arrays larger than 256 x 256. Figure 2 shows an example of the typical resistor bridge structure.

The isolated thin film resistor approach is by far the most profilic technology which has been or is being considered for IR projector applications. At this time, devices are being developed by several companies. Unlike the fabrication of the cavity backed devices, the fabrication of these structures requires on the order of 200 independent processing steps which functions to reduce yields even further. Resistor temperatures of 700 K have been demonstrated. The fill factor and emissivity characteristics are substantially better than those with the cavity backed devices. Fill factors on the order of 50% and emissivities of 0.50 have been achieved. Again, the effective black body temperature simulated over the pixel will be less than the active resistor temperature. The structure of these devices yields a longer time constant and a slower frame rate. The frame rates are limited to the 30 to 60 Hz area. Because the resistors are not completely isolated from adjacent components in the array crosstalk will be evident in any simulated scene. Cooling of the substate also presents a difficult problem which must be considered in any projector design using this technology. Arrays of 100 x 100 elements have be fabricated. Arrays with 256 x 256

Figure 2. Cavity Backed Resistor

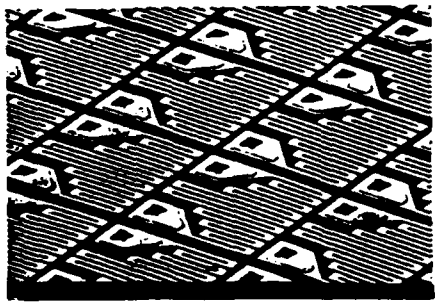

Figure 3. Thin Film Resistor

elements are under development. Because of technology limits it appears that the production of larger arrays is unlikely.

LIGHT MODULATION DEVICES

These technologies can be seperated into two distinct groups. These are the Liquid Crystal Light Valves (LCLV) and the direct amplitude or phase modulation devices. Both function to modulate an IR readout source, but accomplish this in two vey different ways.

The LCLV modulates the readout IR source through polarization effects in either a transmission or reflection manner. Only the reflected mode is suitable for HWIL consideration. In this mode, the IR source is first polarized and then, through the appropriate optics, illuminates the liquid crystal material. Depending on the alignment of the liquid crystal material on a pixel basis the readout light's polarization is altered and reflected back through an analyzer which results in a polarized spatially modulated beam. This beam is then collimated and optically directed to the missile sensor under test. The alignment of the liquid crystal is set by addressing it with a CRT and requires a continuous voltage to maintain its alignment once addressing is complete. This presents a problem because the typical CRT can not continuously maintain this charge while addressing the remaining pixels which make up the scene. However, special purpose CRTs have been developed which can maintain a charge distribution and as a result have been used to reduce if not eliminate the flicker problem. These devices are very expensive and are not readily available. As a result, only one of the flicker free LCLVs has been constructed.

The LCLV has excellent spatial resolution which could support test of any current or future missile seeker. However, other inherent characteristics would appear to exclude the LCLV as a candidate for use in HWIL simulations. These are frame rate, contrast, dynamic range and physical size. Frame rates of 30 Hz are achievable with current LCLVs. The contrast is limited because of impurities within the LCLV. This results in temperature gradients occurring in the simulated scene when there should be none. The maximum temperature which can be simulated is around 320 to 370 K. The physical size is a problem if flight table mounting is required. Figure 4 shows a reflection modulator.

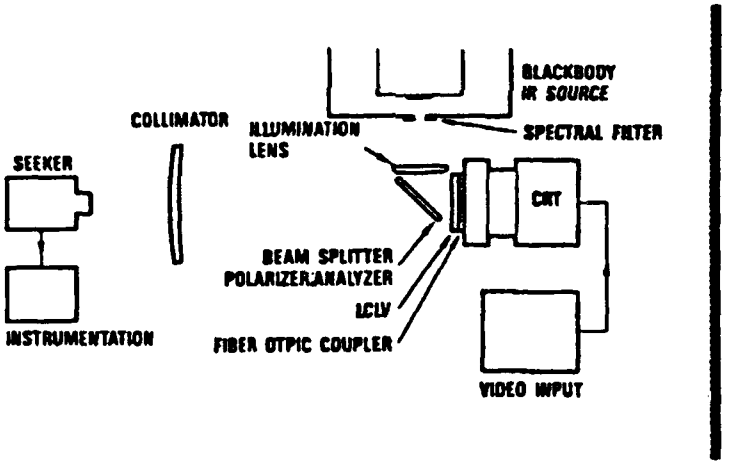


Figure 4. Reflective LCLV IR Modulator

The amplitude or phase Spatial Light Modulators (SLM) are made up of two different concepts. These are the Deformable Mirror Devices (DMiD) and the Deformable Membrane Devices (DMeD). Either can potentially operate as amplitude or phase modulation devices, but the DMeDs are more suited to phase modultion. The DMiDs are made up of individual mirror elements which, depending on the structure, can be either deflected like a piston or tilted along some axis on the element by an electrostatic charge. One example of the angular tilt DMiDs is given in Fig. 5. The DMeDs consist of a reflective membrane stretched across a charge transfer plate which has wells etched into it to allow the membrane to deflect into for modulation. An example of this structure is shown in Fig. 6. The devices can be either addressed using a scanning electron beam or through direct addressing. The E-beam is preferred for the DMeDs and the DMiDs use direct addressing through a Charge Coupled Device (CCD).

In phase modulation mode each device operates similarly to modulate a readout IR source. Each element is deflected to selected depth dependent on the required modulation. The readout light is then

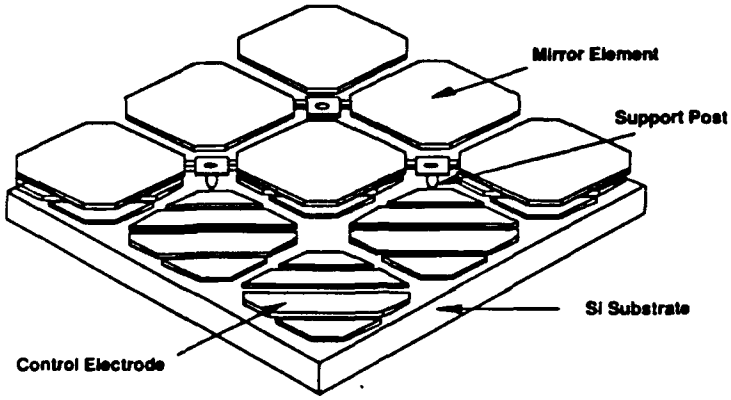


Figure 5. Deformable Mirror Device

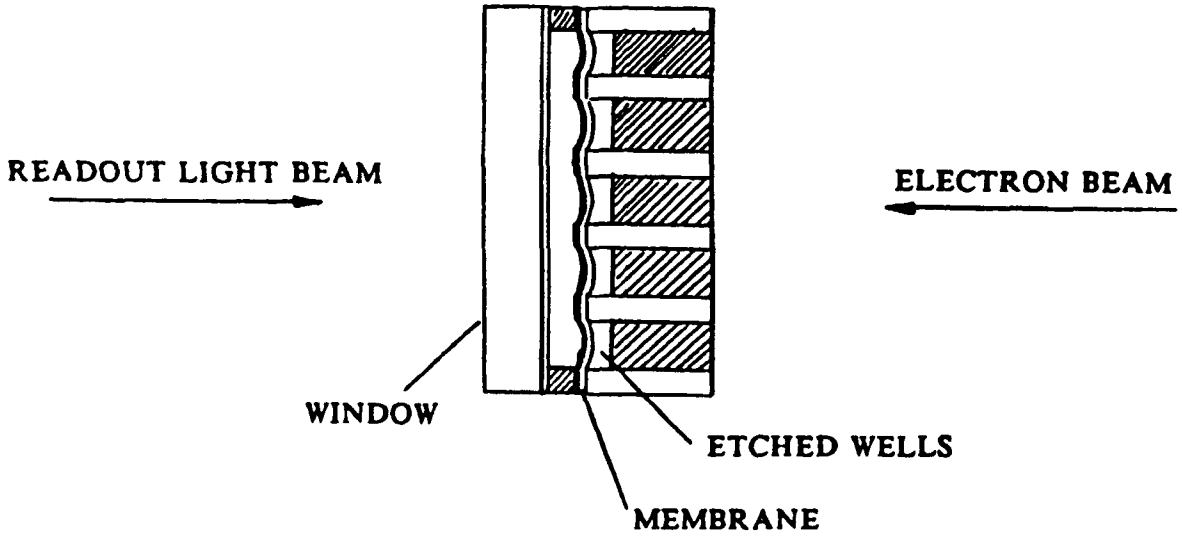


Figure 6. Deformable Membrane Device

deformed based on this deflection and is reflected back through a Schlieren optical system which converts this deformation to amplitude modulation. In amplitude modulation mode only the DMiDs will be considered. In this mode the mirror elements are deflected angularly along the hinge axis. Depending on the amount of this deflection, the IR readout light is modulated by each mirror element based on the amount of energy deflected into collection baffles or out of the line of sight.

The poor efficiency of the Schlieren readout approach of the phase modulation technique in conjunction with the inherently poor modulation efficiency of that technique eliminates it from further consideration. Accordingly, it appears that the DMiDs are better suited for HWIL applications because of the direct amplitude modulation which is offered. The primary disadvantage of DMiD SLM is that only minimal efforts have been taken to develop IR projector prototypes using this technology. However, this is currently changing with several government agencies becoming involved. Also, companies are pursuing this technology for application to high definition television. DMiDs have been fabricated with 256 x 256 elements. Others are under development with resolutions greater than 1000 x 1000. In addtion to the high resolutions, frame rates of 500 Hz should be easily achieved wtih these devices. Because of its reflective nature the device should readily simulate the high temperatures required for some target engagements.

OTHER APPROACHES

Other techniques which have been or are being considered for IR scene projection include IR laser scanners and IR Cathode Ray Tubes (IRCRTs). The laser scanner approach is the newest having been developed over the last few years. On the otherhand, the idea of the IR CRT dates back approximately 20 years, but for the most part the present IR CRTs which are under consideration are very different than those envisioned originally.

The laser scanner functions in a manner that its name implies. An infrared laser within the bandpass of the weapon sensor under test is scanned rapidily across the entrance aperture of the sensor and paints out the IR scene as it progresses. The beam is scanned by passing it through a two axis deflection system made of two acousto-optical modulators. Hence, the beam is deflected horizontally by one modulator and vertically by another. To avoid having the beam deflected to a sensor detector element which is not integrating at that instant, the beam deflection is synched with the readout scan of the sensor under test. This fact presents a problem if a clock signal is not available from the sensor under test. Laser scan projectors with resolutions of 128 x 128 have been built and are nearing operation at some facilities within DOD. Because of limits in the resolution of the modulation system any greater scene resolution is not possible at this time. The laser system offers high dynamic range and high frame rate. A large complex optical system is required which prohibits any kind of interface with a flight table. Techniques are being considered which involve the use of fiber optic bundles to accomplish this interface. Howver, these are only concepts at this time. Another potential problem which depends on the sensor under test is the detector subframe dwell time which is used. Overall, the laser scanner is a good technique to use until other technologies become more advanced.

The initial emphasis in the IR CRT area was in the development of an IR equivalent to the visible wavelength television. Figure 7 shows one of these concepts. However, these have for the most part been discarded because of difficulties in devleoping a phosphor for use in the IR wavebands. Although work is continuing within certain companies on the IR phosphor, the present IR CRTs whcih are being proposed differ substantially from the original idea. These utilize high energy E-beam welding techniques to heat up elements on a target plate. As the element heats up it emits energy inaccordance with Planck's Law. Prototypes of this technique have been built and demonstrated. Temperatures in excess of 1000 K have been achieved. The device also offers good resolution. However, the target plate elements have no sample and hold capability with the time constant directly dependent on their physical structure. Again, synching of the E-beam deflection and sensor undet test scan would be required. The frame rates achievable would be around 30 to 60 Hz. Depending on the E-beam characteristics crosstalk could be a problem.

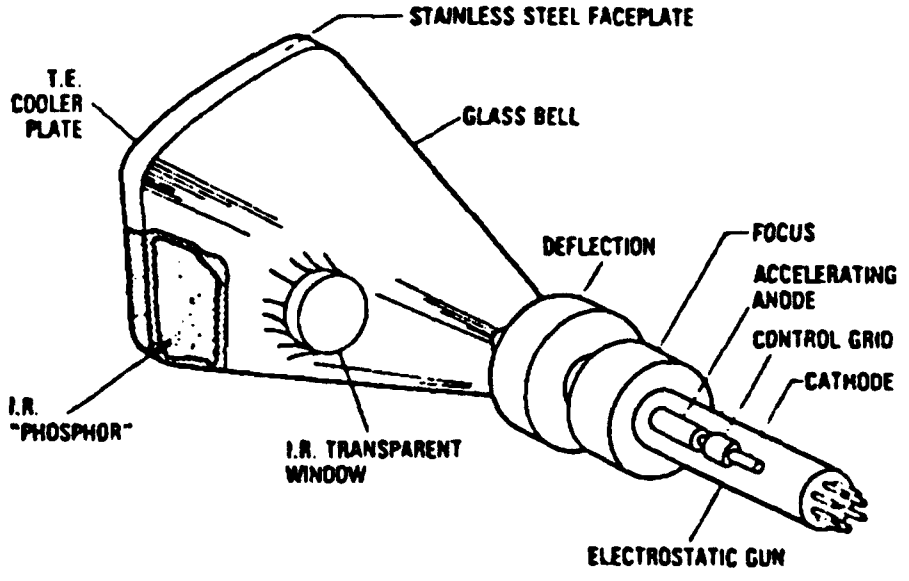


Figure 7. Infrared CRT

## COMPARISON

From the previous discussions the foremost IR projector technologies are the cavity backed resistor array, the thin fim resistor array, the DMiDs, the DMeDs, the LCLV, the laser scanner and the IR CRT. The principal factors for comparison are frame rate, dynamic range, temperature resolution, spatial resolution, flicker and physical size. Table II summarizes the comparison of these technologies on the basis of these characteristics. In the table, a numerical rating is given between one to ten with ten being excellent and one being unacceptable.

Table II. IR Projector Technology Comparison

| Projector Technology | Frame Rate | Dynamic Range | Temperatrue Resolution | Spatial Resolution | Flicker | Size |
|---|---|---|---|---|---|---|
| Resistor Array | | | | | | |
| Cavity Backed | 7 | 5 | 5 | 4 | 6 | 7 |
| Thiin Film | 4 | 5 | 4 | 4 | 6 | 6 |
| Light Modulation | | | | | | |
| LCLV | 4 | 4 | 3 | 10 | 6 | 4 |
| DMiDs | 9 | 8 | 6 | 9 | 8 | 9 |
| DMeDs | 4 | 4 | 3 | 6 | 8 | 9 |
| Other Approaches | | | | | | |
| Laser Scanners | 9 | 9 | 4 | 4 | 4 | 2 |
| IR CRTs | 5 | 7 | 3 | 7 | 3 | 6 |

## CONCLUSIONS

From the preceding discussions it is apparent that given the current status of IR projcetor technologies there is not an ideal device to cover all HWIL simulation requirements. However, several specific simulations can be carried out with the individual devices currently available. At present the DMiDs offer the greatest potential for future support of complete end to end HWIL simulations. As research is directed into this approach and given the prospects of other applications, this technique could prove to be the solution to the long standing problem which has faced the DOD laboratories involved in HWIL simulations of imaging IR systems.

# SIMSTAR - ANATOMY OF A MODERN HYBRID COMPUTER

K.L. Hall
U.S. Army Missile Command
AMSMI-RD-SS-HW, Bldg 5400
Redstone Arsenal, Alabama 35898-5252

## ABSTRACT

Hybrid analog/digital processors have had a hong history, at least in terms of computer age. In recent years, however, this type of processor has suffered a decline in popularity and use, probably because of the difficulties of programming and the relative inaccuracy of its analog components. There is still a place for these processors in missile research and development, as shown by the discussions in this paper.

After a brief survey of hybrid analog/digital systems, this paper discribes the orgins and characteristics of a modern, digitally programmable, hybrid analog/digital processor developed by MICOM RD&EC in cooperation with Electronic Associates, Inc. (EAI). This processor, under the name SIMSTAR, is being marketed commercially within the United States, Europe and Japan. It forms the basis of MICOM's Advanced Simulation Center Hybrid Laboratory where SIMSTARs are heavily used in realtime hardware-in-the-loop (HWIL) simulation of various missile systems.

SIMSTAR's hardware and software characteristics have been tailored for realtime missile HWIL simulation. Two specific examples of SIMSTAR applications are described in order to indicate the demonstrated advantages of SIMSTAR for these applications.

## INTRODUCTION

The most common processors can be lumped into two brances. One branch descended from the idea of finger counting or the abacus and the other from graphical solutions and the slide rule. These two branches are the digital and analog processor branches (1). The following attributes may be associated with processors of the two branches (2):

Analog

1. Dependent variables within the machine are treated as continuous.
2. Static or dynamic accuracy is usually limited to approximately .0001 times the fixed point maximum value and since variables are fixed point scaling in required.
3. Operation is parallel with all processes occuring simultaneously.
4. High speed processing of realtime or faster with speed primarily limited by processor element bandwidths rather than problem complexity.
5. Ability to perform efficient operations of addition, multiplication, integration, complex nonlinear functions, single bit combinational and sequential logic, but limited in capability to store results, provide time delays and handle nonmumerical information.

6. Facility for including analog hardware and input/out devices easily into simulation.

Digital

1. All variables are quantized.
2. Serial or relatively few parallel operation paths.
3. Accuracy relatively independent of quality of system components and determined primarily by the number of bits provided in the processor paths and memory and numerical techniques selected for a specific application. Dynamic accuracy when interfaced to outside realtime hardware is relatively difficult to measure.
4. Solution time is determined primarily by problem complexity and desired numerical accuracy.
5. Provides capability to "trade off" solution time and accuracy.
6. Some numerical operations, such as integration, logs, and sine and cosine are performed by approximate numerical techniques.
7. May store results, either numerical or nonnumerical.
8. May perform logic operations on numerical and nonnumerical variables.
9. Floating point capability usually provided thus avoiding scaling problems.
10. Increased difficulty when programming a parallel processor.

The hybrid processor system is intended to provide the combined strengths of the analog and digital processors while minimizing the weakness of both. Analog/Hybrid processors for high speed simulation applications requiring realtime or faster processing, have evolved from the analog processor shown in Figure 1 in the 1950's and 1960's to the hybrid system shown in

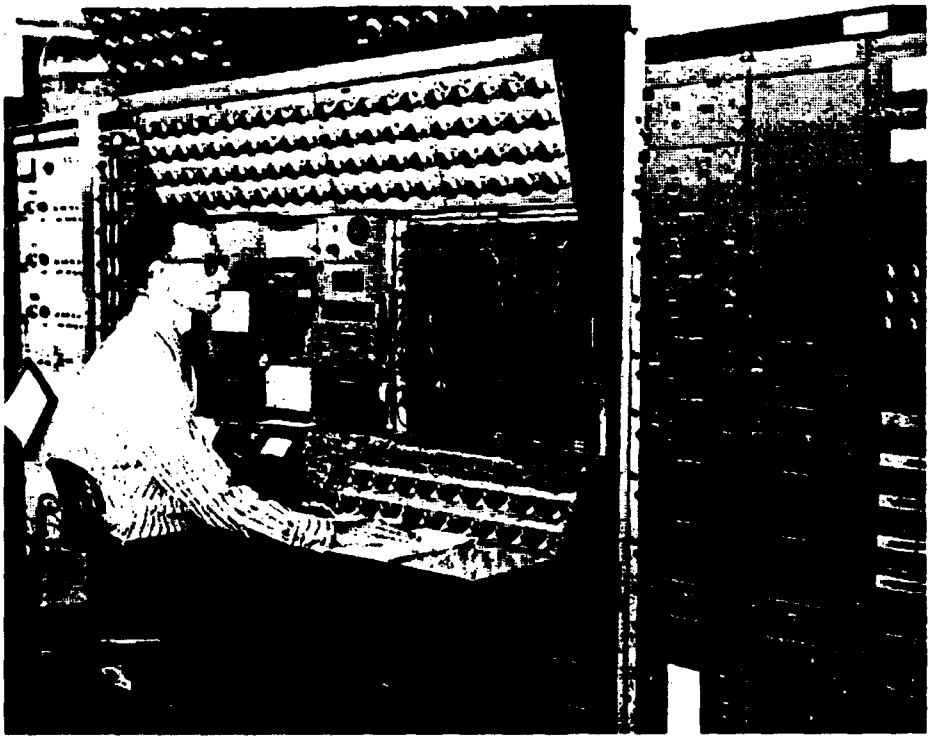

Figure 1 - EAI 231R Analog Processor 1950-1960

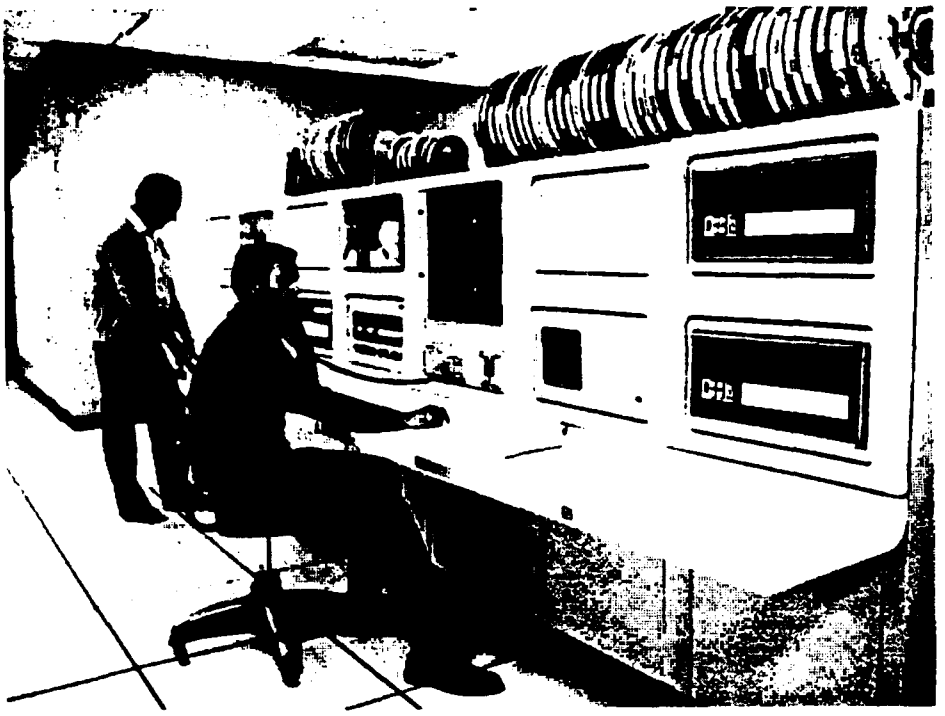

Figure 2 - EAI Automatic Hybrid Setup System 1970's

Figure 3 - EAI 781 Analog/Logic Processor 1970's

Figure 4 - Realtime Terminal CDC/EAI Hybrid 1970's

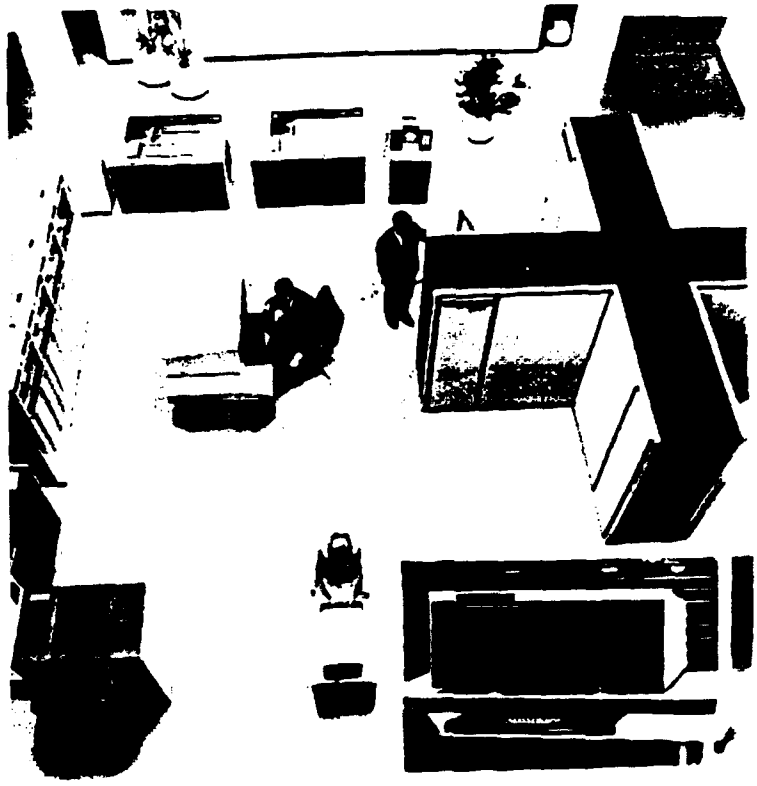

Figure 5 - CDC 6600 Host for 1970's Hybrid Processor

Figures 2, 3, 4 and 5 in the 1970's to the SIMSTAR processor shown in Figure 6.

The practical speed advantage of the 1970's hybrid system can be illustrated by an example of a high fidelity missile simulation which executed at 150 times slower than realtime on the CDC 6600 system alone. This same simulation executed in realtime with additional speed capability remaining on the hybrid system utilizing the same CDC 6600 as the realtime host processor.

While the execution speed was as advantage for the 1970's hybrid systems, programming time and system setup times were long due to a mostly manual setup and programming process. Typical setup times were approximately 1 hour and programming could take 1 to 5 days. These times are reduced to approximately 5 minutes for setup and 30 minutes for recompilation and reloading for the SIMSTAR system. Execution speed for SIMSTAR is approximately the same as for 1970's hybrid systems with small gains in speed in the host processor and function generation processor. Accuracy has improved by a factor of 5 to 10 for the parallel processor subsystem in SIMSTAR over the 1970's type hybrid processor systems.

With SIMSTAR it is practical to expect to share a single hybrid simulation system between 3 or more hardware-in-the-loop tasks during a 2 shift work day with an excellent opportunity for obtaining useful quantity and

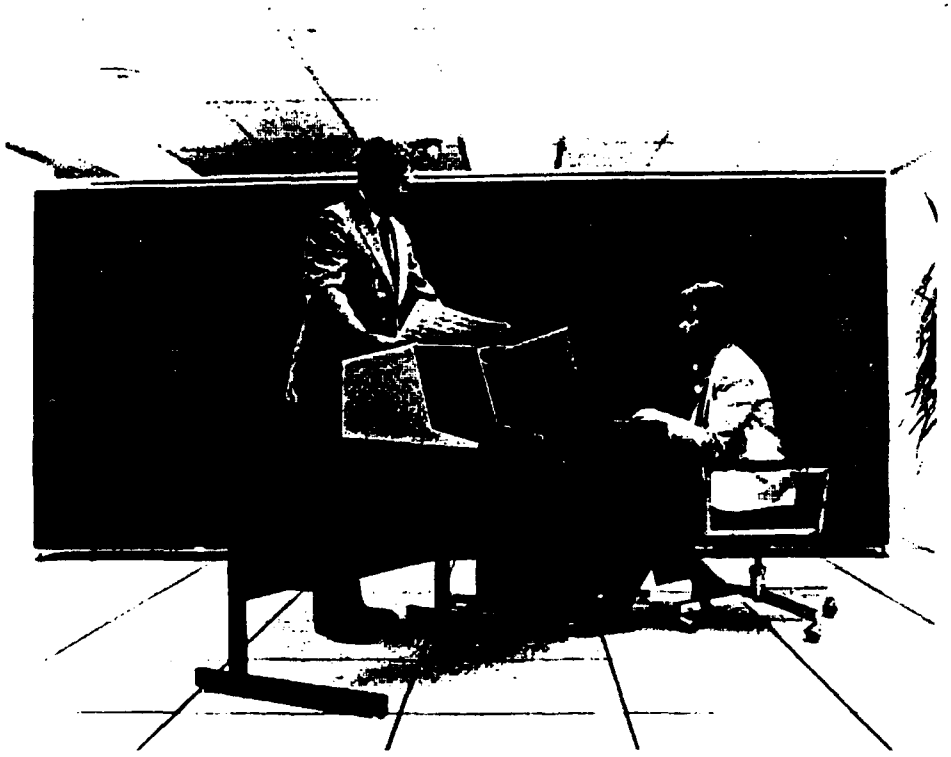

**Figure 6 - SIMSTAR Processor 1980's and 1990's**

quality of results on each task. Complete computer control of all aspects of the setup and modification of the run parameters on the SIMSTAR system permits creation of large predefined run sets. These predefined run sets allow large parametric studies and monte carlo sets to be conducted in a minimum time and with minimum human errors. The SIMSTAR system also provides a real-time workstation human interface including color displays, interactive control and data logging with minimum impact upon host processor speed and data storage capacity. Traditional strip chart functions are available in the real-time workstation which provides display and recording/playback/hardcopy of up to several hundred variables per frame.

The U.S. Army Missile Command Advanced Simulation Center began in the late 1970's development with Electronic Associates, Inc. of a modern simulation simulation processor system currently known commerically as SIMSTAR to provide the speed and accuracy necessary to allow full model fidelity real-time processor capability for Army missile hardware-in-the-loop simulation applications. The first operational system was installed in the Advanced Simulation Center in the mid 1980's. Figure 6 shows this new generation processor which is now the main processor resource in the Hybrid Hardware-in-the-Loop Laboratory.

Currently SIMSTAR is being utilized in such simulation application areas as missiles and aerospace, nuclear, lense and shutter design, dynamic system education, steel rolling mill disign and high speed locomotive design. Simulation activities are utilizing SIMSTAR as a processor system for time critical simulation in the U.S, Europe and Japan.

## CHARACTERISTICS OF A MODERN HYBRID SIMULATION PROCESSOR

Figure 7 is illustrates a typical hardware-in-the-loop application of the SIMSTAR system. Unshaded boxes indicate SIMSTAR subsystems and shaded boxes indicate simulation application elements which are not part of SIMSTAR. The user communicates with this realtime simulation system through the real-time workstation and SIMSTAR host. These communications consists of realtime graphical plots, strip chart and x-y type presentations, numerical values, touch screen, mouse, and normal terminal. The user controls the simulation by means of the touch screen, terminal and procedures prepared to define runs or run sets. Data logging is accomplished within the workstation thus relieving the host of this resource consuming activity. Logged data may be played back from memory in the workstation or stored on optical disk for later review. Hardcopy capability is provided for the graphical and numeric displayed results.

The SIMSTAR host serves as the controller of the realtime simulation and provides high resolution analytical capability for the lower frequency variables in the simulation. High speed aerodynamic table lookup capability is provided by the function generator. High frequency variables are produced by equations implemented on parallel processors 1 and 2. High speed analog and logic variables are provided from the host and parallel processors by way of the analog to digital, digital to analog and logic converters and through the electronic signal allocator which provides program control of the routing of these variables. Analog and logic variables which must be transmitted over long distances, more than 30 to 50 feet, are carried by fiber optic analog trunks and differential hardwired discrete trunks.

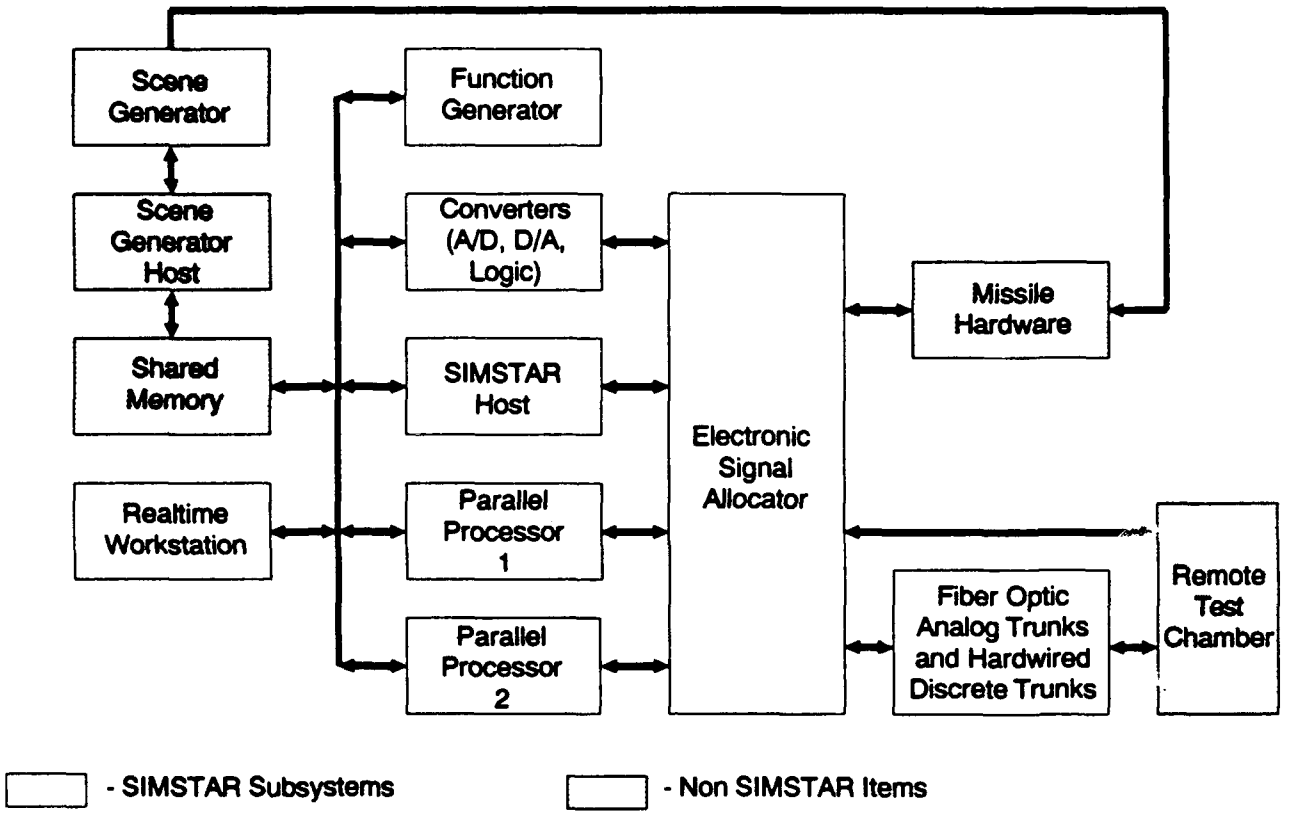


**Figure 7 - SIMSTAR System Configuration**

Variables which define target and missile geometry are sent by the host through the shared memory to the database driven 3-D scene generator host and generator. The scene generator produces a realtime image of the missile field -of-view and provides this image to the missile hardware under test. The missile hardware and software process the image to provide guidance commands to the analytical portiions of the missile models.

The modern hybrid processor system provides the capability for performing realtime execution of complex high fidelity models along with the capability for changing between several hardware-in-the-loop applications with a short, approximately 5 minutes, change over time. All operations are controlled by the host and a complete documentation trail of operations and changes is available to allow selection of the documentation level required for each application. Development of realtime applications is made convenient by the Startran software package which provides a high level simulation language environment for application development and execution.

## TERMINAL HOMING MISSILE APPLICATION

In a typical ground to air application of a modern hybrid computer such as SIMSTAR the math model distribution to system resources is illustrated by Figure 8. Low to medium speed control and dynamic models are typically implemented on the host processor. These models might include overall control of the simulation, aero equations, translation geometry, atmosphere, target motion, thrust, launcher motion and mass properties. The large nonlinear

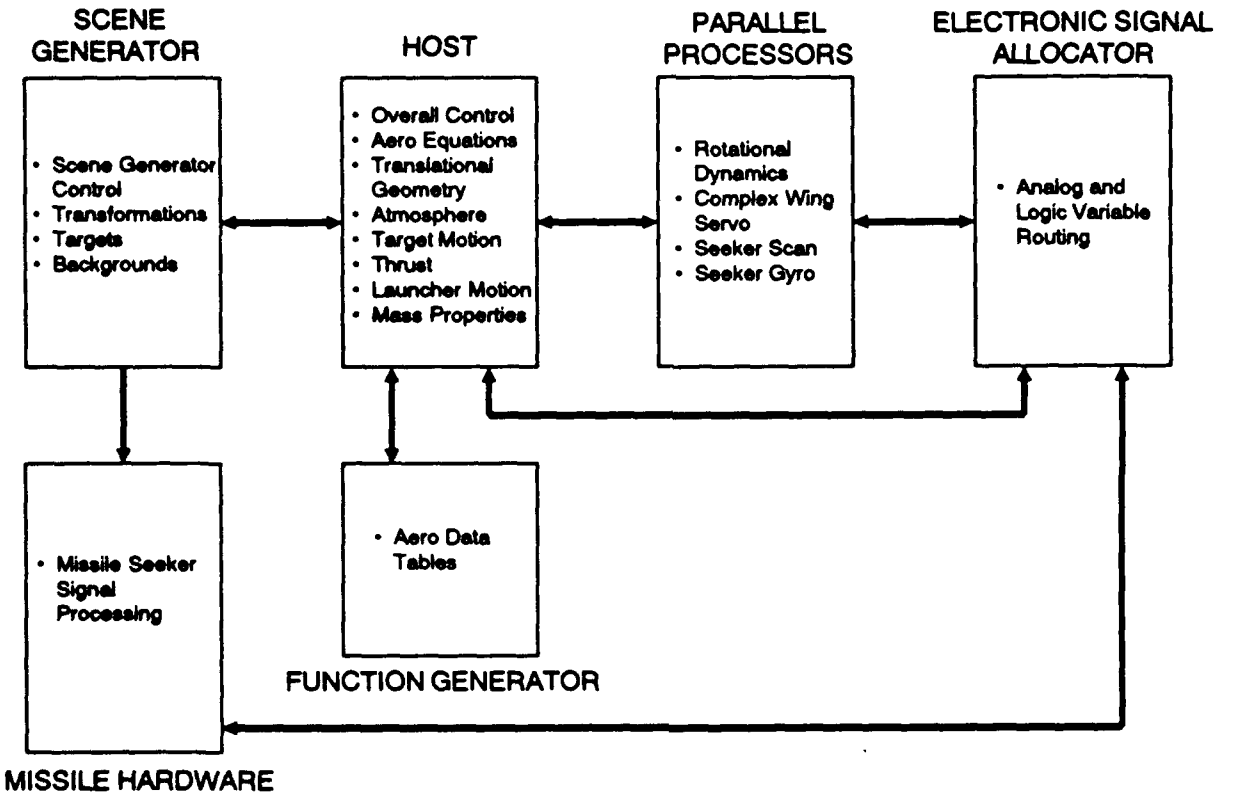


**Figure 8 - Typical SIMSTAR Terminal Homing Application**

aerodynamic tables are best suited to the function generator processor. High speed dynamic models of rotational motion, complex wing servo, seeker scan and seeker gyro are typically implemented on the parallel simulation processors. The remaining functions required to close the control loop of this type missile system simulation are implemented by providing rotational and translational variables for the targets and missile to the scene generator and its host which generates the proper image for the seeker signal processing subsystem to derive guidance commands for input to the wing servo by way of the electronic signal allocator.

## INERTIALLY GUIDED MISSILE APPLICATION

A typical ground to ground inertially guided system is illustrated in Figure 9. For a simulation of this type system all of the missile motion models are typically implemented on the host processor. Along with these motion models such models as the autopilot, launcher control, earth, guidance, mass properties, launcher motion, thrust, atmosphere, aero equations and overall simulation control are often implemented on the host. The more demanding dynmanic models such as the complex actuators, body bending and hinge moments are usually implemented on the parallel simulation processors. The complex aerodynamic data tables is typically implemented on the function generator processor and routing of analog and logic variables between the host and parallel processors is usually accomplished directly or through the electronic signal allocator.

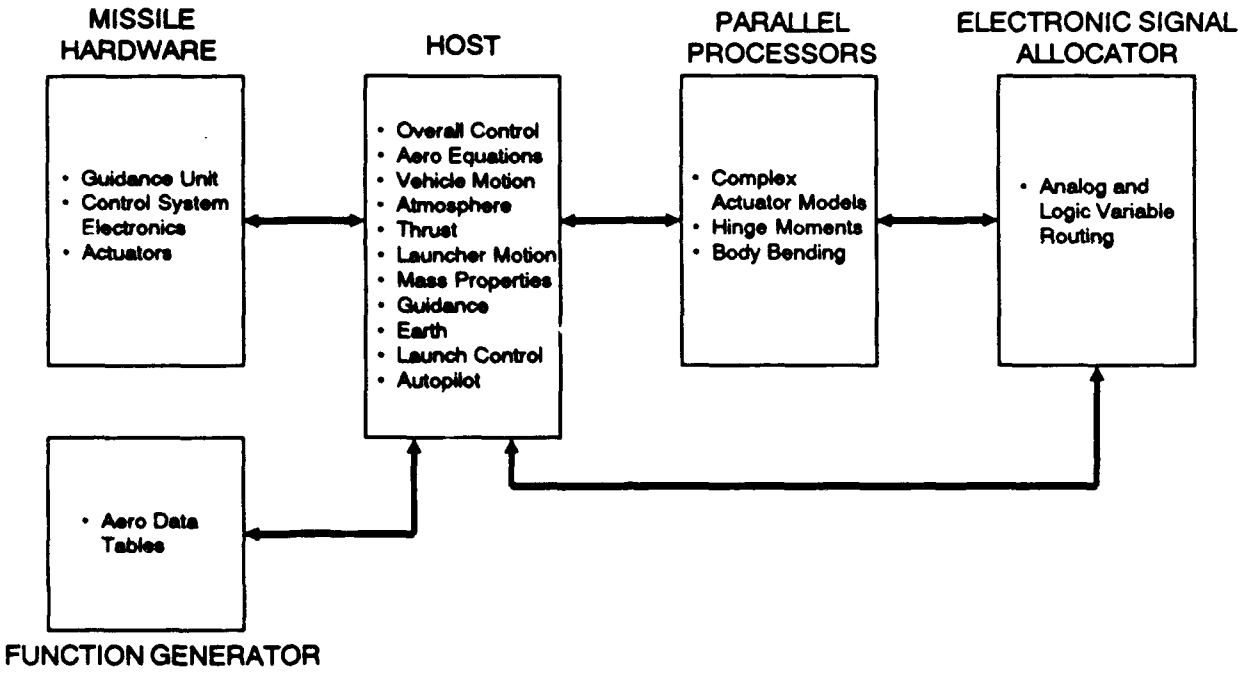


**Figure 9 - Typical SIMSTAR Inertially Guided Application**

Since some missile hardware elements such as control actuator systems can only be utilized for a limited number of simulated flights before degraded performance and the missile hardware/software may be more difficult to utilize when evaluating design changes, the validated math models are typically utilized where a large number of simulated flights are required or where studies and analysis on subsystems are required. Thus in a typical hardware-in-the-loop simulation both the missile hardware/software and the math model representations of each subsystem are provided and either may be selected. In Figure 9 several of the missile hardware/software functions are duplicated in math model implementations.

## CONCLUSION

Modern technology and increased requirement for more complex dynamic models for realtime simulation applications have resulted in a continued need for hybrid simulation processor systems. These hybrid systems now provide a powerful and user friendly tool for many applications where time critical analytical demands are high.

## REFERENCES

1. Jackson, A.S., "Analog Computation", McGraw-Hill Book Company, Inc., 1960, pp. 1-2.

2. Bekey, G.A., Karplus, W.J., "Hybrid Computation", John Wiley & Sons, Inc., 1968, pp. 3-6.

# Simulation as a Tool in Assessing Millimeter-Wave Smart Weapon Systems

Dr. James C. Bradas
U.S. Army Missile Command
Research, Development, and Engineering Center
Guidance & Control Directorate
Technology/Terminal Homing
Redstone Arsenal, AL 35898-5254

## ABSTRACT

The use of simulation as a tool in assessing weapon system performance has seen a tremendous increase in the last decade. Computer speed and memory have all contributed to the ability to build better and more complex models and simulations of weapon system components such as seekers of various types, missile and aircraft airframes, etc. The availability of high-speed mainframe computers (not necessarily supercomputers) of the Dec VAX variety and the like, have made it possible to model very complex, real-world situations involving radars, infrared seekers, RF and thermal targets and backgrounds, and the like. The increasing emphasis on the design of "smart" and/or "brilliant" munitions which use both RF and IR seekers to locate and track armored vehicles, has resulted in a need for accurate simulations capable of modeling the real-world in the laboratory in order for the engineer and algorithm designer to develop systems which can perform the extremely difficult tasks of target detection, discrimination, and tracking. The focus of all-weather "smart" munition systems in the 1980's has been using RF seekers operating in the millimeter-wave regime of the electromagnetic spectrum. In this paper, we discuss simulations currently in use at MICOM and future simulations, to be used in the assessment of performance of weapons which use millimeter-wave seekers and complex RF signal processing techniques.

## INTRODUCTION

During the past 10 years, much work has gone into the development of so-called "smart" and "brilliant" weapon systems to be used in defeating massed armor formations at beyond visual ranges. In order for a weapon to classified as "smart" or "brilliant" requires that the weapon perform many of the same functions as would normally be performed by a human operator. Many of the functions to be performed by "smart" and "brilliant" weapons include the detection and discrimination of armored target vehicles sitting in a typical European battlefield environment. Some of these weapons are designed to be fired in the general vicinity of known target formations, with the process of target location, detection, discrimination, and tracking carried out by the weapon with no human intervention or outside information. Needless to say, such performance by a machine

requires an extremely sophisticated signal processing technique which utilizes information from the sensor (whatever type) in arriving at a decision to attempt to destroy a particular target vehicle.

Of particular interest in sensor development to carry out the functions of "smart" or "brilliant" target detection, discrimation, and tracking, has been the development of active millimeter-wave seekers. Millimeter-wave seekers have many advantages over Infrared sensors, particularly in their ability to work in all-weather environments, in the presence of fog, haze, smoke, and various countermeasures which cause problems for IR. In addition, active millimeter-wave seekers do not depend on target temperature contrast with the background for target detection, and as such, are much less susceptible to simple countermeasures (such as flares or burning decoys). Because millimeter-wave sensors operate in a Radio-Frequency (RF) regime just above traditional microwave bands, radar signal processing techniques using polarimetric signature information are available to the weapon designer.

In this paper, we will briefly discuss some of the current simulations being used to evaluate millimeter-wave systems under development by MICOM.

## TARGET MODELING

Millimeter-wave sensors which perform the task of target detection and discrimination require very sophisticated signal processing techniques. Current radar techniques which are capable of such functions include various polarimetric techniques, range resolution, doppler processing, and various imaging techniques like SAR (Synthetic Aperture Radar). In order for the weapon designer to successfully design and implement a signal processing algorithm which accomplishes the necessary task at hand, it becomes necessary to test the algorithm with sensor data representative of the target and background scenario which the system is likely to encounter. Unfortunately, the availability of millimeter-wave target and background data has been extremely limited. Because of the limited amount of data of sufficient quality for the designer to work with in designing his system, the ability to accurately assess and predict which signal processing techniques are best able to accomplish system requirements. Because of a lack of target data in the early 80's, and because of the natural desire to develop a generic target signature model which would accurately predict target backscatter characteristics at all RF frequencies, much effort has been expended over the last decade to develop target signature models. Some of these models are quite detailed and complex, and require a computer of Cray-type capacities to perform signature calculations. Because of a lack of a supercomputer at RDEC, efforts were made to develop a millimeter-wave target signature model which could accurately

predict the fully polarimetric backscatter millimeter-wave signature characteristics of armored vehicles and still be fast enough to use with typical digital weapon simulations running in a VAX 11/780 environment. These efforts led to the development of a target signature model called 3DSCAT.

Many methods of predicting RF backscatter from complex objects have been developed over the years. Physical optics, the method employed in 3DSCAT, is a fairly accurate method of calculating the backscattered electromagnetic field from a complex object. Techniques must be included to include the effects of multiple reflections on the object itself, since physical optics by itself predicts only the scattered field for a single reflection. Other methods, such as the Geometric Theory of Diffraction, Physical Theory of Diffraction, Method of Moments and so on, are more accurate, but require many more calculations for complex objects. We have been able to show that for the purposes of current millimeter-wave "smart" and "brilliant" weapons, that Physical Optics provides more than a sufficient means of accurately predicting target signature characteristics. These predicted target signatures have been compared with data from real targets and have been shown to be in excellent agreement.

3DSCAT models complex targets as a complex of simple geometric shapes, called geometric "primatives", whose radar signature characteristics are well known. To model a target, one decomposes the vehicle into the following primatives.

1. Flat polygons
2. Cone frusta
3. Flat disks
4. Spheres
5. Arbitrary ellipsoids
6. Prolate spheroids
7. Oblate spheroids
8. Ring Disks or Annuli
9. Cavities
10. Toroids
11. Circular wire loops
12. Ogives
13. Top hats
14. Rectangular Slots
15. Curved Circular Cylinders
16. Cylinder/Plate Dihedrals
17. Edges
18. Dihedrals
19. Trihedrals

By specifying size, orientation, and surface reflectivity (perfect conductor or dielectric can be specified) as well as the range of aspect

angles over which each primative is visible to the radar. The coherent radar signature for each primative visible to the radar is calculated, summed coherently, and output to a data file. Several options are available as to the type of data output. One option calculates the coherent signature and outputs this data to a file. Another option ranks each scattering primative with respect to signature amplitude, and outputs this information, along with coordinate information, to a file. The 3DSCAT model is extremely versatile, and output can be easily tailored to specific needs. In addition, excellent agreement between simulation prediction and real target data has been achieved. Figure 1 shows a typical tank vehicle along with two types of reflections typically seen using a polarimetric radar. Odd reflections are the result of the radar pulse making an odd number of reflections before reflection back toward the radar, while even reflections are the result of an even number of reflections. In addition, for two target sections, namely the turret and a tool bolx on the fender, we list scattering primatives appropriate for use in modelling these portions of the target. Thus, for example, modeling the main gun on the tank might mean decomposing it into:

1. Circular cylinder (main barrel)
2. Circular cavity (opening on barrel)
3. Cylinder plate dihedral (muzzle gas evacuator)
4. Ring Disk (front of muzzle evacuator)

Figure 2 shows the various scattering primatives used in 3DSCAT. Figure 3 and 4 show the signature characteristics as a function of aspect angle for a right-angle dihedral with side lengths as shown at 35 GHz for both linear and circular polarizations. Figures 5 and 6 show a 1 meter long edge as a function of aspect angle in a plane perpendicular and parallel to the edge surface, respectively, at 94 GHz. Figure 7 shows a 5.5 cm circular disk at 94 GHz. Figure 8 shows a 2 cm by 2 cm top hat at 92.7 GHz. Figure 9 shows a 1 meter long circular cylinder at 94 GHz. Figures 10 through 12 show various samples of polar signature plots of typical main battle tanks. Figure 12 shows a comparison of real data (top), with frequency averaged data (left side) and single frequency (right side). Figure 13 shows a typical output file which contains a ranked (from highest to lowest) scattering primatives. Figure 14 shows a typical output in which target glint (apparent centroid of all scattering primatives making up the target) is plotted at 64 different frequencies, typical of a frequency agile radar. Figure 15 shows a table comparing model prediction with real target data of 6 different polarimetric features for a main battle tank. Again, it can be seen that agreement between simulation and real target data is excellent.

## FUTURE DIGITAL SIMULATIONS

Although we have focussed on target modeling in this paper, a realistic simulation capable of representing real-world conditions to a millimeter-wave seeker must be capable of presenting target and background signatures to the radar/seeker model. Since clutter modeling at millimeter-wave frequencies is not nearly as advanced as is the case with target models, problems still remain in using all digital simulations of seeker, target, and background in the assessment of weapon system performance.

One simulation which is in the beginning stages at MICOM will use Synthetic Aperture Radar (SAR) collected by MIT/Lincoln Lab using a 35 GHz radar. This SAR data is fully polarimetric and images a scene with a resolution of 1 foot by 1 foot. Typical scenes include both targets sitting in grassy fields, targets near tree-lines, and targets on dirt and paved roads. Since scenes which contain both targets and surrounding clutter have all target and clutter interactions "built into" the data, this type of target/background signature model would represent a completely realistic database for use by the radar/seeker model.

Our current plans in building a realistic all-digital millimeter-wave simulation are as follows. A typical scene consisting of an armored vehicle in representative clutter will be chosen. This millimeter-wave database consists of a 400 meter x 400 meter array of point scatterers placed at 1 foot intervals in both downrange and crossrange. Each array element contains the full polarimetric scattering matrix associated with that particular scatterer. Before this database is interfaced with the radar model, a geometric model of the target contained in the scene will be layed over the database at the correct aspect angle. The scatterers in the scene which correspond to the target will be given a z-direction (up) coordinate by determining where each target scatterer touches the top of the geometric model of the target. After this has been done, the polarimetric data will be transformed into whatever polarimetric basis is appropriate (the SAR data is linearly polarized). This database will be used to "feed" into the radar/seeker model contained in the simulation. By using such a database, it should be possible to simulate both the target search and terminal homing phase of a millimeter-wave "smart" munition.

Figure 16 shows a color photograph of one of these SAR images received from MIT/LL. The image on the left is the SAR image taken with a resolution of 1 meter by 1 meter. The image on the right is an optical photograph taken of the same scene. It can be seen from the SAR image that individual background objects are clearly identifiable (see, for example, lines in the plowed field, trees, and roads). Figure 17 contains an enlargement of the lower left-hand corner of the SAR image showing trees and a portion of plowed fields. Clearly visible in

the image is a road which winds through the trees from right to left and then down. Also clearly visible are the shadows due to the trees (the radar is looking from the top of the SAR image down toward the bottom of the image). Figure 18 shows an enlargement of a farm-house which is also contained in the scene. Again, trees and roads, as well as lines in the plowed field are clearly visible. In addition, the roof and roof-line are visible in the approximate upper center of the image.

Figure 19 shows a geometric model of an M-47 tank. This type of model will be used in associating a z-direction (up) with target vehicle scatterers contained in the SAR image. Although no plans are currently in place to associate terrain elevation with the background scene, this will be a future avenue of research.

## CONCLUSIONS AND RECOMMENDATIONS

It is clear that the development of realistic millimeter-wave target and background simulations presents a clear challenge to current modelers. It is also clear that such simulations are desperately needed in order to successfully evaluate and investigate newer and better signal processing techniques designed to detect, discriminate, identify, and track armored vehicles. The cost of real-world data gathering can be prohibitively expensive, possible under only very controlled and ideal weather conditions. Simulation is the only other viable and cost-effective alternative to the successful development of current and future millimeter-wave munitions..

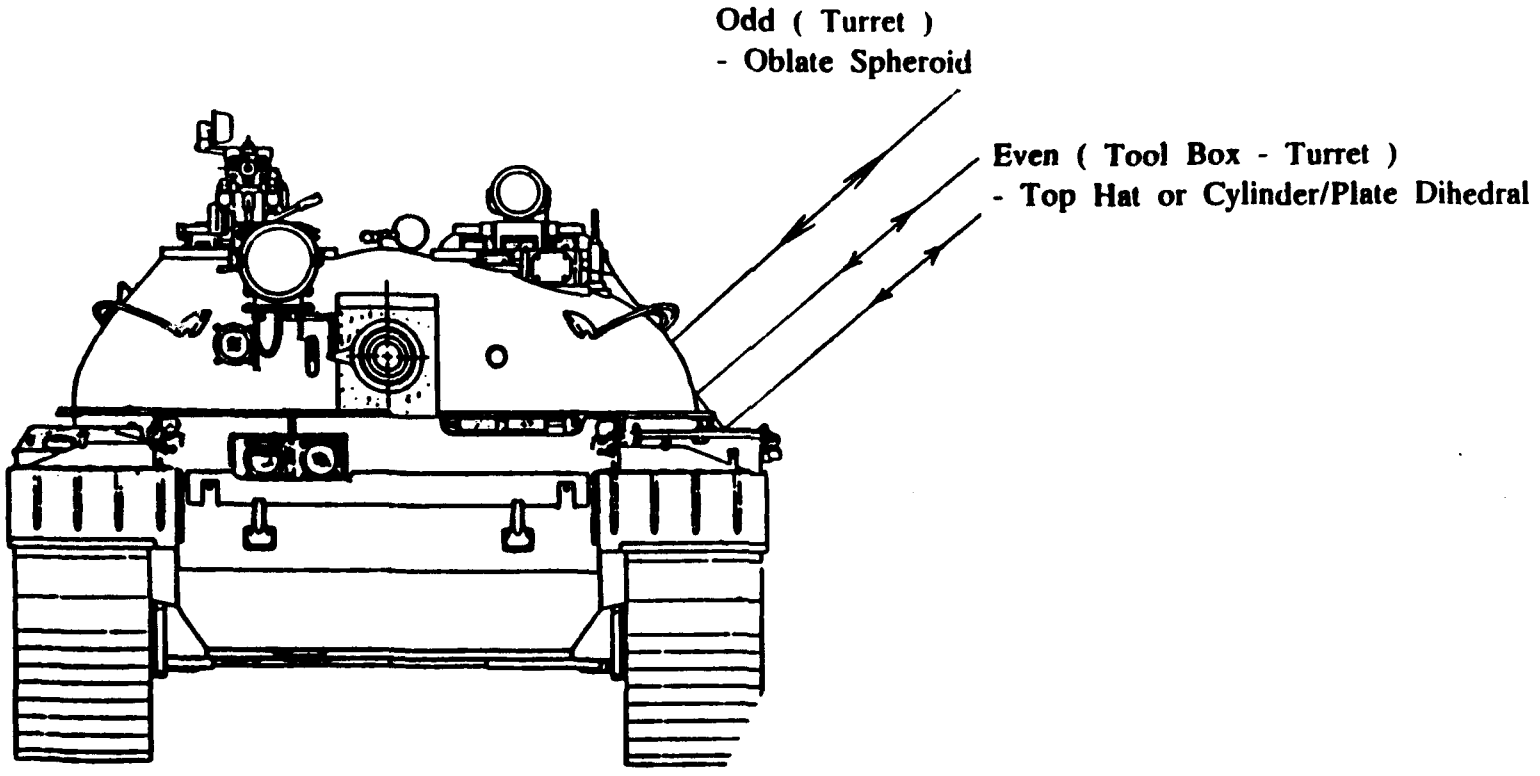


Figure 1. Examples of Reflection Types and Geometric Primatives Used to Model a Complex Target.

## 3DSCAT - SCATTERING CLASSIFIERS

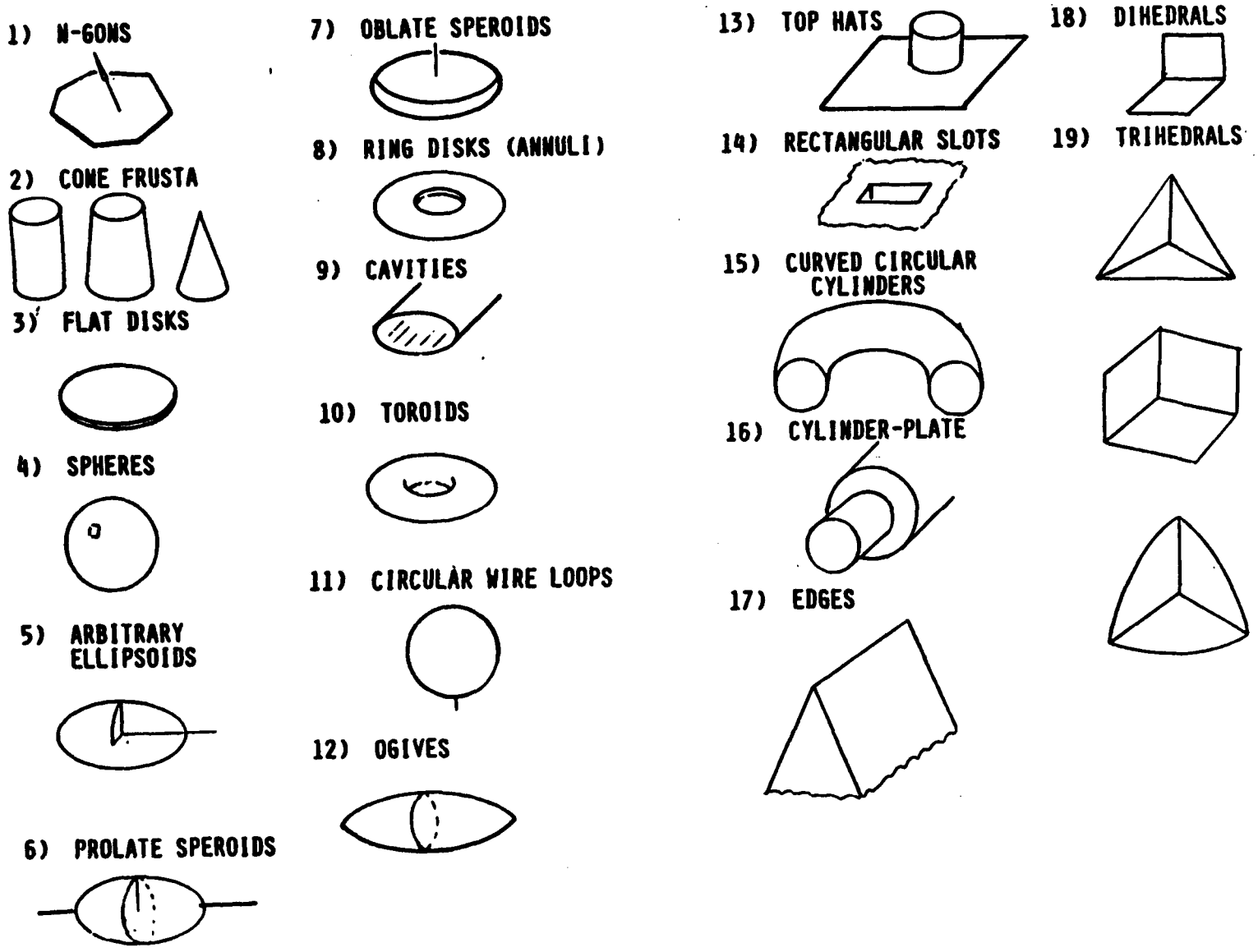


Figure 2. Scattering Primatives.

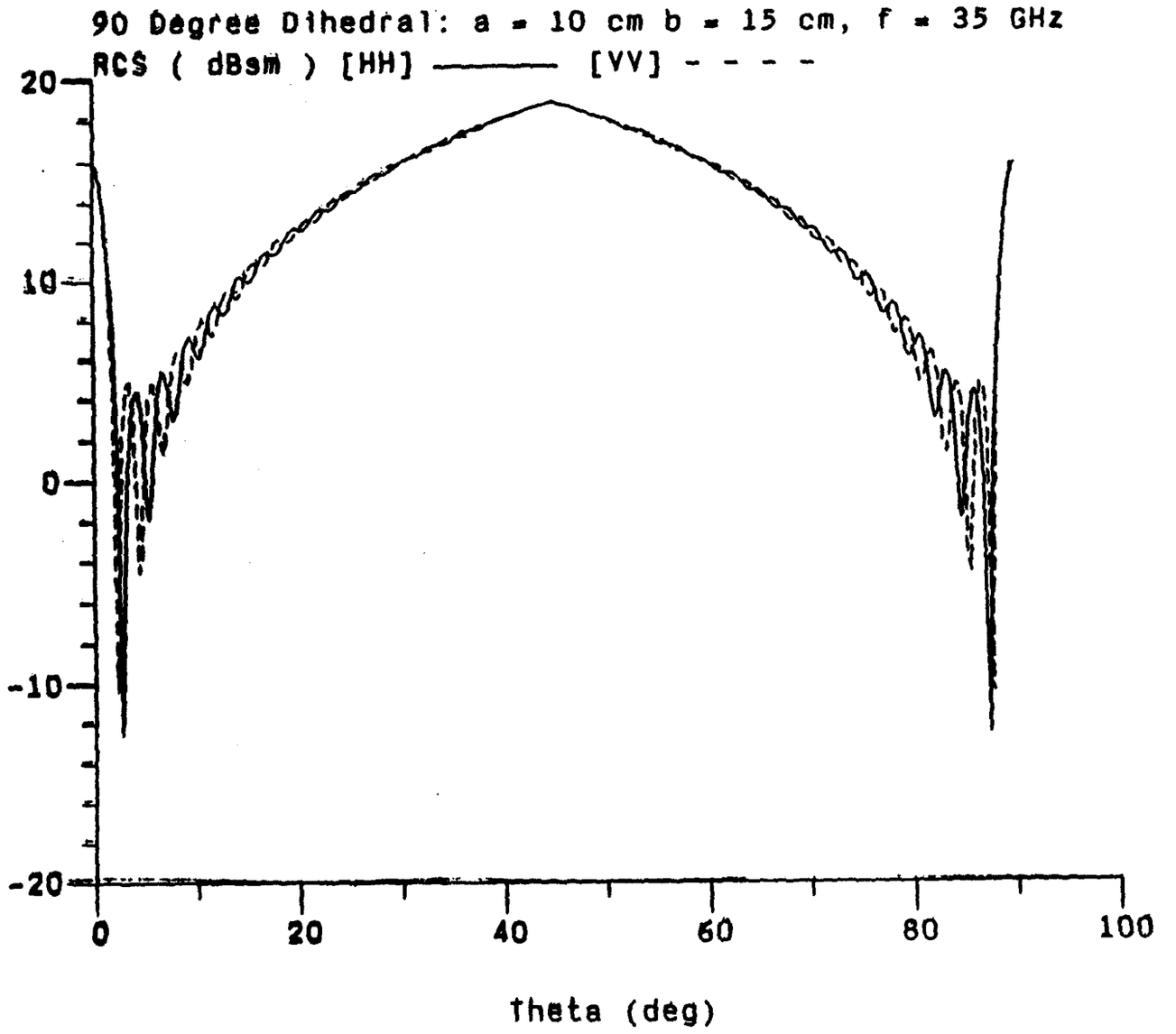


Figure 3. 90 Degree Dihedral RCS, Linear Polarization.

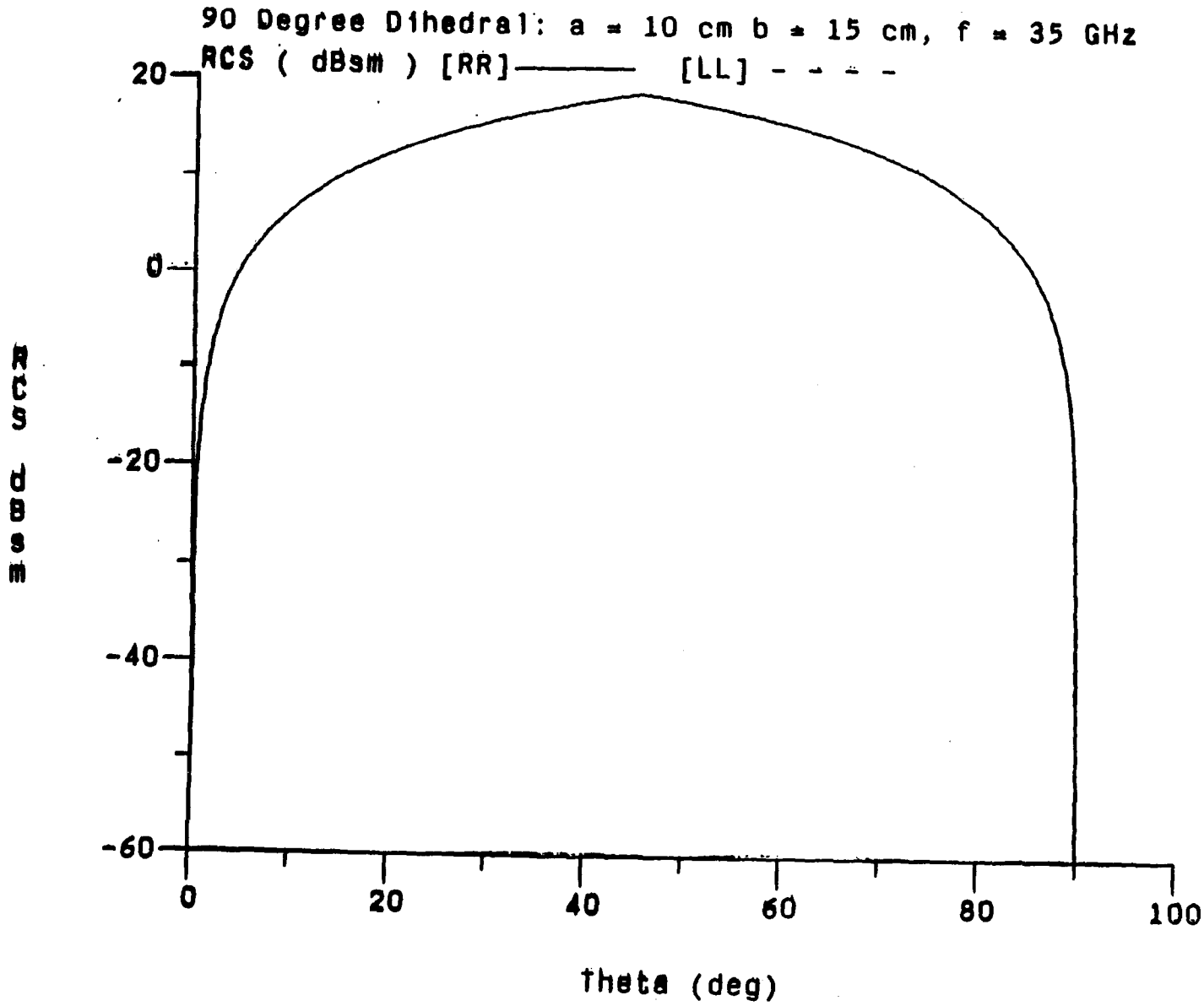


Figure 4. 90 Degree Dihedral RCS, Circular Polarization.

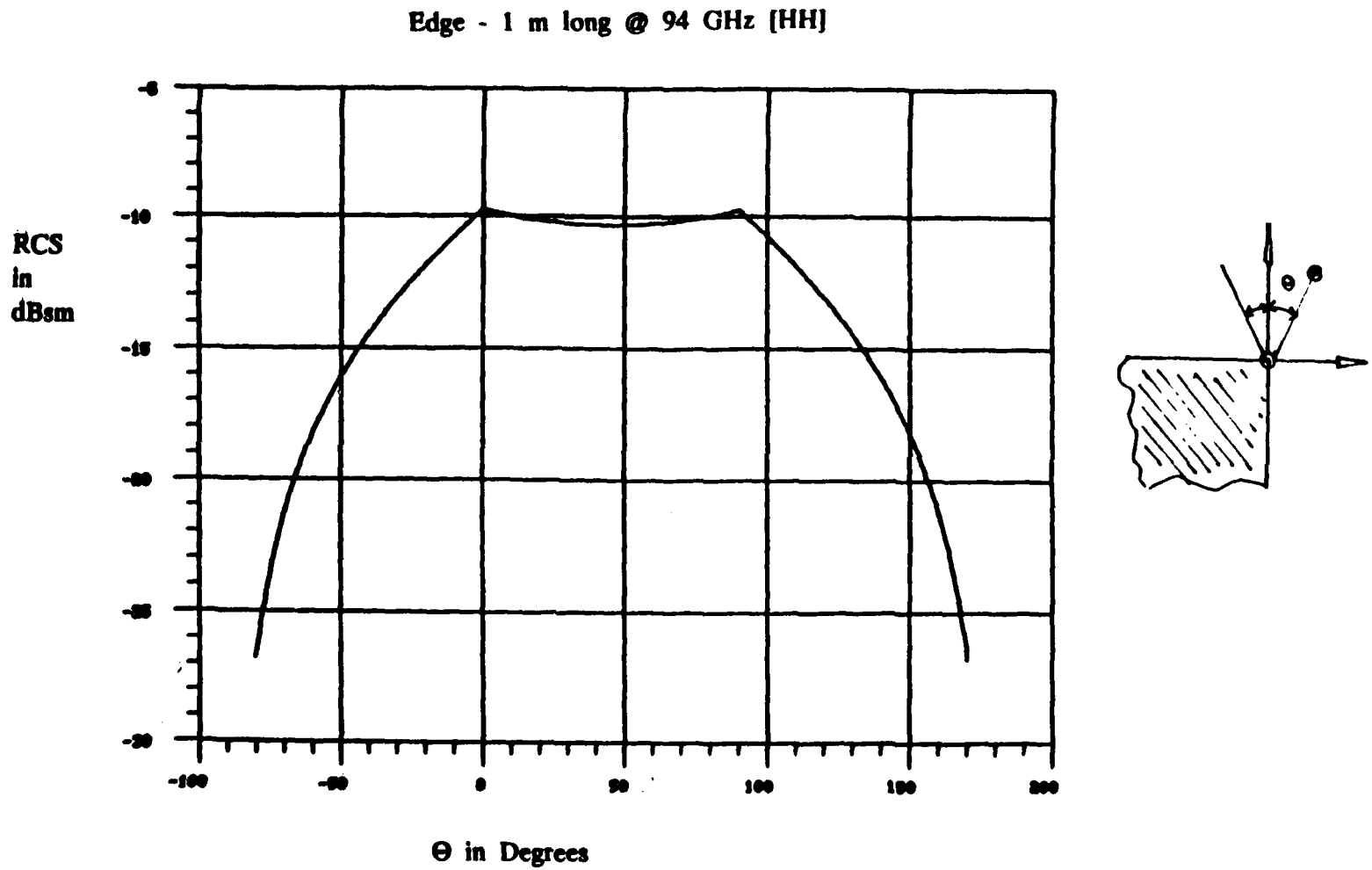


Figure 5. 90 Degree Edge RCS, Linear Polarization.

## Examples of 3DSCAT ( Version 2.0 ) RCS Calculations

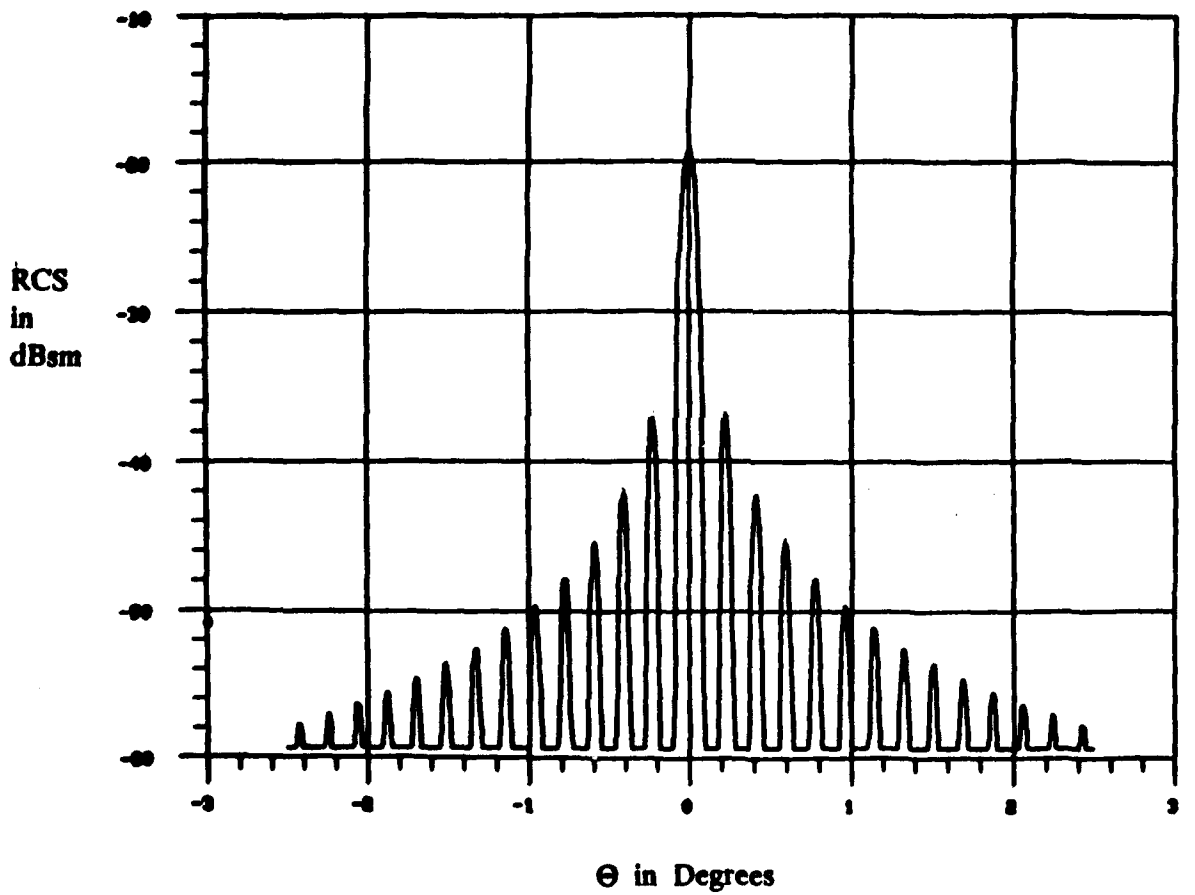


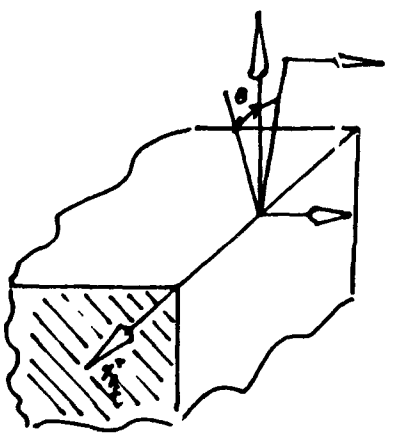

Figure 6. 90 Degree Edge RCS, Linear Polarization.

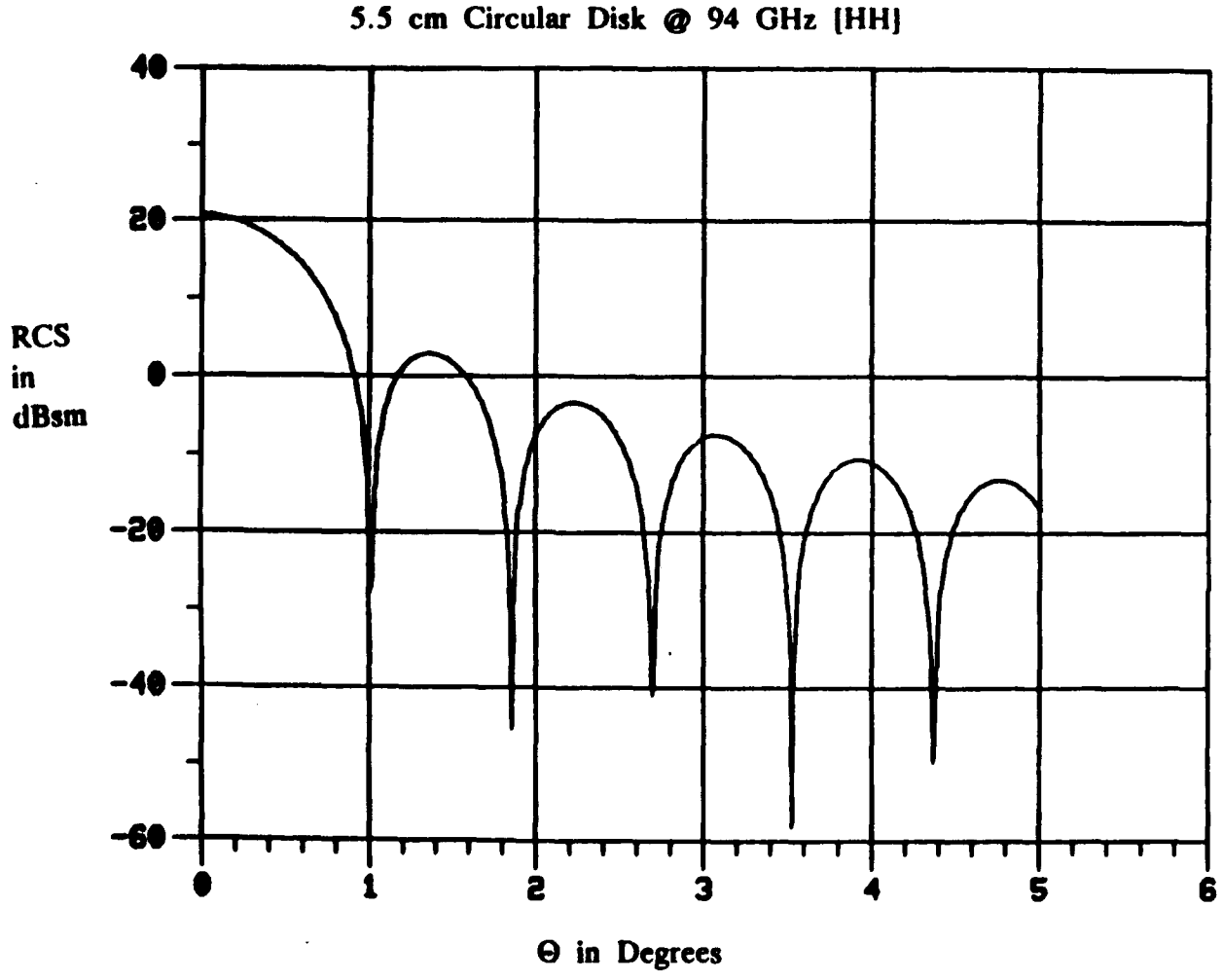


Figure 7. Circular Disk RCS, Linear Polarization.

## Examples of 3DSCAT ( Version 2.0 ) RCS Calculations

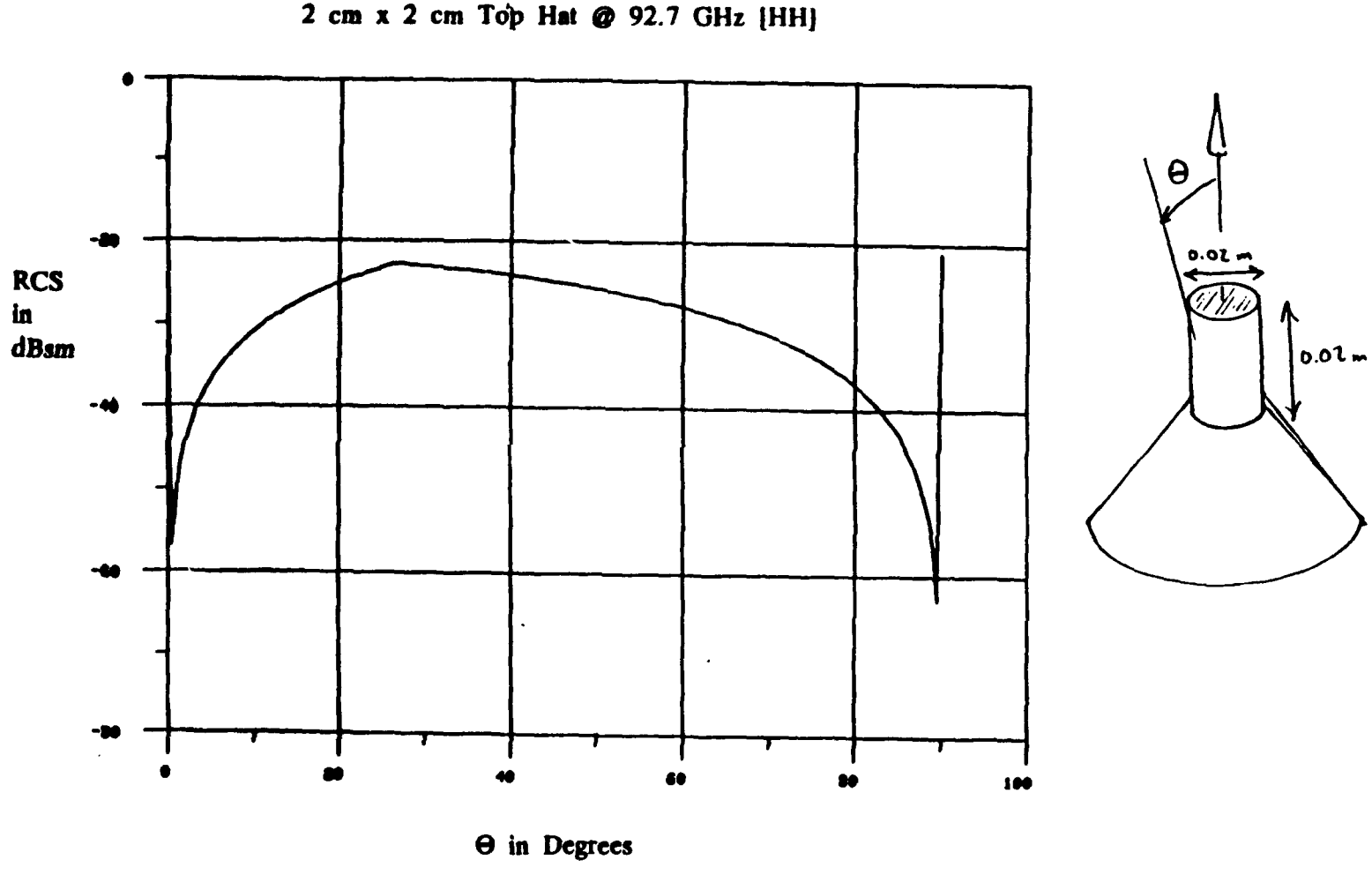


Figure 8. Top Hat RCS, Linear Polarization.

## Examples of 3DSCAT ( Version 2.0 ) RCS Calculations

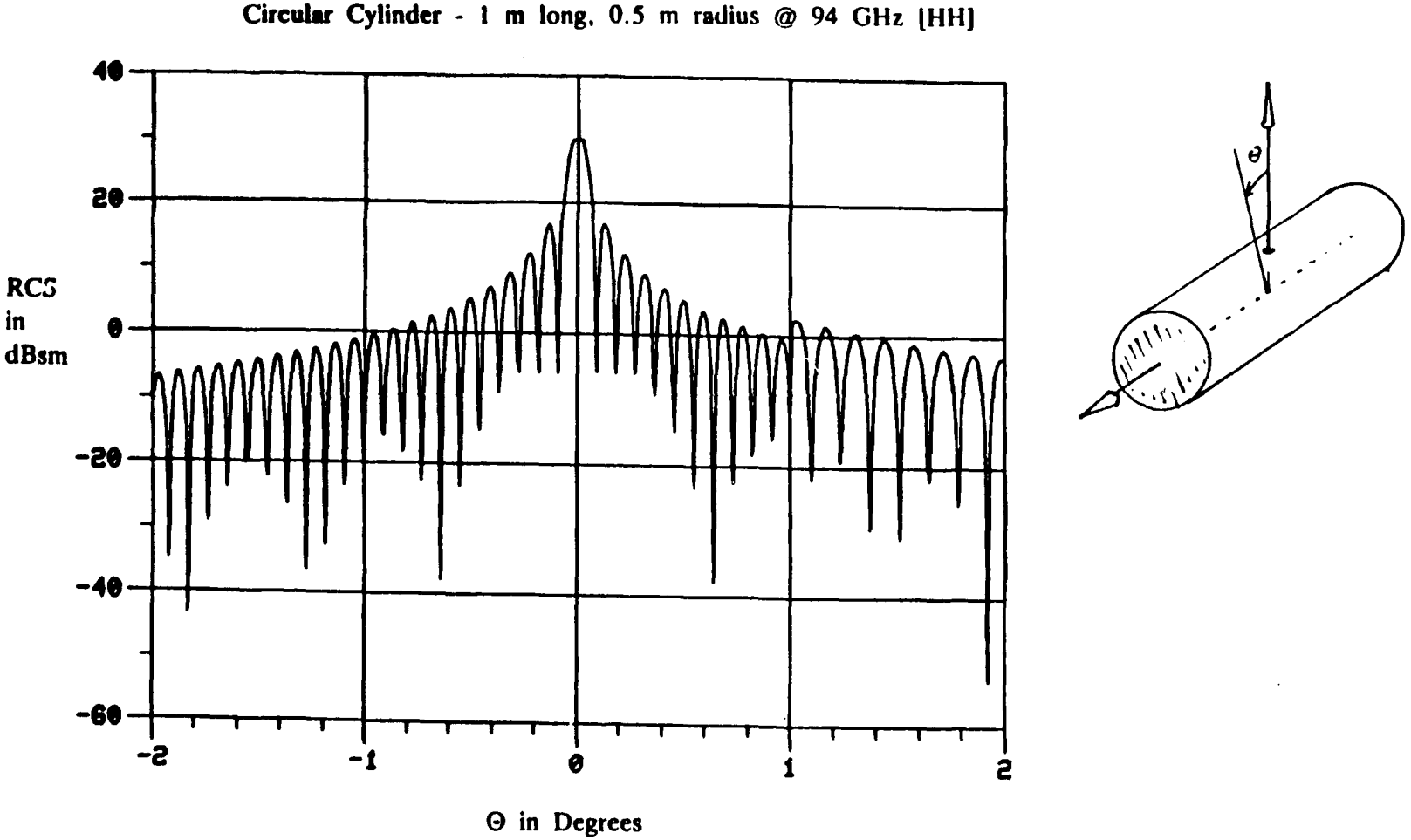


Figure 9. Circular Cylinder RCS, Linear Polarization.

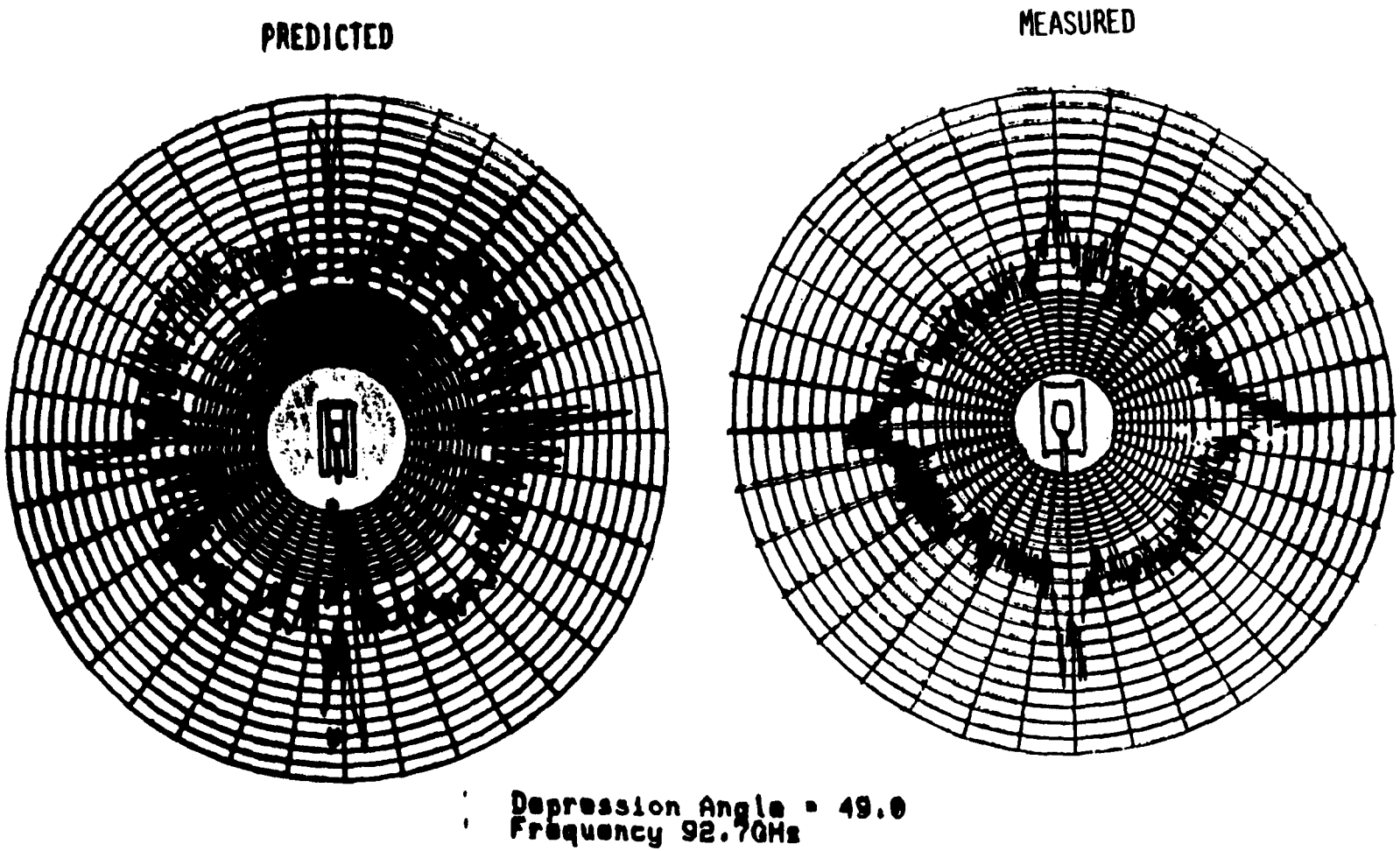


Figure 10. Comparison of 3DSCAT RCS vs. Measured RCS of Main Battle Tank.

RCS in dBsm

PREDICTED

MEASURED

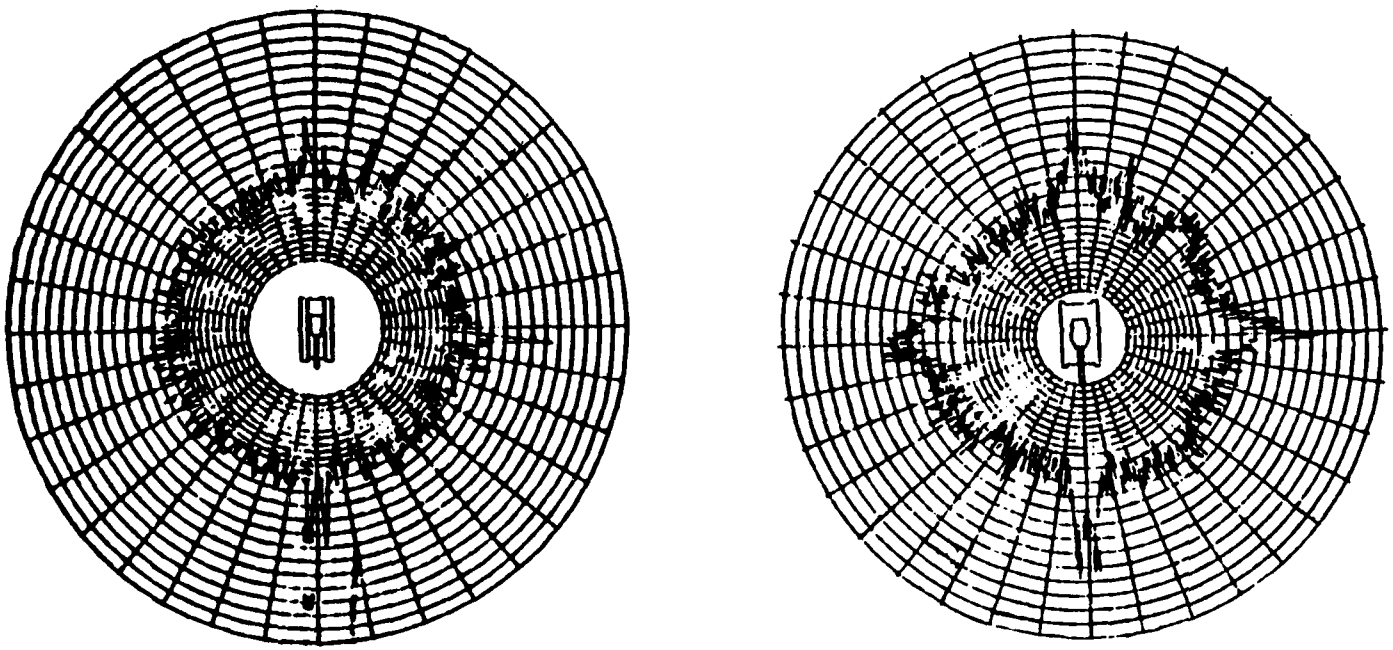

92.7 GHz
49 Degree Depression Angle
HH

Figure 11. Comparison of 3DSCAT RCS vs. Measured RCS of Main Battle Tank.

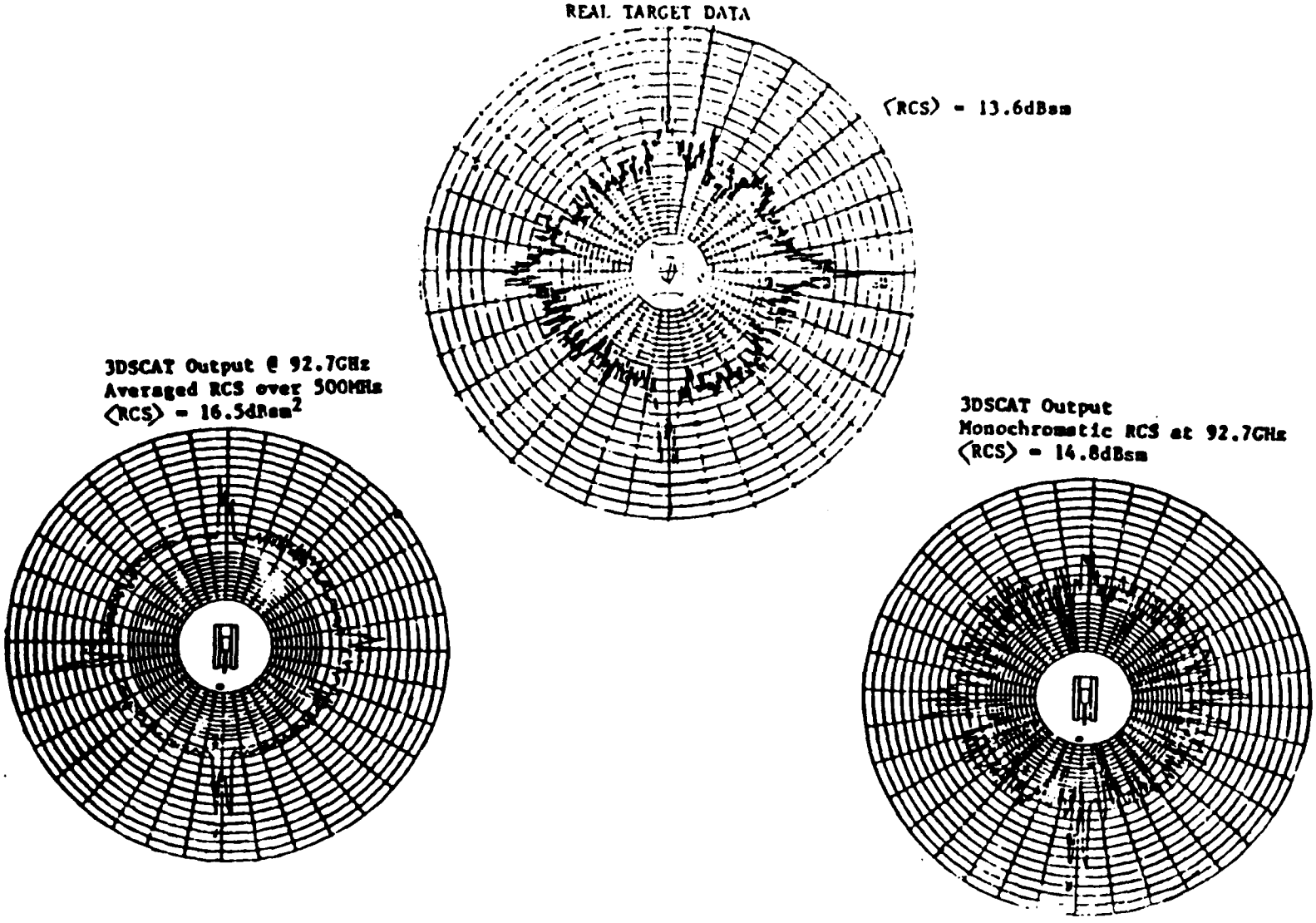


Figure 12. Comparison of 3DSCAT RCS vs. Measured RCS of Main Battle Tank.

3DSCAT Output: Detailed Scatterer Information
Scatterers > 0.01 m2

Target ID: Main Battle Tank
Frequency: 92.7 GHz
No. Samps: 1
Depress : 49.0 Degrees
Azimuth : 85.0 Degrees
Single Frequency Pulse Data
Pulse Number: 1
Linear RCS : 13.176 m2
Odd RCS : 14.056 m2
Even RCS : 13.001 m2

| No. | Type | No. | Part Name | RCS(m2) | RCS(dBsm) | X(m) | Y(m) | Z(m) |
|---|---|---|---|---|---|---|---|---|
| 1 | Dihedral | 52 | Hull Flange | 27.04 | 14.3 | 2.4 | 0.0 | 1.1 |
| 2 | Frusta | 45 | 5th Section | 18.57 | 12.7 | 2.7 | 0.0 | 1.0 |
| 3 | Obl Sph | 1 | Turret Structure | 7.68 | 8.9 | 0.0 | 0.0 | 1.0 |
| 4 | Trihedral | 13 | Hull Flange | 3.13 | 5.0 | 2.4 | -0.9 | 1.1 |
| 5 | Slot | 1 | Blackout Shield | 2.35 | 3.7 | 2.5 | -0.5 | 1.1 |
| 6 | Top Hat | 9 | Turret/Hull Dbl Bnc | 1.56 | 1.9 | 0.0 | 0.0 | 1.7 |
| 7 | Gen Ellip | 1 | Search Light | 0.83 | -0.8 | 1.3 | -0.5 | 2.0 |
| 8 | Cyl Plt Dih | 2 | Snorkel | 0.80 | -1.0 | -1.5 | -0.1 | 1.7 |
| 9 | Frusta | 33 | Blackout Shield | 0.66 | -1.8 | 2.5 | -0.5 | 1.4 |
| 10 | Sphere | 2 | Commander Hatch | 0.53 | -2.8 | -0.5 | 0.1 | 2.2 |



Figure 13. RCS of Scattering Primatives of Main Battle Tank.

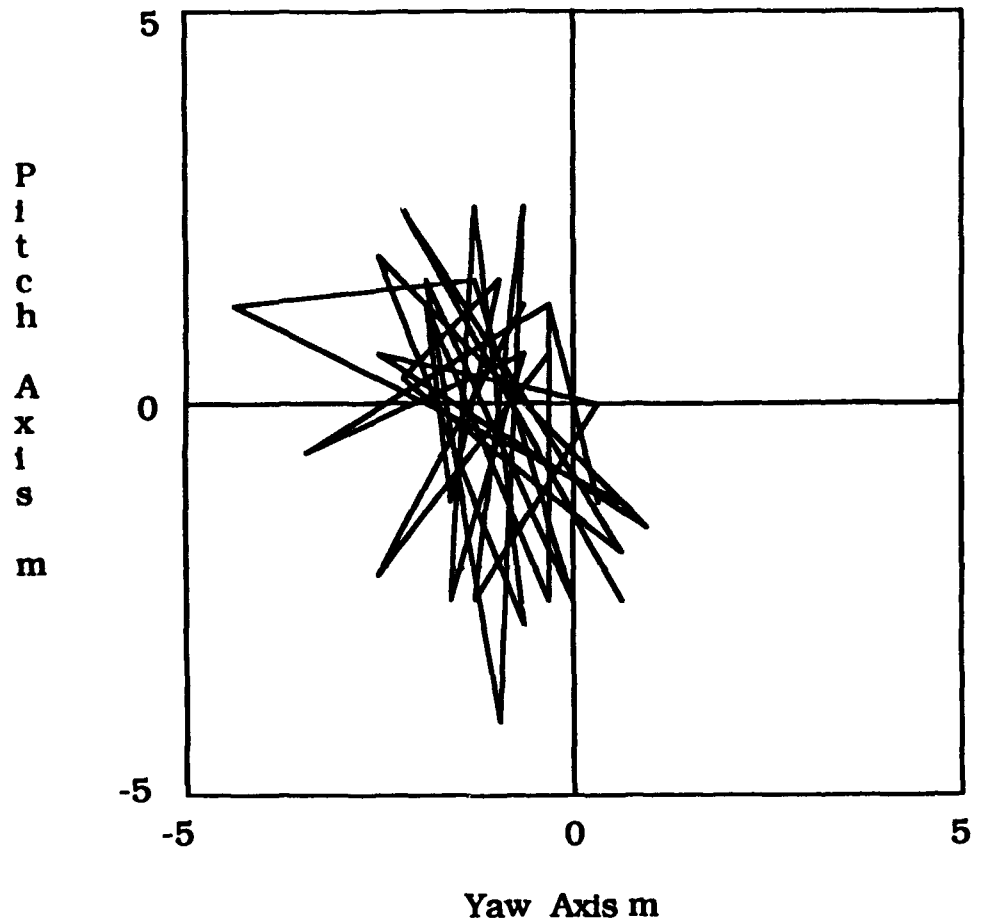


Figure 14. Target Glint Measured in Target Coordinates in Pitch and Yaw.

| Feature No. | | Cerberus ( TABILS 13 ) | 3DSCAT | Difference |
|---|---|---|---|---|
| 1 | Total DC | 15.9 | 14.2 | 1.7 |
| 2 | Odd/Even | 1.6 | -1.0 | 2.6 |
| 3 | In/Out Odd | 2.4 | 3.4 | 1.0 |
| 4 | In/Out Evn | 1.6 | 2.6 | 1.0 |
| 5 | In/Out +Pr | 2.1 | 4.2 | 2.1 |
| 6 | In/Out -Pr | 2.8 | 2.1 | 0.7 |

All 6 Features within 3 dB or less
3 Features within 1 dB or less

Figure 15. Table Comparison of Signal Processing Features Generated by 3DSCAT vs. Real Main Battle Tank Date from Cerberus (TABILS 13).

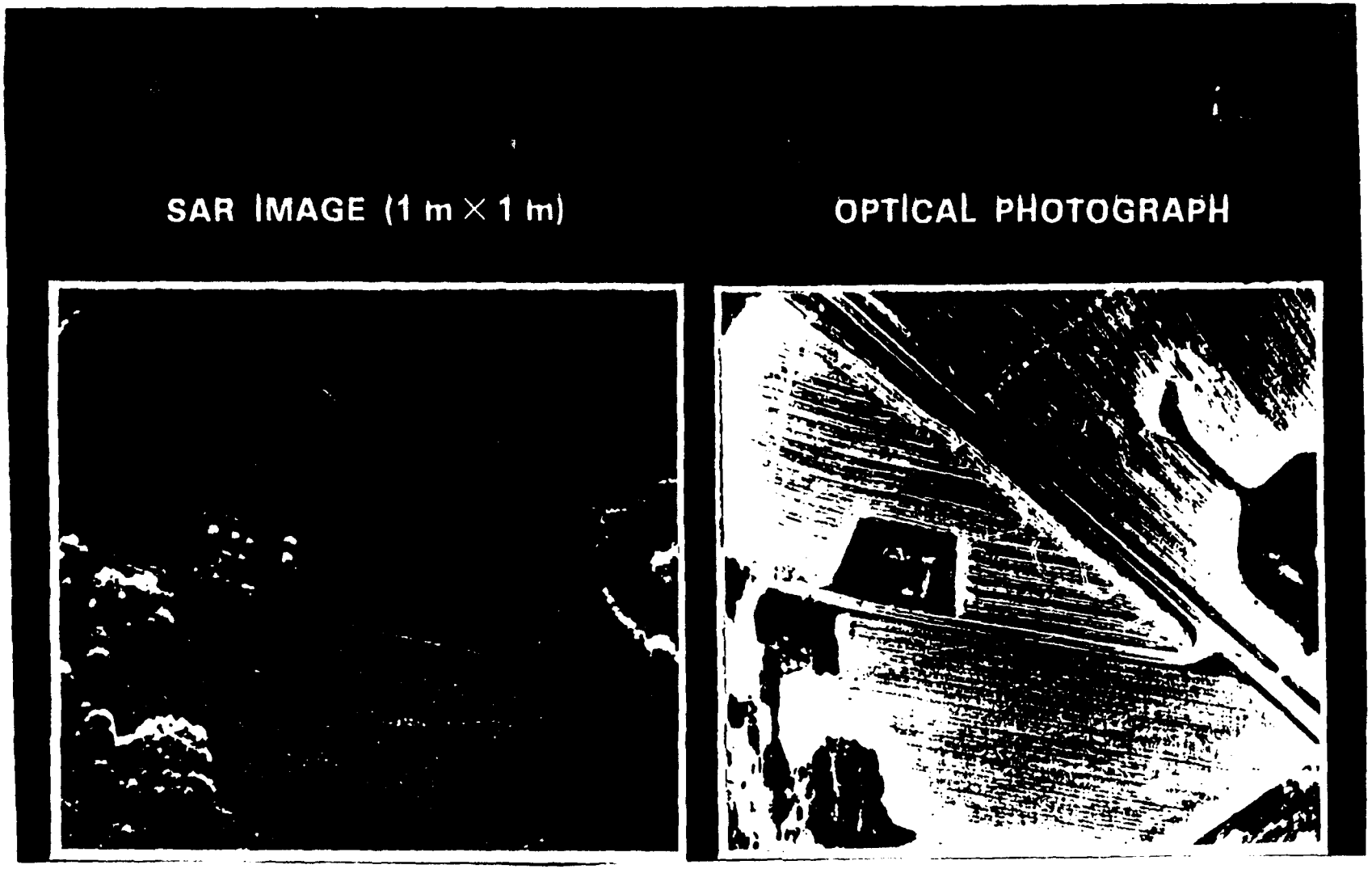


Figure 16. SAR Image vs. Optical Photograph at 35 GHz Obtained from MIT/Lincoln Laboratories.

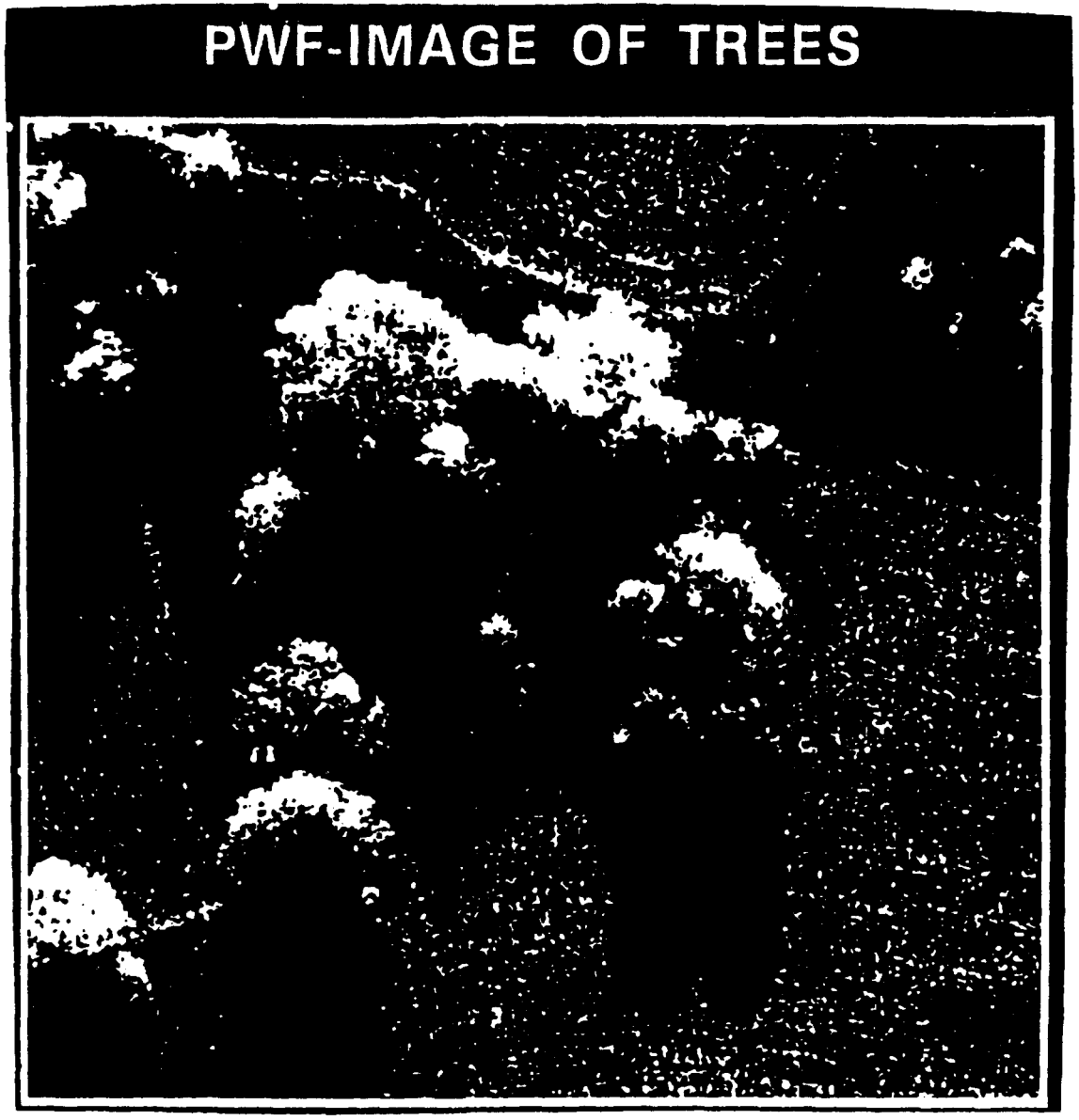


Figure 17. Enlargement of SAR Image of Trees at 35 GHz Obtained from MIT/Lincoln Laboratories.

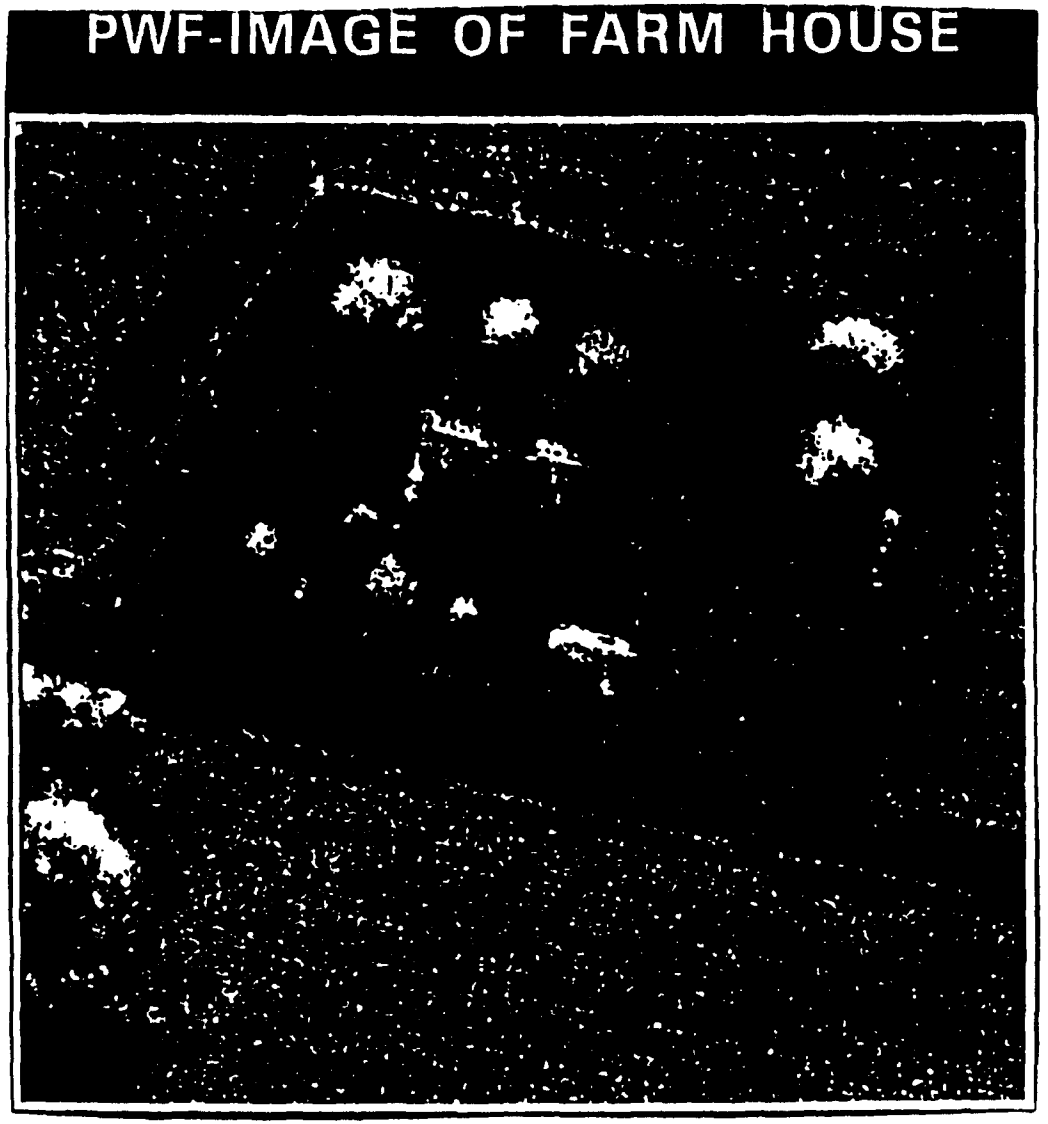


Figure 18. Enlargement of SAR Image of Farmhouse at 35 GHz Obtained from MIT/Lincoln Laboratories.

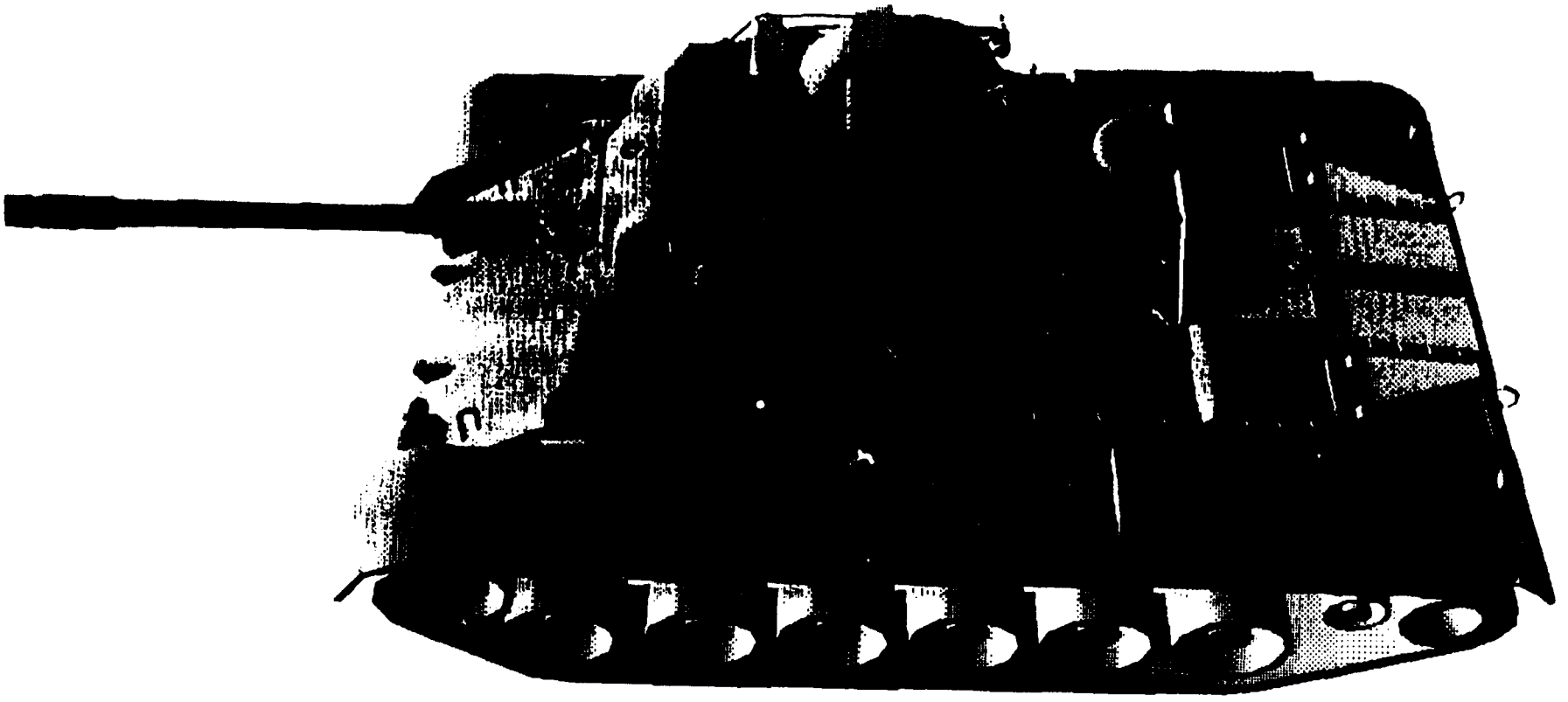

Figure 19. Geometric Model of M-47 Tank.

# CFD in Tactical Missile Aero-Propulsion Technology

Clark D. Mikkelsen, Kevin D. Kennedy, and Billy J. Walker
US Army Missile Command
Redstone Arsenal, Alabama

## ABSTRACT

PARCH, a fully elliptic, three-dimensional, two-phase (gas-particle), Navier-Stokes flow solver has been developed to model combined tactical missile external flow/plume flowfields with turbulent mixing and finite-rate chemistry. This paper describes the PARCH code capabilities, shows the results for three code validation cases, and demonstrates the potential PARCH contribution to tactical missile aero-propulsion technology with the solution for a transonic missile with bifurcated propulsive nozzles, blunt nose, and a large base.

## INTRODUCTION

One long standing weakness in the state-of-the-art of tactical missile aero-propulsion interaction technology has been the ability to model combined missile and rocket exhaust plume flowfields even though total flowfield solutions are fundamental to the prediction of vehicle aerodynamics, missile/plume signature, and plume/signal interference.

Combined missile external flow/plume flowfields have been difficult to model because of the complexity of the physical processes that occur. These include aerodynamic flow separation of the missile afterbody boundary layer due to the high pressures at the rocket nozzle exit plane; the recirculation, mixing, and chemical reaction in the the base region; the mixing, complex shock structure, and afterburning of the fuel rich rocket exhaust in the near plume region; and the mixing in the far plume region. These difficulties are further increased by three-dimensional effects due to angle-of-attack, multiple exhaust nozzles, or bifurcated nozzles, and the two-phase, gas-particle constituents of most tactical missile rocket exhaust plumes.

The technical approach taken toward resolution of this shortcoming in flowfield prediction capability has been to use proven numerical methods of computational fluid dynamics (CFD) and apply them successively to this problem; i.e. to build on a known flowfield code while adding the capability to handle more complex physical processes with each step. Running jointly with

---

Approved for public release: distribution is unlimited.

this model development effort has been a program to verify the methodology for each process using simpler validation cases based on experimental measurements or known analytical solutions. This joint approach insures that each step in the development process accurately models the physical phenomena while reducing the risks inherent in code development.

The objective of this paper is to describe the capabilities incorporated into PARCH, the missile external flow/plume flowfield model developed under this program, to show the results of three simple code validation cases, and to demonstrate the full PARCH potential with the solution for a complex but realistic tactical missile configuration.

## PARCH MODEL

The PARCH Navier-Stokes code is based on the ARC code developed at NASA Ames Research Center by Pulliam and co-workers and subsequently upgraded to the PARC code for generalized grid blanking/boundary conditions by Cooper at Arnold Engineering Development Center, AEDC[1]. PARCH incorporates several upgrades to the original ARC methodology with regards to thermochemical capabilities, multi-phase gas-particle non-equilibrium flow, turbulence modeling, numerical algorithms, and grid handling. As such, the PARCH model contains rather broad based capabilities and has been applied to rocket and scramjet propulsive flowfields, and to aerodynamic, reentry wake, and film cooling problems.

Code upgrades to Parch provide significant flexibility. The choice of algorithms include central difference, 1st order upwind Roe schemes, and 2nd order upwind Roe schemes with TVD extensions. The basic algorithm is solved with either the diagonalized or banded block tridiagonal matrix inversions techniques. Thermochemical options include perfect gas, equilibrium air, one-step complete combustion, generalized multi-component finite-rate chemical kinetics, and thermal equilibrium. inviscid, laminar, or turbulent viscosity models may be specified with PARCH, but the original Baldwin-Lomax algebraic turbulence model has been replaced with the two-equation Chien low Reynolds number $\kappa$-$\varepsilon$ model with corrections added for compressibility and curvature. In addition, a generalized multi-zoning or grid blocking capability has been implemented for the analysis of tactical missile flow problems of extreme geometric complexity.

The governing Navier-Stokes equations use conventional implicit time stepping and linearization procedures. Approximate factorization is utilized to cast the equations into the conventional delta or strong conservation law form. The code can treat two-dimensional planar, two-dimensional axisymmetric, and

three-dimensional forms of the equations. Artificial viscosity is added both implicitly and explicitly and follows the switched fourth-order and second-order form of Jameson. Variable spatial and temporal time-steps are used for improved algorithm efficiency and robustness.

## GRID GENERATION

Experience has shown that obtaining a numerical solution to the Navier-Stokes equations for a given flowfield is as equally dependent on the grid which defines the flowfield as on the algorithm which represents the fluid dynamic equations; i.e., a poorly constructed grid may never give a valid solution regardless of the flow solver. Factors which determine the relative merits of a given grid include (1) the total number of grid points, (2) packing of the grid points to resolve specific features of the flowfield, (3) skewness of the grid lines, particularly at grid boundaries, (4) the ratio of width to height to depth of the cells formed by the grid points, and (5) the location of the grid boundaries relative to specific features of the flowfield. Furthermore, grid generation is rarely a one step process, but rather a continuous refinement through packing to resolve shock waves, boundary layers, and other features of the flowfield as they develop.

The grid generation code chosen for use with PARCH was INGRID, an interactive, user-oriented code designed to generate two-dimensional and three-dimensional computational grids for flow solvers such as the PARCH code. INGRID uses several techniques either separately or in combination to generate grids for arbitrary geometries. The computational mesh is formed using algebraic and/or partial differential equation methods with proper forcing functions. User defined grid clustering is accomplished with either exponential or hyperbolic tangent routines that allow for a desired grid point distribution. Grid optimization is accomplished using an elliptic solver and/or variational methods[2,3].

## PARCH CODE VALIDATION CASES

The following three flowfield calculations were completed as PARCH code validation cases. The cases were chosen because they represent fundamental fluid dynamic problems with known analytical solutions or experimental measurements for validation comparisons. These cases do not in any way validate the PARCH model for all possible flowfield conditions. Rather, validation is a process which adds credibility to the model as more validation cases of wider range and complexity are successfully completed. Quality validation cases, however, are difficult to

obtain for anything but the most simplistic configurations since more complex validation tests are restricted by cost, instrumentation, and technical problems.

## SUPERSONIC INVISCID FLOW OVER A WEDGE

The first case chosen for code validation was a simple, two-dimensional, supersonic wedge flow configuration since solutions for the shock angle are given by compressible, isentropic flow theory. The specific case was a sharp wedge inclined at 15 degrees to a Mach 6 air ($\gamma = 1.4$) free stream.

The grid defining the flowfield over the wedge of interest is shown in Figure 1. The wedge is 9 units long and 2.41 units in height at the base giving a wedge angle of 15 degrees. The grid extends 0.5 units in front of the wedge tip and rises to 5 units above the wedge centerline at the base. There are 250 grid points along the axis parallel to the wedge centerline and 100 grid points extending normal to the wedge surface. Grid points were packed toward the wedge surface in the normal direction and toward the wedge tip in the longitudinal direction. The outer boundary of the grid represents the freestream and was located far enough away from the wedge surface so as not to interfere with the shock emanating from the wedge tip. The grid shown in Figure 1 is an end product, not an initial guess, and was based on both experience with the PARCH code and a priori knowledge of the theoretical shock location based on two-dimensional shock tables. No special attempt was made to pack grid points so as to better resolve the shock.

PARCH was compiled and executed for this wedge flow configuration on a 64-bit word length machine. The initial flowfield, as defined by the density, velocity components, and energy at each grid point, was given as a uniform Mach 6 flow parallel to the wedge centerline. For this case, PARCH was run in an Euler or inviscid mode; hence, the initial flowfield conditions and the reference conditions are not unique, and any consistent set of conditions fixing a Mach 6, $\gamma = 1.4$ freestream and uniform Mach 6 initial flowfield condition should give identical results.

The results for the PARCH wedge flow calculations are shown in the Mach number contours of Figure 2. The computed shock angle is at approximately 23 degrees which is consistent with the theoretical solution from the two-dimensional shock tables[4].

## SUPERSONIC TURBULENT FLOW OVER A CONE

The second case chosen for code validation was a simple, axisymmetric, supersonic flow over a sharp, 7 degree half-angle cone. Turbulent boundary layer profiles for this configuration were taken in the AEDC Supersonic Wind Tunnel (A) at a freestream Mach number of 4 and freestream unit Reynolds number of 3 million per foot using probe techniques[5].

The grid defining the flowfield over the cone is shown in Figure 3. The cone is 1.016 m (40 inches) long and 0.249 m (9.82 inches) in diameter at the base giving a cone half-angle of 7 degrees. The grid extends 0.0127 m (0.5 inches) in front of and above the cone tip. The grid rises to 0.296 m (11.65 inches) above the cone centerline at the base. There are 150 grid points along the axis parallel to the cone centerline and 100 grid points extending normal to the cone surface. Grid points were packed towards the cone tip, toward the cone surface, and in the region of the shock. The outer boundary of the grid represents the freestream and was located such that the shock generated by the cone at Mach 4 would lie just inside the grid boundary. Packing of grid points toward the cone surface was altered as the PARCH flowfield developed to insure resolution of the turbulent boundary layer. Grid points were distributed, as recommended[6], to give at least one grid point within a $y^+$ of 1 and 10 grid points with a $y^+$ of 50.

The PARCH code was compiled and executed for this case on a 64-bit word length machine. The initial flowfield, as defined by the density, velocity components, and energy at each grid point, was calculated using one-dimensional, isentropic flow theory and the wind tunnel freestream conditions. PARCH was run in the viscous mode using the modified, two-equation $\kappa$-$\varepsilon$ turbulence model.

Results for the PARCH flowfield calculations are shown in the turbulent boundary layer profile of Figure 4 where measured and calculated velocities compare well at the measurement station 0.902 m (35.5 inches) downstream of the cone tip. The velocity, U, was normalized by the constant edge velocity, $U_e$; and the distance normal to the cone surface, y, was normalized by the boundary layer thickness, $\delta$, which was defined as the location corresponding to $U/U_e = 0.995$. This PARCH calculation required 7,550 iterations for convergence with no significant changes in the flowfield properties occurring between 7,550 and 8,550 iterations.

## SUPERSONIC LAMINAR FLOW OVER A CONE

The third case chosen for code validation was identical to the second case above except that probe data for laminar boundary layer profiles over the sharp, 7 degree half-angle cone were taken in the AEDC Supersonic Wind Tunnel (A) at a freestream Mach number of 4 and freestream unit Reynolds number of 0.6 million per foot[5].

The grid defining the flowfield over the cone was identical to the grid for the second case above as shown in Figure 3; however, it was necessary for this laminar case to add some bluntness, 1/2000 of the base, to the tip of the cone.

For laminar flow, the PARCH code requires a characteristic length scale to resolve the local Reynolds number; hence, a finite cone tip radius is necessary to avoid laminar boundary layer growth starting with an infinite local Reynolds number. This bluntness requirement does not occur in the previous turbulent case since the local length scale is derived from the turbulent mixing model[6].

The PARCH code was again compiled and executed for this case on a 64-bit word length machine with an initial flowfield as calculated using one-dimensional isentropic flow theory and the wind tunnel freestream conditions.

Results for the PARCH flowfield calculations are presented in the laminar boundary layer profile of Figure 5 where measured and calculated velocities compare well at the measurement station 0.902 m (35.5 inches) downstream of the cone tip. As in the turbulent boundary layer results of Figure 4, the velocity, U, was normalized by the constant edge velocity, $U_e$; and the distance normal to the cone surface, Z, was normalized by the boundary layer thickness, $\delta$, which was defined as the location corresponding to $U/U_e \approx 0.995$. The measured data in Figure 5 does not extend below $Z/\delta = 0.35$ in this laminar flow case because of probe interfence with the flow. This PARCH calculation required 9,000 iterations for convergence with no significant changes in the flowfield properties occurring between 9,000 and 10,000 iterations.

## PARCH CODE DEMONSTRATION CASE

A final case demonstrates the capability of the PARCH model to treat complex but realistic tactical missile configurations. The case of interest was a 12 caliber, optical-fiber guided, transonic missile with a blunt nose, boat tail, and a large base. Missile propulsion was provided by a monopropellant hydrazine

flight motor with bifurcated nozzles located upstream of the boat tail. Motivation for this demonstration case was provided by the need to satisfy design requirements limiting skin temperature aft of the propulsive nozzles and limiting turbulent intensity in the missile wake or optical-fiber trail.

Analysis of this problem exercised many features of the PARCH code including finite-rate chemistry, and the two-equation $\kappa$-$\varepsilon$ turbulence model. Some 270,000 grid points were required for a zero angle-of-attack calculation with quarter plane symmetry, and the PARCH multi-zoning capability was a direct outgrowth of this analysis effort.

A sample of the results from this PARCH calculation are illustrated in the Mach number contours of Figure 6. This figure views the missile body from the aft end and shows the missile cylindrical surface, boat tail, and one of the bifurcated nozzles. The Mach number contours lie in the vertical symmetry plane passing through the nozzle and depict the diffusion of the high Mach number exhaust into the missile external flowfield.

## CONCLUSIONS

The PARCH model is currently the most advanced model of a missile in flight. The code has successfully completed a limited number of fundamental fluid dynamic cases as part of an on- going and extensive validation program to build confidence in the PARCH model; and the ability of the code to treat realistic, complex tactical missile problems has been demonstrated.

## REFERENCES


1. Cooper, G.K., "The PARC Code: Theory and Usage," AEDC-TR-87-24, October 1987.

2. Dorrel, E.W., Jr. and Soni, B.K., "INGRID: Interactive Two-Dimensional Grid Generation," AEDC-TR-86-49, February 1987.

3. Dorrel, E.W., Jr. and McClure, M.D., "3D INGRID: Interactive Three-Dimensional Grid Generation," AEDC-TR-87-40, April 1988.

4. John, J.E.A., Gas Dynamics, 2nd Edition, Boston, Massachusetts, Allyn and Bacon, Inc., 1984, pp. 388-397.

5. Donaldson, J.C., "Laser Doppler Velocimeter Application in Supersonic Boundary-Layer Flow," AEDC-TR-86-44, March 1987.

6. Dash, S.M., Science Applications International Corporation, Ft. Washington, Pennsylvania, Personal Communication.

## NOMENCLATURE

$\gamma$ = specific heat ratio

$J$ = total velocity

$U_e$ = constant edge velocity

$Z$ = distance normal to the surface

$\delta$ = local boundary layer thickness

$\rho_w$ = local density at the wall

$\tau_w$ = local shear stress at the wall

$\mu_w$ = local viscosity at the wall

$y^+$ = dimensionless distance normal to the surface

$= z\sqrt{\rho_w \tau_w}/\mu_w$

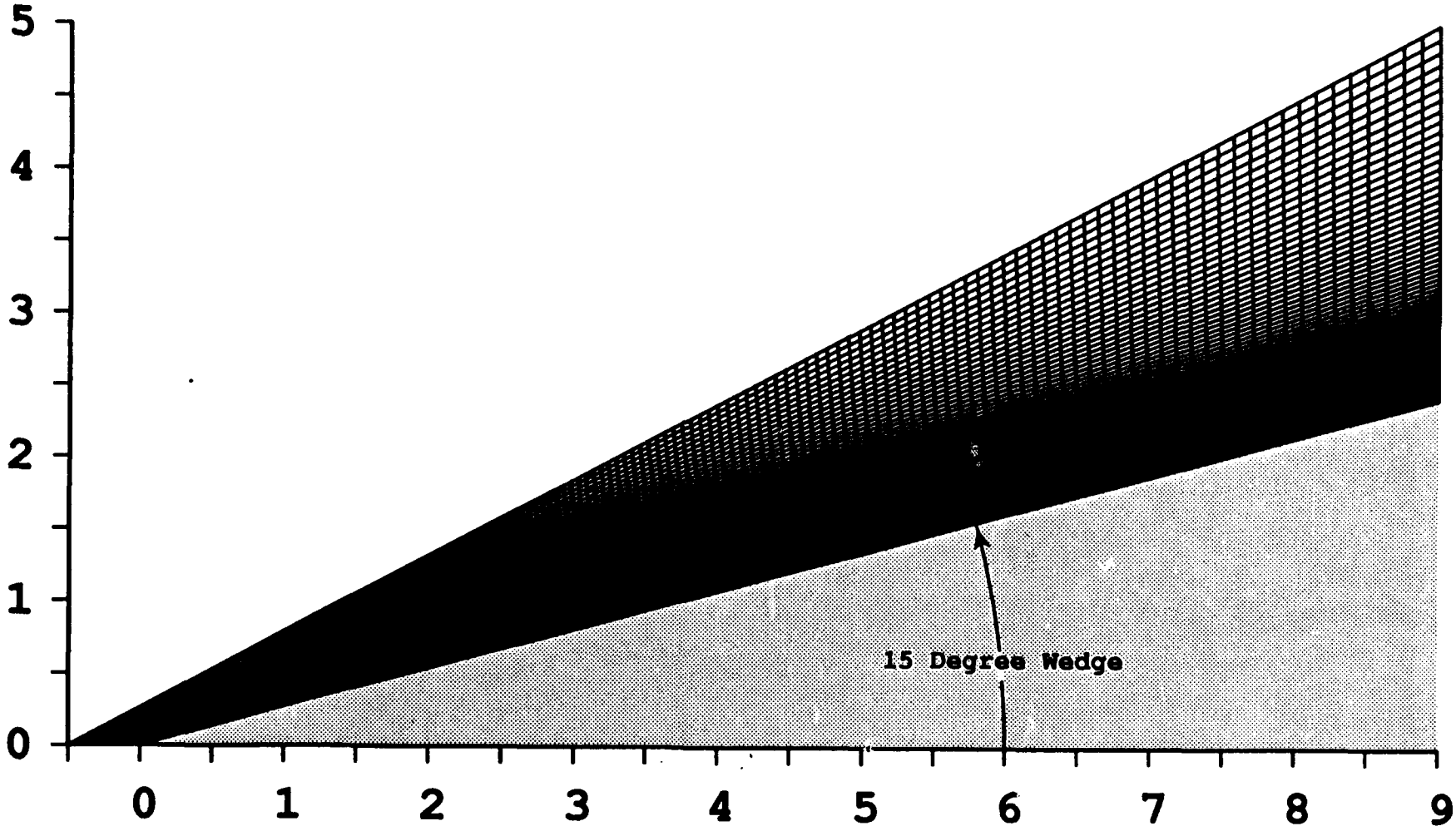


Fig. 1. Wedge Flowfield Grid

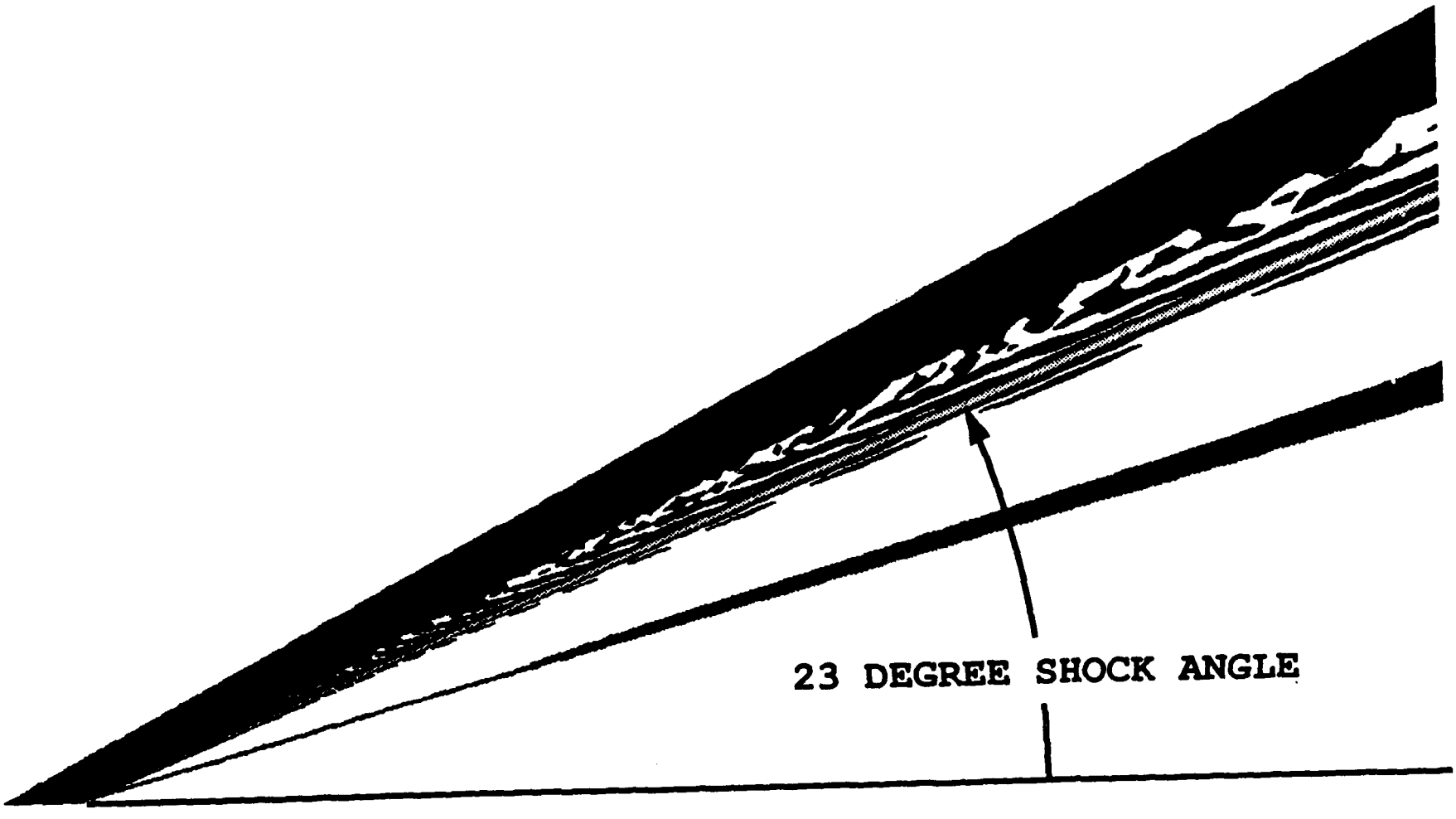


Fig. 2. Wedge Flow Mach Number Contours

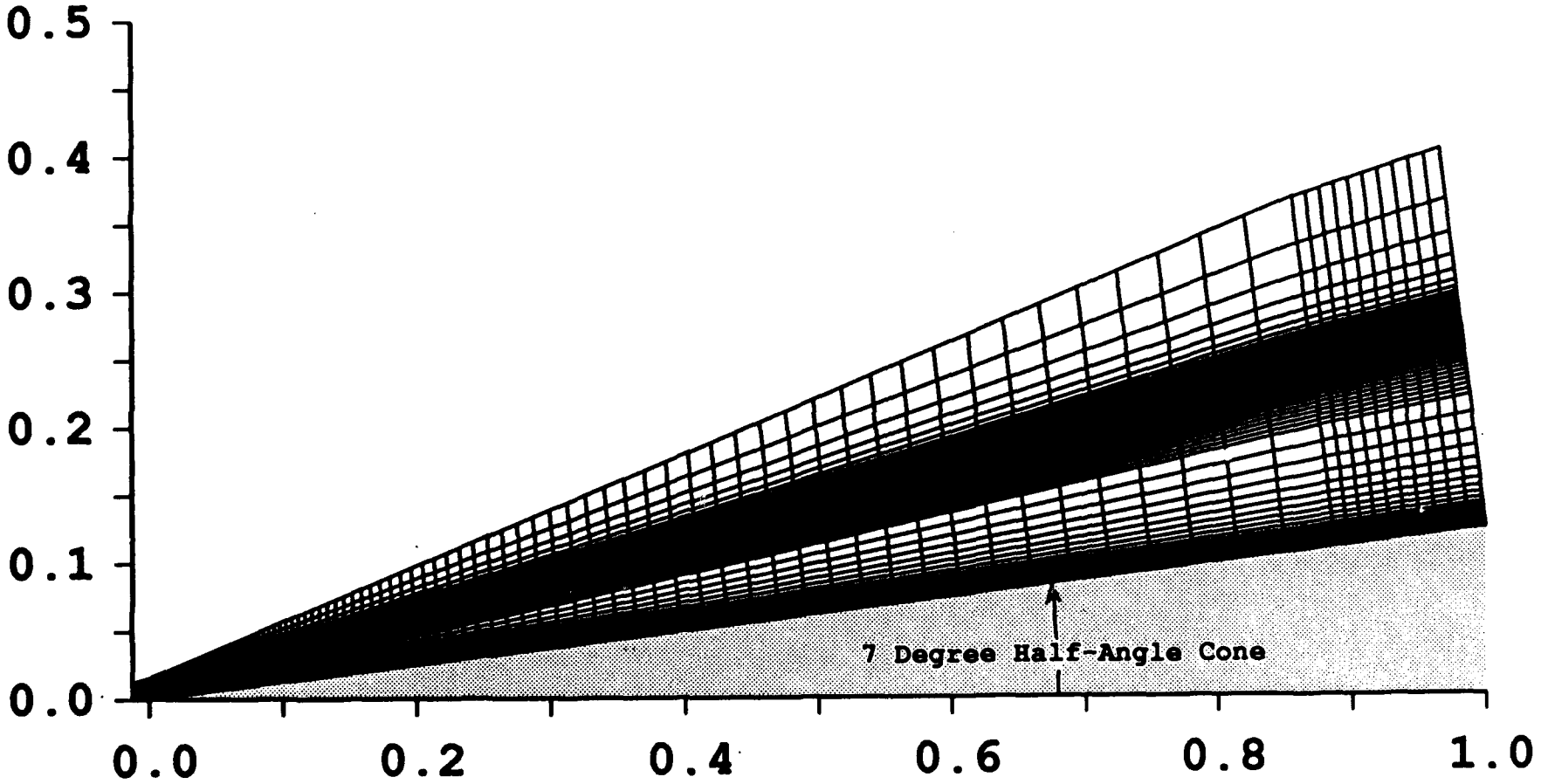


Fig. 3. Cone Flowfield Grid

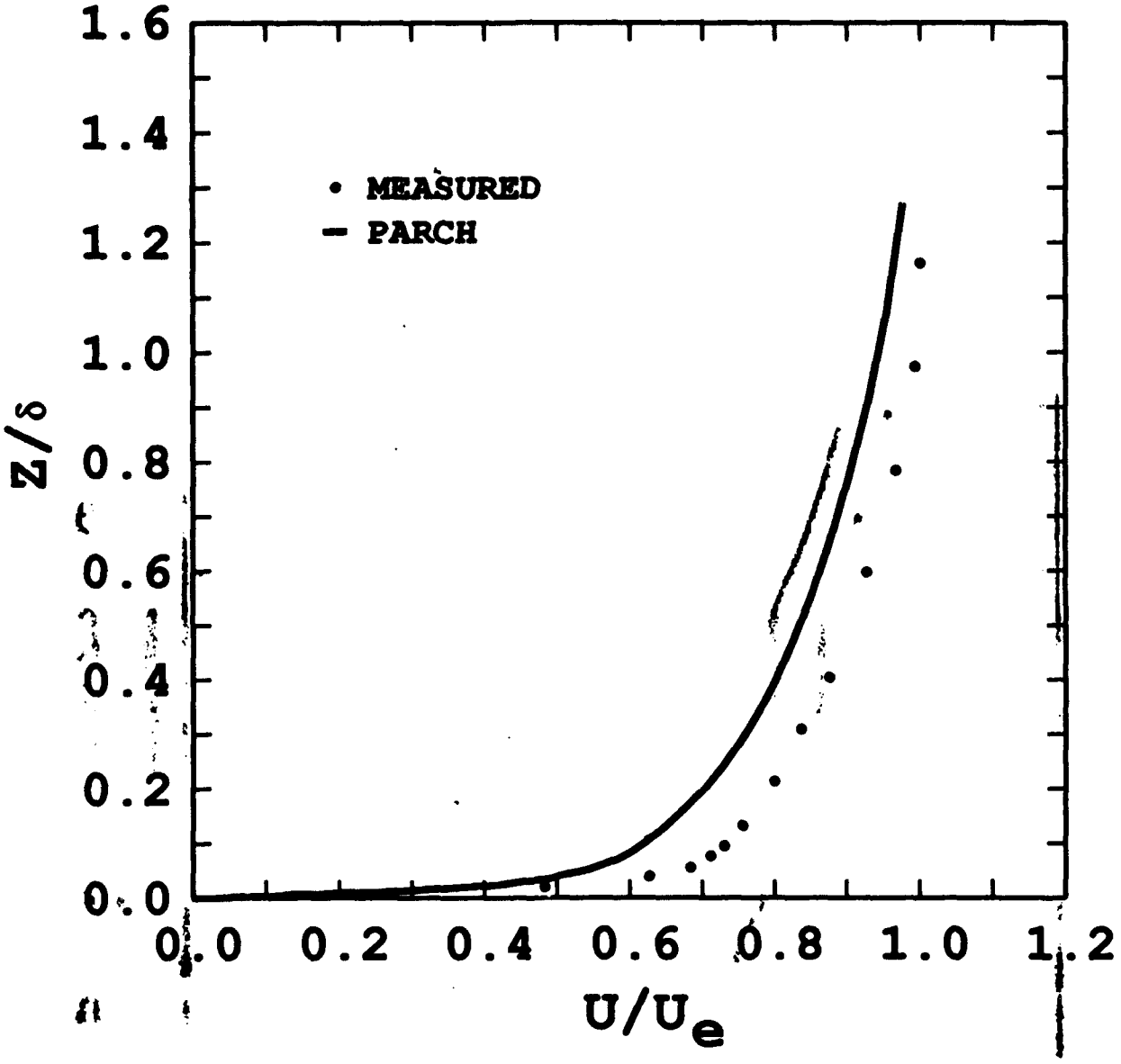


Fig. 4. Turbulent Boundary Layer Profile

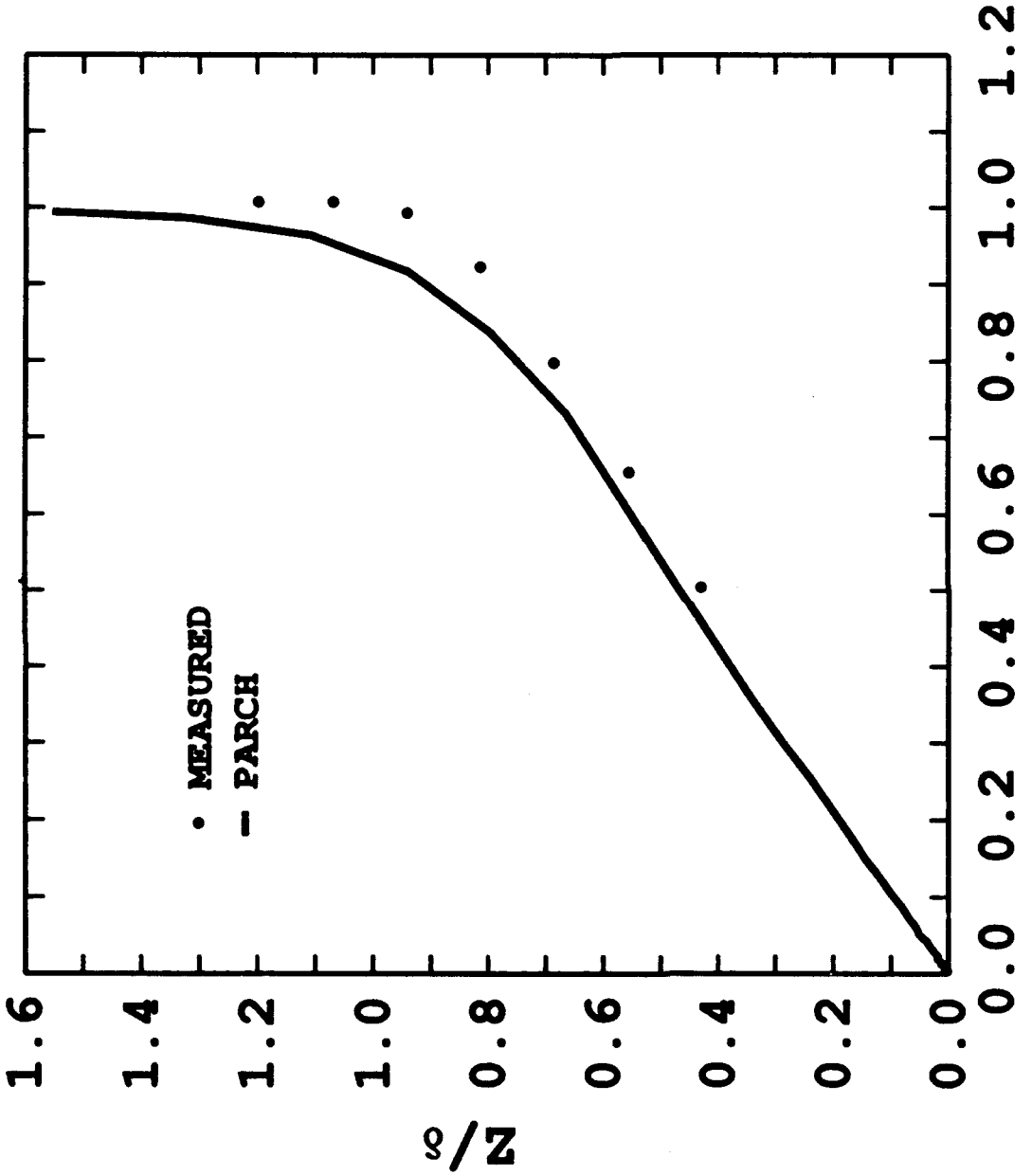


Fig. 5. Laminar Boundary Layer Profile

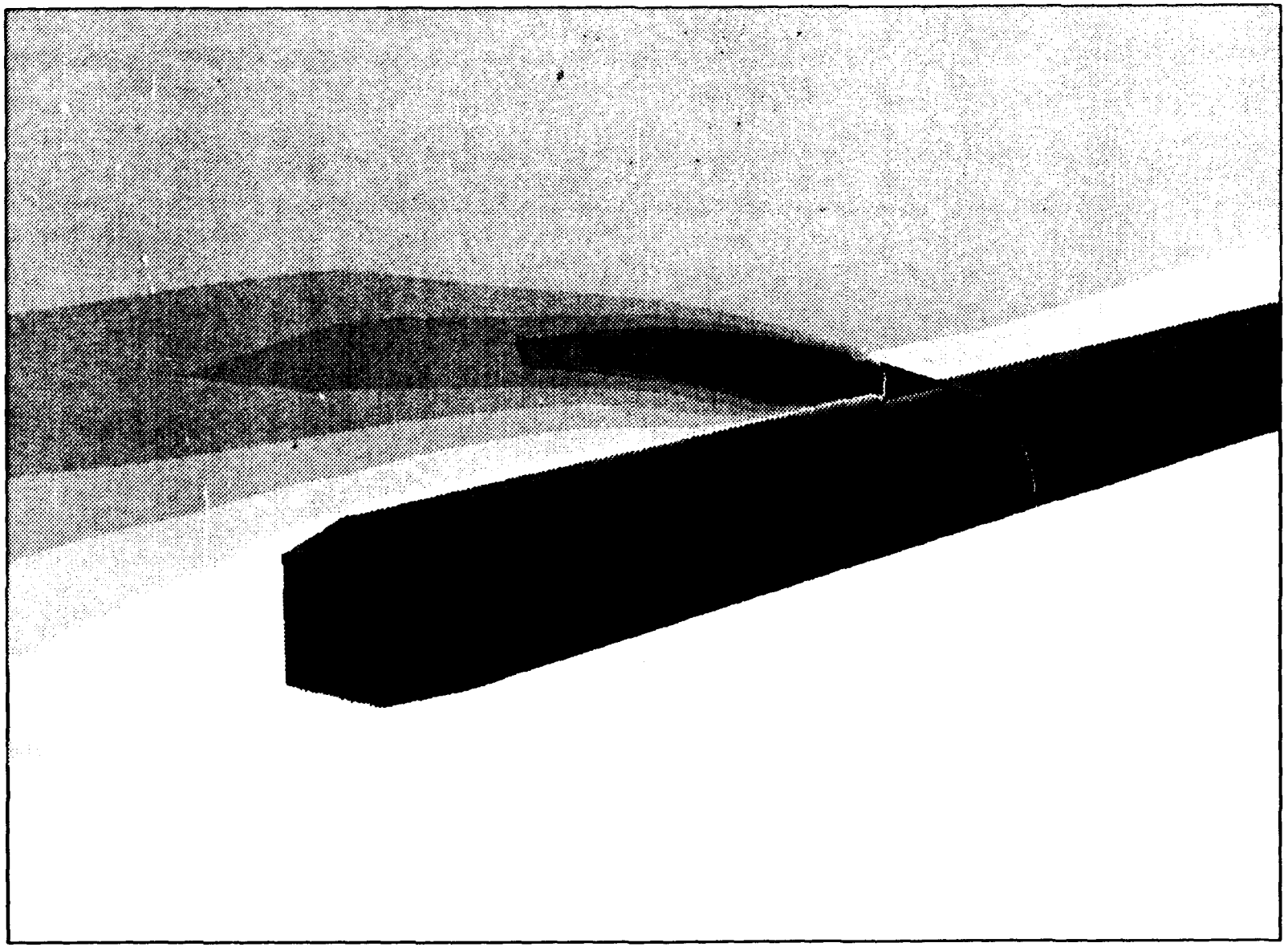

**Fig. 6. Tactical Missile Mach Number Contours**

## - SESSION VI -

PROPULSION

# SAFE DISPOSAL OF ROCKET MOTORS

William S. Melvin
Propulsion Directorate
Research, Development, and Engineering Center
U. S. Army Missile Command
Redstone Arsenal, AL 35898-5249

## ABSTRACT

The U.S. Army Missile Command (MICOM) has been successful in applying critical fluid extraction (CFE) technology for propellant and explosive demilitarizations. A specific process that is ready for transition from research to pilot plant demonstration is the near-critical liquid (NCL) ammonia demilitarization of rocket motors containing ammonium perchlorate (AP) composite propellants. This demilitarization method consists of a straightforward, four-step, continuous process. Step one involves removing the AP propellant from the rocket motor by hydraulic erosion using NCL ammonia. Step two extracts the oxidizer (AP) and separates the AP/liquid ammonia solution and binder residue (crumb). Step three recovers the AP by evaporating the ammonia. Step four condenses the ammonia vapor and recycles the liquid ammonia for a continuous removal/extraction operation. The CFE process is efficient and is conducted at ambient temperatures and low operating pressures.

This paper summarizes the recommendations of a two-phase engineering design study to finalize a process and build a pilot plant facility to demilitarize rocket motors containing AP composite propellants. Phase I is intended to demonstrate the technical feasibility of the process, to determine the effects of process variables, and to demonstrate the safe operation of the ammonia CFE demilitarization process. Phase II includes the design, construction, and operation of a pilot plant to demonstrate that the critical fluid method is nonpolluting, cost effective, and environmentally acceptable.

## INTRODUCTION

MICOM has successfully demonstrated an innovative application of critical fluid extraction (CFE) technology for the demilitarization of propellant, explosive, and pyrotechnic (PEP) munitions. The MICOM method of CFE demilitarization represents a radical departure from traditional open burning/open detonation (OB/OD) disposal methods. It offers an environmentally safe and straightforward approach for resource recovery, reclamation, and/or in situ neutralization of otherwise hazardous munitions and ingredients. The method circumvents traditional ingredient solvation processes, avoids the use of water or hazardous organic solvents, and does not generate additional hazardous wastes. This demilitarization process is nonpolluting, cost effective, and environmentally acceptable.

Cleared for public release; distribution is unlimited.

In the MICOM CFE demilitarization method, gases are compressed and "fluidized" under pressure to near-critical liquid (NCL) and supercritical fluid (SCF) conditions. These fluids serve as nontraditional extraction solvents when used in their NCL or SCF conditions. The unusual solvating properties of critical fluids can enhance selective and rapid extraction of PEP ingredients from complex munition compositions. The CFE demilitarization process takes advantage of gas-to-liquid and liquid-to-gas phase transitions which occur during the compression and expansion (pressure reduction) of all confined gases. Because the CFE process is similar to the operation of closed-loop air-conditioning and refrigeration systems, continuous recycling of the solvent is possible. The main differences reside in the selection of an appropriate critical fluid solvent and the incorporation of an extraction vessel and a pressure reduction (expansion) chamber for ingredient recovery. Complete recovery of soluble ingredients is obtained by controlling the phase transition of the NCL or SCF solvent to the gaseous state. Liquefaction and recompression of the original CFE solvent completes the continuous demilitarization cycle. A simplified schematic of a CFE system is shown in Fig. 1.

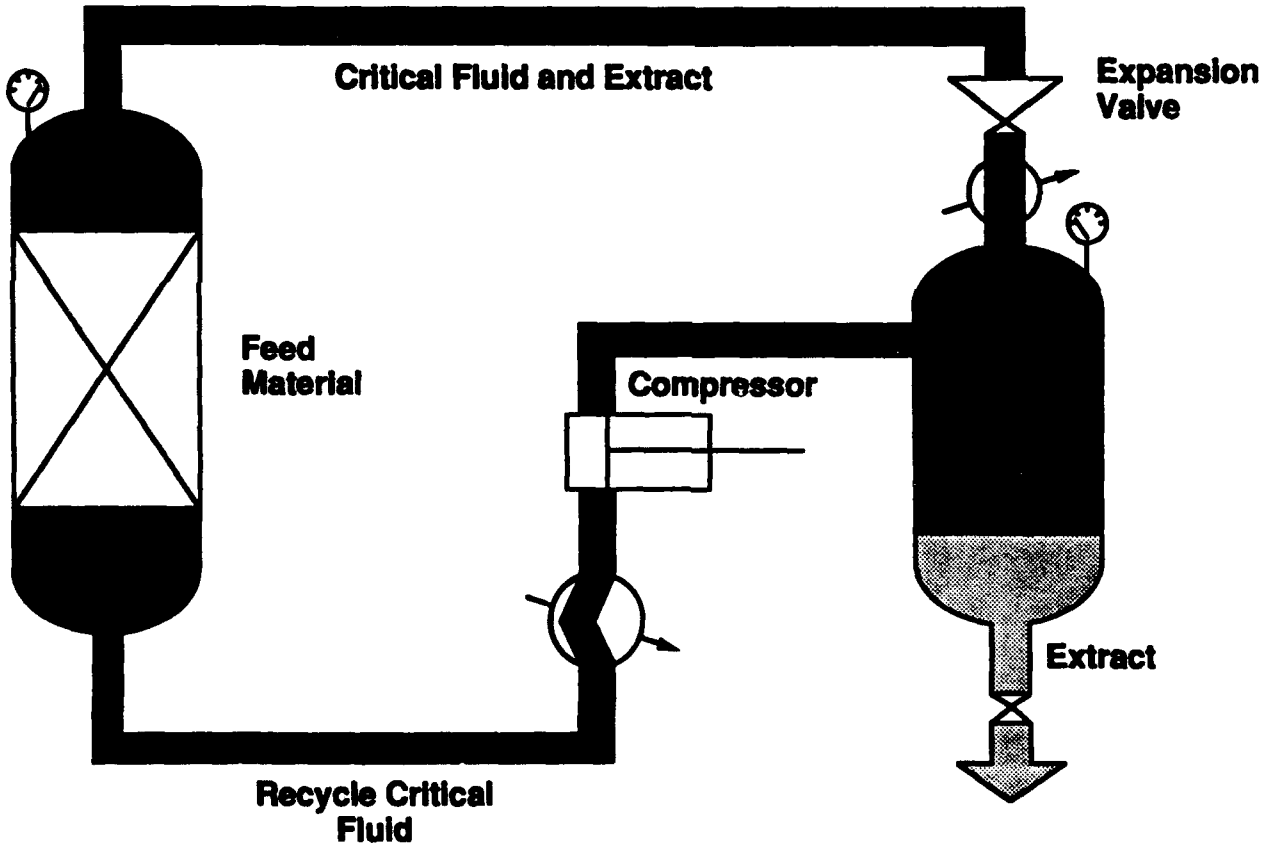


Fig. 1. Critical Fluid Extraction by Pressure Reduction Technique.

The MICOM CFE demilitarization process, albeit simple in design, has been experimentally shown to be extremely effective for class 1.3 AP composite propellants and has similar usage potential for related PEP munitions. The

MICOM demilitarization program is broad-based and has included the investigation of several CFE solvent systems. The MICOM method offers a unique alternative to current OB/OD disposal practices and provides high payoff potential for propellant and conventional ammunition demilitarization. MICOM has tested the CFE process at the laboratory scale for a variety of conventional munitions and high energy materials. Plans for system engineering design, prototype scale-up, and testing of system specific processes are in progress.

The primary advantages of the CFE demilitarization process are:

1. It uses mature, well-developed technologies. CFE technology is a proven industrial process that can be applied to munitions demilitarization and hazardous waste minimization.

2. The process is environmentally acceptable. The system is completely self-contained, meaning no pollution of air or water environments.

3. The method is economically advantageous. Strategic raw materials can be recovered. CFE solvents are low cost, recyclable for continuous processing, and do not generate additional hazardous wastes.

4. Transportable facilities appear to be feasible. This process lends itself to mobility, as the various components can be designed in modular form.

## DISCUSSION

The use of critical fluids at conditions above and below their critical temperatures and pressures for demilitarization has been under active investigation by MICOM.[1,2] Investigations have examined the extraction of both fuels and oxidizers using a variety of NCL and SCF extraction solvents which include carbon dioxide, ammonia, and nitrous oxide. Of particular interest is the process using ammonia to extract ammonium perchlorate from hydroxy-terminated polybutadiene (HTPB) and polybutadiene-acrylic acid-acrylonitrile (PBAN) composite propellants. Tests have shown that liquid ammonia will dissolve considerably more than its own weight of AP.[3] This effort is the basis of the demilitarization process principally described in this paper.

Ammonia is in the liquid state at approximately 120 psi and 70 °F. Because of its affinity for AP, ammonia can be used at these conditions for extracting AP from propellant binders. To facilitate a rapid extraction process, the propellant is best cut or comminuted into small pieces. Dissolved AP can be recovered by use of heat to evaporate the ammonia. Fortunately, composite propellant binders are not greatly affected by ammonia.[1,4]

The physical characteristics of ammonia and its affinity for AP suggests a unique process for demilitarization of rocket motors. In this process the rocket motor serves as the extraction vessel. Liquid ammonia is injected at a high velocity stream that cuts or erodes the propellant into small pieces suitable for rapid extraction of the AP. The ammonia CFE method of demilitarization of rocket motors consists of a straightforward, four-step, continuous process. The first step involves propellant removal by hydraulic erosion of the propellant surface using NCL ammonia at moderately high pressures. The

second step includes extraction of the AP oxidizer and separation of the AP/ammonia solution and binder residue (crumb). Partial extraction of the AP occurs during propellant removal. In the third step, the AP is recovered by evaporation of the ammonia. The fourth step involves condensation (liquefaction) of the ammonia vapor by compression and cooling. The liquid ammonia is then recycled for continuation of the cutting/extraction operations.

Ample data exist on the processing of ammonia because of its use in the chemical and refrigeration industries. MICOM experiments have demonstrated that 100% of the AP can be rapidly extracted from composite propellants. Traditional water cutting of propellants suggests that liquid ammonia can similarly be used to cut or erode propellants.[5] These conclusions are the basis for a CFE demilitarization pilot plant design carried out by Stone Engineering on behalf of the U. S. Army.[6] The remainder of this paper is a summary discussion of the design study conducted in support of pilot plant implementation.

MICOM has requested funding for a two-phased program to finalize a process and build a pilot plant facility to demilitarize rocket motors containing ammonium perchlorate (AP). The proposed 1,100 pound capacity rocket motor demilitarization facility will validate the engineering and processing requirements for applying this technology to AP composite propellants that comprise the major portion of the DoD and NASA large rocket motor inventories. Phase I is intended to demonstrate the technical feasibility of the process, to determine the effects of process variables in three critical steps (propellant removal, AP extraction, and AP recovery), and to demonstrate the safe operation of the ammonia demilitarization process. Phase II will include the design, construction, and operation of a pilot plant to demonstrate that the critical fluid method is non-polluting, cost effective, and environmentally acceptable.

## PHASE I - TECHNOLOGY DEVELOPMENT

### EROSIVE PROPELLANT CUTTING

Tests will be conducted to determine optimum conditions for erosive cutting of bulk composite propellant using high pressure liquid ammonia jets. The effects of pressure, nozzle size and configuration, impingement velocity, and nozzle-to-propellant surface distance requirements will be assessed. These tests will provide the baseline data on propellant surface erosion efficiencies, surface penetration depths, cutting phenomena, and binder communition that are required for engineering design scale-up. An apparatus has been designed to conduct these tests.

### AP EXTRACTION

The AP extraction tests will determine how the AP extraction rate is affected by the surface-to-volume ratio of the propellant sample, contact time, and AP concentration in the AP/ammonia solution. An apparatus has been designed to conduct these tests.

## AP RECOVERY

A simulated falling film evaporator and linear delivery nozzle will be employed in this investigation. Tests will be accomplished to determine the rate of AP recovery with respect to factors such as AP concentration, operating pressure, rate of solution input, temperature of evaporator plate, and top-to-bottom temperature gradient. Other factors in the evaporation/recovery process that will be investigated include: (1) the minimum operating pressure at which ammonia evaporation can be conducted without causing flashing of the feed solution, resulting in entrainment of AP dust in the ammonia vapor, and (2) the determination of whether the AP will fall freely from the evaporator plate and collect in the bottom of the evaporator vessel, or whether a mechanical means will have to be incorporated to remove the solid AP from the evaporator plate. An apparatus suitable for conducting these measurements has been designed.

## SAFETY TESTS

Safety tests will be conducted to identify any potential hazards associated with the demilitarization process and to determine if there is a need to establish limits for processing variables (such as temperature, pressure, and AP concentration) to ensure a safe pilot plant operation.

Both the crumb (binder/Al residue) and AP/ammonia solutions will be evaluated with respect to safety characteristics. Crumb that contains excessive amounts of residual AP (up to 10%--two to three times the expected concentration) will be subjected to standard compression, thermal, electrostatic, impact, and friction tests.

Ammonium perchlorate/ammonia solutions at AP concentrations up to 95% of saturation (67% by weight) will be evaluated. The safety tests that will be conducted include thermal, electrostatic, impact, friction, pressure, detonation, and critical height to explosion. In addition, low and high pressure pumping tests (at pressures that will encompass the range of pressures that will be employed in the high and low pressure sections of the pilot plant) will be accomplished.

## PHASE II - PILOT PLANT DESIGN

The pilot plant concept, as depicted in Fig. 2, consists of a four-step CFE process. The entire process is contained in a closed system where high pressure jets of liquid ammonia are used to cut composite solid propellants into small pieces. These propellant pieces are transferred to a crumb separator where the liquid ammonia dissolves the ammonium perchlorate (AP) oxidizer out of the binder. The AP/ammonia solution is transferred to an evaporator where the ammonia is evaporated from the solution and the AP is recovered. The ammonia vapor is compressed and colled and recondensed to a liquid and then is transferred to a liquid ammonia storage tank to be recycled through the system. Because the system is closed, the entire process continued until all the propellant has been removed from the rocket motor and all the AP has been separated from the propellant binder without loss of the ammonia. The crumb separator and evaporator are sized to contain all the inert binder and all of the AP from one 1,100 pound rocket motor.

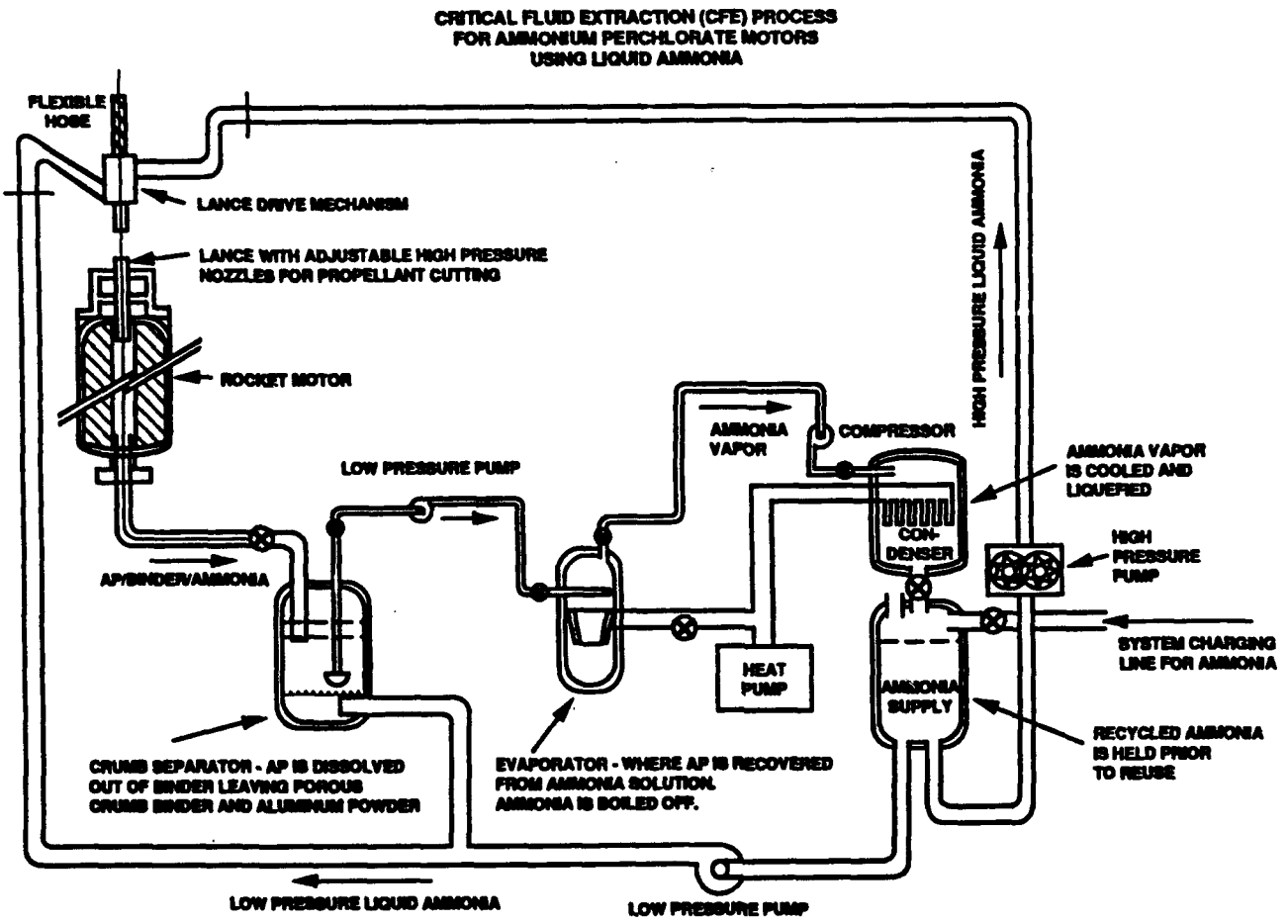


Fig. 2. Pilot Plant Schematic

The first step of the process is to remove the propellant from the rocket motor. To do this, the motor is mounted into a holding structure with the nozzle end up. Special fittings for each type of rocket motor are mounted on each end of the motor. The lower (head) end is connected to the inlet pipe to the crumb separator. The upper (nozzle) end is connected to the lance drive mechanism. Both end fittings must be pressure tight to prevent the loss of ammonia during the process.

The lance contains two (or more) adjustable high pressure nozzles which direct jets of liquid ammonia into the propellant to cut (erode) the propellant. Low pressure jets of liquid ammonia are used to flush the surface of the propellant and carry off the cut pieces of propellant. The lance rotates slowly and moves down the axis of the rocket motor while the high pressure jets of ammonia cut the propellant and the low pressure jets wash away the loose pieces. As the propellant is removed, the adjustable nozzles are moved closer to the new propellant surface for more efficient cutting. The lance is moved up and down the axis of the propellant while rotating until all the propellant is removed from the motor case. The lance is designed to accommodate a fiber optics light source to illuminate the cutting location, and a TV monitor to observe the cutting and to determine when all propellant has been removed.

The second step of the process is to collect the propellant pieces in the crumb separator. Here the liquid ammonia will dissolve the AP leaving a porous crumb of rubber binder which contains the powered aluminum fuel. The crumb separator tank consists of a fixed upper section and a removable lower section which is sized to contain all of the propellant crumb from the rocket motor. The upper section contains the crumb and liquid ammonia inlet pipe, a pipe to the vacuum pump, an over-pressure relief pipe, and two liquid ammonia outlet pipes (one to a recirculating pump for the crumb separator and the other to the high- and low-pressure recirculating pumps to the rocket motor). The lower section contains one inlet pipe from the recirculation pump. Between the two sections is a screen to prevent propellant crumb from floating to the upper liquid level. Above the inlet pipe in the lower sections is a fluidized bed screen through which the upward flow of liquid ammonia agitates the crumb in the liquid ammonia to increase the efficiency of the AP extraction.

The crumb separator also contains pressure, temperature, liquid-level, and concentration sensors. The liquid level sensor determines when, and how much, solution is recirculated to the rocket motor. The concentration sensor determines when to divert solution to the evaporator after a predetermined AP/ammonia concentration level has been reached.

In the third s tep of the process, the AP is recovered from the AP/ammonia solution by evaporation of the ammonia. The evaporator tank consists of a fixed upper section and a removable lower section which is sized to contain all of the AP from the rocket motor propellant. The upper section contains the solution inlet pipe, an outlet pipe to the vacuum line, and an outlet pipe for the ammonia vapor. It also contains a heated falling-film evaporator which separates the AP from the ammonia. The incoming solution is discharged through a ring-type nozzle around the upper edge of the falling-film evaporator. The solution flows down a smooth, Teflon-coated conical surface (large diameter at the top) where it is heated, and the ammonia is boiled off. The precipitated AP falls into the lower section of the tank. To minimize AP sticking to the evaporator wall, a vibrator may be required to shake it loose. The lower end of the evaporator probably will require more heat because the boiling point of the AP/ammonia solution increases as the concentration level increases. The pressure in the evaporator tank is lowered as the vapor is drawn out through a filter (to remove any AP dust) and a dryer (to remove any water) to a compressor which recompresses the vapor before it is pumped into a condenser.

The fourth step of the process takes place in the condenser where the ammonia vapor is cooled and reliquefied. The liquid ammonia is then transferred into the liquid ammonia storage tank where it is ready to be recycled. (A heat pump will be used to supply the heat to the evaporator and the cooling for the condenser.)

To ensure safe and efficient operation of the pilot plant, pressure, temperature, liquid level, and concentration sensors are strategically located throughout the system. Pressure and temperature sensors are located in each of the four tanks, in the drain line from the rocket motor, and in the high- and low-pressure lines to the rocket motor. Readings from any of these sensors which exceed the predetermined levels will cause an alarm to sound and will shut down the system automatically.

Liquid level sensors are located in the crumb separator and in the liquid ammonia storage tank. The sensor in the crumb separator controls the liquid level by controlling the recirculating pumps to the rocket motor. The sensor in the ammonia storage tank monitors the amount of liquid ammonia in the system.

Concentration sensors are located in the crumb separator and in the inlet pipe to the high-pressure pump. The sensor in the crumb separator controls the pump which transfers the AP/ammonia solution to the evaporator. The sensor in the inlet line to the high-pressure pump shuts the system down if the concentration level exceeds a predetermined level. Additional sensors in the process building are provided to detect ammonia leaks in the system. Any leaks will cause an alarm to sound and the system will be shut down automatically.

All pilot plant instruments and sensors will be monitored by the computer-controlled system. The control system will measure and record all parameters, store this information for each rocket motor, and provide a printout for each selected parameter. Two sets of limits, upper and lower, for each parameter will be input into the computer. Whenever any of the lower limits are exceeded in a predetermined time, the control will cause an alarm to sound and if the operator cannot bring that parameter back within limits in a predetermined time, the computer will cause the process to shut down. If any of the upper limits are exceeded, the computer will cause the process to shut down immediately.

## SUMMARY

### CAPACITY

The simplicity of the MICOM CFE demilitarization process makes it particularily amenable to system scale-up. System specific processes are considered viable for applications which range from large ICBM rocket motors to small hand grenade munitions.

### OPERATING COST

Operating cost is believed to be low. Costs will vary in accordance with system specific requirements, size of munitions, and whether smaller munitions can be demilitarized in bulk (soak) processes. Small and mobile designs are feasible.

### PROCESS CONTROL

All system configurations are intended to utilize existing technologies and off-the-shelf industrial components.

### RECLAMATION QUALITY

The CFE process provides high quality, high yield ingredient reclamation. The process has an extensive industrial base which can be readily adapted to meet the needs of the munitions industry.

## WASTE STREAMS GENERATED

The process is designed to eliminate or minimize hazardous waste generation.

## ENVIRONMENTAL CONSTRAINTS

Minimal constraints are anticipated as the CFE demilitarization method addresses emerging Environmental Protection Legislative Acts on Clean Air, Clean Water, Hazardous Waste Reduction, Resource Conservation and Recovery, and Federal Facility Contamination. Therefore, the MICOM critical fluid demilitarization method offers defense contractors, NASA, and the DoD a "clean" process which will be economical and meet EPA environmental concerns.

## DATA GAPS

The CFE demilitarization process for recovery of ammonium perchlorate from composite propellants is ready for transition from research to pilot plant demonstration. This effort will provide an extensive data base in support of other munition demilitarization applications which are presently under consideration.

## CONSTRUCTION COSTS

Construction costs are believed to be highly competitive with cost savings through joint ventures with private industries.

## DEVELOPMENTAL COSTS

Costs will vary in accordance with the specific demilitarization effort. Typical system engineering design, testing, and evaluation costs are estimated to be $1.5M per system.

## DEVELOPMENTAL STATUS

A process to meet the demilitarization requirements for Class 1.3 large rocket motors is ready for transition to pilot plant demonstration. Similar processes for conventional munition applications have been demonstrated at the laboratory scale. Funding is required for prototype engineering design and evaluation.

## REFERENCES


1. Melvin, W. S., "Demilitarization Method for Composite Propellants," 1989 JANNAF Propulsion Meeting, CPIA Publication No. 515, Vol. III, pp 103-111.

2. Melvin, W. S., and Graham, J. F., "Method to Demilitarize, Extract, and Recover Ammonium Perchlorate from Composite Propellants Using Liquid Ammonia," Propulsion Directorate, U.S. Army Missile Command, Redstone Arsenal, AL, U.S. Patent 4,854,982, Filed 31 January 1989.

3. Boggs, T. L., Bradley, H. H., McBride, W. R., and Prentice, J. L., "A New Class of Propellants: Solution Monopropellants Part I: What is a Solution Monopropellant?," 12th JANNAF Combustion Meeting, CPIA Publication No. 273, Vol. III, pp 89-103.

4. McBride, W. R., "Sensitivity and Characterization of Selected Liquid Ammonia Systems," NWC TP 5836, pp 33-38.

5. Brown, E. D., "Propellant Removal by Water Washout (Hydromining)," Morton Thiokol, Inc., Brigham City, UT, 1985 JANNAF Safety and Environmental Protection Subcommittee Meeting, 4-8 November 1985, CPIA Pub. 436, pp 99-103.

6. Davis, R. T., and McGill, H. L., "Critical Fluid Demilitarization of Rocket Motors," Technical Report No. 35801-90001, Stone Engineering Company, April 1990; Performed under MICOM Contract No. DAAH01-89-C-0099.

# INSENSITIVE MUNITIONS SOLID PROPELLLANT DEVELOPMENT

Eric J. Herring
Propulsion Directorate
U.S. Army Missile Command
Redstone Arsenal, AL 35898-5249

## INTRODUCTION

Recently the U.S. Army has adopted an Insensitive Munitions (IM) policy for current and future missile systems. Army missile systems will need to meet IM requirements in the fielded motor/launch configuration. This policy will significantly reduce the severity of personnel and equipment losses in the handling of munitions during production, storage, shipping, and combat operations. A much publicized incident occurred several years ago in West Germany. This was the accidental ignition and subsequent overpressurization of the first stage PERSHING rocket motor which resulted in three deaths and nine injuries to Army personnel. The cause was attributed to electrical discharge during the removal of this motor from its shipping container. Another example is the 1967 incident on the aircraft carrier, U.S.S. Forrestal off the coast of Vietnam which resulted in 134 deaths/161 injuries and considerable cost to repair the ship. This incident involved a jet fuel fire and munitions cook-off from the fire. These heavy losses did not result from direct enemy fire.

Potential losses of lives, planes, ships, helicopters, tanks, etc. can also result from the initiation to explosion/detonation of the impacted munitions during combat, and may lead to the detonation of other munitions on board. This paper is a presentation of a general background on propellants, approaches to the research and development of IM solid propellants, motor cases, shipping cases, mitigation, which will meet the Army's policy of Insensitive Munitions and the IM testing required for all U.S. munitions of the future.

## BACKGROUND

Rocket motor propellants can be divided into three general types: solids, liquids, and gells. Solid propellants are typically composed of a polymeric binder system with plasticizer, metallic fuels, oxidizers, and additives such as combustion or chemical stabilizers, burn rate catalysts, etc. Solid propellants can be classified as high performance aluminized composite smokey and minimum signature formulations. Minimum signature formulations are especially important in Army tactical

missile systems to minimize detection of the launch platforms during an engagement (radar/visual/flash signature) and to lessen interference of guidance (visual/or mm. wave). Minimum signature solid propellants are detonable, while higher performance smokey propellants are non-detonable. This is due to the presence of high energy "smokeless" explosive ingredients used to formulate the minimum signature propellants.

Liquid propellant systems typically consist of oxidizers and fuels. Oxidizers such as liquid oxygen, hydrogen peroxide, and inhibited red fuming nitric acid react in the motor chamber with liquid fuels such as liquid hydrogen or hydrocarbons. Most oxidizers and fuels are hypergolic and do not need igniter systems. Gelled propellant systems also consist of oxidizers and fuels. Silicon dioxide (very fine particle size) is typically used to gel the oxidizer and fuel in IRFNA gel oxidized systems. Gelled systems are considered insensitive as the fuel and oxidizer are separated.

Solid propellants are classified as Class 1.1 or Class 1.3 depending on the detonation sensitivity of the propellant as tested per Army TB700-2, "DOD Explosives Hazard Classification Procedures," the primary Class 1.1/1.3 test criteria has been the Naval Ordnance Laboratory (NOL) Card Gap Test. The general setup for this type of test is shown in Figure 1. The attenuating material, plexiglass disks, 0.01-inch thick are placed between the explosive Pentolite initiator and the propellant test sample, and serves to dampen the shock wave from the detonation of the Pentolite pellets. The number of these disks, or cards as most often referred, required to attenuate and prevent a detonation of the propellant, is the measure of sensitivity of the propellant (or explosive). The higher the card (0.01-inch) value, the more sensitive the propellant. A positive test is one in which a hole is punched through the 3/8 inch thick steel witness plate which is placed beneath the test sample. For Class 1.1 propellants a negative test is greater than 69 cards while for Class 1.3, it is less than 70. Examples of positive and negative test results are shown in Figure 2.

Composite propellants usually contain an oxidizer such as ammonium perchlorate (AP) and/or the metallic fuel aluminum, which form hydrogen chloride (HCl) and aluminum oxide during combustion. The HCl readily combines with the moisture in the air to produce a very smokey exhaust while metals form solid oxide particulates which contribute to radar signature.

## APPROACHES TO DEVELOPING IM SOLID PROPELLANTS

Several approaches are available to develop IM solid propellants. These approaches are being investigated and developed at the Propulsion Directorate through in-house or Army funded contractual work. The initial, and most obvious, is to

decrease the amount of high energy explosive ingredients in the propellant such as HMX, RDX, and nitroglycerin. Decreasing or eliminating these highly energetic ingredients would make the propellant less sensitive; however, rocket motor performance will suffer, often times significantly. Therefore, more propellant weight would be required to perform the same missile mission. In general, the higher the specific impulse of the propellant, the greater the sensitivity. A viable method to boost the performance of lower energy propellant formulations is to design the rocket motor to burn at higher combustion pressures. For example, a propellant formulation with a specific impulse of 224.6 at 1,000 psia will have an impulse of approximately 235.5 at 2,000 psia. Composite motor cases are stronger than metal ones and for the same case weight, they can be designed to operate at these higher pressures.

Another option is the development of new polymers, plasticizers, and oxidizers to enable the necessary tradeoff of energy and sensitivity of the propellant. Current formulations use inert polymers which decrease propellant performance. New energetic polymers such as the trifunctional hydroxy glycidyl azide can be used in propellant formulations to increase performance while allowing a reduction of more sensitive explosive ingredients such as HMX, RDX, etc. In addition, research and development in ongoing new plasticizers and oxidizers will provide energetic and insensitive ingredients for propellant formulations. These more energetic, less sensitive ingredients require less quantity for the same performance and will make the overall system less sensitive.

Another approach is to physically separate the oxidizer and the fuel elements of the propellant systems; e.g. bipropellant systems. An example of this is the hybrid rocket propulsion, with a solid fuel grain (no oxidizer) and liquid or gelled oxidizer in a separate tank. Gelled oxidizers provide an extra IM benefit by immobilizing a dangerous liquid component of the bipropellant system. The gelled oxidizer flows when pressurized. Air-oxidized propulsion systems also offer IM features as no oxidizer is needed, and only fuel is carried on the rocket system. Examples of these are the ducted rocket and turbojet propulsion systems.

In addition to the propellant options listed above, several external protective options are available. The first of these deals with the development and evaluation of IM rocket motor cases, shipping containers, and launchers. The Propulsion Directorate is currently investigating filament wound, braided, fabric wrapped, strip laminate, and hybrid motor cases. These motor concepts operate by attenuating kinetic energy of fragments/bullets, and by softening of the resins used to bind the various fibers, metal strips, etc. during exposure to heat

from a fire. The later phenomena prevents motor pressure buildup and motor explosions/detonations will not occur. Another means to vent rocket motor pressure is by passively opening the head or aft closures of the motor. These typically operate by mechanical or physical disruption of the closure locking mechanism.

IM TEST REQUIREMENTS

There are seven required IM tests; however, only four of these are mandatory for Army propulsion systems. These tests are: fast cook-off, bullet impact, sympathetic detonation, fragment impact, slow cook-off, shaped charge jet impact, and spall impact. The latter three tests are required if a threat assessment evaluation shows they are required. A brief description of each of these tests follows.

a. "The fast cook-off test consists of engulfing the test item in the flame envelope of a liquid fuel fire, and recording its reaction as a function of time."[1] An average fuel flame temperature of at least 1600 degrees F as measured by thermocouples, neglecting the contributing heat from the burning motor, will be considered a valid test. The passing criteria is "no reaction more severe than burning."

b. The bullet impact test consists of firing three 50 caliber armor-piercing (AP) bullets at 2600 to 3000 feet/second at the test item. The time between each bullet impact should be between 90 and 110 milliseconds. A configuration for a bullet impact test is shown in Figure 3. The passing criteria is "no reaction more severe than burning."

c. The sympathetic detonation test consists of detonating one munition (donor) adjacent to one or more like munitions (acceptors)."[3] The reasoning behind this test is that the detonation reaction may propagate from one munition to another within a stockpile or group of munitions. A possible sympathetic detonation configuration is shown in Figure 4. The passing criteria is "no detonation of any acceptor."

d. The fragment impact test consists of firing a one-half inch, 250 grain, mild-steel cube traveling at 8000 to 8600 feet/second into the test item. A configuration for fragment impact is shown in Figure 5. The passing criteria is "no reaction more severe than burning."

e. "The slow cook-off test (SCO) is used to determine the reaction temperature and to measure the overall response of major munition subsystems to a gradually increasing thermal environment."[2] This test involves subjecting the test item to a gradual temperature rise of 6 degrees F per hour till a reaction occurs. The passing criteria is "no reaction more severe than burning."

f. The shaped charge jet impact test subjects the test item to a jet of a M42/M46 grenade, representative of a top attack or an 81-mm precision shaped charge (or both), representative of a hand-held high explosive anti-tank attack. The decision on which jet to use shall be based upon the threat assessment. A configuration for the shaped charge jet impact test is shown in Figure 6. The passing criteria is "no detonation as a result of the shaped charge impact."

g. The spall impact test subjects the test item to hot spall fragments produced by impacting a 1-inch thick rolled homogeneous armor plate with the shaped charge jet of an 81-mm precision shaped charge. A configuration for the spall impact test is shown in Figure 7. The passing criteria is "no sustained burning" shall occur as a result of the spall impact.[4]

The Propulsion Directorate, in the development of IM propellants, is developing less costly subscale IM test articles for quick propellant screening for IM characteristics. The test article is prepared by casting propellant into a tube of Kevlar or graphite composite for subscale testing. A schematic diagram is shown in Figure 8, which shows the composite tube without propellant before hydroburst testing. Since less propellant is involved this is a more safe and cost effective screening tool for IM propellants.

## CLOSING REMARKS

The above is an overview of the Army's efforts to develop IM propulsion technology for future missile systems. The Propulsion Directorate is playing a vital and active part in this IM technology area. The Army missile systems will be required to meet rigorous and challenging IM Test Requirements as stated earlier in this paper. The IM technology development is still in an early stage; however, the cost benefits in personnel and equipment during the manufacture, storage, usage and demilitarization shipment of propellants makes Insensitive Munitions well worth the effort.

## GLOSSARY

| | |
|---|---|
| HMX | Cyclotetramethylenetetramine |
| IM | Insensitive Munitions |
| RDX | Cyclotrimethylenetrinitramine |

References 1-4: MIL-STD-2105A, (DRAFT) 19 JAN 90, Hazard Assessment Tests for Non-Nuclear Munitions

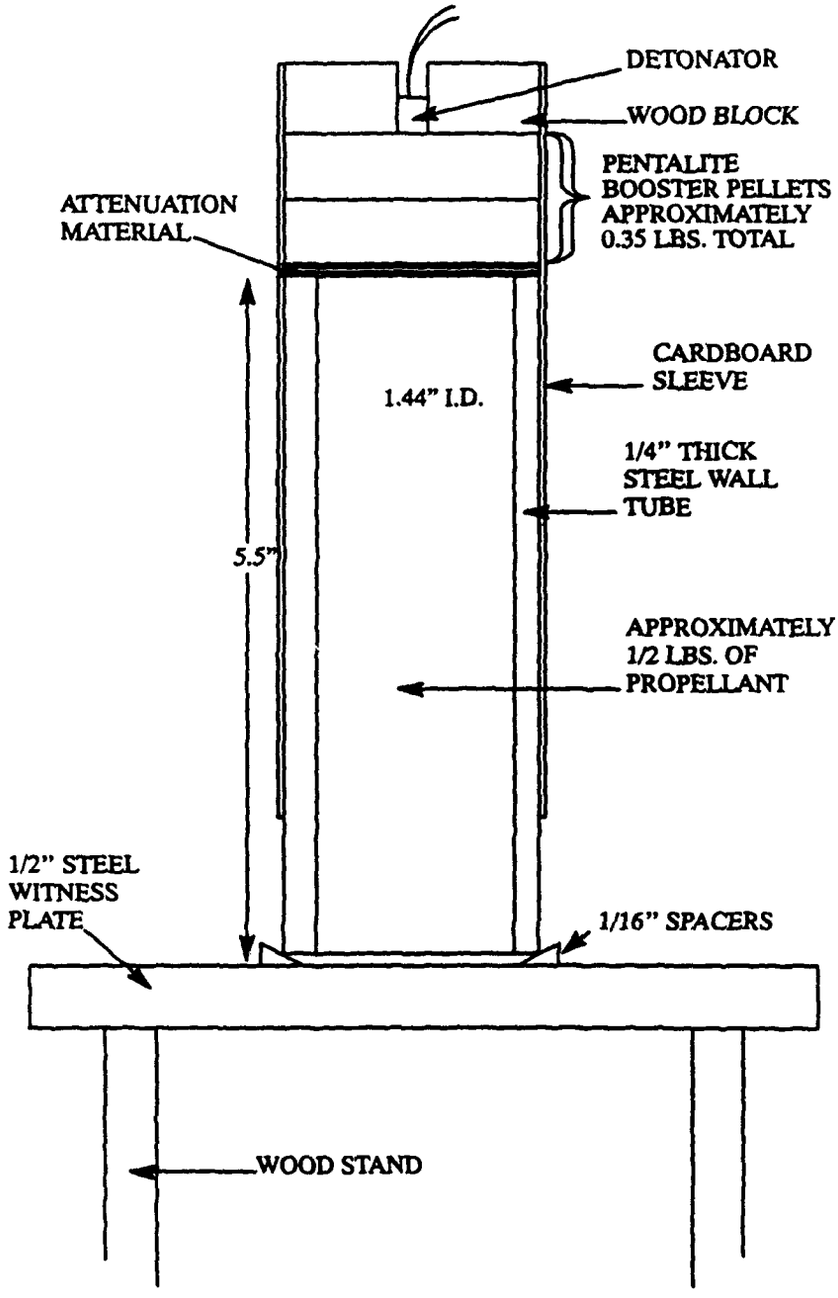


Figure 1. NOL Card Gap Test.

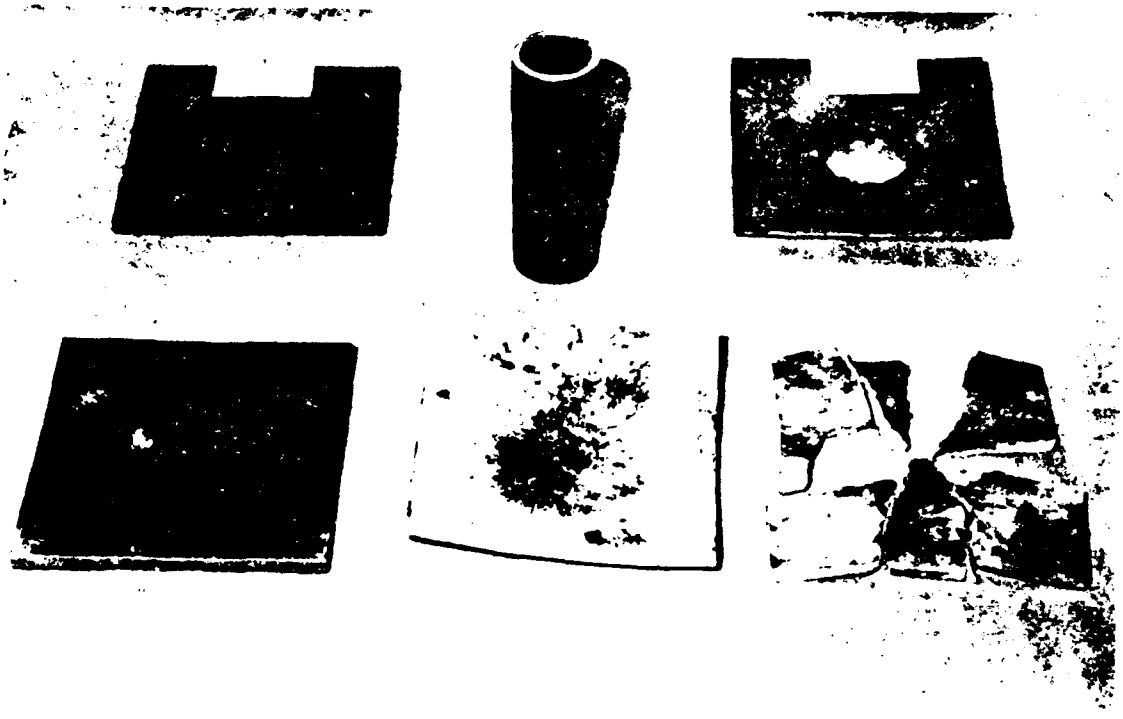

Figure 2. Typical Card Gap Test Results.

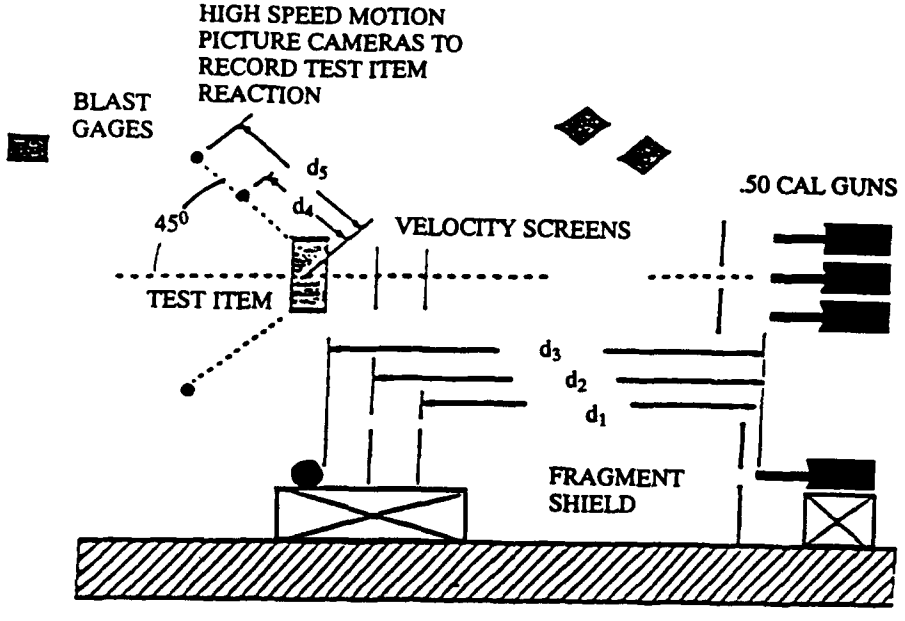


NOTES:

$d_1$ = DISTANCE TO FIRST VELOCITY SCREEN
$d_2$ = DISTANCE TO SECOND VELOCITY SCREEN
$d_3$ = DISTANCE TO TEST ITEM
$d_4$ = DISTANCE TO FIRST BLAST GAGE
$d_5$ = DISTANCE TO SECOND BLAST GAGE(S)

**Figure 3. Bullet Impact Test Configuration.**

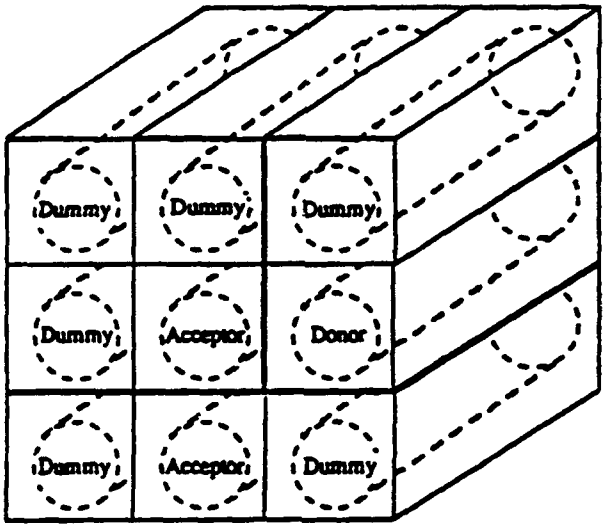


Figure 4. Possible Sympathetic Detonation Configuration.

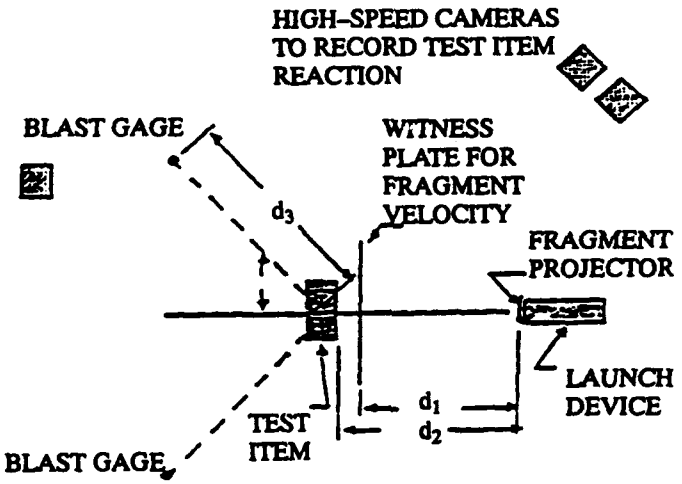


$d_1$ = DISTANCE FROM FRAGMENT MAT TO WITNESS PLATE
$d_2$ = DISTANCE FROM FRAGMENT MAT TO TEST ITEM
$d_3$ = DISTANCE FROM TEST ITEM TO BLAST GAGE(S)

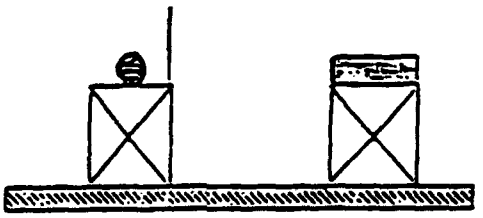

Figure 5. Fragment Impact Test Configuration.

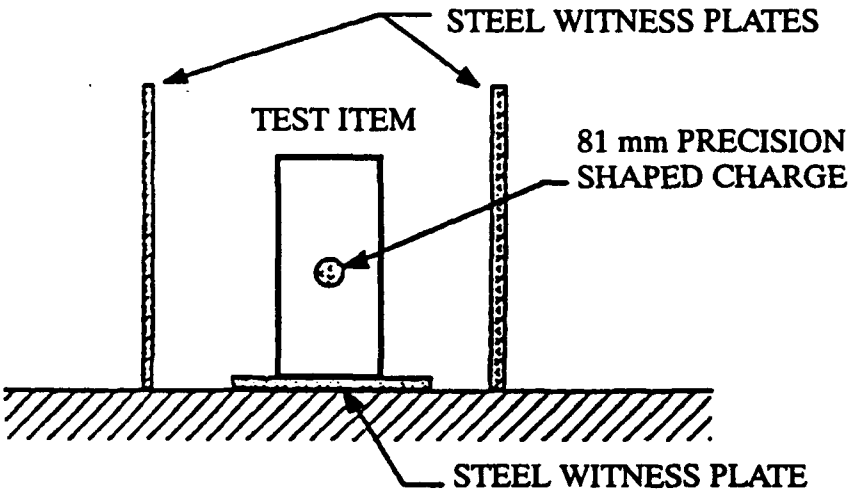


ELEVATION VIEW

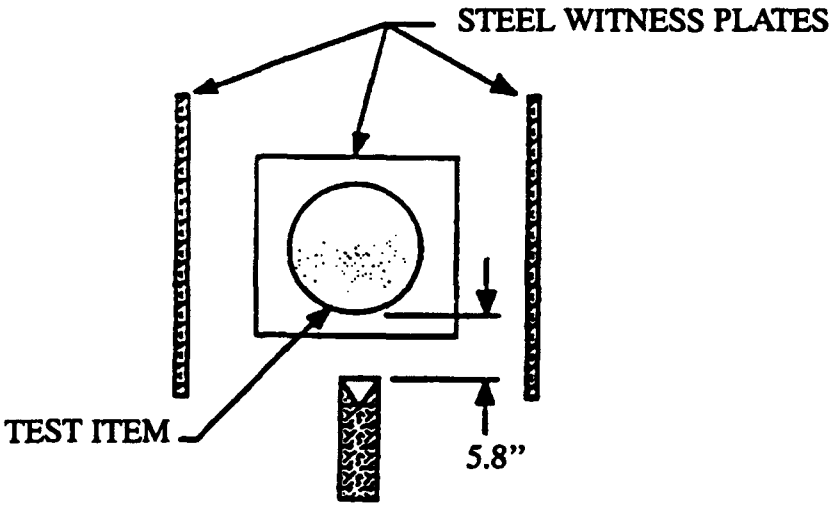


PLAN VIEW

Figure 6. Shaped Charge Jet Impact Test Configuration.

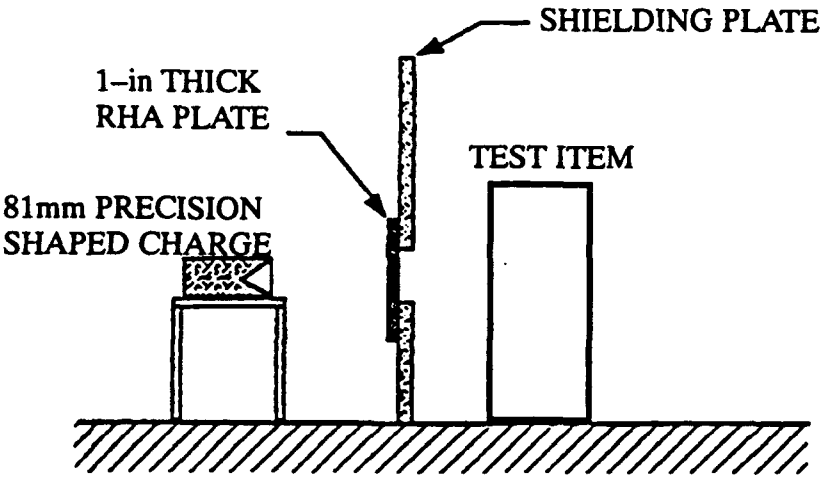


ELEVATION VIEW

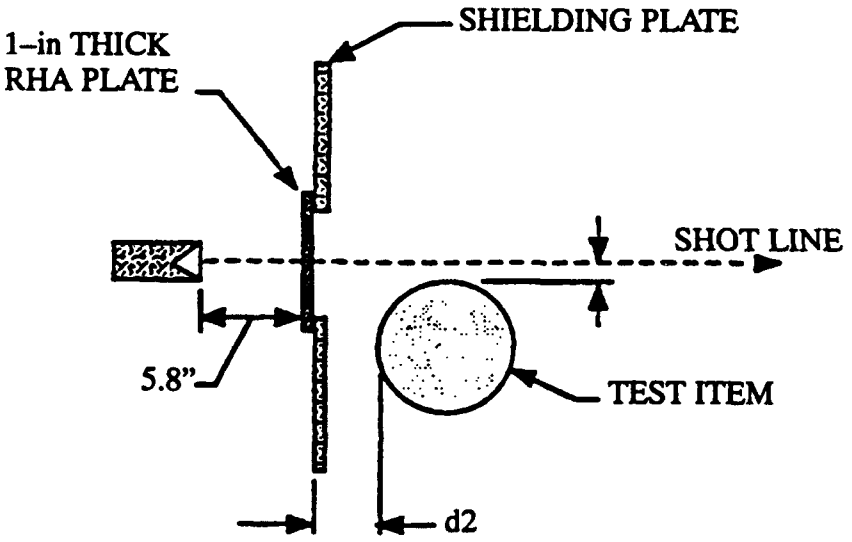


PLAN VIEW

Figure 7. Spall Impact Test Configuration.

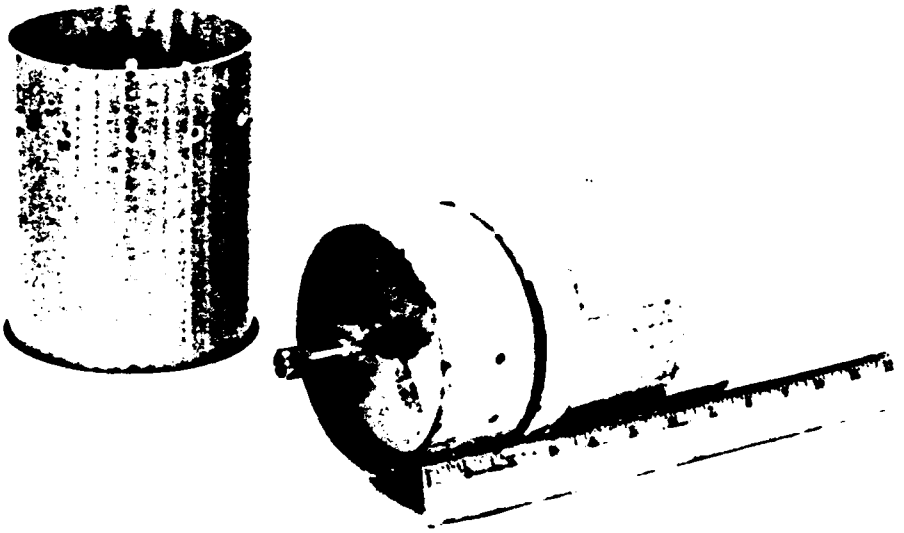

Figure 8. Epoxy End-Capped Kevlar Braided Tube for Hydroburst Testing.

# COMPOSITE MOTOR CASE TECHNOLOGY

Kelly B. McGuire
Propulsion Directorate
Research, Development, and Engineering Center

## ABSTRACT

Composite motor case technology has matured over the past twenty years, with great advances in the manufacture of the fibers used to fabricate motor cases. In addition to the advances in fiber technology, significant improvements to the manufacturing hardware have also taken place. The advantages and disadvantages of composite motor fabrication are discussed, along with three alternate methods for manufacturing a composite motor case: filament winding, braiding, and steel strip laminate. The response of composite cases to the Insensitive Munitions requirements outlined in MIL-STD-2105 is also discussed.

## I. INTRODUCTION

Ever since man became interested in rocket propulsion, he has constantly sought to optimize his propulsion vehicle. Rocket technology has evolved over the past thousand years from simple paper and gunpowder rockets to complex liquid and solid rocket motors. In the 50's and 60's the rocket motor designer opted to stuff as much energetic material into the rocket motor case as possible to enhance its performance. However, the payoffs from this effort became smaller and smaller in recent years. The next approach to enhance the performance of the motor was to minimize the inert weight of the motor case. Significant weight savings were not possible until the 70's and 80's when there were great advances in the manufacturing of the fibers required to fabricate composite motor cases.

A typical solid rocket motor configuration is shown in Fig. 1. The primary elements in a solid rocket motor are: the igniter, propellant grain, insulation, liner, motor case, and nozzle assembly. Of these components, the motor case and nozzle are ideal candidates for composite fabrication. Substantial weight savings can be achieved by replacing these components with composite materials. This paper will only address the benefits of a composite motor case.

The Propulsion Directorate has been active in composite motor case research over the past several years by participating in manufacturing technology programs such as: "The Collapsible Net Metal Mandrel Program," "The Integral Wound Composite Adaptor Program," and "The Low Cost Free Flight Motor Program." Many of the results from these programs are currently being used in industry.

## II. ADVANTAGES AND DISADVANTAGES OF COMPOSITE FABRICATION

### ADVANTAGES

There are several advantages to using a composite motor case rather than the traditional monolithic case. The primary benefit of using a composite motor case is weight savings, which can improve the overall performance of the motor. The weight savings are easily visible when comparing the motor case materials currently used in Army systems. Bar graph representations of the material density and tensile strength of these materials are shown in Fig. 2 and Fig. 3, respectively. The results of a laminate analysis of a 6-inch diameter tube subjected to a 3,000 psi internal pressure are given in Table 1. The results presented in this table demonstrate that a graphite tube is approximately 7 times lighter than a comparable 4130 steel tube.

Composite motor case fabrication offers the following advantages:

* Tailorable case stiffness to weight ratio
* Non-strategic materials
* Light weight
* Short lead time for special configurations
* No welds
* Corrosion resistent
* Low Thermal Expansion of graphite/epoxy

### DISADVANTAGES

Some of the disadvantages of composite motors are listed below:

* More susceptible to damage during handling operations
* Require more complex inspection (Ultrasonics, X-ray)
* Analysis more difficult (requires additional materials transformations)
* High cost for small tactical motors
* Closures and attachment hardware present significant challenges in the design of composite cases
* Dilatation can be a problem for propellant grains
* Extra case thickness can create problems for volume limited applications

## III. TYPES OF COMPOSITE MOTOR CASES

There are three basic methods of fabricating composite motor cases: filament winding, braiding, and steel strip laminate. The first two methods utilize fibers and a resin matrix material to form the structure, and the latter utilizes thin steel strips and an epoxy. Each of the manufacturing methods are described in greater detail below.

### FILAMENT WOUND

Filament wound cases generally have a higher strength to weight ratio than monolithic cases. This strength is primarily due to the advances in fiber technology during the past decade. Filament winding is also cost effective, especially when manufacturing large motor cases.

Filament winding became a proven technology in the early 60's as a viable method for fabricating pressure vessels. In the early days of filament winding the machines consisted of a modified lathe which had the capability of rotating the mandrel while traversing along the longitudinal axis. The winding patterns were obtained by selecting the appropriate gears to achieve the desired mandrel rotation and traverse speed. The modern filament winding machine is computer controlled and has six degrees of freedom, enabling the machine to wind complex geometries with relative ease.

The procedure for fabricating a filament wound case consists of several steps. The winding time ranges from a few hours for a small case to 14 days for the proposed Filament Wound Case (FWC) for the Space Shuttle Solid Rocket Booster. The first step involves preparing a mandrel made of plaster, sand, salt, or more recently, a collapsible net metal mandrel. Following this step, the insulators are installed on the mandrel and spliced in preparation for the case winding. The case body or pressure vessel is formed by winding a series of helical and hoop layers, as depicted in Fig. 4 and Fig. 5. The helicals provide the primary structure for ensuring the integrity of the domes, while the hoop layers provide the pressure carrying capability of the cylindrical section. The fibers used during the winding process are either preimpregnated with resin or dipped in a resin bath during the winding process. Upon completion of the winding, the case is placed in an oven or microwave and cured. Following this step the cases are exposed to a series of leak and hydroproof tests to ensure joint and case integrity.

### BRAIDED

The use of low cost, light weight, mass produced fabrication concepts for tactical motor cases has been a goal of several Army technology programs for the past decade. The principal concepts which have been pursued are strip laminate, line pipe, and braiding, all of which rely on rapidly produced tube type fabrication methods. Such construction becomes increasingly attractive as the motor L/D requirement increases since the closure design, weight, and cost all become less significant with larger L/D ratios. The braided composite construction discussed here was previously used for launch tubes and similar open ended applications. However, the more stringent requirements for free flight artillery rockets indicated an excellent potential application. This potential was most fully exploited and developed in a recent Manufacturing Methods and Technology (MM&T) Program, as outlined in Reference 1.

Braiding is an extremely old process which was first mechanized during the industrial revolution. The methodology used today was developed for the textile and rope industries. The major factor in making braiding a viable concept for rocket motor cases is the advance in the materials industry. Fibers today are lighter and stronger than other structural materials, making composite cases an attractive alternative to the monolithic equivalent.

The braiding process utilized the over and under placement of adjacent strands of yarn in a specified pattern around a mandrel. The typical pattern interlaces helical and longitudinal yarns into layers of fiber (fiberglass, Kevlar 49, graphite, etc.) reinforcement in a sequence optimized for specific strength and stiffness requirements. These layers are impregnated with resin and used to complete this unique composite structure. By adjusting the braid angle, the hoop and longitudinal strength can be optimized. The greater the braid angle, the greater the longitudinal strength.

The braiding equipment used to fabricate motor cases at the Propulsion Directorate consists of the Wardwell 144 carrier braider shown in Fig. 6. The major components for braiding rocket motor cases are the braiding wheel, braider support structure, mandrel traverse mechanism, component mandrel, and support equipment for the mixing, application and curing of the resin. A schematic of the braider is shown in Fig. 7. This figure identifies the components previously mentioned. A balanced braid is obtained when the width of fiber lies flat and adjacent so that no gaps occur between widths. The braid angle is controlled by adjusting the number of carriers, the speed of the carriers around the braid wheel, and the feed rate of the mandrel through the braid ring. The machine shown in Figs. 6 and 7 has the capacity of 144 helical cops of fiber and 72 cops of longitudinal fiber. The braid angle can be altered to achieve the optimum configuration for various diameters and shapes. Longitudinal fiber of the same or different material can be interwoven around the circumference to increase the bending stiffness. Each of the carriers travels about the braid ring along a serpentine guide path, producing an over and under braid effect. These layers can be optimized for specific load cases by tailoring the winding pattern to accommodate the burst or stiffness requirement. The fibers are impregnated with epoxy resin and cured, resulting in a bonded composite structure.

## STEEL STRIP LAMINATE

Steel strip laminate (SSL) motor cases are fabricated by winding a 3-inch wide continuous strip of 301 stainless steel approximately 0.003 inches thick over a cylindrical mandrel. The steel strips are held in place by epoxy. A typical SSL c ase will consist of four to six layers of steel. The resulting case has strength and weight properties similar to a monolithic case. This technology is best suited for fabrication of motor cases with a large L/D ratio. Although there are limits as to the tailorability of the SSL design, initial test results indicate the SSL case could meet the Insensitive Munitions requirements.

## IV. INSENSITIVE MUNITIONS

One of the areas of concern in the military is safety in storage and handling of munitions. A program is under way to make the munitions less susceptible to low energy impact, fragment impact, fuel fires, and prolonged exposure to a heat source. Many of these requirements are addressed in great detail in MIL-STD-2105A. There are two primary ways to meet the requirements of MIL-STD-2105A. The first method is to obtain a propellant formulation which is rugged and non-detonable. The propellant chemists are currently striving to arrive at a propellant formulation which is non-detonable, yet has sufficient mechanical and ballistic properties to perform as a tactical propellant. The second method of meeting the requirements of MIL-STD-2105A is to encase the propellant in a rugged energy absorbing motor case. Some of the tests currently under investigation are described below.

### INSENSITIVE MUNITION (IM) TSTS CURRENTLY UNDER INVESTIGATION

Slow Cook-Off. The slow cook-off test is used to determine the reaction temperature and to measure the overall response of a rocket motor to a gradually increasing thermal environment. The test consists of preconditioning the test article to 100 °F before increasing the temperature at a rate of 6 °F per hour until reaction occurs. Passing this test requires no reaction more severe than burning.

Fast Cook-Off. Fast cook-off consists of engulfing the test item in the flame envelope of a liquid fuel fire and recording its reaction as a function of time. This test is accomplished by placing a common jet fuel (JP-5, JP-8, etc.) in a basin whose dimensions are at least 10 feet larger than the dimensions of the motor being tested. The flame temperature is measured via thermocouples. Passing this test requires no reaction more severe than burning.

Bullet Impact. The bullet impact test consists of impacting the test article by at least three 50 caliber armor-piercing bullets at 2800 ± 200 ft/s. Passing this test requires no reaction more severe than burning.

Fragment Impact. The fragment impact test consists of striking the test article with a 250 grain steel cube traveling at 8300 ± 300 ft/s. Passing this test requires no reaction more severe than burning.

### COMPOSITE MATERIALS CONTRIBUTIN TO THE IM PROBLEM

Utilizing composite motor cases can maximize safety of the rocket motor during storage and handling. Safety can be accomplished through the proper selection of fiber and matrix material. For example, to achieve the desired results from the bullet and fragment impact tests, a composite motor case must be capable of absorbing a large portion of the energy of the projectile upon initial impact, thus minimizing the shock to the propellant grain. Another benefit is the non-sparking characteristic of the organic composite fibers.

A composite case can minimize the threat of detonation of a motor due to either the fast or slow cook-off test by allowing the pressure inside the case to vent. Methods currently under investigation to achieve this goal involve the selection of matrix materials. An ideal candidate for a matrix material would be one that has sufficient strength to ensure the integrity of the motor under operating conditions, yet would melt at temperatures below the propellant's auto-ignition temperature if exposed to a heat source for a prolonged period of time, thus allowing the case to vent in the event of ignition. In addition to this desired thermal response, the potential exists for adding an ablative coating to the matrix material which could prolong the time a motor could be subjected to a heat source prior to ignition.

## V. CONCLUSIONS

Composite motor technology is constantly improving, primarily due to major advances in the manufacture of fibers used during the winding process. Composite motor cases offer high strength to weight ratios and tailorable case stiffness properties. The fa brication process has been proven over the past 25 years. Composite cases offer several solutions to the Insensitive Munitions problems facing the industry today.

## REFERENCES


1. Crownover, W. S., and McGuire K. B., "Use of Braided Composite Construction for Tactical Rocket Motor Cases," U.S. Army Missile Command, TR-RD-PR-86-7, January 1987.

2. Christensen, Paul, "Filament Wound Rocket Motor Cases - Where Are We Now And Where Are We Going?", Hercules, January 1987.

TABLE 1 STRUCTURAL COMPARISON UNDER INTERNAL PRESSURE
6 INCH DIAMETER TUBE, 3000 PSI [2]

| MEASURE | STEEL 4130 | ALUMINUM 7075-T6 | S GLASS | KEVLAR 49 | AS GRAPHITE | IM GRAPHITE |
|---|---|---|---|---|---|---|
| HOOP STRESS (KSI) | 180 | 83 | 180 | 140 | 175 | 253 |
| RADIAL GROWTH (IN) | 0.015 | 0.021 | 0.099 | 0.058 | 0.042 | 0.054 |
| WEIGHT (LB/FT) | 5.0 | 3.9 | 1.2 | 1.1 | 1.0 | 0.7 |

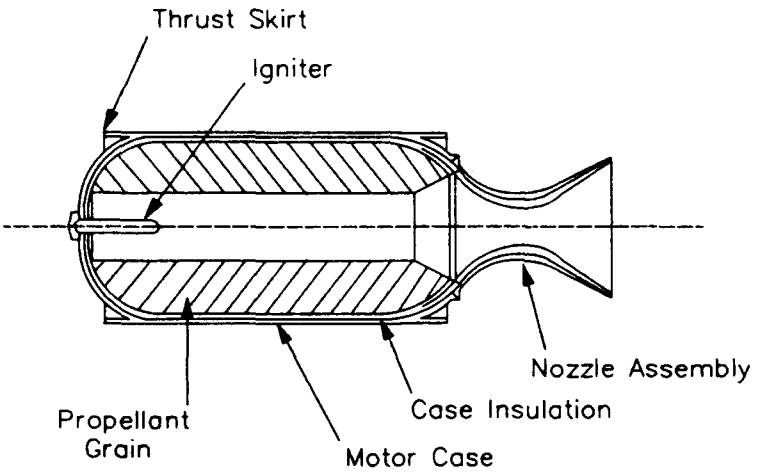


**Figure 1. Typical Solid Rocket Motor Configuration**

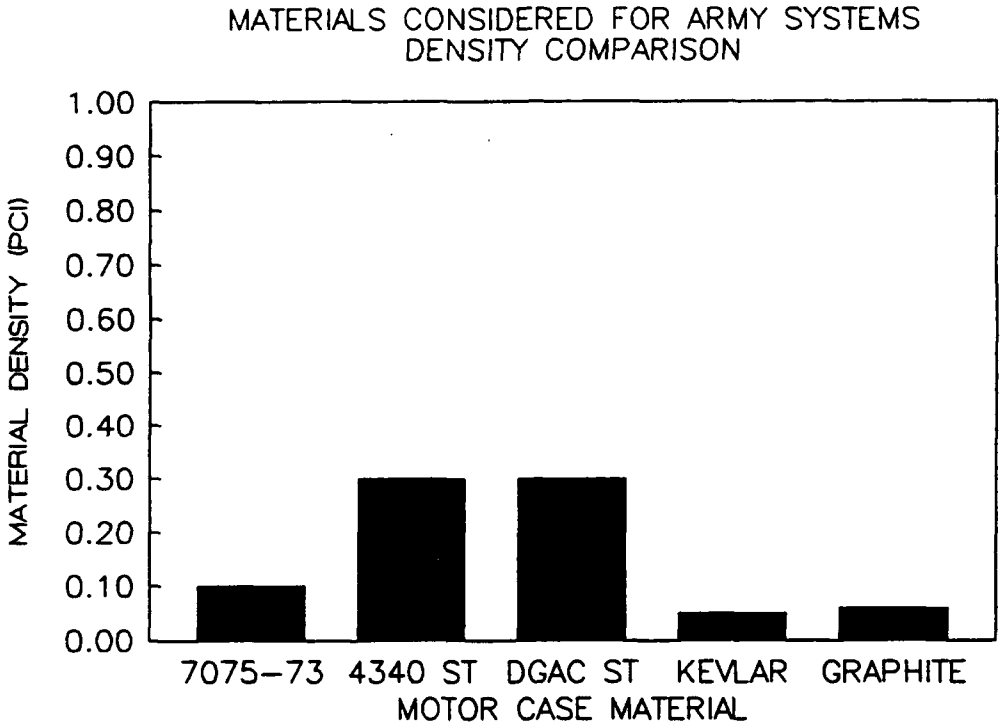


**Figure 2 Density of The Materials Considered For Army Systems**

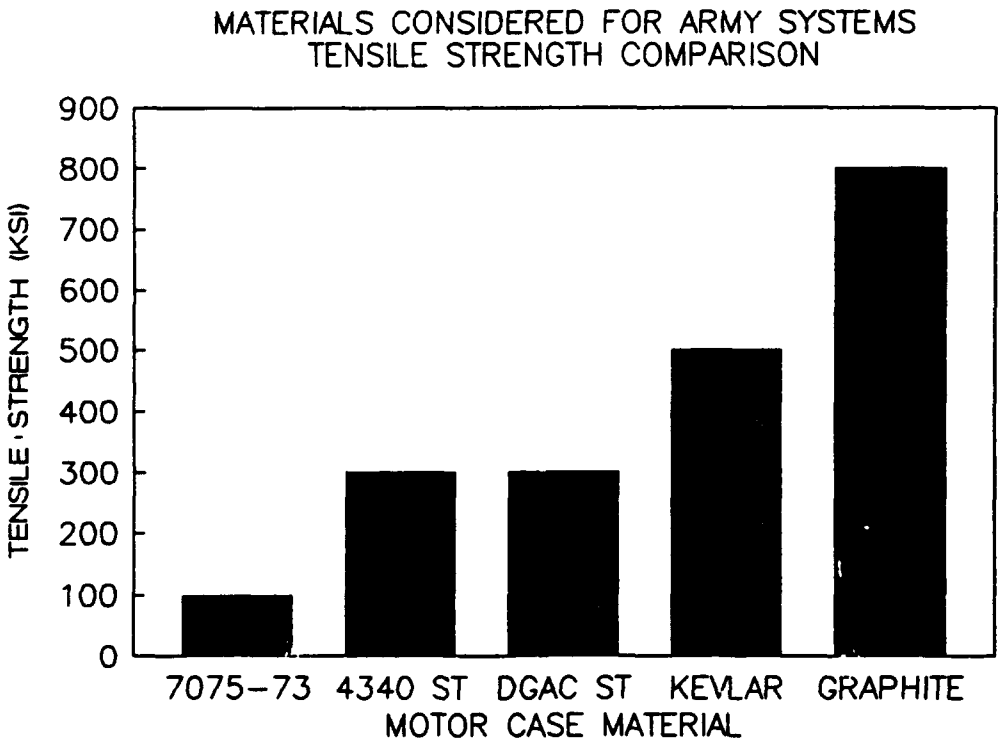


**Figure 3 Tensile Strength of Materials Considered For Army Systems**

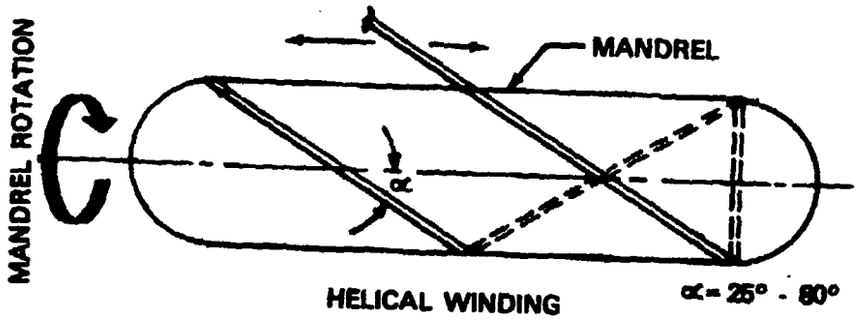


Figure 4 Filament Winding Helical Pattern

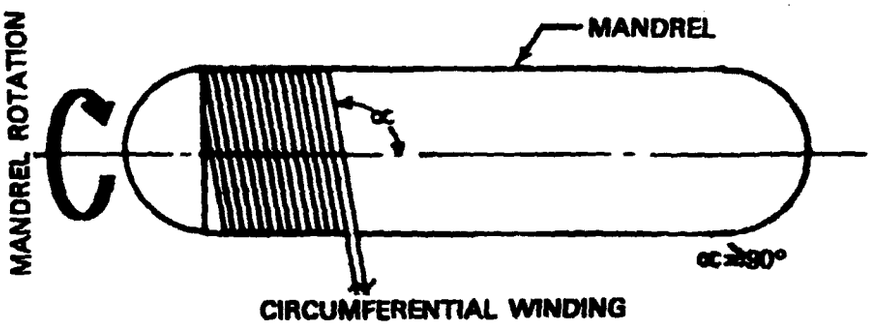


Figure 5 Filament Winding Hoop Pattern

Figure 6 Wardwell 144 Carrier Braiding Machine

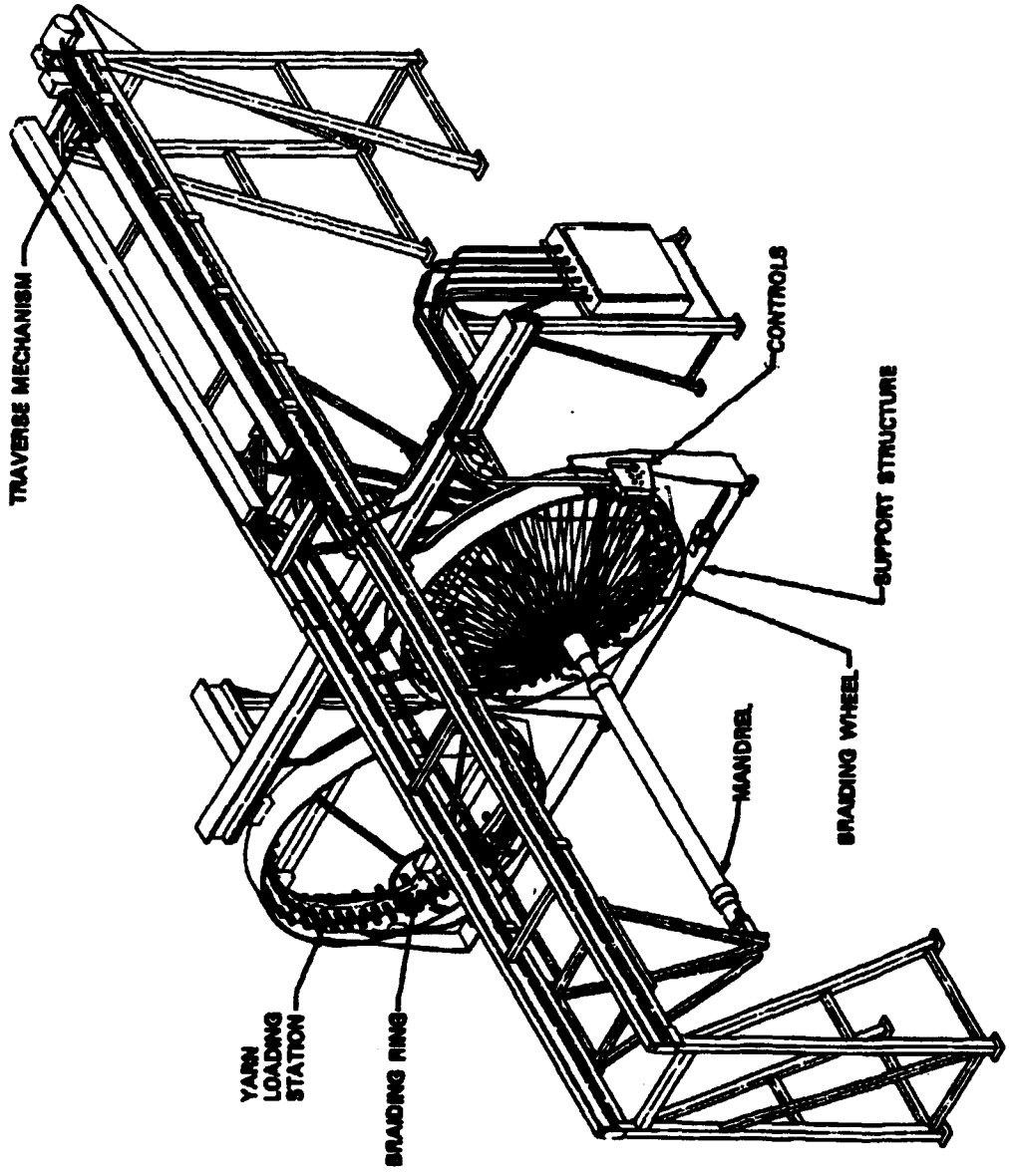


Figure 7 Braiding Machine Configuration

# Rocket Motor Testing at the Propulsion Directorate

Robert W. Milton
Propulsion Directorate
Research, Development, and Engineering Center

## ABSTRACT

The U.S. Army MICOM Propulsion Directorate at Redstone Arsenal, Huntsville, Alabama, has the job of improving the propulsion systems of existing Army missile systems and designing and implementing new and innovative propulsion technology in future systems. This broad assignment encompasses a large number of interrelated tasks, including the topic of this paper, Propulsion Directorate Testing, that are all focused upon the improvement of propulsion technology.

## INTRODUCTION

Since propulsion technology improvement is a research and development effort, the best way to evaluate the success or failure of new ideas is by testing and analysis. Many prototypes that seemed ideal on paper have failed to produce the desired results when put on the test stand or laboratory bench. In addition, a good, well planned test program allows technical personnel and engineers to evaluate specific parameters of a propulsion system without being burdened with interference effects from non-contributing items. In effect, testing is the acid test for new ideas and concepts, and the Propulsion Directorate recognizes the need for an advanced test capability.

## DISCUSSION

A major percentage of the test work being performed at the Propulsion Directorate relates directly to the Insensitive Munitions (IM) program. This program was created to evaluate and desensitize munitions to accidental and combat induced environments that could lead to failure of the system. Each system must undergo a battery of tests to determine its sensitivity characteristics and reaction to damaging stimulus, such as being hit by hot metal fragments, accidental impact, or gunfire.

The Propulsion Directorate also devotes considerable effort investigating mysteries of propellant related mishaps in the commercial world and in the military arena. Some of the investigations have had worldwide repercussions and have given the Propulsion Directorate an excellent reputation for thoroughness and effectiveness.

The Propulsion Directorate, in its mission of improving missile propulsion technology, is able to test a wide range

of new concept hardware and ideas. A very capable on site testing environment is a necessity. Complete chemical as well as physical analysis can be performed efficiently with a minimum of logistical problems. Elemental propellant formulation analysis, surveillance work, quality control, ageing studies, mechanical properties testing, static firing, and exhaust signature evaluation can all be accomplished in the Propulsion Lab complex.

The Propulsion Lab has an extensive chemical analytical capability and is continually faced with new challenges. Chemical testing and analysis can be performed efficiently and effectively at the Propulsion Lab. The fundamental characteristics of solid or liquid propellant are determined by its chemical composition and properties. In order to achieve comprehensive knowledge of new and existing propellants, a modern and capable chemical analysis capability is a must. Propellant compositions must by analyzed throughout their development to insure that the various individual ingredients are combined to achieve the desired finished product. Constant monitoring of fielded missile propellant is done routinely to insure the continued operationability of the system. In addition, quality control testing and service life investigations of propellant are an important role in chemical testing. Gas chromatography, infrared and ultraviolet spectroscopy, atomic absorption and propellant extraction and analysis are only a few of the chemical testing capabilities of the Propulsion Directorate.

The Propulsion Directorate realizes that the physical properties of a propellant are as important as the chemical ones, and has an entire function and test area dedicated to achieving the desired combinations of strength, flexibility, and longevity in its propellants. Physical propellant properties can be characterized exactly the same way as more commonly recognized structural materials, such as steel or aluminum. Propellants have a measurable ultimate tensile and yield stress, a modulus of elasticity, and creep and fatigue limits. In order for these characteristic propellant properties to be experimentally determined, a tensile test specimen is loaded until failure. The resulting strain curve allows the determination of the unique properties of the specific propellant sample.

The Propulsion Directorate has a multiple bay static test firing range and extensive ballistic data acquisition capability. Figure 1 is a photograph of the static test stand.

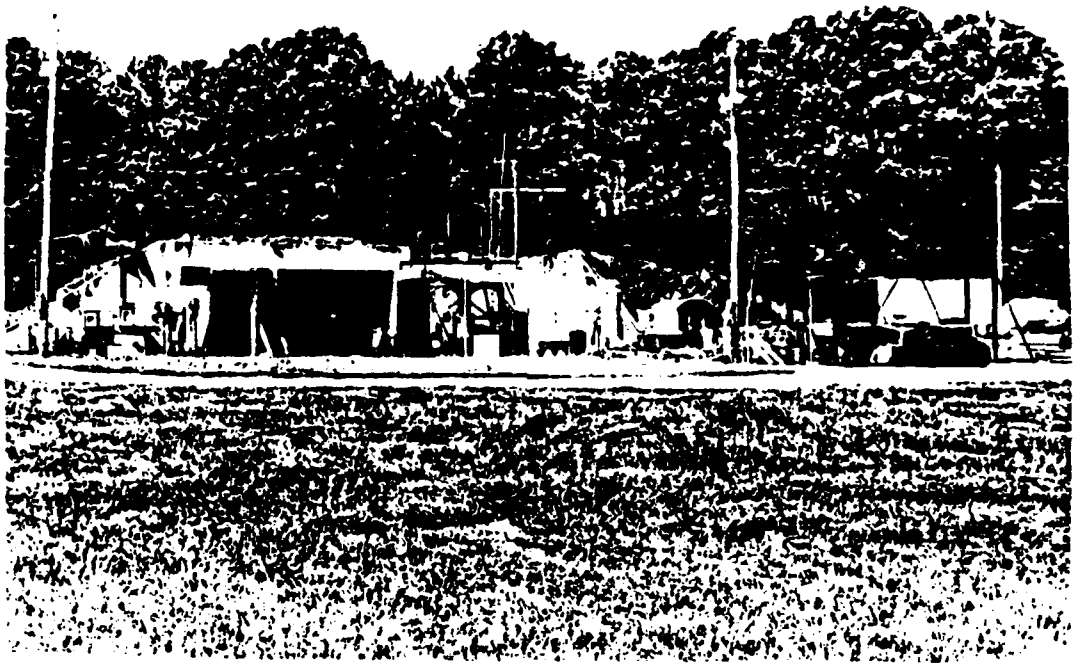

Figure 1. Static Test Stand.

Experimental missile propellant, no matter how promising it appears in the design stage, must be proven by being fired in a static test facility. The Propulsion Directorate has an excellent capability for static test firing and can handle motors from 2 inches to over 5 feet long. On average, between seven hundred and one thousand motors are statically tested each year at the static test facility. In order to collect and process the large amounts of motor performance data that is necessary, an efficient control center utilized. Some of the measurement capabilities for statically fired motors are chamber pressures, thrust, torque, temperature, noise and recoil.

The Propulsion Directorate also tests many different varieties of small gas turbine engines, and has a dedicated test facility strictly for that purpose. As an alternative to the more conventional methods of missile propulsion, gas turbine engines are showing great promise. Gas turbine engines have some significant advantages over conventional missile propulsion systems in that they have almost no exhaust signature, are throttleable, and can be produced quickly and cheaply. Figure 2 is a photograph of a disassembled turbojet engine and its component parts.

Figure 2. Turbine Engine.

The stringent material requirements of a flight ready, high thrust, small diameter, light weight turbine engine has helped push technology forward. For example, there is a huge difference in the operating stresses and material property constraints that are imposed upon an ordinary car engine and a missile turbojet. A standard automobile has an engine that can run at approximately 6000 RPM and 300 degrees Fahrenheit, while a missile rated turbojet will run at 120,000 RPM and 800 degrees Fahrenheit. Obviously, the same materials that will work perfectly in the automobile engine will not withstand the necessary operating stress and temperatures imposed by the turbojet. For these reasons, new and exotic materials like high temperature ceramics and alloys are being tested for their potential.

One of the most unique permanent test facilities in place at the Propulsion Directorate complex is the Signature Characterization Facility (SCF). A critical factor concerning the acceptability of a new or existing propellant is its characteristic exhaust signature when burning. The lower or smaller the exhaust signature of the missile, the less chance of interference with guidance signals, and the less vulnerable the launch crew will be toward counter attack. If a missile, when fired at the enemy, leaves a highly visible smoke trail, then the enemy will be able to follow the missile trail backward along its course and find the launching vehicle. In addition, a propellant that has a high infrared signature is much more easily tracked by heat seeking means than a propellant that has a low infrared signature. The amounts of toxic and corrosive chemicals in

the exhaust of a missile could possibly negate the ability of the weapon system to be fired from an enclosed space, such as a room in a building, or a tank turret. The Signature Characterization Facility has the capability to test all these signature parameters, and more. Essentially, the test facility consists of a twenty foot long, climactically controlled, static test chamber, and a separate data acquisition and control room. The chamber is temperature and humidity controlled, and can be set in the range of -40 degree F to 140 degrees F. Small scale motors are fired in the chamber and their signature is evaluated with monitoring equipment. Figure 3 is a photograph of the control room of the SCF showing the complex array of instrumentation utilized to collect signature data.

Figure 3. SCF Control Room.

A small scale motor is mounted on a static firing stand in the environmental chamber, and ignited. During the burn, the actual motor flame can be tested for its visible and infrared components, and utilizing special interferometry techniques, the chemical composition of the flame can be investigated. After the motor has extinguished itself, the exhaust plume is contained in the chamber while comprehensive tests are run. Data on toxicity, particle size, chemical composition, and light transmission on various wavelengths is gathered, and the typical sampling time is on the order of five minutes.

The Propulsion Lab is committed to Insensitive Munitions work, and the bullet test program is a good example. The small caliber bullet test work done at the Propulsion Lab was performed in order to gain a better understanding of a small arms bullet impact threat, and the nature of any inhibiting mechanisms that may permit the survival of the developed weapon system against bullet impact stimulus. The test setup consisted of a remotely mounted and fired rifle that was used to shoot a variety of propellant filled, analog motor test cylinders, each five inches in diameter and ten inches tall. In addition to high speed data sampling equipment and VHS video, a 40,000 frames per second camera was used to record the response of the bullet striking the test motor. The high speed camera is fast enough to photograph a bullet in flight, so it is an excellent tool to record the fast responses of reacting propellant.

A propellant sample can actively react in three distinct ways when struck by a bullet.[1] The sample can burn, explode, or detonate. Good evidence of a reaction is obtained by the high speed camera or video recorder, such as what recorded the series of photographs below. Figure 4 is a video camera picture of a motor that exploded when struck by a bullet. The sample was destroyed by the explosion, and large pieces of propellant and motor case were recovered from over 150 feet away.

Figure 4. Picture of Sample Exploding.

The picture clearly shows the bullet hole in the front of the case, and the exhaust flame coming from the nozzle area. This figures illustrate how dangerous a bullet strike on a missile motor can be, and how, under certain circumstances, the missile could become propulsive and inadvertently launch. At the very least, both the reactions caused by bullet impact and illustrated by Figures 4 and 5 would have damaged the missile launching vehicle and threatened the crew.

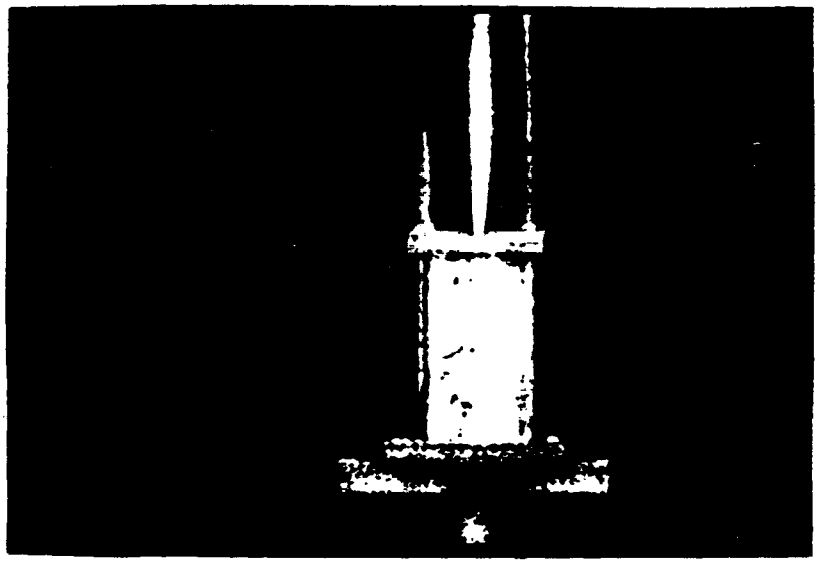

Figure 5. Picture of Propulsive Burn.

Some of the testing performed by the Propulsion Lab, because of the uniqueness of the test, takes existing data acquisition and measurement technology to the limit. For example, a special propellant sensitivity test, called the RND test, measures the actual speed of a detonation wave as it travels down the length of a 15 inch long propellant sample.[2] Contrary to popular belief, when a substance such as an explosive or propellant detonates, the entire piece of material does not react at exactly the same time. A detonation wave front is created by a certain, specific stimulus and travels radially outward in all directions. In an example where the detonation stimulus is applied to the end of a long narrow sample, as it is in the RND test, the detonation wave travels down the length of the propellant with great speed. Detonation waves, unlike acoustical or other vibration waves, travel supersonically through the detonating material. Some of the detonation waves travel at more than 11,000 miles per hour, almost 15 times the speed of sound in air. The extreme velocity of the detonation wave is one reason why it is so difficult to accurately measure. Since the entire RND test specimen is only 15 inches long, it is obvious that some specialized equipment is necessary to accurately record the high velocity detonation wave as it travels down the length of the test specimen. The solution to such a problem is to measure the elapsed time the detonation wave takes to travel between two points that are a known distance apart. Five small piezoelectric pins are inserted into the test sample at equally spaced distances down the length of the sample. Figure 6 is a photograph of a RND test specimen with the pins installed.

These pins have an extremely fast electrical response time and give off a characteristic voltage spike when impacted by an object or a shock wave. The time between the voltage spikes of the successive piezoelectric pins is recorded by an extremely fast recording oscilloscope that has the capability to collect data at a rate of 27 billion samples a second. The high acquisition speed allows the oscilloscope to record the elapsed time for the detonation front to pass successive pins as it travels down the detonating sample. An actual data trace is shown below in fig 7.

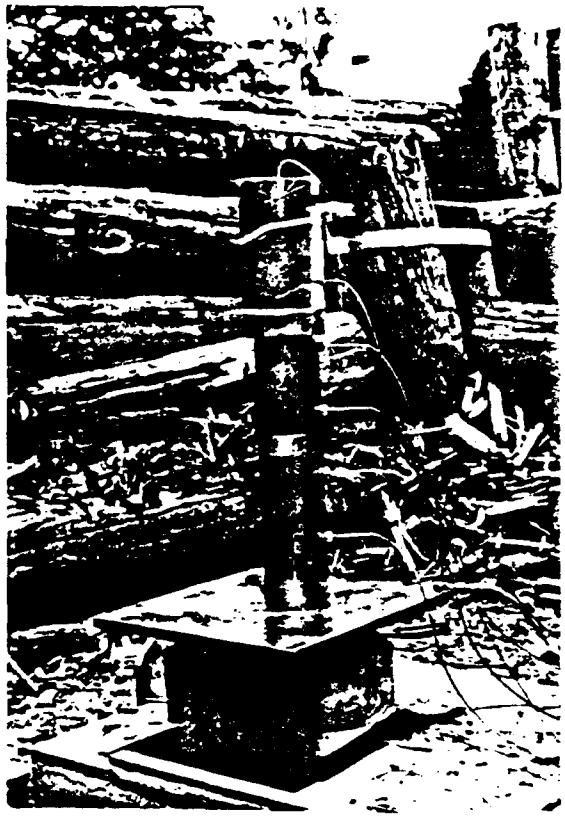

Figure 6. RND Test Specimen.

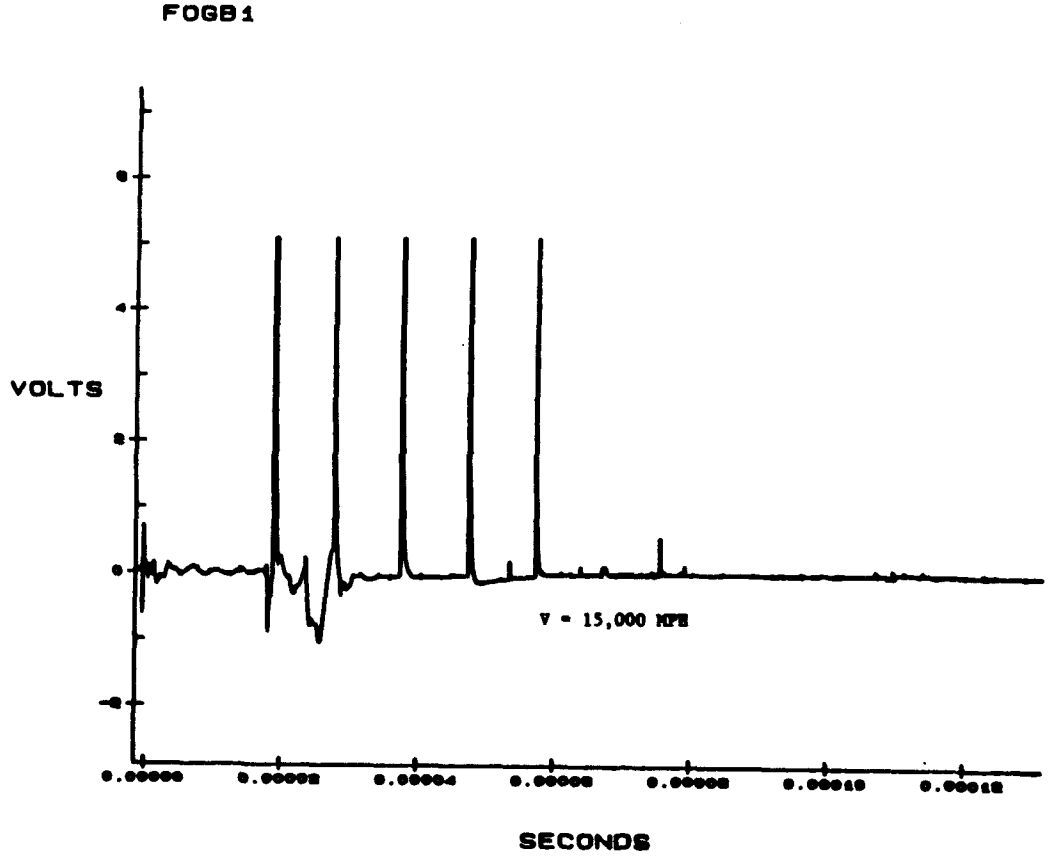


Figure 7. RND Voltage Response.

The trace clearly shows each individual voltage spike that was produced when the detonation front passes and activates a piezoelectric pin. The average velocity of this detonation wave front is approximately 15,000 miles per hour, or 20 times the speed of sound in air.

Some of the most interesting test work has been performed as a direct result of investigations into missile related accidents or mishaps.

One noteworthy investigations was initiated in 1985, when, in Germany, a Pershing missile that was being unloaded from its packing crate ignited and burned, killing 5 U.S. Servicemen. The event was given a national defense priority and an investigation was launched. There were no immediately apparent reasons for the failure, although sabotage was one of the considerations. An unusual set of circumstances of the normally routine uncrating procedure had been noted by a professional observer. Apparently, there was some difficulty in the uncrating process, and the motor could not be removed in one smooth operation. The motor had been binding in the crate, and was raised and lowered repeatedly from the shipping container. The observer said that he heard a sharp electrical pop just before the missile ignited, and because of this testimony, the theory was put forth that somehow, as an effect of the repeated attempts at uncrating the motor, an electrical charge built up in the motor case due to friction with the crate, and the missile was ignited. The motor case was made of Kevlar and the portions of the packing crate that had been in contact with the missile were made of rubber. These two materials are both excellent electrical insulators. The Propulsion Lab was given the task, along with other directorates at MICOM, of finding the reason for the motor failure. A subsequent investigation revealed that an electrical effect known as triboelectrification had taken place between the motor case and the rubber shock mounts of the packing crate during the uncrating process.[3] Triboelectrification is the creation of a charge of electricity in two contacting materials due to friction. In the case of the Pershing incident, triboelectrification took place between two good electrical insulators, namely the Kevlar motor case and rubber shock mounts in the crate. Normally, triboelectrification is not a concern in metallic materials because the conductive materials disperse the electrical charge. Triboelectrification was a factor in the Pershing incident because neither the motor case or the packing crate that contacted the motor were electrical conductors. Since the triboelectric charge was caused by the friction of two insulators, the charge could not dissipate through either material, and built up to a possible 5000 volts. The subsequent discharge of this high voltage is what ignited the motor. Once triboelectrification and its effect on insulated motor cases was understood, it was easily fixed.

Simply painting the outer motor case of the missile and the inner bearing surfaces of the packing container with a metallic paint allows the electrical charge to dissipate and has prevented any future incidents with this and other missile systems.

Triboelectrification was the culprit in another fatal incident, one that occurred on Redstone Arsenal. An FBI trainee was killed when a water cannon exploded. The effect of triboelectrification was suspect, and an investigation was started with the help of the Propulsion Lab. The evidence revealed that a triboelectric charge of sufficient magnitude to fire the cannon was built up by the simple action of unwrapping some adhesive tape from the body of the water cannon. The charge was on the order of 6000 volts, as demonstrated by a laboratory investigation.[4] The results of the experiments are shown in Figure 8. This figure depicts the high voltages created by the act of separating different types of adhesive tapes from each other. In order to prevent the accident from occurring in the again in the future, a less adhesive packing tape is now being used.

| Material | Width (in) | Voltage |
|---|---|---|
| Reinforced Plastic | 1.0 | 6,000 |
| Black Plastic | 0.5 | 5,000 |
| Black Plastic | 1.0 | 9,000 |
| Cloth | 0.75 | 700 |

Figure 8. High Voltages Created by Adhesive Tape Separation

Other types of missile systems have had problems, and these have also been investigated by the Propulsion Lab. In the mid 1980's, several TOW missile launch motors failed in the form of a pressure burst in which dangerous fragments of the motor were thrown about. These failure of the launch motors raised the questions of safety and reliability in a major missile system, and a "DO NOT USE" notice was sent from MICOM to the various armies in the world that fielded the TOW weapon. The Independent Review Board that was formed to conduct an investigation of the accidents felt that there should be an effort to determine the actual chamber pressure levels at the time of the motor failures. If this could be defined, then failure scenarios and causes could be better refuted or justified. Sample TOW launch motors were tested and caused to fail at various pressures by machining a notch of different sizes in the side of the motor. The resulting pieces of the exploded motors were gathered up after each induced failure and weighed.[5] A resulting average weight of fragments versus failure pressure was established, and when this data was compared to the actual TOW motors that failed in the field, it was a relatively simple task to estimate the approximate chamber pressures of the Tow launch motor failures.

The Propulsion Lab also is involved in commercial propellant related accidents. Ammonium Perchlorate, AP, is an oxidizer, and is used in many solid fueled rocket propellants. In May, 1988, the PEPCON Ammonium Perchlorate facility in Nevada was completely destroyed by an explosion. The devastation of the production facility was a result of 8 million pounds of AP going up in smoke and flame. The destruction of the facility was a severe blow to the missile industry because it cut the U.S. production of AP in half, and taxed the capabilities of NASA and defense programs that utilized AP as a propellant ingredient. Concerns about possible future incidents created an urgent need to increase the knowledge base of AP transportation and storage safety issues. A panel of technical representatives was formed that included personnel from the Propulsion Directorate, and was tasked to perform specific tests that were designed to simulate the conditions of the destroyed AP facility. The resulting data helped the panel review current shipping and storage regulations concerning Ammonium Perchlorate and make the proper recommendations for changes in procedure to keep similar incidents from happening in the future.

## CONCLUSION

The Propulsion Directorate has an international reputation and an exceptional ability to perform complex and unusual tests of missile propellant systems. These experiments range from chemical analysis, physical properties studies, and static tests of conventional and turbine propulsion systems to complex investigations into missile related accidents and failures.

## REFERENCES


1. Milton, R., and Thorn, L. B., "Small Arms Bullet Impact on Analog Motors," JANNAF Propulsion Meeting, Cleveland, Ohio., May 1989.

2. Thorn, L. B., and Wharton, W. W., "Screening of Nondetonable Minimum Smoke Propellants for Army Applications," JANNAF Propulsion Meeting, San Diego, Ca., December 1987.

3. Dreitzler, D. R., "Electrostatic Voltage Generation Measurements on Missile System Materials," JANNAF Subcommittee Meeting, Monterey, Ca., April 1986.

4. Dreitzler, D., "Electrostatic Voltage Generation Measurements on Missile System Materials," JANNAF Subcommittee Meeting, Monterey, Ca., April 1986.

5. Sanders, S., et al., "Investigation of 1986 Yakima and Oahu TOW Launch Motor Failures", Technical Report RD-PR-87-7, March 1988.

# AN OVERVIEW OF THE ARMY ROCKET MOTOR SERVICE LIFE PROGRAM

J. M. Fisher
Propulsion Directorate
U.S. Army Missile Command
Redstone Arsenal, AL

## ABSTRACT

The objective of service life technology is to understand, predict, and verify the effects of loads, environments, material response and aging on the shelf life and structural integrity of rocket motors. Work conducted by the U.S. Army Research, Development, and Engineering Center, Propulsion Directorate and its contractors has led to the development of analytical models which account for thermal/vibrational loads, mechanical property variability, aging, cumulative damage, solar radiation, wind velocity, viscoelastic propellant behavior, internal gas generation/solubility/diffusivity and stress-free temperature shift. These models have been implemented in several computer codes and applied to Army rocket motors. In several instances application of these service life techniques has led to the extension of the effective service life for rocket motors. For example, HAWK service life has been extended from 10 to 17 years with a further extension to 20 years planned for late FY90; PATRIOT service life has been doubled from 7 to 14 years; and MLRS service life will be extended from 10 to 15 years in late FY90. These extensions represent significant savings of over 800 million dollars by delaying required rebuys. In addition, service life technology provides for more efficient production planning, lower costs for stockpile reliability programs, improved management of rocket motor inventories and more reliable structural margin prediction.

## INTRODUCTION

An important factor in the development, deployment, and use of any missile system is: How long is it good for? While care is taken in designing and manufacturing rocket motors to insure sufficient motor performance and safety margins at production, effort is also required to monitor and maintain this performance during the lifetime of the motor. In fact, analysis is even required to determine what this lifetime should be. Unfortunately, rocket motors do not yet come equipped with turkey buttons to let the user know when its service life is "done". Service life evaluation is the technology area which addresses the experimental and analytical work involved in determining and verifying useful shelf life for solid rocket motors.

## FAILURE MODES/STRUCTURAL ANALYSIS

The first step in evaluating service life for a solid rocket motor is to determine the critical failure mode or modes. This is a function of the motor and system configuration, components, design application, and constituent materials. Failure modes may include phenomena such as internal fissuring of the propellant grain due to gas generation from chemical degradation, bondline failures due to stresses induced by thermal cycling and/or cracks in the propellant at the bore or other internal surface due to thermally induced strains. The critical mode for failure can be determined by finite element analyses, full-scale or analog testing, actual field failures and combinations of these.

### COMPOSITE PROPELLANTS

Solid rocket motors containing composite propellants are primarily susceptible to failure from thermal cycling. The coefficient of thermal expansion for metallic or composite case materials is typically an order of magnitude lower than the coefficient of thermal expansion for solid propellant. This causes the case to act as a rigid restraint as the propellant tries to swell and shrink with the temperature cycling. The resulting stresses that build up in the propellant grain and bondline damage and weaken them, ultimately leading to failure. This phenomenon is referred to as cumulative damage.[1]

Linear cumulative damage based on maximum principal stress as shown in Equation (1), is used as the failure criterion in SLife, an in-house computer code for evaluating service life.

$$D = \sum_{i=1}^{n} \frac{\Delta t_i}{a_t \, T_o} \left( \frac{\sigma_i}{\sigma_o} \right)^{\beta} \qquad (1)$$

where

$D$ = cumulative damage
$\Delta t_i$ = time at $\sigma_i$
$a_t$ = temperature dependent shift function
$T_o$ = reference temperature, °F
$\sigma_i$ = average stress during $\Delta t_i$
$\sigma_o$ = critical stress, psi, (at $a_t/t=0$)
$\beta$ = inverse slope of log stress-vs-log reduced time at $a_t/t=0$

Figure 1 Shows bore temperature calculated by SLife as a function of time for a composite motor. Figures 2 and 3 show stress and strain, respectively, at the bore associated with the thermal loads from Figure 1. SLife then calculates the resulting cumulative damage values shown in Figure 4.[2]

## DOUBLE BASE PROPELLANTS

Modified double base, or minimum smoke, propellants are less susceptible to stress and strain damage induced by thermal cycling than the composite propellants. However, the minimum smoke propellants tend to degrade chemically and generate gasses as a byproduct of this degradation. If the rate of gas generation exceeds the rate at which the gas can diffuse through the propellant web, internal cracks develop which can lead to motor failure. The internal pressure at which these cracks will develop is a function of the propellant's mechanical properties. This critical pressure parameter is determined from Equations (2), (3), and (4), and serves as the failure criterion in the in-house service life code GASLife.[3]

$$Pcr = \sigma_m (1 + \epsilon_m) \left( \frac{\alpha - 1}{\alpha} \right) \quad (2)$$

$$\alpha = 1 + \Delta v/v \quad (3)$$

$$\frac{\Delta v}{v} = \epsilon_m \phi_f \left\{ \frac{\ln (E/F)}{1 + \ln (E/F)} \right\} \quad (4)$$

where

| | | |
|---|---|---|
| Pcr | = | critical pressure for cracking, psi |
| $\sigma_m$ | = | maximum stress |
| $\epsilon_m$ | = | strain at maximum stress |
| $\alpha$ | = | volume change ratio |
| $\Delta v/v$ | = | strain dilatation |
| $\phi_f$ | = | volume fraction of filler particles |
| E | = | initial slope modulus, psi |
| F | = | secant modulus at max stress, psi ($\sigma_m/\epsilon_m$) |

Figure 5 shows internal pressure values for a minimum smoke motor stored at Yuma, AZ. With time, the gas generation rate increases as chemical stabilizers in the propellant are consumed. There is a critical level of stabilizer below which the gas generation rate increases exponentially. Until this critical level is reached, stabilizer depletion follows a fairly linear relation with time. Figure 6 shows percent stabilizer loss for minimum smoke motors which have been stored at Yuma, AZ and Fort Greely, AK for 1, 4, and 5 years.[4]

## MATERIAL CHARACTERIZATIONS

As with any empirical analysis, the results of service life evaluation are only as good as the inputs. Therefore, it is vital to have complete and accurate data on all the material properties for the constituent materials in a rocket motor. This includes thermal, chemical, and physical properties for the case material, any liner and/or insulating materials and the solid propellant. Properties are experimentally determined for thermal conductivity, coefficient of thermal expansion, density, Young's modulus, bondline strength, maximum stress and strain, solubility, diffusivity and gas generation as appropriate. Materials are also subjected to accelerated aging in order to develop aging models for critical properties.

Values for the maximum stress obtained for the propellant at various strain rates over a temperature range are shifted according to the time-temperature equivalence principle.[5] Equation (6) is used to apply this principle numerically or the shifting can be done by hand.

$$\text{Log } a_t = \frac{C_1 (T - T_s)}{C_2 (T - T_s)} \qquad (6)$$

where

$a_t$ = reduced time shift function
$C_1$ and $C_2$ = material constants
$T$ = temperature, F
$T_s$ = reference temperature, F

The resulting reduced time plots are then used to obtain critical stress, $\sigma_o$, and beta, $\beta$, parameters required for cumulative damage calculations. Figure 7 shows maximum stress versus reduced time data for minimum smoke motors tested after being stored at Fort Greely, AK for 1 and 4 years.

## SHELF LIFE SURVEILLANCE PROGRAMS

To monitor changes in motors due to time and temperature cycling, long term surveillance programs are established. In these programs, motors are stored at various sites with representative climatic environments. These sites include Yuma, AZ representing a hot, dry climate; Albrook, Panama representing a hot, humid climate; Fort Greely, AK representing an arctic climate; locations in Germany representing actual deployment sites, and Redstone Arsenal, AL representing igloo storage. Periodically, motors stored at these sites are brought to MICOM, RD&E Center for testing. This testing includes both static firing for performance evaluation and dissection for propellant and bondline evaluation. Results from surveillance programs provide real time aging data vital to development and validation of aging models and service life evaluations.

Depending on the propellant type and the associated failure mode, tests conducted on these dissected motors include the following:

(1) Time-Temperature Characterization - Viscoelastic characterization of the propellant provides material property inputs for structural and service life analysis.

(2) Gradient Tests - Radial and longitudinal gradients in mechanical properties of the propellant may be present due to casting flow phenomenon, chemical migration or other causes and must be considered in evaluating possible failure sites and modes.

(3) Joint-in-Tension - A reduced time-temperature characterization is conducted using bond joint specimens from dissected motors to monitor the bondline strength as a function of time in storage and storage location.

(4) Adhesive Fracture Energy - The energy required to promote growth of a crack or debond is determined as a function of age and storage location.

(5) Crosslink Density Test - Crosslink density is determined for the propellant to correlate with changes in mechanical properties with time and temperature cycling.

(6) Nozzle Mechanical Properties - Mechanical properties of the nozzle material are monitored to detect and model any degradation which may adversely affect motor performance.

(7) Motor Case Tests - Hydroproof testing of static fired motor cases validates safety margins. Specialized tests may also be developed for system specific critical, potential failure modes.

(8) Igniter Tests - Pyrotechnics contained in igniters are analyzed chemically to monitor changes in composition which may adversely affect performance. Squib resistance is also measured to insure adequate performance.

(9) Stabilizer Level Determination - The level of stabilizer present in the propellant following the storage time is measured to determine the percent lost during storage.

(10) Gas Generation Rate - The rate of outgassing, or gas generation, is measured for propellant removed from the aged motors in order to monitor any effects from aging.

Data from such tests conducted on dissected motors as well as the baseline material characterizations serve as inputs to the in-house service life codes.

## THERMAL LOAD MODELS

In order to simulate the thermal load histories experienced by surveillance motors during their storage, temperature profiles have been developed for each of the storage sites. These thermal models consist of Fourier series representations fitted to hourly temperature readings from a 10-year period. Igloo storage is represented by the cosine function in Equation (7).

$$T = 64 + 20 \cos\left[\left(\frac{t}{4380} - 1\right)\pi\right] \qquad (7)$$

The in-house computer codes used to evaluate service life calculate ambient temperatures from these models. The effects of solar radiation and wind velocity may also be included depending on the storage scenario being simulated.

## PREDICTIVE MODELING

The results obtained from either SLife or GASLife represent service life evaluations based on mean properties, mechanical or chemical, for one motor. In order to make a predictive service life evaluation for a population of motors it is necessary to adjust these results according to the variability which might be seen in this population. One way is to quantify the variability in quality control data for the population in question and use this correlation to modify the code results.

Statistical analysis of quality control data on 475 propellant mixes for a composite motor led to the following relation.[6]

$$D^* = D\left(\frac{E^* \cdot \sigma}{E \cdot \sigma^*}\right)^{\beta} \qquad (8)$$

where

$D^*$ = cumulative damage for the motor population
$D$ = cumulative damage based on a single motor
$E^*$ = mean modulus from quality control data
$E$ = modulus from the single motor
$\sigma_m^*$ = mean maximum stress from quality control data
$\sigma_m$ = maximum stress from the single motor

The predicted service life for any motor from this population stored at the site considered is then the reciprocal of $D^*$. Table I shows service life estimates for the composite motor based on properties from a single motor and the predictive values adjusted for the mean motor population.[6]

TABLE I. Service Life Predictions For A Composite Motor

| Storage Site | Motor Service Life | Population Service Life |
|---|---|---|
| Alaska | 33 | 45 |
| Arizona | 125 | 172 |
| Igloo | 93 | 128 |

## RESULTS/CONCLUSIONS

The testing and analyses discussed previously have been applied to several Army rocket motors. The resulting service life evaluations have increased the original expected lifetimes of some of these motors. Such service life extensions delay rebuys and thereby lower the cost of maintaining a functional inventory. Table II below lists some of the systems along with their original expected service life, the extended service life expected, and the resulting savings.

TABLE II. Service Life Extensions/Savings

| Systems | Original Service Life | Extended Service Life | Dollar Savings |
|---|---|---|---|
| HAWK | 10 | 15 | 44M |
| | | 20 | undetermined |
| MLRS | 10 | 15 | 750M |
| PATRIOT | 7 | 14 | 24M |

Analyses conducted as part of service life evaluations provide verification of the structural integrity and margins of safety for solid rocket motors. Service life technology facilitates more efficient production planning, improved management of rocket motor inventories, lower costs for stockpile reliability programs and more reliable structural margin predictions. Service life evaluation and its related technologies play a vital role in the development, deployment, and maintenance of the Army's solid rocket motors.

## FUTURE EFFORTS IN SERVICE LIFE

Efforts in the future will be directed toward improving and verifying service life evaluation techniques. This includes both the experimental and analytical aspects. Experimental procedures and specimens may be improved to better simulate loading conditions actually seen in the motor. Analog or subscale tests would also be beneficial in applying and calibrating damage calculations. This is of particular interest in systems which have bondline failure modes since measurement of bondline stresses in the motor configuration are difficult at best.

Other experimental efforts are underway to validate and model the shift in stress-free temperature with time. This phenomenon has been shown to exist in certain propellants and significantly lowers the damage resulting from temperature cycling. Service lives for motors with propellants which exhibit this tendency may far exceed original calculations.

A desirable analytical improvement would be to have the ability to model actual three dimensional geometries found in rocket motors. Solid rocket motors may have rather complicated internal geometries due to things such as stress relief grooves and finocyl bore designs. With the current service life codes equivalent thermal models must be derived for motors with geometries other than a cylindrical bore. Inhomogeneity and anisotropy of material properties are also real world problems which cannot be evaluated with current service life techniques.

The development and implementation of service life evaluation techniques has provided unique and vital benefits to the entire solid rocket motor community. It is, however, a technology area which needs continued research, development, and application to promote growth and evolution.

## REFERENCES


1. Bills, K. W., Jr., et al. "Solid Propellant Cumulative Damage Program," Aerojet General Corporation, Sacramento, CA, RPL-TR-68-131, October 1968.

2. Davis, Louise M. and Patterson, Joel E., "Analysis and Prediction of the MLRS Rocket Motor Service Life," TR-RD-PR-87-3, U.S. Army Missile Command, Redstone Arsenal, AL, May 1987.

3. Martin, D. L., "Service Life Prediction of Smokeless Propellant Motors," TR-RK-75-6, U.S. Army Missile command, Redstone Arsenal, AL, January 1975.

4. Fisher, J. M., "CHAPARRAL Service Life Evaluation," 1988 JANNAF Joint Propulsion Meeting, San Diego, CA, December 1988.

5. Ferry, J. D., "Viscoelastic Properties of Polymers," John Wiley and Sons, New York, NY, 1961.

6. Martin, D. L., "Structural Service Life Analysis for Rocket Motor Grains," TR-RD-PR-86-6, U.S. Army Missile Command, Redstone Arsenal, AL, April 1987.

7. Martin, D. L., and Siron, R. E., "Service Life Prediction of the MLRS Propellant Grain," TR-RK-82-1, U.S. Army Missile Command, Redstone Arsenal, AL, October 1981.

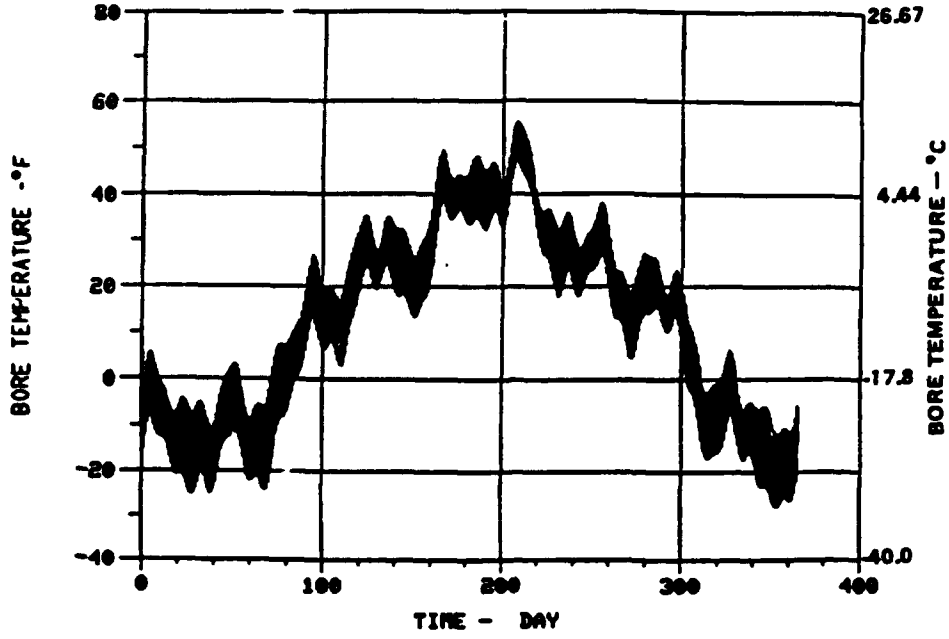


Figure 1. Bore temperature versus time for a composite motor stored at Ft. Greely, AK.

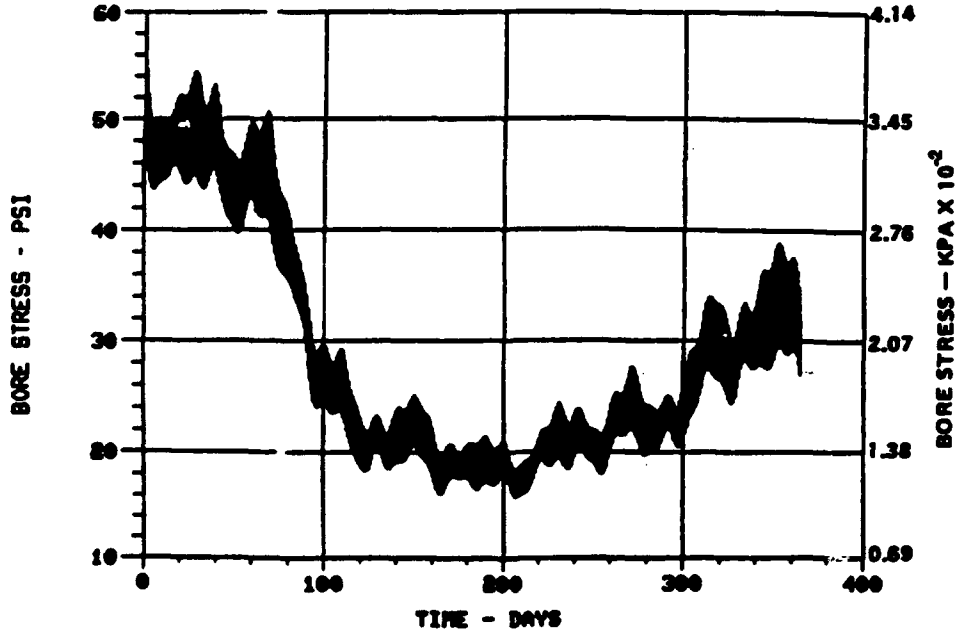


Figure 2. Bore stress versus time for a composite motor motor stored at Ft. Greely, AK.

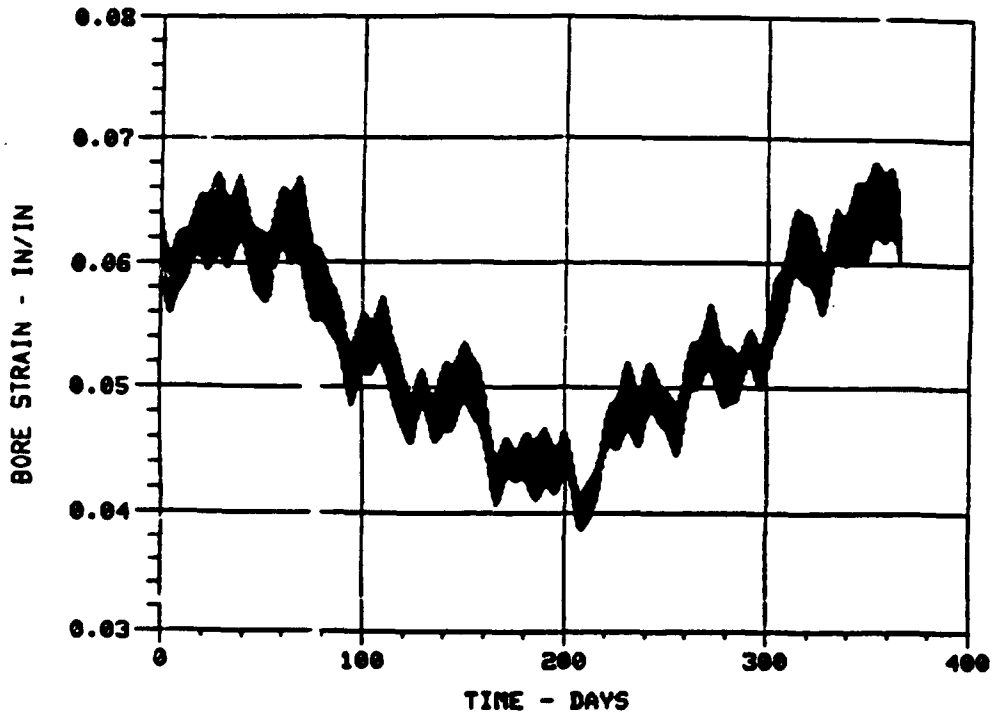


Figure 3. Bore strain versus time for a composite motor stored at Ft. Greely, AK.

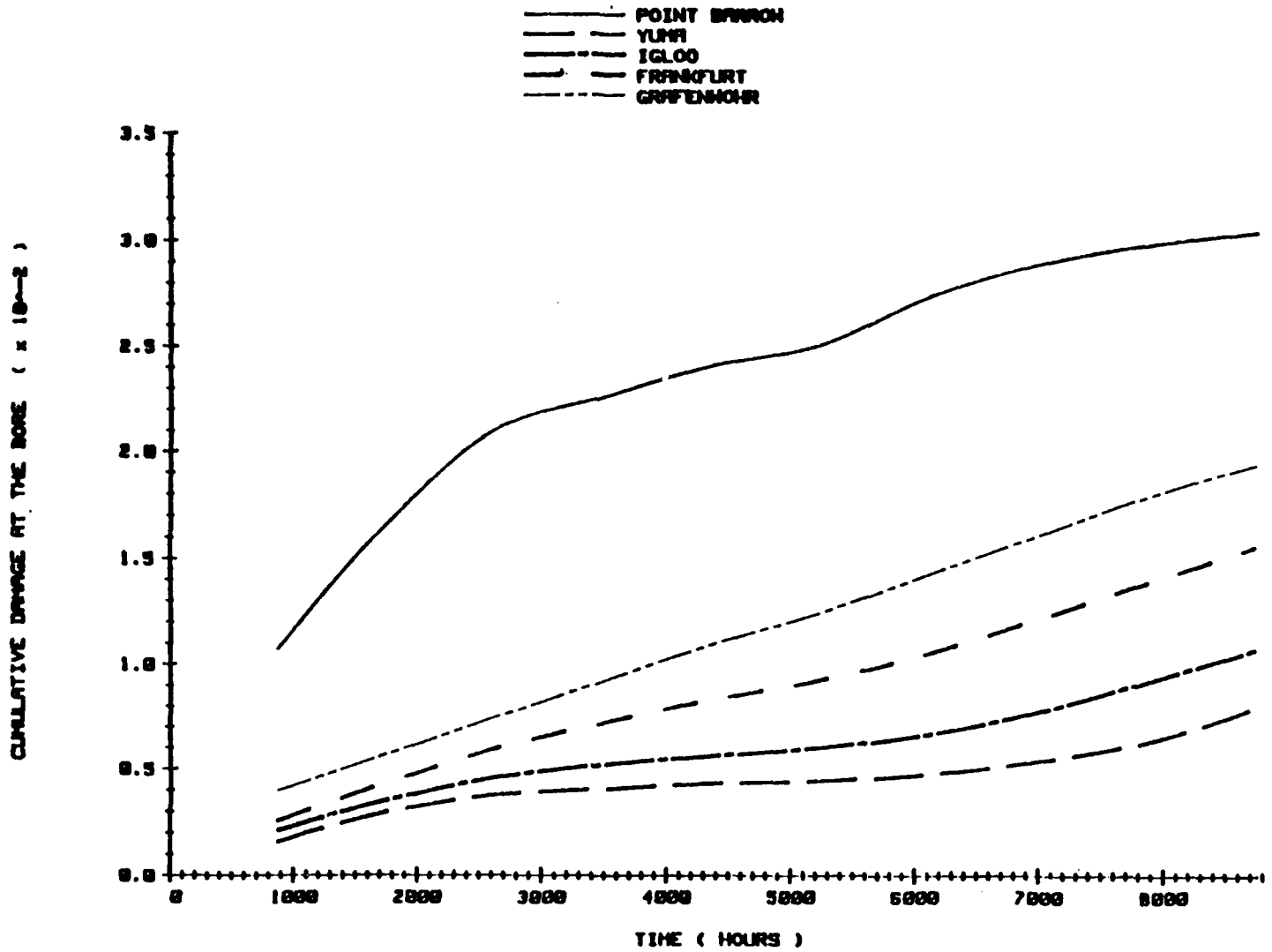


Figure 4. Cumulative damage at bore for a composite motor.

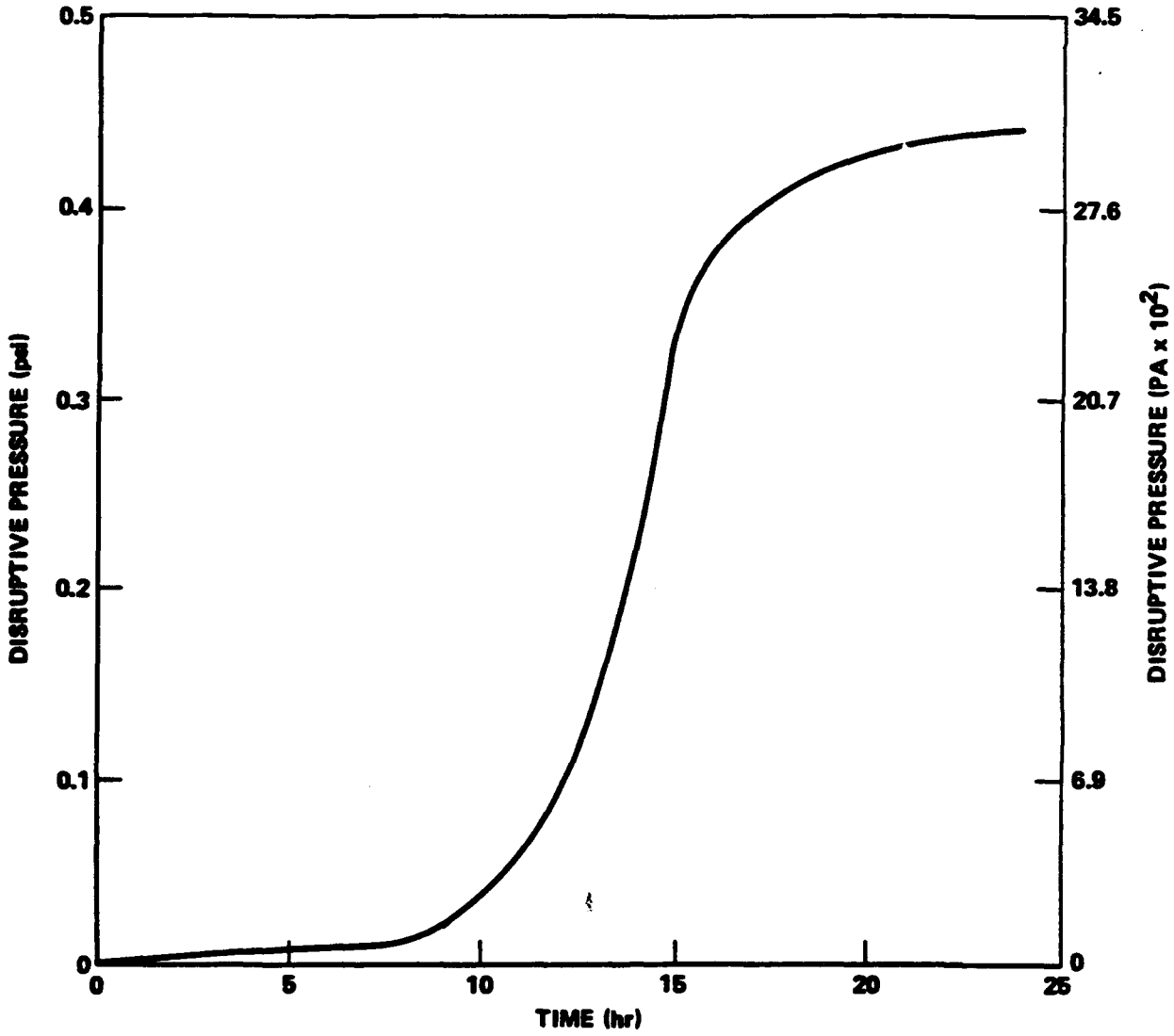


Figure 5. Internal disruptive pressure versus time for a minimum smoke motor stored at Yuma, AZ.

Fig 6. Minimum Smoke Motor–Stabilizer Depletion versus Storage Time

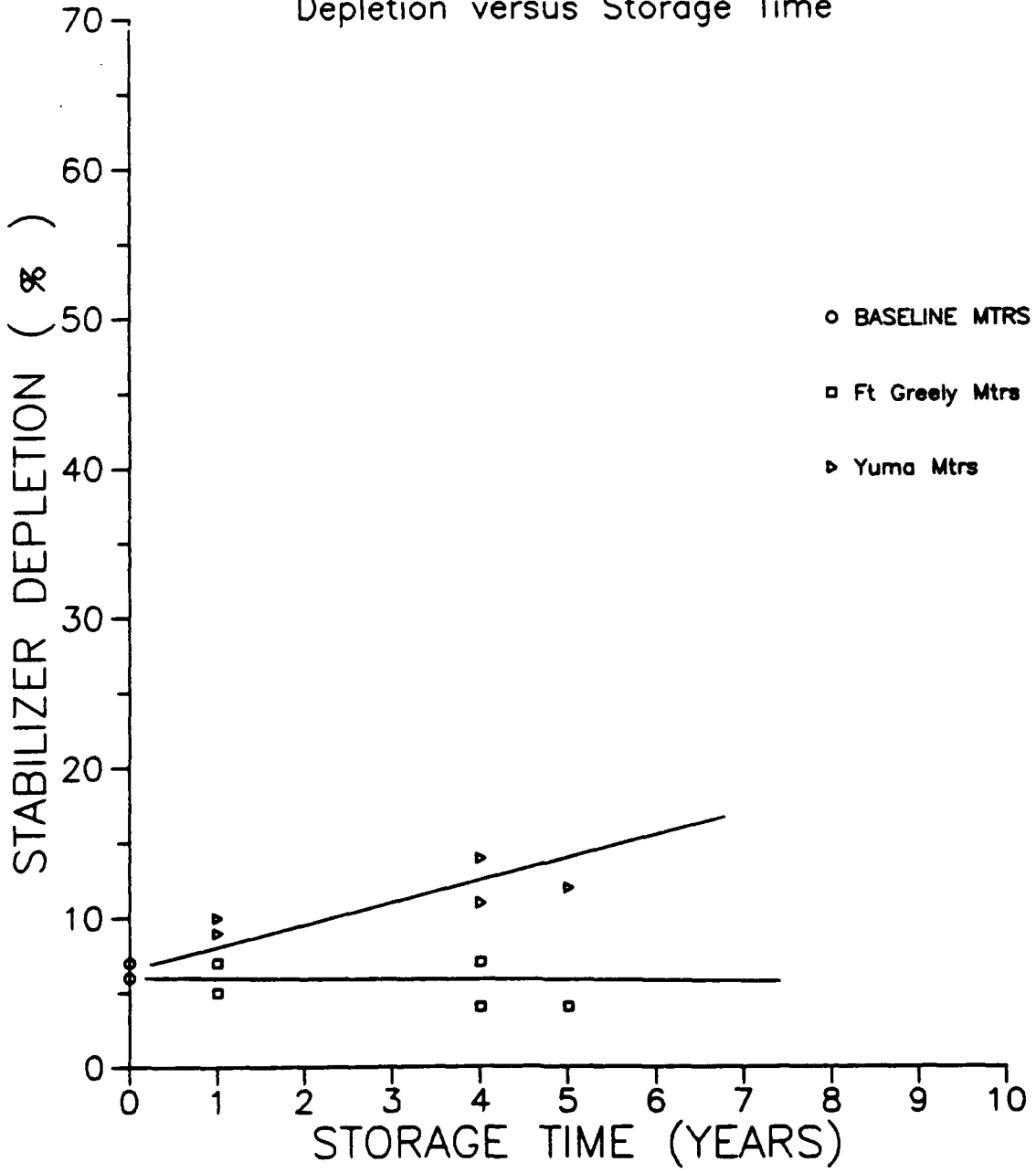


Figure 6. Minimum smoke motor-stabilizer depletion versus storage time.

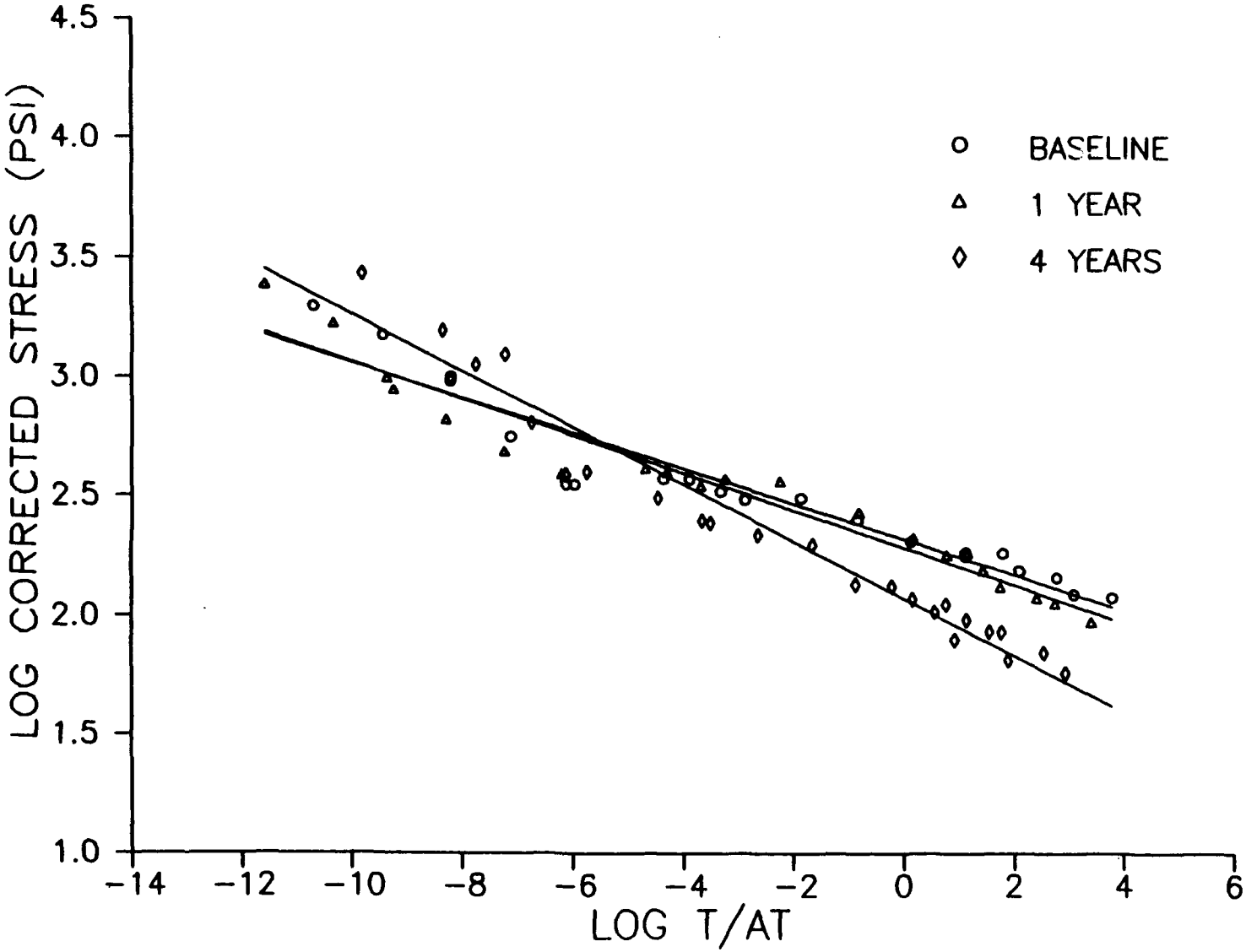


Figure 7. Log corrected stress-vs-log reduced time for motors stored at Ft. Greely, AK.

# BIPROPELLANT GELS (U)

W. M. Chew and B. D. Allan
Propulsion Directorate
U.S. Army Missile Command
Redstone Arsenal, Alabama

## ABSTRACT

This paper discusses the status and current research in gel bipropellant propulsion. Gel propulsion is a novel technology that is a practical alternative to solid or liquid propellant systems. In particular, gels are an attractive solution for systems that require both high performance (high density impulse and/or energy management) and compliance with the Insensitive Munitions Guidelines. Gel propulsion has a similar density impulse to solids, the controllability of liquids, and is safer than either. Gel propulsion is versatile and can be applied to a wide range of applications from low cost fixed thrust systems to advanced systems requiring sophisticated energy management. Gel propellants can be formulated to give a wide variety of performance, signature, and density characteristics. This paper reviews the status and direction of research/development of each subsystem (propellants, pressurization, storage and expulsion, and engine). This review shows that gel propulsion technology is ready for full scale engineering development.

## INTRODUCTION

The Army's propulsion research and development programs are currently working toward three primary goals. First, missile systems currently under development are requiring significant increases in performance. This includes longer range, higher velocity, and the ability to turn on and off, throttle, and/or pulse the propulsion system (energy management). The propulsion systems are also required to be packaged within smaller and lighter envelopes. Secondly, Joint Service Requirements for Insensitive Munitions (JSRIM) requires all DOD munitions to comply with the DOD Mil Std 2105 Insensitive Munitions (IM) Guidelines. Finally, propellants with minimum signature exhaust are desired to prevent identification of the launch site and interference with target acquisition and missile control systems.

At present, no Army missiles can pass all the IM guidelines. State-of-the-art aluminum containing ammonium perchlorate composite solid propellants leave a distinct exhaust trail containing aluminum oxide and hydrogen chloride. They also fail the slow cook-off IM test requirement. Ammonium nitrate propellants are a possible insensitive replacement, especially for minimum signiture propelllants. Ammonium nitrate propellants, however, are significantly less energetic, and a

significant performance penalty is paid for minimum signature IM solid propellants.

Gel propulsion systems are a good solution for future IM Army missiles because it is inherently insensitive and gel propellants can be easily formulated to give high performance and/or minimum signature. The characteristically high Isp of liquids and high density-impulse of solids propulsion can be obtained through by gelling liquid propellants with high energy solids. The Navy has recently demonstrated that a gel propulsion system will pass bullet impact and fast and slow cook-off IM tests. Gel propulsion systems should easily pass the other four tests because the oxidizer and fuel gels are non-detonable, immobilized, and are separate components. Minimum signature is obtained by proper selection of liquid and solid ingredients.

Table 1 lists several key properties of gel propulsion that make this technology attractive. Isp is high because of the liquid propellant components, and the high density Isp is obtained through solids loading. The combination of gel propulsion's IM and density-impulse properties make it ideal for volume limited systems such as ADKEM. Because gels can be throttled and pulsed, they are ideal for applications such as N-LOS, which require energy management, or "smart" missiles that have feedback between the propulsion and guidance and control systems, which dramatically increases the range and kill probability. The advantage of energy management is clearly shown in Table 2.

Gel propellants are immobilized at rest and can move only under shear conditions. Fuel gels and oxidizer gels are hypergolic at the contact surface and will extinguish as the fuel and oxidizer burns away from the interface. Both the monomethyl hydrazine based fuel gel (MICOM gel) and inhibited red fuming nitric acid based oxidizer gel (IRFNA gel) are soluble with water, except for the aluminum in the fuel gel. Accidents or hostile action that results in contact of the two gels, therefore, can be easily extinguished with water flushing and their active components neutralized. This property also makes demiliterization easy.

The motor components of a gel propulsion system are similar to liquid motor components (Figures 1 and 2): a pressurization subsystem that expels gel propellants from a storage/expulsion subsystem into a bipropellant engine. The engine can have a simple fixed thrust injector or a more sophisticated injector with throttling and/or pulsing capability.

Gel propellants are formulated by mixing liquid propellants, a gellant, and generally an energetic, high density solid. The resulting gel has high viscosity and will flow only if a shear force has been applied to overcome the yield point. This property prevents sloshing and ullage changes in center-of-

gravity during in flight that can be a problem with liquid propellants in some types of missiles. Gel propellants become less viscous when increasing shear forces are applied (shear thinning). Gels reduce the high evaporation rate that is typical of liquid oxidizers and fuels, which minimizes toxicity concerns. When a gel is exposed to air, a crust forms that inhibits further evaporation. The high viscosity, yield point, and self sealing properties of gels minimize the hazards caused by tank ruptures. If the rupture occurs, the gel will flow slowly through the rupture; crusting, however, starts immediately and the leak is stopped.

The gelled fuels Alumizine (Air Force), Notsgel (Navy) and MICOM gel (Army), were developed in the 1960's. They are hydrazine/hydrazine derivative gels loaded with aluminum which were hot-fire tested in engines using liquid oxidizers. These programs were drastically reduced in the 1970's because ammonium perchlorate based solid propellants had higher density impulse, the toxicity of the volatile components was of concern, and control of optimum oxidizer/fuel (O/F) flows were difficult due to the difference in rheology between fuel gels and liquid oxidizers. The Army is now actively pursuing gel propellants for four reasons:

1. the desire for propulsion systems with energy management capabilities
2. The development of microelectronics that can maintain feedback between propulsion and guidance and control
3. the requirement for Insensitive Munitions
4. the development of an oxidizer gel that matches the rheological flow properties of the fuel gel under all operating conditions.

During the 1980's subsystems were developed and a successful all up system feasibility demonstration test was conducted. A solid warm gas generator expelled MICOM fuel and IRFNA oxidizer gels from piston tanks into four 1500 lbf engines. The engines were controlled with 2 - 10 msec electronic signals to the servovalves at a slew rate of 1 per 10 msec. This test demonstrated that 8 msec electronic signals results in reproducible full thrust pulses and 2 msec signals results in reproducible pulses of roughly 50% full thrust. The schematic for this system is given in Figure 3.

## DISCUSSION

This section discusses current research/development for each gel subsystem and gel propulsion systems.

## GEL PROPELLANTS

MICOM fuel and IRFNA oxidizer gels pass centrifuge settling tests, environmental vibration tests, and accelerated compatibility tests with aluminum, stainless steel, and several elastomer materials. Together, these tests indicate a gel propulsion life cycle of over 20 years. Gels have been reproducibly manufactured in 130 lbm batches. Properties of MICOM and IRFNA gels are summarized in Tables 3 and 4.

The rheology of MICOM and IRFNA gels have been extensively studied. The viscosity has been measured between -65° and +165° F using a Ferranti-Shirley cone plate, Haake rotating concentric cylinder, and capillary flow viscometers (Figures 4 and 5). The yield points have been determined with cone penetrometers and by extrapolating the viscosity curve to zero shear. The pressure drops produced by different flow rates through an extensive set of geometric flow passages have been determined at ambient temperature. These geometries simulate the flow passages within typical propulsion system hardware such as straight tubes and orifices of different diameters and gradual and sudden expansions and contractions. The difference between viscosities measured by viscometers and straight tube flow tests are significant as shown in Table 5. Engineers, therefore, should use flow data when optimizing engine and propellant flow line designs. As an example of the data from non-tubular geometries, the results from the orifice plate tests are given in Figures 6 and 7. These figures show that 0.2 inch diameter orifices almost cause gel cavitation. Gels can cavitate, and cavitating venturis are used to control gel flow rates during engine hot-fire tests.

One advantage of gel propulsion is that gels of differing composition can be used in the same, or very similar, hardware to tailor the propulsion system to specific requirements. For example, when minimum signature gels were required, carbon was substituted for aluminum in the fuel gel to eliminate smoky aluminum oxide in the exhaust, and lithium nitrate was removed to eliminate smoky lithium oxide. These minimum signature gels have been developed and are awaiting engine testing. Similarly, when a safer replacement for liquid hydrogen was desired for a booster application, two different aluminum loaded RP-1 gels were formulated.

Our current areas of research involve formulating hydrocarbon fuel gels for air breathing applications, interhalogen oxidizer gels for increased Isp, testing of minimum smoke oxidizer and fuel gels, and determining the compatibility of gels with bladder, flow line, and injector materials.

## PRESSURIZATION SYSTEMS

Solid propellant hot and warm (2000° F) gas generators and monopropellant and bipropellant liquid gas generators have been developed and tested to expel gels from storage/expulsion tanks.

Current research in this area is focused on developing cool, on demand gas generators. Solid gas generator development is based around glycidyl azide polymer (GAP), an energetic binder. Other generator concepts include catalytic decomposition of gas mixtures and the use of fuel rich (off optimum) liquid bipropellants. These key improvements will reduce the cost and weight of gel propulsion systems by reducing the quantity of pressurant propellant and allowing the use of elastomer bladders in the expulsion subsystem.

## EXPULSION SYSTEMS

Gel propellants have been expelled from piston and bonded rolling diaphragm (BRD) tanks. The advantages of BRD tanks are that they can be welded to seal the propellants completely and do not require an elastomer to withstand the friction occurring within a piston. An engineering sketch of a tandem BRD tank is given in Figure 8. Elastomers that can be used as bladders have been shown to be compatible with both MICOM fuel and IRFNA oxidizer gels in accelerated aging tests.

Research in this area includes advanced development of BRD tanks with in lighter and smaller subsystems, and development of tanks with elastomeric bladders that will result in inexpensive, light, and small subsystems.

## ENGINES

Several unmodified liquid engines have been used successfully to hot fire gel propellants. Two types of engines, using face shut-off pintle (Figure 9) and impinging stream platelet (Figure 10) injectors, have been designed specifically for gel propellants, fabricated, and hot-fire tested with gels. Both straight and turn-flow nozzles have been used.

Hot fire tests have demonstrated that gel engines are capable of energy management. Several engines have demonstrated throttling, one with a 19:1 throttling range. Other engines demonstrated reproducible pulsing with as short as 2 msec electronic signals. Face shut-off injectors have been turned off for over an hour and re-started with no evidence of plugging.

The impinging stream injectors have faster mixing than face shut-off injectors as evidenced by their shorter $L^*$ of 4 inches vs. 30 inches. Both injectors have demonstrated a $C^*$ combustion efficiency of approximately 98%.

Conventional materials have been successfully used as ablatives and throat materials in gel engines. Graphonol and quartz epoxy ablatives have been used in combustion chambers and quartz and silica epoxies have been used in nozzles. Graphite inserts in face shut-off injector engines have demonstrated minimal throat erosion rates ( Figure 11).

Research in this area is focused on improved designs incorporating state-of-the-art composite materials to increase engine performance and decrease engine size and weight.

SYSTEMS

System studies have been made for various Army and Navy anti-aircraft missiles, close range fire support, and ballistic fire support. These studies predict gels to give similar, if not improved performance to the existing solid propellants. IM and energy management characteristics make gels very attractive. An example of the results from one of these studies is given in Figure 12.

Research in this area includes understanding the interconnections between the various subsystems to optimize system designs and identifying one or more candidate point designs for full scale engineering development.

## CONCLUSIONS

Gel propulsion is a mature technology and a practical alternative to solid and liquid systems. It is versatile and will meet current and future propulsion requirements. Gels are particularly well suited to high performance systems requiring IM compliance and energy management.

The Propulsion Directorate has an active program that is aimed at developing low cost, low weight gel propulsion systems with long shelf-lives.

REFERENCES

Allan, B. D., "Development and Testing of MICOM Gel," RD-TR-71-11, U.S. Army Missile Command, June 1971.

Allan, B. D., "A Gelled Oxidizer for Tactical Missiles," presented at U.S. Army Science Conference, June 1982.

Allan, B. D., "Thixotropic Gels for Tactical Missiles," JANNAF Propulsion Meeting, February 1983.

Gould, R. A., "Full Scale Hazard Testing of Gelled Liquid Propellants for the Insensitive Munitions Advanced Development Program," NWC TP 7060, Naval Weapons Center, China Lake, CA,; April, 1990.

Giola, G.P., Chew, W. M., Ryder, D. D., "Propulsion Systems Hazards Evaluation and Liquid/Gel Propulsion Component Development Program," TR-CR-RD-PR-90-1, Final Report by TRW Inc, December, 1989.

Smith, A. L., and Anderson, R. E., "Propulsion System Hazard Evaluation and Liquid/Gel Propulsion Component Development," TR-CR-RD-PR-90-2, Final Report by Aerojet TechSystems, January, 1990.

Chew, W. M., Denson, J. R., and Jones, J. F., "Metallized Hydrocarbon Gel Propellant," JANNAF Propellant Development and Characterization Subcommittee Meeting, CPIA Publication No. 527, 67 (1990).

Schaplowsky, R. K., Anderson, R. E., Cabeal, J. A., and VanderWall, E. M., "Characterization of Gelled RP-1 Containing Aluminum," JANNAF Propellant Development and Characterization Subcommittee Meeting, CPIA Publication No. 527, 77 (1990).

TABLE 1. ADVANTAGES OF GEL PROPULSION

HIGH PERFORMANCE

- HIGH Isp - >300 lbf·sec/lbm
- HIGH DENSITY Isp - >495 lbf·sec·g/lbm·$cm^3$
- CAPABLE OF MULTIPLE STARTS
- CAPABLE OF THROTTLING - 19:1 Demonstrated
- CAPABLE OF PULSING - 2 msec demonstrated minimum reproducible pulse width

SAFE

- COMPLIES WITH IM GUIDELINES
- GELS ARE INSENSITIVE TO SHOCK, FRICTION, AND ESD
- GELS ARE SELF SEALING
- GELS HAVE LOWER EVAPORATION RATES THAN LIQUID PROPELLANTS
- FUEL AND OXIDIZER GELS ARE NON EXPLOSIVE ON CONTACT

VERSATILE

- HARDWARE AVAILABLE FROM SIMPLE FIXED THRUST TO SOPHISTICATED ENERGY MANAGEMENT SYSTEMS
- GELS PROPELLANTS CAN BE FORMULATED FOR SPECIFIC MISSIONS SUCH AS HIGH VELOCITY, LONG RANGE, AND MINIMUM SIGNATURE

EASILY HANDLED

- HAS >20 YEAR SHELF LIFE
- RHEOLOGICALLY MATCHED TO MAINTAIN OPTIMUM O/F RATIO OVER ENTIRE TEMPERATURE RANGE
- GELS HAVE REDUCED SLOSH
- ARE EASILY PUMPED

TABLE 2. RANGE IMPROVEMENTS USING MICOM/IRFNA GEL FOR THE LANCE MISSILE SYSTEM

| Propellants | Range, % of Baseline |
|---|---|
| UDMH/IRFNA Baseline | 100 |
| MICOM gel/IRFNA gel | 200 |
| UDMH/IRFNA (new guidance & control) | 235 |
| MICOM gel/IRFNA gel (new guidance & control) | 375 |

TABLE 3. PROPERTIES OF MICOM FUEL GEL

Composition (Wt%)

| | |
|---|---|
| Aluminum | Approximately 60 |
| Monomethyl Hydrazine | Approximately 38 |
| Gellant/Stabilizer | Approximately 2 |

Density (g/cc)

| | |
|---|---|
| 135° F | 1.39 |
| 77° F | 1.49 |
| -40° F | 1.55 |

Freezing Point -65° F

Accelerated Settling

No settling after 30 minutes at 500 g acceleration

Sensitivity

Shock and compression - negative
Auto decomposition - exotherm at 380° F

TABLE 4. PROPERTIES OF IRFNA OXIDIZER GEL

Composition (Wt%)

| | |
|---|---|
| Lithium Nitrate | Approximately 30 |
| IRFNA | Approximately 65 |
| Gellant | Approximately 5 |

Density (g/cc at 77° F)

| | |
|---|---|
| 20% $LiNO_3$ | 1.71 |
| 30% $LiNO_3$ | 1.78 |
| 40% $LiNO_3$ | 1.85 |

Freezing Point <- 65 °F

Accelerated Settling

No settling after 30 minutes at 500 g

Vapor Pressure, Long Term Storage, Sensitivity

Same as IRFNA

TABLE 5 DIFFERENCES BETWEEN MICOM AND IRFNA GEL VISCOSITIES (POISE = g/cm·s) DETERMINED BY CAPILLARY FLOW VISCOMETER AND STRAIGHT TUBE FLOW MEASUREMENTS AT AMBIENT TEMPERATURE

| SHEAR RATE ($sec^{-1}$) | VISCOMETER | | STRAIGHT TUBE | |
|---|---|---|---|---|
| | MICOM | IRFNA | MICOM | IRFNA |
| $10^4$ | 1.5 | 0.37 | 13.2 | 11.7 |
| $10^5$ | 0.63 | 0.24 | 2.7 | 4.3 |
| $10^6$ | 0.54 | 0.22 | 0.55 | 1.61 |

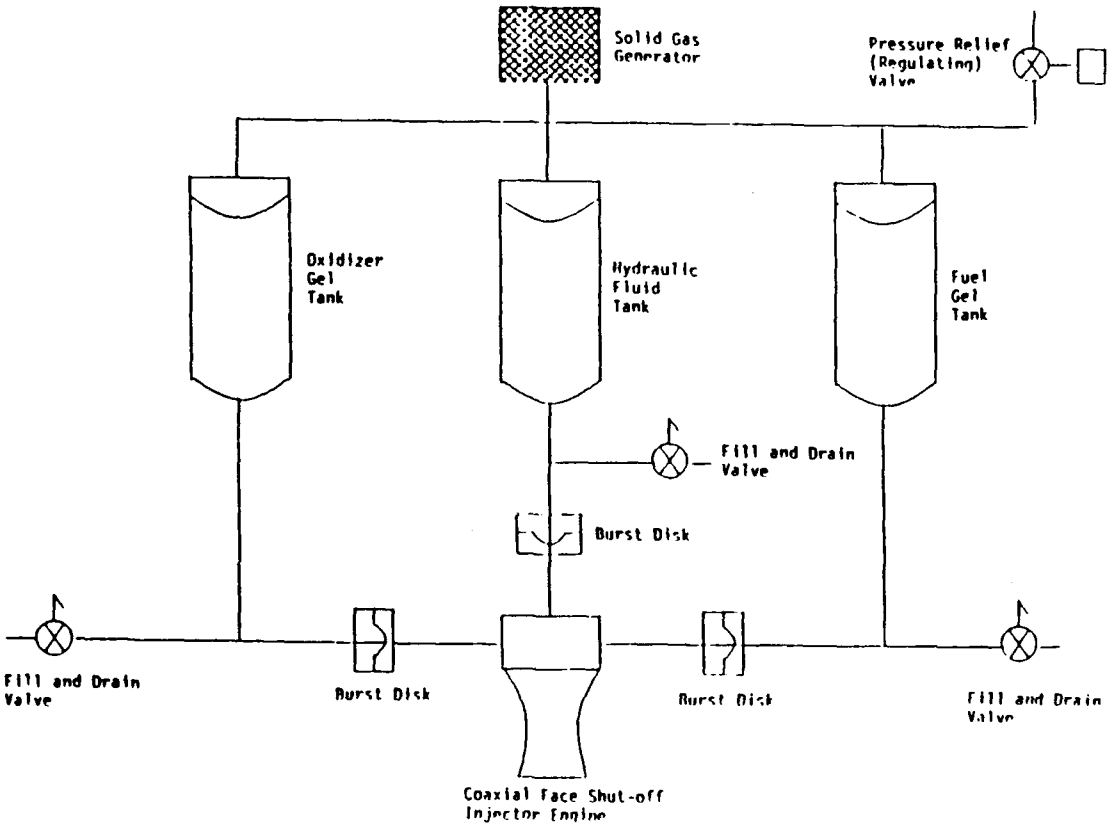


Figure 1. Schematic diagram of a typical gel propulsion system with energy management capability.

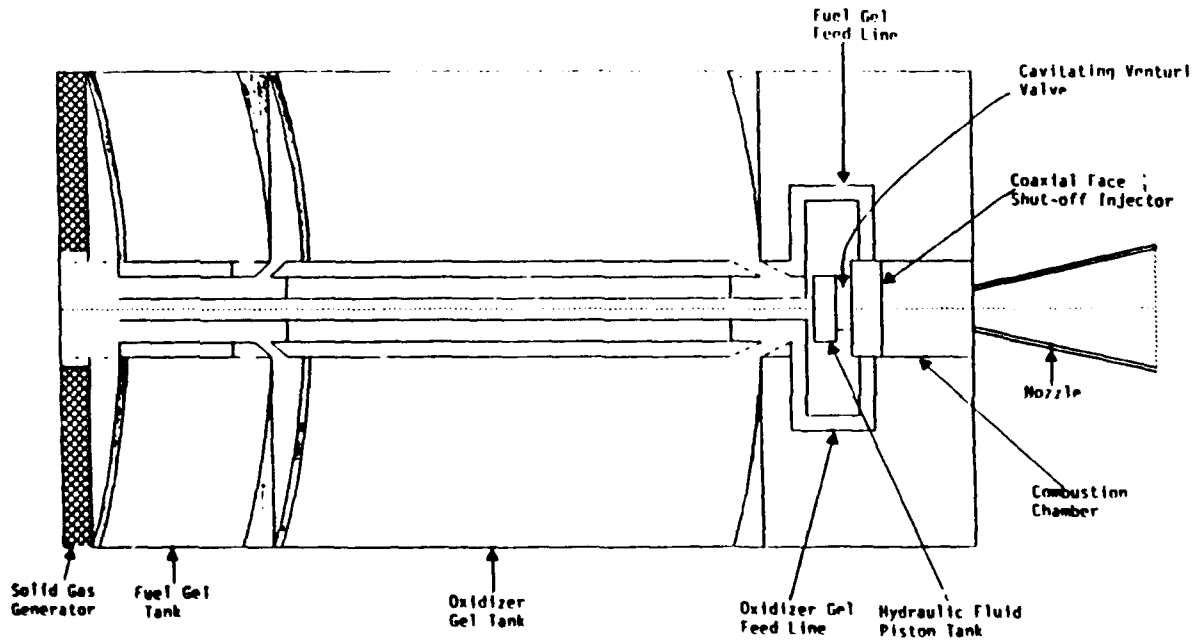


Figure 2. Conceptual engineering sketch of a typical gel propulsion system showing how the subsystems can be integrated into a flight motor.

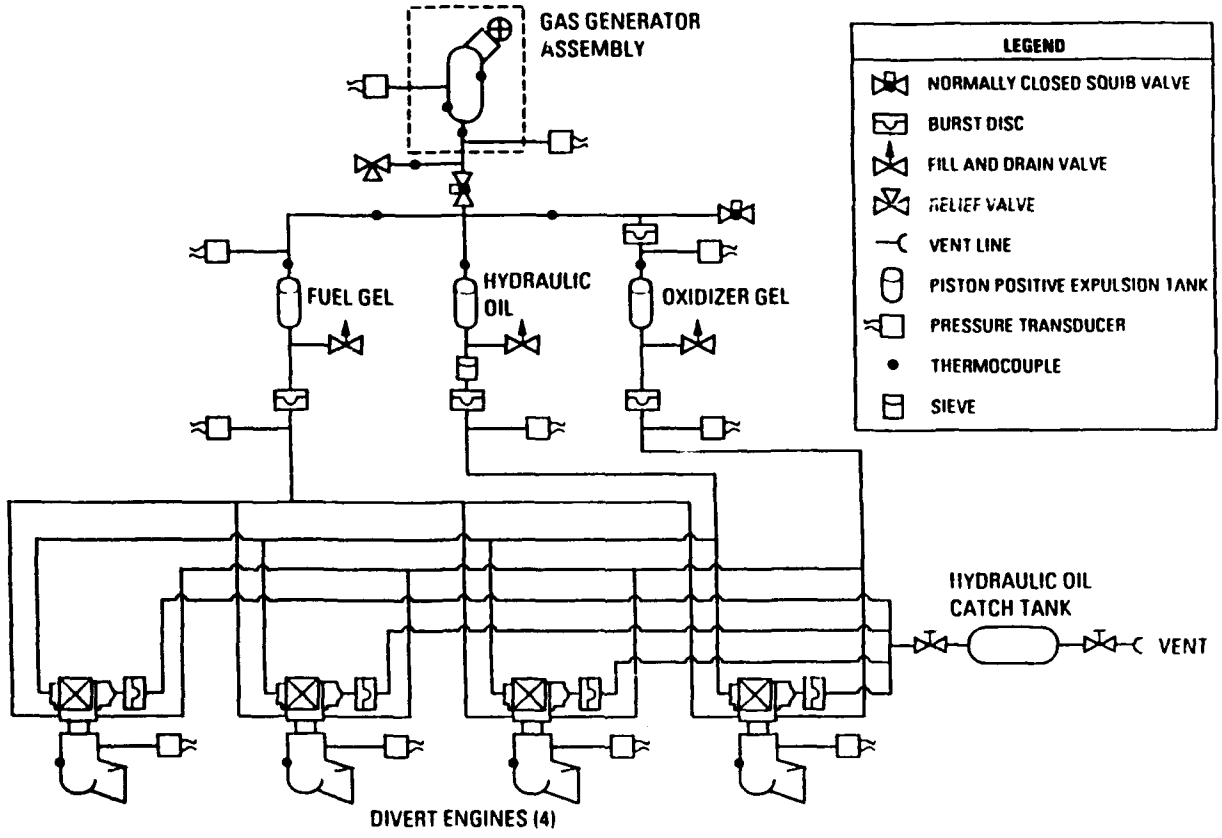


Figure 3. Schematic diagram of the ACES-X system that demonstrated reproducible 2 msec pulsing.

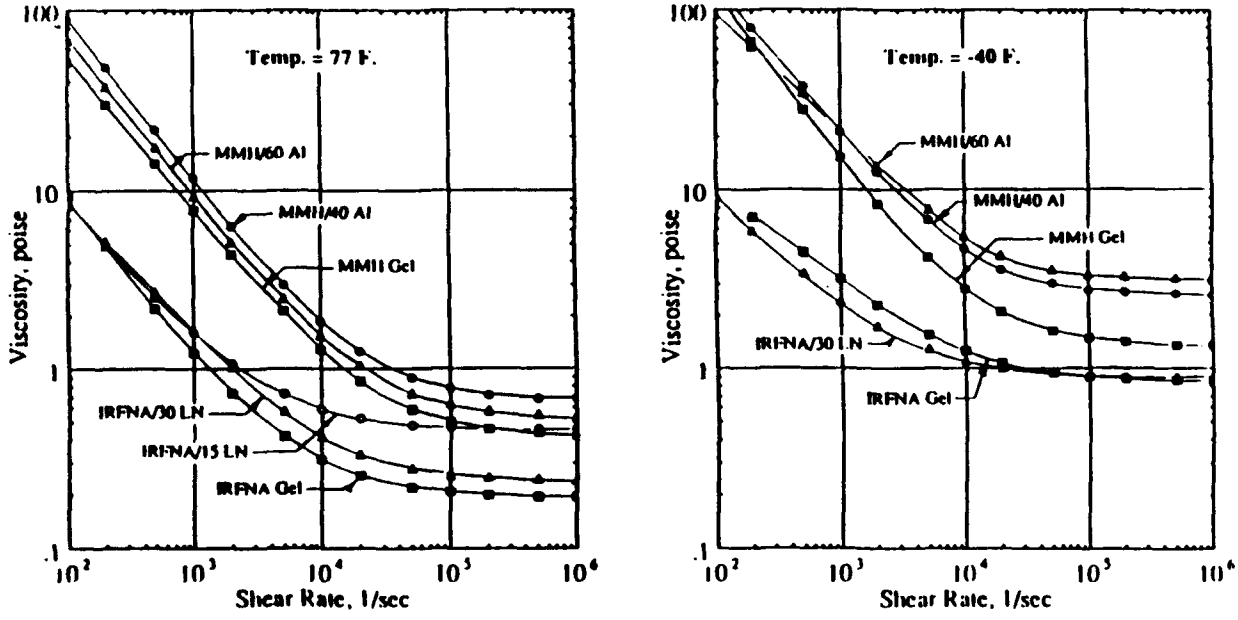


Figure 4. Shear thinning property of MICOM and IRFNA gels. This Figure shows the decrease of gel viscosities with shear rate measured with a capillary flow viscometer. The variation of viscosity with per cent loading of aluminium (Al) and lithium nitrate (LN) is also shown.

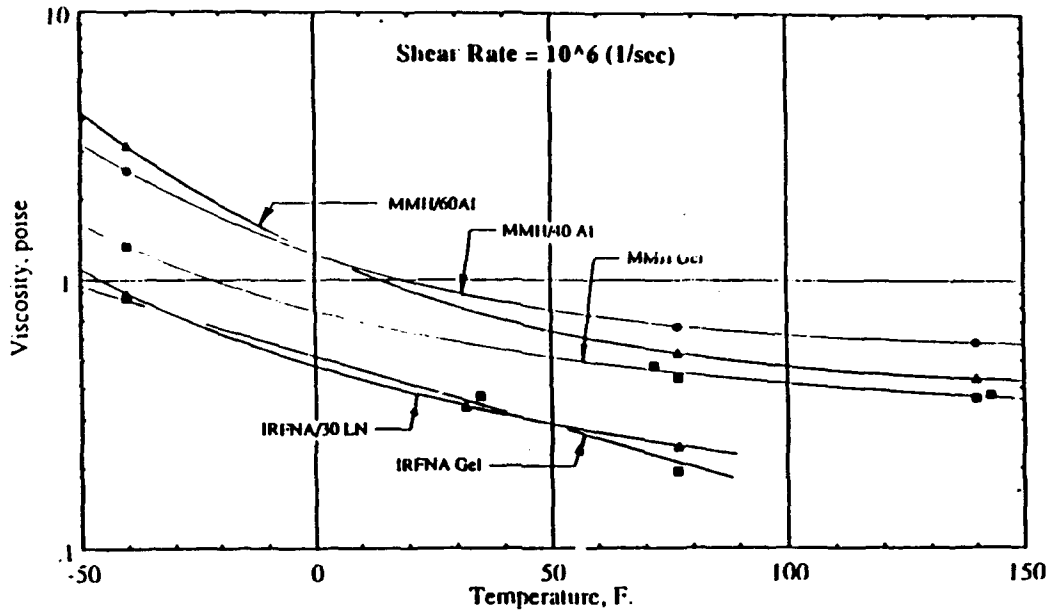


Figure 5. Temperature dependence of MICOM and IRFNA gels showing the decrease of viscosity with increasing temperature measured with a capillary flow viscometer. The variation of viscosity with per cent loading of aluminum (Al) and lithium nitrate (LN) is also shown.

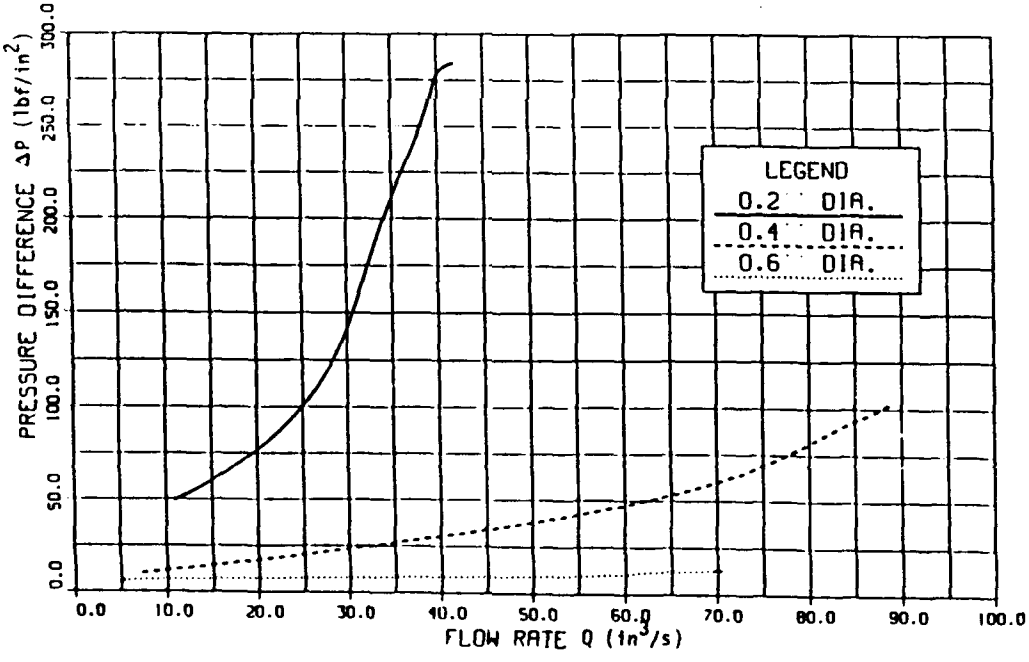


Figure 6. The effect of orifices on MICOM gel flow properties showing increasing pressure drop with decreasing orifice diameter. Note that the 0.2 inch diameter orifice almost produces cavitation.

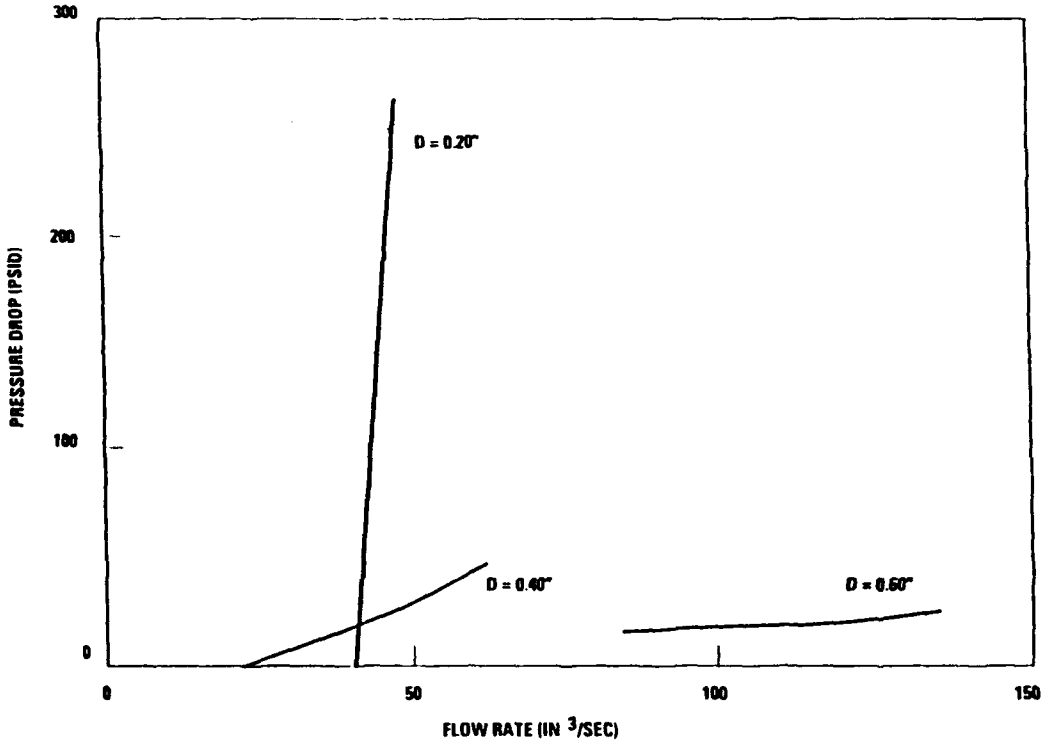


Figure 7. The effect of orifices on IRFNA gel flow properties showing increasing pressure drop with decreasing orifice diameter. Note that the 0.2 inch diameter orifice almost produces cavitation. Comparison of this Figure with Figure 6 confirms that the rheology of the fuel and oxidizer gels are matched for flow through orifices.

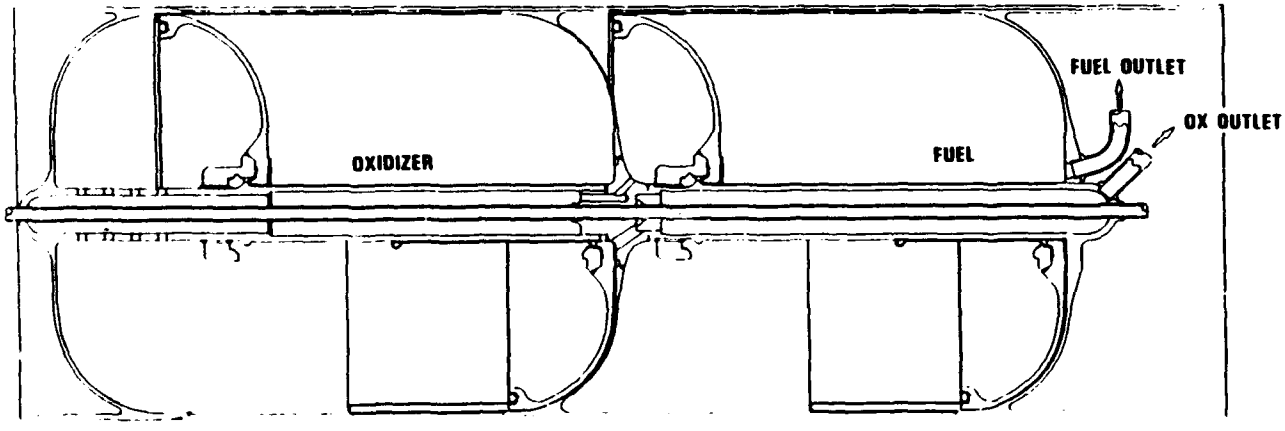


Figure 8. Engineering sketch of a tandem bonded rolling diaphragm tank showing the position of the piston before (above center line) and after (below center line) expulsion.

**Baseline Gel Hot-Fire Tests Engine Design**
**1100 $lb_f$ Thrust Rating**

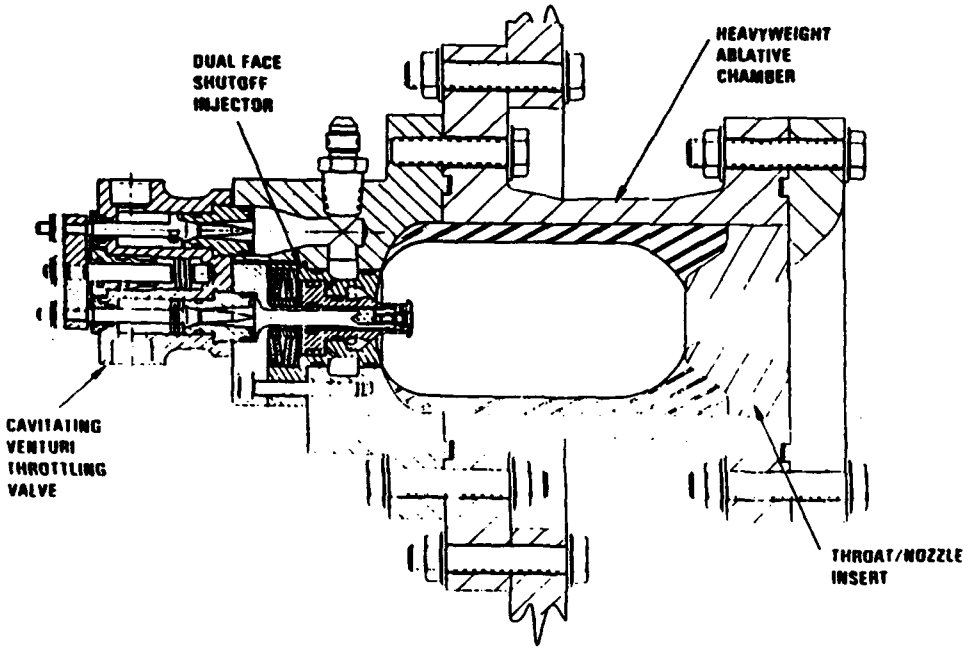


Figure 9. Engineering sketch of a gel engine developed by TRW Inc. with a face shut off injector and a throttling valve.

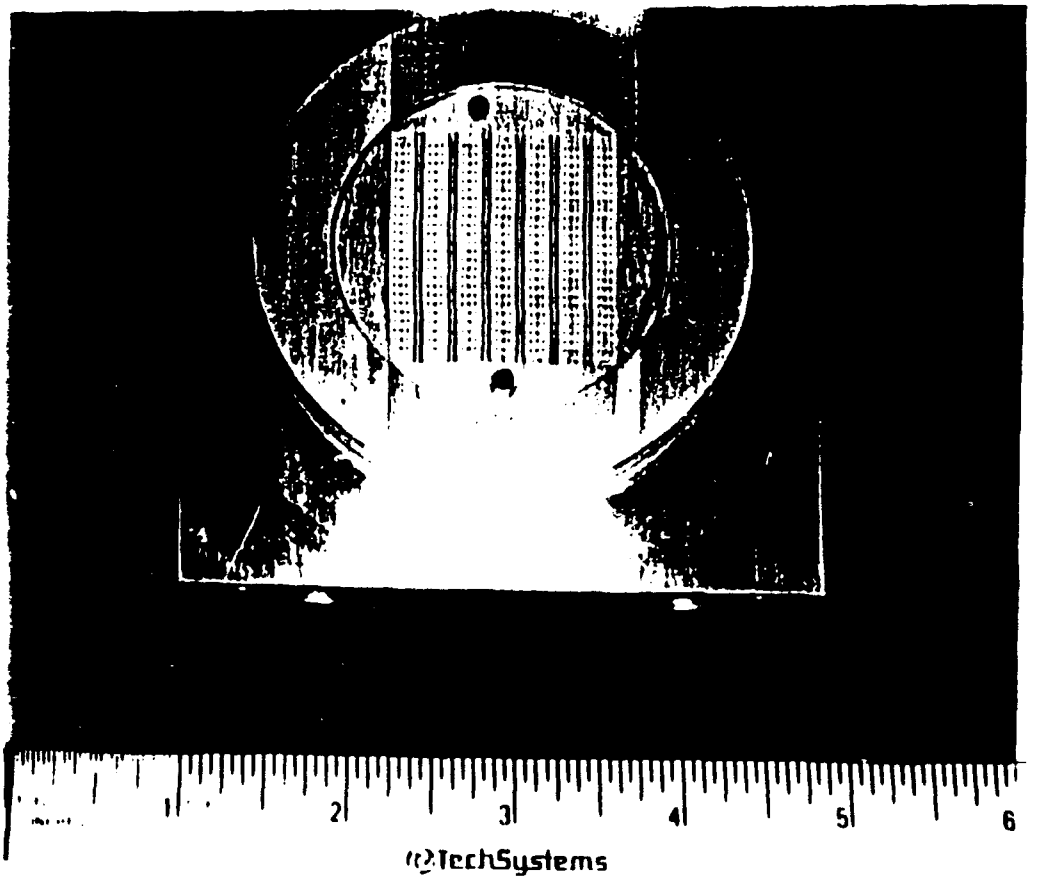


Figure 10. Photograph of an impinging stream platelet injector from a gel engine developed by Aerojet TechSystems.

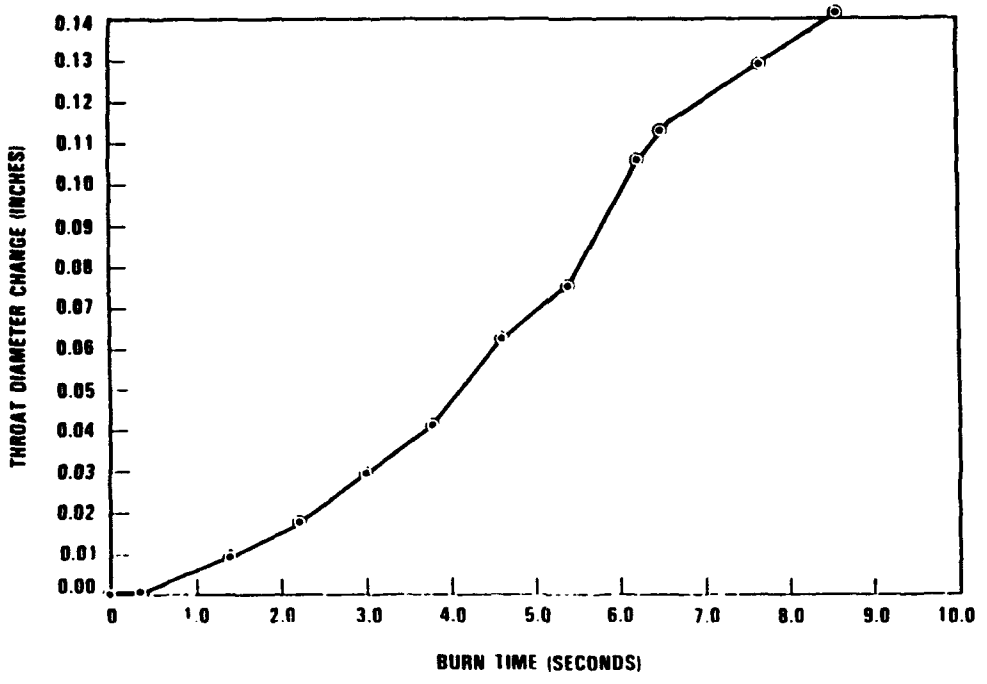


Figure 11. Demonstration of minimal throat erosion rate (0.0098 in/sec) during a 1500 lbf thrust engine test with MICOM and IRFNA gel propellants.

| Parameter | PATRIOT/Solid | PATRIOT/Gel* |
|---|---|---|
| Fuel/oxidizer composition | HTPB | MICOM Gel/IRFNA Gel |
| Mass of fuel/oxidizer | 1098 $lb_m$ | 1184 $lb_m$ |
| Total impulse | 100 | 116 |
| Maximum thrust | 25,400 $lb_f$ | 26,080 $lb_f$ |
| Specific impulse | 100 | 105 |
| Throttling range | N/A | 65 – 100% |
| Chamber pressure | 1500 psia | 2200 psia |
| Time-of-flight | 100 | 127 |
| Intercept velocity | 2297 ft/sec | 3937 ft/sec |
| Range | 100 | 125 |

*Due to performance classification, gel system performance increase over solid system performance is shown as percentage increase

Figure 12. System study results obtained by TRW Inc., showing the advantage of gel propulsion over solid propulsion for the Patriot missile.